

The background of the cover is a dark, textured image of microfossils, likely foraminifera, in shades of blue and grey. Overlaid on this is a circular map of Antarctica in a light blue color, centered on the South Pole. The map includes a grid of latitude and longitude lines. A solid blue vertical bar is on the left side of the cover.

Exploring the use of organic biotic remains for reconstructing Antarctic cryosphere variability

Sea ice dwellers as storytellers

Julian Hartman

Exploring the use of organic biotic remains for reconstructing Antarctic cryosphere variability

Sea ice dwellers as storytellers

Utrecht Studies in Earth Sciences 290

ISBN: 978-90-6266-661-4

ISSN: 2211-4335

USES No.: 290

Cover design by: Margot Stoete

This research was carried out at Utrecht University and financially supported by NWO
Netherlands Polar Program project number 866.10.110

Copyright © 2023 Julian Hartman

All rights reserved. No part of this publication may be reproduced in any form, by print or
photo print, microfilm or any other means, without written permission by the publishers.

This thesis was printed in the Netherlands by Proefschriftmaken.nl

Exploring the use of organic biotic remains for reconstructing Antarctic cryosphere variability

Sea ice dwellers as storytellers

Verkenning van het gebruik van organische biotische overblijfselen voor het reconstrueren van de variabiliteit van de Antarctische cryosfeer
(met een samenvatting in het Nederlands)

Proefschrift

ter verkrijging van de graad van doctor aan de Universiteit Utrecht op gezag van de rector magnificus, prof. dr. H.R.B.M. Kummeling, ingevolge het besluit van het college voor promoties in het openbaar te verdedigen op

vrijdag 29 september 2023 des middags te 2:15 uur

door

Julian Diede Hartman
geboren op 20 juni 1988 te Hilversum

Promotores

Promotor	–	Prof. dr. Henk Brinkhuis	–	Utrecht University
Co-promotor	–	Dr. Francesca Sangiorgi	–	Utrecht University
Co-promotor	–	Dr. Peter K. Bijl	–	Utrecht University

Members of the dissertation committee

Prof. dr. Carlota Escutia	–	Instituto Andaluz de Ciencias de la Tierra, Universidad de Granada, Granada, Spain
Prof. dr. Amy Leventer	–	Colgate University, Hamilton, New York, USA
Prof. dr. Lucas Lourens	–	Utrecht University, Utrecht, The Netherlands
Dr. Fabienne Marret-Davies	–	University of Liverpool, Liverpool, UK
Prof. dr. ir. Stefan Schouten	–	Utrecht University, Utrecht, The Netherlands & Royal Netherlands Institute for Sea Research, 't Horntje, The Netherlands

Contents

Chapter 1. General introduction	7
Chapter 2. A review of the ecological affinities of marine organic microfossils from a Holocene record offshore of Adélie Land (East Antarctica) <i>J.D. Hartman, P.K. Bijl, F. Sangiorgi</i> (published in Journal of Micropalaeontology)	31
Chapter 3. <i>Nucicla umbiliphora</i> gen. et sp. nov.: a Quaternary peridinioid dinoflagellate cyst from the Antarctic margin <i>J.D. Hartman, F. Sangiorgi, P.K. Bijl, G.J.M. Versteegh</i> (published in Palynology)	101
Chapter 4. Holocene paleoenvironment and paleoclimate at the Adélie Basin (East Antarctica): the marine palynological signature in the IODP Site U1357 record <i>J.D. Hartman, P.K. Bijl, H. Brinkhuis, S. Schouten, F. Sangiorgi</i>	117
Chapter 5. Sea-ice, primary productivity and ocean temperatures at the Antarctic marginal zone during late Pleistocene <i>J.D. Hartman, F. Sangiorgi, M.A. Barcena, F. Tateo, F. Giglio, S. Albertazzi, F. Trincardi, P.K. Bijl, L. Langone, A. Asiola</i> (published in Quaternary Science Reviews)	173
Chapter 6. Paleoceanography and ice sheet variability offshore Wilkes Land, Antarctica - Insights from Oligocene-Miocene TEX86-based sea surface temperature reconstructions <i>J.D. Hartman, F. Sangiorgi, A. Salabarnada, F. Peterse, A.J.P. Houben, S. Schouten, H. Brinkhuis, C. Escutia, P.K. Bijl</i> (published in Climate of the Past)	249
References	285
Nederlandse samenvatting	343
Dankwoord (Acknowledgements)	347
Short curriculum vitae	351

Chapter 1

General introduction

1 Research context

Global warming resulting from the increase in greenhouse gas emissions since the beginning of the industrial era is affecting life on Earth. Compared to average atmospheric temperature during 1850-1900, global surface temperature on Earth increased 1.1°C (2011-2020) and it is projected for the year 2100 that the policies that have been implemented so far will result in an increase of 2.5 to 4°C, causing loss of biodiversity, more extreme weather events and a rise in global sea level of about 70 cm (IPCC AR6 Synthesis report, 2023). These changes will increase the risk of water and food scarcity, infrastructural damage, and loss of habitable areas, particularly in coastal areas due to sea level rise. To assess how climate warming through increased greenhouse gas emissions will affect the globe, an understanding of the Earth's systems (biosphere, hydrosphere, geosphere, atmosphere, and cryosphere) and how these systems interact with each other is essential. The cryosphere, that is all land-based ice and sea ice, is mostly situated in the polar regions.

In these polar regions primary productivity and therefore marine life in general is governed by the seasonal insolation changes and concomitant waxing and waning of sea ice. The ice in the polar regions is not only affected by atmospheric warming, but also, and even mainly by warming of the ocean waters. This has already resulted in a reduction of Arctic sea ice with important implications for the Earth's albedo, sea ice-dependent ecosystems, burial of organic carbon, and ocean current dynamics (e.g., Post et al., 2013). At the beginning of 2014, when this PhD research started, the implications of climate warming around Antarctica were much less understood. The IPCC AR5 report that had been published in 2013 has '*change of many characteristics of Antarctic sea ice*' and '*mass loss from glaciers from the Antarctic and the observational record of ice-ocean interactions*' listed as two of the key uncertainties in observation of changes in the climate system. It is, however, expected that a reduction of sea ice around Antarctica will have even greater implications on the global climate system in comparison to the Arctic, considering that Southern Ocean primary productivity accounts for 5% of the global primary productivity (Arrigo et al., 2008) and is responsible for on average 4%, but seasonally up to 25% of the uptake of atmospheric CO₂ (Takahashi et al., 2002, 2009). However, while sea ice concentrations in the Arctic are declining (Comiso and Nishio, 2008; Kay et al., 2011; Notz and Marotzke, 2012), sea ice concentrations around Antarctica show a minor increasing trend on average, although with strong local differences (Comiso and Nishio, 2008; Turner et al., 2009; Parkinson and Cavalieri, 2012; Parkinson, 2019). It is worth noting that the sea ice extent around Antarctica reached a record low in February 2023 (article by Gautier, 2023, National Snow and Ice Data Center). Numerical models have difficulties modeling the trends in sea ice concentration observed around Antarctica, as

ice-ocean interactions are not well incorporated, which makes future Antarctic sea-ice projections highly uncertain (Arzel et al., 2006; Bracegirdle et al., 2008; Bintanja et al., 2015). Furthermore, the sensitivity of the Antarctic land-based ice to warming is not clearly understood as sea level reconstructions suggest fluctuations of 20 meter or more have occurred over the past 25 million years within 1-thousand-to-1-million-year timespans, but ice sheet models have difficulties modeling such a dynamic Antarctic ice sheet. However, in more recent years, incorporation of complex processes in response to warming, such as hydrofracturing and cliff failure (see Figure 1), into numerical ice sheet models show that the Antarctic ice sheet can be more vulnerable to warming than was previously thought (Pollard et al., 2015). In addition, warming of the Southern Ocean could potentially result in the collapse of Antarctic land-based ice, since today much of the Antarctic ice sheet is grounded below sea level (Smith et al., 2019; Colleoni et al., 2022). Intrusion of warmer waters below the ice shelves will melt the ice sheet from below, destabilizing the grounding of these ice sheets and subsequently causing them to collapse (see Figure 1). This would result in a global sea level rise. Notably, one third of Antarctica's ice sheet – equivalent to up to 20 meter sea level rise – sits below sea level and is vulnerable to collapse from ocean heating (DeConto and Pollard, 2016).

One avenue of research that may provide clues to sea ice dynamics under warmer climatic conditions is to turn to periods in Earth's geological past that have experienced warming. Detailed analysis of these ancient records may provide better understanding of how warming of the ocean waters may affect the stability of the Antarctic ice sheet, and surface water conditions around Antarctica in general.

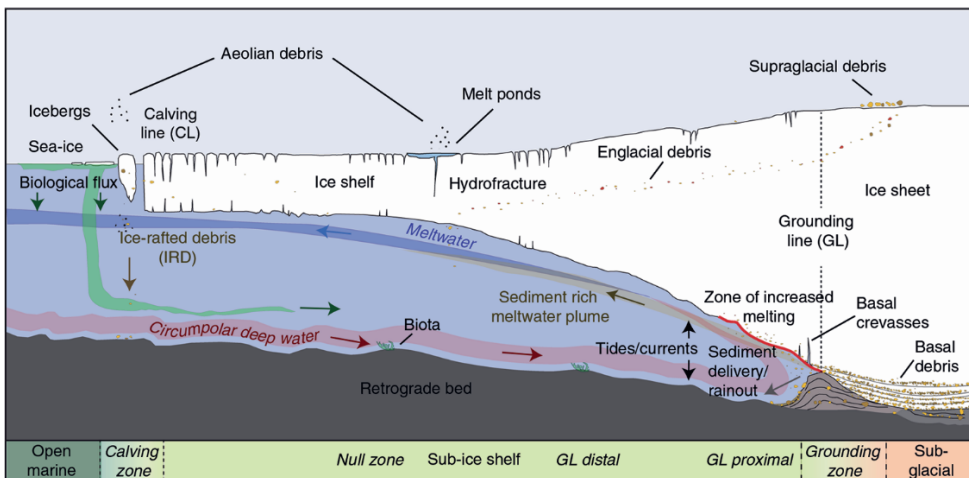


Figure 1: Simplified view of an Antarctic ice shelf and ice sheet resting on a retrograde bed and being influenced by warm ocean waters from below (figure obtained from Smith et al., 2019).

2 Sedimentary archives and proxies

Because environmental conditions of (sea-ice covered) ocean surface waters in the past cannot be measured directly, we must rely on indirect inferences, so-called proxies, based on (present-day) relations and/or correlations between the (modern) environmental parameters and what is deposited as sediments on the ocean floor, typically recovered by scientific ocean drilling. Lithogenic and biogenic particles are the major constituents of sediments around Antarctica. The specific Antarctic environmental conditions of the surface water such as extremely varying temperature, salinity, availability of light and availability of nutrients are home for very specific types and species of microscopic plankton. Many of these produce an outer wall made of carbonate, such as foraminifers and coccolithophores, or biosilica, as diatoms and radiolarians do, or types of resistant organic material, produced by e.g., dinoflagellates, tintinnids (zooplankton) and various prasinophytes (green algae). Remains of these organisms, either morphologically recognizable or molecular, will eventually sink to the ocean floor and form part of the sediments. However, due to various processes taking place in the water column, such as dissolution, scavenging by predators, and transport by ocean currents, what is eventually buried on the ocean floor is often only a fraction of what is produced in surface waters. Nevertheless, correlations between microplankton remains (microfossils) in ocean floor surface sediments and/or their chemical composition and surface water environmental parameters have been demonstrated (e.g., Lear et al., 2000; Armand et al., 2005; Crosta et al., 2005b; Prebble et al., 2013; Zonneveld et al., 2013; Marret et al., 2020) and successfully applied to reconstruct past surface water conditions from sedimentary records, also in the Southern Ocean (Gersonde et al., 2003; Crosta et al., 2008; Bijl et al., 2011; Sluijs et al., 2011; Bohaty et al., 2012; Houben et al., 2013; Riesselman and Dunbar, 2013).

Typically, however, such studies are based on calcareous or biosiliceous microfossil groups, and their biochemistry. Research employing organic biotic remains, including more or less *in situ* and transported elements (e.g., from land), is so far scarcer. Yet, accurate reconstructions of, for example, ancient polar environmental conditions have been demonstrated for many categories of organic walled microfossils (Bijl et al., 2011, 2013a; Houben et al., 2013; Sangiorgi et al., 2018), and specific molecular remains derived from plankton species, bacteria and/or archaea that are preserved within sediments (Brassell et al., 1986; Schouten et al., 2002; Hopmans et al., 2004; Belt et al., 2007).

Here we explore the organic remains of organisms (such as dinoflagellate cysts and archaeal membrane lipids) obtained from the sediments below the ocean floor around Antarctica further in terms of providing paleoenvironmental clues during periods of warming since the establishment of the Antarctic ice sheets.

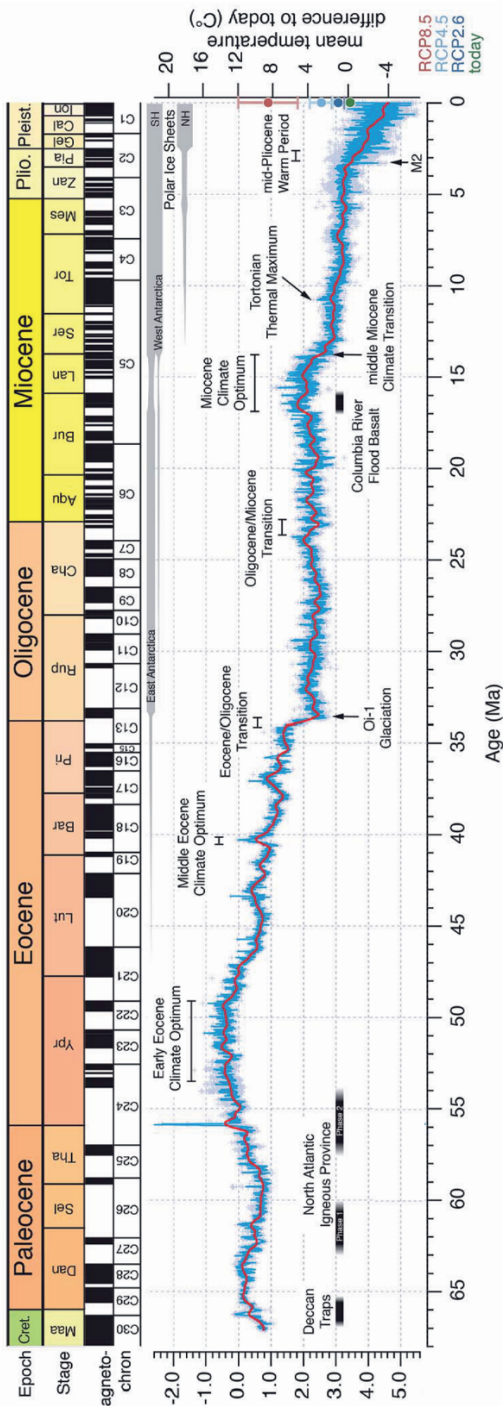


Figure 2: Cenozoic Global Reference benthic foraminiferal oxygen isotope dataset from ocean drilling core sites spanning the past 66 Myr (figure obtained from Westerhold et al., 2020).

3 Critical periods in the history of the Antarctic ice sheets

To study the effects of climate warming on the Antarctic ice sheet in an icehouse state, the focus of this thesis lies on the period since the establishment of a large Antarctic ice sheet around 34 million years before present (Ma), mid-way the Cenozoic era (the past 66 million years). Much of our understanding of global climate change during the Cenozoic era comes from high-resolution deep-sea oxygen isotope records obtained from foraminiferal shells living on the bottom of the ocean (benthic foraminifera) (Zachos, 2001; Lisiecki and Raymo, 2005; Zachos et al., 2008; Westerhold et al., 2020) (see Figure 2). Cooling of the bottom ocean waters as well as the formation of continental ice sheets results in a loss of the lighter ^{16}O isotope from the ocean waters and therefore incorporation of relatively more of the heavier ^{18}O isotope in benthic foraminifera. This ratio between lighter and heavier oxygen isotopes is expressed as $\delta^{18}\text{O}$ and increases with declining temperatures and/or ice sheet expansion. Based on this and various sedimentary archives from around Antarctica (Zachos et al., 1992; Ivany et al., 2006; Sorlien et al., 2007; Houben et al., 2013; Galeotti et al., 2016) it is clear that a large Antarctic Ice Sheet (AIS) was established during the Eocene-Oligocene Transition (EOT), which is marked by a stepwise increase of about 1.5‰ in the benthic foraminiferal $\delta^{18}\text{O}$ record around 34 Ma (Zachos, 2001; Coxall et al., 2005). As $\delta^{18}\text{O}$ ratio incorporates both a temperature and an ice volume signature, increases in the benthic foraminiferal $\delta^{18}\text{O}$ record after the establishment of the AIS at 34 Ma thus represent periods of either warming of bottom ocean waters or AIS decline or a combination of both.

Key periods of global warming, represented by relatively low $\delta^{18}\text{O}$ values, have been identified in the benthic foraminiferal $\delta^{18}\text{O}$ record. These periods are of particular interest when studying sedimentary records near the Antarctic margin because they may provide insight into how much of the $\delta^{18}\text{O}$ signal is related to ice sheet decline and how much to a temperature increase, in other words: the sensitivity of the Antarctic ice sheet to global warming.

The IPCC AR6 report (2023) states that it is *very likely* that greenhouse gases are the main driver for current global warming. Of these greenhouse gases carbon dioxide (CO_2) accounts for most of the radiative forcing today with atmospheric concentrations well over 400 ppmv (National Oceanic and Atmospheric Administration, Global Monitoring Laboratory). Periods in the past with a similar atmospheric CO_2 concentration as today may provide important insights into the sensitivity of the Antarctic ice sheet under current CO_2 radiative forcing. During the Oligocene (~34 - 23 Ma) atmospheric CO_2 concentrations dropped from around 650 ppmv to 400 ppmv and thus correspond to modern and future

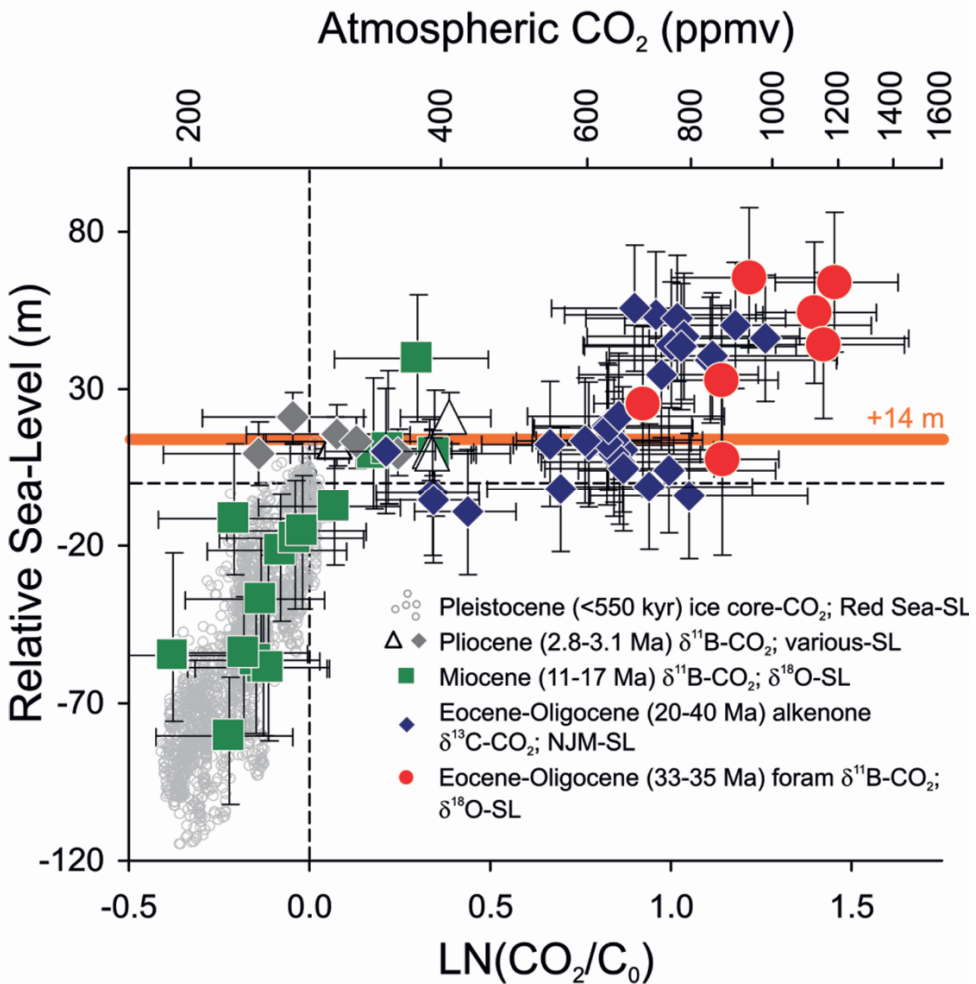


Figure 3: The relation between reconstructed atmospheric CO₂ concentrations and reconstructed relative sea level in the Cenozoic Era; figure obtained from Foster & Rohling (2013).

projections. The Oligocene is therefore a key period for understanding the stability of the future Antarctic Ice Sheet. Note that based on the relationship of CO₂ concentrations and sea level obtained from paleoclimatic reconstructions, global sea level would have been 14 meters higher than today if the Earth's system were to reach an equilibrium state under modern CO₂ forcing (see Figure 3) (Foster and Rohling, 2013). For the main part, this 14-meter global sea level rise represents the deglaciation of the West Antarctic Ice Sheet (WAIS, ~3.5 meter) and the Greenland Ice Sheet (GIS, ~7 meter). Furthermore, it seems that while CO₂ concentrations in the atmosphere declined during the Oligocene, the East

Antarctic Ice Sheet (EAIS) was very stable. However, as continental configuration and paleotopography and therefore ocean circulation during this period was different from today, other factors such as ocean heat transport might have played a role in the stability of the Antarctic Ice Sheet. It is therefore also important to consider more recent periods of global warming as analogues for future warming, such as the Miocene Climatic Optimum (MCO) (~17-14.5 Ma), the mid-Pliocene warm period (~3 Ma), the Last Interglacial (LIG) (~125 thousand years ago (ka)) and the mid-Holocene warm period/thermal maximum (~ 8 ka) (see Figure 2).

4 Neogene changes in continental configuration affecting ocean currents of the Southern Ocean

When reconstructing past climate conditions, it is important to consider that ocean currents may have been different in the past due to a different continental configuration. The formation of the eastward-flowing Antarctic Circumpolar Current (ACC) has been considered important for the establishment and subsequent expansion of the Antarctic ice sheet, as it isolates the Antarctic continent from warmer ocean currents originating from lower latitudes. The ACC may therefore have promoted cooling of the Antarctic continent by preventing transport of warmer ocean water to the Antarctic coast (Lagabriele et al., 2009; Katz et al., 2011; Bijl et al., 2013a). During the Eocene, Oligocene and Miocene periods, Antarctica was positioned more eastwards than today (van Hinsbergen et al., 2015), and Australia and South America were positioned closer the Antarctic continent. Separation of Australia from Antarctica through the formation of the Tasmanian Gateway and separation of South America from Antarctica through the opening of Drake Passage eventually resulted in the establishment of the strong flowing ACC we have today. However, the timing of the opening of these ocean gateways and the establishment of a strong flowing ACC is controversial. Based on dinoflagellate cyst biogeography and sea surface temperature reconstructions it is established that the earliest throughflow of a westward Antarctic Circumpolar Counter Current (ACCC) at the Tasmanian Gateway was established in the middle Eocene around 49 Ma (Bijl et al., 2013a). However, a deeper ocean eastward flowing circulation was not present until around 33 Ma (Stickley et al., 2004; Scher et al., 2015). At Drake Passage, a deep-water throughflow has been suggested around 41 Ma (Scher and Martin, 2006). The various tectonic plates around Drake Passage have been subject to various phases of spreading but also to uplift which may have limited throughflow. Therefore, the timing of a strong ACC through Drake passage has been much debated (Lawver and Gahagan, 2003; Livermore et al., 2007; Lagabriele et al., 2009; Maldonado et al., 2014). However, a strong ACC through Drake passage must have developed between 24 and 10 Ma. Before that time, throughflow at Drake Passage may

have been temporarily limited, in which case the westward flowing ACCC would have been more dominant than the eastward flowing ACC (Hill et al., 2013) (see Figure 4). The presence of a weaker ACC during the Eocene, Oligocene and Miocene is important to consider as warming along the Antarctic coast may not be (only) due to warming of the

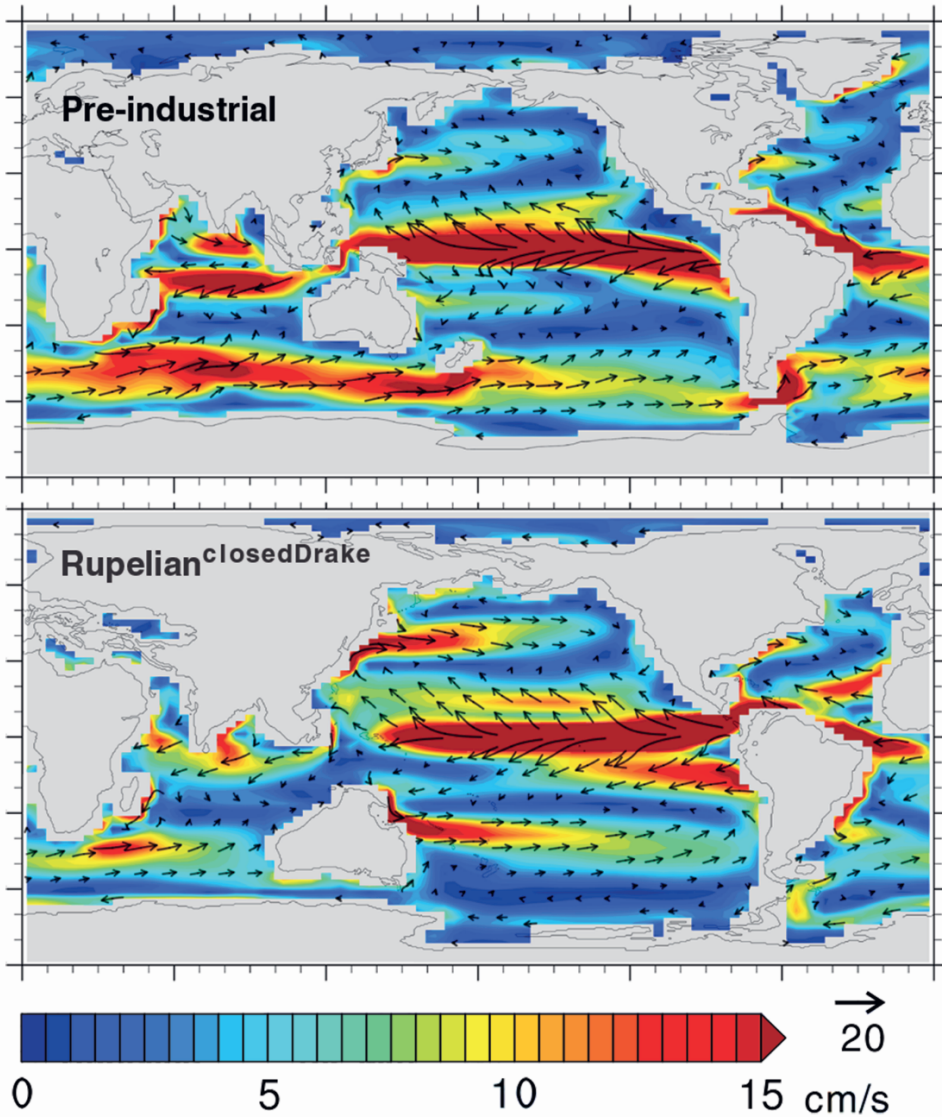


Figure 4: Modelled global ocean surface current speed for a modern and early Oligocene (Rupelian) continental configuration with a closed Drake Passage (Hill et al., 2013).

climate but also due to the influence of warmer ocean currents. Currents that flow along the southern coast of Australia and the western coast of South America would have been able to reach (closer to) the coast of Antarctica, which would have limited the development of sea ice around Antarctica and the presence of large ice shelves extending from the continent into the ocean.

5 Glacial-interglacial variability

Another aspect to consider when reconstructing past climate conditions is that a more short-term variability is overimposed on the warming or cooling trends due to changing long-term greenhouse gas concentrations in the atmosphere and changing continental configurations. This variability is caused by cyclical changes in the shape of Earth's orbit around the Sun (eccentricity cycle of 100 kyr), the Earth's tilt (obliquity cycle of 41 kyr) and the movement of the solstices and equinoxes along Earth's orbit due to the wobbling of the Earth's axis and the rotation of the trajectory around the Sun (precession cycles of 23 and 19 kyr). Due to the combination of these orbital cyclicities the amount of insolation that a specific latitude receives during a specific month varies cyclically. In this way the amount of insolation received at 65°N during the summer months has controlled the expansion and decline of the northern hemisphere ice sheets during the Pliocene and Pleistocene, with periods of low summer insolation leading to ice sheet expansion (Ruddiman, 2003). As previously stated, the formation of ice sheets results in the loss of the ^{16}O isotope from the ocean waters and thus the orbital variation of ice sheet expansion and decline is also reflected in $\delta^{18}\text{O}$ records of benthic foraminifera around the globe. By combining the $\delta^{18}\text{O}$ records of 57 globally distributed sites a stack was created for the past 5.3 Myr, known as the LR04 stack (Lisiecki and Raymo, 2005). The various highs and lows within this stack are known as Marine Isotope Stages (MIS) with an assigned number and Substages with an assigned letter. Generally, positive excursions (glacial stages) are even-numbered, and the negative excursions (interglacial stages) are odd-

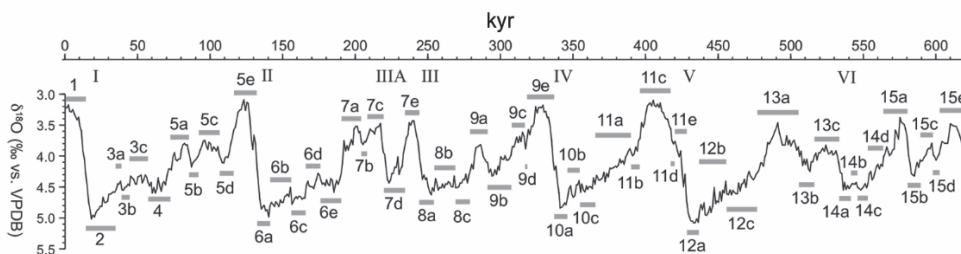


Figure 5: Scheme of marine isotope stage (MIS) numbering for the last 600 kilo years according to Railsback et al. (2015).

numbered. Glacial-interglacial transitions can be recognized as large shifts from higher to lower $\delta^{18}\text{O}$ values and mark the end of an ice age, also known as a glacial Termination, and have been numbered with Roman numerals. The Last Interglacial (LIG) is also known as MIS5e and the Last Glacial Maximum (LGM) is also known as MIS2. The latest scheme for naming and duration of the individual isotope stages has been proposed by Railsback et al. (2015) (see Figure 5).

Orbitally induced glacial-interglacial variability within $\delta^{18}\text{O}$ records has not only been observed during the Pliocene and Pleistocene periods, but also further back in time. The Oligocene and Miocene periods show fluctuations within the $\delta^{18}\text{O}$ record of up to 1‰ with glaciations following a 110-kyr eccentricity cycle (Liebrand et al., 2017) (see Figure 6). Considering that no northern hemisphere ice sheet was present during these periods, fluctuations in $\delta^{18}\text{O}$ are the result of deep-sea temperature changes and changes in the size of the Antarctic Ice Sheet. Fluctuations of 50% to 125% of the present-day East Antarctic Ice Sheet have been reconstructed for the Oligocene, depending on how much of the $\delta^{18}\text{O}$ signal is related to deep sea temperature (Pekar et al., 2006; DeConto et al., 2008; Pekar and Christie-Blick, 2008).

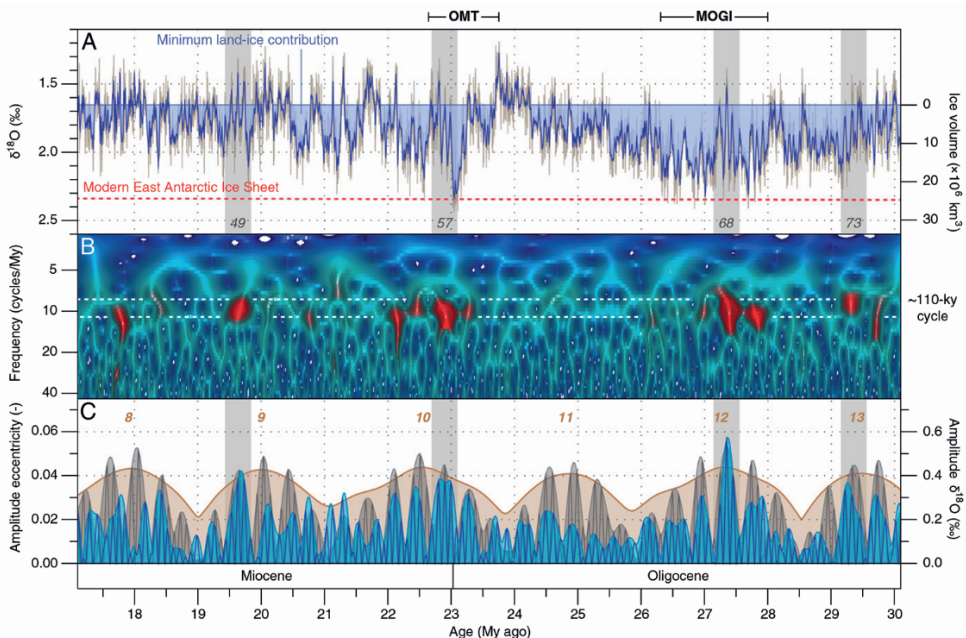


Figure 6: $\delta^{18}\text{O}$ record from ODP Site 1264 (A) and the 110-kyr eccentricity cycle obtained from wavelet analysis (B) and filtered from the $\delta^{18}\text{O}$ -record as shown by the dark blue line in C (Liebrand et al., 2017). Earth's 110-kyr, 405-kyr and 2.4-Myr eccentricity cycles are shown with a grey line, light grey and brown shading, respectively. OMT = Oligocene-Miocene Transition, MOGI = Mid-Oligocene Glacial Interval.

6 The rationale for using indicators (proxies) of surface water properties.

To be able to distinguish between the temperature signal and the ice sheet volume signal in the $\delta^{18}\text{O}$ record, independent proxies for temperature reconstruction are necessary. To reconstruct deep-sea temperatures, the ratio between magnesium (Mg) and calcium (Ca) in benthic foraminiferal shells has been used, since incorporation of Mg increases with increasing temperature (Lear et al., 2000). However, the use of proxies based on foraminifer shells (oxygen isotopes, elemental ratios) is limited due to poor preservation of carbonates at the high-latitude Southern Ocean sea floor because deep waters are undersaturated in carbonate so foraminifera hardly preserve and the proxy-temperature relation is based on critical assumptions on the past composition of ocean seawater. Therefore, alternative temperature proxies should be considered. As the Southern Ocean is a source of deep-water formation today and likely was in the past, there should be a strong relation between the temperature of the surface waters and the temperature of the bottom waters close to the Antarctic margin. Therefore, the long-term surface water temperature trends of the surface waters and deep waters should be very similar, which allows the use of surface water temperature proxies to estimate the contribution of temperature to the $\delta^{18}\text{O}$ record, thereby allowing a reconstruction of the stability and size of the Antarctic ice sheet. The size and stability of the Antarctic ice sheet will also affect the surface water conditions along the Antarctic coast through sea-ice formation, meltwater run-off and stratification. As mentioned, there are many proxies based on the remains of plankton, so-called microfossils, to reconstruct surface water conditions. As preservation of carbonate-based microfossil remains in the Southern Ocean is poor, records around Antarctica are characterized by a high silica content instead. Therefore, reconstructions of sea ice concentrations mainly rely on the use of diatoms. However, diatom frustules can be susceptible to dissolution because shelf waters around Antarctica generally contain low concentrations of dissolved silica. Furthermore, due to burial, the diatom frustules will be affected by diagenesis where the biogenic opal dissolves and precipitates as cristobalite and tridymite. Due to this diagenetic front, preservation of siliceous microfossils in the sediments is limited below a certain depth. So, instead of planktic foraminifera and diatoms for reconstruction of surface water environmental conditions, it is important to consider alternatives. Therefore, in this thesis we employ the use of organic remains of organisms (organic proxies) and explore their potential. The organic proxies we use are organic-walled microfossils (palynomorphs) and membrane lipids produced by a group of marine Archaea called Thaumarchaeota and by some bacteria.

6.1 Organic walled microfossils as a proxy for paleoenvironmental conditions

'Organic (walled) microfossils' encompass a broad group composed of typically single, sometimes colonial, cells of aquatic and terrestrial origin, ranging across many phyla, ranging from terrestrial floras to minute marine and fresh water algal remains. These remains are also known as palynomorphs and study of these remains is known as palynology, derived from the Greek word *παλύνω*, which translates to "strewn particles". Palynomorphs have been recovered from Southern Ocean sediments before (Hannah et al., 2000, 2001; Esper and Zonneveld, 2002; Sluijs et al., 2003; Storkey, 2006; Warny et al., 2009), but their application for environmental reconstructions at high-latitudes is challenging for various reasons and requires further study. Various species of dinoflagellate cysts have been successfully applied for 'deep time' reconstructions of shifts of Southern Ocean fronts during the Oligocene and Miocene, when opening of the Tasmanian Gateway and Drake Passage isolated Antarctica to allow the build-up of the Antarctic Ice Sheet (Houben et al., 2013; Prebble et al., 2013; Bijl et al., 2018b; Sangiorgi et al., 2018; Hoem et al., 2021a, 2021b). Furthermore, dinoflagellate cysts have been employed to reconstruct Pleistocene glacial-interglacial variability at sites near Southern Ocean fronts (Howe et al., 2002; Esper and Zonneveld, 2007), but the use of dinoflagellate cysts for reconstructing paleoenvironmental conditions in the Southern Ocean in more recent geological (e.g., icehouse) times is limited, due to the scarcity of the material and because species diversity in modern surface sediment samples decreases towards the Antarctic coast (Esper and Zonneveld, 2002, 2007; Zonneveld et al., 2013; Marret et al., 2020). Considering this, it is important to expand our knowledge on (other) palynomorphs in the Southern Ocean as this could potentially enlarge the toolbox to reconstruct paleoenvironmental change near the Antarctic coast. Particularly because, as stated above, preservation of siliceous and carbonate microfossils may be limited on the Southern Ocean sea floor and palynology can be an alternative. But also, when other proxies are available, the use of organic walled biotic remains can be an important addition for reconstructing paleoenvironmental, allowing for the reconstruction of a larger portion of the ecosystem, including not only primary producers, but also secondary producers, zooplankton and bottom-dwelling detritus feeders, which may all respond differently to (future) climatic changes.

6.2 Membrane lipids and the TEX₈₆ paleothermometer

Lipids from the cell membranes of marine Thaumarchaeota are used for reconstructing past surface water temperatures. Marine Thaumarchaeota are one of the dominant prokaryotes in today's ocean and at higher ambient temperature they biosynthesize more cyclopentane moieties in their membrane lipids. Because particularly

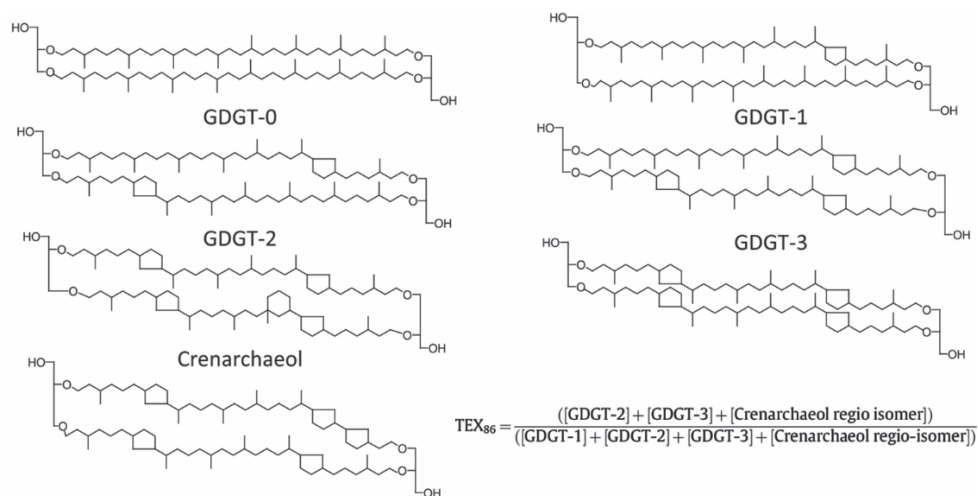


Figure 7: Molecular structures of GDGT-0 to GDGT-3 and Crenarchaeol, and the TEX_{86} formula (Schouten et al., 2013).

those membrane lipids that are synthesized in the surface ocean get exported to the ocean sediments, where they preserve well, the relative abundance of the cyclopentane moieties of these lipids can be used as a proxy for SST. This proxy is known as TEX_{86} and is based on the distribution of isoprenoid glycerol dialkyl glycerol tetraethers (GDGTs), which are the lipid remains preserved in sediments (Schouten et al., 2002) (see Figure 7). For calibration to temperature, a core-top calibration is used: an assembly of TEX_{86} surface sediments from global oceans and their associated modern temperatures. Since the original core-top calibration, which is based on a comparison between a TEX_{86} index consisting of 4 different GDGTs and mean annual sea surface temperature (Schouten et al. 2002), the calibration dataset has been expanded and improved upon and new calibrations based on satellite-derived temperature data have been developed (Kim et al., 2008, 2010). Multiple proxies and calibrations based on GDGTs now exist, which are all based on the same or a similar set of GDGTs (GDGT-0 to GDGT-3, Crenarchaeol and its regio-isomer) (Schouten et al., 2013).

Similar to palynomorphs, the application of TEX_{86} has been challenging at high latitudes, because there is a large scatter at the low-temperature end (<5°C) of the TEX_{86} -SST relationship. A large part of the various calibrations is developed mainly to resolve the non-linearity in the TEX_{86} -SST relationship that results from this large scatter. Kim et al. (2010) resolved this non-linearity by applying two different indices each with their own logarithmic calibration depending on the temperature range. These calibrations, known as

$\text{TEX}_{86}^{\text{H}}$ (which uses the original TEX_{86} index for the higher temperatures) and $\text{TEX}_{86}^{\text{L}}$ (which uses the ratio of [GDGT-2] over [GDGT-1], [GDGT-2] and [GDGT-3] for the lower temperatures) show a better fit to both core-top and mesocosm studies than older calibrations. Both $\text{TEX}_{86}^{\text{L}}$ and $\text{TEX}_{86}^{\text{H}}$ will produce similar SST estimates above SSTs of 15°C, but below 15°C $\text{TEX}_{86}^{\text{L}}$ better fits the core-top data (Kim et al., 2010).

For this reason, $\text{TEX}_{86}^{\text{L}}$ has most often been applied in the polar regions. Nevertheless, the application of either proxy does not resolve the large scatter in the low-temperature domain. Ho et al. (2014) have extensively compared the $\text{TEX}_{86}^{\text{L}}$ and linear TEX_{86} calibrations of Kim et al. (2010) for the polar regions, and concluded that most of the scatter is caused by regional differences in the Arctic but that the Southern Ocean TEX_{86} values of core tops show good correlation to today's yearly mean SSTs derived from the World Ocean Atlas of 2009 (WOA09). Instead, Southern Ocean $\text{TEX}_{86}^{\text{L}}$ values appear to be biased towards warmer temperatures and correlate best with annual summer temperatures (Ho et al., 2014). Another complicating factor is the fact that the ratio between GDGT-2 and GDGT-3 in the sediments seems to depend on water depth. Shallow water sites consistently have a lower GDGT-2/GDGT-3 ratio than deep water sites (Taylor et al., 2013), because the 'deep water' Thaumarchaeota produces relatively more GDGT-2 than the 'shallow water' Thaumarchaeota (Villanueva et al., 2015). As $\text{TEX}_{86}^{\text{L}}$ is much more sensitive to changes in the GDGT-2/GDGT-3 ratio than TEX_{86} because GDGT-3 is not included in the nominator of this index, water depth and/or the relative abundance of these 'deep water' Thaumarchaeota throughout the water column will have a strong effect on $\text{TEX}_{86}^{\text{L}}$ -derived sea surface temperatures. Because the distribution of GDGTs throughout the water column and the mechanisms by which these GDGTs end up in the sediments will likely vary regionally, the type of calibration is likely to be regionally dependent in paleoclimatic studies (Bijl et al., 2009; Liu et al., 2009; Shevenell et al., 2011; Sluijs et al., 2011; Kim et al., 2012a). A later addition to the available calibration methods that aims to resolve this regional variability is the BAYSPAR calibration model developed by Tierney & Tingley (2014; 2015). This calibration is based on a Bayesian spatially varying regression model, which infers a best estimate for intersection and slope of the calibration based on an assembly of 20° by 20° spatial grid boxes that statistically fit best with a prior estimate of average SST in the region. This latest calibration method offers opportunities to apply TEX_{86} also at high latitude Southern Ocean sites based on a calibration that does not include sites with a different TEX_{86} -SST relationship, such as the Arctic (Ho et al., 2014; Tierney and Tingley, 2014). A more regionally based calibration will give a more accurate sea surface temperature estimate and will therefore aid our understanding of the climate conditions close to the Antarctic ice sheet during periods of warming in the past.

7 Material

To reconstruct environmental conditions close to the Antarctic margin using marine palynology and TEX₈₆ for (key) periods in Earth's history, we rely on cores drilled from the ocean floor near the Antarctic coast. Relatively shallow cores of a few meters deep can be obtained using piston coring from smaller research vessels. Several expeditions have been carried out by German, French and Italian Antarctic cruises. However, these generally contain material that has been deposited over the past 10.000 to a few 100.000 years and therefore do not allow for reconstructing environmental conditions deeper in time. For this drill cores of hundreds of meters below the ocean floor are obtained by specially equipped drilling ships. Particularly the International Ocean Discovery Program (IODP) and its predecessors (ODP and DSDP) have carried out expeditions to obtain such sedimentary records. However, because of the harsh conditions near the Antarctic coast due to sea ice, strong winds and cold temperatures, drill cores obtained by the DSDP/ODP/IODP expeditions from near Antarctica are relatively scarce. At the start of this PhD research, only seven expeditions were carried out close to the Antarctic coast and generally with poor core recovery: Leg 28 (Ross Sea), Legs 35 and 178 (West Antarctic Peninsula), Leg 113 (Weddell Sea), Legs 119 and 188 (Prydz Bay), and Expedition 318 (Wilkes Land). During IODP Expedition 318, which was carried out in 2010, seven cores (U1355 – U1361) were drilled, thereby expanding the available sedimentary archives around Antarctica and along the previously unexplored East-Antarctic margin of Wilkes Land (Expedition 318 Scientists, 2011a). This region is of particular interest as it is located at the seaward termination of the Wilkes Subglacial Basin, which is largely below sea level with steep reversed (retrograde) slopes (Fretwell et al., 2013), making the overlying ice sheet potentially vulnerable to intrusion of warm ocean waters (see Figure 1). With the retrieval of IODP cores U1355 – U1361 sedimentary material spanning the past 54 million years has been obtained, allowing for a detailed analysis of some critical periods in Earth's climate history during which the East Antarctic Ice Sheet (EAIS) evolved to its present-day, relatively stable configuration.

8 Synopsis

As is evident from the above, our understanding of the environmental conditions close to the Antarctic margin in a warmer-than-today world is limited. In this thesis sediments from the cores that were obtained at Sites U1356 (offshore Wilkes Land) and U1357 (Adélie Basin) during IODP Expedition 318 to offshore east Antarctica and core AS05-10 obtained during the XX Italian Antarctic Cruise are studied to expand our knowledge on Southern Ocean palynology and the use of TEX₈₆ as a paleothermometer in

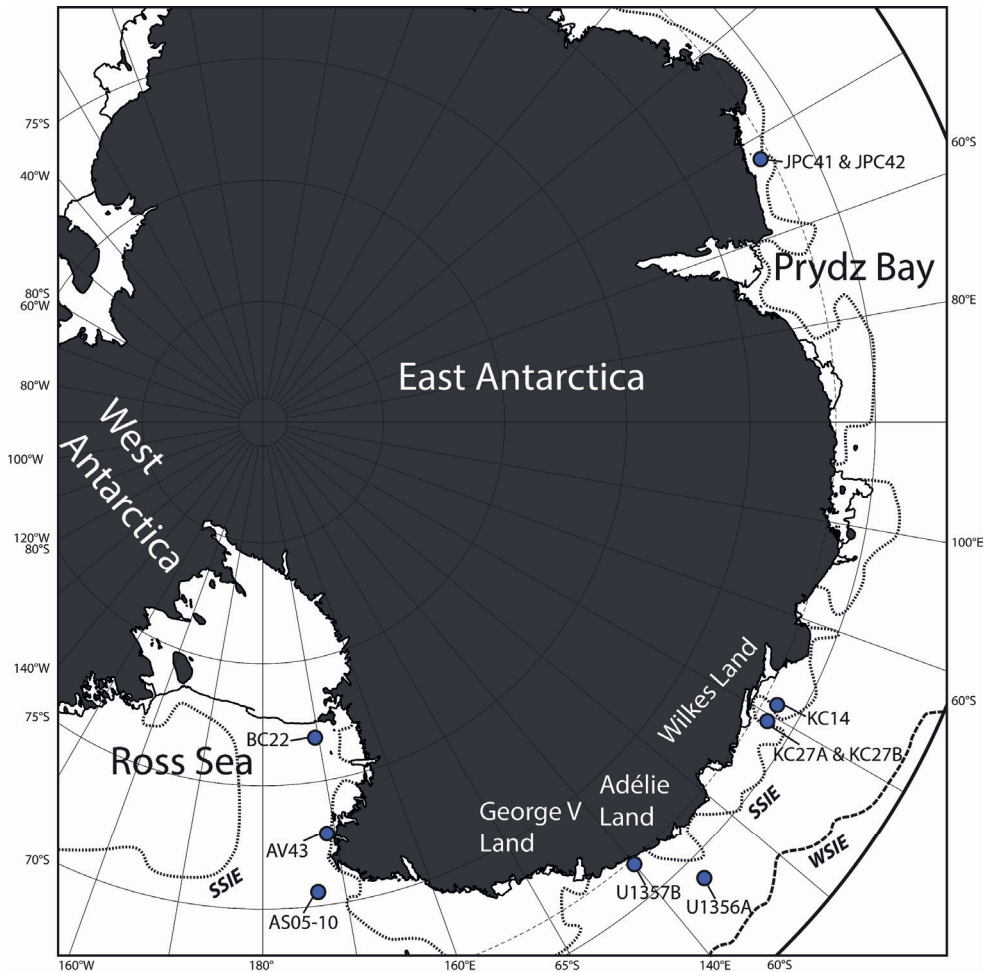


Figure 8: Map of East Antarctica with sample locations used in this thesis. SSIE = summer sea ice edge, WSIE = winter sea ice edge.

the polar regions (see Figure 8). In addition, sea surface samples were used from a variety of other cores along the East Antarctic margin for Chapter 3.

Samples were taken from various time intervals with different continental configurations and/or atmospheric CO_2 concentrations. Notably, the various sedimentary records used show alternations in lithology, which can be linked to climate (glacial-interglacial) or seasonal variability. In such cases, samples were taken from both types of lithologies to investigate if there is any correlation to the lithology and palynology and/or TEX_{86} . To aid our understanding of these proxies, new and existing paleoclimate records

based on the diatom content of Southern Ocean cores are compared to our palynological and TEX₈₆ results.

Chapters are organized to follow the stratigraphic order of the studies conducted: from the Holocene to the Oligocene (see Figure 9).

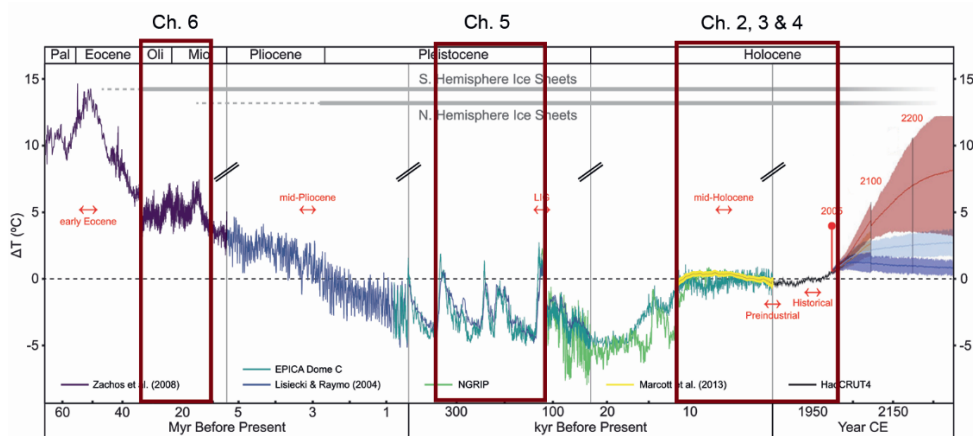


Figure 9: Temperature trends for the past 65 Ma and potential geohistorical analogues for future climates (red arrows) (Burke et al. 2018). The time intervals studied in the various chapters are indicated.

In **Chapter 2** we explore the palynological content samples from the 170 m-long and laminated Holocene core that was drilled at IODP Site U1357 in the Adélie Basin, East Antarctica. Sedimentation rates at this site are exceptionally high, which allowed for exceptional preservation of organic material and show potential for ultra-high (annual) resolution studies. The remains of 74 different mainly marine microfossil taxa and/or types have been described together with their biological origin and their ecological affinities, if known. The remains include phytoplanktonic and zooplanktonic organisms, as well as detritus feeders and bottom-dwelling scavengers from across three eukaryotic kingdoms. Because of the good preservation, digital images of new and known species are included. Therefore, this chapter contains photographic material and environmental interpretation of most of the palynomorphs so far discovered in Antarctic sediment and can hence serve as a reference work for future palynological paleoenvironmental studies in the Southern Ocean.

One of the dinoflagellate cyst species encountered at Site U1357 and included in the photographic material of Chapter 2 is *Nucicla umbiliphora*, which we formally describe In **Chapter 3**. This species was depicted as an unknown (protoperidinioid) dinoflagellate cyst in four previous studies but lacked a formal description. It was found in sediments spanning a time period from the Last Interglacial to Recent. Based on material from nine

additional core sites, *Nucicla* is described as an acavate, dorsoventrally compressed cyst with a rounded pentagonal outline. It has a hypocyst that is twice as large as the epicyst, a large sulcus with the posterior sulcal plate at the antapex and an archaeopyle formed by the loss of the three anterior intercalary plates. The species *N. umbiliphora* is defined based on the cyst wall ornamentation and archaeopyle shape. Given that the occurrence of this species seems to be limited to the Antarctic shelf, it can be an indicator of quasi-annual sea-ice cover in paleoenvironmental studies. Sediments where *N. umbiliphora* has been found are in areas where sea-ice cover is at least 9 months.

The palynological content of Site U1357 throughout the entire Holocene is explored further in **Chapter 4**. Here the shifts in the palynological record of (mostly) surface-water dwelling species allowed the determination of several intervals, which are likely the result of ecosystem turn-overs due to paleoenvironmental changes. We compare the timing of these shifts to a TEX₈₆-based reconstruction of the subsurface water temperatures from the same core. We make use of the laminations (alternating light and dark laminae) present in the core which could indicate spring and summer deposition, respectively. Reconstructed spring subsurface temperatures especially show a strong relation to the faunal turn-over events within the palynological record. In addition, a proxy for export productivity based on the palynological remains of benthic foraminifera is introduced to compare with the palynological content that is derived from surface-water dwelling species. Furthermore, a recently published reconstruction of the meltwater flux to Site U1357 (Ashley et al., 2021), based on the deuterium isotopes within fatty acids and diatom-based paleoenvironmental reconstructions of the well-studied nearby core MD03-2601 (Crosta et al., 2008; Denis et al., 2009b) are used for comparison. In this way, we get a better understanding of the ecological affinities of the organic microfossils (from tintinnids, dinoflagellates and prasinophytes) obtained from the record of Site U1357 and even some of the microfossil remains with an unknown biological origin. In this chapter we highlighted the existence of a degradational bias affecting some palynomorphs, as some of the tintinnid and dinoflagellate remains with typically thinner walls are only present in the upper sediment record regardless the exceptional overall preservation. This means that some palynomorphs may not be present downcore even in a record with such exceptional preservation of organic matter because of selective preservation. In this chapter we conclude that true faunal turn-over events occur at the transition from the early Holocene to the mid-Holocene, when subsurface water temperatures increase by about 2°C and sea ice concentrations decline; and around 3.0 ka, when the meltwater flux to the study site decreases and increased mixing with deeper waters leads to more nutrient availability, resulting in increased primary productivity. This underlines the fact that increased meltwater flux from the Antarctic mainland and/or reduction of sea-ice concentrations

due to current global warming can have strong implications for ecosystems around Antarctica as a whole.

How ecosystem changes near Antarctica reflect the waxing and waning of the Antarctic ice sheet and the associated paleoenvironmental changes in the surface waters on glacial-interglacial timescales is discussed in **Chapter 5**. In this chapter microfossil remains, including dinoflagellates as well as diatoms and benthic foraminifera, TEX₈₆ together with other organic and inorganic geochemistry proxies, and sedimentology obtained from core AS05-10 will be combined to reconstruct the paleoenvironmental conditions off the Ross Sea margin (Adare Basin) during Marine Isotope Stages 9 to 5 (350 to 70 ka). For each of the glacial-interglacial transitions a clear succession of events is recognized: after (near-)permanent sea ice cover during the glacial stages, ice-shelf break-up follows with episodic ice-free areas and surface water stratification due to meltwater release. This is followed by the establishment of the high productivity Marginal Sea-ice Zone (MIZ) over site AS05-10 and a further retreat of the summer sea ice margin south of site AS05-10 during the interglacials. For MIS5e (peak warming of the Last Interglacial) it is established that highest productivity was reached due to an increased length of the blooming season and an increased nutrient supply. TEX₈₆-based temperatures reconstructed for this period suggest (summer) temperatures of 2.5°C warmer than today. The paleoenvironmental changes at the onset of each glacial Termination resemble global warming effects around Antarctica today, considering that surface water temperatures west of the Antarctic Peninsula have already risen by 1°C since 1955 (Meredith and King, 2005) and the release of meltwater from the Antarctic mainland into the Southern Ocean has increased, resulting in freshening of the Ross Sea (Jacobs et al., 2002). It is therefore not unreasonable that future global warming is likely to result in a reduction of the sea ice concentrations around Antarctica, despite the fact that sea ice concentrations around Antarctica currently show no clear trend with local increases opposed to recent declines (Comiso and Nishio, 2008; Yuan et al., 2017; Parkinson, 2019).

At site AS05-10, preservation of GDGTs and dinoflagellate cysts is not exceptional resulting from a combination of limited productivity in the surface waters due to high sea ice concentrations during the glacial periods and generally well-oxygenated bottom waters at the site. Although an increased preservation of organic matter, including dinoflagellate cysts and GDGTs, during the interglacial periods is indicative of paleoenvironmental change reflecting decreased bottom water oxygenation and/or enhanced primary productivity, most paleoenvironmental changes at AS05-10 are inferred from the diatom record. However, for paleoenvironmental reconstructions further back in time, preservation of diatoms can become limited due to diagenetic alteration of biogenic opal. So, deep-time

reconstructions of paleoenvironmental conditions rely much more on the preservation of organic microfossils and biomarkers.

IODP Expedition 318 offshore Wilkes Land (East Antarctica) was designed to recover material that would provide insight into the Antarctic cryosphere dynamics, i.e. the waxing and waning of the Antarctic ice sheet, during periods with higher than present CO₂ concentrations and the initiation of the sea-ice (eco)system. CO₂ concentrations in the atmosphere today (constantly higher than 400 ppm since 2013, National Oceanic and Atmospheric Administration, Global Monitoring Laboratory) are comparable to those during (most of) the Oligocene (34 – 23 Ma) and the Miocene (23 – 5 Ma). It is therefore very fortunate that the core that was obtained from Site U1356 covers the nearly the entire Oligocene period and parts of the Miocene period and that preservation of organic matter, including dinoflagellate cysts and GDGTs, was also reasonable to good. Based on the lithology of this core, glacial and interglacial facies were distinguished (Salabarnada et al., 2018). This distinction between colder glacial and warmer interglacial periods during the Oligocene-Miocene is confirmed by the palynological content (dinoflagellate cysts) (Bijl et al., 2018b) and for the Oligocene also by reconstructed TEX₈₆-based sea surface temperatures, which are presented in **Chapter 6**. In this chapter we show that during the Oligocene temperatures off the Wilkes Land coast were on average about 17°C and decrease towards about 11°C during the Mid-Miocene Climate Transition in agreement with the general lack of sea-ice dinoflagellate cysts and mostly oligotrophic species in this part of the record (Bijl et al., 2018b). Compared to average sea surface temperatures of 1°C today, these conditions are extremely warm, and likely the result of Antarctica not being fully isolated by a strong Antarctic Circumpolar Current. Site U1356 was also positioned more northerly than today and was possibly still under the influence of warm ocean currents coming from the southern coast of Australia. A novelty presented here is that this represents the first study that considers retrieving temperature proxies from sediments of which detailed lithology is known with clear alternations (likely) related to glacial-interglacial variability. This has allowed us to conclude that the temperatures obtained from the interglacial facies are significantly warmer (1.5 – 3.1°C) than those obtained from the glacial facies. The reconstructed long-term temperature trends follow the long-term trends of the benthic δ¹⁸O records. Assuming that bottom-water formation occurred near the Antarctic margin, the long-term temperature trends as well as the glacial-interglacial temperature variability that is reconstructed for the surface waters off the Wilkes Land coast, will be relayed to the deep ocean. This means that a large part of the long-term trends and variability during the Oligocene within the δ¹⁸O record is due to the bottom-water temperature component within the δ¹⁸O signal rather than the ice volume component. This would suggest that during the Oligocene the Antarctic ice sheet

was relatively stable with little effect on global sea level while CO₂ concentrations declined, which is in agreement with Foster and Rohling (2013) (Figure 2). It is likely, that, in contrast to today, much of the Antarctic ice sheet was grounded above sea level during the Oligocene, making it less vulnerable to basal melt (Miller et al., 2020; Colleoni et al., 2022).

9 Concluding remarks and future research

This thesis shows that the analysis of organic biotic remains and notably the TEX₈₆-based paleothermometer is an important component in paleoenvironmental research in circum-Antarctic sediment records.

However, as with many proxies, a preservation bias should always be considered as is clear from the richness of organic remains obtained from Site U1357 in comparison to the poor preservation of organic material in core AS05-10. It has been my experience that considering the scarcity of available material from around Antarctica, all available proxies should be used to build a complete history of paleoenvironmental changes. For example, the samples with palynological content and a sufficient amount of GDGTs in core AS05-10 were few and mainly obtained from the interval that represents MIS5e, but as such they are an important indicator for how exceptional MIS5e was compared to other interglacials during the Pleistocene.

Taking into account sedimentology (glacial versus interglacial deposits and light versus dark lamina) prior to sampling has proven to be a beneficial approach. As is shown by the different temperature trends obtained from glacial and interglacial deposits at Site U1356, climate conditions and trends may differ between glacial and interglacial periods. Determining independently whether samples are derived from glacial or interglacial deposits will also prevent any apparent trends that could result from sampling relatively more interglacial deposits versus glacial deposits in one part of the record, or vice versa. Similarly, changes in surface water temperature through time can be very different for each season as demonstrated by the spring and summer temperature trends at Site U1357.

Future research needs to focus on finetuning and expanding the available proxies that can be used for paleoclimate research at high latitudes. Further analysis of the palynomorphs obtained from Site U1357 described in Chapter 2 will aid Southern Ocean palynological studies in the years to come and that the origin of some of the unknowns will be discovered. Although an effort has been made to compare shifts in the palynological content to paleoenvironmental change recorded in existing records near Site U1357, it would be best when the palynological content of Site U1357 is compared to the diatoms from Site U1357. Currently, a detailed diatom record of Site U1357 has not been published.

Considering TEX_{86} , the BAYSPAR calibration method may be considered by some an improvement to previous calibrations. Nevertheless, it relies on assumptions about the water column depth the GDGTs are derived from and a prior estimate of average seawater temperature. In addition, it is not always clear whether there is any seasonal bias or if there is a bias due to changes in the relative contribution of ‘shallow water’ versus ‘deep water’ communities. In general, I believe that TEX_{86} -based temperature reconstructions are a good reflection of the temperature trend, but absolute temperature estimates should be tuned to other available temperature proxies. It is therefore still tricky to find the ideal calibration and I hope that additional proxies will be developed. Recently a new calibration technique has been developed for TEX_{86} based on modern machine learning tools (Dunkley Jones et al., 2020), which has already been applied at the TEX_{86} dataset of Site U1356 (Duncan et al., 2022). In addition, some pilot studies have been carried out by using indices based on hydroxy-GDGTs, which are more abundant in polar regions and may be temperature dependent. I have done some testing with hydroxy-GDGTs obtained from the samples and cores used in this thesis (results are not published nor part of this thesis) and I hope this work will be continued to further improve our GDGT-based temperature reconstructions.

Lastly, with the retrieval of cores from Site U1356, the first near-complete record of the Oligocene was obtained from near the Antarctic Coast. Chapter 5 (Hartman et al., 2018c) and publications by Bijl et al. (2018b) and Salabarnada et al. (2018) have given us a better understanding of the paleoenvironmental conditions near the Antarctic coast during the Oligocene, however this is just one record. Moreover, considering that the Wilkes Land coast was under influence of the warmer proto-Leeuwin current flowing along the south coast of Australia during the Eocene and possibly to some degree during the Oligocene as well, Site U1356 would have been one of the warmest sites around Antarctica at that time. It is therefore necessary that more cores from this period are obtained from around Antarctica. Steps to a more complete understanding of the Oligocene Southern Ocean have already been taken by Hoem et al. (2021a, 2021b) and Duncan et al. (2022). Reiterating that atmospheric CO_2 concentrations today are similar to that during the Oligocene and the Miocene, getting a more and more complete picture of cryosphere variability during the Oligocene and Miocene is essential for future climate projections.

Chapter 2

**A review of the ecological affinities
of marine organic microfossils from a
Holocene record offshore of Adélie
Land (East Antarctica)**

Abstract

Integrated Ocean Drilling Program (IODP) Expedition 318 recovered a ~170 m long Holocene organic-rich sedimentary sequence at Site U1357. Located within the narrow but deep Adélie Basin close to the Antarctic margin, the site accumulated sediments at exceptionally high sedimentation rates, which resulted in extraordinary preservation of the organic sedimentary component. Here, we present an overview of 74 different mainly marine microfossil taxa and/or types found within the organic component of the sediment, which include the remains of unicellular and higher organisms from three eukaryotic kingdoms (Chromista, Plantae and Animalia). These remains include phytoplanktonic (phototrophic dinoflagellates and prasinophytes) and very diverse zooplanktonic (heterotrophic dinoflagellates, tintinnids, copepods) organisms. We illustrate each marine microfossil taxon or type identified by providing morphological details and photographic images, which will help with their identification in future studies. We also review their ecological preferences to aid future (palaeo)ecological and (palaeo)environmental studies. The planktonic assemblage shows a high degree of endemism related to the strong influence of the sea-ice system over Site U1357. In addition, we found the remains of various species of detritus feeders and bottom-dwelling scavengers (benthic foraminifers and annelid worms) indicative of high export productivity at Site U1357. This study shows the potential of organic microfossil remains for reconstructing past environmental conditions, such as sea-ice cover and (export) productivity.

1 Introduction

Site U1357 was drilled as part of the Integrated Ocean Drilling Program (IODP) Expedition 318 and is located in the Adélie Basin downwind and downcurrent from the Mertz Glacier Polynya. Polynyas are seasonal openings within the sea ice formed through the vertical mixing of warmer subsurface waters or through advection from the coast by wind or currents (Arrigo et al., 1998a; Arrigo and van Dijken, 2003; Morales Maqueda et al., 2004). These polynyas overlying the Antarctic shelf fuel increased primary productivity through nutrient release and sustain entire ecosystems including marine mammals and birds (Stirling, 1997; Arrigo and van Dijken, 2003). The Mertz Glacier Polynya is one of the larger and more productive coastal polynyas of the Antarctic margin (Arrigo and van Dijken, 2003). Annually, the Mertz Glacier Polynya is open between December and March, which allows for blooms of primary productivity (on average over the bloom period $0.31 \pm 0.26 \text{ g C m}^{-2} \text{ d}^{-1}$) and therefore increased particle fluxes to the sea floor (Arrigo and van Dijken, 2003). Over the Holocene, this process has accumulated 172 meters of diatomaceous ooze. In addition to the diatoms, the sediments from Site U1357 contain abundant microfossil remains left behind by a large variety of phytoplankton species and their predators. Although organic microplankton remains are less commonly used for reconstructing past environmental conditions (e.g., sea ice, temperature, productivity) in the Southern Ocean because not all organic remains are able to withstand lithification processes and/or oxygen degradation, the organic microplankton remains of Site U1357 are exceptionally well preserved. The high organic carbon content of these sediments includes not only dinoflagellate cysts, but also less commonly preserved material such as tintinnid loricae. In addition, the remains of higher animal taxa, foraminifers, chlorophytes and ciliates were mentioned (Expedition 318 Scientists, 2011b). The whole organic microfossil abundance and diversity of the unique sediments from Site U1357 has the potential of increasing our knowledge on Holocene environmental changes within a polynya-controlled environment closer to the Antarctic margin than the generally less diverse dinoflagellate cyst assemblages south of the sea-ice edge.

Future changes in sea-ice concentration due to global warming will likely affect Southern Ocean primary productivity, but how the seasonal sea-ice concentrations will change under current global warming and how this will affect primary productivity is still highly uncertain (Deppeler and Davidson, 2017). With respect to coastal polynyas there is even higher uncertainty on how climate change will affect them because the expected increased temperatures and increased precipitation have counteracting effects on polynya size (Marsland et al., 2007). In this regard, there is a growing need for high-resolution sedimentary archives from close to the Antarctic margin, which straddle past warmer time intervals, and accurate proxies that can be used to reconstruct past sea surface conditions

(e.g., sea-ice concentrations, sea surface temperature, and productivity). However, before we can interpret the diverse and highly abundant organic microfossil assemblages from the polynya sediments from Site U1357 and other Antarctic coastal records in terms of palaeoenvironmental changes, an accurate review of their ecological preferences is required. To this end, we have compiled an overview of the palynomorphs that we encountered in IODP Hole U1357B, and reviewed the palaeoenvironmental affinities of known marine organic microfossils.

2 Material

Site U1357 was triple cored to ensure maximum recovery of the sequence. Hole U1357B was drilled at a depth of 1017 meter below sea level and recovered about 172 of the sedimentary succession (Expedition 318 Scientists, 2011b). The lithology of Hole U1357B consists of dark black sediment, the surface of which oxidizes post-recovery into an alternation of centimetre-scale lighter and darker green layers of diatomaceous ooze, with a diatom content of 80–99% (Expedition 318 Scientists, 2011b). Throughout the core the total organic carbon (TOC) has been consistently high with values between 1 and 2 wt% (Expedition 318 Scientists, 2011b). For this review a total of 34 samples, taken throughout the 172 meters of recovery, were examined for their palynological content. Samples were obtained from both dark- and light-coloured laminae and covering the entire Holocene record to anticipate potential differences in the palynological assemblage between lamina types and shifts in the palynological composition through time. In **Chapter 4** we will discuss the changes in palynological content through time for palaeoenvironmental interpretations.

3 Methods

3.1 Palynological processing

For palynological processing, samples were freeze-dried, weighted, and ground manually in a mortar. For quantitative analyses a tablet of *Lycopodium clavatum* spores was added, and the sediment was wetted with an Agepon dilution (1:200). To remove carbonates and silicates, the samples were treated with 30% cold HCl and 38% cold HF respectively. Subsequently, samples were shaken for 2 h at 250 rpm, after which the samples were diluted with tap water and left to settle for 24 h. After decantation, 30% HCl was added to remove fluoride gels, tap water was added and the samples were centrifuged, after which the samples were decanted again. The material was treated once more with 38% HF and all subsequent steps. The organic residue was sieved using a 10- μ m mesh sieve and clumps were fragmented using ultrasound. Heavy minerals were removed by pouring the residue from the sieve into an evaporating dish floating in an ultrasonic

bath and decanting this back into the sieve after 5 minutes. No oxidation was applied. The fraction > 10- μ m was concentrated to ~1 ml of glycerine-water and a fraction thereof was mounted on a microscope slide using glycerine jelly. Samples are stored in the microscope slide collection of the Laboratory of Palaeobotany and Palynology at Utrecht University.

3.2 Microscope photography

Images were taken at either 400x, 630x or 1000x magnification using a Leica DM2500 LED microscope with mounted Leica MC170 HD camera. In some cases the live z-stacking tool Live Image Builder (LIB) within the Leica Application Suite software 4.0 was used. Z-stacking constructs a two-dimensional (2D) image from a 3D object by combining the areas in focus from multiple images, which is ideal for 3D microscopic objects.

3.3 Taxonomic framework

Because we have encountered palynomorphs derived from taxa within various eukaryote kingdoms, we have chosen to structure this review of organic microfossils according to the most recent systematic classifications of these taxa. The classification we use is based on the publications of Ruggiero et al. (2015) for the Chromista, and on a lower taxonomic level Fensome et al. (1993) and the online classification Dinoflag3 (Williams et al., 2017) for the dinoflagellate cysts; and Agatha and Strüder-Kypke (2012) and Agatha and Strüder-Kypke (2013) for the tintinnids. For the classification of chlorophytes we rely on several molecular phylogenetic and classification studies (Nakayama et al., 1998; Guillou et al., 2004; Marin and Melkonian, 2010; Tragin et al., 2016). In cases in which we were able to identify the remains of higher organisms at class level at least, they have been structured according to known classifications as well: Marley et al. (2011) for the tardigrades and Fauchald (1977) and Struck et al. (2006) for the eunicid polychaete worms. Acritarchs are classified according to Downie et al. (1963). Remaining unidentified organic microfossils and reworked palynomorphs are listed at the end of our review.

4 Background and terminology

Because this review comprises the remains from a very broad array of organic microplankton, we first provide background information for the larger microplankton groups. First, relevant descriptive terminology for each of the palynomorph types is given to aid the morphological descriptions of each species in the Results section. Second, we explain on a superordinate level the relationship between the microfossils in the sediments and their species living in the water column from which they originate and how we can interpret these in terms of environmental conditions. Species-specific ecological preferences are discussed in the Results section in more detail.

4.1 Dinoflagellates and their cysts

4.1.1 Descriptive terminology

Dinoflagellate cysts are produced as part of a dinoflagellate's life cycle. Dinoflagellate cysts are characterized by a cingulum and sulcus, the shallow depressions that mark the position of the two flagella of the dinoflagellate and an archaeopyle, the hole through which the living dinoflagellate escapes its cyst (Evitt, 1985). Dinoflagellate cysts can be produced by thecate (armoured) and athecate (naked) dinoflagellates. In the case of thecate dinoflagellates the tabulation of the cyst (paratabulation) reflects the tabulation (plate arrangement) of the theca, which is unique for each species (Evitt, 1985). In these cysts, the archaeopyle is often formed through the loss of a distinct set of paraplates, which is used for classification (Fensome et al., 1993). Furthermore, dinoflagellate cysts can possess a wide variety of wall ornamentations that either reflect the tabulation of the theca of the motile cell or do not correspond to this tabulation at all (Evitt, 1985). The larger morphological diversity of dinoflagellate cysts versus motile dinoflagellates as well as their stratigraphic application has led to a taxonomic classification for cysts separate from the classification of the biological species (Evitt, 1985). Because the biological species is unknown for many dinoflagellate cysts, we also apply the classification of dinoflagellate cysts and primarily list the dinoflagellate cyst taxa below unless the dinoflagellate cyst has none, in which case we use 'Cyst of [*biological taxon*]'

4.1.2 Fossil-plankton-ecosystem relationships

In the Southern Ocean, dinoflagellates form one of the largest microplankton group after diatoms and *Phaeocystis*, blooming in late summer in response to the sea-ice decline and phytoplankton (i.e. diatom) blooms (Garrison and Buck, 1989; Andreoli et al., 1995; Clarke and Leakey, 1996; Assmy et al., 2014). The taxonomic diversity includes species with various life strategies including heterotrophic and phototrophic lifestyles, parasitism, symbiosis and phagotrophy (Evitt, 1985). Among heterotrophic dinoflagellates, a wide variety of feeding strategies is applied to a large variation of prey, including prey that is larger than the dinoflagellates themselves (Jacobson, 1999). Therefore, they can be important for top-down control of phytoplankton blooms (Bjørnsen and Kuparinen, 1991). However, because only a minority of dinoflagellates produces cysts, which can be preserved in the sediments (Evitt, 1985), the cysts found in Hole U1357B are not representative of the total dinoflagellate abundance and diversity in the surface waters. The cysts of dinoflagellates have, however, proven to be powerful tools for reconstructing past sea surface-water conditions, because their distribution in the surface sediments has been linked to specific surface-water environmental conditions, such as temperature and

productivity (e.g., Pross & Brinkhuis 2005; Esper & Zonneveld 2007). Although dinoflagellate cyst assemblages do not show much species diversity in most Holocene ice-proximal Southern Ocean records (Harland et al., 1999; Howe et al., 2002; Esper and Zonneveld, 2007) or within recent sediments (Marret and De Vernal, 1997; Harland et al., 1998; Wrenn et al., 1998; Harland and Pudsey, 1999; Marret et al., 2001; Esper and Zonneveld, 2002, 2007; Pieńkowski et al., 2013b; Prebble et al., 2013), the distribution of dinoflagellate cysts in the sediments has been linked to the Southern Ocean fronts and the sea-ice extent (Marret and De Vernal, 1997; Harland et al., 1998; Esper and Zonneveld, 2002, 2007; Prebble et al., 2013). As they become generally very scarce south of the maximum sea-ice edge (Marret and De Vernal, 1997; Harland et al., 1998), dinoflagellate cyst abundances have been useful for inferring the position of the maximum sea-ice edge throughout the Quaternary (Harland et al., 1999; Howe et al., 2002). South of the Subantarctic Front, the dinoflagellate cyst assemblage in the surface sediments is dominated by heterotrophic species (Marret and De Vernal, 1997; Harland et al., 1998; Esper and Zonneveld, 2002, 2007; Prebble et al., 2013). This means that prey availability likely determines their distribution in the surface sediments. For example, it has been shown that the dominance of a certain heterotrophic dinoflagellate species in the water column is in part controlled by the size of the available prey, as certain prey is too large for some types of feeding strategies that dinoflagellates apply (Assmy et al., 2014).

While dinoflagellate cysts are usually found in surface sediments, the cyst of the photosynthetic dinoflagellate *Polarella glacialis* is abundant in the sea ice and underlying waters (Montresor et al., 1999, 2003 and references therein), but it has seldom been found in surface sediments (Ichinomiya et al., 2008; Heikkilä et al., 2014). Instead, its biogeographic distribution is based on reports from fast ice along the Antarctic coast (Thomson et al., 2006) and DNA extraction from water column and sediment samples (Rengefors et al., 2008; Boere et al., 2009).

4.2 Tintinnid loricae

4.2.1 Descriptive terminology

Unlike other spirotrich ciliates, tintinnids are the only group that produces a shell, the so-called lorica. These loricae have an oral opening at the anterior end through which adoral membranelles (used for swimming and feeding) of the ciliate protrude when the tintinnid is in its extended state (Agatha et al., 2013). In most cases the lorica is larger than the cell proper so that it is able to retract within the lorica for protection (Agatha et al., 2013). The posterior end of the lorica can have various forms (a.o. conical, globular or tubular) and the anterior collar can possess openings (fenestrae). The vast majority of tintinnids build a transparent lorica, known as a hyaline lorica (Agatha et al., 2013).

However, a selection of tintinnid genera agglomerates mineral or biogenic particles to their lorica to form a so-called hard lorica, or a lorica with a hard bowl if the particles only stick to the posterior end (Agatha et al., 2013). Palynological treatment with hydrochloric and hydrofluoric acid will dissolve the siliceous and carbonate microfossils (e.g., diatom frustules and coccoliths) of the tintinnids with hard lorica. However, most of the underlying organic shells of hard loricae and hyaline loricae are able to withstand these acid treatments (Agatha and Simon, 2012). The lorica is probably built from crystalline proteins (Agatha and Simon, 2012; Agatha et al., 2013), which also makes it resistant to a certain degree of diagenesis. For this reason, tintinnids can be used as environmental proxies in palynological studies. This is, however, not common practice. Tintinnids have been used in Antarctic paleoenvironmental reconstructions before (Ace Lake, Antarctica), although no palynological treatment was applied here (Cromer et al., 2005).

Because the shape of the lorica is species specific, identification can be achieved at species level based on the lorica only. However, there is an increasing awareness of considerable morphological plasticity within species, which is related to the life cycle stages of the ciliate (Boltovskoy et al., 1990; Wasik, 1998; Agatha et al., 2013; Dolan et al., 2013b). The intraspecific morphological varieties of several Antarctic species were recently confirmed by a genetic study (Kim et al., 2013).

4.2.2 Fossil-plankton-ecosystem relationships

Within the Southern Ocean there is a large diversity of endemic and more widespread species (Dolan et al., 2012). The geographic distribution of Southern Ocean tintinnids, based on plankton studies, shows that there is a relation between the distribution of tintinnids and the Southern Ocean fronts (Dolan et al., 2012). In general, however, tintinnids are only a minority component of the microzooplankton in the Southern Ocean compared to, for example, heterotrophic dinoflagellates (Dolan et al., 2012). Tintinnids feed on a wide variety of prey ranging from picozooplankton to microzooplankton size, including diatoms, dinoflagellates and chlorophytes (Montagnes, 2013). Remains of the latter two taxonomic groups in particular have also been found in Hole U1357B. Furthermore, it has been shown that species endemic to the Antarctic coastal waters become relatively more abundant when the phytoplankton community is dominated by *Phaeocystis* (Dolan et al., 2013b). It is, however, uncertain whether a predator-prey relationship is involved here, as spirotrich ciliates in general are known to have difficulty preying on *Phaeocystis* colonies and only feed on individual cells (Dolan et al., 2013b). The range of organisms that feed on tintinnids is also extensive, but reported predators of the tintinnids endemic to the Antarctic are limited to copepods, small malacostracans (e.g., krill) and ostracods (Stoecker, 2013).

4.3 Foraminifer linings

4.3.1 Descriptive terminology

Mainly benthic foraminifera produce a foraminiferal lining between their cytoplasm and their calcareous or arenaceous shell (De Vernal, 2009). However, planktonic species produce an inner lining as well (Hemleben et al., 1977), some of which may be preserved in the sediments (Arai and Koutsoukos, 1998). Our focus here lies on the linings of benthic foraminifera, which remain after the calcareous or arenaceous shell has been dissolved. Dissolution can occur in the sediment pore waters or after palynological processing. Foraminiferal linings are composed of a complex mixture of polysaccharide and protein macromolecules with some chitin derivatives and even traces of lignin derivatives (Ní Fhlaithearta et al., 2013), which makes most linings resistant to lithification processes and palynological acid treatments. However, not all foraminiferal linings survive lithification and acid treatment. It has been suggested for calcareous benthic foraminifera that the thickness, and therefore its preservation potential, is linked to the thickness of the calcareous test and therefore the capacity of the foraminifer to bind magnesium (Ní Fhlaithearta et al., 2013). At Site U1357, calcareous tests of benthic foraminifera have been recorded (Expedition 318 Scientists, 2011b). Similar to the tests, the foraminiferal linings occur in various forms, and can be recognized as a series of spherical or half-moon-shaped, reddish brown chambers arranged in a spiral form (trochospiral or planispiral), as a bunch of grapes (triserial), or as a bead necklace (uniserial).

4.3.2 Fossil-organism-ecosystem relationships

Because benthic foraminiferal linings are preserved better than the calcareous shell, which may dissolve in the sediment pore waters, they have been considered a better representation of benthic (paleo)productivity than the calcareous shells (De Vernal, 2009). Benthic productivity is controlled mainly by the availability of free oxygen in the bottom waters and the nutrient supply from the surface waters (Jorissen et al., 1995; Thomas et al., 1995), which links the productivity at the sea floor to surface-water productivity. It has been suggested that the abundance of epifaunal versus infaunal species is directly related to the amount of organic material that reaches the sea floor (Thomas et al., 1995). However, high abundances of epifaunal species could also reflect a well-ventilated bottom-water environment with pulsed high primary productivity in the surface waters (Jorissen et al., 1995; Thomas et al., 1995; Costello and Bauch, 1997). Conversely, high abundances of infaunal species could reflect regions with high surface-water productivity and a sustained flux of organic matter to the sea floor, which consumes oxygen and could result in low oxygen concentrations in the bottom waters (Thomas et al., 1995). Although it is not always possible to determine the foraminifer species from the benthic foraminifer linings,

uniserial or triserial forms are generally infaunal, while trochospiral forms are more commonly epifaunal (Corliss, 1991).

4.4 Prasinophyte phycomata

4.4.1 Descriptive terminology

Phycomata are the reproductive cysts formed during the asexual reproduction of scaled green algae (prasinophytes). Although many prasinophytes produce cysts (e.g., Daugbjerg 2000; Moro et al. 2002; Moestrup et al. 2003), these appear to be mostly polysaccharide in nature and are therefore not preserved in the sediments (O’Kelly, 2007). However, within the order of Pyramimonadales, one of the most basal clades of green algae (Nakayama et al., 1998; Guillou et al., 2004; Suda et al., 2013), the family of Halosphaeraceae make a multilayered phycoma (resting spore) of which at least one of the layers is made from sporopollenin, which makes them fossilizable (Colbath and Grenfell, 1995). Originally the phycomata of prasinophytes found in the fossil record were classified as acritarchs until the resemblance was noticed between the former acritarchs *Cymatiosphaera* and *Pterospermella* and the phycomata of species of *Pterosperma* (Martin, 1993). Various types of prasinophyte phycomata are known from palynological records (Martin, 1993; Colbath and Grenfell, 1995; Mudie et al., 2011). Because many of them were originally formally described from sedimentary deposits, these phycomata have their own taxon (Colbath and Grenfell, 1995). The surface wall of prasinophyte phycomata can be smooth or ornamented, including the presence of pores and (equatorial) wings or ridges, which are termed alae (Parke et al., 1978; Colbath and Grenfell, 1995).

4.4.2 Fossil-plankton-ecosystem relationships

Prasinophytes are predominantly marine plankton (Parke et al. 1978; O’Kelly, 2007). In addition, studies based on pigment signatures of Antarctic seawater show that prasinophyte abundances in general increase during periods of decreased stratification (Rozema et al., 2017) with the highest prasinophyte pigments found offshore below the mixed layer depth (Hashihama et al., 2008; Kozłowski et al., 2011). Because stratification along the Antarctic coast is directly related to the presence of sea ice and/or meltwater run-off from the continent, increased amounts of prasinophytes should instead reflect more open ocean conditions (Rozema et al., 2017). However, some prasinophytes occur in fresh and brackish water environments, and fossil phycomata of prasinophytes have mainly been found in association with inshore shallow lagoonal and deltaic environments (Mudie et al., 2010). Also in the Arctic, pigment signatures show that the highest prasinophyte concentrations are located in cool, nitrogen-depleted, meltwater-influenced surface waters (Fujiwara et al., 2014). It is possible that these Arctic prasinophytes are different species than those living offshore of Antarctica and therefore have different

environmental preferences, but species-specific ecological preferences for phycomate prasinophytes (i.e. Halosphaeraceae) are not available. Species-specific biogeographic information has been mainly obtained from phytoplankton checklists (Moita & Vilarinho 1999; Hällfors 2004; Guilloux et al. 2013; Medvedeva & Nikulina 2014; Veen et al. 2015; Cărauş 2017) and the online Global Biodiversity Information Facility (GBIF: <https://www.gbif-iat.org/>, last access 23 September 2018) and is therefore rather patchy. Ecological inferences based on the presence of prasinophyte phycomata should therefore be made carefully, in particular because ecologically the Pyramimonadales (including Halosphaeraceae) only represent a minor component of the green algae (Tragin et al., 2016). It is known, however, that several species within Pyramimonadales have been associated with sea-ice-dominated environments of the Antarctic (Daugbjerg, 2000; Moro et al., 2002). This is also evident from the fossil record in which fossil prasinophyte phycomata have been found in sediment cores and surface sediments from the shelves of the Ross Sea, Prydz Bay and the Antarctic Peninsula (Hannah et al., 1998; Wrenn et al., 1998; Hannah, 2006; Warny et al., 2006, 2009; Warny, 2009; Clowes et al., 2016). In sea-ice-dominated environments, fossil prasinophyte phycomata have been associated with the sea-ice edge and increased stratification after sea-ice retreat (Mudie et al., 1992; Wrenn et al., 1998; Hannah, 2006). Pyramimonadales are considered important spring bloomers around Antarctica (Varela et al., 2002) and Greenland (Harðardóttir et al., 2014) and might be important in maintaining the heterotrophic microbial community during the winter (Harðardóttir et al., 2014). Although prasinophytes are predominantly autotrophic, mixotrophy has also been reported as a means to survive the cold light-limited Antarctic winters (Bell and Laybourn-Parry, 2003).

4.5 Scolecodonts

4.5.1 Descriptive terminology

While annelids are soft-bodied organisms and generally do not fossilize, the hardened jaw parts of eunicid annelids are commonly found in fossil assemblages dating back to the late Cambrian (Struck et al., 2006). In this context they are commonly known as ‘scolecodonts’ (Struck et al., 2006). The eunicid jaw apparatus consists of mandibles and rows of maxillary pieces with or without carrier (Fauchald, 1977; Struck et al., 2006). Jaw morphologies are quite similar between taxa, but in general three major types are distinguished based on the number of maxillae and the shape of the carrier: ctenognath, prionognath and labidognath (Struck et al., 2006).

4.5.2 Fossil-plankton-ecosystem relationships

Scolecodonts have been reported from Cretaceous, Oligocene and Miocene Antarctic drill holes or outcrops (Szaniawski and Wrona, 1987; Hannah et al., 2000;

Amenábar et al., 2014; Warny et al., 2016), but never as such from Antarctic or Southern Ocean Holocene deposits. Considering that scolecodonts are the remains of benthic organisms, their presence is indicative of oxygenated bottom-water conditions. Still, when part of the palynological assemblage, scolecodonts are generally not used for paleoenvironmental interpretation because eucnid mandible parts are often difficult to relate to extant taxa and difficult to distinguish from the sclerotized mouthparts of cladocerans and chaetognaths (Mudie et al., 2011). Possible scolecodonts are discussed in section 5.7 'Palynomorphs of unknown affinity'. The characteristics of eucnid jaw apparatuses have, however, been extensively compared at family level and their phylogenetic relationships have been discussed (Fauchald, 1977; Struck et al., 2006). We are therefore fairly certain that the eucnid jaws found in the samples of Hole U1357B are of the ctenognath type (relatively large basal maxillae and symmetrical rows of numerous anterior denticles in longitudinal series without carriers) and therefore belong to the family of Dorvilleidae (Struck et al., 2006).

The knowledge of Antarctic or Southern Ocean dorvilleids is limited, but recently the experimental deployment of whale bones off the coast of Deception Island (South Shetland Islands) has led to the discovery of some new dorvilleid species: these include *Parougia diapason* (Taboada et al., 2015), *Ophryotrocha clava* and *Ophryotrocha orensanzi* (Taboada et al., 2013).

4.6 Arthropod remains

4.6.1 Descriptive terminology

Some of the remains in the samples of Hole U1357B were identified as derived from copepods, but for other thick-walled, yellow, chitinous remains the true biological affinity is unknown. These palynomorphs are possibly derived from crustacean exoskeletons as their appearance resembles that of known copepod remains. We discuss these in section 5.7 'Palynomorphs of unknown affinity'. The palynomorphs that were identified as belonging to copepods are listed under the subclass Copepoda in the Results section. Among these remains are chitinous body parts, but also copepod eggs and spermatophores.

Copepod egg sizes can range between 60 and 300 μm (Koga 1968; van Waveren 1992; Belmonte 1998) and can be a common component in palynological assemblages (van Waveren 1992; Mudie et al. 2010; Mudie et al. 2011; Candel et al. 2013). In general copepods produce two types of eggs: quiescent subitaneous eggs, which are produced under unfavourable environmental conditions and hatch open within a few weeks when conditions improve; and diapause eggs, which are produced when copepod production is highest and during population decline, and will not open until after a gene-controlled

refractory phase is over (Marcus, 1996; Castellani and Lucas, 2003; Katajisto, 2003; Hansen et al., 2010; Berasategui et al., 2012). These diapause eggs are able to remain viable for several decades (Marcus, 1996). Both subitaneous and diapause eggs can be smooth or ornamented, but diapause eggs possess a thicker egg envelope consisting of multiple layers (Santella and Ianora, 1990; Marcus, 1996). Various ornamentation types of subitaneous and diapause eggs have been described, ranging from smooth to reticulate, covered with short, long, and/or branched spines, or with a equatorial wing (Koga, 1968; Santella and Ianora, 1990; Belmonte, 1992, van Waveren 1992; Belmonte, 1998; Hansen et al., 2010). It has been suggested that such surface ornamentation provides protection against carnivores or serves as a floating device (Koga, 1968; Dumont et al., 2002). Some eggs might appear smooth under the light microscope but when viewed under scanning electron microscope are rough or finely tuberculated (Belmonte, 1998; Berasategui et al., 2012). The morphology of the eggs is not known for all of the Southern Ocean species, and studies on copepod reproduction generally report the amount of copepod egg (and also spermatophore) observations and do not describe their morphology (e.g., Swadling 1998; Loots et al. 2009).

4.6.2 Fossil-organism-ecosystem relationships

In palynological studies, fragments of chitinous body parts of arthropods are common components of the non-pollen palynomorph assemblage (Mudie et al., 2011). Marine arthropods (i.e. crustaceans) include the Antarctic krill *Euphausia superba* and amphipods, but in particular copepods as they can comprise more than 75% of the Southern Ocean standing biomass (Atkinson et al., 2012). Copepods are important grazers in the Southern Ocean, feeding predominantly on large-range diatom species (Pasternak and Schnack-Schiel, 2001). However, some species supplement their diets by a certain degree of carnivory, preying on dinoflagellates, small crustaceans and protozoans during early spring, when phytoplankton is still scarce (Atkinson, 1998; Pasternak and Schnack-Schiel, 2001). The production of faecal pellets by copepods is an important mechanism for the export productivity of organic material to the sea floor (Harris, 2001), also in coastal high-latitude water (Fabiano et al., 1997; Smith Jr. et al., 2011), and therefore has likely contributed to the high sedimentation rates in the Adélie Basin. Today, only three species of copepods are found in the sea ice and water column close to our study site in the Adélie Basin: *Drescheriella glacialis*, *Stephos longipes*, and *Paralabidocera antarctica*, the latter of which was the most abundant (Loots et al., 2009).

Taxonomy on the species level is not possible on the exoskeleton parts found in Hole U1357B, because these are fragmentary. However, using the online database “Diversity and Geographic Distribution of Marine Planktonic Copepods” of Razouls et al.

(2005-2017) we have been able to identify several copepod exoskeleton parts. In particular mandibular gnathobases can potentially provide information on the different copepod taxa from which we find the remains in the samples of Hole U1357B. Mandibular gnathobases are the basal parts of the copepod mandibles and are used for crushing and mincing food (Michels and Gorb, 2015). Mandibular gnathobases consist of a chitinous exoskeleton with sockets on which opal teeth (crown- or cap-like structures) are located (Michels and Gorb, 2015). Palynological processing of the material from Hole U1357B will have dissolved these opal teeth, making identification on the species level more difficult. It also means that the sizes, both absolute and relative, of the preserved chitinous tooth sockets do not necessarily represent the original sizes of the teeth that have been dissolved from these sockets. In future studies, it might be possible to quantify copepod diversity if, e.g., eggs and mandibular gnathobases can be identified on the genus or species level. Changes in the diversity of copepod species in the sediments could be related to the sea-ice extent (Swadling, 1998; Loots et al., 2009; Kramer et al., 2011). Because of the difficulties with assigning copepod remains to particular genera or species, a geographic distribution and environmental interpretation are generally not provided for the copepod remains.

4.7 Acritarchs

4.7.1 Descriptive terminology

Acritarchs are hollow, organic-walled and have a wide range of morphologies and surface-wall ornamentations (Martin, 1993). Surface-wall ornamentations can include ridges (septa) or processes (Martin, 1993). Most of the acritarchs described here have a single circular opening or pylome. By convention a single circular opening is said to be apical and a pylome is defined as a (sub)circular opening whose periphery is distinct before excystment (Martin, 1993). The pylome is closed off by a lid, the operculum (Martin, 1993).

4.7.2 Fossil-plankton-ecosystem relationships

Acritarchs are the remains of a variety unicellular biological affinity (red and green algae), although their exact origin is uncertain. Under the group Acritarcha we discuss known acritarchs that have a genus and species name. Other palynomorphs (including hollow organic-walled specimens) with unknown biological affinity are listed in section 5.7 'Palynomorphs of unknown affinity'. The geographic distribution of acritarch species is primarily based on palynological studies of recent marine surface sediments.

4.8 Reworked material

Pollen, spores, and some dinoflagellate cysts recovered from Hole U1357B are considered part of the reworked assemblage as they clearly reflect input from older strata.

The eutardigrade egg found in Hole U1357B is also probably derived from the Antarctic mainland. Modern-day biogeographic information and ecological preferences for these species are therefore not relevant for this study and generally not provided here. However, qualitatively, increased abundances of reworked material could be related to increased iceberg discharge and/or ice-shelf collapse, or submarine slope instability, since early Cenozoic and Cretaceous strata do surface on the Antarctic continental shelf in the region (Expedition 318 Scientists, 2011b).

5 Results

5.1 Dinoflagellate cysts

Kingdom CHROMISTA Cavalier-Smith 1981
Subkingdom HAROSA Cavalier-Smith 2010
Infrakingdom HALVARIA Cavalier-Smith 2010
Superphylum ALVEOLATA Cavalier-Smith 1991
Phylum MIOZOA Cavalier-Smith 1987
Division DINOFLAGELLATA (Bütschli, 1885) Fensome et al. 1993
Subdivision DINOKARYOTA Fensome et al. 1993
Class DINOPHYCEAE Pascher 1914
Subclass GYMNODINIPHYCIDAE Fensome et al. 1993
Order GYMNODINIALES Apstein 1909
Suborder GYMNODINIINEAE Fensome et al. 1993
Family GYMNODINIACEAE Lankester 1885
Genus *Gymnodinium* Stein 1878
Cyst of *Gymnodinium microreticulatum* Bolch et al. 1999 (Plate 2, figure 9–16)

Morphology and identification: These are spherical brown-coloured microreticulate cysts with chasmic archaeopyles. Sometimes only half-cysts are found, when the chasmic archaeopyle has ruptured the cyst in two. Only four modern dinoflagellate species are known to produce these kind of fossilizable cysts and they all belong to the naked (unarmoured) dinoflagellate genus *Gymnodinium*, namely *Gymnodinium catenatum* Graham (cyst described by Anderson et al. 1988), *Gymnodinium nolleri* Ellegaard & Moestrup 1999, *Gymnodinium microreticulatum*, and *Gymnodinium trapeziforme* Attaran-Fariman & Bolch 2007 in Attaran-Fariman et al. (2007). *G. trapeziforme* is, however, not spherical like the specimens found in the samples of Hole U1357B, but subrectangular (Attaran-Fariman et al., 2007). The cysts of the other three species are spherical and look very similar under the light microscope, but they can be distinguished primarily by their colour and size (Bolch et al., 1999). Cysts of *G. microreticulatum* are the smallest of the three species (17–28 µm) and have a pale brown

or purplish brown colour versus the reddish brown of *G. nolleri* and *G. catenatum*. There is, however, some overlap between the size ranges of *G. nolleri* and *G. microreticulatum* (Bolch et al., 1999; Ribeiro et al., 2012a). Still, *G. nolleri* possesses fewer rows of relatively larger paravesicles in the paracingular area (Ribeiro et al., 2012a). In addition, the chasmic archaeopyle *G. microreticulatum* runs along the parasulcus and not along the paracingulum as is the case for the other two species (Bolch et al., 1999). However, paracingular ruptures could be present due to damage during sedimentation (Bolch et al., 1999). Based on the size and pale brown colour of the microreticulate cysts encountered in the samples of Hole U1357B we assign these cysts to *G. microreticulatum*. We have not been able to distinguish a paracingulum due to the small size of the paravesicles, but as *G. nolleri* possesses a paracingulum with better-recognizable larger vesicles this also suggests that our specimens are *G. microreticulatum*.

Biological taxon: *Gymnodinium microreticulatum*.

Dimensions: Cysts diameters range between 28 and 36 μm (average: 31 μm , n=8).

Geographic distribution: The distribution of microreticulate *Gymnodinium* cysts in coastal marine sediments is rather patchy and is probably influenced by ship ballast water (Hallegraeff, 1998; Bolch and Reynolds, 2002). The highest abundances of cysts of *G. microreticulatum* have been found in surface sediments of southern Australia and Tasmania, but also in Uruguay, Hong Kong, the Chinese coast, the Russian east coast and Portugal (Amorim et al., 2001; Bolch and Reynolds, 2002; Orlova et al., 2004; Ribeiro et al., 2012a, 2016).

The fossil record: Palynological records of cyst-forming *Gymnodinium* species are sparse. To our knowledge records are only available from the Kattegat (south-western Scandinavia) (Thorsen et al., 1995; Fjellså and Nordberg, 1996), the Adriatic Sea (Sangiorgi and Donders, 2004), and the Portuguese margin (Ribeiro et al., 2012a, 2016). There are therefore no published records of *G. microreticulatum* in the Southern Ocean. However, there is one account that states that *G. microreticulatum* has only been introduced in southern Australian waters within the past 50 years (McMinn, 2002).

Ecological preferences and environmental interpretation: The large distribution area renders this species a generalist: the associated broad temperature and salinity range makes it difficult to infer ecological preferences. Culture experiments have only been performed with a temperature range of 17°C - 25°C and 26-35 g/L (Bolch et al., 1999). However, its occurrence in samples of Hole U1357B suggests it is able to live under much cooler temperature conditions. All three spherical cyst-forming *Gymnodinium* species are autotrophic, and increased abundances of the three species have been associated with an increased influence of warmer waters and surface-water stratification (Ribeiro et al., 2016). Notably, however, cysts of *Gymnodinium* cf. *catenatum* have also been found in

northern high latitudes along the Russian east coast (Orlova et al., 2004), thereby confirming the ability of spherical cyst-forming *Gymnodinium* species to live in relatively colder waters.

Order SUESSIALES Fensome et al. 1993

Family SUESSIACEAE Fensome et al. 1993

Genus *Polarella* Montresor, Procaccini & Stoecker 1999

Cysts of *Polarella glacialis* Montresor, Procaccini & Stoecker 1999 (Plate 2, figure 21-23)

Morphology and identification: This is a small, ovoidal, transparent cyst with more than 40 solid, spiny processes. The cyst wall is relatively thick. Most specimens have been found with cell content. Paratabulation is not visible on the cyst underneath the light microscope, but it is known from scanning electron microscope images that each spiny process reflects a paraplate (Montresor et al., 1999). This species was described from the brine in upper sea ice at McMurdo Sound, Ross Sea and is the first account of a free-living species in the order Suessiales, which before its official description only included fossil taxa and symbionts (Montresor et al., 1999).

Biological taxon: *Polarella glacialis*.

Dimensions: The cyst length is $14 \pm 1 \mu\text{m}$ ($n=3$).

Geographic distribution: The occurrence of its cysts in fast ice of the Weddell Sea (Buck et al., 1992), Ross Sea (Stoecker et al., 1997; Montresor et al., 1999; Andreoli et al., 2000) and Prydz Bay areas (Thomson et al. 2004; 2006), but also in water samples from Prydz Bay (Rengefors et al., 2008) and the Arctic (Montresor et al. 2003 and references therein), indicate an Antarctic circumpolar and bipolar distribution for *Polarella glacialis*. There are only a few accounts of cysts of *P. glacialis* in surface sediments: from the Hudson Bay area (Heikkilä et al., 2014) and off the coast near Syowa station, Queen Maud Land, Antarctica (Ichinomiya et al., 2008), and the Ross Sea (Francesca Sangiorgi, unpubl. data).

The fossil record: Cysts (and fossil 18S rDNA) of *P. glacialis* have rarely been found in surface sediments and never below the upper few centimetres of sediment cores (Ichinomiya et al., 2008; Boere et al., 2009; Heikkilä et al., 2014), which may be because the cyst lacks dinosporin allowing for long-term preservation (Montresor et al., 1999). The fact that we find cysts of *P. glacialis* several metres deep underlines the exceptional preservation of organic matter in Hole U1357B.

Ecological preferences and environmental interpretation: In Hole U1357B *Polarella glacialis* is one of the three autotrophic dinoflagellate species (the others being *G. microreticulatum* and *Impagidinium pallidum*) that were found *in situ*. It has been shown that the highest concentrations of *P. glacialis* occur in the upper ice layers of fast ice, but are generally poorly represented in pack ice (Stoecker et al., 1997; Andreoli et al., 2000;

Thomson et al., 2006). Mass excystment of *P. glacialis* occurs at -6°C and 100 psu in austral spring (around early November) after which the number of cells increases until early December (Stoecker et al., 1997; Thomson et al., 2006). Sexual reproduction takes place at around -2°C and 37 psu followed by encystment (Thomson et al., 2006). Large amounts of these cysts are released into the water column through brine rejection in late spring (Thomson et al., 2006). Considering the low preservational potential, the presence of *P. glacialis* is indicative of the nearby fast ice extending from the Antarctic coast, but should be interpreted as a preservation signal as the disappearance of *P. glacialis* from the sedimentary record does not necessarily mean the fast ice has retreated.

Subclass PERIDINIPHYCIDAE Fensome et al. 1993
Order GONYAULACALES Taylor 1980
Suborder GONYAULACINEAE (autonym)
Family GONYAULACACEAE Lindemann 1928
Subfamily GONYAULACOIDEAE Fensome et al. 1993
Genus *Impagidinium* Stover & Evitt 1978
Impagidinium pallidum Bujak 1984 (Plate 1, figure 29–35)

Morphology and identification: This species possesses very high septa (up to 15 µm) compared to the cyst diameter. Unlike other *Impagidinium* species these septa are not placed on a central body, but together form a thin-walled envelop with polygonal fields. The cyst is very transparent and can therefore be easily overlooked. However, in the samples of U1357B it is commonly found with a spherical body with cell content inside the transparent cyst.

Biological taxon: Cyst of *Gonyaulax* sp. indet. (Head, 1996; Zonneveld et al., 2013).

Dimensions: The cyst lengths range between 59 and 102 µm (average: 77µm, n=5) and the diameter of the central spherical body is 39±10 µm (n=3).

Geographic distribution: The highest relative abundances of *I. pallidum* are observed in areas influenced by the melt-back of seasonal sea ice in both the Arctic and the Antarctic (Mudie, 1992; Marret and De Vernal, 1997; De Vernal et al., 2001; Kunz-Pirrung et al., 2001; Esper and Zonneveld, 2007; Bonnet et al., 2010; Pieńkowski et al., 2013b; Zonneveld et al., 2013). In the Southern Ocean, it is generally restricted to waters south of the Subtropical Front (Marret and De Vernal, 1997; Crouch et al., 2010; Verleye and Louwye, 2010; Prebble et al., 2013), but remarkably very low amounts of *I. pallidum* have been found in surface samples of the south-east Atlantic Ocean (Esper and Zonneveld, 2002). In the Arctic, highest abundances of *I. pallidum* cysts are found in sediments of the deeper parts of the Arctic basins underlying the pack-ice margin (Mudie,

1992; Mudie and Harland, 1996). However, specimens of *I. pallidum* have been found in the Mediterranean and equatorial east Atlantic (Zonneveld et al., 2013).

The fossil record: *I. pallidum* is a particularly long-ranging species. Notably, it was first described from North Pacific sediments with ages ranging from the late Eocene to Pleistocene (Bujak, 1984). Also in the Southern Ocean, occurrences of *I. pallidum* date back as far as the Oligocene (Stocchi et al., 2013; Bijl et al., 2018b). Temperatures close to the Antarctic margin at that time were much warmer than today (Petersen & Schrag 2015; **Chapter 6**) and it has been suggested that it was still able to tolerate much warmer temperatures during Pliocene-Pleistocene times, which could explain its modern bipolar distribution (De Schepper et al., 2011). This is also supported by accounts of *I. pallidum* from Oligocene to Pliocene strata from the Mediterranean area (Versteegh and Zonneveld, 1994; Zevenboom et al. 1994). In more recent Quaternary records of the Southern Ocean, the highest abundances of *I. pallidum* have been found during the interglacial stages south of the Subantarctic Front (SAF) (Esper and Zonneveld, 2007). North of the SAF the highest abundances are found during the glacial stages (Marret et al., 2001).

Ecological preferences and environmental interpretation: This is one of the three autotrophic dinoflagellate cyst species encountered in the samples of Hole U1357B. In both the Arctic and the Antarctic, cysts are associated with temperatures between -1.7°C and 5.4°C (Mudie, 1992; De Vernal et al., 1997; Marret and De Vernal, 1997; Esper and Zonneveld, 2007; Zonneveld et al., 2013). In palynological records it is therefore also generally treated as a cold-water species (De Vernal et al., 2001; Brinkhuis et al., 2003), although it seems to have been more tolerant to warmer temperatures in the past (Versteegh and Zonneveld, 1994; Sangiorgi et al., 2018). Its affinity for the pack-ice margin in the Arctic could mean an affinity for the seasonal meltback and the associated stratification and nutrient release (Mudie, 1992; Mudie and Harland, 1996). Also around Antarctica it is most abundant in nutrient-rich waters south of the APF and the seasonal sea-ice zone (Marret and De Vernal, 1997; Marret et al., 2001; Esper and Zonneveld, 2007).

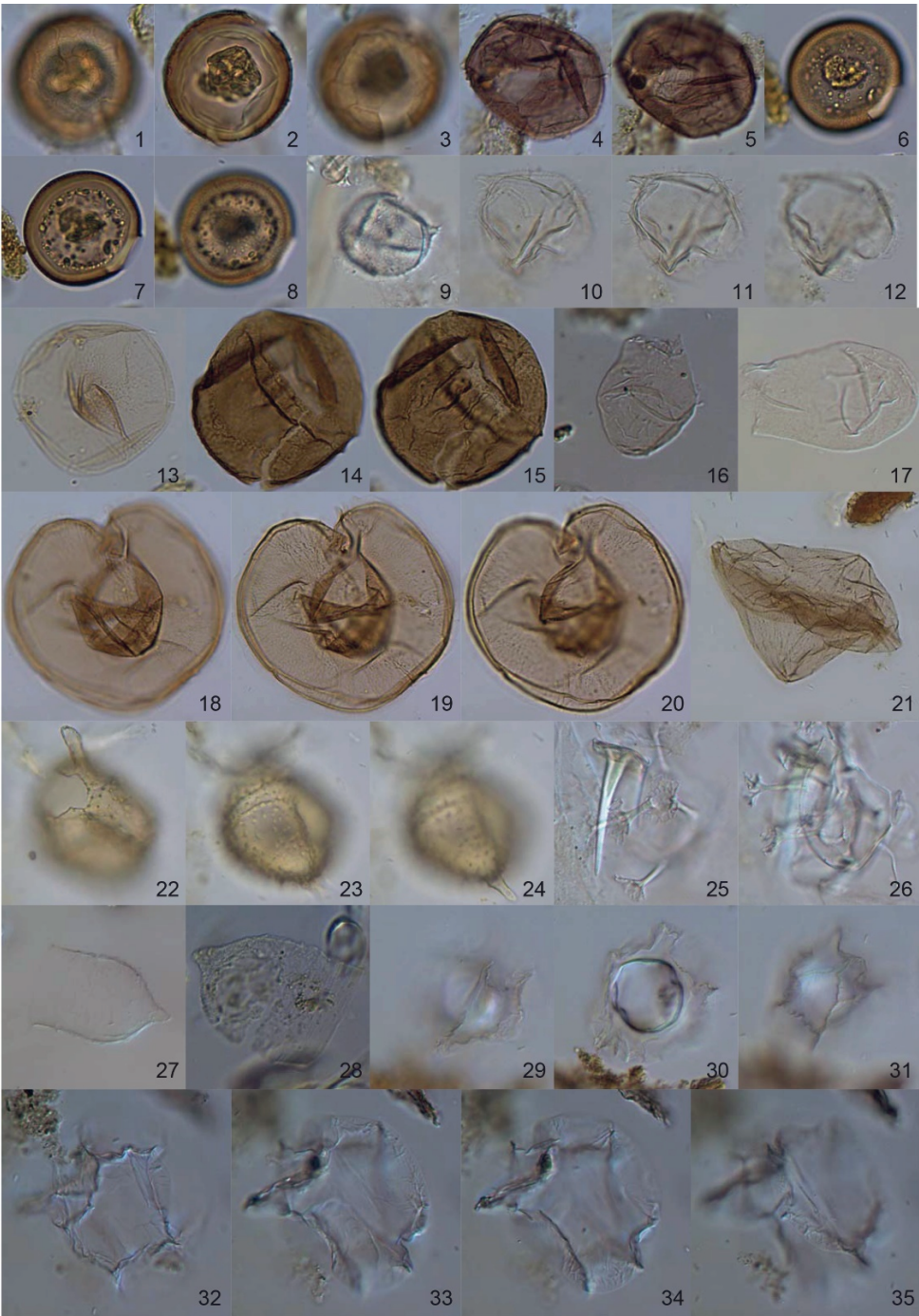


Plate 1 (previous page):

Figure 1-3: *Cryodinium meridianum* with cell content and faint septa, U1357B-16H-1W 63–65 cm, slide 1, E.F.: E17.2, upper, mid and lower focus.

Figure 4-5: *Cryodinium meridianum* flattened with clear septa, U1357B-8H-3W 54–56 cm, slide 1, E.F.: U28.4, upper and lower focus.

Figure 6-8: *Cryodinium* sp. 1 with cell content, U1357B-16H-1W 63–65 cm, slide 1, E.F.: O18.2, upper, mid and lower focus.

Figure 9: *Vozzhennikovia* aperture, oblique antapical view, U1357B-3H-7W 10–12 cm, slide 1, E.F.: J23.4, lower focus.

Figure 10-12: *Spinidinium colemani*, oblique dorsal view, U1357B-2H-4W 111–113 cm, slide 1, E.F.: E20.2, upper, mid and lower focus.

Figure 13: *Selenopemphix antarctica*, (ant)apical view, U1357B-18H-4W 2–3 cm, slide 1, E.F.: D35.2, upper focus.

Figure 14-15: *Nucicla umbiliphora*, dorsal side up, U1357B-6H-4W 86–88 cm, slide 1, E.F.: K24.1, upper and lower focus.

Figure 16: *Dictyocystid lorica* sac, U1357B-16H-1W 63–65 cm, slide 1, E.F.: G21.4.

Figure 17: *Dictyocystid lorica* sac, U1357B-17H-1W 18–20 cm, slide 1, E.F.: E25.1.

Figure 18-20: *Selenopemphix* sp. 1 sensu Esper & Zonneveld 2007, antapical side up, U1357B-6H-4W 86–88 cm, slide 1, E.F.: T30.4, upper, mid and lower focus.

Figure 21: *Selenopemphix* sp. 1 sensu Esper & Zonneveld 2007, lateral view, U1357B-19H-2W 39–41 cm, slide 1, E.F.: J29.4, LIB image.

Figure 22-24: *Vozzhennikovia netrona*, oblique apical view, U1357B-19H-2W 39–41 cm, slide 1, E.F.: F24.1, upper and lower focus, and lower focus on the antapical horn.

Figure 25-26: *Enneadocysta dictyostila*, lateral view, U1357B-6H-6W 123–125 cm, slide 1, E.F.: J28.3, upper focus on the ragged clypeate processes and mid focus.

Figure 27: *Codonellopsis glacialis*, U1357B-1H-2W 40–42 cm, slide 1, E.F.: K24.1, LIB image.

Figure 28: *Codonellopsis glacialis*, U1357B-5H-7W 5–7 cm, slide 1, E.F.: N31.3.

Figure 29-31: *Impagidinium pallidum* with internal spherical body, U1357B-17H-5W 97–99 cm, slide 1, E.F.: H32.4, upper, mid and lower focus.

Figure 32-35: *Impagidinium pallidum*, U1357B-18H-4W 2–3 cm, slide 1, E.F.: K33.1, upper focus, mid focus on upper right septa, mid focus on lower septa and lower focus.

Order PERIDINIALES Haeckel 1894

Suborder PERIDINIINEAE Fensome et al. 1993

Family PROTOPERIDINIACEAE (Bujak and Davies *in* Fensome et al 1998) (Fensome et al. 1998)

Subfamily PROTOPERIDINIOIDEAE Bujak and Davies 1983

Genus *Cryodinium* Esper et Zonneveld 2002

Cryodinium meridianum Esper et Zonneveld 2002 (Plate 1, figure 1–5)

Morphology and identification: *Cryodinium meridianum* is a brown, spherical, scabrate dinoflagellate cyst with septa (ridges) reflecting the paratabulation (Esper and Zonneveld, 2002). As in the original description of the species, the height of the septa of the specimens in Hole U1357B is highly variable and can be very faint in the specimens of Hole U1357B. The combination of scabration and low septa is very characteristic and allows for identification even if the archaeopyle, which is formed through the loss of two

intercalary plates (Esper and Zonneveld, 2002), is not very clear. Some specimens in the samples of Hole U1357B still contain cell content.

Biological taxon: Cyst of unknown dinoflagellate (Esper and Zonneveld, 2002).

Dimensions: Cyst diameters range between 40 and 56 μm (average: 46 μm , $n=13$).

Geographic distribution: This species has been first described from surface sediments as endemic between the Antarctic Polar Front (APF) and the Weddell Sea Gyre with its highest abundances most distal from the coastline (Esper and Zonneveld, 2002). In later studies it has been reported from surface samples and Quaternary records from the South Atlantic (Esper and Zonneveld, 2007), the Prydz Bay area (Storkey, 2006; Boere et al., 2009), the south-eastern Pacific (Zonneveld et al., 2013), and most recently from the northern South China Sea (Li et al., 2017).

Ecological affinities and interpretation: Infrared analyses of modern cysts suggest that the brown protoperidinioid dinoflagellate cysts have a cyst wall chemistry that is distinctly different from the cyst wall chemistry of transparent autotrophic gonyaulacoid cysts, but similar to cyst of the distantly related heterotrophic gymnodinioid *Polykrikos* spp. (Ellegaard et al., 2013). It is therefore likely that the chemical composition of the cyst wall is determined by lifestyle (Ellegaard et al., 2013). This is also the reason why modern brown dinoflagellate cysts are generally considered heterotrophic. In the original description of *C. meridianum*, it is also considered as such and associated with the high phytoplankton concentrations within the Polar Frontal Zone (PFZ) and the Antarctic Zone (AZ) (Esper and Zonneveld, 2002). Because of this exclusive distribution within the PFZ and the AZ it is restricted to waters with a maximum summer temperature of 13.7°C (Zonneveld et al., 2013). Recently, however, *C. meridianum* has been reported from the northern South China Sea, where it is oddly listed as an autotrophic species by Li et al. (2017). The species is, however, not discussed by Li et al. (2017) and no pictures of the species are provided rendering the validity of its occurrence in the South China Sea difficult to prove.

Cryodinium sp. 1 (Plate 1, figure 6–8)

Morphology and identification: In addition to *Cryodinium meridianum*, we regularly encountered cysts similar to *C. meridianum*, but which lack the septa. Still, these cysts have the typical scabration and 2I archaeopyle of *C. meridianum*.

Biological taxon: Cyst of unknown dinoflagellate.

Dimensions: They are of equal size as *C. meridianum* (48 ± 1 μm , $n=3$).

Geographic distribution: There are no previous reports of this species from modern-day surface sediments. This is a new species, which will be formally described elsewhere.

The fossil record: Although there are no previous reports of granulated round brown cysts with a 2I archaeopyle, granulated round brown cysts (archaeopyle unknown) have been reported from Quaternary cores from the southern Atlantic Ocean as *Protoperidinium* sp. 1 (Esper and Zonneveld, 2007). These cysts are particularly abundant during Marine Isotope Stage 2 just north of the modern-day Antarctic Polar Front (APF), and also during marine isotope interglacial stages south of the modern-day APF (Esper and Zonneveld, 2007).

Ecological preferences and environmental interpretation: It is possible that these cysts belong to the same biological species as *C. meridianum* but that the cyst morphology is controlled by environmental conditions. There are other examples of morphological variations in cysts due to changes in environmental parameters. For instance, *Lingulodinium* and *Operculodinium* cyst process lengths have been related to changes in salinity (De Vernal et al., 1989; Mertens et al., 2009).

Genus *Echinidinium* Zonneveld 1997 ex Head, Harland & Matthiessen 2001
Echinidinium sleipnerensis Head, Riding, Eidvin & Chadwick 2004 (Plate 2, figure 1–8)

Morphology and identification: In most of the core samples of Hole U1357B brown dinoflagellate cysts with numerous solid and/or apiculocavate processes can be found. Multiple round brown spiny dinoflagellate cyst taxa have been described, which can be distinguished based on the shape and hollowness of their processes and the granulation of the central body (Radi et al., 2013). Identification by archaeopyle type is often difficult, as the archaeopyle is rarely observed and/or not known for certain species. Based on the absence of granulation in all specimens encountered in Hole U1357B and some specimens exhibiting an archaeopyle that resembles a therophylic slit, we have identified the round brown spiny cysts of Hole U1357B as *Echinidinium sleipnerensis* (Head et al., 2004; Radi et al., 2013).

Biological taxon: Cyst of unknown dinoflagellate. However, like all other modern-day round brown spiny cysts the motile cell is likely protoperidinioid and heterotrophic (Radi et al., 2013; Ellegaard et al., 2013).

Dimensions: Cysts are between 29 and 46 μm in diameter (average: 41 μm , $n=8$).

Geographic distribution: No record of *E. sleipnerensis* has been published since its formal description by Head et al. (2004), except for a single mentioning as 0.003% of the total dinoflagellate cyst abundance in a surface sediment survey of a Tunisian lagoon (Fertouna-Bellakhal et al., 2014). Because the archaeopyle of brown spiny cysts is generally difficult to distinguish, it is possible that earlier finds of *E. sleipnerensis* were misidentified (Radi et al., 2013). For example, *Islandinium minutum* cysts look very similar to *E. sleipnerensis*, but instead possess an apical archaeopyle and granulation (Head et al., 2001;

Radi et al., 2013). In sediments around Antarctica, *Islandinium minutum* has been found in the fjords of Prydz Bay (Boere et al., 2009) and on both sides of the Antarctic Peninsula (as *Algidasphaeridium? minutum* in Harland et al. 1999; Harland & Pudsey 1999). Although the archaeopyle in the specimens from Prydz Bay is well distinguishable, other reports of *Islandinium minutum* could be misidentified *E. sleipnerensis*.

The fossil record: The original description of *E. sleipnerensis* is based on samples from Upper Pliocene sediments of the northern North Sea (Head et al., 2004). Apart from that there is no other record of this species.

Ecological preferences and environmental interpretation: Because *E. sleipnerensis* has not been recorded in any surface sediment samples apart from a Tunisian lagoon (Fertouna-Bellakhal et al., 2014), its ecological preferences are unclear. However, brown spiny cysts are generally found in sediments underlying high-productivity surface waters (Zonneveld et al., 2013). In the Southern Ocean, the cysts identified as *I. minutum* have been associated with locations where sea-ice cover is longer than 3 months per year (Harland and Pudsey, 1999).

Genus *Nucicla* Hartman et al. (2018b)

Nucicla umbiliphora Hartman et al. (2018b) (Plate 1, figure 14–15)

Morphology and identification: This species was first depicted as Dinocyst sp. A in Wrenn et al. (1998), and has recently been formally described (Hartman et al., 2018b) (see also **Chapter 3**). In the U1357B record fragments of this species have been more often found than whole cysts. This could be due to the large 3I archaeopyle that favours rupture. Because of its unique 3I archaeopyle, relatively large hypocyst, and surface ornamentation (see **Chapter 3**) the fragmentary remains were also easily identified.

Biological taxon: Cyst of unknown dinoflagellate.

Dimensions: Its size measured along the cingulum is $60\pm 8\ \mu\text{m}$ (n=3).

Geographic distribution: Prior to its formal description *N. umbiliphora* was found in surface samples from the Prydz Bay area (Storkey, 2006; Boere et al., 2009). In addition to that, **Chapter 3** shows its occurrence in surface sediments from the Ross Sea and the East Antarctic coastal margin, including Hole U1357B.

The fossil record: *N. umbiliphora* has been reported from multiple Quaternary records in the Ross Sea (Wrenn et al., 1998; Warny et al., 2006; **Chapter 3**). The oldest sample with a known age containing *N. umbiliphora* was obtained from Marine Isotope Stage 5e in the Ross Sea (see **Chapter 3**).

Ecological preferences and environmental interpretation: This species appears to be endemic to the shallow marginal ice zone (MIZ): the (East) Antarctic shelf and the Ross Sea (see **Chapter 3**).

Genus *Selenopemphix* (Benedek 1972) Head 1993

Selenopemphix antarctica Marret et De Vernal 1997 (Plate 1, figure 13)

Morphology and identification: This is a brown, scabrate cyst that is polarly compressed, which is why under the light microscope they are typically in polar view (Marret and De Vernal, 1997). In polar view they possess a circular outline. Furthermore, it possesses one apical and two antapical horns and an intercalary archaeopyle, although this is not always visible (Marret and De Vernal, 1997).

Biological taxon: Cyst of unknown dinoflagellate (Zonneveld et al., 2013).

Dimensions: The diameter of the cyst in (ant)apical view ranges between 52 and 68 μm (average: 60 μm , n=8).

Geographic distribution: *Selenopemphix antarctica* is restricted to and common in the sediments underlying the cool marine waters south of the Subantarctic Front (SAF) and dominant south of the Antarctic Polar Front (APF) (Marret and De Vernal, 1997; Harland and Pudsey, 1999; Esper and Zonneveld, 2002, 2007; Crouch et al., 2010).

The fossil record: In Quaternary records south of the modern-day SAF, this species is generally one of the most dominant during both glacial and interglacial stages (Harland et al., 1999; Marret et al., 2001; Howe et al., 2002; Esper and Zonneveld, 2007).

Dinoflagellate cysts that are morphologically very similar to *S. antarctica* have been recorded as far back as the Oligocene (Houben et al., 2013; Bijl et al., 2018a).

Ecological preferences and environmental interpretation: High abundances of *S. antarctica* are generally associated with sea surface summer temperatures (SSSTs) below 5°C, relatively low sea surface summer salinity (SSSS) (34-35 psu), and high chlorophyll-*a* waters, and it is not found in oligotrophic regions (Marret and Zonneveld, 2003; Prebble et al., 2013). It is the dominant dinoflagellate cyst species in Antarctic waters that are influenced by seasonal sea-ice cover and has therefore been used as an indicator for the presence of seasonal sea ice in the past (Marret and De Vernal, 1997; Harland et al., 1999; Marret et al., 2001; Howe et al., 2002; Houben et al., 2013). As this is probably a heterotrophic species, its high abundances in the sediments underlying these sea-ice-dominated waters can be explained by the high primary (mainly diatom) productivity in the Antarctic summer when upwelling at the Antarctic Divergence enhances nutrient availability (Harland and Pudsey, 1999; Harland et al., 1999).

Selenopemphix sp. 1 sensu Esper & Zonneveld (2007) (Plate 1, figure 18–21)

Morphology and identification: Although similar to *Selenopemphix antarctica*, *Selenopemphix* sp. 1 sensu Esper & Zonneveld (2007) is much larger and has a deep sulcus and a pronounced conical apical complex (Esper and Zonneveld, 2007). Nevertheless, this

species is sometimes combined with *S. antarctica* as they have very similar morphology (Esper and Zonneveld, 2007; Prebble et al., 2013). In Harland et al. (1998) specimens of *Selenopemphix* sp. 1 are depicted as *S. antarctica*.

Biological taxon: Cyst of unknown dinoflagellate.

Dimensions: The diameter of the cyst in (ant)apical view ranges between 82 and 98 μm (average: 88 μm , $n=4$).

Geographic distribution: The full geographic distribution of *Selenopemphix* sp. 1 is unknown because apart from its original description from the South Atlantic Ocean by Esper & Zonneveld (2007) both older (Harland et al., 1998) and newer studies (Prebble et al., 2013) did not differentiate between *Selenopemphix* sp. 1 and *S. antarctica*. Nevertheless, it is expected that the geographic distribution is similarly restricted to the Southern Ocean south of the Subantarctic Front, as is *Selenopemphix antarctica*.

The fossil record: From Quaternary sedimentary records of the South Atlantic it is clear that *Selenopemphix* sp. 1 is more abundant during interglacial stages south of the Antarctic Polar Front (APF), while it is more abundant during glacial stages north of the APF (Esper and Zonneveld, 2007). No other records of *Selenopemphix* sp. 1 exist.

Ecological preferences and environmental interpretation: It has been suggested that *Selenopemphix* sp. 1 is a larger species endmember of *S. antarctica* that only forms under ideal environmental conditions, although it is unclear what ideal environmental conditions (Esper and Zonneveld, 2007). Assuming that a larger cyst is also produced by a larger motile dinoflagellate, such dinoflagellates will have a lower surface-to-volume ratio. Dinoflagellates with a lower surface-to-volume ratio are known to sink faster and swim slower (Kamykowski et al., 1992). It is therefore possible that specific oceanographic conditions or an increased availability of prey, such that slower swimming does not limit the chance to capture prey, allows for larger dinoflagellate sizes. The larger cell size of *Selenopemphix* sp. 1 could also be related to temperature. For a Holocene core obtained from Disko Bay, Greenland, it has been shown that the dinoflagellate cysts obtained from the colder time interval were significantly larger than the dinoflagellate cysts obtained from the warmer time interval (Mousing et al., 2017). Alternatively, being larger could be a defense against predators that can only consume a restricted prey size, such as tintinnids (Dolan and Pierce, 2013).

5.2 Tintinnid loricae and lorica sacs

Phylum CILIOPHORA Doflein 1901

Class SPIROTRICHEA Bütschli 1889

Subclass CHOREOTRICHIA Small & Lynn 1985

Order TINTINNIDA Kofoid & Campbell 1929

Family DICTYOCYSTIDAE Haeckel 1873

Palynomorph: Dictyocystid lorica sac (Plate 1, figure 16–17)

Morphology and identification: This palynomorph is one of the most abundant in Hole U1357B. They are bulb-shaped, transparent, hyaline vesicles. On the microscope slide they are pressed flat, but folds in their wall suggest they originally had a more 3D form. Their size and shape resemble that of tintinnid loricae such as *Codonellopsis pusilla*, but without the scars of now-dissolved diatom frustules. Unlike the loricae of tintinnids, the oral opening of the vesicle looks torn or ragged and very thin-walled, instead of a continuous rim. We believe that these vesicles are the lorica sacs of Dictyocystid tintinnids. The lorica sac is a non-ornamented membrane that lines the lorica wall (Agatha, 2010; Agatha and Strüder-Kypke, 2013). At the oral opening it merges into a foldable closing apparatus that closes off the lorica opening in disturbed or contracted tintinnids (Agatha, 2010; Agatha and Strüder-Kypke, 2013). In contrast to the lorica sac the foldable closing apparatus is ornamented with furrows and/or ribs (Agatha, 2010). The membrane of the closing apparatus is just 0.1 – 0.2 μm thick (Agatha, 2010), and it is therefore not surprising that the closing apparatuses of the palynological remains of the lorica sacs of Hole U1357B are damaged either due to the sedimentation process or palynological processing.

Biological taxon: Recent phylogenetic analyses based on small subunit rRNA (Strüder-Kypke and Lynn, 2008) and the recognition of a shared morphological character, i.e. the lorica sac (Agatha, 2010), have resulted in the combination of the tintinnid families Codonellidae, Codonellopsidae and Dictyocystidae into the oldest of these families, the Dictyocystidae (Agatha and Strüder-Kypke, 2012). Genera for which a lorica sac was observed are *Codonella*, *Codonellopsis*, *Dictyocysta*, and *Codonaria*. Of the genera that possess a lorica sac only *Codonellopsis* is an abundant genus endemic to the Southern Ocean (Dolan et al., 2012). Known Southern Ocean endemic species are *Codonellopsis gausi*, *Codonellopsis glacialis* and *Codonellopsis balechi* (Alder and Boltovskoy, 1991; Clarke and Leakey, 1996; Wasik et al., 1996; Wasik, 1998; Fonda Umani et al., 2005; Dolan et al., 2012, 2013b). However, no lorica sac was observed in *C. gausi* and it might therefore not belong to the Dictyocystidae (Kim et al., 2013). For the other two species the presence of a lorica sac has not been studied in detail, but if the lorica sac does indeed belong to one of these species, it more closely resembles the more bowl-shaped species *C. balechi*. No loricae of *C. balechi* have been found, but the preservation potential of the loricae of *C. balechi* might be lower than the lorica sacs. Alternatively, the lorica sacs could belong to *Codonellopsis*, *Dictyocysta*, or *Codonella* that have a widespread distribution but are also frequently encountered in the Southern Ocean (for a full overview see Dolan et al., 2012). Of these widespread species *Codonella amphorella*, *Codonella aspera*,

Dictyocysta elegans, and *Dictyocysta lepida* are known to possess a foldable closing apparatus and lorica sac (Agatha, 2010). Furthermore, *Codonellopsis pusilla* is particularly abundant in the PFZ (Dolan et al., 2012; Malinverno et al., 2016), and the loricae of *C. pusilla* have been found in some of the samples in Hole U1357B. However, for this species the closing apparatus and lorica sac have not been studied in detail. Also, in this case it could be that the loricae of *C. pusilla* have less preservation potential than the lorica sacs.

Dimensions: The lorica sacs are $60\pm 11\ \mu\text{m}$ in length ($n=4$).

Geographic distribution: Lorica sacs have not been reported in palynological studies before. However, identical forms have been reported from Prydz Bay as *Sphaeromorph* by Storkey (2006; plate 2, fig. 7).

The fossil record: Tintinnid lorica sacs have not been reported from sedimentary records before.

Ecological preferences and environmental interpretation: Considering that most genera and species occurring in the Southern Ocean that possess a lorica sac have a more widespread distribution, we interpret higher abundances of lorica sacs in the sediments as reflecting an influence of more northerly sourced waters, in particular if the sacs belong to *C. pusilla*, which is known to be very abundant in the Polar Front Zone (Dolan et al., 2012; Malinverno et al., 2016).

Genus *Codonellopsis* Jörgensen 1924

Lorica of *Codonellopsis pusilla* (Cleve) Jörgensen 1924 (Plate 3, figure 1–2)

Morphology and identification: This species has a globular posterior bowl on its lorica and an anterior hyaline part of the lorica that is characterized by a row of circular fenestrae. On the hyaline remains of the lorica the scars of diatom frustules can be recognized on the posterior end. The genus *Codonellopsis* generally builds a hard bowl at the posterior end of its lorica by agglutinating mineral particles, diatoms and radiolaria (Petz et al., 1995; Wasik, 1998; Agatha et al., 2013). However, in *Codonellopsis pusilla* this hard bowl is typically built from coccoliths (Malinverno et al., 2016). On the other hand, photographs of *C. pusilla* in Dolan et al. (2012) and Dolan et al. (2013b) show that its lorica can also contain diatoms.

Biological taxon: *Codonellopsis pusilla*

Dimensions: The length of the lorica is $46\pm 2\ \mu\text{m}$ ($n=4$).

Geographic distribution: This is a widespread species originally described from the North Atlantic Ocean (Cleve, 1899). In the Southern Ocean, *Codonellopsis pusilla* can be found predominantly in the Polar Front Zone (PFZ) (Malinverno et al., 2016) and can be as common as the Antarctic endemic genera *Cymatocylis* and *Laackmanniella* (Dolan et al., 2012).

The fossil record: No fossil record of *C. pusilla* exists so far, as even published records of relatively young sedimentary core material containing tintinnid remains do not distinguish between individual species (see e.g., Roncaglia, 2004a; Cromer et al., 2005).

Ecological preferences and environmental interpretation: Because of its high abundances in the PFZ, increased abundances of *C. pusilla* in samples of Hole U1357B could suggest an increased influence of northerly sourced waters.

Lorica of *Codonellopsis glacialis* Laackmann 1907 (Plate 1, figure 27–28)

Morphology and identification: *Codonellopsis glacialis* has a straight short lorica. The palynological remains show the scars of diatoms that were attached to the posterior end of the lorica. Furthermore, it has a posterior acuminate tip. Fragments that consist of the hyaline anterior and miss part of the agglutinated bowl could have been mistakenly identified as *Laackmanniella naviculaefera*.

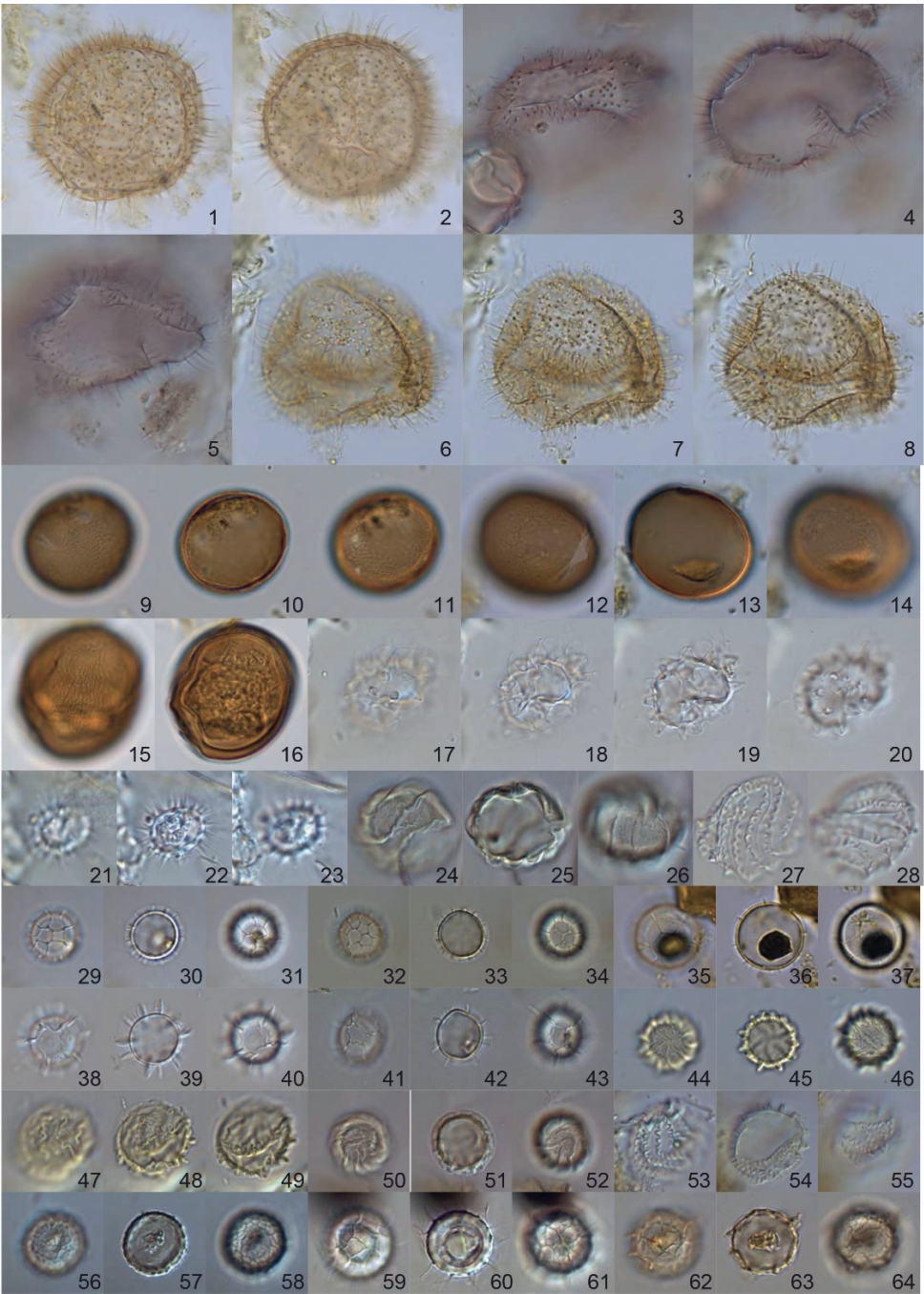
Biological taxon: Multiple authors have suggested that *Codonellopsis glacialis* is synonymous to *Codonellopsis gaussi* Laackmann 1907 based on the presence of transitional forms and the position of the kineties (ciliary rows), but genetic studies have yet to confirm this (Balech, 1958a; Balech, 1973; Kim et al., 2013). In comparison to *C. glacialis*, the lorica of *C. gaussi* sensu stricto is longer (140-180 μm , see junior synonym *Leprotintinnus gaussi* in Laackmann 1910) and is characterized by a much expanded posterior bowl and a posterior acuminate tip. However, only whole specimens of *C. glacialis* were found in Hole U1357B with no (fragments of) expanded bowls of *C. gaussi*.

Dimensions: Specimens in Hole U1357B are 60 ± 6 μm long ($n=3$), which is relatively short compared to the range of 60-125 μm in the original description (see junior synonym *Leprotintinnus glacialis* in Laackmann 1910).

Geographic distribution: Both *C. glacialis* and *C. gaussi* are endemic to the Southern Ocean (Dolan et al., 2012; Dolan and Pierce, 2013).

The fossil record: No fossil record of *C. glacialis* exists, as even published records of relatively young sedimentary core material containing tintinnid remains do not distinguish between individual species (see e.g., Roncaglia, 2004a; Cromer et al., 2005).

Ecological preferences and environmental interpretation: *C. glacialis* and *C. gaussi* have both been associated with the sea-ice edge (Garrison and Buck, 1989). Petz et al. (1995) have also found *C. glacialis* within grease ice (sea ice of <1 cm thickness), comprising 50% of the total ciliate community. A preferred seawater temperature range was given by Petz et al. (1995) of -1.8°C to 0.0°C .



20 μm

Plate 2 (previous page):

Figure 1-2: *Echinidinium sleipnerensis*, U1357B-7H-3W 49–50 cm, slide 1, E.F.: V24.2, upper and lower focus.

Figure 3-5: *Echinidinium sleipnerensis*, U1357B-2H-3W 72–74 cm, slide 1, E.F.: R34.1, upper, mid and lower focus.

Figure 6-8: *Echinidinium sleipnerensis*, U1357B-13H-1W 108–110 cm, slide 1, E.F.: D28.3, upper focus on processes, upper focus on archaeopyle and lower focus.

Figure 9-11: *Gymnodinium microreticulatum*, U1357B-1H-1W 11–13 cm, slide 1, E.F.: G30.1, upper, mid and lower focus.

Figure 12-14: *Gymnodinium microreticulatum* with visible archaeopyle or rupture, U1357B-8H-3W 54–56 cm, slide 1, E.F.: G26.4, upper, mid and lower focus.

Figure 15-16: *Gymnodinium microreticulatum*, U1357B-17H-1W 18–20 cm, slide 1, E.F.: V24.1, upper and mid focus.

Figure 17-20: *Macrobiotoid tardigrade* egg, U1357B-3H-5W 28–30 cm, slide 1, E.F.: M22.4, upper focus on the tips of the conical projections, upper focus on the sides of the conical projections, mid and lower focus.

Figure 21: *Polarella glacialis*, U1357B-1H-2W 40–42 cm, slide 1, E.F.: J34.4, upper focus, mid and lower focus.

Figure 24-26: *Pterosperma parallelum*, large with straight alae, U1357B-3H-1W 97–99 cm, slide 1, E.F.: M36.1, upper, mid and lower focus.

Figure 27-28: *Pterosperma* cf. *parallelum*, U1357B-10H-7W 15–17 cm, slide 1, E.F.: G15.2, upper and lower focus.

Figure 29-31: *Pterosperma cristatum*, U1357B-17H-1W 117–119 cm, slide 1, E.F.: D21.4, upper, mid and lower focus.

Figure 32-34: *Pterosperma cristatum*, U1357B-17H-5W 97–99 cm, slide 1, E.F.: L24.3 upper, mid and lower focus.

Figure 35-37: *Pterosperma polygonum*, U1357B-8H-3W 54–56 cm, slide 1, E.F.: J15.2, upper, mid and lower focus.

Figure 38-40: *Pterosperma marginatum*, U1357B-10H-1W 58–60 cm, slide 1, E.F.: G15.4, upper, mid and lower focus.

Figure 41-43: *Pterosperma cristatum* or early developmental stage of *Pterosperma marginatum*, U1357B-17H-5W 97–99 cm, slide 1, E.F.: E25.3, upper, mid and lower focus.

Figure 44-46: *Pterosperma parallelum*, small with straight alae, U1357B-3W-1H 97–99 cm, slide 1, E.F.: H35.4, upper, mid and lower focus

Figure 47-49: *Pterosperma parallelum*, large with undulating alae, U1357B-3H-1W 97–99 cm, slide 1, E.F.: J35.2, upper, mid and lower focus.

Figure 50-52: *Pterosperma parallelum*, small with relatively thick alae, U1357B-3H-1W 97–99 cm, slide 1, E.F.: J36.4, upper, mid and lower focus.

Figure 53-55: *Pterosperma* cf. *parallelum*, U1357B-8H-3W 54–56 cm, slide 1, E.F.: J24.1, upper, mid and lower focus.

Figure 56-58: *Pterosperma* aff. *reticulatum*, U1357B-16H-1W 63–65 cm, slide 1, E.F.: E23.3, upper, mid and lower focus.

Figure 59-61: *Cymatiosphaera* sp. 1, U1357B-3H-1W 97–99 cm, slide 1, E.F.: G29.4, upper, mid and lower focus.

Figure 62-64: *Cymatiosphaera* sp. 1 with degraded alae, U1357B-17H-1W 117–119 cm, slide 1, E.F.: L25.3, upper, mid and lower focus.

Incertae sedis *Laackmanniella* Kofoid & Campbell 1929

Laackmanniella naviculaefera (Laackmann 1907) Kofoid & Campbell 1929

(Plate 3, figure 7–10)

Morphology and identification: Like *Codonellopsis*, *Laackmanniella* agglutinates mineral particles and diatoms to its lorica (Petz et al., 1995; Wasik et al., 1996; Agatha et al., 2013), the scars of which are visible on the hyaline palynological remains. This species is often considered also including *Laackmanniella prolongata*, which is suggested to be a morphological variety and therefore synonymous (Petz, 2005; Dolan et al., 2012; Kim et al., 2013 and references therein). *L. naviculaefera* differs from *L. prolongata* by having a shorter lorica (138 μm versus 308 μm) (Laackmann, 1907) and a slightly bulging bowl. In Hole U1357B often fragments consisting of both a long hyaline spiraling anterior and part of an agglutinated posterior bowl are found. Although the anterior part of the lorica of *Codonellopsis gausi* is similar to that of *L. naviculaefera*, it is more likely that the remains in Hole U1357B belong to *L. naviculaefera* because the typical lorica of *C. gausi* with large posterior bulge was never found.

Biological taxon: After the formation of the families Codonellidae, Codonellopsidae, and Dictyocystidae into the family Dictyocystidae, the genus *Laackmanniella* (formerly part of Codonellopsidae) was left as affiliated incertae sedis because it was unknown whether *Laackmanniella* possessed a lorica sac and the associated folded closing apparatus (Agatha and Strüder-Kypke, 2012). In a later phylogenetic study based on small subunit rDNA by Kim et al. (2013) it is mentioned that no lorica sac was observed in either *Codonellopsis gausi* or *Laackmanniella prolongata* (*Laackmanniella naviculaefera*) and that they are very closely related. The validity of the genus *Laackmanniella* has therefore been questioned and it has been suggested that *C. gausi* and *L. prolongata* should be united into one genus outside of Dictyocystidae (Kim et al., 2013).

Dimensions: The specimens encountered in Hole U1357B are often not intact, but the most complete specimens are 122 ± 3 μm long ($n=3$), which is consistent with the description of *L. naviculaefera* by Laackmann (1907), and the specimens depicted by Wasik (1998), Dolan et al. (2012), and Dolan et al. (2013b).

Geographic distribution: *Laackmanniella* (and its possible senior synonym *C. gausi*) are endemic to the Antarctic and Subantarctic waters, and most dominant south of the Polar Front (Dolan et al., 2012). Notably, *L. naviculaefera* was already described from the waters off Adélie Land in the 1950's (Balech, 1958b)

The fossil record: No fossil record of *L. naviculaefera* exists, as even published records of relatively young sedimentary core material containing tintinnid remains do not distinguish between individual species (see e.g., Roncaglia, 2004a; Cromer et al., 2005).

Ecological preferences and environmental interpretation: A seawater temperature range was given for *L. naviculaefera* by Petz et al. (1995) of -0.8°C to -0.5°C and it is particularly dominant in inshore high-productivity environments associated with the retreat of the sea-ice edge and upwelling of modified Circumpolar Deep Water (Garrison and Buck, 1989; Garzio and Steinberg, 2013). It has been shown that *L. naviculaefera* actively selects the diatoms it incorporates into its lorica (Wasik et al., 1996), and it has been suggested that it adheres to the diatom frustules after ingesting their protoplasts (Gowing and Garrison, 1992). But living diatom frustules have also been found on loricae of *L. naviculaefera*, although it is uncertain whether these diatoms have been actively selected by the tintinnid or whether the diatoms have used the lorica as an ideal substrate for attachment (Armbrecht et al., 2017). A preference for a high-productivity environment and a diatom-based diet are consistent with the high sedimentation rates of diatom ooze in Hole U1357B.

Family PTYCHOCYLIDIDAE Kofoid & Campbell 1929

Genus *Cymatocylis* Laackmann 1910

Cymatocylis convallaria Laackmann 1910

(Plate 3, figure 11; Plate 4, figure 1–2, 5; Plate 6, figure 1–4)

Morphology and identification: These are relatively large transparent loricae with an oral opening that is ornamented with acuminate tips along its rim. The surface of the anterior part of the lorica has a honeycomb structure. The posterior ends in a tip, which is either blunt or long and acuminate. Many samples of Hole U1357B contain high amounts of these hyaline acuminate horns and only a few specimens are found whole. These all belong to the various formae of tintinnid *Cymatocylis convallaria*. Because the larger formae of *C. convallaria* in Hole U1357B are often broken, the individual formae of *C. convallaria* can therefore not be quantified. However, formae with a long, narrow antapical horn (i.e., forma *cylindrica* and forma *calyciformis*) can be distinguished from (the posterior ends of) the formae without (i.e., forma *affinis* and forma *drygalskii*). Specimens of *C. convallaria* sensu stricto and forma *affinis* are generally preserved whole.

Biological taxon: Originally multiple species of *Cymatocylis* were differentiated based on the length of the apical horn of the lorica versus the total lorica length (Laackmann, 1910). It was concluded later that the species *C. convallaria* without an apical horn and *Cymatocylis affinis* Laackmann 1910 and its four formae with apical horn were in fact the same (Boltovskoy et al., 1990). Therefore, the species name *Cymatocylis convallaria-affinis* was proposed (Boltovskoy et al., 1990). A recent genetic study has confirmed that species with much larger lorica and apical horns, *Convallaria drygalski* (Laackmann 1907) Laackmann 1910 and *Cymatocylis calyciformis* (Laackmann 1907)

Laackmann 1910 (including their formae described by Laackmann (1910), e.g., forma *subrotundata* and *cylindrica*), are also in fact *C. convallaria-affinis* (Kim et al., 2013). Consequently, these former species and formae have been called *C. affinis-convallaria* forma *calyciformis*, forma *drygalskii*, forma *subrotunda*, forma *cylindrica* by Dolan et al. (2013b). We refer to *C. affinis-convallaria* and all its synonyms as *Cymatocyliis convallaria* following Petz et al. (1995) and Petz (2005).

Dimensions: The smaller *C. convallaria* sensu stricto and *C. convallaria* formae *affinis* are $112 \pm 16 \mu\text{m}$ ($n=3$) and the larger formae that were found intact show a range in length between 290 and 415 μm ($n=4$).

Geographic distribution: *C. convallaria* is endemic to the Southern Ocean, but in contrast to *Laackmanniella*, *C. convallaria* is also regularly found in areas outside the winter sea-ice edge (Dolan et al., 2012). Still, *C. convallaria* was already reported off the coast of Adélie Land in the 1950's as *C. affinis* (Balech, 1958b).

The fossil record: No fossil record of *C. convallaria* exists, as even published records of relatively young sedimentary core material containing tintinnid remains do not distinguish between individual species (see e.g., Roncaglia, 2004a; Cromer et al., 2005).

Ecological preferences and environmental interpretation: A temperature range was given by Petz et al. (1995) of -1.2°C to -0.5°C . With respect to the other Antarctic endemic species the lorica of *Cymatocyliis* has a much larger oral diameter, which suggests that these tintinnids feed on larger prey (Dolan and Pierce, 2013). It has been shown that there is a relation between the size of the loricas of *C. convallaria* and the environmental conditions in the surface waters, with higher amounts of the smaller *C. convallaria* forma *affinis* present in food-rich surface waters, both spatially (Boltovskoy et al., 1990) and seasonally (during summer) (Wasik, 1998). It is, however, unknown whether there is any relation between all the other formae of *C. convallaria* and the environmental conditions.

Family uncertain

The *coxliella* form (Plate 3, figure 3–4)

Morphology and identification: This is a hyaline lorica with a pointed tip and a wall structure resembling a spiraling ribbon. This type of lorica is known as the *coxliella* form.

Biological taxon: *Coxliella* is considered an artificial genus as it is a phenotype of other tintinnid taxa (Agatha and Strüder-Kypke, 2012, 2013; Agatha et al., 2013). Various species of *Coxliella* have, however, been described from around Antarctica (Laackman, 1907; Balech, 1958a; 1958b; 1973).

Dimensions: This particular specimen is 55 μm long.

Geographic distribution: *Coxliella* forms are often abundant in both Arctic and Antarctic assemblages (Dolan et al., 2012).

The fossil record: No fossil record of *coxiella* form loricae exists, as even published records of relatively young sedimentary core material containing tintinnid remains do not distinguish between individual species (see e.g., Roncaglia, 2004a; Cromer et al., 2005).

Ecological preferences and environmental interpretation: It is possible that this type of morphology is characteristic of a rapidly growing population (Dolan et al., 2012).

Palynomorph: Lorica (possibly) type 1 (Plate 3, figure 13–14)

Morphology and identification: This palynomorph is a bottle-shaped, transparent vesicle with a narrow oral opening and a broad, flat posterior end. There are no scars present of formerly agglutinated (biogenic) material. It does resemble some of the hyaline tintinnid loricae without an apical horn, but the narrow oral opening is atypical. We believe this is the lorica of a tintinnid, but we have not been able to identify the genus.

Biological taxon: Unknown because we have not been able to ascribe the lorica to a genus.

Dimensions: The length of the lorica is $63 \pm 3 \mu\text{m}$ ($n=3$).

Geographic distribution: Unknown because we have not been able to ascribe the lorica to a genus.

The fossil record: No similar forms have been found in other published palynological records.

Ecological preferences and environmental interpretation: Unknown because we have not been able to ascribe the lorica to a genus.

5.3 Foraminifer linings

Infrakingdom RHIZARIA Cavalier-Smith 2002

Phylum FORAMINIFERA d'Orbigny 1826

Palynomorph: Foraminifer linings of benthic foraminifera
(Plate 3, figure 5–6; Plate 4, figure 4, 8)

Morphology and identification: Within Hole U1357B we find trochospiral (Plate 3, figure 5), triserial (Plate 3, figure 6) and uniserial foraminifer linings (Plate 4, figure 4, 8). Triserial and uniserial forms are usually more transparent than the trochospiral forms. Only few specimens were found completely intact within the samples of U1357B. However, even the damaged specimens can often still be distinguished by the darker-coloured central chamber lining (the proloculum, see also Wrenn et al. 1998).

Biological taxon: The biological calcareous or arenaceous taxa corresponding to the linings cannot be determined. To be able to do so, the original calcareous and arenaceous shells should be picked before palynological treatment.



20 µm

Plate 3 (previous page):

Figure 1-2: *Codonellopsis pusilla*, U1357B-9H-4W 79–81 cm, slide 1, E.F.: G26.4, upper and lower focus.

Figure 3-4: *Coxiella* form lorica, U1357B-2H-2W 6–8 cm, slide 1, E.F.: J30.1, upper and lower focus.

Figure 5: Trochospiral foraminifer lining, U1357B-17H-5W 97–99 cm, slide 1, E.F.: E26.3.

Figure 6: Triserial foraminifer lining, U1357B-17H-5W 97–99 cm, slide 1, E.F.: H21.2.

Figure 7-9: *Laackmanniella naviculaefera*, U1357B-1H-2W 40–42 cm, slide 1, E.F.: K24.2, upper, mid and lower focus.

Figure 10: *Laackmanniella naviculaefera*, U1357B-10H-1W 58–60 cm, slide 1, E.F.: K24.2, LIB image.

Figure 11: *Cymatocyclus convallaria* sensu stricto, U1357B-7H-5W 4–6 cm, slide 1, E.F.: W26.2, LIB image.

Figure 12: P-type maxillary apparatus of *Ophryotrocha orensanzii*, U1357B-4H-3W 61–63 cm, slide 1, E.F.: G21.4, LIB image.

Figure 13-14: Lorica? type 1, U1357B-2H-4W 111–113 cm, slide 1, E.F.: L17.3.3, upper and lower focus.

Figure 15: Anterior denticle of maxillary apparatus of *Ophryotrocha*, U1357B-5H-7W 5–7 cm, slide 1, E.F.: H35.3.

Figure 16: Anterior denticle of maxillary apparatus of *Ophryotrocha*, U1357B-16H-4W 64–65 cm, slide 1, E.F.: L20.3.

Figure 17: Copepod mandibular gnathobase 2, U1357B-3H-3W 8–10 cm, slide 1, E.F.: Q29.4.

Figure 18: Pollen grain of *Nothofagus*, U1357B-17H-1W 18–20 cm, slide 1, E.F.: F22.1, LIB image.

Figure 19: Pollen grain of Podocarpaceae, U1357B-7H-5W 4–6 cm, slide 1, E.F.: K11.2, LIB image.

Figure 20: Forceps of a P-type maxillary apparatus of *Ophryotrocha orensanzii*, U1357B-9H-1W 112–114 cm, slide 1, E.F.: G22.4, LIB image.

Figure 21: Copepod mandibular gnathobase 1, U1357B-3H-3W 8–10 cm, slide 1, E.F.: V24.1.

Figure 22: Forceps of K-type maxillary apparatus of *Ophryotrocha*, U1357B-16H-1W 63–65 cm, slide 1, E.F.: P26.1, LIB image.

Figure 23: Forceps of K-type maxillary apparatus of *Ophryotrocha*, U1357B-16H-4W 64–65 cm, slide 1, E.F.: G21.4, LIB image.

Figure 24-27: Copepod spermatophore (Type AB-33), U1357B-17H-5W 97–99 cm, slide 1, E.F.: G30.2, upper focus on the distal end of the tube-like neck, upper focus on the proximal part of the tube-like neck, mid and lower focus.

Figure 28: Copepod spermatophore (Type AB-33), U1357B-17H-1W 117–119 cm, slide 1, E.F.: D27.2.

Figure 29: Copepod thoracopod, U1357B-16H-4W 64–65 cm, slide 1, E.F.: H21.4, LIB image.

Figure 30-31: *Leiosphaeridia* sp. 2, U1357B-9H-1W 112–114 cm, slide 1, E.F.: K19.4, upper and mid focus.

Figure 32: *Leiosphaeridia* sp. 2 with an apparent second membrane, U1357B-16H-1W 63–65 cm, slide 1, E.F.: E21.3, upper, mid and lower focus.

Dimensions: These vary strongly between specimens and the original size cannot usually be determined, because the specimens are broken.

Geographic distribution: Although benthic foraminifera are common around Antarctica and can be quite diverse (Mikhalevich, 2004), they are often not preserved because the Antarctic shelf waters are highly undersaturated with respect to calcite (Expedition 318 Scientists, 2011a), and the remineralization of organic matter causes acidic pore waters which dissolve the foraminifera post-depositional. The inner linings of benthic foraminifera within palynomorph assemblages are found more commonly at sites along the Antarctic coast (Wrenn et al., 1998; Warny et al., 2006; Warny, 2009). However, because around Antarctica tilted Paleogene and Neogene strata are exposed due to glacial erosion, such foraminifer linings could also be reworked (Warny, 2009).

The fossil record: Foraminiferal linings have been found in fossil assemblages obtained from marine cores as well as continental outcrops around Antarctica with ages

ranging between the Cretaceous and the Quaternary. An extensive overview of Antarctic records of fossil foraminiferal linings is given by Concheyro et al. (2014)

Ecological preferences and environmental interpretation: Considering that the majority of palynological remains from Hole U1357B are deposited *in situ*, and the preservation potential of foraminifera in these sediments is far better than those of the Eocene sediments in the region (Expedition 318 Scientists, 2011a) the benthic foraminiferal linings are probably *in situ*. In general, the presence or absence of benthic foraminiferal linings in palynological records is associated with well-ventilated or anoxic bottom waters, respectively (Sluijs et al., 2006, 2008; Frieling et al., 2018). High abundances of benthic foraminifera (and their linings) could also reflect high surface-water productivity as benthic fauna is directly dependent of the organic carbon flux from the surface waters (Jorissen et al., 1995; Thomas et al., 1995; Costello and Bauch, 1997). The ratio between infaunal versus epifaunal species is used as a paleoproductivity proxy, as infaunal species tend to increase during sustained periods of high productivity, while epifaunal species are more dominant when surface-water productivity occurs in pulses (Thomas et al., 1995; Costello and Bauch, 1997). Because trochospiral (more commonly epifaunal), triserial and uniserial (more commonly infaunal) foraminifer linings have been found within Hole U1357B, they could potentially be used to qualitatively reconstruct surface-water productivity changes and/or changes in bottom-water oxygenation (Corliss, 1991).

5.4 Prasinophyte phycomata

Kingdom PLANTAE Haeckel 1866

Phylum CHLOROPHYTA Pascher 1914

“Prasinophytes” (paraphyletic taxon, see Nakayama et al. 1998; Guillou et al. 2004)

Order PYRAMIMONADALES Chadeffaud 1950

Family HALOSPHAERACEAE Haeckel 1894

Genus *Pterosperma* Pouchet 1893

Phycoma of *Pterosperma cristatum* Schiller 1925

(Plate 2, figure 29–34 and possibly figure 41–43)

Morphology and identification: Specimens from Hole U1357B closely resemble the phycoma of *P. cristatum* as depicted by Bérard-Therriault et al. (1999). These specimens possess straight alae (ridges) that form square or pentagonal compartments. *P. cristatum* is very similar to *Pterosperma polygonum*, but in contrast to *P. polygonum* *P. cristatum* does not possess pores on its central body (see Inouye et al. 1990, fig. 3). Because we cannot distinguish any pores on our specimens and because of the strong similarity with the specimens depicted by Bérard-Therriault et al. (1999), we have identified most of our

specimens as *P. cristatum*. However, it has been shown that in early developmental stages of *P. polygonum* the pores cannot be resolved (Parke et al., 1978). Even the large central pore of *Pterosperma marginatum* is not visible in non-fully developed specimens, while the alae are present (Parke et al., 1978). It is therefore possible that we have identified some non-fully developed specimens of *P. polygonum* and *P. marginatum* as *P. cristatum*. Light microscope photographs of *P. polygonum* and *P. cristatum* by Bérard-Therriault et al. (1999) show that *P. polygonum* has relatively higher alae. On the other hand, the alae on *P. polygonum* of Parke et al. (1978) and *P. cf. polygonum* of Marchant (2005) are relatively low.

Biological taxon: *Pterosperma cristatum*

Dimensions: The specimens within Hole U1357B are 13 to 21 μm in diameter (average: 15 μm , n=6).

Geographic distribution: The full geographic distribution of *P. cristatum* in the surface waters is unclear, but it has been reported from around the world: Gulf of Saint Laurent in Canada (Bérard-Therriault et al., 1999), in coastal bays of Japan (Inouye et al. 1990; Kawachi, 2017), off the coast of Portugal (Moita and Vilarinho, 1999), the Baltic Sea area (Hällfors, 2004), the German Wadden Sea (Scholz and Liebezeit, 2012), freshwaters in the Russian Far East (Medvedeva and Nikulina, 2014), the Danube River Basin in Romania and the Black Sea (Cărăuș, 2017), and in Norwegian fjords (Hoem, 2018).

The fossil record: Mudie et al. (2010) noticed the remarkable similarity between the fossil specimens of *Cymatiosphaera globulosa* from the Black Sea (Wall et al. 1973) and the phycocyst stage of *P. cristatum*. Originally, *C. globulosa* was described from Oligocene strata in Japan (Takahashi, 1964) and later from Upper Cretaceous strata in Japan (Takahashi, 1967). Similar-looking *Cymatiosphaera* (*Cymatiosphaera* sp. 1, diameter 11 μm) have been recorded in a Miocene record from Prydz Bay, Antarctica (Hannah, 2006), as well as in Quaternary, Miocene and Oligocene sections from the Ross Sea (Hannah et al., 1998, 2000). It is, however, uncertain whether these old prasinophyte phycocysts belong to the same biological species *P. cristatum* with similar environmental preferences as today. On the other hand, Holocene records of *C. globulosa* likely originate from *P. cristatum* in the surface waters. For example, *C. globulosa* is known from several Quaternary records from the Black Sea area where it first appeared in the deeper waters around 9600 cal. yr BP (Atanassova, 2005; Filipova-Marinova, 2007; Filipova-Marinova et al., 2013).

Ecological preferences and environmental interpretation: Although *Pterosperma* is considered a fully marine genus (Parke et al., 1978), the geographic distribution of *P. cristatum* suggests that it is also tolerant to more brackish environments and/or coastal areas influenced by freshwater input. Notably, *C. globulosa* is considered a euryhaline

species and therefore able to tolerate large salinity fluctuations (Wall et al., 1973; Atanassova 2005; Filipova-Marinova 2007; Filipova-Marinova et al. 2013). In the fossil records from the Black Sea increases of *C. globulosa* together with other euryhaline dinoflagellate species mark the transition from a freshwater lake to increased marine (more saline) conditions (Wall et al., 1973; Atanassova 2005; Filipova-Marinova 2007; Filipova-Marinova et al. 2013). Increased amounts of *Cymatiosphaera* in the Miocene record from Prydz Bay are associated with increased freshwater and stratified oceanic waters resulting from increased warming during the Mid-Miocene Climatic Optimum (Hannah, 2006).

Phycoma of *Pterosperma marginatum* Gaarder 1954
(Plate 2, figure 38–40 and possibly figure 41–43)

Morphology and identification: The phycoma of *Pterosperma marginatum*, like *P. cristatum*, possesses alae that form polygonal compartments. However, *P. marginatum* typically possesses a large pore placed centrally within each compartment (Thronsen 1997; Bérard-Therriault et al., 1999). The alae of this specimen are undulate, which is different from, e.g., the specimen depicted by Parke et al. (1978, plate 1, fig. F) with more straight alae. Specimens with similar undulating ridges have been found lacking these pores (Plate 2, figure 41–43). Since the central pores are absent in not fully developed phycmata, it is possible that these are also *P. marginatum*.

Biological taxon: *Pterosperma marginatum*

Dimensions: Specimens of *P. marginatum* are $14 \pm 1 \mu\text{m}$ ($n=2$).

Geographic distribution: As with the other *Pterosperma* species, it has a global but patchy distribution. It has been recorded off the coast of Portugal (Moita and Vilarinho, 1999), in the Gulf of Saint Laurent in Canada (Bérard-Therriault et al., 1999), the Norwegian Sea and the Arctic Ocean (Ocean Biogeographic Information System, accessed in 2018)

The fossil record: *P. marginatum* is not known from the fossil record.

Ecological preferences and environmental interpretation: *Pterosperma* is considered a fully marine genus (Parke et al., 1978). Considering it has been found together with *P. polygonum* (Moita & Vilarinho 1999; Bérard-Therriault et al., 1999) it likely prefers a similar habitat.

Phycoma of *Pterosperma parallelum* Gaarder 1938 (Plate 2, figure 24–26, 44–52)

Morphology and identification: The phycoma of *Pterosperma parallelum* possesses low, curved, parallel alae (Thronsen, 1997; Marchant, 2005). In the samples of Hole U1357B there is some variation in the appearance of the alae. The thickness, smoothness,

and straightness vary between specimens. Some specimens have relatively thick and/or undulate alae (Plate 2, figure 47–52).

Biological taxon: *P. parallelum*

Dimensions: Phycomata of *P. parallelum* in Hole U1357B range in size between 10 and 25 μm , which compares well with reported sizes of 9–20 μm (Thronsen, 1997; Marchant, 2005).

Geographic distribution: Southern Ocean, near the Polar Front (Marchant, 2005; Australian Antarctic Data Centre, 2017), and in inland waters of the Netherlands (Veen et al., 2015).

The fossil record: *P. parallelum* is not known from the fossil record.

Ecological preferences and environmental interpretation: Although *Pterosperma* is considered a fully marine genus (Parke et al., 1978), the multiple recordings of *P. parallelum* in the sea-ice-influenced waters of the Southern Ocean suggest some tolerance to fluctuating surface-water salinities.

Phycoma of *Pterosperma* cf. *parallelum* (Plate 2, figure 27–28, 53–55)

Morphology and identification: This palynomorph resembles *P. parallelum* as described by Thronsen (1997) and Marchant (2005), but the alae are not simple straight ridges. Instead, this phycoma possesses parallel rows of small, flat, square protuberances. The phycoma wall is thinner than *P. parallelum*.

Biological taxon: It is uncertain whether these phycomata belong to an unknown species of *Pterosperma* or whether they represent an early developmental stage of *P. parallelum*. However, considering that phycomata grow in size during asexual reproduction (Colbath and Grenfell, 1995) and the fact that we find both smaller and larger specimens of *P. cf. parallelum* as well as smaller *P. parallelum* within our samples, the latter is less probable.

Dimensions: The size of *P. cf. parallelum* ranges between 19 μm and 26 μm ($n=3$), comparable to *P. parallelum*.

Geographic distribution: Unknown because no previous record of this species exists.

The fossil record: Unknown because this species has not been recorded in palynological studies before.

Ecological preferences and environmental interpretation: Unknown because no previous record of this species exists.

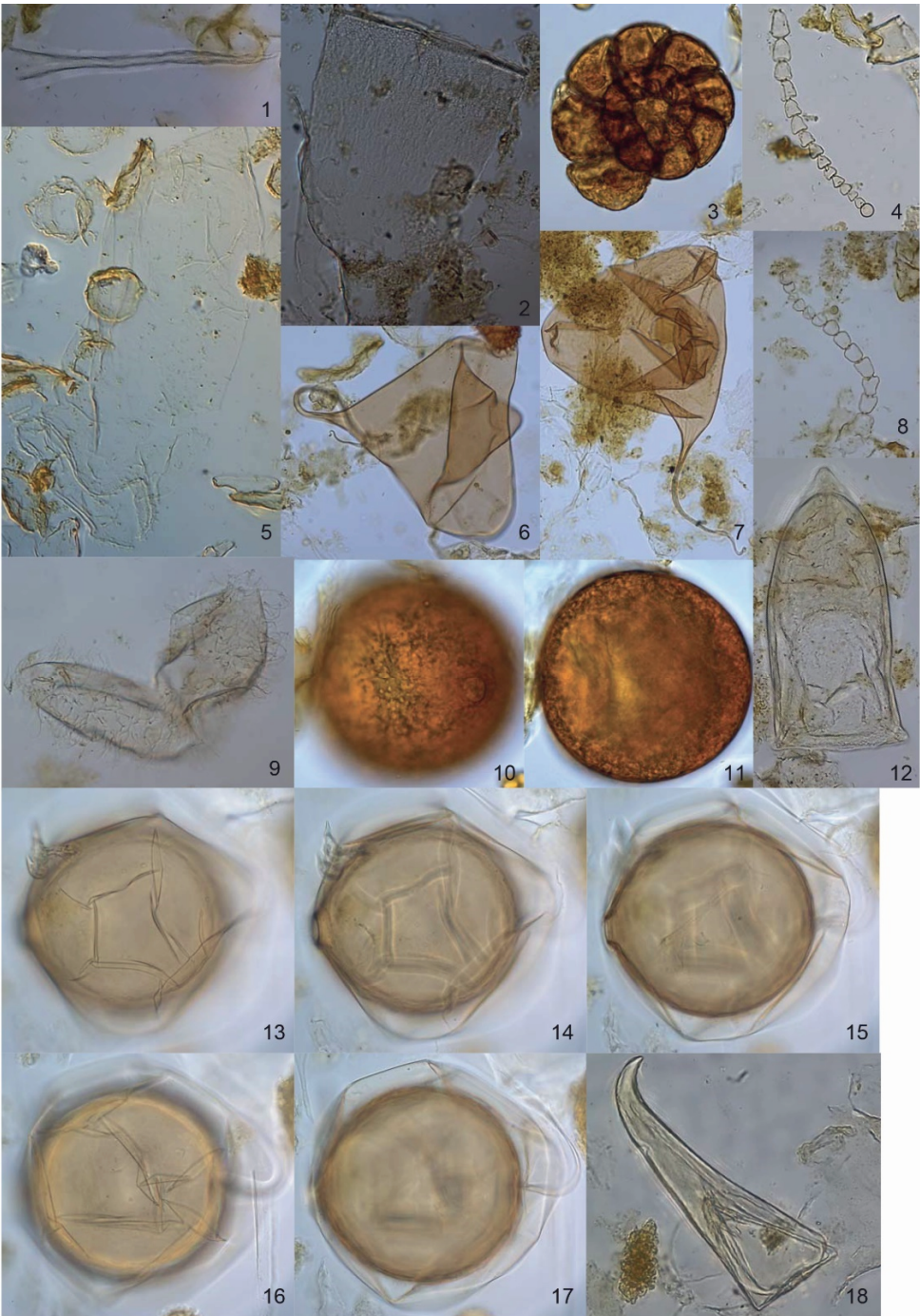


Plate 4 (previous page):

Figure 1: *Cymatocyliis convallaria* forma *calyciformis* or *cylindrica* apical lorica horn, U1357B-3H-1W 97–99 cm, slide 1, E.F.: K36.4, LIB image.

Figure 2: *Cymatocyliis convallaria* forma *calyciformis*, detail of the anterior part of Plate 6, figure 1, U1357B-8H-3W 54–56 cm, slide 1, E.F.:K20.1, upper focus.

Figure 3: Trochospiral foraminiferal lining, U1357B-6H-4W 86–88 cm, slide 1, E.F.: V27.2.

Figure 4: Uniserial foraminiferal lining, U1357B-2H-2W 6–8 cm, slide 1, E.F.: K30.1, LIB image.

Figure 5: *Cymatocyliis convallaria* forma *cylindrica*, detail of the anterior part of Plate 6, figure 3, U1357B-6H-6W 123–125 cm, slide 1, E.F.: K24.1, LIB image.

Figure 6: Copepod? spermatophore (Type AB-22), U1357B-7H-5W 4–6 cm, slide 1, E.F.: J21.3.

Figure 7: Copepod? spermatophore (Type AB-22), U1357B-14H-5W 48–49 cm, slide 1, E.F.: H19.2.

Figure 8: Uniserial foraminifer lining, U1357B-7H-5W 4–6 cm, slide 1, E.F.: D16.3.

Figure 9: Copepod egg that has split open, U1357B-2H-6W 6–8 cm, slide 1, E.F.: K34.1, upper focus.

Figure 10–11: *Palaeostomocystis sphaerica* with content, pylome visible on the right, U1357B-5H-7W 5–7 cm, slide 1, E.F.: Q21.1, upper and mid focus.

Figure 12: Type AB-27c, bullet-shaped, U1357B-2H-6W 6–8 cm, slide 1, E.F.: O32.4, LIB image.

Figure 13–17: *Palaeostomocystis sphaerica* with outer envelope with tail, U1357B-1H-2W 40–42 cm, slide 1, E.F.: U23.3, upper focus on envelope, upper focus on cyst, mid focus, lower focus on envelope and lower focus on tail..

Figure 18: Type AB-27f, falcate, U1357B-1H-2W 40–42 cm, slide 1, E.F.: L27.1, LIB image.

Phycoma of *Pterosperma polygonum* Ostenfeld in Ostenfeld and Schmidt 1902 (Plate 2, figure 35–37)

Morphology and identification: This species is very similar to *Pterosperma cristatum*. As mentioned above, what distinguishes the phycomata of *P. polygonum* from *P. cristatum* is the presence of small pores covering the central body (Thronsdén et al., 1997; Bérard-Therriault et al., 1999). However, these are lacking in earlier developmental stages of the phycoma (Parke et al., 1978). In addition, pores can be easily overlooked underneath the light microscope, which is why some specimens of *P. polygonum* can be misidentified as *P. cristatum*. Although originally *Pterosperma polygonum* was described as being twice as large (40 µm) in comparison to our specimens (Ostenfeld and Schmidt, 1902), it is known that phycomata vary in size depending on the stage of asexual reproduction within a phycoma (Colbath and Grenfell, 1995). Notably, smaller phycomata resembling *P. polygonum* have been described (*Pterosperma* cf. *polygonum* in Marchant, 2005). Scanning electron microscope images of *P. cf. polygonum* of Marchant (2005) also show the presence of pores.

Biological taxon: *Pterosperma polygonum*

Dimensions: The specimens in Hole U1357B are 17±1 µm (n=2).

Geographic distribution: Documentation of *P. polygonum* is rather patchy with reports from the Red Sea and the Gulf of Aden (Ostenfeld and Schmidt, 1902), the Gulf of Saint Laurent in Canada (Bérard-Therriault et al., 1999), off the coast of Brittany (France) in the western English Channel (Guilloux et al., 2013), freshwaters of the Russian Far East (Medvedeva and Nikulina, 2014), inland waters of the Netherlands (Veen et al., 2015), the

North Sea (Marine Biology Laboratory, MICROBIS accessed in 2018), off the coast of Japan (Ocean Biogeographic Information Center, accessed in 2018), the White Sea (Russia) and the Arctic Ocean (Hopcroft, 2016), the Southern Ocean (Davies & Watts, 2017) and *P. cf. polygonum* from Davis Station, East Antarctica (Marchant, 2005).

The fossil record: *P. polygonum* is not known from the fossil record.

Ecological preferences and environmental interpretation: *Pterosperma* is considered a fully marine genus (Parke et al., 1978), but like *P. cristatum* the geographic distribution of *P. polygonum* suggests some tolerance to lower salinities.

Phycoma of *Pterosperma* aff. *reticulatum* Ostenfeld in Ostenfeld and Schmidt 1902 (Plate 2, figure 56–58)

Morphology and identification: The original description of *Pterosperma reticulatum* in Ostenfeld and Schmidt (1902) is based on a specimen of about 80 µm with lamellae (alae) forming a finely reticulated surface. We follow Thornington-Smith (1970) in assigning similar-looking phycomata but with a much smaller size to *Pterosperma* aff. *reticulatum*. The specimens encountered in Hole U1357B are ornamented with numerous low alae that form a reticulate surface of irregular polygonal fields. The size and wall ornamentation of the specimens from Hole U1357B therefore also resemble *Pterosperma parvareopunctatum* Thornington-Smith 1970, but they lack the central pores that are present in each of the irregular polygonal fields.

Biological taxon: It is unknown whether the specimens described by Thornington-Smith (1970) are biologically the same as those described by Ostenfeld and Schmidt (1902), although phycomata are known to grow in size during asexual reproduction (Colbath and Grenfell, 1995).

Dimensions: The specimens encountered in Hole U1357B are 17±1 µm (n=2).

Geographic distribution: Originally, *P. reticulatum* was described from the Red Sea and the Gulf of Aden (Ostenfeld and Schmidt, 1902). For the smaller *P. aff. reticulatum* no other record exists apart from its description from the surface waters in the western Indian Ocean (Thornington-Smith, 1970).

The fossil record: This species is not known from the fossil record.

Ecological preferences and environmental interpretation: Unknown due to the scarce information about its geographic distribution.

Cymatiosphaera sp. 1 (Plate 2, figure 59–64)

Morphology and identification: This is a transparent sphere with alae forming irregularly shaped polygonal fields. The alae are so high (about 5 µm) and transparent compared to the vesicle diameter that it seems as if bifurcating processes extend to the

point at which some of the alae intersect. In some more degraded specimens, bifurcating processes are what is left of the alae (Plate 2, figure 62–64).

Biological taxon: Unknown, but the size, transparency and wall ornamentation are very similar to the phycomata of prasinophytes.

Dimensions: The diameter of *Cymatiosphaera* sp. 1 is $17\pm 1\ \mu\text{m}$ ($n=4$).

Geographic distribution: To our knowledge this species has not been recorded from the surface waters or modern-day surface sediments before.

The fossil record: Although *Cymatiosphaera* is a common genus in fossil records, we have not been able to assign the specimens from Hole U1357B to a specific species. *Cymatiosphaera* sp. 1 differs distinctly from most other *Cymatiosphaera* species found in fossil records close to the Antarctic margin (Hannah et al., 1998; Wrenn et al., 1998; Hannah et al., 2000; Hannah, 2006; Warny et al., 2006; Clowes et al., 2016) by the irregular polygonal fields formed by its high septa. *Cymatiosphaera* sp. 2 recorded by Hannah (2006) in a Miocene record from Prydz Bay, Antarctica, also seems to possess such irregular polygonal fields, but its septa are lower. Also, the specimen depicted by Hannah (2006) is larger ($32\ \mu\text{m}$ in diameter) than *Cymatiosphaera* sp. 1 recorded in Hole U1357B

Ecological preferences and environmental interpretation: Unknown because to our knowledge this species has not been recorded from the surface waters or modern-day surface sediments before. Species of *Cymatiosphaera* (including *Cymatiosphaera* sp. 2 of Hannah (2006)) close to the Antarctic margin have, however, been associated with increased freshwater release and stratified oceanic waters during the Mid-Miocene Climatic Optimum (Hannah, 2006).

5.5 Eggs, spermatophores, teeth and other animal remains

Kingdom ANIMALIA Linnaeus 1758

Phylum ANNELIDA Lamarck 1809

Class POLYCHAETA Grube 1850

Order EUNICIDA Fauchald 1977

Family Dorvilleidae Chamberlin 1919

Genus *Ophryotrocha* Claparède & Mecznikow 1869

Palynomorph: P-type maxillary apparatus of *Ophryotrocha orensanzi* Taboada et al. 2013
(Plate 3, figure 12, 20)

Morphology and identification: Within the samples of Hole U1357B we find a variety of serrated dark red palynomorphs of various sizes. Some of these have a jaw-like shape, being serrated at one side of an elongated sclerotized part. Notably, the most distal tooth of the serrated side of the ‘jaw’ is the largest. Regularly, longitudinal series are found consisting of multiple jaw-like forms attached together. We have identified these as the P-

type maxillary apparatus of the polychaete worm *Ophryotrocha*. Of all the Southern Ocean species of *Ophryotrocha*, *O. orensanzi* possesses maxillary pieces within its P-type mandibular apparatus that have a very prominent distal tooth similar to the specimens found in Hole U1357B (Taboada et al., 2013; Paxton et al., 2017). This distal tooth is especially prominent on the forceps of the maxillary apparatus and is formally described as a 'lateral fang' on the P-type forceps in the emended diagnosis of *O. orensanzi* by Paxton et al. (2017).

Biological taxon: We believe these are the remains of *Ophryotrocha orensanzi*. It could be, however, that these maxillary apparatuses belong to *Ophryotrocha claparedii*, for which the jaw apparatus is poorly known (Szaniawski and Wrona, 1987), or to an unknown species of *Ophryotrocha*, considering that the fauna around the Antarctic coast is poorly explored and the amount of new *Ophryotrocha* species that have been discovered away from the Antarctic coast has increased enormously in recent years (Paxton and Åkesson, 2007; Paxton and Davey, 2010; Taboada et al., 2013; Ravara et al., 2015; Paxton et al., 2017). Species of the dorvilleid *Ophryotrocha* possess a P-type maxillary apparatus when they are young or female (Paxton and Åkesson, 2007). Once they become a sexually mature male or change from female to male (hermaphrodites) this P-type jaw gets replaced by a K-type jaw, which has greatly enlarged basal parts (forceps) (Paxton and Åkesson, 2007; Paxton et al., 2017).

Dimensions: The largest specimens are about 160 µm long and the smallest specimens about 16 µm long (average: 38 µm, n=9).

Geographical distribution: Four species of *Ophryotrocha* are known from shallow-water Southern Ocean sites. The species *Ophryotrocha claparedii* has been reported from the Ross Sea (Gambi et al., 1994; Morehead et al., 2008). Recently discovered new species include *Ophryotrocha orensanzi* and *Ophryotrocha clava* discovered on experimentally deployed whale bones off the coast of Deception Island (Taboada et al., 2013), and *Ophryotrocha shieldsi* from underneath a fish farm in Tasmania (Paxton and Davey, 2010). Recently, *O. orensanzi* has also been reported from near Casey Station, East Antarctica (Paxton et al., 2017), which is not too far from Hole U1357B.

The fossil record: Scolecodonts of several *Ophryotrocha* species have been described from the Cape Melville Formation (Lower Miocene) of King George Island (Szaniawski and Wrona, 1987).

Ecological preferences and environmental interpretation: Although *Ophryotrocha* species are generally associated with high-nutrient littoral conditions, whale falls and hydrothermal vents (Taboada et al., 2013; Paxton et al., 2017), the recent find of *O. orensanzi* near Casey Station in clean, unpolluted waters has led to the suggestion that *Ophryotrocha* are not specialists of organically enriched substrates, but rather

unspecialized opportunists that rapidly increase their population size in nutrient-rich environments (Paxton et al., 2017).

Palynomorph: Basal part (forceps) of a K-type maxillary apparatus of *Ophryotrocha* (Plate 3, figure 22–23)

Morphology and identification: These are falcate, dark red sclerotized parts. We have identified these as the basal parts of the K-type maxillary apparatus of *Ophryotrocha*.

Biological taxon: Likely they belong to the same species as the P-type maxillary apparatus, *O. orensanzi*, or an unknown Antarctic species. They belong to male individuals or formerly male individuals, as hermaphrodite *Ophryotrocha* retain their K-type maxillary apparatus once they change from the male to the female sex (Paxton and Åkesson, 2007). The length of the K-type forceps is, however, half the size of the specimen of *O. orensanzi* drawn by Paxton et al. (2017). It is unclear what the size range of the K-type forceps of *O. orensanzi* can be and thus whether the specimens found in Hole U1357B truly belong to this species.

Dimensions: These palynomorphs are $76 \pm 3 \mu\text{m}$ in length ($n=2$).

Geographic distribution: For this information, see the P-type maxillary apparatus of *Ophryotrocha orensanzi* above.

The fossil record: For this information, see the P-type maxillary apparatus of *Ophryotrocha orensanzi* above.

Ecological preferences and environmental interpretation: For this information, see the P-type maxillary apparatus of *Ophryotrocha orensanzi* above.

Palynomorph: Anterior denticles of the maxillary apparatus of *Ophryotrocha* (Plate 3, figure 15–16)

Morphology and identification: These are ovate or lobe-shaped, dark red serrated sclerotized parts. The serration is symmetrical with respect to the central axis of the lobe-shaped part and only present at the distal end. We have identified these exoskeleton parts as the anterior denticles of either a P-type or a K-type mandibular apparatus of the dorvilleid *Ophryotrocha*. The shapes of anterior denticles of *Ophryotrocha* range from ovate to subtriangular (Paxton and Åkesson, 2007; Paxton and Davey, 2010; Taboada et al., 2013; Ravara et al., 2015; Paxton et al., 2017).

Biological taxon: Considering the presence of P-type mandibular apparatuses of *O. orensanzi* (or possibly an unknown species of *Ophryotrocha*), these anterior denticles likely belong to the same species.

Dimensions: They are $56 \pm 3 \mu\text{m}$ in length ($n=2$).

Plate 5 (next page):

Figure 1-3: Copepod egg, U1357B-2H-6W 6–8 cm, slide 1, E.F.: F28.2, upper, mid and lower focus.

Figure 4: *Leiosphaeridia* sp. 3, U1357B-8H-3W 54–56 cm, slide 1, E.F.: H19.2, mid focus.

Figure 5: Copepod endites, U1357B-2H-6W 6–8 cm, slide 1, E.F.: J36.3, LIB image.

Figure 6: Detail of the right copepod seta of Plate 4, figure 13, U1357B-8H-3W 54–56 cm, slide 1, E.F.: T30.1.

Figure 7-9: *Leiosphaeridia* sp. 2, U1357B-18H-2W 114–116 cm, slide 1, E.F.: G26.3, upper, mid and lower focus on which an opening with sharp edges is visible.

Figure 10-12: *Palaeostomocystis* cf. *fritilla*, U1357B-6H-6W 123–125 cm, slide 1, E.F.: K24.1, upper, mid and lower focus.

Figure 13: *Palaeostomocystis* cf. *fritilla* with operculum attached, U1357B-6H-4W 86–88 cm, slide 1, E.F.: K33.3, upper focus.

Figure 14-16: *Palaeostomocystis* cf. *reticulata*, U1357B-12H-2W 1-3 cm, slide 1, E.F.: H23.4, upper, mid and lower focus.

Figure 17-19: *Palaeostomocystis* cf. *reticulata*, U1357B-6H-6W 123–125 cm, slide 1, E.F.: L14.4, upper, mid and lower focus.

Figure 20-22: *Palaeostomocystis* sp. C, U1357B-3H-3W 8–10 cm, slide 1, E.F.: U28.3, upper, mid and lower focus.

Figure 23-25: *Palaeostomocystis sphaerica*, U1357B-1H-1W 11–13 cm, slide 1, E.F.: L30.3, upper, mid and lower focus.

Geographic distribution: For this information, see the P-type maxillary apparatus of *Ophryotrocha orensanzi* above.

The fossil record: For this information, see the P-type maxillary apparatus of *Ophryotrocha orensanzi* above.

Ecological preferences and environmental interpretation: For this information, see the P-type maxillary apparatus of *Ophryotrocha orensanzi* above.

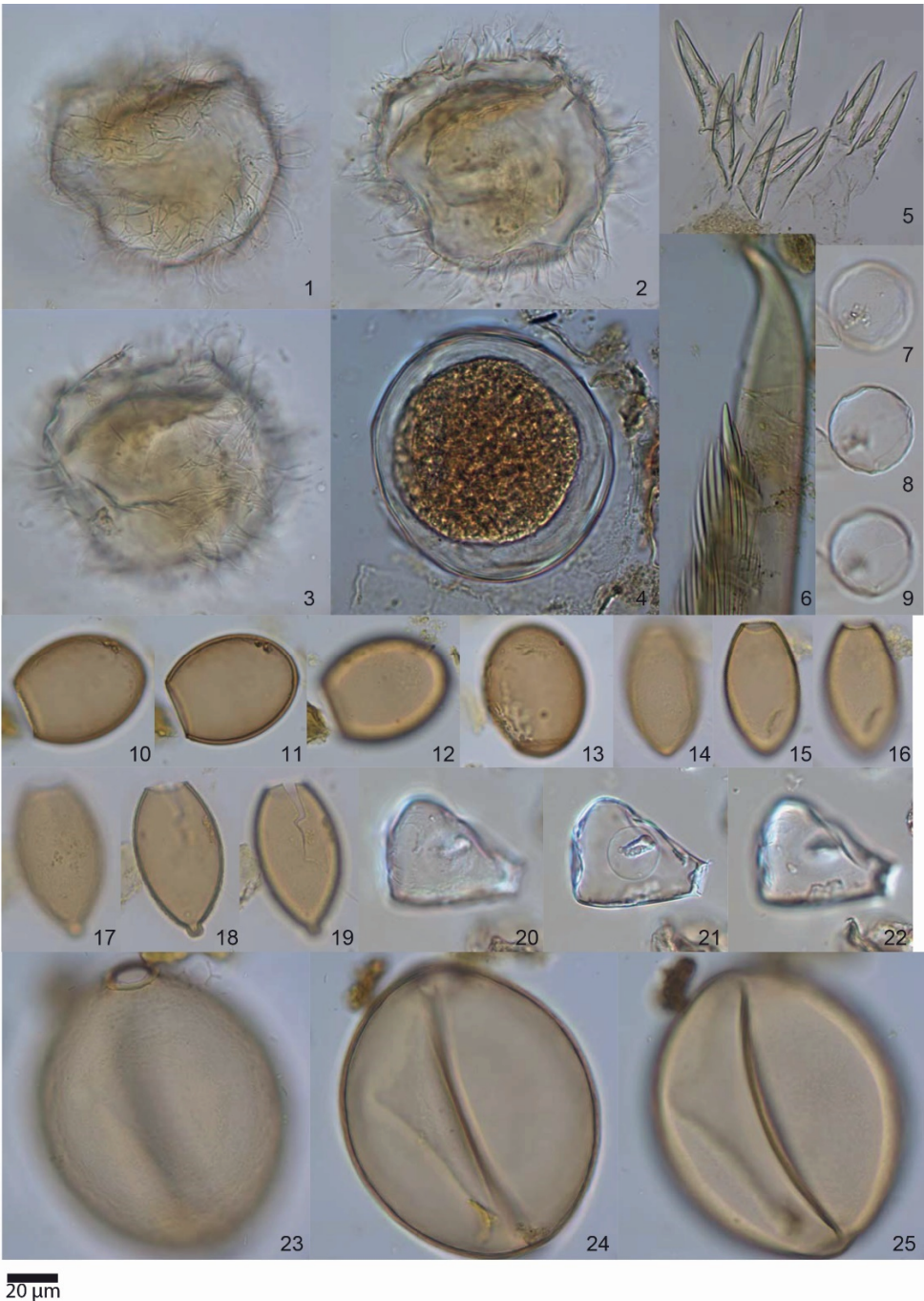
Phylum ARTHROPODA von Siebold 1848
Subphylum CRUSTACEA Brünnich 1772
Class MAXILLOPODA Dahl 1956
Subclass COPEPODA Milne-Edwards 1840

Copepod spermatophores

Palynomorph: Copepod spermatophore Type AB-33 (Plate 3, figure 24–28)

Morphology and identification: Among the palynological remains in Hole U1357B, club-shaped, transparent vesicles have also been found, which are most likely copepod spermatophores. Copepod spermatophores are generally club-shaped or flask-shaped and taper towards the proximal end into a tube-like neck (Subramoniam, 2017).

Biological taxon: It is unknown to which copepod species this spermatophore belongs. Like most crustaceans, copepods produce a spermatophore to aid sperm transfer and avoid loss of sperm (Subramoniam, 2017). The spermatophore is attached to the female genital orifice with some adhesive material around the neck, after which sperm is released through the tube-like neck (Subramoniam, 2017).



Dimensions: The spermatophore is 37 ± 5 μm in length ($n=2$) when the tube-like neck is not included.

The fossil record: Similar-looking forms have been recovered from a peat section in Tierra del Fuego (Borromei et al., 2010).

Palynomorph: Copepod (possibly) spermatophore Type AB-22 (Plate 4, figure 6–7)

Morphology and identification: Type AB-22 large, orangish brown tetrahedral casing. The three angles at the ‘base’ of the tetrahedron have rounded edges, while the ‘top’ acuminate into an extended tube-like neck. Due to flattening on the microscope slide the tetrahedral shape can appear more triangular with one of the base angles folded. The tetrahedron casing and tube-like neck show a resemblance to the spermatophores of some crustaceans, copepods in particular (Subramoniam, 2017). If that is the case, Type AB-22 is 4 times larger than Type AB-33, suggesting it is produced by a larger copepod species than the species that produced Type AB-33.

Biological taxon: Possibly a larger copepod species. Larger copepods can produce spermatophores that exceed a length of 100 μm (e.g., Hopkins 1978; Defaye et al. 2000), but the tetrahedron shape of Type AB-22 is different from the typical elongated club-shaped copepod spermatophores (Hopkins, 1978; Defaye et al., 2000; Subramoniam, 2017). We can therefore not be certain that this is indeed a copepod spermatophore. Alternatively, it is produced by another order of small crustaceans that we have not been able to identify.

Dimensions: The width of the casing ranges between 124 and 141 μm and the tube-like neck is 115 ± 20 μm long ($n=4$).

Geographic distribution: Identical specimens derived from surface sediment samples from Prydz Bay have been depicted as an “egg case” by Storkey (2006, plate 12, fig. 7–10).

Copepod eggs

Palynomorph: Copepod egg (Plate 4, figure 9; Plate 5, figure 1–3)

Morphology and identification: A transparent sphere, which is densely covered in spines. The thickness of the egg envelopes in diapause eggs can be several micrometres thick (Santella and Ianora, 1990; Berasategui et al., 2012). Therefore, these eggs are likely quiescence subitaneous eggs because their walls appear relatively thin.

Biological taxon: Considering that *Paralabidocera antarctica* is the most common copepod species at the Adélie coast (Loots et al., 2009) and that *P. antarctica* produces similar-sized eggs (Swadling, 1998), it is possible that these belong to *P. antarctica*. The

morphology of subitaneous (and diapause) eggs of *P. antarctica* is, however, unknown to us.

Dimensions: The egg diameter is $115\pm 15\ \mu\text{m}$ ($n=3$) and the spines have a length of $16\pm 3\ \mu\text{m}$ ($n=11$).

Copepod mandibular gnathobases

Palynomorph: Copepod mandibular gnathobase 1 (Plate 3, figure 21)

Morphology and identification: This mandibular gnathobase is rectangular with a toothed edge at one side consisting of nine triangular teeth, which decrease in size towards one side. It somewhat resembles the mandibular gnathobase of the local copepod *Stephos longipes*. However, this species has a large separation between the ventral (largest) tooth and the first central tooth (Razouls et al., 2005-2017), which is not the case in this specimen. Instead, it is more similar to the mandibular gnathobase of *Centropages hamatus* (Michels and Gorb, 2015), but this is not a Southern Ocean species.

Biological taxon: Although we have not been able to assign it to any specific copepod species, such robust gnathobases with compact relatively short teeth at the distal ends typically belong to species that feed on phytoplankton (i.e. diatoms) (Michels and Gorb, 2015).

Dimensions: It is $68\pm 5\ \mu\text{m}$ wide and $30\pm 3\ \mu\text{m}$ high ($n=2$).

Palynomorph: Copepod mandibular gnathobase 2 (Plate 3, figure 17)

Morphology and identification: Compared to mandibular gnathobase 1, this specimen is more square-shaped. It possesses five triangular teeth (chitinous tooth sockets). The ventral tooth is smaller than the two teeth (first and second central tooth) adjacent to it. Both the square-shaped dimensions and the number of teeth strongly resemble the mandibular gnathobase of *Rhincalanus gigas* (Michels and Gorb, 2015). Also, confocal laser scanning micrographs show that the ventral tooth socket is indeed smaller than the first central tooth (Michels and Gorb, 2015).

Biological taxon: Probably *Rhincalanus gigas*.

Dimensions: It has a width of $35\ \mu\text{m}$ and height of $50\ \mu\text{m}$ ($n=1$).

Geographic distribution: *R. gigas* is a Southern-Ocean-wide species, but is most common in the Antarctic Circumpolar Current (Atkinson, 1998).

Ecological preferences and environmental interpretation: Being one of the most herbivorous species (feeding mostly on phytoplankton) of the Southern Ocean, *R. gigas* feeds predominantly on diatoms (Atkinson, 1998; Atkinson et al., 2012). Populations of *R. gigas* descend to deeper waters in winter when they do not feed (diapause), although

some populations have been found feeding in open surface waters during winter (Atkinson, 1998).

Exoskeleton parts

Palynomorph: Copepod thoracopod (Plate 3, figure 29)

Morphology and identification: This is a segmented exoskeleton part. Towards the distal end the segments become smaller stepwise. We have identified this as the distal part of a thoracopod (swimming leg) of a copepod.

Biological taxon: Considering its size it probably belonged to a small copepod species.

Dimensions: It is 92 μm long (n=1).

Palynomorph: Copepod endites (Plate 5, figure 5)

Morphology and identification: Within the samples of Hole U1357B groups transparent conical palynomorphs are encountered, which are attached together at their base by a thin transparent surface. In some cases spines protrude from the base of an individual transparent cone. Although we cannot be certain, we believe that these could be the endites of a copepod maxilla.

Biological taxon: These are probably copepod mandible remains.

Dimensions: The transparent cones are typically $42 \pm 12 \mu\text{m}$ long (n=9).

Palynomorph: Copepod setae (Plate 5, figure 6; Plate 6, figure 5)

Morphology and identification: The most frequently encountered remains of copepods in the samples of U1357B are the setae of copepod thoracopods. Fans of bristles are positioned on one side of the seta at constant intervals.

Biological taxon: Such specimens likely belong to the larger copepod species such as *Rhincalanus gigas* (Razouls et al., 2005-2017), of which mandibular gnathobases were also found (see above).

Dimensions: The setae are often fragmented, but the largest specimen that was measured is 527 μm long.

Phylum TARDIGRADA Spallanzani 1776

Class EUTARDIGRADA Marcus 1927

Order PARACHELA Schuster et al. 1980

Superfamily MACROBIOTOIDEA Thulin 1928 in Marley et al. 2011

Palynomorph: Macrobiotoid tardigrade egg (Plate 2, figure 17–20)

Morphology and identification: The eutardigrade superfamily Macrobiotioidea (Marley et al., 2011) comprises several genera of tardigrades that produce eggs with an ornamentation consisting of tapered, conical projections with or without distal bifurcations or dishes (Bertolani and Rebecchi, 1993; Pilato et al., 2004; Gibson and Zale, 2006; Bartels et al., 2009; Altiero et al., 2010; Zawierucha et al., 2016). Within the samples of Hole U1357B we encountered one palynomorph that strongly resembles a macrobiotoid tardigrade egg. This palynomorph is transparent and smooth-walled with transparent, hollow, conical processes (about 20 are visible on one side of the egg). Each conical projection is about 4 μm high and possesses a thread-like extension at its tips, which can be as long as the conical projection itself.

Biological taxon: The egg found in Hole U1357B resembles the eggs of *Macrobiotus krynaui* (Dastych and Harris, 1995) or *Macrobiotus blocki* (see Gibson et al. 2007), although it is much smaller in size and has longer thread-like extensions at its processes. The exact macrobiotoid tardigrade species to which this egg belongs remains unknown.

Dimensions: Without its processes the egg is 19 μm in diameter ($n=1$).

Geographic distribution: Macrobiotoid eutardigrades are found worldwide in freshwater and semiterrestrial environments (Bertolani et al., 1996). Also on Antarctica, tardigrade eggs have been found in freshwater and slightly brackish lake sediments (Gibson and Zale, 2006; Gibson et al., 2007; Cromer et al., 2008) as well as on sparsely vegetated and ice-free areas (Dastych and Harris, 1995; Convey and McInnes, 2005; Convey et al., 2008).

The fossil record: The eggs of tardigrades are also known to be preserved in sediments (Gibson and Zale, 2006; Gibson et al., 2007; Cromer et al., 2008; Borrromei et al., 2010; Mudie et al., 2011). However, species-specific environmental reconstructions are scarce. Recently, multiple Holocene tardigrade egg records from Antarctic lakes were generated that give insight into Holocene tardigrade dispersal and how they are affected by regional climate change (Gibson and Zale, 2006; Gibson et al., 2007).

Ecological preferences and environmental interpretation: Notably, only eutardigrades, which comprise the freshwater and semiterrestrial tardigrades, produce ornamented eggs in contrast to the marine heterotardigrades, which produce smooth-walled eggs (Bertolani et al., 1996). Within sedimentary records increased amounts of such ornamented tardigrade eggs have been associated with restricted freshwater conditions, such as lakes or ponds (Gibson and Zale, 2006; Gibson et al., 2007; Cromer et al., 2008; Borrromei et al., 2010; Mudie et al., 2011). The presence of tardigrade eggs in samples of Hole U1357B is therefore a surprise given the marine conditions as indicated by the other plankton groups. Since we have only found one and because tardigrades are also common on sparsely vegetated and ice-free areas of the Antarctic continent (Dastych and Harris,

1995; Convey and McInnes, 2005; Convey et al., 2008), it is likely that it has been transported (through icebergs or wind) from the Antarctic mainland.

5.6 Acritarchs

Group *incertae sedis* ACRITARCHA Evitt 1963

Subgroup SPHAEROMORPHITAE Downie, Evitt & Sarjeant 1963

Genus *Leiosphaeridia* Eisenack 1958

Leiosphaeridia sp. 1–3 (Plate 3, figure 30–34; Plate 5, figure 4, 7–9; Plate 7, figure 1–3)

Morphology and identification: The genus *Leiosphaeridia* includes all simple, smooth, spherical palynomorphs, which may or may not exhibit dehiscence through partial rupture (Colbath and Grenfell, 1995). Within Hole U1357B we can distinguish three morphotypes: *Leiosphaeridia* sp. 1 (Plate 7, figure 1–3), *Leiosphaeridia* sp. 2 (Plate 3, figure 30–34; Plate 5, figure 7–9), and *Leiosphaeridia* sp. 3 (Plate 5, figure 4). All three species are transparent spheres, but *Leiosphaeridia* sp. 2 can be more yellow. Also, some specimens of *Leiosphaeridia* sp.2 appear to be covered by a second membrane (Plate 3, figure 32–34) or have a hole (Plate 5, figure 9).

Biological taxon: The genus *Leiosphaeridia* has been the subject of considerable taxonomic debate, in part due to its uncertain biological affinities (Martin, 1993; Colbath and Grenfell, 1995). An affinity with green algae, such as *Chlorella* Beijerinck 1890 and the prasinophyte *Halosphaera* Schmitz 1879, has been suggested for some *Leiosphaeridia* species, but the genus could very well be polyphyletic (Martin, 1993; Colbath and Grenfell, 1995). Because of its uncertain taxonomic position, we retain it under Acritarcha.

Dimensions: *Leiosphaeridia* sp. 1 is only 16 ± 1 μm in diameter ($n=2$). *Leiosphaeridia* sp. 2 is 30 ± 2 μm in diameter ($n=6$) and has a relatively thicker wall. *Leiosphaeridia* sp. 3 is 70 ± 30 μm in diameter ($n=3$) and has a relatively thin wall, which is sometimes difficult to distinguish and easily ruptured.

Geographic distribution: Smooth-walled transparent spheres can be found in marine sediments worldwide. In the Southern Ocean, *Leiosphaeridia* have been reported from modern-day surface sediments of the Prydz Bay area (Storkey, 2006) and the Ross Sea (Wrenn et al., 1998).

The fossil record: Different sizes of *Leiosphaeridia* spp. have been common near the Antarctic margin since at least the late Eocene (Kemp, 1975; Wrenn et al., 1998; Hannah et al., 2000, 2001; Troedson and Riding, 2002; Hannah, 2006; Warny et al., 2006, 2009, 2016). It is therefore possible that the more yellow specimens are reworked.

Ecological preferences and environmental interpretation: In the Arctic high abundances of *Leiosphaeridia* have been found in the low-salinity surface meltwater within disintegrating pack ice during the spring thaw (Mudie 1992; Mudie & Harland,

1996). Mudie (1992) has shown that in the Arctic increased abundances of *Leiosphaeridia* are associated with the presence of a fixed ice margin. Therefore, increased abundances of *Leiosphaeridia* have been associated with glacial retreat and freshwater discharge in palaeoreconstructions at the Antarctic margin (Hannah, 2006; Warny et al., 2006, 2016). It is uncertain whether the different sizes of *Leiosphaeridia* are related to environmental conditions, produced by different organisms, or represent different growth stages similar to prasinophyte phycomata during internal cell division.

Subgroup UNCERTAIN

Genus *Mecsekia* Hajós 1966 emend. Schrank 2003

Mecsekia cf. *Mecsekia* sp. A of Schrank (2003) (Plate 7, figure 4–9)

Morphology and identification: Within Hole U1357B, transparent spheres ornamented with about 50 pillar-like, subtriangular spines have been found. These spines are evenly distributed and the distance between them is at least 3 times the diameter of the spines. Such acritarchs belong to the genus *Mecsekia*. The genus *Mecsekia* comprises small spherical or ovoidal vesicles with numerous subtriangular spines (Schrank, 2003). The spines are solid apart from a thin central canal (Schrank, 2003). Generally no excystment structure is present (Schrank, 2003). The different species of *Mecsekia* are generally distinguished from each other based on the distribution and space between the spines, and the wall structure between the spines (Schrank, 2003). Also in the specimens from Hole U1357B, the thin central canal within the spines can be distinguished. Based on the distance between the spines, the specimens from the samples of Hole U1357B resemble *Mecsekia* sp. A of Schrank (2003). However, the spines of *Mecsekia* sp. A of Schrank (2003) are more unevenly distributed than the specimens from Hole U1357B. Palynomorph Type 115 of Pals et al. (1980), described from a Holocene peat section of the Klokkeweel bog (the Netherlands), is likely also a species of *Mecsekia* and shows resemblance to the specimens from Hole U1357B. However, Type 115 of Pals et al. (1980) has also relatively more processes.

Biological taxon: The biological affinity of this species is unknown.

Dimensions: Specimens are $15 \pm 2 \mu\text{m}$ in diameter ($n=3$).

Geographic distribution: To our knowledge this particular *Mecsekia* species is not known from modern-day sediments. However, other species of *Mecsekia* have been recovered from sediments underlying brackish water, such as the Black Sea (as *Micrhystridium* cf. *ariakense* in Mudie et al. 2011) and more dynamic coastal marine waters, such as the shallow marine Great Bahama Bank (as *Varia*-1 type in Traverse & Ginsburg 1966).

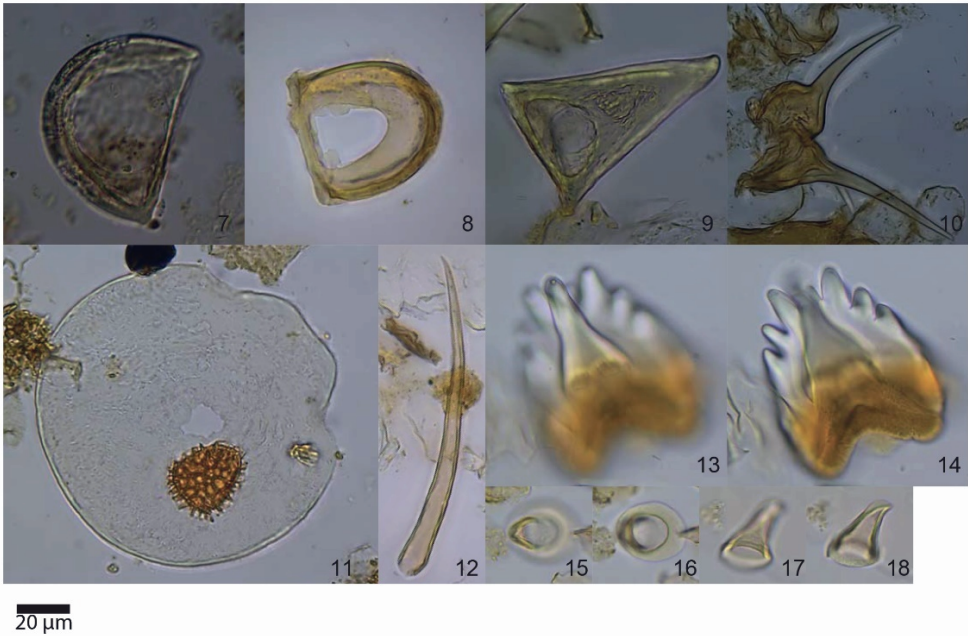
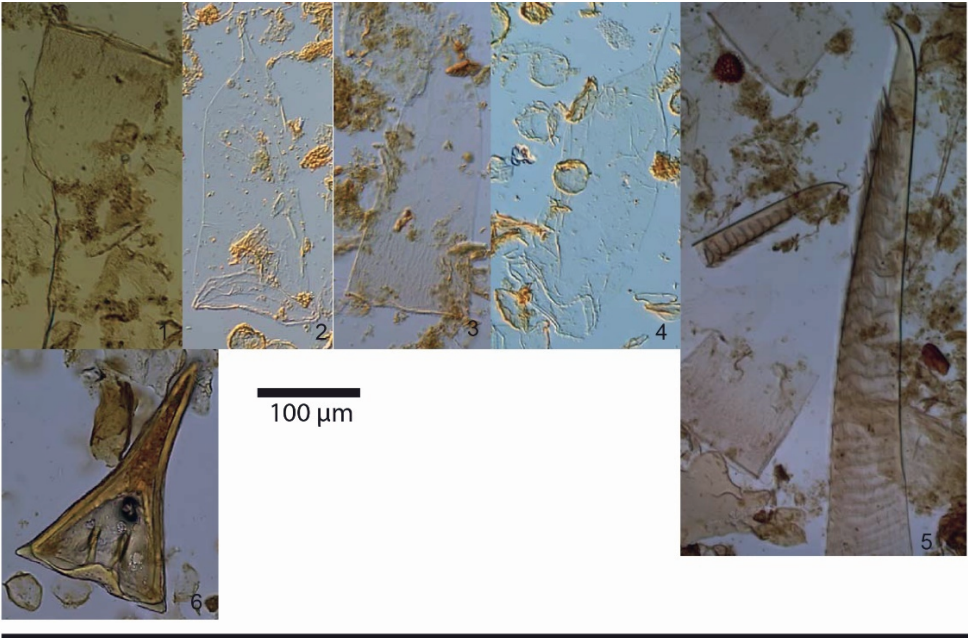


Plate 6 (previous page):

- Figure 1: *Cymatocyclus convallaria* forma *calyciformis*, U1357B-8H-3W 54–56 cm, slide 1, E.F.:K20.2.
Figure 2: *Cymatocyclus convallaria* forma *cylindrica*, U1357B-5H-5W 12–14 cm, slide 1, E.F.: S17.2, LIB image.
Figure 3: *Cymatocyclus convallaria* forma *cylindrica*, U1357B-8H-3W 54–56 cm, slide 1, E.F.: F17.3.
Figure 4: *Cymatocyclus convallaria* forma *cylindrica*, U1357B-6H-6W 123–125 cm, slide 1, E.F.: K24.1, LIB image.
Figure 5: Copepod setae: a large seta on the right and a smaller seta on the left (anterior ends of *Cymatocyclus convallaria* are also present on the left side), U1357B-8H-3W 54–56 cm, slide 1, E.F.: T30.1.
Figure 6: Type AB-27e, triangular with acute tip, U1357B-5H-7W 5–7 cm, slide 1, E.F.: H27.1, LIB image.
Figure 7: Type AB-27a, dome-shaped with broad base, U1357B-8H-3W 54–56 cm, slide 1, E.F.: Q31.3, LIB image.
Figure 8: Type AB-27b, dome-shaped, U1357B-17H-1W 117–119 cm, slide 1, E.F.: G17.3, LIB image.
Figure 9: Type AB-27d, triangular, U1357B-5H-7W 5–7 cm, slide 1, E.F.: D32.4, LIB image.
Figure 10: Type AB-29, U1357B-5H-7W 5–7 cm, slide 1, E.F.: E34.4, LIB image.
Figure 11: Type AB-28, U1357B-10H-1W 58–60 cm, slide 1, E.F.: L23.2, LIB image.
Figure 12: Type AB-30, U1357B-15H-2W 75–76 cm, slide 1, E.F.: F22.2, LIB image.
Figure 13-14: Type AB-32, U1357B-2H-2W 114–116 cm, slide 1, E.F.: N32.3, upper and lower focus.
Figure 15-16: Type AB-31, top view, U1357B-6H-6W 123–125 cm, slide 1, E.F.: J26.3, upper and lower focus.
Figure 17-18: Type AB-31, lateral view, U1357B-17H-5W 97–99 cm, slide 1, E.F.: O28.4, upper and lower focus.
-

The fossil record: *Mecsekia* sp. A of Schrank (2003) was described from Maastrichtian deposits in Egypt.

Ecological preferences and environmental interpretation: Based on the distribution pattern of the various *Mecsekia* species, Schrank (2003) infers that *Mecsekia* prefers a shallow marine environment. Notably, Type 115 of Pals et al. (1980) was also only found in the marine clay deposits underlying the lake deposits of this peat section (Pals et al., 1980). However, the fact that *Mecsekia* has also been associated with more restricted brackish water settings today (Mudie et al., 2011) suggests some tolerance to lower salinities. A tolerance to lower salinities is also suggested by fossil accounts of *Mecsekia*, such as the Miocene restriction of the Pannonian Lake and the associated stratification (Magyar et al., 1999; Sütő and Szegő, 2008; Sütőné Szentai, 2012).

Genus *Palaeostomocystis* Deflandre 1937

Palaeostomocystis cf. *fritilla* (Bujak 1984) Roncaglia 2004b (Plate 5, figure 10–13)

Morphology and identification: Ovoidal, yellow, smooth, thick-walled vesicles with a single polar pylome (opening) with an undulate margin have been found within the samples of U1357B. These belong to the genus *Palaeostomocystis*, which comprises all single-walled vesicles with a large pylome. They resemble *Palaeostomocystis fritilla* in particular, but lack faveolated wall, resembling a fine-meshed reticulate network of muri (Bujak, 1984; Roncaglia, 2004b; Warny, 2009).

Biological taxon: The biological affinity of *P. fritilla* is unknown (Warny, 2009) and it is uncertain whether *Palaeostomocystis* cf. *fritilla* is produced by a different biological species than the species producing *P. fritilla*. Alternatively, *Palaeostomocystis* cf. *fritilla* are

diagenetically altered forms of *P. fritilla*. *P. fritilla* shows some similarity to the egg capsules (oocytes) produced by Turbellaria (Platyhelminthes), which are ovoidal capsules with an single operculum (Harmsworth, 1968). Such oocytes are known to be preserved (Harmsworth, 1968; Borromei et al., 2010; Mudie et al., 2011). For example, larger but similar-looking oocytes with a smooth pylome margin have been reported from a peat core derived from a mire in Tierra del Fuego (Borromei et al., 2010). Nevertheless, different Turbellaria species produce different shapes and sizes of oocytes. Turbellaria are known to live in Antarctic sea ice and release their eggs upon ice melt (Janssen and Gradinger, 1999; Kramer et al., 2011). However, the studied species by Janssen & Gradinger (1999) do not seem to produce egg capsules and release globular-shaped eggs of 30-90 µm directly into the surface waters.

Dimensions: Specimens of *Palaeostomocystis* cf. *fritilla* are 49±5 µm long and 41±3 µm wide (n=5).

Geographic distribution: *Palaeostomocystis* species in general have been associated with a (sub)polar environment (Warny, 2009). *P. fritilla* has also been reported from surface sediments of the Weddell Sea, Antarctica, although it is possible that these are reworked from older Pleistocene sediments (Yi et al., 2005; Warny, 2009; Pieńkowski et al., 2013b). *P. fritilla* has also been reported from surface sediments in the Prydz Bay area (Storkey, 2006), the (Canadian) Arctic (Pieńkowski et al., 2011), Disko Bay, west Greenland (Roncaglia, 2004b; Seidenkrantz et al., 2008), and the Faroe Islands (Roncaglia, 2004a). Notably, it has also been reported from surface sediments in the more temperate semi-marine environment of the Marmara Sea, although rare in abundance (Mudie et al., 2011).

The fossil record: Originally *P. fritilla* was described from Pleistocene sediments in cores derived from the northern North Pacific and the Bering Sea (Bujak, 1984). Other reports of *P. fritilla* come from middle and late Holocene core sections obtained in Tierra del Fuego, Argentina (Candel et al., 2013), Disko Bay, west Greenland (Roncaglia, 2004b; Seidenkrantz et al., 2008; Ribeiro et al., 2012b), the Faroe Islands (Roncaglia, 2004a), and the Canadian Arctic (Pieńkowski et al., 2011, 2013a, 2014). In addition, Pieńkowski et al. (2014) reports smooth-walled varieties of *P. fritilla*, referred to as *Palaeostomocystis* sp. A, from mid-Holocene deposits of the Canadian Arctic.

Ecological preferences and environmental interpretation: In paleoenvironmental records increased abundances of *P. fritilla* have been associated with the proximity of the sea-ice margin, the establishment of a seasonal sea-ice environment (Roncaglia, 2004a; Pieńkowski et al., 2013a, 2014), and glacial freshwater discharge and/or stratification (Seidenkrantz et al., 2008). In the Canadian Arctic Archipelago the highest abundances are associated with the modern-day 9-10 months per year of sea-ice cover (Pieńkowski et al., 2013a, 2014).

Palaeostomocystis cf. reticulata (Plate 5, figure 14–19)

Morphology and identification: This species of *Palaeostomocystis* is ovoidal, but more slender than *Palaeostomocystis cf. fritilla*, and has reticulate surface-wall ornamentation. It has a yellow thick wall, but the reticulate surface-wall structure is thin, barely visible, and colourless. At one pole a large pylome is present that is almost half the diameter of the vesicle. Because of these characteristics it strongly resembles *Palaeostomocystis reticulata* of Deflandre (1937), which has been described from Cretaceous flint pebbles in the Paris Basin. However, the specimens of *P. cf. reticulata* in Hole U1357B possess a conical antapex often with a (prominent) knob that is lacking in *P. reticulata*.

Biological taxon: The biological affinity of this taxon is unknown.

Dimensions: Specimens of *Palaeostomocystis cf. reticulata* are 57 ± 4 μm long and 31 ± 2 μm wide (n=5).

Geographic distribution: These palynomorphs have not been reported from modern-day surface sediments.

The fossil record: This is the first account of *Palaeostomocystis cf. reticulata* in the fossil record. However, *P. reticulata* has been reported from Upper Eocene to Pliocene reworked surface sediments around the Antarctic Peninsula (Warny, 2009) apart from its original description from the Paris Basin (Deflandre, 1937).

Ecological preferences and environmental interpretation: Because the biological affinity is unknown, the ecological preferences are unknown for this palynomorph. However, *Palaeostomocystis* have been associated with (sub)polar environments in general (Warny, 2009).

Palaeostomocystis sphaerica Deflandre 1937 sensu Warny 2009
(Plate 4, figure 10–11, 13–17; Plate 5, figure 23–25)

Morphology and identification: These acritarchs are yellow-brown, thick-walled, granulated spheres with a single collared pylome in the middle of a frustoconical collar (Deflandre, 1937). They strongly resemble the specimens of *P. sphaerica* depicted by Warny (2009). However, some specimens encountered in Hole U1357B are found with an additional transparent envelope with a long transparent tail (Plate 4, figure 13–17). This is similar to the specimens depicted as *Zooplankton* spp. from Prydz Bay (Storkey 2006, plate 8, figures 7–12 and plate 9, figures 1–9). However, this envelope is generally not present and probably lost due to the process of lithification.

Biological taxon: The original description of Deflandre (1937) for *Palaeostomocystis sphaerica* was based on a single specimen derived from a Cretaceous flint pebble from the

Paris Basin. Although the original specimen of Deflandre (1937) was just 20 μm , Warny (2009) also included specimens sampled from Upper Eocene to Pliocene reworked material around the Antarctic Peninsula, which ranged in size between 40 and 120 μm . Although different in size, these specimens are very similar in shape and wall ornamentation (Warny 2009: plate 1, figure 9; Deflandre, 1937: plate XII, figure 6).

Dimensions: The spheres in Hole U1357B range between 123 and 167 μm in diameter (average: 138 μm , $n=7$).

Geographic distribution: Specimens of *P. sphaerica* identical to those of Hole U1357B and similar to the large specimen depicted by Warny (2009) have also been found in surface samples in Prydz Bay (Storkey 2006, plate 8, figures 7–12 and plate 9, figures 1–9). The specimens described by Warny (2009) from surface sediments of the Weddell Sea are considered reworked.

The fossil record: *P. sphaerica* has not been described from prehistoric deposits apart from the original description from the Paris Basin (Deflandre, 1937). *P. sphaerica* sensu Warny (2009) is not known from the fossil record, although the specimens from the Weddell Sea are considered reworked from older strata (Warny, 2009).

Ecological preferences and environmental interpretation: In contrast to the specimens of Warny (2009), the occasional occurrence of this transparent envelope and the presence of cell content in some specimens of Hole U1357B could suggest that these specimens are not reworked from older sediments. Like *P. fritilla*, it has been suggested that *P. sphaerica* is also indicative of a (sub)polar environment and that the older species such as *P. sphaerica* might have evolved a preference for colder surface waters since the Cretaceous (Warny, 2009). However this assumes that the different *Palaeostomocystis* species are phylogenetically related, despite the fact that their biological affinity is uncertain (Warny, 2009). Instead, there is a possibility that the different *Palaeostomocystis* species are biologically unrelated. It is even very possible that the smaller *P. sphaerica* described by Deflandre (1937) from the Cretaceous was produced by a very different species than the specimens encountered in modern surface sediments. Today, similar spherical cysts with a single collared pylome are produced by both parasitic perkinsozoans (Leander and Hoppenrath, 2008; Choi and Park, 2010; Mangot et al., 2011) and spirotrich ciliates (Reid and John, 1983; Reid, 1987; Müller and Wünsch, 1999; Kamiyama, 2013). Resting cysts of the tintinnid ciliates encountered in Hole U1357B (i.e., *Codonellopsis*, *Laackmanniella*, *Cymatocylis*) are, however, unknown and cannot be compared to *P. sphaerica*. The manner in which some of the specimens found in Hole U1357B and in Prydz Bay are enveloped by a tailed transparent sac does, in fact, resemble a host organism (e.g., dinoflagellate) with a parasitic perkinsozoan cyst that has penetrated the host's cell wall with its germ tube (i.e. pylome) to release its newly formed zoospores (see Leander &

Hoppenrath 2008). On the other hand, it is unlikely that the cell wall of the host organism would be preserved. The biological affinity and ecological preferences of *P. sphaerica* sensu Warny (2009) therefore remain uncertain.

Palaeostomocystis sp. B (Plate 7, figure 10–15)

Morphology and identification: This is a yellowish, ovoidal vesicle with one polar pylome. The surface of the wall is covered by a yellowish to colourless reticulate network of membranes. In this respect it is very similar to *Palaeostomocystis reticulata* of Deflandre (1937) found in Cretaceous flint pebbles in the Paris Basin. However, the width of the pylome of *P. reticulata* is almost half the diameter of the vesicle and possesses no collar, while the specimens from Hole U1357B have a relatively small pylome with an outward-extending collar more similar to the smooth-walled *Palaeostomocystis* sp. 1 of Warny (2009). In addition, the reticulate network appears to be denser than the original drawings of *P. reticulata* of Deflandre (1937).

Biological taxon: Like the *P. sphaerica* specimens of Hole U1357B, *Palaeostomocystis* sp. B resembles some of the cysts produced by spirotrich ciliates (Reid and John, 1983; Reid, 1987; Müller and Wünsch, 1999; Kamiyama, 2013), which are known to also produce various kinds of surface-wall ornamentation (Foissner et al., 2007).

Dimensions: These palynomorphs are 33 ± 5 μm long and 22 ± 5 μm wide ($n=4$).

Geographic distribution: *Palaeostomocystis* sp. B is not known from modern-day surface sediments.

The fossil record: *Palaeostomocystis* sp. B is not known from other fossil records.

Ecological preferences and environmental interpretation: Because the biological affinity is unknown, the ecological preferences are unknown for this palynomorph. However, *Palaeostomocystis* have been associated with (sub)polar environments in general (Warny, 2009).

Palaeostomocystis sp. C (Plate 5, figure 20–22)

Morphology and identification: A transparent globular vesicle with one polar collared pylome. The rounded shape of this vesicle is somewhat flattened at the opposite site of the pylome.

Biological taxon: Smooth spherical cysts with a single collared pylome are produced by both parasitic perkinsozoans (Leander and Hoppenrath, 2008; Choi and Park, 2010; Mangot et al., 2011) and spirotrich ciliates (Reid and John, 1983; Reid, 1987; Müller and Wünsch, 1999; Kamiyama, 2013). As mentioned above, cysts of the Antarctic spirotrich tintinnids are unknown, so it is uncertain whether *Palaeostomocystis* sp. C belongs to any of these tintinnids.

Dimensions: These palynomorphs are 50 ± 5 μm long and 50 ± 5 μm wide ($n=3$).

Geographic distribution: *Palaeostomocystis* sp. C is not known from modern-day surface sediments.

The fossil record: *Palaeostomocystis* sp. C is not known from other fossil records.

Ecological preferences and environmental interpretation: Because the biological affinity is unknown, the ecological preferences are unknown for this palynomorph. However, *Palaeostomocystis* have been associated with (sub)polar environments in general (Warny, 2009).

5.7 Palynomorphs of unknown affinity

Palynomorph Type AB-2 (Plate 7, figure 22–24)

This is a 17 ± 1 μm sized sphere ($n=3$) with a very thick wall and can appear relatively flat under the light microscope. The wall thickness is about one-fifth of the sphere's diameter. It is transparent without any wall ornamentation. It could therefore be considered as a leiosphere, but because there are also 10 μm sized *Leiosphaeridia* without such a distinct thick wall, we treat Type AB-2 separately.

Palynomorph Type AB-3 (Plate 7, figure 31–37)

Type AB-3 consists of a flattened spherical “body”, such that the cross section is ovoidal, and a “tail” shaped like an open cylinder positioned on one of the flattened surfaces. The membrane forming the cylindrical tail expands around one-half of the body and forms a crenulated crest that decorates the equator of the body. The distal end of the cylindrical membrane is slightly tapered. On the flattened surface of the body across from the tail, a single pylome is present without any collar. The diameter of the pylome is about half the size of the diameter of the flattened surface of the body, which has a diameter of 18 ± 1 μm ($n=4$). The length of body and tail together is 28 ± 1 μm .

Palynomorph Type AB-4 (Plate 7, figure 38–41)

Type AB-4 is a transparent sphere of about 18 ± 2 μm in diameter ($n=3$) that is ornamented with 35 to 50 solid processes with a length of about 10 μm . At their distal ends the processes are dendritic, showing multiple bifurcations in a tree-like fashion. These distal ‘branches’ do not seem to interconnect between processes.

Palynomorph Type AB-5 (Plate 7, figure 25–26)

This palynomorph has a fuzzy appearance, but seems to consist of an inner body with cellular content and an outer spongy layer. Although the cellular content in Type AB-5 is contained in a spherical body, the spongy outer layer of the palynomorph seems to be a polyhedron (edges can be distinguished in the outline). Its size is 23 μm in diameter ($n=1$).

Palynomorph Type AB-13 (Plate 7, figure 16–21)

This palynomorph consists of a transparent sphere with a diameter of $11\pm 2 \mu\text{m}$ ($n=3$). From this sphere an equatorial, undulating crest extends from which a transparent membrane extends towards both poles. This membrane is striated and/or folded longitudinally and is open at the polar ends. Including the membrane the total length of the palynomorph is about 25 μm . The presence of an equatorial membrane is similar to the equatorial alae of some phycomata of prasinophyte algae (Parke et al., 1978).

Palynomorph Type AB-19 (Plate 7, figure 27–30)

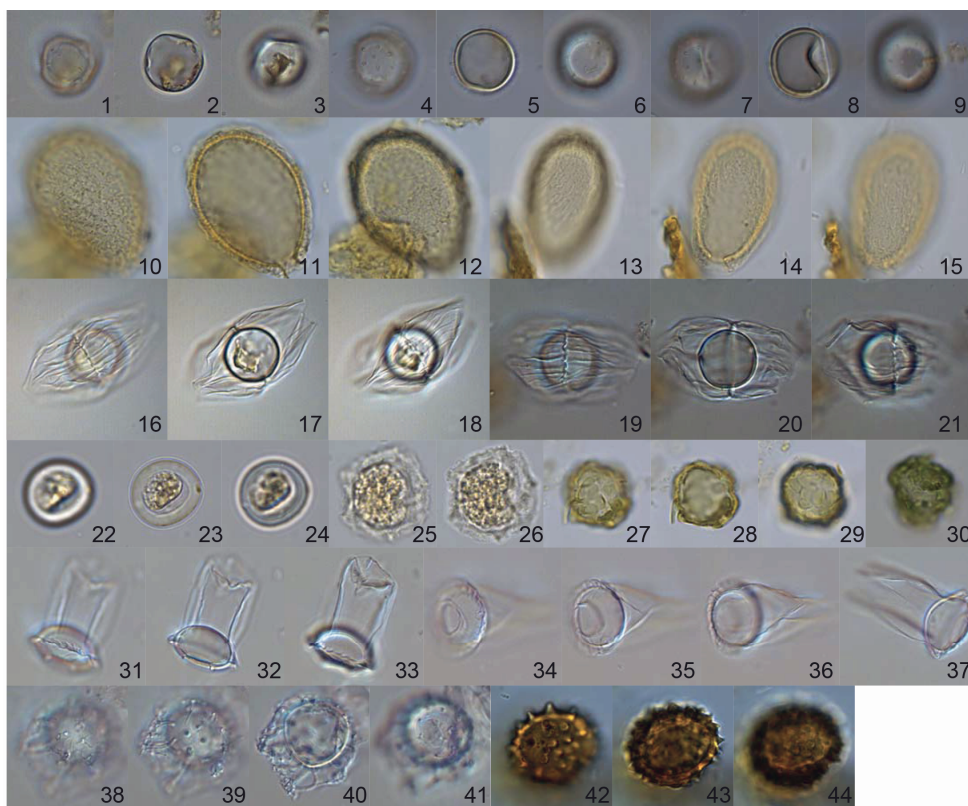
A green or yellowish green subspherical body that is covered with wart-like protrusions. Type AB-19 is about $17\pm 2 \mu\text{m}$ in diameter ($n=4$). The wart-like protrusions are solid, circular, or ovoid thickenings of the wall surface about 2–3 μm in diameter.

Palynomorph Type AB-21 (Plate 7, figure 42–44)

Type AB-21 is thick-walled, slightly ovoidal, and ornamented with solid triangular short spines, which are distributed irregularly at some parts of the wall surface. It has a dark yellow colour and is 22 μm in diameter ($n=1$). The spines resemble those of a tardigrade egg, but tardigrade eggs are transparent and do not possess such a thick wall. Alternatively, it could be an ornamented pollen grain.

Palynomorph: Type AB-27a – f (Plate 4, figure 12, 18; Plate 6, figure 6–9)

Within the samples of Hole U1357B there is a variety of thick-walled domes and cones that all share a characteristic semicircular to subtriangular cavity at the base. Their sizes range from 52 to 243 μm long (average: 124 μm , $n=8$). Some shapes resemble the lorica of a tintinnid ciliate, but tintinnid loricae have a much thinner hyaline wall. Also, all specimens have a thick-walled base and therefore cannot house a single-celled organism. Instead, the cavity is open laterally. If these are in fact parts of a crustacean exoskeleton, it is unknown to which part they belong. We distinguish six different morphotypes: a) dome-shaped with a broad base, b) dome-shaped with height and width being equal, c) bullet-shaped, d) triangular, e) triangular with long acute tip, and f) falcate.



20 µm

Plate 7:

Figure 1-3: *Leiosphaeridia* sp. 1, U1357B-17H-5W 97–99 cm, slide 1, E.F.: L33.4, upper, mid and lower focus.

Figure 4-6: *Mecsekia* cf. *Mecsekia* sp. A of Schrank (2003), U1357B-18H-4W 2–3 cm, slide 1, E.F.: D23.3, upper, mid and lower focus.

Figure 7-9: *Mecsekia* cf. *Mecsekia* sp. A of Schrank (2003) with dent, U1357B-18H-4W 2–3 cm, slide 1, E.F.: H30.3, upper, mid and lower focus.

Figure 10-12: *Palaeostomocystis* sp. B, U1357B-6H-6W 123–125 cm, slide 1, E.F.: E30.3, upper, mid and lower focus.

Figure 13-15: *Palaeostomocystis* sp. B, U1357B-3H-7W 10–12 cm, slide 1, E.F.: O19.1, upper, mid and lower focus.

Figure 16-18: Type AB-13, U1357B-17H-1W 117–119 cm, slide 1, E.F.: D25.4, upper, mid and lower focus.

Figure 19-21: Type AB-13, U1357B-18H-4W 2–3 cm, slide 1, E.F.: F21.2, upper focus, mid and lower focus.

Figure 22-24: Type AB-2, U1357B-18H-2W 114–116 cm, slide 1, E.F.: H28.1, upper, mid and lower focus.

Figure 25-26: Type AB-5, U1357B-1H-1W 11–13 cm, slide 1, E.F.: E22.3, upper and mid focus.

Figure 27-29: Type AB-19, U1357B-5H-5W 12–14 cm, slide 1, E.F.: F32.1, upper, mid and lower focus.

Figure 30: Type AB-19, U1357B-7H-5W 4–6 cm, slide 1, E.F.: V21.4, upper focus.

Figure 31-33: Type AB-3, U1357B-1H-1W 11–13 cm, slide 1, E.F.: G23.1, upper, mid and lower focus.

Figure 34-36: Type AB-3, U1357B-3H-7W 10–12 cm, slide 1, E.F.: O22.3, upper, mid and lower focus.

Figure 37: Type AB-3, U1357B-3H-7W 10–12 cm, slide 1, E.F.: G29.2, mid focus.

Figure 38-41: Type AB-4, U1357B-1H-2W 40–42 cm, slide 1, E.F.: H33.1, upper focus on dendritic distal process endings, upper focus on central body, mid and lower focus.

Figure 42-44: Type AB-21, U1357B-5H-7W 5–7 cm, slide 1, E.F.: E32.2, upper, mid and lower focus.

Palynomorph: Type AB-28 (Plate 6, figure 11)

This is a flat, circular palynomorph, but at one side of the palynomorph two rounded indents interrupt the circular outline. Its diameter is about 117 μm ($n=1$). It is possible that this is part of an arthropod exoskeleton.

Palynomorph: Type AB-29 (Plate 6, figure 10)

Sickle-shaped exoskeleton parts extending from a broad base. The sickles are about 44 ± 4 μm long ($n=2$).

Palynomorph: Type AB-30 (Plate 6, figure 12)

These are long, yellow, curved blades that are hollow inside. They are generally longer than 100 μm . The lack of distinct characteristics makes it difficult to assign these types of palynomorphs to a particular organism. As discussed above, such forms can be parts of crustacean mandibles or the jaw apparatus of eunicid annelids, although the remains of the latter have a distinct dark red colour in the samples of U1357B. Alternatively they could be the grasping spines positioned on the posterolateral sides of the heads of chaetognaths, which they use for capturing prey (Ball and Miller, 2006). These grasping spines are also hollow and can be longer than 100 μm (for detailed SEM images see Szaniawski 2002). Chaetognaths are the second most abundant zooplankton group in the Southern Ocean after the copepods, on which they prey (Froneman and Pakhomov, 1998; Terazaki et al., 2013). Also in the Southern Ocean north of the Adélie Coast, chaetognaths, particularly *Eukrohnia hamata* and *Sagitta gazellae*, have been recorded, although their abundance decreases towards higher latitudes due to the scarcity of larger copepod species (Terazaki et al., 2013). However, the number of the deeper-dwelling *E. hamata* particularly increases when the sea ice disappears in spring-summer (Terazaki et al., 2013). It is thus very possible that their grasping spines end up in the sediments of the Adélie Basin.

Palynomorph: Type AB-31 (Plate 6, figure 15–18)

This palynomorph resembles a hollow thorn. It is similar to Type AB-30, but much shorter: 25 ± 1 μm ($n=2$). In addition, the bottom aperture, which is about 10 μm , has an outward-extending rim a few micrometres wide. As with Type AB-30, it is unclear to what organism this palynomorph belongs due to the lack of characteristic features. However, the size of Type AB-31 makes it too small to be the remains of chaetognath grasping spines. Alternatively, we found that the circular rim around the aperture is the same size as the pylome of *Palaeostomocystis sphaerica*, which means that Type AB-31 could be the

plugs of *P. sphaerica*. These plugs would detach when the content of *P. sphaerica* would have been released, similar to the way the cysts of spirotrich ciliates release an operculum to allow the ciliate to escape (Reid and John, 1983; Reid, 1987; Müller and Wünsch, 1999). However, spirotrich cysts with a pointy operculum are not known to us.

Palynomorph: Type AB-32 (Plate 6, figure 13–14)

This is a tooth-like palynomorph with a semicircular outline, one central posterior (proximal) cone, and eight symmetrically arranged anterior (distal) cones. Of the anterior cones the second cone from the centre of the tooth is the largest. The tooth is 82 µm high and 61 µm wide (n=1). It shows resemblance to some conodont teeth, although conodont teeth are generally somewhat larger and conodonts are long extinct (Ulrich and Bassler, 1926). More likely this is a mandible part, the tooth of a eunicid annelid, or a chaetognath unknown to us.

5.8 Reworked palynomorphs

5.8.1 Dinoflagellate cysts

Order GONYAULACALES Taylor 1980

Suborder GONYAULACINEAE (autonym)

Family AREOLIGERACEAE Evitt 1963

Genus *Enneadocysta* Stover & Williams 1995 emend. Fensome et al. 2006

Enneadocysta dictyostila (Menéndez 1965) Stover & Williams 1995 emend. Sarjeant 1981
(Plate 1, figure 25–26)

Morphology and identification: The species *Enneadocysta dictyostila* has been the subject of substantial taxonomic debate (Sarjeant, 1981; Fensome et al., 2006). It can be recognized by its large apical archaeopyle and ragged clypeate processes (processes possessing a distal perforate quadrate or polygonal platform with broken margins) (Fensome et al., 2006). Clypeate processes and an apical archaeopyle are also present in the species *Areosphaeridium diktyoplokum* (Klumpp 1953) Eaton 1971 emend. Stover & Williams 1995; however, *A. diktyoplokum* possesses only one process on its antapical plate, while *E. dictyostila* possesses two (Fensome et al., 2006). Also, the margins of the distal perforate platforms are mostly continuous (entirely clypeate) in *A. diktyoplokum* (Fensome et al., 2006).

Biological taxon: Irrelevant because this species is part of the reworked microfossil assemblage.

Dimensions: The diameter of the cyst not including its processes ranges between 44 µm and 81 µm (average: 65 µm, n=5).

Geographic distribution: This species has no modern-day distribution.

The fossil record: In the Southern Ocean *E. dictyostila* ranges from the mid-Eocene to just past the Eocene-Oligocene boundary (Bijl et al., 2013b). In younger sediments it is a common species in the reworked assemblage (as *Enneadocysta partridgei* in Hannah 2006; Warny et al. 2006)

Order PERIDINIALES Haeckel 1894

Suborder PERIDINIINEAE Fensome et al. 1993

Family PERIDINIACEAE Ehrenberg 1831

Subfamily DEFLANDREOIDEAE Bujak & Davies 1983

Genus *Spinidinium* Cookson & Eisenack 1962 emend. Sluijs et al. 2009

Spinidinium colemanii Wrenn & Hart 1988 (Plate 1, figure 10–12)

Morphology and identification: This circumcavate dinoflagellate cyst is characterized by penitabular capitate spines, an apical horn and a posteriorly attached (adnate) operculum consisting of one intercalary plate (Wrenn & Hart 1988; Sluijs et al. 2009). In terms of ornamentation, it is therefore quite similar to *Vozzhennikovia stickleyae*.

Biological taxon: Irrelevant because this species is part of the reworked microfossil assemblage.

Dimensions: Its length including the apical horn is $57 \pm 5 \mu\text{m}$ ($n=3$).

Geographic distribution: This species has no modern-day geographic distribution.

The fossil record: The stratigraphic range of *S. colemanii* is from the late Paleocene to Eocene (Sluijs et al., 2003).

Genus *Vozzhennikovia* Lentin & Williams 1976

Vozzhennikovia apertura (Wilson 1967) Lentin & Williams 1976 (Plate 1, figure 9)

Morphology and identification: This is a horned, transparent cornucavate dinoflagellate cyst, which can be easily distinguished by its archaeopyle formed through the loss of three intercalary plates and its ornamentation of pointed or flat-tipped short spines (as *Spinidinium aperturum* in Wilson 1967).

Biological taxon: Unknown because this is the cyst of an extinct dinoflagellate.

Dimensions: Its length including the apical horn is about $41 \pm 1 \mu\text{m}$ ($n=2$).

Geographic distribution: This species has no modern-day geographic distribution.

The fossil record: *V. apertura* has a stratigraphic range in the Southern Ocean of Paleocene to Eocene (Bijl et al., 2013b). Despite the fact that its stratigraphic range is restricted to the Paleogene, it is a commonly found species since the Oligocene in other cores drilled near the Antarctic coast, where it is considered part of the reworked assemblage (Hannah et al., 2000; Hannah and Fielding, 2001; Yi et al., 2005; Hannah, 2006;

Warny et al., 2006, 2009; Bijl et al., 2018a), because Eocene strata dip up to the surface on the Wilkes Land margin (Truswell, 1982; Expedition 318 Scientists, 2011a)

Vozzhennikovia netrona Levy & Harwood 2000 emend. Sluijs et al 2009
(Plate 1, figure 22–24)

Morphology and identification: This species has short capitate spines similar to *Vozzhennikovia apertura*, but has in addition to the apical horn a very distinctive antapical horn (Sluijs et al., 2009).

Biological taxon: Irrelevant because this species is part of the reworked microfossil assemblage.

Dimensions: Its length including the apical and antapical horn is 66 μm (n=1).

Geographic distribution: This species has no modern-day geographic distribution.

The fossil record: The stratigraphic range of *V. netrona* is from the middle to late Eocene (Sluijs et al., 2003, 2009).

5.8.2 Pollen and spores

Phylum TRACHEOPHYTA Sinnot ex Cavalier-Smith 1998
Palynomorphs: pollen and spores (Plate 3, figure 18–19)

Morphology and identification: Remains of vascular plants are scarce within Hole U1357B and consist mainly of pollen grains and spores. The most common pollen belong to the genera *Nothofagidites* (Plate 3, figure 18) and *Podocarpidites* (Plate 3, figure 19). The *Nothofagidites* pollen grains are transparent, flattened spheres with a scabrate wall ornamentation and possess seven colpi. The *Podocarpidites* pollen grains are brown-colored, bisaccate pollen grains with a reticulate wall structure on the sacci. We have not identified other pollen and spores down to species level.

Biological taxon: *Nothofagidites* and *Podocarpidites* are pollen of *Nothofagus* trees and Podocarpaceae respectively.

Dimensions: Most pollen and spores found in Hole U1357B are between 20 and 40 μm large.

Geographic distribution: Pollen assemblages dominated by *Nothofagidites* and *Podocarpidites* have been associated with the modern-day (sub)alpine, cold or temperate rainforests of southern South America, Tasmania, Australia, New Caledonia, New Guinea and New Zealand (Kennett and Barker, 1990; Roberts et al., 2003; Pross et al., 2012)

The fossil record: Pollen grains of *Nothofagus* and podocarps are found *in situ* since the Late Cretaceous ranging possibly into the Pliocene and are the dominant vegetation of the Antarctic tundra during the Oligocene and Miocene (Hill and Scriven, 1995; Askin and

Raine, 2000; Troedson and Riding, 2002; Prebble et al., 2006; Warny et al., 2006; Pross et al., 2012; Sangiorgi et al., 2018).

6 Conclusions

We describe a total of 74 palynomorphs, which are discussed based on an extensive literature survey to resolve their biological origin and what they represent ecologically. This review serves as a resource for future studies along the Antarctic margin. All the palynomorphs of Hole U1357B represent at least 40 different *in situ* species. Such diversity illustrates the species richness of a polynya-controlled environment at the Antarctic coast and further highlights the importance of finding well-preserved strata to reconstruct biotic response to past climate or oceanographic changes.

Particularly among the dinoflagellates and tintinnids there is a high degree of Southern Ocean endemism, which reflects the influence of the seasonal sea-ice system. Some of these species have been linked directly to an Antarctic coastal setting (e.g., *Nucicla umbiliphora*; **Chapter 3**) and the formation of sea ice and brine release (e.g., *Polarella glacialis*; Thomson et al. 2006). Among the other palynological remains, particularly prasinophytes, leiospheres and *Palaeostomocystis* have also been linked to a sea-ice-controlled environment (Mudie 1992; Daugbjerg 2000; Moro et al. 2002; Warny 2009). On the other hand, we find the remains of more cosmopolitan species, such as the dinoflagellate *Gymnodinium microreticulatum* and the tintinnid *Codonellopsis pusilla*.

In addition to the richness of the assemblage, the state of preservation in Hole U1357B is truly exceptional. This is evident from the findings of easily degradable species such as cysts of *Polarella glacialis* (Montresor et al., 1999) also in the lower parts of the sedimentary sequence (see **Chapter 4**), while in general the preservation of organic carbon and palynomorphs at the Antarctic margin and on the Antarctic shelves is very poor (Sackett, 1986; Kvenvolden et al., 1987; Venkatesan and Kaplan, 1987; Wrenn et al., 1998) due to intensive oxygen delivery, strong ocean currents, and therefore the effective remineralization of organic matter (De Vernal and Marret, 2007; Zonneveld et al., 2010).

The palynomorph record of Hole U1357B is an important source for reconstructing Holocene Antarctic climate variability for future work. This extensive review of organic microfossil associations provides the basis to implement an additional tool, next to diatoms, to reconstruct palaeoenvironmental and palaeoceanographical changes in sites close to the Antarctic margin, while considering at a wider portion of the ecosystem (primary and secondary producers). This will be presented in **Chapter 4**.

Chapter 3

***Nucicla umbiliphora* gen. et sp. nov.:**
a Quaternary peridinioid dinoflagellate
cyst from the Antarctic margin

Abstract

In the southern high latitudes, dinoflagellate cysts are an important microfossil group for both biostratigraphic and palaeoenvironmental interpretation purposes. In light of this, the peridinioid dinoflagellate cyst *Nucicla umbiliphora* gen. et sp. nov. from the Antarctic margin is formally described. *Nucicla* is dorsoventrally compressed, has a rounded pentagonal outline in dorso-ventral view, an epicyst that is only half as high as the hypocyst, an unusual archaeopyle formed by the loss of the three anterior intercalary plates, and a posterior sulcal plate that is positioned at the antapex. The species *N. umbiliphora* is characterised by a scabrate cyst wall and possesses undulated and/or crenulated folds/ridges. It has been so far exclusively found in Quaternary sediments obtained from the East Antarctic continental shelf and the Ross Sea. Although the dinoflagellate producing this cyst is as yet unknown, its brown colour and the lack of autofluorescence suggest that the motile cell is likely a heterotrophic *Protoperidinium* species. As such, *N. umbiliphora* might benefit from phytoplankton blooms occurring close to the Antarctic margin after seasonal sea-ice retreat.

1 Introduction

Although the Oligocene to Quaternary sediments of the Southern Ocean and Antarctic margin have long been thought to contain no dinoflagellate cysts (McMinn, 1995), several endemic and bipolar species have been discovered during the last two decades. They are important for both biostratigraphic purposes and reconstructing the high-latitude climatic evolution (Marret and De Vernal, 1997; Montresor et al., 1999; Esper and Zonneveld, 2002; Prebble et al., 2013; Clowes et al., 2016; Bijl et al., 2018a).

Here we formally describe *Nucicla umbiliphora* gen. et sp. nov. This species has already been reported without formal description from four localities around Antarctica (Figure 1). These dinoflagellate cysts are now included in *N. umbiliphora*. It was first depicted as Dinocyst sp. A from Quaternary samples from the Cape Roberts Project drill core 1 (CRP-1), Ross Sea (Wrenn et al., 1998). Storkey (2006) reported the species from shelf surface sediments in Prydz Bay. Furthermore, the dinoflagellate cyst is depicted in Warny et al. (2006) as '*Lejeunecysta* cf. sp. 1 and 5 of CRP' (i.e. cf. Hannah et al., 2000) from the Ross Sea shelf edge. Finally, the species has also been reported from a Holocene core from a small meromictic basin upstream Ellis Fjord, which lies at the eastern coastal margin of Prydz Bay (Boere et al., 2009). Here we add occurrences of this species in nine other East Antarctic marine sediment cores and surface sediments (Figure 1, Table 1).

2 Material and methods

Samples obtained from nine cores (see Table 1; Figure 1) were freeze-dried and crushed manually to small chunks in a mortar after which a *Lycopodium* tablet was added with Agepon (1:200). Agepon was used to plump up the shrivelled *Lycopodium* from the tablets and the palynomorphs in general. A small amount of 30% cold hydrochloric acid (HCl) was added to remove carbonate, and to dissolve the *Lycopodium* tablet. Samples were treated with 38% cold hydrofluoric acid (HF) and shaken for 2 h at 250 rpm. Thereafter, samples were diluted with tap water, allowed to settle for 24 h, and decanted. Subsequently, 30% HCl was added to remove fluoride gels, tap water was added and the samples were centrifuged, after which the samples were decanted. No additional neutralisation steps were performed to remove excess HF. Tap water was added to the residue to prevent oxidation of the organic material. The treated material was sieved using a 10- μ m mesh sieve and kerogen clumps were ultrasonically fragmented. Heavy minerals were removed by pouring the residue from the sieve into a porcelain dish that is kept floating in the ultrasonic bath, and by decanting this back into the sieve after 5 minutes. The fraction > 10 μ m was concentrated into ~1 mL of glycerin-water and a fraction thereof was mounted on a microscope slide using glycerine jelly.

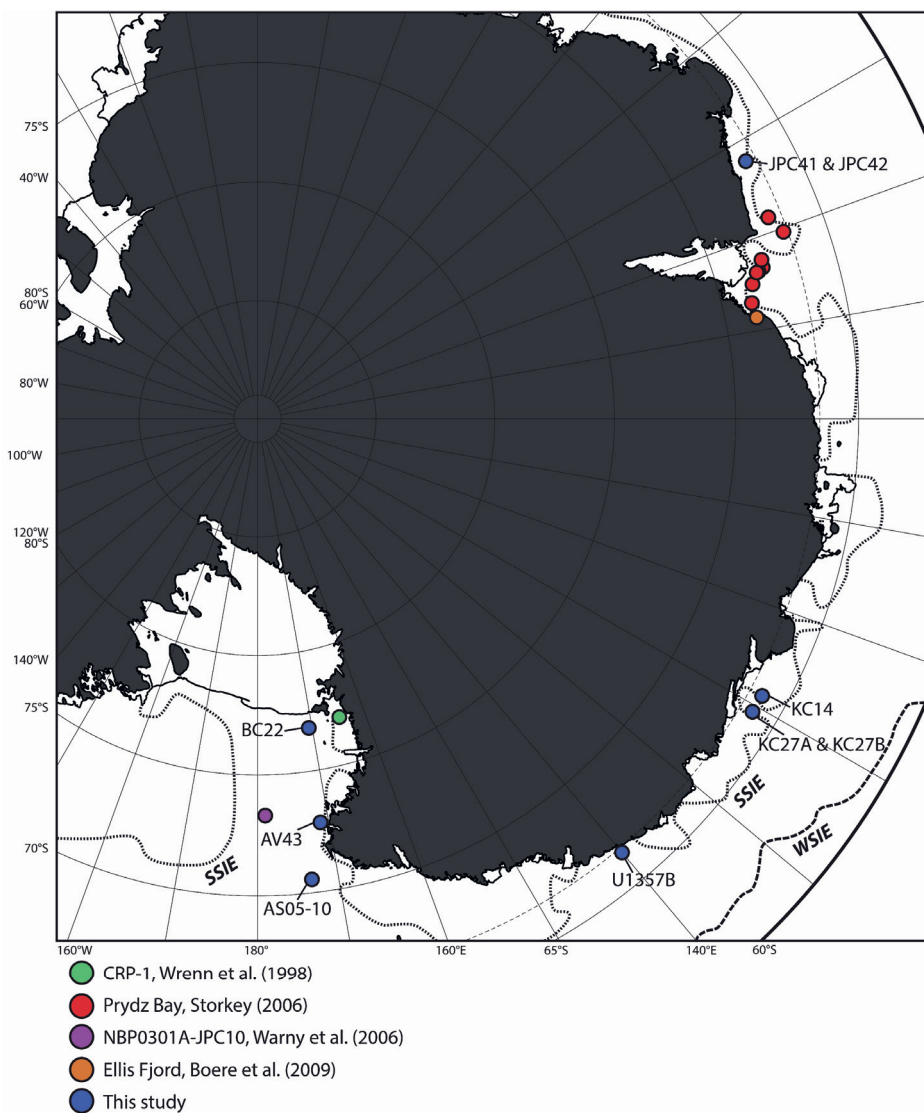


Figure 1: Previously published sites and the sites presented in this study from which samples are derived that contain *Nucifera umbiliphora*. The position of the summer sea ice edge (SSIE) and winter sea ice edge (WSIE) are indicated by dotted and interrupted lines, respectively. The position of the SSIE and WSIE are based on the figure by Arrigo et al. (2008), which shows the averaged satellite-derived, annual sea-ice cover for the period 1997-2006. SSIE: <20 days/year sea-ice cover and WSIE >320 days/year sea-ice cover.

Table 1: Coordinates, core length and water depth of the sampled cores

Core	Locality	Latitude	Longitude	Core length (m)	Water depth (mbsl)	Reference
AS05-10	Western Ross Sea	70°59.11'S	173°03.91'E	7.50	2377	This study
ANTA02-AV43	Western Ross Sea	74°08.45'S	166°04.97'E	2.20	218.5	Del Carlo et al. (2015)
BC22	Southwestern Ross Sea	76°41.59'S	169°04.68'E	0.37	790	This study
IODP U1357B	Adélie Basin	66°24.7990'S	140°25.5705'E	172.44	1017	Exp.318 Scientists (2011)
NBP0101-JPC41	MacRobertson Shelf	67°07.817'S	62°59.436'E	24.12	563	Leventer et al. (2001)
NBP0101-JPC42	MacRobertson Shelf	67°07.479'S	63°00.195'E	24.95	850	Leventer et al. (2001)
NBP1402-KC14	Sabrina Coast	66°52.3691'S	118°14.4022'E	2.63	643	Domack & Leventer (pers. comm.)
NBP1402-KC27A	Sabrina Coast	66°11.092'S	120°30.2403'E	2.952	544	Domack & Leventer (pers. comm.)
NBP1402-KC27B	Sabrina Coast	66°11.0907'S	120°30.2385'E	2.71	547	Domack & Leventer (pers. comm.)

Green autofluorescence of the cyst was tested on a Leica DM2500 LED fluorescence microscope.

Images were taken using a Leica DM2500 LED microscope with mounted Leica MC170 HD camera and for the images of Plate 1 the Live Image Builder (LIB) within the Leica Application Suite software 4.0 was used, which is a live z-stacking tool. Z-stacking constructs a two-dimensional image from a three-dimensional object by combining the areas in focus from multiple images, which is ideal for three-dimensional microscopic objects.

A scanning electron microscope (SEM) photo was made using a JEOL NeoScope JCM-6000 Benchtop SEM, located at the 'Gemeenschappelijk Milieu Laboratorium' building at Utrecht University. For the SEM photo, dinoflagellate cysts were individually picked using a microinjection system, subsequently placed on a stub and coated with a thin (10 nm) layer of platinum.

Plate terminology follows the Kofoid tabulation system (see Kofoid 1911). Archaeopyle descriptive terms follow Bujak & Davies (1983).

3 Results

Nucicla umbiliphora was found in core-top samples of all the examined cores, with the exception of cores AS05-10, NBP0101-JPC41 and -JPC42 for which no core-top samples were available. Dinoflagellate cysts of *N. umbiliphora* were occasionally found with the operculum still attached (Plate 1, figures 1, 2, 6) and in one case also containing cell

content (Plate 1, figure 10–11). The cysts of *N. umbiliphora* did not autofluoresce under fluorescence microscopy (Plate 1, figure 12).

For core ANTA02-AV43 all samples were taken above the interval 1.48–1.51 m below sea floor (mbsf), which has an age of 9.7 ± 5.3 ka based on $^{40}\text{Ar}/^{39}\text{Ar}$ dating (Del Carlo et al. 2015). No age models have been published yet for cores U1357B, BC22, NBP0101-JPC41 or NBP0101-JPC42. However, the latter two are likely of Holocene age as the nearby core NBP0101-JPC43B (23.95 m long) shows bottom ^{14}C ages of about 11.6 ka (Mackintosh et al., 2011). We encountered the species in JPC41 as deep as 17.52 mbsf. The new species has also been encountered throughout core BC22 (36.5 cm long). Unpublished dinoflagellate cyst data from box core BC22 suggest a position for the Last Glacial Termination between 0.25 and 0.28 mbsf, from which the amount of dinoflagellate cysts per gram of dry sediment decreases strongly downcore. It has also been encountered sparsely in Hole U1357B to a depth of 55.06 mbsf. The ^{14}C data from the nearby Hole U1357A provide an age of ~ 4.2 cal. kyr BP at 68.85 mbsf (Yamane et al., 2014). Samples from core AS05-10 have been retrieved from the interval with maximum dinoflagellate cyst preservation, which is associated with the onset of MIS5.5 (see **Chapter 5**). Apart from perhaps the CRP-1 core, for which the age model of the Quaternary section above 43 mbsf is not well resolved, the occurrence in core AS05-10 during MIS5.5 is the oldest record of *Nucicla umbiliphora*.

4 Systematic palaeontology

- Division DINOFLAGELLATA (Bütschli 1885) Fensome et al. 1993
 - Subdivision DINOKARYOTA Fensome et al. 1993
 - Class DINOPHYCEAE Pascher 1914
 - Subclass PERIDINIPHYCIDAE Fensome et al. 1993
 - Order PERIDINIALES Haeckel 1894
 - Suborder PERIDINIINEAE Fensome et al. 1993
 - Family PROTOPERIDINIACEAE Bujak and Davies 1998 in Fensome et al. 1998
 - Subfamily PROTOPERIDINIOIDEAE Bujak and Davies 1983
 - Genus *Nucicla* gen. nov.

Type species. *Nucicla umbiliphora* Hartman, Sangiorgi, Bijl & Versteegh sp. nov.

Derivation of the name. From the Latin *nucicla*, meaning small nut, in reference to the cyst resembling a nut.

Diagnosis. Acavate dorsoventrally compressed cyst with a rounded pentagonal outline, a hypocyst that is twice the size of the epicyst, an archaeopyle formed by the loss

of three anterior intercalary plates, and a large sulcus with the posterior sulcal plate positioned at the antapex.

Differential diagnosis. This genus differs from all other peridinioid dinoflagellate cysts by its combination of (1) a consistent 3I archaeopyle, (2) a well-outlined cingulum and sulcus, (3) the absence of cavation, and (4) a large sulcus with a posterior sulcal plate at the antapex. The late Cretaceous to Early Palaeocene genus *Trithyrodinium* Drugg 1967 also has a 3I archaeopyle, but is cavate. *Vozzhennikovia* Lentin & Williams 1976 has an I or 3I archaeopyle, and is cavate as well. Although the number of archaeopyle plates in *Brigantedinium* Reid 1977 is not limited and therefore can include species with a 3I archaeopyle, *Brigantedinium* is spherical/ovoidal and lacks tabulation other than the archaeopyle. Other genera with dorsoventral compression, a pentagonal outline and consisting of an autophragm include *Votadinium* Reid 1977, *Lejeunecysta* Artzner & Dörhöfer 1978, *Trinovantedinium* Reid 1977, and *Leipokatium* Bradford 1975. Like *Brigantedinium*, *Votadinium* and *Leipokatium* can have an archaeopyle consisting of any number of intercalary plates, but *Votadinium* differs from *Nucicla* in having a shallow or deep depression between the antapical lobes and lacks a well-defined cingulum. *Leipokatium* has very distinct antapical horns and a hypocyst much smaller than the epicyst. Both *Lejeunecysta* and *Trinovantedinium* may have a sulcus and/or cingulum reflected, but have an I archaeopyle. In addition, *Trinovantedinium* has non-tabular proximochorate processes and *Lejeunecysta* has an epicyst and hypocyst of approximately equal size. For all of the above-mentioned genera the position of the posterior sulcal plate is either unclear or not as posterior as in *Nucicla*.

Nucicla umbiliphora sp. nov.

Plate 1, figures 1–12 and Plate 2, figures 1–6

Synonymy.

Dinocyst sp. A. Wrenn et al. 1998, p. 595, figure 5 a–d.

Protoperidinium sp. 2 Storkey, 2006, p. 49, Plate 4, figures 10–12.

Lejeunecysta cf. sp. 1 and 5 of CRP Warny et al. (2006), p. 163, Plate 3, figures 3–4.

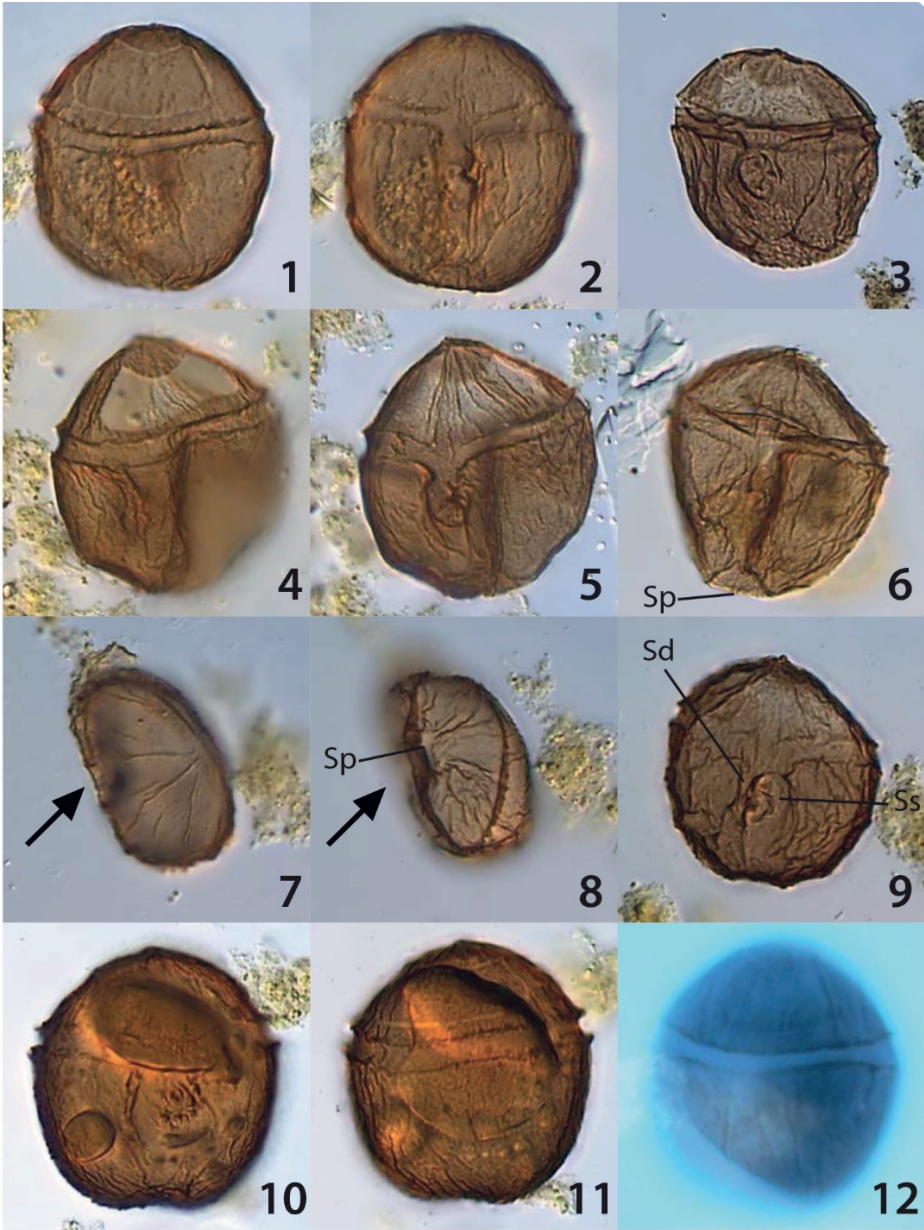
Cyst type 1 Boere et al., 2009, p. 273, figure 5 D, E, (F?).

Holotype. Plate 1, figure 1-2. Cruise NBP0101, core JPC41, 108 cm depth, slide no. 1, England Finder (E.F.) coordinates: U29.2 down left corner.

Repository. Stored at the collection of the Laboratory Marine Palynology and Oceanography, Utrecht, The Netherlands.

Type locality. Iceberg Alley, MacRobertson Shelf, East Antarctica.

Type stratum. Holocene.



20 μ m

Plate 1 (previous page): Light microscope photographs of Nucicla umbiliphora.

Figure 1. Holotype, JPC42, 468 cm depth, slide 1, E.F.: U29.2, dorsal side up: dorsal view with operculum attached but archaeopyle outlined.

Figure 2. Holotype, JPC42, 468 cm depth, slide 1, E.F.: U29.2, dorsal side up: ventral view (mirrored).

Figure 3. AS05-10, slice V-92, slide 1, E.F.: G24.1, dorsal side up: ventral view (mirrored), outline of archaeopyle visible.

Figure 4. JPC41, 108 cm depth, slide 1, E.F.: L35.4, dorsal side up: dorsal view.

Figure 5. JPC41, 108 cm depth, slide 1, E.F.: L35.4, dorsal side up: ventral view (mirrored) with clearly visible flagellar scar.

Figure 6. ANTA02-AV43, 2-3 cm depth, slide 2, E.F.: F19.2, ventral side up: ventral view, a low ridge indicates the position of the posterior sulcal plate.

Figure 7. JPC41, 556 cm depth, slide 1, E.F.: O42.1, antapical side up: apical view (mirrored), sulcus indicated by arrow.

Figure 8. JPC41, 556 cm depth, slide 1, E.F.: O42.1, antapical side up: antapical view, sulcus indicated by arrow, a low ridge can be distinguished at the posterior edge of the posterior sulcal plate.

Figure 9. JPC42, 295 cm depth, slide 2, E.F.: G32.4, ventral side up: ventral view, some of the low ridges within the sulcus may correspond to sulcal plate boundaries.

Figure 10. JPC42, 295 cm depth, slide 2, E.F.: N33.3, dorsal side up: ventral view (mirrored), cell content visible.

Figure 11. JPC42, 295 cm depth, slide 2, E.F.: N33.3, dorsal side up: dorsal view, cell content visible, operculum still attached, but outline visible.

Figure 12. Holotype, JPC42, 468 cm depth, slide 1, E.F.: U29.2, viewed under fluorescence microscope showing no autofluorescence.

Paratype. Plate 1, figure 6. Core ANTA02-AV43, 2-3 cm depth, slide no. 2, E.F.: F19.2 bottom side. Stored in the collection of the Laboratory Marine Palynology and Oceanography, Utrecht, The Netherlands.

Stratigraphic range. Marine Isotope Stage 5.5 to Recent

Derivation of the name. From the Latin *umbilicus* (navel) and the Ancient Greek suffix *-phoros* (bearing), with reference to its large flagellar scar, which resembles a navel.

Diagnosis. A species of *Nucicla* with a scabrate wall structure and with low, undulating or crenulating ridges with no apparent relation to plate boundaries with the exception of the cingulum and sulcus. The sulcus shows a large flagellar scar. Apart from the cingulum and sulcus tabulation is only indicated by the clear 3l archaeopyle, of which the 2a intercalary is large and latideltaform. In the holotype the operculum is still attached; specimens are usually found without operculum.

Dimensions.

Holotype: Height = 70 µm; width measured along the cingulum = 62 µm.

Other specimens (n=10): Height = 57–70 µm, average = 64.5 µm. Width = 52–63 µm, average = 60.0 µm.

Description. A brown cyst with pentagonal outline, which is dorsoventrally compressed. Apical and antapical ‘horns’ are rounded and broad-based so that the cyst appears more rounded than pentagonal. A few specimens show a small acute apical horn (see Plate 1, figures 3 and 11). None of the specimens show acute tips at the antapical ‘horns’. The hypocyst is twice the height of the epicyst. The autophragm has folds that

form low, undulating or crenulating ridges, which are predominantly longitudinal and can be dendritic (resembling a tree branch). With the exception of the cingulum and sulcus, these ridges have no relation to sutures. The cyst wall is scabrate and the degree of scabration varies between specimens (Plate 2, figures 4–6). The clearly distinguishable cingulum is levelled or very slightly descending and outlined by sutural ridges. Within the cingulum, low longitudinal ridges occur, but with no relation to cingular plate boundaries. The sulcus forms a clear depression, and is outlined by sinistral and dextral longitudinal sutural ridges. Some specimens also clearly show a posterior sutural ridge, which outlines the entire posterior sulcal plate (Sp) (Plate 1, figures 6 and 8). The sutural ridge that outlines the Sp extends towards the dorsal side of the cyst, indicating the exceptional antapical position of the Sp. To our knowledge no other protoperidinioid cyst possesses an Sp that is positioned so far posteriorly, thereby pushing the antapical plates to the dorsal side. The sulcus shows a large flagellar scar, with low ridges converging towards it. Applying standard protoperidinioid tabulation to *N. umbiliphora*, low ridges within the sulcus seem to outline the right sulcal plate (Sd) and the left sulcal plate (Ss) (Plate 1, figures 3 and 9). In some specimens (Plate 1, figures 3 and 9) a low ridge is present at the anterior margin of the left and right sulcal plates, indicating the position of the anterior sulcal plate (Sa) (Figure 2).

The 3I archaeopyle is relatively large and spans almost the entire dorsal side of the epicyst. It has a consistent shape with clear angles marking plate junctions, except for the boundaries between the intercalary plates, which are smooth and subtle. Nevertheless, both archaeopyle and operculum outline suggest a 3I archaeopyle for the following reasons: (1) the upper margin of the archaeopyle is concave. Although in dinoflagellate cyst species with a 2a archaeopyle such a concave upper margin could be the result of the inward folding of the apical plates, we are certain that this is not the case for *N. umbiliphora*, because the outline of the operculum is also concave (Plate 2, figure 6); (2) the upper margin of the archaeopyle is three-sided (particularly visible in Plate 2, figure 3), strongly suggesting that these are the three sides of the third apical plate (3') that border each of the anterior intercalaries (green, black and blue lines in the figures of Plate 2); (3) in several instances the lower margin of the 2a intercalary appears slightly but nevertheless clearly elevated with respect to the lower margins of the 1a and 3a intercalaries (indicated by the ^ symbols in the figures of Plate 2). The position of the plate junctions in the lower margin of the archaeopyle suggests that the 1a and 3a intercalaries are very narrow, bordering a large latideltaform 2a intercalary. Although we cannot determine any further tabulation from the cyst of *N. umbiliphora*, the relatively low height of the epicyst in combination with the large 2a suggests that the height of the 3'', 4'', and 5'' precingular plates is suppressed (see Figure 2).

Differential diagnosis. This is currently the only species in the genus. Within Protoperidiniaceae, *Nucicla umbiliphora* with its pentagonal outline, limited tabulation, rounded antapical horns, scabration and brown colour most closely resembles *Lejeunecysta rotunda* Clowes et al., 2016. Instead of erecting a new genus one might consider emending *Lejeunecysta* to include *N. umbiliphora*. However, *Lejeunecysta* differs from *Nucicla* in more than just one aspect. Most importantly, *Lejeunecysta* has a consistent 2a archaeopyle and closely defined archaeopyle shape. *Lejeunecysta* also differs in having the epicyst and hypocyst of approximately equal length, symmetrically located horns which are small pointed and solid, a laevigate or chagriniate wall, and tabulation only indicated near the archaeopyle and cingulum, whereas the sulcus is only marked by a shallow depression. Because of the number and clarity of the differences we found it necessary to erect a new genus. It differs from most other peridinioid genera by its 3I archaeopyle. Other known genera with a 3I archaeopyle are the Cretaceous to Early Palaeocene *Trithyrodinium* and Palaeocene to Oligocene *Vozzhennikovia*, but both these genera are cavate. Typically, the apical and antapical horns of these genera are made up of the periphragm, while *N. umbiliphora* only has an autophragm (see Figure 3). Other brown scabrate dinoflagellate cyst species from the present-day Southern Ocean are *Selenopemphix antarctica* Marret and De Vernal (1997), *Brigantedinium pynei* Hannah et al., 1998 and *Cryodinium meridianum* Esper and Zonneveld, 2002. *Cryodinium meridianum* also has low, sometimes dendritic ridges, but most of these crests reflect tabulation. Furthermore, *C. meridianum* lacks the pentagonal outline and dorsoventral compression, and has a 2I archaeopyle. *Brigantedinium pynei* is reminiscent of *C. meridianum*, but its rugulose surface does not reflect tabulation and it has an I archaeopyle (Clowes et al., 2016). *Selenopemphix antarctica* does not have ridges, has an I-type archaeopyle and the width of the cyst is much larger than its height, so that it typically appears in (ant)apical view on microscope slides. *Nucicla umbiliphora* was found in Quaternary sediments of the Ross Sea together with a similar-looking Dinocyst sp. B (Wrenn et al., 1998). Because Dinocyst sp. B of Wrenn et al. (1998) has antapical ‘horns’ with acute tips, and the number of intercalary plates that comprise the archaeopyle is uncertain, it is not included in *N. umbiliphora*.

Plate 2 (next page): Light microscope photographs of the archaeopyle of Nucicla umbiliphora. Symbols and coloured lines correspond to plate junctions and the upper archaeopyle margin as indicated in Figure 2.

Figure 1. JPC42, 295 cm depth, slide 2, E.F.: O35.4, ventral side up (archaeopyle mirrored).

Figure 2. JPC42, 953 cm depth, slide 2, E.F.: G28.4, ventral side up (archaeopyle mirrored), sinistral side is torn.

Figure 3. JPC41, 1752 cm depth, slide 1, E.F.: P41.1, ventral side up (archaeopyle mirrored), focus on the upper archaeopyle margin.

Figure 4. JPC41, 1752 cm depth, slide 1, E.F.: P41.1, ventral side up (archaeopyle mirrored), focus on the lower archaeopyle margin.

Figure 5. JPC41, 1004 cm depth, slide 1, E.F.: T40.3, dorsal side up.

Figure 6. Holotype, JPC42, 468 cm depth, slide 1, E.F.: U29.2, dorsal side up, operculum attached but outline of the archaeopyle visible.

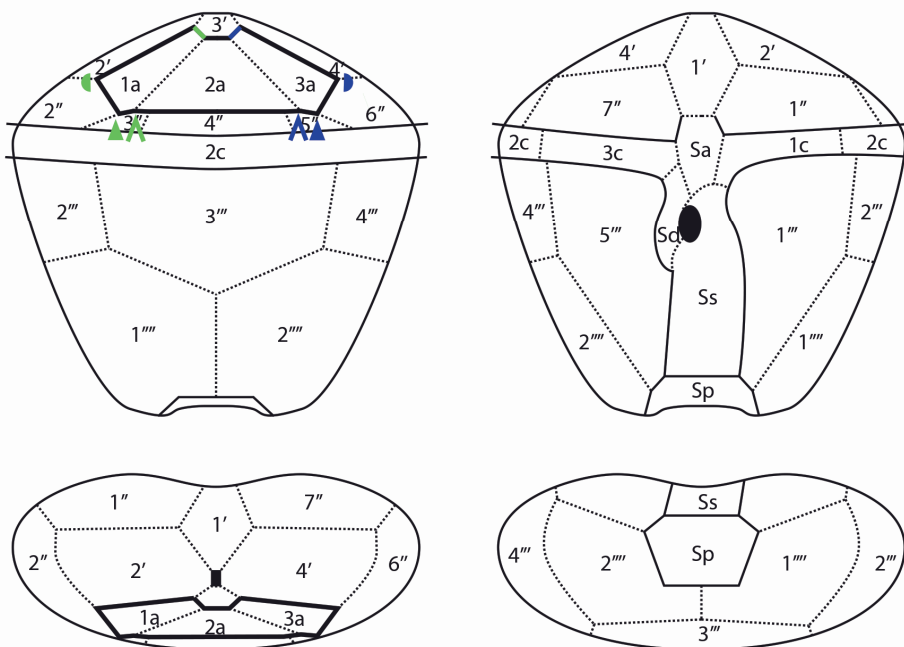
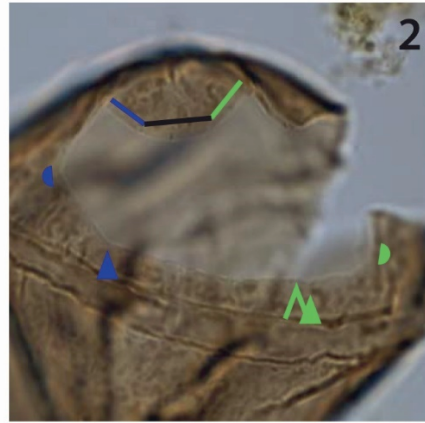
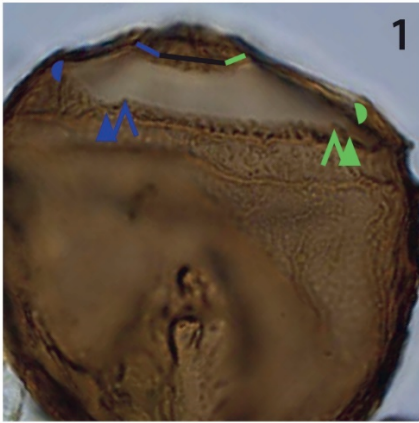
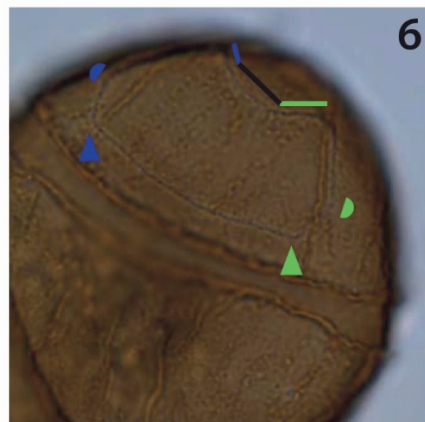
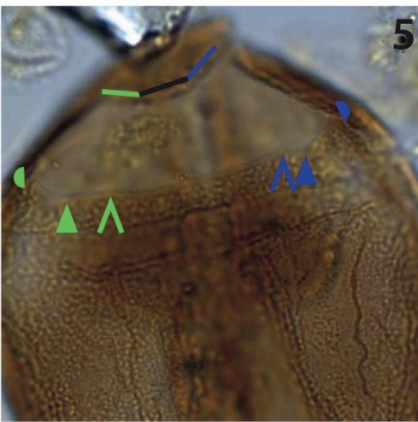
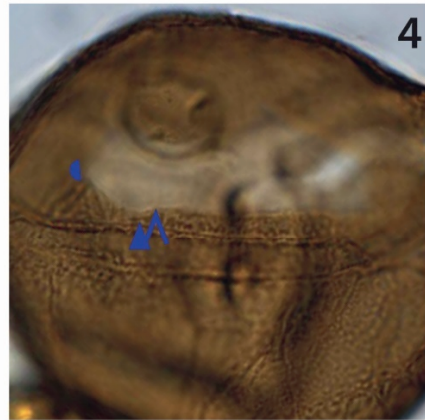
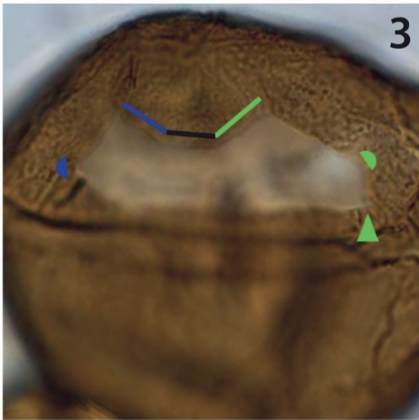


Figure 2: Schematic drawings of the plate boundaries of Nucicla umbiliphora. Top left: dorsal view. Top right: ventral view. Bottom left: apical view. Bottom right: antapical view. Uninterrupted lines indicate archaeopyle (thick), cingulum and sulcal outlines (thin). Dotted lines are hypothetical, based on the standard protoperidinioid plate configuration and deduced from the archaeopyle outline and presumed sutural sulcal ridges. Archaeopyle plate junctions are marked by symbols. The upper archaeopyle margin is indicated by coloured lines. This coding of lines and symbols corresponds to that used in Plate 2.



3



20 μ m

Discussion

4.1 Taxonomy

We placed *N. umbiliphora* within the family Protoperidiniaceae based on the visible tabulation, the absence of cavation and the brown colour. It lacks plate boundaries between the cingular plates which hampers definite placement within Protoperidiniaceae. However, several modern-day cysts with a pentagonal outline and an intercalary archaeopyle but without plate boundaries between the cingular plates do produce *Protoperidinium* thecae, such as *Votadinium*, *Lejeunecysta*, *Selenopemphix* and *Trinovantedinium* (Head, 1996; Matsuoka and Head, 2013; Mertens et al., 2017). In addition, *N. umbiliphora* does not show green autofluorescence, like many *Protoperidinium* cysts (Brenner & Biebow, 2001; Anderson et al., 2003). Currently, the motile stage of *N. umbiliphora* is unknown.

4.2 Ecology

Nucicla umbiliphora occurrences are all near the Antarctic margin and except for site AS05-10 only in sediments from the shelf or inland fjords. This strongly suggests it is endemic to the Antarctic shelf. All sample areas experience at least 9 months of yearly sea-ice cover (Figure 1; Arrigo et al., 2008). Considering that all modern-day dinoflagellates that produce brown cysts are heterotrophic, it is likely that the motile stage of *N. umbiliphora* is heterotrophic as well (see Ellegaard et al., 2013). In the coastal waters of Antarctica, the phytoplankton blooms in the highly stratified surface waters after sea-ice retreat could be an important food source for *N. umbiliphora* (Kang and Fryxell, 1993; Clarke and Leakey, 1996; Arrigo et al., 1998b; Smith Jr. et al., 2000; Hiscock et al., 2003; Smith Jr. et al., 2006; Peloquin and Smith Jr., 2007; Arrigo et al., 2008). At the Antarctic shelf, these conditions typically arise within the marginal ice zone in late summer (Fitch and Moore, 2007; Arrigo et al., 2008) and within coastal polynyas (Arrigo et al., 1999; Arrigo and van Dijken, 2003). Notably, the occurrence of *N. umbiliphora* at Hole U1357B confirms a preference for polynya environments, as U1357B has been drilled directly downwind and downcurrent of the Mertz Glacier Polynya (Expedition 318 Scientists, 2011b).

5 Conclusions

Nucicla umbiliphora gen. et sp. nov. (Peridinales, Protoperidinioideae) occurs in Quaternary sediments from the East Antarctic margin and the Ross Sea. It has a 3l archaeopyle, which is unique among protoperidinoids. Furthermore, it has a rounded to pentagonal outline with a hypocyst twice as large as the epicyst, a sulcus with a distinct flagellar scar and a posterior sulcal plate positioned at the antapex. It has a scabrate wall

ornamentation with low somewhat crenulating ridges. The species is probably endemic to the Antarctic shelf environment during the Holocene and may prove to be bound to the high primary productivity after spring sea-ice retreat.

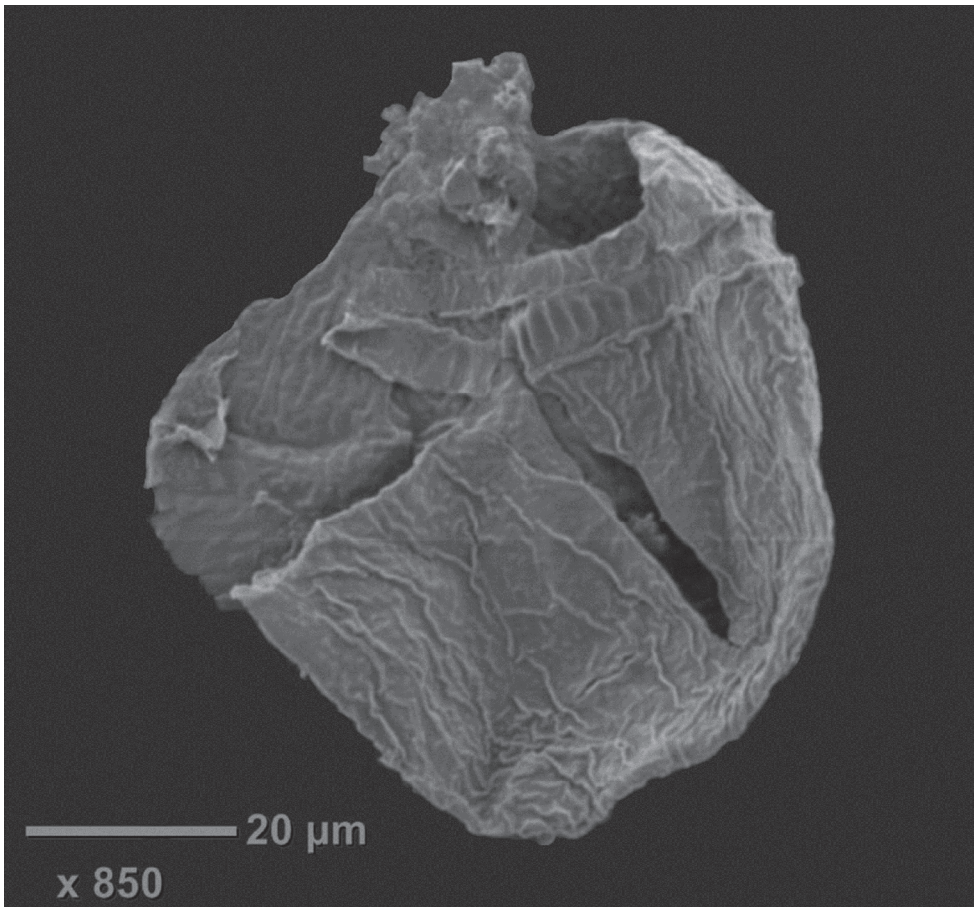


Figure 3: Benchtop SEM photograph of *Nucicla umbiliphora* (dorsal view). No tabulation pattern is visible except for the archaeopyle and cingulum. The autophragm with its folded ridges can be seen both externally and internally. Scale bar and magnification in the bottom left corner.

Chapter 4

Holocene paleoenvironment and paleoclimate at the Adélie Basin (East Antarctica): the marine palynological signature in the IODP Site U1357 record

Abstract

In reconstructing past Holocene paleoenvironmental conditions of the surface waters around Antarctica an often used proxy are the siliceous microfossil remains of diatoms and radiolaria. However, when considering only autotrophic primary producers in paleoenvironmental studies, our understanding of the implications of climatic changes, such as changes in sea-ice cover and surface water temperatures, to marine ecosystems around Antarctica remains limited. It is therefore important to also consider other microfossil remains to cover a larger part of the ecosystem that is affected by climate change. With the recovery of Hole U1357B from the Adélie Basin during Integrated Ocean Drilling Program (IODP) Expedition 318, a ~170 m long Holocene record is available containing exceptionally preserved organic microfossil remains. In this study, changes in the palynological content throughout the Holocene at Site U1357 are described, including the remains of primary producers as well as secondary producers, zooplankton and detritus-feeding bottom-dwellers. In addition to a TEX_{86} -based subsurface water temperature reconstruction that is presented in this study, paleoenvironmental reconstructions for the Holocene based on the diatom content from the nearby core MD03-2601 and a recently published reconstruction of meltwater fluxes to Site U1357 allow a direct comparison of the shifts within the palynological record to known (regional) paleoenvironmental changes. In this way, a better understanding of the ecological affinities of some of the biological species that produce these organic microfossil remains is acquired. In addition, a proxy for reconstructing export productivity based on the palynological remains of foraminifera is introduced. The timing of the reconstructed shifts within the palynological record matches with reconstructed subsurface water temperature changes, especially reconstructed spring temperatures, and paleoenvironmental changes known from core MD03-2601.

1 Introduction

The presence and seasonal amplitude of sea ice play a fundamental role in the stability of Antarctic ice shelves and ice sheets (Rintoul et al., 2018). In places where sea ice disappears and the ocean warms, ice shelves are rapidly losing mass (Rintoul et al., 2018; Gudmundsson et al., 2019). In addition, seasonal productivity patterns, linked to yearly sea ice dynamics, determine the capability of the Southern Ocean to function as a carbon source or sink (Sarmiento et al., 2004; Takahashi et al., 2009; Peck et al., 2010; Steinacher et al., 2010; Long et al., 2021). Future changes in sea-ice concentration under continued global warming will likely affect Southern Ocean primary productivity and thereby possibly also its role in the uptake of CO₂ (Deppeler and Davidson, 2017; Fan et al., 2020). Instrumental records have collected a great amount of data on sea-ice dynamics for the past few decades, but they are too short to capture the long-term variability (Comiso and Nishio, 2008; Turner and Comiso, 2017; Parkinson, 2019), which is needed to improve future projections (Arzel et al., 2006; Bracegirdle et al., 2008; Turner et al., 2013; Bintanja et al., 2015).

Studies of the Holocene (~11.5 ka to present day) have shown that the Antarctic climate may have responded differently to quasi-global climate shifts than the Northern Hemisphere, specifically during two major quasi-global climatic events: the 8.2 ka event, which is characterized by a short-lived (century-long) cooling (3–5 °C) episode, particularly over the North Atlantic (Alley and Ágústsdóttir, 2005), and the 4.2 ka event, which is characterized by strong aridification in particularly the low- and middle Northern latitudes (Booth et al., 2005; Walker et al., 2012). These events have been used to informally subdivide the Holocene into an early (11.7–8.2 ka), middle (8.2–4.2 ka), and late (4.2–0 ka) period. Instead, the Holocene Antarctic climate has a strong and variable seasonality depending on the intensity of the summer insolation (Jones et al., 2023) and on multidecadal time scales climate variability around Antarctica is determined by the Southern Annular Mode (SAM) (Thompson and Wallace, 2000; Thompson et al., 2000). The SAM affects annual sea-ice advance and retreat, and therefore primary productivity around Antarctica, with positive SAM (westerly winds positioned closer to the pole) associated with a longer sea-ice season (Stammerjohn et al., 2008; Saba et al., 2014). Associated with the annual sea ice cycle are polynyas: seasonal cavities in the sea ice that either result from oceanic sensible heat flux or result from transport of sea ice away from the Antarctic continent (Morales Maqueda et al., 2004). They are major production areas of phytoplankton as well as sea ice along the Antarctic coast (Arrigo and van Dijken, 2003; Morales Maqueda et al., 2004). The presence and size of especially coastal polynyas are associated with the severity of near-surface wind strength, which is determined by a combination of the pole-to-coast (katabatic) pressure gradient and the multidecadal

variability of the SAM (Stammerjohn et al., 2008; Campagne et al., 2015; Hazel and Stewart, 2019). Changes in sea ice concentration due to the variability of the SAM determines productivity within polynya and has consequences on the entire marine ecosystem (Saba et al., 2014; Campagne et al., 2015; La et al., 2019).

Understanding Holocene ice-sheet and sea-ice variability and behavior, and primary productivity patterns may aid projection of near-future ice mass loss and the potential of the Southern Ocean to act as a sink for CO₂, because of the similarity of Holocene climatic forcings to those in the present and near-future.

To reconstruct past environmental conditions at Antarctic proximal sites, remains of diatoms and radiolarians are often used, as these are very abundant and well preserved in the Southern Ocean surface sediments. Studies on diatoms and radiolarians have defined their modern geographic distribution and ecological niches, which allows correlation to surface water environmental parameters (Armand et al., 2005; Crosta et al., 2005b; Lawler et al., 2021). For example, diatom assemblage work on core MD03-2601 from the Adélie Basin (Fig. 1) has resulted in a detailed reconstruction of Holocene environmental changes. Core MD03-2601 is about 40 m long, covers a period between 1 ka to 11 ka (Denis et al., 2009b) and was analyzed at 10-20 yr resolution, which is approximately the resolution of the SAM variability. However, the siliceous microfossil assemblage constitutes a fraction of the full biodiversity of polynya ecosystem remains, which can be found in Antarctic sediments. In recent years, palynology, the study of dinoflagellate cysts (dinocysts) and other palynomorphs (organic remains of unicellular organisms like algae and zooplankton), has become a complementary tool (**Chapter 5**; Mudie et al., 2021) or even an alternative tool to the study of siliceous remains to reconstruct the circum-Antarctic past environment (Houben et al., 2013; Bijl et al., 2018b; Sangiorgi et al., 2018; Hoem et al., 2021a; Marschalek et al., 2021). The use of dinocysts for reconstructing Holocene paleoenvironmental conditions in the Southern Ocean is still underexploited, partly due to the scarcity of available sediment records and because species diversity, at least in modern surface sediment samples, is low close to the Antarctic coast (Esper and Zonneveld, 2002, 2007; Prebble et al., 2013; Zonneveld et al., 2013; Marret et al., 2020; Thöle et al., 2023). Therefore, including also other palynomorphs in paleoenvironmental reconstructions could potentially enlarge the toolbox to reconstruct paleoenvironmental change near the Antarctic coast. **Chapter 2** provides a qualitative overview of the palynological content of a Holocene record at Integrated Ocean Drilling Program (IODP) Site U1357, in the Adélie Basin. This sequence contains the exceptionally well-preserved organic remains of three eukaryotic kingdoms, and various trophic levels, both from benthic and pelagic organisms, and thus provides a good representation of the lower trophic levels of the ecosystem.

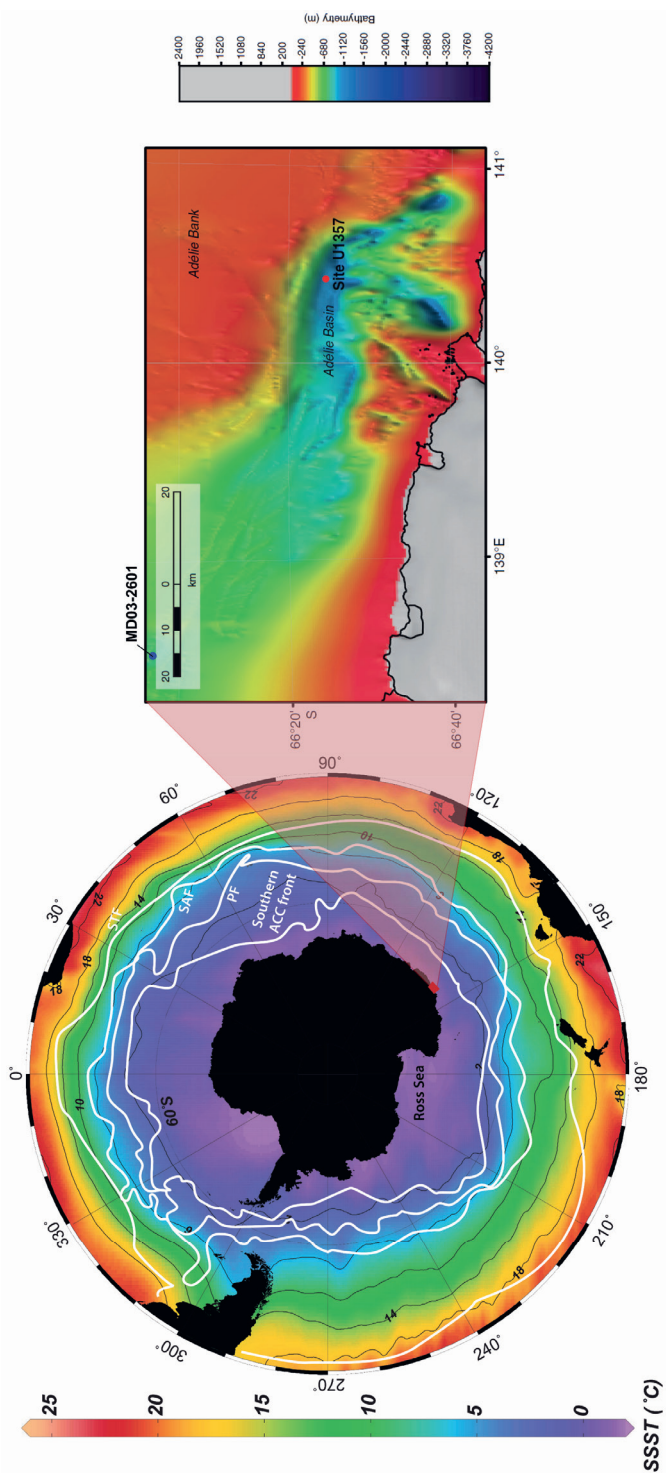


Figure 1: Present-day summer sea surface temperatures (SSST) and frontal systems around Antarctica (on the left) and the location of Site U1357 (current study) and site MD03-2601 at the Adélie Coast plotted on the bathymetry of the Adélie Basin (on the right).

In this study, we examine the Adélie Holocene record from Site U1357 (Hole B) for palynology at a near-centennial resolution and pair our analyses with a TEX₈₆-based sea water temperature reconstruction and recently published reconstructions of the meltwater flux to the site (Hole U1357B, Ashley et al., 2021). In addition, the proximity of Hole U1357B to site MD03-2601 allows direct comparison of the palynological content to reconstructed environmental conditions based on diatoms from MD03-2601. With 10 to 30 laminae deposited every 100 year the record from Hole U1357B can potentially resolve Holocene climate variability for the East Antarctic coastal margin on decadal timescales. Millennial-scale temperature shifts of up to 3°C change have been reconstructed for the Holocene from both Antarctic ice cores and Southern Ocean climate proxy records (Masson et al., 2000; Hodell et al., 2001; Masson-Delmotte et al., 2004; Nielsen et al., 2004; Crosta et al., 2008; Divine et al., 2010; Shevenell et al., 2011; Kim et al., 2012a; Prebble et al., 2017; Jones et al., 2023), allowing insight into ecosystem response to warmer-than-present-day conditions. To this end, we first provide an overview of the expression of key Holocene events in the Southern Ocean, then we report previous work done on Holocene paleoenvironmental reconstructions in the Adélie Basin, and ultimately, we present our palynological study.

2 Background information

2.1 Expression of the Northern Hemisphere 8.2 ka and 4.2 ka events in the Southern Ocean

The 8.2 ka event is linked to a freshwater outburst from the Laurentide lakes Agassiz and Ojibway after reduction of the Laurentide Ice Sheet, which have significantly reduced the formation of North Atlantic Deep Water (NADW), affecting ocean heat transport (Barber et al., 1999; Teller et al., 2002). Coupled ocean-atmosphere-biosphere climate model experiments show a warming Southern Ocean in response to the freshwater release in the North Atlantic due to the so-called ‘bipolar seesaw effect’ (Bauer et al., 2004; Wiersma et al., 2011). However, the Vostok deuterium record is perhaps the only record showing a warming pulse of about 2°C around 8.2 ka, as there is little other evidence for a Southern Hemisphere warming (Ljung et al., 2008; Wiersma et al., 2011), even from West Antarctica (Jones et al., 2023). This is consistent with modeling results, as the magnitude of warming in the Southern Hemisphere resulting from the 8.2 ka event is predicted to be too small to exceed the natural variability in the proxy records (Wiersma and Renssen, 2006). Only one other warming event recorded around 8.5 ka BP in Lake Terrasovoje, Amery Oasis, East Antarctica, has been linked to the 8.2 event (Cremer et al., 2007). In general, the circum-Antarctic during the early Holocene was characterized by relatively warm period around 11 ka, which is known as the Early Holocene Climatic Optimum

(EHCO) (Nielsen et al., 2004; Bentley et al., 2009; Divine et al., 2010). This period of (summer) sea surface temperature (SST) warming and (winter) sea-ice retreat is related to a poleward migration of the westerlies (Divine et al., 2010). Between 10 and 8 ka, ice core sea salt and micropaleontological data show an increase of (winter) sea-ice extent between 10 and 8 ka (Divine et al., 2010; Mezgec et al., 2017; Melis et al., 2021; Winski et al., 2021).

In the southern high and mid-latitudes, a short-lived cooling event has been associated with the 4.2 ka event, which is recorded in surface water proxies from marine sediment cores (Moros et al., 2009) as well as from ice cores from the east Antarctic continent (Masson-Delmotte et al., 2004). However, most reconstructed SST trends derived from marine records show a more gradual temperature shift between 5 and 3 ka. Notably records from between 45 and 55°S in the Atlantic sector of the Southern Ocean show a gradual warming after a relatively cool mid-Holocene period (Nielsen et al., 2004; Denis et al., 2010; Xiao et al., 2016a), while a gradual cooling after a relatively warm mid-Holocene period is recorded in sedimentary cores obtained south of 55°S around Antarctica (Domack et al., 2001; Crosta et al., 2004, 2007, 2008; Bentley et al., 2009; Denis et al., 2010; Melis et al., 2021), resulting in more consolidated pack-ice conditions at Antarctic coastal margins (Mezgec et al., 2017). A new record from the Divide ice core from West Antarctica (Jones et al., 2023) shows a warming summer temperature trend throughout the early and mid-Holocene, with peak warming at 4.1 ka, and then a cooling during the late Holocene, while winter temperatures remain relatively stable.

The timing and expression of the warming/cooling trends during the mid-Holocene apparently varies strongly between the various marine and ice-core records (Masson et al., 2000; Domack et al., 2001; Crosta et al., 2008; Bentley et al., 2009; Divine et al., 2010; Prebble et al., 2017). The differences in the timing of peak warmth and reduced sea-ice extent during the mid-Holocene have in part been attributed to the fact that the different proxies used for environmental reconstruction are biased towards different seasons (Renssen et al., 2005; Crosta et al., 2008). Because changes in orbital parameters over the course of the Holocene result in a decrease in winter insolation as well as an increase in summer insolation (Laskar et al., 2004), proxies reflecting different seasons can show opposing trends, particularly in sedimentary records that cannot capture a seasonal resolution. Notably, it has been demonstrated recently that the mid-Holocene Thermal Maximum is likely an artifact, resulting from the temperature proxies being biased towards seasonal (summer) temperatures (Bova et al., 2021). In addition, during the Holocene the winter Latitudinal Insolation Gradient (LIG) decreased, while the summer LIG increased (Davis and Brewer, 2009). Because the summer and winter LIG are in antiphase, this results in a latitudinal temperature gradient (LTG) that evolves over time differently for each

season (Davis and Brewer, 2009). Therefore, the late Holocene southern high latitudes did experience both a summer strengthening of the westerlies and the associated intrusion of relatively warm nutrient-rich Modified Circumpolar Deep Water (MCDW) onto the Antarctic shelf (Denis et al., 2010; Shevenell et al., 2011; Kim et al., 2012a), as well as a winter decrease in westerly wind strength, which promotes sea-ice expansion (Denis et al., 2010). The seasonal environmental changes have been well-studied in the Adélie Basin (Crosta et al., 2005a; Denis et al., 2006; Crosta et al., 2007, 2008; Denis et al., 2010; Maddison et al., 2012; Ashley et al., 2021), allowing for a comparison to the organic proxies from U1357B without a seasonal bias.

2.2 Holocene environmental conditions in the Adélie Basin (East Antarctica)

Holocene environmental conditions and climate variability near the East Antarctic Ice Sheet has been studied extensively by using material obtained from core MD03-2601 from the Adélie Basin. Paleoclimatological reconstructions include seasonal SST and sea-ice extent reconstructions based on diatoms and diatom biomarkers (Crosta et al., 2005a; Denis et al., 2006; Crosta et al., 2007, 2008; Denis et al., 2010), a subsurface temperature record (Kim et al., 2012a), reconstructions of paleoproductivity and nutrient utilization (Crosta et al., 2005a; Denis et al., 2009b; Panizzo et al., 2014), and reconstructions of deep water formation (Denis et al., 2009a). More recently, biomarker data (deuterium isotopes of C₁₈ fatty acids and highly branched isoprenoids (HBI)) and sedimentological data (grain size, natural gamma radiation and biosiliceous mass accumulation rates) has become available from IODP (Integrated Ocean Drilling Program) record from Site U1357 (Fig. 1) covering the entire Holocene (Ashley et al., 2021). They have been used to reconstruct fresh meltwater fluxes to the Adélie Coast coming either from local glaciers or transported anti-clockwise via the Antarctic Coastal Current from the Ross Sea, where glacial retreat persisted until 3 ka (Ashley et al., 2021). A summarizing figure of the reconstructed surface water conditions at MD03-2601 and U1357 is shown in Fig. 2.

Like today, diatoms were the most dominant phytoplankton group in the Adélie Basin, as the close correspondence between the organic carbon content and the biogenic silica content of M03-2601 suggests (Crosta et al., 2005a). Based on the diatom content of M03-2601 warm and cold periods are distinguished. Most noticeable is a shift in dominance between the open-ocean species *Fragilariopsis kerguelensis* and the sea-ice-loving *Fragilariopsis curta* group (combined *Fragilariopsis* species with similar environmental preferences, such as *Fragilariopsis curta* and *Fragilariopsis cylindrus*) at around 4.5 ka. It marks the transition from the mid-Holocene to the late Holocene (Crosta et al., 2005a, 2007). Based on the relative abundance of these sea-ice loving diatom

species and open-ocean loving species the Holocene period in the Adélie Basin has been subdivided in four climatic stages: the warmer Hypsithermal 1 (~11 to 8.4 ka); a relatively cold period at the end of the early Holocene (~8.4 – 7.4 ka); Hypsithermal 2, which is equivalent to the mid-Holocene (~7.4 – 4.5 ka) and the colder Neoglacial or late Holocene (~4.5 – 1.0 ka) (Denis et al., 2009a). It should be noted that the age model for MD03-2601 was recently updated by Ashley et al. (2021), which implies that the timing of environmental changes based on the proxy data differs from that in the original publications. The reviewed age model affects particularly the data younger than 6.3 ka and therefore includes the onset of the Neoglacial (late Holocene), which was originally dated at ~3.5 ka.

Periods of increased paleoproductivity have been recognized based on total organic carbon (C_{org}), total organic nitrogen (N_{org}) and biogenic silica (BSi) fluxes (Denis et al., 2009b). In general, there appears to be a positive correlation between these paleoproductivity proxies and the relative abundance of summer diatom species, incl. *F. kerguelensis*, that grow in the summer season, as well as the setae diatom group, which are associated with nutrient-rich mixed surface waters in the Adélie Land region (periods around 2.0, 4.8, 6.0, 7.5 and 8.3 ka; Fig. 2b.3 and 2b.4) (Denis et al., 2009b). Instead, a negative correlation to C_{org} , N_{org} and BSi fluxes was shown for *Chaetoceros* resting spores (RS), which are indicative of high spring productivity in stratified surface waters and nutrient limitation, and $\delta^{15}N_{bulk}$, which reflects relative nutrient utilization (Denis et al., 2009b). This suggests that (1) particularly the slow summer diatom production is responsible for organic matter burial in the Adélie Basin and not the spring blooms, and (2) relative nutrient utilization seems to be determined by nutrient availability due to upwelling of nutrient-rich modified Circumpolar Deep Water (Denis et al., 2009b).

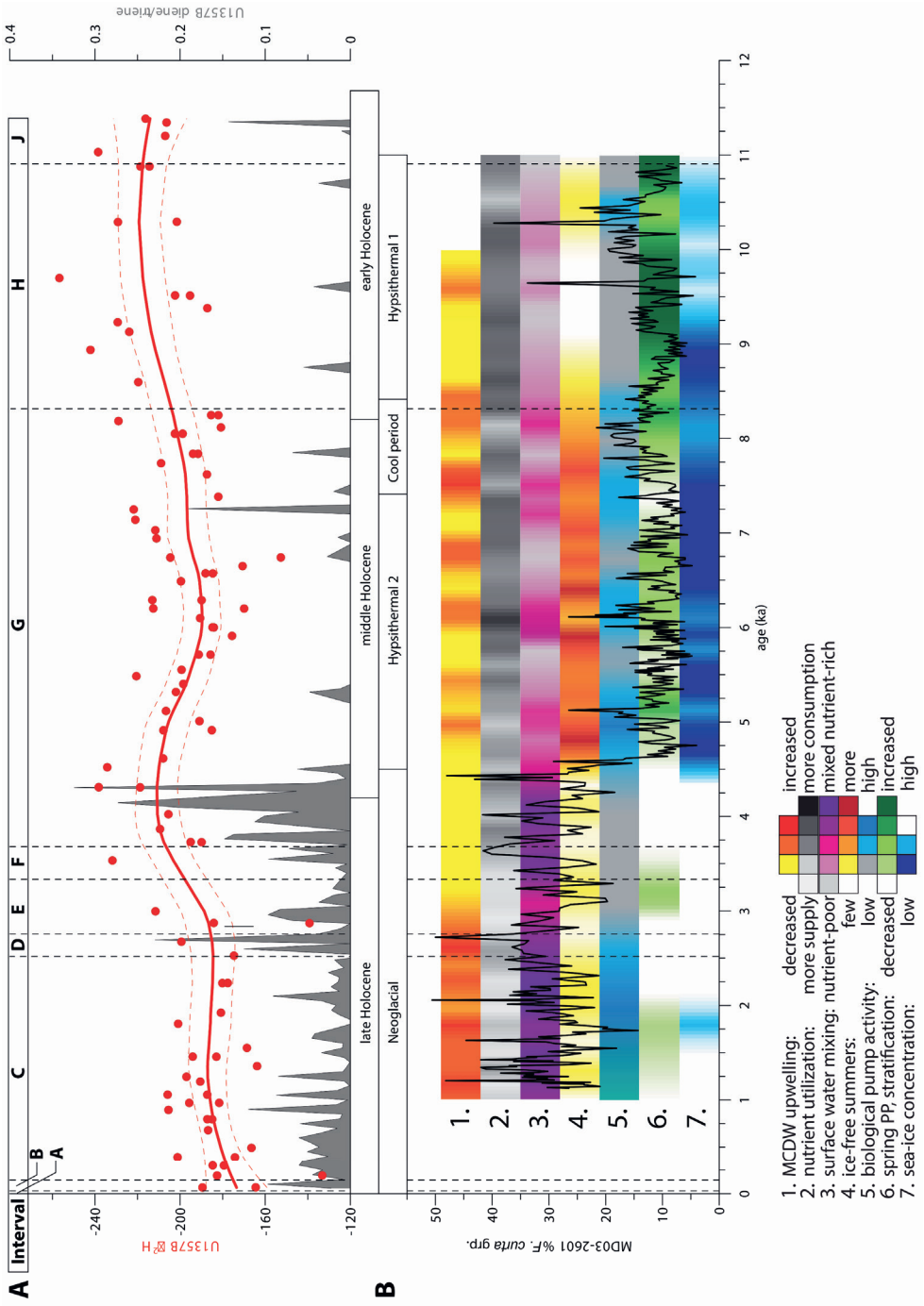


Figure 2 (previous page): **(A)** Proxies for environmental surface water conditions at Site U1357B, based on Ashley et al. (2021): deuterium ratio of fatty acids (red) and diene/triene ratio (grey). Intervals A to J are as defined by the cluster analysis in Figure 3; **(B)** Percentage of *F. curta* grp. at site MD03-2601 (black line) and graphic summary of environmental surface water conditions at site MD03-2601 (see references in the text): (1) MCDW upwelling based on the relative abundance of *Proboscia* spp.; (2) Nutrient utilization (supply vs. consumption) based on $\delta^{15}\text{N}_{\text{bulk}}$; (3) Nutrient-rich mixed surface waters based on the relative abundance of the setae diatom group (Denis et al., 2009b); (4) Ice-free summers and therefore growing season length based on relative abundances of summer diatom group (Denis et al., 2009b); (5) Biological pump activity based on Th-normalized Bsi, C_{org} and N_{org} content; (6) Spring primary productivity and stratification based on relative abundances of *Chaetoceros* resting spores; and (7) Sea-ice concentrations based on the relative abundances of *F. curta* versus *F. kerguelensis*.

3 Material and age model

A 172.44 m-long core from Site U1357 (Hole U1357B) was recovered during Integrated Ocean Drilling Program (IODP) Expedition 318 in 2010 and lies downwind and downcurrent from the Mertz Glacier Polynya in the Adélie Basin (66°24.799'S, 140°25.571'E), East Antarctica (Fig. 1), at 1017 meters water depth. Reaching a depth of 170.7 meter below sea floor (mbsf), a total of 172.44 m core length was obtained. Almost the entire core consists of an alternation of centimeter-scale dark olive-brown and light greenish brown laminae, which consist of 80-99% diatom ooze. The few centimeters below 170.25 mbsf are characterized by an abrupt downward increase in the clay, silt and sand content (Escutia et al., 2010). These light and dark diatomaceous laminations are a common facies for Antarctic shelf deposits and are interpreted as annual spring and summer bloom deposits (Leventer et al., 2002; Stickley et al., 2005; Denis et al., 2006; Maddison et al., 2012).

An age model for U1357B was developed by Ashley et al. (2021) based on 87 ¹⁴C analyses on bulk organic carbon and using BACON, a Bayesian iteration scheme.

For palynological analysis a total of 56 samples were taken. The shallowest sample (U1357B-1H-1W 11-13 cm) was taken from a soupy mixed part of the core. The other 55 samples were taken from single lamina: 12 samples from light-colored lamina, 43 samples from dark-colored lamina.

A total of 173 samples were taken for GDGT analysis. Of these samples 89 samples were taken from light laminae and 83 samples were taken from dark laminae. One sample (U1357B-19H-1W 8-9 cm) was taken from a more orange-colored lamina below a light-colored lamina.

4 Methods and statistical analyses for the interpretation of palynological proxies

4.1 Palynological processing and counting

A total of 56 samples taken for palynological analysis were freeze-dried and grinded manually after which a *Lycopodium clavatum* tablet (containing 18583 ± 762 spores; batch number 483216) was added with some Agepon (1:200) for calculating palynomorph concentrations (Wood et al., 1996). Standard palynological treatment (10% HCl, unheated 40% HF and no oxidation) was applied. The treated material was sieved using a 10-µm mesh sieve and clumps of residue were disaggregated using ultrasound. Heavy minerals were removed by pouring the residue from the sieve into an evaporating dish that is kept floating in the ultrasonic bath and decanting this back into the sieve after 5 minutes. The fraction > 10-µm was concentrated to ~1 ml of glycerin-water and a fraction hereof was mounted on a microscope slide using glycerine jelly. Slides were

analysed until a minimum of 200 palynomorph counts was reached (on average a number 630 palynomorphs were counted per slide). The major palynomorph groups considered were: dinocysts, tintinnid loricae, prasinophytes, acritarchs and reworked palynomorphs, including dinocysts, pollen and spores (for a list of species within each group see Appendix A). Subsequently, the relative abundance of each species or group of palynomorphs was calculated (in %) with respect to the total number of palynomorphs. In addition, relative abundances (%) of dinocyst species were calculated with respect to the total number of dinocysts counted. We also considered two main groups of dinocysts based on the trophic strategy of the dinoflagellate producing the cyst (i.e., autotrophic or heterotrophic). Similarly, the relative abundance of tintinnid (zooplankton) species was calculated with respect to the total number of tintinnid loricae. The relative abundances of dinocysts and tintinnid loricae are considered separately, as these are the most abundant organic-walled micro-organisms. Considering these micro-organism groups separately, allows for studying shifts in the dinocysts and tintinnid loricae assemblages and better comparison to the available literature, as generally relative abundances are described per microfossil group.

4.2 Identification of palynomorphs, grouping and environmental interpretation

Dinoflagellate cyst (dinocyst) taxonomy follows that cited in Williams et al. (2017). An extensive review on the palynomorph species found in the sediments of Hole U357B is published, including also ecological data for interpreting the palynological record is given in **Chapter 2**. We use this overview to interpret the assemblage shifts recorded in Hole U1357B. Individual species of dinocysts and tintinnids are considered here. Moreover, we have grouped the *Cymatiosphaera*-type prasinophytes with polygon-forming algae as *Cymatiosphaera* spp. (*P. cristatum*, *P. polygonum*, *P. marginatum*, *P. aff. reticulatum*, and *Cymatiosphaera* sp. 1) for two reasons. Firstly, differentiation between some of these species is based on the presence of pores, which can be either too small to identify underneath the light microscope or absent in early developmental stages of the phycoma (Parke et al., 1978). Secondly, the ecological affinities of these prasinophytes (green algae) are unknown at species level (see **Chapter 2**). This is also the reason why publications often considered them as one group (*Cymatiosphaera* spp.) (e.g., Hannah et al., 2000; Mudie et al., 2002; Piasecki et al., 2002; Riding and Hubbard, 1999; Warny et al., 2006) and taken to represent increased stratification due to the presence of seasonal sea ice and/or meltwater runoff. Similarly, the prasinophyte *Pterosperma parallelum*-type phycomata with parallel alae (*P. parallelum* and *P. cf. parallelum*) were grouped under *P. parallelum*.

Various types of benthic foraminifer inner wall linings have been recorded. We distinguish between uniserial, triserial and trochospiral foraminifer linings. Trochospiral

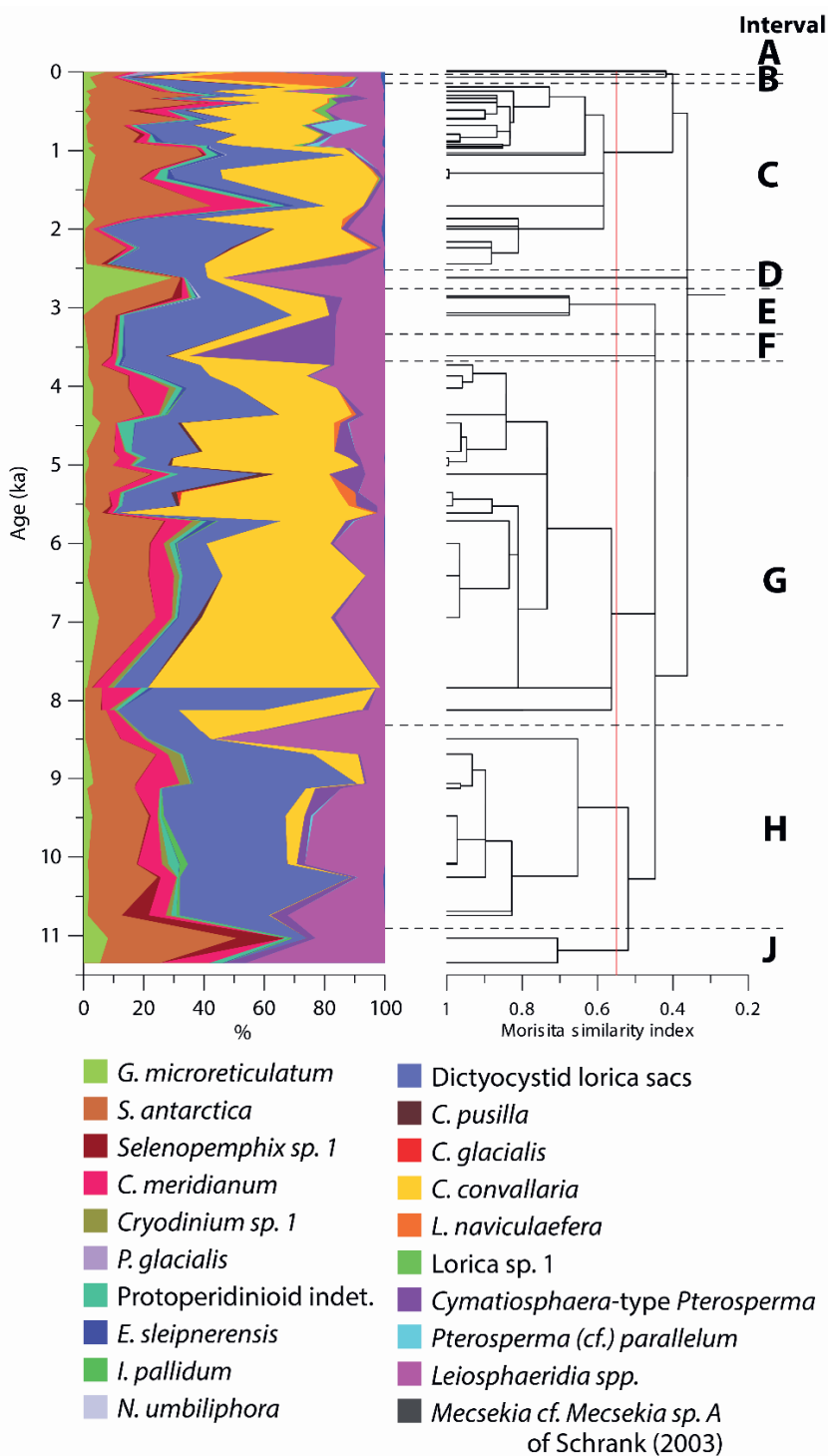
Figure 3 (next page): Relative abundances of surface water dwelling palynomorphs (on the left) used for cluster analysis based on the Morisita similarity index (on the right). Interval boundaries were established by using a cut-off value of 0.55 (red line).

foraminifers are commonly epifaunal species, while uniserial and triserial forms are generally infaunal species (Corliss, 1991). It has been shown that the relative amount of infaunal species increases with respect to the epifaunal species during times of increased productivity (Thomas et al., 1995). We therefore define a paleoproductivity proxy as the ratio of uniserial and triserial foraminifer linings over all foraminifer linings, which approximates the ratio of all infaunal foraminifers over all foraminifers. We call this proxy infaunal foraminifer linings ratio (IFL ratio).

Of the larger zooplankton remains only the copepod remains will be discussed. However, it must be noted that as most remains are fragmentary, they are hard to quantify. To avoid overestimation, counts are limited to the amounts of setae (hair-like structures) with their pointy ends intact. The sum of copepod remains includes these intact setae, copepod eggs, spermatophores and mandibular gnathobases.

4.3 Constrained cluster analysis: turnover events in the palynological record

We performed a constrained cluster analysis on all palynomorphs produced by species living in the surface waters to define intervals based on turnover events in the assemblages (Fig. 3). Organic walled dinocysts, tintinnid loricae (forms within the same species have been grouped together, thereby taking into account intraspecific variation of the tintinnid lorica (Agatha et al., 2013)) and lorica sacs, prasinophytes, the acritarch *Leiosphaeridia* spp. (leiospheres) and the acritarch *Mecsekia* (see **Chapter 2**, Plate 7, 4-9) were considered. The acritarch *Palaeostomocystis* is not included in this analysis, as it has an unknown biological origins (see **Chapter 2**). The cluster analysis has been performed using the Morisita overlap index as a similarity measure (values between 0 and 1, with 1 indicating highest similarity). This index places emphasis on shifts in dominance of common species, which is the focus of this study, and almost neglects the turnover of rare species (Barwell et al., 2015). The dendrogram was constructed using the software PAST (Hammer et al., 2001). A cutoff value of 0.55 for the Morisita similarity index was arbitrarily chosen at about one third of the similarity index range (0.35-1), such that the resulting clusters are relatively more dissimilar with respect to each other (closer to 0) than they are similar (closer to 1).



4.4 Detrended correspondence analysis

We used the software program PAST (Hammer et al., 2001) for multivariate analyses and used a detrended correspondence analysis (DCA) to detect whether the variability in the palynological content is linked to the type of sediment lamina (dark versus light). The DCA was performed on all palynomorphs known to be derived from planktonic organisms by grouping them according to their higher order taxonomic group, trophic level and endemism. The groups used in the DCA analysis are: *Palaeostomocystis*, autotrophic dinocysts, heterotrophic dinocysts, endemic tintinnids, non-endemic tintinnids, prasinophytes, and leiospheres. As described in **Chapter 2**, the endemic tintinnids include species that are typically abundant south of the winter sea ice edge (WSIE) and/or living within sea ice (i.e., *C. glacialis*, *C. convallaria*, and *L. naviculaefera*). The non-endemic tintinnids include cosmopolitan species and/or species more common in the Polar Frontal Zone (i.e., *C. pusilla* and dictyocystid lorica sacs). Furthermore, DCAs have also been performed on the composition of all known planktonic heterotrophic species (all tintinnids and heterotrophic dinoflagellates) and all known planktonic autotrophic species (all prasinophytes, leiospheres and autotrophic dinoflagellates). The distinction between *Selenopemphix antarctica* and *Selenopemphix* sp. 1 *sensu* Esper & Zonneveld (2007) is maintained. Biologically these dinoflagellate cysts could belong to the same species, as *Selenopemphix* sp. 1 appears to be a larger version of *S. antarctica* with a more pronounced, depressed sulcus and larger conical apical complex (Esper and Zonneveld, 2007). However, such morphological differences could be important, as cyst morphology could be dependent on the environment (Mertens et al., 2009). Therefore, environmental and/or ecological conditions could also play a role in the size of *Selenopemphix* sp. 1 versus *S. antarctica* as well as the presence or absence of septae on *Cryodinium* (*C. meridianum* versus *Cryodinium* sp. 1) (**Chapter 2**, Plate 1). Indeed, *Selenopemphix* sp. 1 and *S. antarctica* seem geographically separated (Thöle et al., 2023). In addition, two size classes of acritarch leiospheres are considered here: *Leiosphaeridia* sp. 1 and sp. 2 of **Chapter 2** grouped together (<30 µm in diameter) and *Leiosphaeridia* sp. 3 of **Chapter 2** (>70 µm in diameter). Because of the distinct size difference between *Leiosphaeridia* sp. 3 and the other leiospheres, it is likely that these are produced by different phytoplankton species with possibly different ecological preferences.

4.5 GDGT analysis

For GDGT extraction, couplets of samples (163 in total) have been taken about every two meters from both a light and a dark lamination in order to compare seasonal differences. Samples were then freeze-dried, manually mortar-grinded for homogenization, and extracted with an accelerated solvent extractor (ASE) using

dichloromethane (DCM) and MeOH (9:1 v/v) at 100°C and 7.6×10^6 Pa. An internal standard for GDGT quantification was added to the total extracts. Using Pasteur pipettes column filled with activated Al_2O_3 , the extract was separated into apolar, ketone and polar fractions by eluting it with hexane/DCM (9:1 v/v), hexane/DCM (1:1 v/v) and DCM/MeOH (1:1 v/v), respectively. The polar fractions containing the GDGTs were analyzed according to the procedure described by Schouten et al. (2007). The polar fractions were dried down under nitrogen and subsequently redissolved by sonication using hexane/isopropanol (99:1 v/v) to a concentration of 2 mg/ml and filtered through a $0.45 \mu\text{m}$ PTFE filter attached to a 1 ml syringe. Analysis of the GDGTs was performed using high performance liquid chromatography-atmospheric pressure chemical ionization mass spectrometry (HPLC-APCI-MS). Identification of the different GDGT isomers was carried out via single ion monitoring (SIM, $[\text{M}+\text{H}]^+$ ions at m/z 1302, 1300, 1298, 1296, 1292, 1050, 1036 and 1022, and dwell time of 237 ms. Quantification of the GDGT compounds was achieved by integrating the peak areas and using the C_{46} GDGT internal standard according to Huguet et al. (2006).

4.6 TEX_{86} , $\text{TEX}_{86}^{\text{H}}$ and $\text{TEX}_{86}^{\text{L}}$ proxies and calibrations

Temperatures were calculated using the TEX_{86} index. The TEX_{86} index and its derivatives $\text{TEX}_{86}^{\text{H}}$ and $\text{TEX}_{86}^{\text{L}}$ use the ratio of different isoGDGTs, which are produced by Thaumarchaeota (Schouten et al., 2002; Kim et al., 2010). The relationship between TEX_{86} and sea-surface temperature is non-linear due to the large scatter at the lower temperature end of the calibration. $\text{TEX}_{86}^{\text{H}}$ and $\text{TEX}_{86}^{\text{L}}$ have been developed as a means to overcome this non-linearity (Kim et al., 2010). The $\text{TEX}_{86}^{\text{H}}$ proxy is the logarithmically transformed version of the TEX_{86} proxy, but it is calibrated to sea surface temperature (SST) by excluding all (sub)polar core-tops, thereby eliminating the scatter at the lower temperature end of the calibration (Kim et al., 2010). This makes $\text{TEX}_{86}^{\text{H}}$ unsuitable for reconstructing SSTs at the higher latitudes. Furthermore, it has been shown that exclusion of the (sub)polar core-top values for the $\text{TEX}_{86}^{\text{H}}$ calibration has led to the exclusion of most shallow water core-top sites (Taylor et al., 2013). Because Thaumarchaeota living in the deeper waters (>1000 m) synthesize GDGTs at a different ratio than Thaumarchaeota in shallow waters (Kim et al., 2015; Villanueva et al., 2015), this may have introduced a water-depth dependency limiting $\text{TEX}_{86}^{\text{H}}$ to deep-water sites (>1000 mbsl) (Taylor et al., 2013). Considering that the Adélie Basin is ~ 1000 m deep, this may play a role at Site U1357. We shall therefore not consider $\text{TEX}_{86}^{\text{H}}$ for reconstructing SSTs at Site U1357.

In the study of Kim et al. (2010), the $\text{TEX}_{86}^{\text{L}}$ showed the best correlation to the lower SST values and was established by removing the crenarchaeol regioisomer (Cren') from the $\text{TEX}_{86}^{\text{H}}$ equation and the exclusion of GDGT-3 from its nominator. However, it has

subsequently been shown that $\text{TEX}_{86}^{\text{L}}$ is very sensitive to changes in the GDGT-2/GDGT-3 ratio ([2]/[3]) (Taylor et al., 2013; Hernández-Sánchez et al., 2014). The 'deep water' community of Thaumarchaeota typically synthesize higher concentrations of GDGT-2 relative to GDGT-3 (Kim et al., 2015; Villanueva et al., 2015). Although highest isoGDGT export to the seafloor is linked to highest organic matter, opal (diatom frustules) and lithogenic particle fluxes from the surface and shallow subsurface waters (0-200 mbsl) (Yamamoto et al., 2012; Mollenhauer et al., 2015), a decrease of this export could increase the relative export of isoGDGTs from the deeper waters to the seafloor. Therefore, we consider $\text{TEX}_{86}^{\text{L}}$ also unsuitable for reconstructing SSTs at Site U1357.

As neither $\text{TEX}_{86}^{\text{L}}$ nor $\text{TEX}_{86}^{\text{H}}$ appears to be suited for Site U1357, we limit ourselves to TEX_{86} . The reliability of TEX_{86} and derived temperatures can be affected by input of soil, input by methanotrophic and methanogenic archaea, and other non-thermal biases (Koga et al., 1998; Pancost et al., 2001; Schouten et al., 2013; Elling et al., 2014; Qin et al., 2015). We therefore screen the TEX_{86} values by using Branched and Isoprenoid Tetraether index (BIT index) (Hopmans et al., 2004) to account for soil-derived and non-Thaumarchaeotal isoGDGTs (BIT >0.3) (Weijers et al., 2006). Using the Methane Index (MI) (Zhang et al., 2011) and the GDGT-2/crenarchaeol ratio (Weijers et al., 2011), the potential influence methanotrophs has been checked (MI > 0.3 and GDGT-2/crenarchaeol > 0.4). The GDGT-0/crenarchaeol ratio is used to identify the potential input of isoGDGTs by methanogenic archaea (values >2) (Blaga et al., 2009; Sinninghe Damsté et al., 2009). And finally, the Ring Index ($|\Delta\text{RI}|$) has been applied to investigate any other non-thermal biases (values >0.6) (Zhang et al., 2016). However, none of these indices exceeded the limits for which TEX_{86} becomes less reliable, and this no data were discarded.

To convert TEX_{86} into temperature we used the Bayesian spatially-varying regression model (BAYSPAR) of Tierney & Tingley (2014; 2015). This method renders a local linear regression based on TEX_{86} core-top values and World Ocean Atlas 2009 temperature data (Locarnini et al., 2010) within a 20° x 20° grid cell that encompasses the study site (Tierney and Tingley, 2014). We used the subT (0-200m) calibration because Thaumarchaeota are absent in the upper 0-45 m of the water column in the seasonally ice-covered waters of the Southern Ocean (Kalanetra et al., 2009).

Local regression (LOESS) was applied to analyze the long-term (1-kyr) trends. In contrast to a 10-point average curve, a LOESS curve generates a confidence interval that takes into account uneven sample spacing.

5 Results

5.1 Palynology

The palynomorph assemblage consists of dinoflagellate cysts (dinocysts), pollen and spores, tintinnid loricae, zooplankton remains, prasinophytes, foraminifer linings, and acritarchs (see **Chapter 2** for a taxonomic overview). Based on the statistical clustering of the *in situ* palynological remains of surface-dwelling organisms, the record has been divided into nine intervals (A to J) (Figure 3). By using a cutoff value of 0.55 there are some intervals that only consist of one datapoint. We are aware of the fact that these may be statistical outliers and might not be representative of actual environmental conditions. We are therefore cautious in interpreting these intervals individually and rather discuss them together with the neighboring intervals as part of a trend.

Firstly, we describe the *in situ* palynological remains of these surface-dwelling organisms for each interval. Ages (in ka) for the interval boundaries are based on the average between the age of lowest sample in the upper interval and age of the highest sample in the lower interval. Relative abundances of the palynomorph groups (i.e., relative abundances of dinocysts, tintinnid loricae, prasinophytes, and acritarchs (leiospheres and *Mecsekia*) and total concentration of palynomorphs (in number/gram dry sediments) are presented in Fig. 4. This figure shows that in general tintinnid loricae and lorica sacs (both remains of planktonic zooplankton) form the dominant part of the assemblage throughout most of the core. In Fig. 5 the % of individual dinocyst species within the dinocyst assemblage are indicated (e.g., % *Selenopemphix antarctica* within the dinocyst assemblage). Fig. 6 shows the % of individual tintinnid species within the tintinnid assemblage.

Secondly, we present the relative abundances of foraminifer lining types (Fig. 7). And thirdly, species of *Palaeostomocystis* and undescribed acritarchs will be presented as relative abundances with respect to the total palynomorph assemblage (Fig. 8).

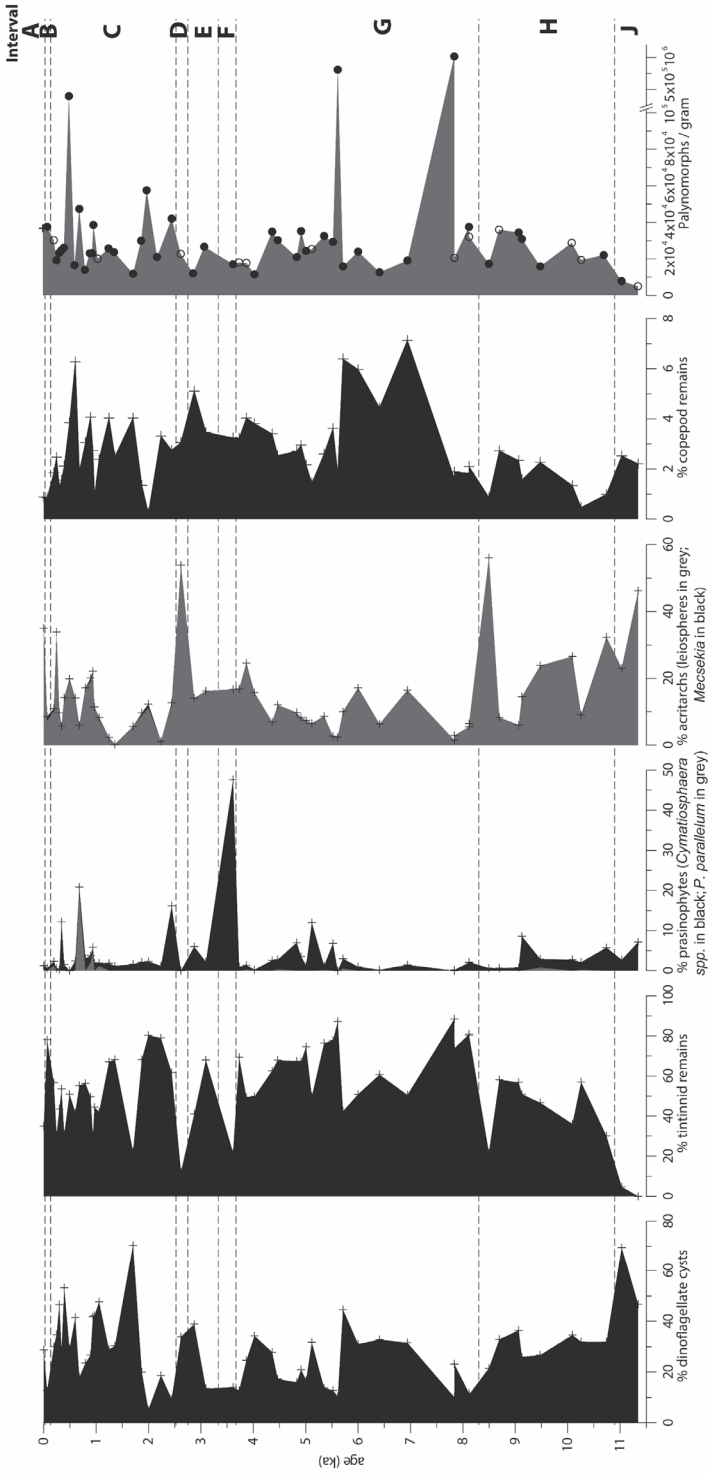


Figure 4: Relative abundances of higher-order taxonomical palynological groups. Percentages reflect the relative abundance of a group with respect to the total number of palynomorphs. Most right figure shows the total amount of palynomorphs per gram sediment with open circles being samples obtained from light coloured laminae and filled circles being samples obtained from dark coloured laminae.

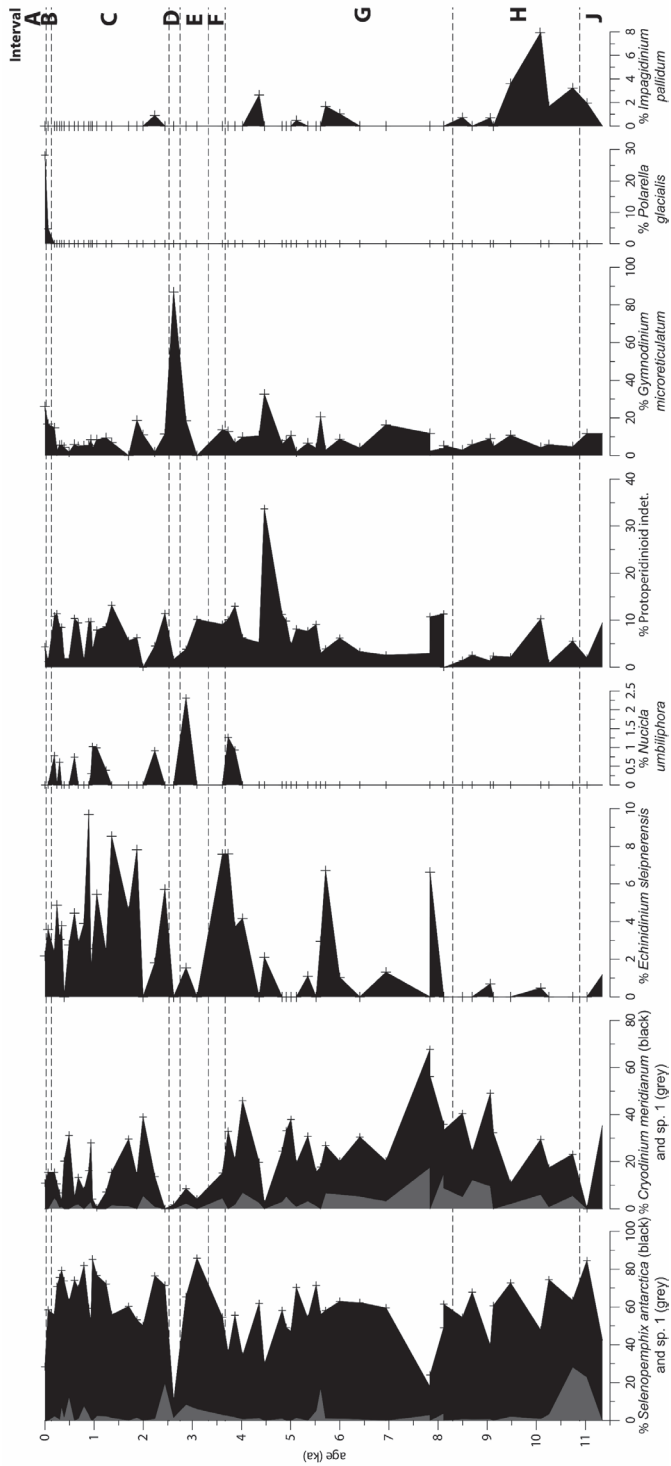


Figure 5: Relative abundances of dinocysts. Percentages reflect the relative abundance of a species with respect to the total number of dinocysts.

Interval J (11.35 – 10.89 ka)

This interval consists of the deepest two samples taken from Hole U1357B. With respect to the younger intervals, interval J is characterized by high relative abundances of dinocysts and the lowest relative abundances of tintinnid remains (Fig. 4). Furthermore, leiospheres are also well represented (~46%). Notably, the lowest sample (169.7 – 169.71 mbsf) does not contain any tintinnids. The tintinnid remains that are present in the top sample of this interval (165.88 – 165.89 mbsf) are only dictyocystid lorica sacs (Fig. 6). Prasinophytes comprise about 5% of the total assemblage (Fig. 4). The dinocyst assemblage consists mostly of *Selenopemphix antarctica* and *Gymnodinium microreticulatum* (Fig. 5). The lower sample of this interval contains high relative amounts of *Cryodinium meridianum*, while the upper sample shows an increase of *Selenopemphix* sp. 1 *sensu* Esper & Zonneveld (2007) (~23%) and *Impaginium pallidum* (~2%) towards interval H.

5.1.1 Interval H (10.89 – 8.31 ka)

With respect to interval J, interval H shows a significant increase in tintinnid remains and contains significantly less abundant dinocysts. Leiospheres vary strongly between 6 and 56% in this part of the record (about 30 m), but particularly the top sample in this interval is characterized by very high amounts of leiospheres (Fig. 4). Within the tintinnid assemblage in interval H, the dictyocystid lorica sacs are almost the only tintinnid-derived palynomorphs in the assemblage (Fig. 6). The relative abundance of the tintinnid *Cymatocylis convallaria* shows an increasing trend. The dinocyst assemblage is dominated by *S. antarctica* and *C. meridianum* with relative abundances around 60% and 25%, respectively (Fig. 5). In the lower part of interval H, there is an increase and decrease of both *I. pallidum* and *Selenopemphix* sp. 1 *sensu* Esper & Zonneveld (2007). *I. pallidum* reaches an optimum of ~8% of the dinocyst assemblage at ~10.1 ka and is almost absent above 9.1 ka. The presence of higher relative abundances of *I. pallidum* coincides with slightly elevated abundances of prasinophytes. *Selenopemphix* sp. 1 reaches an optimum of ~28% at ~10.7 ka and disappears almost entirely above ~10.1 ka.

5.1.2 Interval G (8.31 – 3.67 ka)

The largest part of Hole U1357B falls within this interval (about 75 m). Highest relative abundances of tintinnid loricae are found within this interval and are generally above 50% (Fig. 4). The amount of leiospheres is relatively low with respect to intervals H and J. On average, the relative amount of dinocysts is somewhat lower in comparison to interval H, fluctuating between 15% and 40%. The tintinnid lorica assemblage consists almost entirely out of *C. convallaria* at the expense of the dictyocystid lorica sacs, which show a strong relative decline in the transition from interval H to G (Fig. 6). In the lowest

part of this interval there are large shifts in dominance between *C. convallaria* and the dictyocystid lorica sacs within the tintinnid assemblage. The composition of dinocysts is quite constant throughout this interval with *S. antarctica* and *C. meridianum* showing relative abundances of ~50% and ~30%, respectively (Fig. 5). However, in the lowest part of this interval, *C. meridianum* abundances reach above 40%, replacing *S. antarctica*. In this part of the record also the highest relative abundances of the septa-less *Cryodinium* sp. 1 (Chapter 2, Plate 1) are found. Relative abundances of *Echinidinium sleipnerensis* increase towards the top part of this interval but show occasional sharp peaks throughout the interval. Between 5.5 and 4.5 ka some peaks of *Cymatiosphaera*-type prasinophytes (Fig. 4) as well as peaks of the agglutinating tintinnid species *Codonellopsis pusilla*, *Codonellopsis glacialis* and *Laackmanniella naviculaefera* (Fig. 6) occur. Particularly the sample at 5.1 ka shows high amounts of the prasinophyte *Pterosperma* aff. *reticulatum* (Chapter 2, Plate 2) and the tintinnid lorica of *C. pusilla*. At the uppermost part of this interval is the first appearance of *Nucicla umbiliphora*. Although this species is a minor fraction of the total dinocyst assemblage, its presence is clearly characteristic for the upper part of the record from this point upwards.

5.1.3 Interval F (3.67 – 3.35 ka)

This interval, consisting of one sample (51.87 – 51.89 mbsf) from a dark lamina, shows the highest relative amount of prasinophytes recorded in Hole U1357B (47%), all of which are *Cymatiosphaera*-type (Fig. 4). Most of these belong to the species *Cymatiosphaera* sp. 1 as described in Chapter 2 (Plate 2). This increase of prasinophytes coincides with a significant drop in the amount of tintinnid remains and dinocysts, while leiospheres remain unchanged transitioning from interval G to interval F. In contrast to interval G, dictyocystid lorica sacs again dominate the tintinnid assemblage (Fig. 6), while the relative abundance of *C. convallaria* has dropped. Among the dinocysts, *S. antarctica* still dominates the dinocyst assemblage (Fig. 5). However, within the dinocyst assemblage there is an increase of *E. sleipnerensis* when transitioning from interval G to interval F.

5.1.4 Interval E (3.35 – 2.75 ka)

This interval consists of two samples, both from dark laminae (Fig. 4). Both have elevated leiosphere (~15%) and low prasinophyte (~4%) abundances (Fig. 4). However, the upper sample is dominated by dinocysts (Fig. 4), while the lower sample contains significantly less dinocysts. Within the dinocyst assemblage, both samples are dominated by *S. antarctica* and show elevated amounts of the larger *Selenopemphix* sp. 1 *sensu* Esper & Zonneveld (2007) (Fig. 5). *E. sleipnerensis* is almost absent in this interval and *C. meridianum* has declined significantly in comparison to the intervals F and G. Highest abundances within the record (2.3% of dinocysts) of *Nucicla umbiliphora* are recorded

within the upper sample of this interval. Within the tintinnid assemblage, the relative abundance of the dictyocystid lorica sacs reaches an optimum of 82% in the lowest sample of this interval.

5.1.5 Interval D (2.75 – 2.53 ka)

The one sample that represents this interval (43.24 – 43.26 mbsf), which is obtained from a light lamina, stands out from the other intervals by the relatively high amounts of leiospheres (54%) (Fig. 4). Interval D shows increased abundances of dinocysts (34%). Noticeably, the dinocyst assemblage is dominated by *G. microreticulatum* (87%) at the expense of *S. antarctica* (Fig. 5). Percentages of *C. meridianum* remain very low.

5.1.6 Interval C (2.53 – 0.13 ka)

This interval consists of about 35 meters and is characterized by a dominance of tintinnid remains varying mostly between 40 and 80%, while dinocysts are generally less than 40% (Fig. 4). However, dinocysts are relatively abundant here compared to the rest of the record, particularly at 1.7 ka, which results in a drop in the relative abundance of tintinnids to ~20%. The dinocyst assemblage is dominated by *S. antarctica* and to a lesser degree by *C. meridianum*, like interval H (Fig. 5). Characteristic for this interval is the occurrence of *E. sleipnerensis*, which is common in all samples and reaches its highest values in this interval. The tintinnid assemblage is dominated by *C. convallaria* and dictyocystid lorica sacs, with the latter generally less abundant than the former (Fig. 6). Peak abundances (up to 11% of the total amount of tintinnid remains) of Lorica type 1 are recorded in the top part of interval C. The relative abundance of leiospheres is relatively low but increases upcore to about 20% (Fig. 4). Also, there are some peak relative abundances of prasinophytes, noticeably of *Pterosperma parallelum* (up to 19%), which does not peak in any other interval (Fig. 4).

5.1.7 Interval B (0.13 – 0.03 ka)

Interval B consists of only one sample (1.9 – 1.92 mbsf), which was taken from a dark lamina. This interval is characterized by a relatively high abundance of tintinnid loricae (78%) (Fig. 4). The composition of the dinocyst is comparable to interval C, but with a relative increase of *G. microreticulatum*. *Polarella glacialis* makes its first appearance, where it reaches 4% abundance (Fig. 5). Within interval B the tintinnid species *L. naviculaefera*, *C. glacialis*, and *C. pusilla* reach peak abundances, which results in a relative decrease of dictyocystid lorica sacs and *C. convallaria* (Fig. 6). Within acritarchs *Mecsekia* cf. *Mecsekia* sp. A of Schrank (2003) reaches peak abundances (Fig. 4).

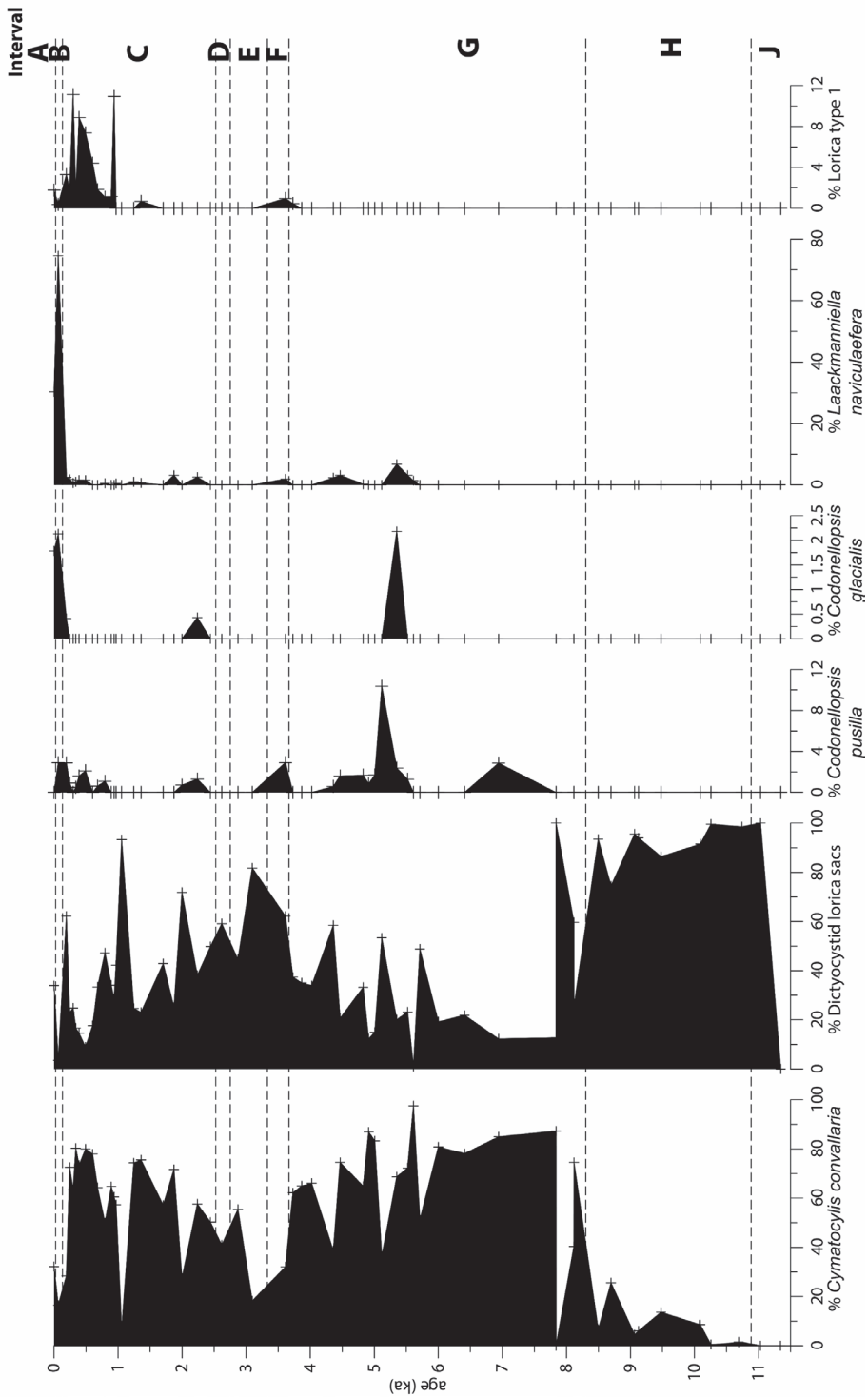


Figure 6: Relative abundances of tintinnid loricae. Percentages reflect the relative abundance of a species with respect to the total number of tintinnid loricae.

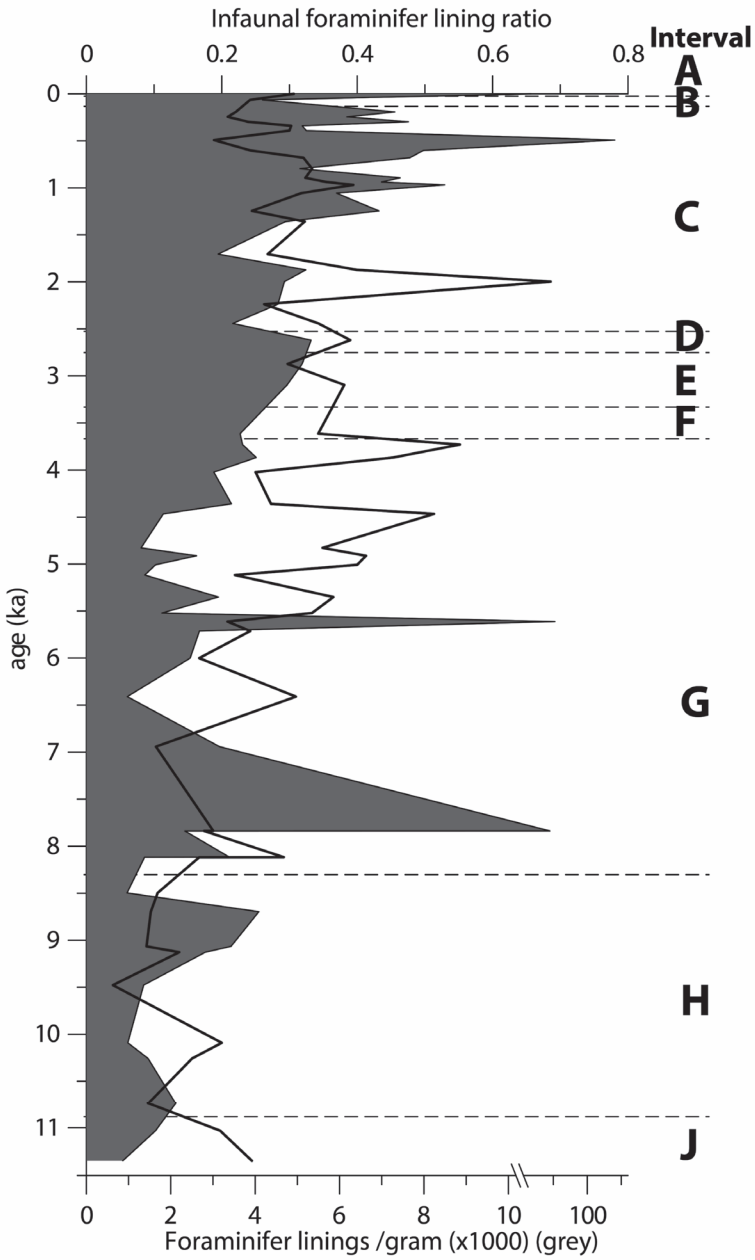


Figure 7: Total amount of foraminifer linings per gram sediment (grey) and the infaunal foraminifer lining ratio (black line).

5.1.8 Interval A (0.03 to present-day)

This interval, which is only the uppermost sample that is analyzed (0.11 – 0.13 mbsf), consists of the slurry representing modern sediment close to the sediment-water interface. Among the remains of planktonic organisms, tintinnid loricae, leiospheres and dinoflagellates contribute about equally (between 28 and 35%) to the palynological assemblage (Fig. 4). The dinocyst assemblage changes drastically compared to the sample below and is dominated by *G. microreticulatum*, *S. antarctica*, and *P. glacialis*, each comprising about 25% to the total dinocyst assemblage (Fig. 5). *P. glacialis* shows the highest abundances of the entire record. Within the tintinnid assemblage *C. convallaria*, *L. naviculaefera* and dictyocystid lorica sacs each comprise 30 to 33% (Fig. 6). *C. glacialis* is also still present.

5.1.9 Foraminifer linings

Both the amount of foraminifer linings per gram as well as the infaunal foraminifer lining (IFL) ratio show relatively low values in intervals H and J (Fig. 7). Within interval G the amount of foraminifer linings per gram is still relatively low except for two samples with very high palynomorph content in general (see Fig. 4). However, the IFL ratio increases upcore within interval G. In intervals A to F both the amount of foraminifer linings per gram as well as the IFL ratio are relatively high. In the upper part of interval C the highest amounts of foraminifer linings per gram are observed. The IFL ratio decreases slightly going upcore from interval C to A.

5.1.10 Copepod remains

The relative amount of copepod remains generally varies between 2 and 7% (Fig. 4). During intervals H and J, the relative abundance of copepod remains is relatively low (around or below 2%). Within interval G the relative abundance of copepod remains increases and reaches its maximum values between 8 and 5.5 ka. During the younger intervals the relative amount of copepod remains is at a constant 4%.

5.1.11 Other frequently observed palynomorphs and reworked material

The most frequently occurring acritarchs, for which it is uncertain whether they are derived from the surface waters and/or represent a single individual, are *Palaeostomocystis*, Type AB-2, Type AB-3, Type AB-4 and Type AB-13 (see **Chapter 2**). The relative abundances of these palynomorphs within the total palynological assemblage of Hole U1357B are presented in Fig. 8. *Palaeostomocystis sphaerica* sensu Warny (2009) is the most common species, showing relative abundances of around 2% throughout most of the core (Fig. 8). It shows highest relative abundances of almost 10% within interval J. However, it is nearly absent in interval H. Other species of

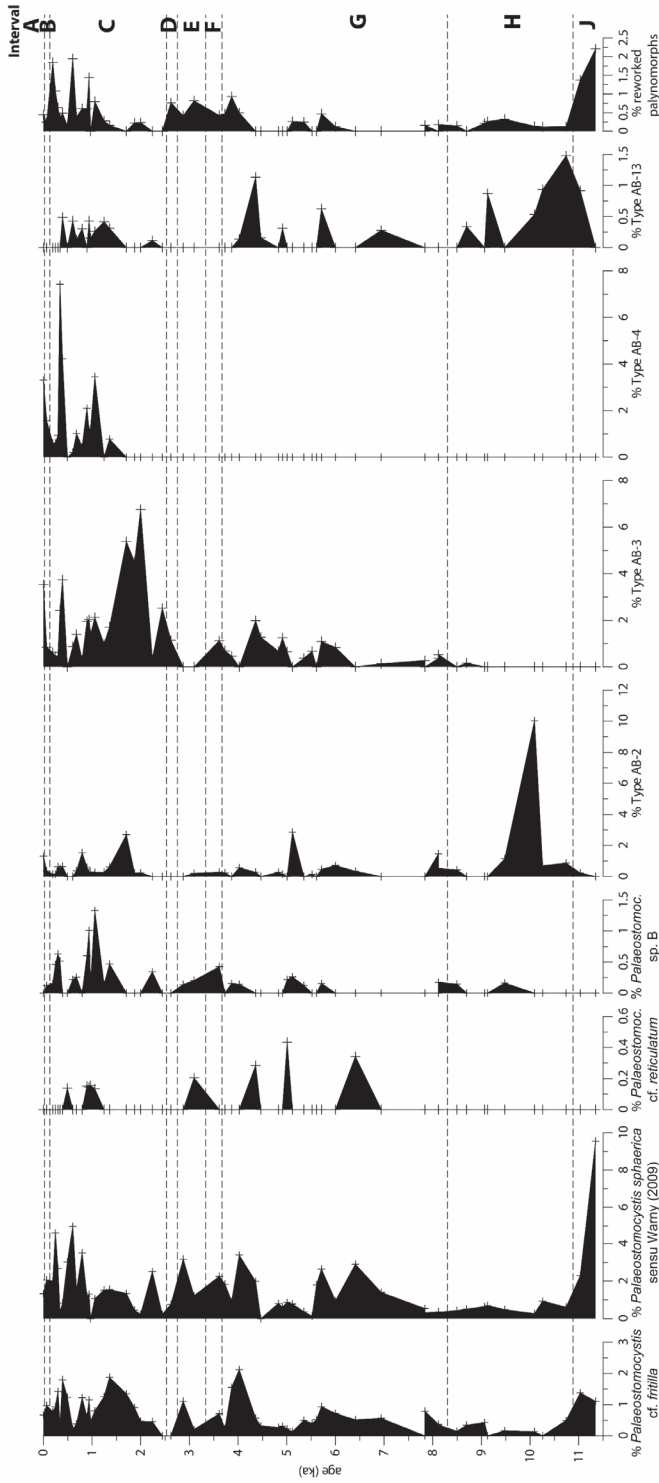


Figure 8: Relative abundances of acritarchs and palynomorphs of unknown origin (codes as in Chapter 2), and the relative abundance of reworked palynomorphs. Percentages reflect the relative abundance of a palynomorph with respect to the total number of palynomorphs.

Palaeostomocystis are even less common, although *Palaeostomocystis* cf. *fritilla* is present throughout the core with highest abundances in interval A to C, the upper part of interval G, and interval J. Among the nameless acritarchs Type AB-3 and AB-4 are particularly abundant within interval A and C, both reaching nearly 8% of the total palynomorph assemblage. Type AB-3 is most common in the lower part of interval C, while Type AB-4 is most common in the upper part of interval C. Type AB-2 and AB-13 show increased abundances in interval H, but are generally less common in intervals A to G. Within interval H, Type AB-2 even reaches relative abundances of more than 10% of all palynomorphs.

The reworked material includes pollen and spores, dinocysts of Paleogene age, and tardigrade eggs, which are likely derived from lichens or lakes on the Antarctic continent (see **Chapter 2**). Together they generally form less than 0.5% of the total palynomorph assemblage. Notably, however, both samples that comprise interval J have a reworked assemblage higher than 1% of the total palynomorphs assemblage. Peaks of nearly 2% reworked material are also present in the upper part of interval C. Furthermore, there are elevated amounts of reworked material (nearly 1%) in intervals D to F and the most upper part of interval G.

5.2 TEX₈₆ values and reconstructed subsurface temperatures

The TEX₈₆ values show a stable long-term trend with an average and standard deviation of 0.416 and 0.026, respectively. The highest TEX₈₆ value is at ~5.6 ka, where TEX₈₆ reaches a value of 0.49 (see Suppl. Table S1). TEX₈₆-based subTs generated by BAYSPAR show an average of 1.2±2.8°C (± 1 s.e.), which is higher than the modern-day average spring and summer temperatures of -1.7°C for 0–200 m depth (World Ocean Atlas data). The BAYSPAR reconstructed subT long-term trend is stable over time (Fig. 9A). However, the LOESS curve shows a long-term subT increase between 8.3 and 6.0 ka and a decrease between 6.0 and 3.6 ka. After 3.6 ka the long-term subT trend remains rather constant around 2°C. The short-term variability generally lies within a 2°C range but is higher in some parts of the record: around 1.8 ka, around 5.6 ka with a notable transient subT peak of 6.1°C, and from 10 ka to the end of the record.

Although the TEX₈₆ values obtained from dark and light lamina are not statistically different (F-test p-value = 0.33), the long-term trends reconstructed from the dark (summer) and light (spring) laminae are distinctly different (Fig. 9B). The long-term subT trend obtained from the dark (summer) laminae is at a constant value of 1.3°C, with the exception of the period between 7.0 and 5.0 ka where the long-term subT trend increases towards 2.1°C and then decreases back to 1.3°C. In contrast, the long-term subT trend obtained from the light (spring) laminae is much more variable. It shows an optimum of about 1.9°C around 6.0 ka, like the summer subT trend, but also shows optima of 2.1 and

1.7°C around 10.0 and 1.0 ka, respectively. The minima in the spring subT trend lie around 8.5 (0.8°C) and 2.8 ka (0.5°C). The general trend of subT reconstructed from both spring and summer laminae does show little change through time, because the summer subT trend is rather flat and therefore diminishes the spring subT fluctuations. Notably, minima in the subT reconstructions seem to co-occur with interval boundaries, particularly for the spring subT reconstruction. Minima in spring subT occur at the boundary between intervals C and D-E, and intervals G and H.

5.3 Variability analyzed by detrended correspondence analysis

The DCA analysis performed on the higher-order taxonomic plankton groups shows that samples derived from the light laminae and the dark laminae do not form separate clusters (Fig. 10A). The same holds true for the DCA analysis performed only on all known heterotrophic species (Fig. 10B), and the DCA analysis performed on all known autotrophic species (Fig. 10C).

Instead, samples belonging to the same interval, as determined by the constrained cluster analysis, form separate clusters in both the DCA analysis performed on the higher-order taxonomic groups (Fig. 10D) and the DCA analysis performed on all known heterotrophic species (Fig. 10E). When looking only at the larger intervals C, G and H in both figures, interval C and G plot separate from interval H.

Looking at the position of the DCA *species* in the DCA analysis performed on the higher-order taxonomic plankton groups (Fig. 10A, D), autotrophic species (leiospheres, prasinophytes and autotrophic dinoflagellates) and heterotrophic species (tintinnids and cysts derived from heterotrophic dinoflagellates) plot on opposite sides of diagonal Φ , which is the line where DCA axis-1 is equal to DCA axis-2. In Figure 10D, samples from intervals A, D, F and G plot above diagonal Φ , while most of the samples belong to the other intervals plot below.

Considering the DCA analysis performed only on the heterotrophic species (Fig. 10B, E), the cysts of heterotrophic dinoflagellates plot on the left side of the diagonal Φ , while tintinnids plot on the right side with the exception of Lorica type 1. In Figure 10E, samples from interval H and J plot above diagonal Φ , while samples from interval A and B and most samples from interval G plot below diagonal Φ . Samples from the other intervals plot mostly on diagonal Φ .

In the DCA analysis performed on all known autotrophic species (Fig. 10C, F) all *samples* cluster between *G. microreticulatum*, *Cymatiosphaera*-type prasinophytes and the two size classes of leiospheres, which are generally the most abundant. The other autotrophic species (*Impagidium pallidum*, *Polarella glacialis* and *Pterosperma*

parallellum) only occur in a few samples and are therefore positioned very distant from the samples.

Discussion

5.4 Comparison of the constructed subsurface temperature trends based on TEX₈₆ to other known records

Based on the relative abundances of *F. curta* and *F. kerguelensis* at site MD03-2601 it was established that the Neoglacial experienced ~1-2 °C cooler surface water temperatures in comparison to Hypsithermal 2 (Crosta et al., 2007). How the Neoglacial environmental conditions differ from the preceding Hypsithermal 2 is also evident on a seasonal scale (Denis et al., 2006), as spring laminae deposited during Neoglacial period are dominated by *F. curta*, while the spring laminae of Hypsithermal 2 are dominated by *Fragilariopsis rhombica* (Denis et al., 2006), which prefers slightly warmer temperatures (Armand et al., 2005). Although, the transition from the Hypsithermal 2 into the Neoglacial is rather sudden when considering the diatom record, it has been suggested that this sudden transition is the result of the crossing of an ecological threshold and that the actual temperature decline was much more gradual (Crosta et al., 2007). Between ~5.5 and 3.5 ka the reconstructed summer and spring subT values from Site U1357 show a gradual decline to resulting in about 1-2°C cooler for the Neoglacial in comparison to Hypsithermal 2 in good agreement with the diatoms.

Although the subT reconstruction based on TEX₈₆ obtained from the summer laminae only shows increased temperatures during Hypsithermal 2 (7.4 tot 4.5 ka), the subT reconstruction based on TEX₈₆ obtained from the spring laminae of Hole U1357B is much more dynamic. The spring subT trend also matches the other diatom-based climatic periods: the relatively warm Hypsithermal 1 and the relatively cool period between 8.4 and 7.4 ka (Crosta et al., 2008; Denis et al., 2009b). Furthermore, the good fit between the maxima and minima in this spring subT record and the palynology-based interval boundaries further supports that the reconstructed temperatures reflect a true climate signal. Noticeably, the reconstructed spring subT trend also matches the deuterium-based atmospheric temperature anomalies reconstructed from the Dome C ice core (Masson-Delmotte et al., 2004): a temperature optimum is located at 11 to 10 ka, a minimum is located at 8 ka, followed by a period of relatively stable warm temperatures between ~7 and ~4 ka, a temperature minimum at 2.5 ka and an optimum at 1.0 ka.

An explanation for the mismatch between the spring and summer subT trends could be that changes in the intensity of late summer storm activity and/or upwelling of MCDW has significantly influenced the summer subT record. For example, increased upwelling of warmer MCDW during a relatively cool period could have nullified the cooling

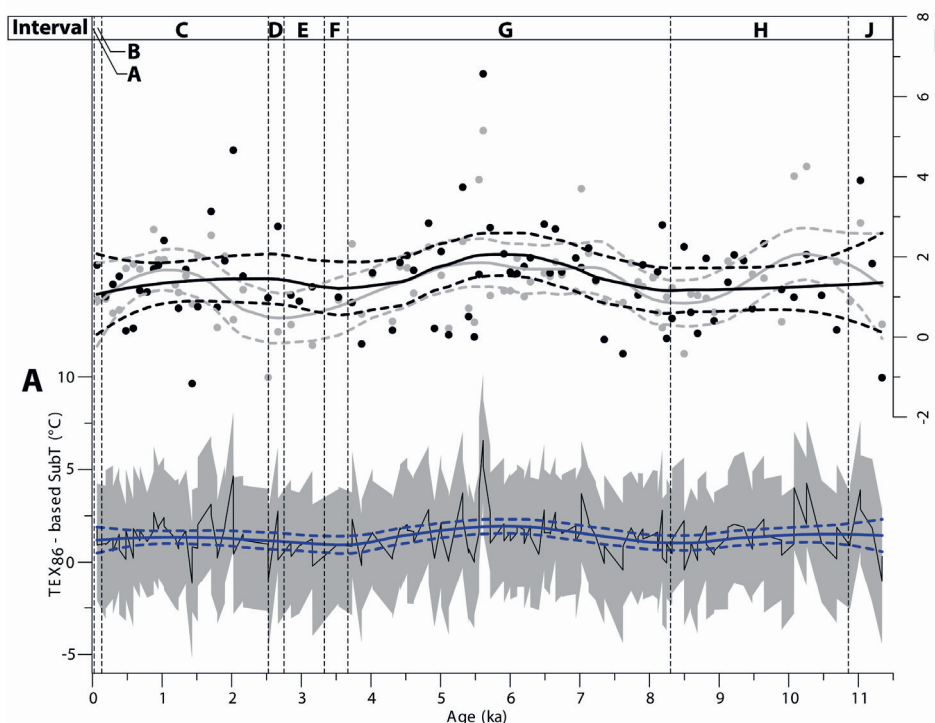


Figure 9: TEX_{86} -based subsurface temperatures with a thin black line (A) or black and grey dots (B) representing the original data and the thick lines representing the LOESS curves with 90% confidence intervals (dotted thick lines). A) TEX_{86} -based BAYSPAR subT reconstruction (black line) with 90% confidence interval (light grey area). B) TEX_{86} -based BAYSPAR subT values separated based on light (spring) laminations (plotted in grey) and dark (summer) laminations (plotted in black).

trend seen in spring during the summer, resulting in a minor or no change in the reconstructed summer subT record. Based on the diatom record from MD03-2601, this could be the case for the Neoglacial, where high relative abundances of *Proboscia spp.* suggest increased upwelling of MCDW (Fig. 2B.1) (Kim et al., 2012a).

So, although reconstructed subT lie about 2-3°C higher than modern-day average spring/summer temperatures between 0 and 200 m depth (World Ocean Atlas data), we are confident that the reconstructed LOESS-integrated temperature trends reflect the regional long-term Holocene seasonal surface water temperature trends.

5.5 Short- and long-term variability within the palynological record

The DCA analyses on the different groups of species (higher-order taxonomic plankton groups, heterotrophic species and autotrophic species) show that variability is

mostly determined by the relative amount of heterotrophic versus autotrophic species and/or the relative amount of (heterotrophic) dinocysts versus (heterotrophic) tintinnid loricae, independent from the type of lamina where the sample was taken from. Therefore, there is no significant difference between the palynological content of light versus dark colored laminae. This means that if each lamina represents a season, short-term (seasonal) variability is not directly reflected by the palynological content. Consequently, parts of the core in which relatively more samples are taken from dark (light) laminae, are therefore not significantly biased towards the summer (spring) season.

Instead, the intervals, as determined by the constrained cluster analysis, are reflected in the sample clustering in the DCA-analysis, meaning that most of the variability along the DCA axes 1 and 2 is the result of long-term variability.

5.6 Interpretation of the DCA analyses

In the DCA analysis performed on the higher-order taxonomic groups (Fig. 10A, D) the separation of autotrophic species above diagonal Φ and heterotrophic species below diagonal Φ can be interpreted in terms of primary productivity. In that case, samples from intervals A, D, F and G that contain relatively less heterotrophic species with respect to autotrophic species (plotting above diagonal Φ in Fig. 10D), can be interpreted as periods with relatively lower primary productivity. Intervals B, C, E and G would then be periods of relatively higher primary productivity. Notably, peak amounts of palynomorphs per gram sediment are recorded within intervals C and G.

The position of mostly dinocyst species above diagonal Φ and tintinnid species below diagonal Φ in the DCA analysis performed on the cysts derived from heterotrophic species (Fig. 10B, E) can have various reasons as dinoflagellates and tintinnids may depend on other types of available prey, water temperature and salinity. Whatever the determining paleoenvironmental factors are, this DCA analysis shows that the palynological content, and therefore also the paleoenvironmental conditions of intervals C and G are similar (showing overlap in Fig. 10D, E), while interval H differs from these intervals (forming a separate cluster in Fig. 10D, E). The similarity of intervals C and G is related to the dominance of *C. convallaria*, as is also obvious from Fig. 3. Apart from an environmental interpretation, the relative abundance of dinocysts versus tintinnid lorica can also be the result of a different sensitivity of the walls of the two groups of organisms to oxygen degradation. The proteinaceous tintinnid loricae degrade more easily than the organic wall of dinocysts (Agatha and Simon, 2012; Dolan et al., 2013a; Bogus et al., 2014), which is also the reason that tintinnid loricae are not commonly used for palaeoenvironmental reconstructions, while dinocysts are (see **Chapter 2**). A preservation bias in the palynological record can therefore not be excluded.

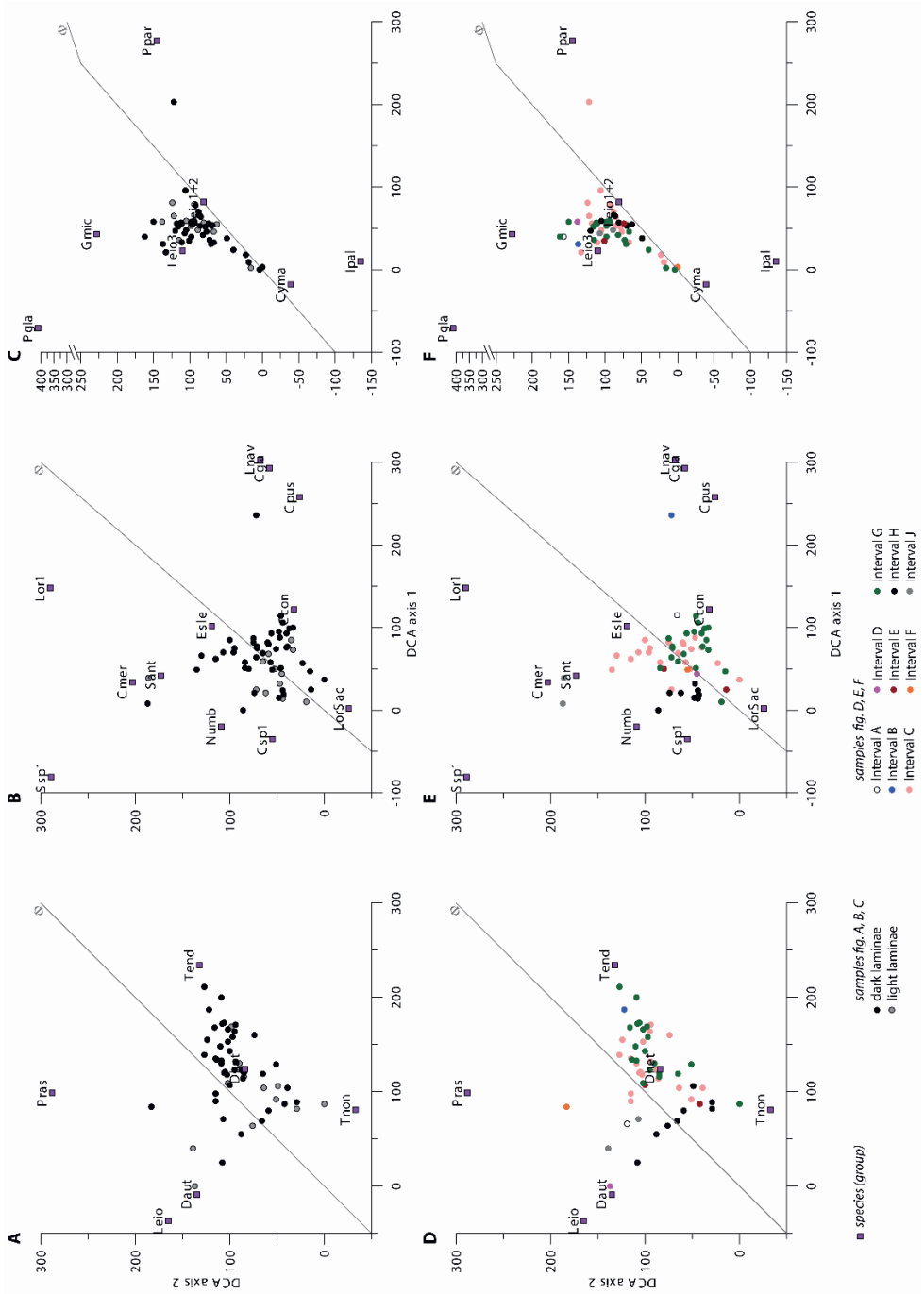


Figure 10 (previous page): DCA plots of the higher-order taxonomic groups (A and D), heterotrophs (B and E), and autotrophs (C and F) with colors representing dark/light laminae (A to C) and the intervals based on the cluster analysis (D to F). Acronyms: *Pras* = *Prasinophytes*, *Leio* = *Leiosphaerites*, *Daut* = autotrophic dinoflagellates, *Dhet* = heterotrophic dinoflagellates, *Tend* = endemic tintinnids, *Tnon* = non-endemic tintinnids, *Ssp1* = *Selenopemphix* sp. 1, *Sant* = *S. antarctica*, *Lor1* = *Lorica* type 1, *Cmer* = *C. meridianum*, *Csp1* = *Cryodinium* sp. 1, *Numb* = *N. umbiliphora*, *Eise* = *E. sleipnerensis*, *Con* = *C. convallaria*, *Lnav* = *L. naviculalefera*, *Cpus* = *C. pussilla*, *Cgla* = *C. glacialis*, *LorSac* = *dictyocystid lorica sacs*, *Gmic* = *G. microreticulatum*, *Pgla* = *P. glacialis*, *Ipal* = *I. pallidum*, *Leio1+2* = *Leiosphaeridia* sp. 1 and 2, *Leio3* = *Leiosphaeridia* sp. 3, *Cyma* = *Cymatiosphaera*-type phycoma, *Ppar* = *P. parallelum*-type phycoma

5.7 Preservation bias in the palynological record

The preservation potential for agglutinated and organic-walled tintinnids in general is quite low, as they are only seldom found in the fossil record while they can be found abundantly in surface sediments (Lipps et al., 2013). Records that contain tintinnid lorica generally do not consider individual taxa (Roncaglia, 2004a; Cromer et al., 2005). Even in anoxic bottom-waters where there is a greater potential of tintinnid preservation, fragmentation of the lorica during the lithification process also results in tintinnid loricae being rare in palynological records (Cromer et al., 2005). Notably, whole loricae are only seldom found within the samples of Hole U1357B. Likely, too small lorica pieces get lost during sieving when processing the palynological samples.

The size of the lorica and the wall texture (monolaminar versus trilaminar) could play a role in the resistance to lithification. This seems to be confirmed by the dominance of hyaline tintinnid *C. convallaria* in the tintinnid assemblage record of Hole U1357B versus *C. glacialis* and *L. naviculaefera*, which are particularly dominant in the upper two palynological samples (intervals A and B). All formae of *C. convallaria* are larger than *C. glacialis* and *L. naviculaefera*. In addition, *C. convallaria* has a trilaminar wall texture with thick inner and outer layers (in particular the posterior ends, which are used for counting in this study), while the wall textures of *Laackmanniella* and *Codonellopsis gaussi* (of which *C. glacialis* is possibly a junior synonym (Balech, 1958a, 1973; Alder, 1999) are monolaminar with alveoli (Wasik, 1998; Agatha et al., 2013). It seems plausible that a trilaminar wall texture would make a lorica much more resistant against lithification processes. Hence, the much lower abundances of monolaminar tintinnid species below ~2 mbsf. Notably, the tintinnid species with a monolaminar lorica wall (*C. glacialis* and *L. naviculaefera*) plot to the far right of the DCA plots in Fig. 10B and E, while *C. convallaria* with a trilaminar lorica wall plots to the left, closer to the more oxygen resistant dinocysts. The only other known tintinnid lorica that did preserve further down the record is the agglutinated lorica of *C. pusilla*. The wall texture of this species is not known, but under the light microscope it seems to have a thicker hyaline wall in comparison with the agglutinated loricae of *C. glacialis* and *L. naviculaefera*. This could make the lorica of *C. pusilla* more resistant to lithification processes. The same could be true for the dictyocystid lorica sacs and Lorica sp. 1. The continuous presence of particularly the lorica sacs does suggest that these have a high preservation potential. It is, however, unknown what the lorica sac is composed of. Lorica sp. 1 is an unknown species and its assignment to the Tintinnida is simply based on overall shape and the presence of a large oral opening. It could very well be that this palynomorph is not a tintinnid lorica and that it does not consist of crystalline proteins (Agatha et al., 2013), but of something more resistant.

Organic walls of dinocyst are hypothesized to be composed of resistant biopolymers (e.g. Bogus et al., 2012). Although these biopolymers are highly resistant to degradation, also given the fact that dinocysts are found in sediments as old as the late Triassic, there seems to be some variation in the structure between walls of proteroperidinioid cysts, generally produced by heterotrophic dinoflagellates, and gonyaulacoid cysts, generally produced by autotrophic dinoflagellates (Versteegh and Zonneveld, 2002; Bogus et al., 2014) and even within genera (Bogus et al., 2012, 2014). Given the fact that the dinocyst composition of the samples is dominated by proteroperidinioids, oxygen degradation likely did not strongly affect the dinocyst assemblage throughout the record. The only exception to this is the upper two samples of the palynological record, where cysts of *P. glacialis* have been found. The cyst of *P. glacialis*, found within the sea-ice (Montresor et al., 1999), has been rarely found in surface sediments and never below the upper few centimeters of sediment cores (Ichinomiya et al., 2008; Boere et al., 2009; Heikkilä et al., 2014). Although its small size (~ 12-17 microns) could be a reason that it passes through sieving during sample preparation when samples are sieved at 15 or 20 microns, it has also been suggested that the lack of resilient biopolymers in the cysts of *P. glacialis* is the reason for its absence in sediment cores (Montresor et al., 1999).

In conclusion, preservation of palynomorphs at Hole U1357B is very good, but even more exceptional in the upper 1,90 mbsf (intervals A and B), as is evident from the relatively high abundance of *P. glacialis*, *C. glacialis*, and *L. naviculaefera*. When interpreting intervals A and B in terms of environmental changes, this preservation bias should also be considered. Due to the low preservation potential of these three species, it is possible that these were lost from intervals C-J. There is no evidence that other species are significantly influenced by oxygen degradation throughout the record. These should therefore reflect primarily a palaeoenvironmental signal.

5.8 Regional environmental changes and palynological signature

Here, we compare our palynological and subT results with the previously published paleoenvironmental data from the region (Fig. 2). The goal here is to provide paleoenvironmental context to the shifts in species composition at Hole U1357B, as reflected in the intervals obtained by cluster analysis of the palynological record. A detailed paleoenvironmental reconstruction based on palynology alone would be difficult as ecological preferences of the various dinoflagellates and tintinnids is very limited (see **Chapter 2**). In general, most heterotrophic dinocyst species encountered in Hole U1357B have been reported as endemic to south of the Antarctic Polar Front (APF) and are indicative of high-productivity surface waters related to the seasonal waxing and waning of sea ice (**Chapter 2**, Zonneveld et al., 2013). Other species of dinocysts, such as cysts of

Gymnodinium and *Impagidinium pallidum*, but also prasinophytes and leiospheres have been associated with meltwater discharge and/or surface water stratification (Chapter 2; Mudie, 1992; Hannah, 2006; Warny et al., 2006; Ribeiro et al., 2016). Also the presence of the dinocyst *Islandinium minutum* in surface sediments has been correlated to overlying high-nutrient, low-salinity surface waters but seems to be present mainly in the southern Atlantic Ocean (Thöle et al., 2023) and has not been found at Site U1357. Tintinnid lorica have not been used in paleoenvironmental reconstructions on a species level before and dictyocystid lorica sacs have not been reported from other records. Therefore, we will describe the intervals and interval boundaries in relation to known paleoenvironmental data in a more general sense.

Confirmation that the palynological content of Hole U1357B indeed reflects the long-term environmental conditions in the Adélie Basin comes from the fact that the interval boundaries of intervals C to J occur on or close to the boundaries between the Hypsithermal and the Neoglacial periods in core MD03-2601 (Fig. 2B). In addition, minima in the reconstructed spring subT occur consistently at interval boundaries (Fig. 9). Furthermore, changes in the diene/triene ratio as well as the $\delta^2\text{H}$ of fatty acids obtained from Hole U1357B seem to be reflected in the palynology-based intervals of Hole U1357B (Fig. 2A). A more detailed comparison follows below. Unfortunately, we cannot compare the palynological content of U1357B between 0 and 1 ka to the environmental reconstructions from core MD03-2601, because this core does not contain samples younger than 1 ka.

5.8.1 Early Holocene / Hypsithermal 1 (intervals J and H)

Intervals J and H are considered together as a comparison of interval J to existing paleoenvironmental data is limited, because no data exists from core MD03-2601 prior to 11 ka. Interval J differs mostly from interval H by the (near) absence of tintinnid lorica (Fig. 4). Notably, it also contains the most reworked palynomorphs (Fig. 6). The fact that reworked palynomorphs are limited to interval J during the early Holocene is in line with the sedimentology at Site U1357. The relatively high terrigenous component, increased sorting of the terrigenous sediments and the lack of ice-rafted debris (IRD) between 11.4 and 11 ka at Site U1357 (Ashley et al., 2021) indicates some influence of local glacial meltwater input from local glaciers at the beginning of Hypsithermal 1. However, based on the sedimentology (higher IRD content) and geometry of the Adélie Drift, the grounding line retreat of local glaciers and their contribution as a meltwater source is much reduced when compared to the period prior to 11.4 ka (Ashley et al., 2021).

A grounding-line retreat and the associated southward migration of the sea-ice front in the Adélie Basin would have resulted in an increased meltwater flux to the Adélie

Basin. In general, both core MD03-2601 as well as Site U1357 show that the Adélie Basin was highly stratified due to meltwater. At Site U1357, this meltwater flux is evidenced by compound-specific hydrogen isotopes of fatty acids ($\delta^2\text{H}_{\text{FA}}$). Between 11.4 and 8 ka, the $\delta^2\text{H}_{\text{FA}}$ values indicate a large influx of Antarctic meltwater, as Antarctic glacial ice is highly depleted in ^2H compared to ocean water (Ashley et al., 2021). As the meltwater contribution from local glaciers is much reduced after 11.4 ka, it is hypothesized that during Hypsithermal 1 meltwater is likely increasingly derived from the east, i.e. the Ross Sea, via the Antarctic Coastal Current (Ashley et al., 2021). In addition, warmer conditions combined with fewer storms would result in earlier and more rapid sea-ice break-up leading to increased surface water stratification. At site MD03-2601, this has promoted *Chaetoceros* (*Hyalochaete*) blooms and subsequently the formation of resting spores when nutrient availability becomes limited, resulting in the deposition of relatively high amounts of *Chaetoceros* RS between 11 and 9 ka (Fig. 2B.6) (Denis et al., 2006; Crosta et al., 2008).

In our palynological data from Site U1357B, this high increased meltwater flux is during Hypsithermal 1 is reflected in the relatively high amounts (between 20 and 60%) of leiospheres in interval J and H in comparison to other intervals and the slightly elevated abundances of prasinophytes (~5%). Leiospheres and prasinophytes have been associated with low-salinity surface meltwater in both the Arctic and the Antarctic (Chapter 2; Mudie, 1992; Warny et al., 2006).

At site MD03-2601, Hypsithermal 1 is characterized by a decreasing trend of relative abundances of *F. curta* versus increasing relative abundances *F. kerguelensis*, indicating progressively ice-free surface waters (Fig. 2B.7) (Crosta et al., 2008; Denis et al., 2009a). The low sea-ice concentrations, especially with respect to the Neogene, is also evidenced by the low diene/triene ratio (di-unsaturated versus tri-unsaturated Highly-Branched Isoprenoids) at Site U1357 (Ashley et al., 2021). On the other hand, with respect to the mid-Holocene the relative abundance of diatom species that bloom in summer is relatively low at site MD03-2601 (Fig. 2B.4) (Denis et al., 2009b), suggesting that summers were not sea-ice free and relatively cold. With average temperatures of $1\pm 2.8^\circ\text{C}$, our TEX_{86} -based subT support relatively cold summers during interval H and J with respect to the mid-Holocene TEX_{86} -based subT of $\sim 2^\circ\text{C}$ (Fig. 9). Furthermore, spring sub-surface temperatures show a declining trend during interval H. In our palynological record, the transition from interval J to interval H is marked by a strong increase in tintinnid remains at the expense of the dinoflagellates (mostly *S. antarctica*) and leiospheres. At species level the tintinnid assemblage of interval H is dominated (nearly 100%) by the dictyocystid lorica sacs, suggesting that the tintinnid species that produce these lorica sacs are truly endemic to the Antarctic, cold, sea-ice covered, low-salinity surface waters in comparison to other tintinnid remains.

At site MD03-2601, reconstructions based on C_{org} , N_{org} and BSi fluxes indicate low paleoproductivity and/or burial of organic matter during Hypsithermal 1 (Denis et al., 2009b). Based on these proxies, only a short period between approximately 10.5 and 10 ka has been identified as a period of increased biological pump activity and nutrient supply through deep water mixing (Fig. 2B.5, PE1 in (Denis et al., 2009b)). Peak abundances of the dinoflagellates *Selenopemphix* sp. 1 and *I. pallidum* around this period of increased nutrient supply, which may suggest a preference to these conditions. For *I. pallidum* this is in line with its bipolar distribution in regions with high-nutrient-low-chlorophyll surface waters with seasonally reduced salinities and sea-ice cover (Zonneveld et al., 2013). As an autotrophic species, *I. pallidum* may have profited directly from the increased nutrient supply around 10 ka. Instead the heterotrophic *Selenopemphix* sp. 1, which has been suggested to be a larger species end member of *S. antarctica* (Esper and Zonneveld, 2007), would have profited from the increased productivity of diatoms, such as *Chaetoceros Hyalochaete*. Still, as we compare cores from two different sites although in the proximity of each other, conclusions need to be drawn carefully.

Export productivity at Site U1357 seems to have been relatively low, based on the number of foraminifers per gram sediment as well as the relatively low amount of infaunal versus epifaunal foraminifer linings (IFL ratio) in interval J and H. The foraminiferal remains do not show any indication of increased export productivity around 10.5 ka. A low export productivity in a polynya environment is, however, consistent with observations in the Amundsen Sea Polynya where despite high productivity in the surface waters, intrusion of Circumpolar Deep Water (CDW) prevents sequestration of carbon at the seafloor (Lee et al., 2017).

5.8.2 Middle Holocene / Hypsithermal 2 (interval G)

Based on our palynological and subT data, this interval has relatively high abundances of the tintinnid *C. convallaria* and relatively warm spring and summer subsurface temperatures of $\sim 2^{\circ}\text{C}$ (Fig. 9). The warmer subsurface temperatures are in line with summers becoming more ice-free (Fig. 2B.4) and lower sea-ice concentrations in general (Fig. 2B.7), as is suggested based on the diatom assemblages of MD03-2601 (Crosta et al., 2007). Furthermore, following Hypsithermal 1, the long-term decreasing amounts of *Chaetoceros* RS at site MD03-2601 suggest increasingly less stable surface waters and lower primary productivity during spring (Fig. 2B.6) (Crosta et al., 2005a, 2008). At Site U1357, $\delta^2\text{H}_{\text{FA}}$ is generally higher during Hypsithermal 2 than during Hypsithermal 1 in line with a reduced influx of low-salinity meltwater. However, the period between 6 and 4.5 ka is characterized by a negative $\delta^2\text{H}_{\text{FA}}$ excursion (Fig. 2A), which is interpreted as

enhanced glacial meltwater flux to the site, related to the final retreat of the ice-sheet grounding line in the Ross Sea (Ashley et al., 2021).

While spring productivity decreases, summer productivity increases as summers become more ice-free, which results in a higher relative nutrient utilization (Fig. 2B.2). Short periods of decreased nutrient utilization are generally linked to increased nutrient supply due to surface water mixing, MCDW upwelling and increased biological pump activity (Fig 2B, around 7.3, 6.0 and 5.0 ka) (Denis et al., 2009b).

Heterotrophic species that are relatively more abundant in interval G of our palynological record, such as the tintinnid *C. convallaria* and the dinocyst *C. meridianum*, seem to profit from the increased summer productivity. Considering *C. meridianum* is considered endemic to the Antarctic Circumpolar Current south of the Antarctic Polar Front (Zonneveld et al., 2013), it is not a typical species for the Antarctic margin. Notably, *C. meridianum* is particularly abundant at Site U1357 during the transition from interval H to interval G, which is identified as a relatively cool period prior to Hypsithermal 2 based on equal amounts of *F. curta* and *F. kerguelensis* (Fig. 2B.7) (Crosta et al., 2008). In support of this, the TEX₈₆-based subT record of U1357B shows lower spring temperatures during this time interval. This suggests that these cooler spring temperatures, but ice-free summers are surface water conditions that promote *C. meridianum* or rather promote the autotrophic species that *C. meridianum* feeds on. When the relative abundances of *C. meridianum* decline at the onset of Hypsithermal 2 with surface water conditions becoming warmer and more ice-free, the dinoflagellate assemblage is dominated again by *S. antarctica* similar as during Hypsithermal 1.

The increased summer production during Hypsithermal 2 is considered to be mainly responsible for the increased export of organic matter to the seafloor (Denis et al., 2009b). However, at Site U1357, export productivity remains relatively low at the beginning of interval G, based on the IFL ratio. Instead, copepod remains are particularly abundant between 8 and 5.5 ka (Fig. 4), suggesting that the high productivity in the surface waters due to lower sea-ice concentrations has been beneficial for zooplankton. This is consistent with observations of zooplankton abundance, primary productivity and sea ice concentrations in the Amundsen Sea polynya in relation to SAM (La et al., 2019). Scavenging by zooplankton may have prohibited export of carbon to the seafloor in addition to intrusion of CDW (Lee et al., 2017). Kim et al. (2012) have suggested that high relative abundances of *Proboscia* spp. correspond to increased upwelling of modified CDW at site MD03-2601. Notably, the IFL ratio increases towards the end of interval G with highest values between 5.0 and 4.0 ka when also the influence of modified CDW at site MD03-2601 diminishes. In addition, highest primary productivity and biological pump activity based on N_{org}, C_{org} and BSI is observed around 5.0 ka in core MD03-2601. Increased

productivity and reduced influence of CDW could explain the increased export productivity at Site U1357.

5.8.3 Late Holocene / Neoglacial (upper part of interval G to interval C)

The onset of the Neoglacial period at 4.5 ka in Hole U1357B is marked by an increase in the relative abundances of di-unsaturated versus tri-unsaturated Highly-Branched Isoprenoids (diene/triene ratio in Fig. 2A), relatively higher $\delta^2\text{H}_{\text{FA}}$ and a peak in the Ba/Ti ratio (Ashley et al., 2021). These proxies suggest denser sea-ice cover, an increased influx of meltwater and increased primary productivity, potentially driven by meltwater-induced stratification. At site MD03-2601 diatoms suggest Neoglacial surface water conditions are cooler with higher concentrations of sea ice in spring (high concentrations of *F. curta* versus *F. kerguelensis*). It has been recently proposed that the Neoglacial cooling and sea-ice expansion is the result of the formation of a cool, freshwater mass formed on the continental shelf in the ice shelf cavities of large glaciers, such as the Ross Sea Ice Shelf (Ashley et al., 2021). The formation of such a cool water mass feeding into the Antarctic Surface Waters is only possible once the ice shelf cavities become sufficiently large due to grounding-line retreat, such that intrusion of warmer CDW onto the continental shelf is prevented (Ashley et al., 2021). Furthermore, diatoms at site MD03-2601 suggest relatively warmer and stormier conditions during the summer/autumn months from 4.5 ka onwards (lower concentrations of *Thalassiosira antarctica* and higher concentrations of setae diatoms), which would have resulted in increased mixing (Fig. 2B.3) and high nutrient supply to the surface waters (Fig. 2B.2) (Denis et al., 2009b).

Cluster analysis of the palynological record of Hole U1357B did not result in the placement of an interval boundary at the onset of the Neoglacial. Instead, the boundary between intervals G and F is at 3.5 ka and thus follows 1 kyr after the onset of the Neoglacial. The period between 4.5 and 3.5 ka does, however, show increasing relative abundances of leiospheres, which has been associated with increased meltwater influx. Among the dinocysts, the Neoglacial period can be distinguished by the near continuous presence of *E. sleipnerensis*. The relative abundance of this species starts increasing prior to the interval boundary of intervals G and F. In addition, the dinocyst *N. umbiliphora* starts appearing just prior to this interval boundary. It seems therefore that these species are indicative of the denser sea ice cover and/or increased late summer mixing and nutrient availability of the Neoglacial period, as their prey might have become more available. Notably, a recent study shows that spiny dinocysts such as *E. sleipnerensis* and the very similar *Islandinium* spp. show a preference for low-salinity surface waters around Antarctica (Thöle et al., 2023). Among the tintinnids, the dyctiocystid lorica sacs start

increasing around 4.5 ka, and is generally more abundant during the Neoglacial than during Hypsithermal 2, but not as dominant as during Hypsithermal 1. The presence of these lorica sacs during the Neoglacial as well as Hypsithermal 1, supports a preference of the tintinnid species that makes these lorica sacs, to the cooler, low-salinity waters and denser sea-ice cover of the Neoglacial.

Between 3.5 and 2.5 ka the palynological record is divided into multiple intervals that consist of only one or a few samples (intervals D, E and F). This part of the palynological record, and intervals D and F in particular, is dominated by peaks of leiospheres, *Pterosperma*, and *Gymnodinium*. Therefore, it seems that environmental conditions during this period promoted blooms of autotrophic species, while the rest of the Neoglacial period is dominated by heterotrophic species. Based on the increasing $\delta^2\text{H}_{\text{FA}}$ during this period the influx of meltwater to Site U1357 was much reduced (Ashley et al., 2021). This has been linked to the grounding line of the Ross Sea glaciers reaching their modern-day location by ~ 3.5 ka (Ashley et al., 2021). In addition, the spring cooling during the Neoglacial may have limited meltwater release and therefore surface water stratification (Crosta et al., 2008). However, increased *Chaetoceros* RS (Fig. 2B.6) and decreased setae diatoms (Fig. 2B.3) at site MD03-2601 suggest a period of increased stratification in spring and reduced mixing around 3.0 ka, which would suggest a short period of increased meltwater flux to the Adélie Coast. This short period of increased meltwater influx is not visible in the LOESS regression curve of the $\delta^2\text{H}_{\text{FA}}$ record of U1357 due to the relatively low resolution, but individual datapoints of the $\delta^2\text{H}_{\text{FA}}$ record in intervals E and F are relatively low (Fig. 2A), suggesting there may be some meltwater signal there. Nevertheless, this increased meltwater flux seems to be recorded in the palynological record as blooms of prasinophytes, leiospheres and *G. microreticulatum*, which all have been associated with low salinity surface waters and stratification (**Chapter 2**; Mudie et al., 2002). Based on the diene/triene ratio of Site U1357, the prasinophytes (Fig. 4) seem to prefer the sudden reduction in coastal sea ice during interval F (Fig. 2A), while the peaks of leiospheres (Fig. 4) and *G. microreticulatum* (Fig. 5) coincide with peak coastal sea-ice concentrations during interval D (Fig. 2A). Furthermore, the highest relative abundance of dictyocystid lorica sacs in interval E (Fig. 6) supports the hypothesis that this palynomorph is a good indicator of surface water stratification. In contrast, *E. sleipnerensis*, which was more abundant at the onset of the Neoglacial has disappeared during this interval, even though other spiny brown dinocysts, such as *I. minutum* have been associated with low-salinity surface waters (Thöle et al., 2023). As surface water mixing was somewhat diminished during this interval, it is possible *E. sleipnerensis* and/or its prey prefer the higher nutrient conditions resulting from mixing of the surface waters.

As discussed earlier, the reconstructed subT values from Site U1357 are also about 1°C cooler for the Neoglacial in comparison to Hypsithermal 2 in agreement with the diatom-based temperature reconstructions. During intervals D, E and F, spring temperatures even drop by 2°C to values of around 0.5°C, which might be related to the presence of a cool meltwater lens during this period.

Interval C is characterized by a notable increase of the relative abundance of the dinocyst *E. sleipnerensis*, in line with the decreased $\delta^{15}\text{N}_{\text{bulk}}$ and increased abundance of setae diatoms at site MD03-2601, indicating increased nutrient availability (Fig. 2B.2) through mixing (Fig. 2B.3) (Denis et al., 2009b). Although its biological origin is unknown, highest relative abundances of AB-3 and AB-4 within interval C, while their abundances are much lower or absent during the preceding intervals, suggests the producers of these palynomorphs also respond well to the increased availability of nutrients (Fig. 8). The resulting increase in primary productivity is supported by increased biological pump activity (Fig. 2B.5) in this period (Denis et al., 2009b). At Site U1357 it seems that export productivity based on the IFL-ratio has remained relatively high since the onset of the Neoglacial, but shows a slight decline towards present-day (Fig. 7). Increased relative abundances of *Proboscia* spp. at site MD03-2601 would suggest an increased influence of modified CDW at the study site (Kim et al., 2012a), reducing export productivity (Lee et al., 2017). However, nearer to the Antarctic coast at Site U1357 it is possible that higher sea-ice concentrations have promoted deep-water formation over Site U1357 thereby reducing the intrusion of CDW, and thus allowing more carbon sequestration and burial at the seafloor than expected based on the abundances of *Proboscia* spp. at site MD03-2601.

As discussed, intervals A and B are characterized by palynomorphs that do not easily preserve. Apart from these easily degradable palynomorphs, the two samples that make up this part of the record do not show a significant difference with interval C.

6 Conclusions

Based on the above we show that palynology can be a valuable tool in reconstructing Holocene surface water conditions around Antarctica. With the cluster analysis performed on the surface water dwelling palynological species, interval boundaries based on faunal turn-over events were established that seem to fit to known climatic shifts and local environmental changes. Nevertheless, a preservation bias should always be considered, as demonstrated by the less oxygen-resistant monolaminar tintinnid loricae and the dinocyst *Polarella glacialis*. The transition from the early Holocene to a warmer mid-Holocene with lower sea-ice concentrations matches the boundary between intervals H and G. The transition from the mid-Holocene to the late Holocene is not marked by an interval boundary, although increases in the dinocyst species *E. sleipnerensis*

and *N. umbiliphora* could be indicative of the onset of the late Holocene. Instead, faunal turn-over events as marked by the interval boundaries between intervals G to C occur around 3.0 ka and are characterized by a decrease in meltwater flux to the site and increased surface water mixing and nutrient availability, leading to increased biological pump activity.

With this study we have gained a better understanding of the relation between environmental conditions in the surface water and the presence of certain palynomorphs in the sediments. Although additional studies at other sites around Antarctica are needed to confirm these relationships, we have established the following:

- A relation between the presence of leiospheres, prasinophytes, *Gymnodinium microreticulatum* and an increased meltwater flux and stratification, as suggested in previous studies, seems to be confirmed.
- A relation between the presence of dictyocystid lorica sacs and cold, low-salinity surface water conditions and relatively high sea-ice concentrations is established. The dinocysts *Echinidinium sleipnerensis* and *Nucicla umbiliphora* also seem to prefer these conditions but rely on increased nutrient availability due to late summer mixing too.
- Ice-free summers promote *Cymatocylis convallaria* and *Cryodinium meridianum*, the latter showing an additional preference to cool springs.
- There seems to be a relation between the dinocysts *Selenopemphix* sp. 1 and *Impagidinium pallidum* and nutrient-rich, low-salinity surface waters.
- Zooplankton remains are most abundant when sea-ice concentrations are relatively low and (summer) primary productivity is high.
- Considering the acritarchs with unknown biological origin, it seems that mainly AB-3 and AB-4 show a strong response to the increased sea-ice concentrations and increased nutrient availability of the late Holocene.

Furthermore, we have introduced a proxy for export productivity based on the ratio of infaunal versus epifaunal foraminifer linings. Although further testing of this proxy is necessary to establish its use, the reconstructed export productivity at Site U1357 seems limited during the mid- and late Holocene (lower part of interval G to interval J), while the relatively higher amounts of heterotrophic species in intervals C and G suggest that these periods experienced highest primary productivity (in accordance with highest biological pump activity reconstructed for site MD03-2601). Possibly, export productivity was influenced by the intrusion of (Modified) Circumpolar Deep Water, limiting carbon sequestration and burial at the study site during interval G.

Lastly, we have established that TEX₈₆-based summer and spring subsurface temperatures do not follow the same long-term trend. Specifically, the spring temperature trend shows a strong relation to faunal turn-over events indicated by the interval boundaries that were established by cluster analysis.

Altogether, future changes in surface water temperature, meltwater flux from the Antarctic mainland and sea-ice concentrations will have implications for marine ecosystems around Antarctica, including primary and secondary producers, zooplankton and bottom-dwelling organisms.

Supplementary information of chapter 4

Appendix A: List of taxa

Dinocysts (in situ)

Gymnodinium microreticulatum

Selenopemphix antarctica

Selenopemphix sp. 1 *sensu* Esper & Zonneveld (2007)

Cryodinium meridianum

Cryodinium sp. 1 *sensu* Hartman et al. (2018a)

Polarella glacialis

Echinidinium sleipnerensis

Impagidinium pallidum

Nucicla umbiliphora

Dinocysts (reworked)

Vozzhenikovia apertura

Vozzhenikovia netrona

Eneadocysta dictyostila

Spinidinium colemani

Tintinnids

Remains of dictyocystid lorica sacs

Codonellopsis pussilla

Codonellopsis glacialis

Cymatocylis convallaria (-*affinis*)

Laackmanniela naviculaefera

Lorica type 1 *sensu* Hartman et al. (2018a)

Prasinophytes

Cymatiosphaera-type phycoma of:

Pterosperma cristatum

Pterosperma marginatum

Pterosperma polygonum

Pterosperma reticulatum

Cymatiosphaera sp. 1 *sensu* Hartman et al. (2018a)

Pterosperma parallelum-type phycoma of:

Pterosperma parallelum

Pterosperma cf. *parallelum sensu* Hartman et al. (2018a)

Acritarchs

Leiosphaeridia spp. (sp. 1, 2 and 3 *sensu* Hartman et al. 2018a)

Mecsekia cf. *Mecsekia* sp. A *sensu* Schrank (2003)

Palaeostomocystis cf. *fritilla*

Palaeostomocystis cf. *reticulata*

Palaeostomocystis sphaerica sensu Warny (2009)

Palaeostomocystis sp. B *sensu* Hartman et al. (2018a)

Appendix B: TEX₈₆ data

EXP	SITE	HOLE	CORE	SECTION	upper interval	lower interval	upper depth (mbsf)	lower depth (mbsf)	average depth (mbsf)	Age (yr BP)	GDGT-0	GDGT-1	GDGT-2	GDGT-3	Crenarchaeol	Crenarchaeol regio-isomer	GDGT-I	GDGT-II	GDGT-III
318	U1357	B	1	H	2	W	40	42	1.9	1.92	65.3	2.18E+07	6.37E+05	2.20E+05	1.34E+05	1.58E+07	1.30E+04	1.76E+04	1.86E+04
318	U1357	B	1	H	2	W	42	44	1.92	1.94	66.5	5.63E+06	1.60E+05	5.24E+04	3.32E+04	4.01E+06	4.63E+03	5.54E+03	5.94E+03
318	U1357	B	1	H	2	W	4	6	4.04	4.06	191.4	1.28E+07	3.62E+05	1.16E+05	6.97E+04	9.99E+06	2.57E+04	1.64E+04	1.62E+04
318	U1357	B	2	H	3	W	6	8	4.06	4.08	192.5	1.19E+07	2.94E+05	1.01E+05	6.45E+04	9.23E+06	4.45E+04	8.75E+03	1.10E+04
318	U1357	B	2	H	3	W	72	74	6.22	6.24	297.9	2.66E+07	7.27E+05	2.46E+05	1.53E+05	2.17E+07	1.33E+05	2.69E+04	3.16E+04
318	U1357	B	2	H	3	W	74	76	6.24	6.26	298.9	1.66E+07	5.04E+05	1.63E+05	9.39E+04	1.28E+07	8.59E+04	1.63E+04	1.80E+04
318	U1357	B	2	H	4	W	111	113	8.11	8.13	391.1	5.07E+06	1.49E+05	4.89E+04	2.96E+04	3.70E+06	3.14E+04	6.70E+03	7.39E+03
318	U1357	B	2	H	4	W	113	115	8.13	8.15	392.2	4.20E+06	1.42E+05	4.64E+04	2.79E+04	3.01E+06	2.54E+04	5.09E+03	5.52E+03
318	U1357	B	2	H	6	W	6	8	10.06	10.08	10.07	1.18E+07	3.39E+05	1.06E+05	6.24E+04	9.08E+06	5.29E+04	1.35E+04	1.48E+04
318	U1357	B	2	H	6	W	8	10	10.08	10.1	10.09	4.92E+06	2.10E+05	9.74E+04	6.26E+04	8.09E+06	4.82E+04	1.05E+04	9.68E+03
318	U1357	B	2	H	CC	W	0	2	12.05	12.07	12.06	6.02E+06	1.99E+07	5.24E+05	1.72E+05	1.05E+05	1.57E+07	6.35E+04	2.04E+04
318	U1357	B	2	H	CC	W	4	4	12.07	12.09	12.08	6.03E+06	1.88E+07	4.47E+05	1.70E+05	1.08E+05	1.39E+07	7.94E+04	1.35E+04
318	U1357	B	3	H	5	W	97	99	12.97	12.99	12.98	6.79E+06	2.45E+07	6.55E+05	2.18E+05	1.34E+05	1.86E+07	1.19E+05	1.78E+04
318	U1357	B	3	H	5	W	99	101	12.99	13.01	13	6.81E+06	2.05E+07	5.91E+05	2.03E+05	1.21E+05	1.57E+07	1.04E+05	1.35E+04
318	U1357	B	3	H	3	W	8	10	15.08	15.1	15.09	7.95E+06	3.80E+07	1.08E+06	3.38E+05	1.95E+05	2.84E+07	2.21E+05	2.82E+04
318	U1357	B	3	H	4	W	70	72	17.2	17.22	17.21	8.93E+06	3.26E+07	8.54E+05	2.85E+05	1.89E+05	2.74E+07	1.57E+05	2.70E+04
318	U1357	B	3	H	4	W	72	74	17.22	17.24	17.23	8.94E+06	2.08E+07	4.99E+05	1.80E+05	1.17E+05	1.57E+07	1.01E+05	2.07E+04
318	U1357	B	3	H	5	W	97	99	18.97	18.99	18.98	9.68E+06	2.74E+07	7.20E+05	2.31E+05	1.53E+05	2.24E+07	1.42E+05	2.86E+04
318	U1357	B	3	H	5	W	99	101	18.99	19.01	19	9.69E+06	1.76E+07	4.56E+05	1.57E+05	1.03E+05	1.40E+07	8.12E+04	1.56E+04
318	U1357	B	3	H	7	W	8	10	21.08	21.1	21.09	1.05E+07	4.48E+07	1.18E+06	3.69E+05	2.41E+05	3.92E+07	2.68E+05	4.68E+04
318	U1357	B	3	H	7	W	10	12	21.1	21.12	21.11	1.05E+07	1.92E+07	5.36E+05	1.74E+05	1.11E+05	1.65E+07	1.03E+05	2.86E+04
318	U1357	B	4	H	2	W	95	97	23.95	23.97	23.96	1.19E+07	5.17E+05	1.61E+05	1.00E+05	1.39E+07	1.07E+05	2.80E+04	
318	U1357	B	4	H	3	W	61	63	25.11	25.13	25.12	1.24E+07	2.95E+07	7.78E+05	2.58E+05	1.69E+05	2.38E+07	1.10E+05	4.40E+04
318	U1357	B	4	H	3	W	63	64	25.13	25.14	25.13	1.24E+07	1.03E+07	2.64E+05	8.95E+04	5.89E+04	7.97E+06	3.45E+04	1.47E+04
318	U1357	B	4	H	4	W	118	120	27.18	27.2	27.19	1.35E+07	2.60E+07	6.94E+05	2.33E+05	1.47E+05	2.23E+07	1.39E+05	4.80E+04
318	U1357	B	4	H	4	W	120	122	27.2	27.22	27.21	1.35E+07	2.48E+07	7.34E+05	2.30E+05	1.47E+05	1.93E+07	1.65E+05	4.02E+04
318	U1357	B	4	H	6	W	17	19	29.17	29.19	29.18	1.45E+07	2.97E+07	8.96E+05	2.79E+05	1.71E+05	2.30E+07	9.39E+04	4.35E+04
318	U1357	B	4	H	6	W	19	21	29.19	29.21	29.2	1.45E+07	5.87E+06	1.71E+05	5.31E+04	3.47E+04	4.41E+06	3.32E+04	8.71E+03
318	U1357	B	4	H	7	W	37	39	30.87	30.88	30.88	1.55E+04	4.43E+07	1.33E+06	4.26E+05	2.57E+05	3.32E+07	2.19E+05	3.83E+04
318	U1357	B	4	H	7	W	39	41	30.89	30.91	30.9	1.55E+04	1.88E+07	5.00E+05	1.65E+05	1.00E+05	1.38E+07	1.13E+05	1.86E+04
318	U1357	B	5	H	1	W	122	124	32.22	32.24	32.23	1.70E+07	7.43E+06	1.92E+05	6.32E+04	4.63E+04	5.97E+06	4.42E+04	1.55E+04
318	U1357	B	5	H	1	W	124	126	32.24	32.26	32.25	1.70E+07	7.79E+06	2.28E+05	7.61E+04	4.92E+04	5.70E+06	4.50E+04	1.47E+04
318	U1357	B	5	H	3	W	6	8	34.06	34.08	34.07	1.80E+07	1.55E+08	4.22E+06	1.30E+06	8.64E+05	1.32E+08	7.68E+05	2.55E+05
318	U1357	B	5	H	3	W	8	10	34.08	34.1	34.09	1.80E+07	1.40E+07	3.80E+05	1.30E+05	8.44E+04	1.03E+07	1.60E+04	1.50E+04
318	U1357	B	5	H	4	W	52	54	36.02	36.04	36.03	1.92E+07	4.66E+07	1.14E+06	3.85E+05	2.35E+05	3.80E+07	2.34E+05	6.39E+04
318	U1357	B	5	H	4	W	54	56	36.04	36.06	36.05	1.92E+07	2.22E+07	6.06E+05	1.94E+05	1.28E+05	1.70E+07	1.31E+05	3.42E+04
318	U1357	B	5	H	5	W	114	116	38.14	38.16	38.15	2.06E+07	2.44E+07	6.68E+05	2.18E+05	1.40E+05	2.06E+07	2.25E+05	6.28E+04
318	U1357	B	5	H	5	W	116	118	38.16	38.18	38.17	2.06E+07	1.57E+07	4.70E+05	1.45E+05	8.87E+04	1.26E+07	7.88E+04	2.72E+04
318	U1357	B	5	H	7	W	5	7	40.05	40.07	40.06	2.23E+07	5.43E+06	1.55E+06	4.77E+05	2.88E+05	3.18E+05	1.10E+05	1.28E+05
318	U1357	B	5	H	7	W	7	9	40.07	40.09	40.08	2.23E+07	1.98E+06	2.71E+05	8.50E+04	5.33E+04	7.87E+06	1.90E+04	1.88E+04
318	U1357	B	6	H	2	W	15	17	42.15	42.17	42.16	2.52E+07	3.32E+07	9.70E+05	3.18E+05	1.93E+05	2.52E+07	1.64E+05	4.10E+04
318	U1357	B	6	H	2	W	17	19	42.17	42.19	42.18	2.52E+07	4.98E+06	1.59E+05	4.87E+04	2.91E+04	3.57E+06	1.83E+04	7.93E+03
318	U1357	B	6	H	3	W	44	45	43.94	43.95	43.94	2.67E+07	1.39E+07	4.12E+05	1.36E+05	7.88E+04	1.17E+07	1.08E+05	2.41E+04
318	U1357	B	6	H	3	W	45	46	43.95	43.96	43.95	2.67E+07	9.91E+06	2.92E+05	9.46E+04	5.36E+04	7.41E+06	4.08E+04	1.31E+04
318	U1357	B	6	H	4	W	86	88	45.86	45.88	45.87	2.87E+07	4.36E+07	1.20E+06	3.84E+05	2.33E+05	3.54E+07	2.27E+05	5.49E+04
318	U1357	B	6	H	4	W	88	89	45.88	45.89	45.88	2.87E+07	6.63E+07	2.02E+06	6.58E+05	3.83E+05	5.50E+07	3.44E+05	9.39E+04
318	U1357	B	6	H	6	W	16	18	48.03	48.05	48.04	2.99E+07	3.59E+05	1.14E+05	6.86E+04	1.01E+07	5.90E+04	1.42E+04	1.45E+04
318	U1357	B	6	H	7	W	69	71	50.06	50.08	50.07	3.20E+07	1.55E+07	4.56E+05	1.45E+05	8.80E+04	1.42E+07	3.39E+04	2.39E+04

4

EXP	SITE	HOLE	CORE	SECTION	upper interval	lower interval	upper depth (mbsf)	lower depth (mbsf)	average depth (mbsf)	Age (yr BP)	GDGT-0	GDGT-1	GDGT-2	GDGT-3	Crenarchaeol	Crenarchaeol regio-isomer	GDGT-I	GDGT-II	GDGT-III
318	U1357	B	6	H	7	71	50.08	50.1	50.09	3207.6	1.39E+07	4.40E+05	1.42E+05	8.12E+04	1.08E+07	5.94E+04	2.04E+04	1.95E+04	2.93E+04
318	U1357	B	7	H	1	107	51.07	51.09	51.07	3532.4	1.95E+07	5.69E+05	1.88E+05	1.19E+05	1.52E+07	9.42E+04	3.01E+04	2.80E+04	2.84E+04
318	U1357	B	7	H	1	109	51.09	51.1	51.095	3534.5	1.58E+07	4.91E+05	1.66E+05	1.08E+05	1.24E+07	6.88E+04	2.52E+04	2.10E+04	2.70E+04
318	U1357	B	7	H	3	47	49	53.05	53.07	3728.1	2.33E+07	6.35E+05	2.00E+05	1.25E+05	1.75E+07	1.10E+05	2.68E+04	2.75E+04	3.60E+04
318	U1357	B	7	H	3	49	53.07	53.08	53.075	3729.5	1.41E+07	4.13E+05	1.36E+05	8.16E+04	9.88E+06	1.09E+05	1.43E+04	1.35E+04	1.63E+04
318	U1357	B	7	H	5	2	4	55.04	55.06	3865.5	2.78E+07	7.96E+05	2.59E+05	1.44E+05	2.11E+07	1.02E+05	2.49E+04	2.81E+04	3.16E+04
318	U1357	B	7	H	5	4	55.06	55.08	55.07	3867.3	2.94E+07	8.32E+05	2.56E+05	1.62E+05	2.34E+07	1.39E+05	3.65E+04	3.43E+04	3.94E+04
318	U1357	B	7	H	6	43	44	56.95	56.96	4022.4	4.31E+07	1.26E+06	4.14E+05	2.63E+05	4.08E+07	2.50E+05	6.83E+04	7.73E+04	1.04E+05
318	U1357	B	7	H	6	44	46	56.96	56.98	4033.2	1.02E+07	5.90E+05	1.01E+05	6.42E+04	7.63E+06	4.33E+04	1.12E+04	1.22E+04	2.62E+04
318	U1357	B	8	H	1	66	68	60.16	60.18	4308.2	2.13E+07	5.77E+05	1.85E+05	1.17E+05	1.81E+07	8.03E+04	3.24E+04	3.09E+04	4.31E+04
318	U1357	B	8	H	1	68	70	60.18	60.2	4309.4	9.63E+06	2.68E+05	8.96E+04	5.67E+04	7.42E+06	3.70E+04	1.39E+04	1.28E+04	1.55E+04
318	U1357	B	8	H	2	109	111	62.09	62.11	4416.9	2.66E+07	7.00E+05	2.27E+05	1.36E+05	2.27E+07	1.52E+05	4.74E+04	4.42E+04	5.32E+04
318	U1357	B	8	H	2	111	113	62.11	62.13	4418.1	3.27E+07	9.15E+05	2.95E+05	1.69E+05	2.73E+07	1.90E+05	6.23E+04	5.37E+04	5.95E+04
318	U1357	B	8	H	4	12	12	64.11	64.12	4520.3	1.51E+07	3.91E+05	1.29E+05	8.49E+04	1.25E+07	9.28E+04	2.75E+04	2.68E+04	3.09E+04
318	U1357	B	8	H	4	12	14	64.12	64.14	4521.0	1.38E+07	3.68E+05	1.19E+05	8.50E+04	1.08E+07	5.98E+04	2.16E+04	2.09E+04	2.30E+04
318	U1357	B	8	H	5	77	79	66.27	66.29	4613.0	1.41E+07	3.81E+05	1.29E+05	8.53E+04	1.17E+07	6.27E+04	2.11E+04	2.14E+04	2.49E+04
318	U1357	B	8	H	5	79	81	66.29	66.31	4614.0	3.07E+07	8.28E+05	2.69E+05	1.85E+05	2.39E+07	1.19E+05	4.67E+04	4.36E+04	5.02E+04
318	U1357	B	9	H	1	112	114	70.12	70.14	4827.7	2.65E+07	7.10E+05	2.28E+05	1.58E+05	2.24E+07	1.81E+05	4.63E+04	4.15E+04	4.36E+04
318	U1357	B	9	H	1	116	114	70.16	70.15	4828.8	1.60E+07	4.00E+05	1.42E+05	9.94E+04	1.28E+07	5.84E+04	2.72E+04	2.33E+04	2.62E+04
318	U1357	B	9	H	3	13	15	71.92	71.94	4911.8	3.12E+07	9.15E+05	3.02E+05	1.85E+05	2.34E+07	1.70E+05	3.95E+04	3.82E+04	3.97E+04
318	U1357	B	9	H	4	79	81	74.08	74.1	5007.9	2.25E+07	5.91E+05	1.97E+05	1.38E+05	1.91E+07	1.15E+05	4.11E+04	3.90E+04	4.70E+04
318	U1357	B	9	H	4	81	83	74.1	74.11	5009.1	2.27E+07	6.01E+05	2.06E+05	1.43E+05	1.96E+07	8.48E+04	4.34E+04	3.87E+04	4.56E+04
318	U1357	B	9	H	5	137	138	76.16	76.17	5116.2	1.23E+07	3.52E+05	1.11E+05	7.83E+04	1.03E+07	4.92E+04	1.77E+04	1.90E+04	2.27E+04
318	U1357	B	9	H	5	138	139	76.17	76.18	5116.8	1.77E+07	5.05E+05	1.63E+05	1.02E+05	1.42E+07	7.00E+04	5.70E+04	3.05E+04	3.47E+04
318	U1357	B	10	H	1	4	5	78.54	78.55	5317.8	1.66E+07	4.11E+05	1.46E+05	9.61E+04	1.42E+07	9.33E+04	2.50E+04	2.15E+04	2.51E+04
318	U1357	B	10	H	1	5	6	78.55	78.56	5318.5	2.36E+07	6.06E+05	2.07E+05	1.51E+05	1.86E+07	8.86E+04	3.25E+04	2.89E+04	3.01E+04
318	U1357	B	10	H	2	30	30	80.28	80.3	5402.0	2.72E+07	7.89E+05	2.55E+05	1.63E+05	2.01E+07	1.14E+05	3.53E+04	2.80E+04	3.40E+04
318	U1357	B	10	H	2	32	32	80.3	80.31	5403.3	1.73E+07	5.45E+05	1.74E+05	1.14E+05	1.43E+07	7.63E+04	3.34E+04	2.54E+04	2.81E+04
318	U1357	B	10	H	3	78	80	82.26	82.28	5484.3	2.28E+07	6.71E+05	2.10E+05	1.21E+05	1.96E+07	1.15E+05	4.14E+04	4.04E+04	4.50E+04
318	U1357	B	10	H	3	80	82	82.28	82.3	5485.4	2.38E+07	7.09E+05	2.25E+05	1.33E+05	1.86E+07	1.27E+05	3.82E+04	3.60E+04	4.14E+04
318	U1357	B	10	H	4	97	98	83.9	83.905	5551.7	1.28E+07	3.96E+05	1.26E+05	7.86E+04	1.11E+07	8.35E+04	2.73E+04	2.55E+04	2.81E+04
318	U1357	B	10	H	4	99	99	83.91	83.915	5552.2	2.22E+07	6.17E+05	2.12E+05	1.20E+05	1.81E+07	1.98E+05	4.37E+04	3.74E+04	4.24E+04
318	U1357	B	10	H	5	73	74	85.16	85.17	5611.5	2.19E+07	5.53E+05	1.99E+05	1.39E+05	1.86E+07	2.05E+05	3.14E+04	3.36E+04	3.69E+04
318	U1357	B	10	H	5	74	76	85.17	85.19	5612.2	2.33E+07	6.10E+05	2.11E+05	1.45E+05	2.00E+07	1.88E+05	4.33E+04	3.88E+04	4.16E+04
318	U1357	B	10	H	7	15	17	87.09	87.11	5712.0	4.37E+07	1.17E+06	3.74E+05	2.37E+05	3.94E+07	3.02E+05	7.13E+04	8.06E+04	7.83E+04
318	U1357	B	10	H	7	19	19	87.11	87.13	5713.1	4.66E+07	1.21E+06	3.89E+05	2.58E+05	3.89E+07	1.91E+05	2.11E+05	8.74E+04	9.39E+04
318	U1357	B	11	H	2	50	52	89.13	89.15	5910.1	1.02E+07	3.04E+05	9.86E+04	6.50E+04	8.36E+06	6.62E+04	1.54E+04	1.54E+04	1.61E+04
318	U1357	B	11	H	2	52	53	89.15	89.16	5911.0	1.34E+07	4.42E+05	1.33E+05	8.51E+04	1.08E+07	7.38E+04	2.02E+04	1.91E+04	2.31E+04
318	U1357	B	11	H	3	100	102	91.12	91.14	6000.5	2.22E+07	5.78E+05	1.85E+05	1.25E+05	1.79E+07	1.23E+05	3.05E+04	3.06E+04	3.43E+04
318	U1357	B	11	H	3	102	103	91.14	91.15	6001.6	6.60E+07	1.76E+06	5.78E+05	3.56E+05	5.57E+07	3.27E+05	9.28E+04	8.92E+04	1.08E+05
318	U1357	B	11	H	5	12	14	93.04	93.06	6097.7	2.26E+07	6.22E+05	1.96E+05	1.36E+05	1.89E+07	1.26E+05	5.10E+04	4.98E+04	5.58E+04
318	U1357	B	11	H	5	14	16	93.06	93.07	6099.0	1.03E+07	2.78E+05	9.28E+04	5.93E+04	7.95E+06	5.42E+04	2.59E+04	2.37E+04	2.58E+04
318	U1357	B	11	H	6	74	74	95.14	95.16	6200.2	2.19E+07	6.14E+05	1.99E+05	1.33E+05	1.78E+07	1.22E+05	3.09E+04	2.98E+04	3.17E+04
318	U1357	B	11	H	6	74	76	95.16	95.18	6201.1	2.34E+07	6.47E+05	2.19E+05	1.39E+05	1.76E+07	1.08E+05	3.44E+04	3.07E+04	3.44E+04
318	U1357	B	11	H	CC	13	15	97.18	97.2	6289.2	1.88E+07	5.16E+05	1.59E+05	1.15E+05	1.55E+07	1.13E+05	3.73E+04	3.19E+04	3.79E+04
318	U1357	B	11	H	CC	15	16	97.2	97.205	6290.0	2.13E+07	5.90E+05	1.88E+05	1.24E+05	1.67E+07	1.04E+05	4.02E+04	3.43E+04	3.70E+04
318	U1357	B	12	H	2	3	4	98.09	98.11	6410.5	1.58E+07	4.42E+05	1.32E+05	8.66E+04	1.21E+07	8.77E+04	3.02E+04	2.91E+04	3.27E+04
318	U1357	B	12	H	2	4	5	99.99	100.01	6488.1	4.09E+07	1.19E+06	4.07E+05	2.62E+05	4.36E+07	2.83E+05	1.19E+05	1.20E+05	1.43E+05

EXP	SITE	HOLE	CORE	SECTION	upper interval	lower interval	upper depth (mbsf)	lower depth (mbsf)	average depth (mbsf)	Age (yr BP)	Crenarchaeal regio-isomer	GDGT-I	GDGT-II	GDGT-III						
318	U1357	B	12	H	3	W	46	100.01	100.03	100.02	6889.2	2.00E+07	5.39E+05	1.82E+05	1.16E+05	1.63E+07	4.63E+04	4.17E+04	4.68E+04	
318	U1357	B	12	H	4	W	116	118	102.03	102.05	6572.0	2.81E+07	7.96E+05	2.54E+05	1.58E+05	2.42E+07	1.68E+05	4.57E+04	4.67E+04	5.30E+04
318	U1357	B	12	H	4	W	118	102.03	102.07	6573.1	2.36E+07	6.63E+05	2.18E+05	1.38E+05	1.93E+07	1.19E+05	4.11E+04	4.03E+04	4.21E+04	
318	U1357	B	12	H	6	W	10	103.99	103.98	6649.0	1.24E+07	3.43E+05	1.10E+05	7.33E+04	1.02E+07	8.89E+04	1.96E+04	1.87E+04	3.79E+04	
318	U1357	B	12	H	6	W	12	103.99	103.98	6649.7	2.03E+07	5.51E+05	1.78E+05	1.21E+05	1.68E+07	1.10E+05	3.43E+04	3.38E+04	2.07E+04	
318	U1357	B	12	H	7	W	81	83	106.18	106.2	6740.0	1.73E+07	4.85E+05	1.58E+05	1.03E+05	1.36E+07	8.78E+04	2.76E+04	2.49E+04	2.81E+04
318	U1357	B	12	H	7	W	83	84	106.2	106.21	6740.8	1.46E+07	3.99E+05	1.27E+05	8.33E+04	1.18E+07	8.59E+04	2.80E+04	2.76E+04	3.60E+04
318	U1357	B	13	H	1	W	108	109	108.08	108.05	6941.5	1.94E+07	5.28E+05	1.71E+05	1.11E+05	1.71E+07	1.02E+05	3.65E+04	3.53E+04	2.80E+04
318	U1357	B	13	H	1	W	109	110	108.09	108.1	6942.0	4.86E+07	1.34E+06	4.19E+05	2.83E+05	4.54E+07	2.39E+05	8.32E+04	8.63E+04	8.33E+04
318	U1357	B	13	H	3	W	29	31	110.02	110.04	7029.0	2.53E+07	6.07E+05	2.13E+05	1.38E+05	1.21E+07	1.59E+05	4.17E+04	4.03E+04	4.94E+04
318	U1357	B	13	H	3	W	31	32	110.04	110.05	7030.0	1.78E+07	4.87E+05	1.61E+05	1.06E+05	1.38E+07	1.27E+05	3.07E+04	2.75E+04	2.99E+04
318	U1357	B	13	H	4	W	83	85	112.06	112.08	7140.0	2.48E+07	6.45E+05	2.13E+05	1.32E+05	1.34E+07	1.34E+05	3.59E+04	3.94E+04	3.49E+04
318	U1357	B	13	H	4	W	85	86	112.08	112.09	7141.0	1.25E+07	4.73E+05	1.19E+05	7.72E+04	9.60E+06	6.92E+04	1.93E+04	2.06E+04	1.94E+04
318	U1357	B	13	H	6	W	12	14	114.13	114.14	7249.3	9.62E+07	2.63E+06	8.50E+05	5.08E+05	8.41E+07	4.99E+05	1.16E+05	1.28E+05	1.31E+05
318	U1357	B	13	H	6	W	14	16	114.14	114.16	7250.9	6.26E+07	7.99E+05	2.59E+05	1.58E+05	2.11E+07	1.44E+05	3.65E+04	2.94E+04	3.24E+04
318	U1357	B	13	H	7	W	46	47	115.96	115.97	7382.4	1.91E+07	5.95E+05	1.81E+05	1.02E+05	1.44E+07	1.00E+05	3.01E+04	2.82E+04	2.77E+04
318	U1357	B	13	H	7	W	47	49	115.97	115.99	7383.5	4.78E+07	1.35E+06	4.35E+05	2.80E+05	3.76E+07	2.29E+05	7.60E+04	6.13E+04	6.32E+04
318	U1357	B	14	H	2	W	98	99	118.09	118.1	7618.9	1.25E+07	5.44E+05	1.74E+05	9.28E+04	9.21E+06	7.43E+04	1.49E+04	1.28E+04	1.41E+04
318	U1357	B	14	H	2	W	99	101	118.1	118.12	7620.2	9.68E+06	3.42E+05	1.12E+05	6.07E+04	7.32E+06	6.38E+04	1.52E+04	1.34E+04	1.43E+04
318	U1357	B	14	H	4	W	4	5	120.15	120.16	7737.8	1.06E+07	3.34E+05	1.07E+05	6.36E+04	7.79E+06	7.78E+04	1.72E+04	1.85E+04	1.88E+04
318	U1357	B	14	H	5	W	48	49	122.09	122.1	7837.5	2.02E+07	6.49E+05	2.18E+05	1.22E+05	1.50E+07	1.10E+05	2.43E+04	2.31E+04	2.52E+04
318	U1357	B	14	H	5	W	49	51	122.1	122.12	7838.2	3.21E+07	9.01E+05	3.01E+05	1.81E+05	2.51E+07	1.76E+05	4.83E+04	4.89E+04	5.05E+04
318	U1357	B	14	H	6	W	92	94	124.02	124.04	7906.6	1.66E+07	5.44E+05	1.74E+05	9.28E+04	1.32E+07	1.34E+05	3.81E+04	2.93E+04	3.44E+04
318	U1357	B	14	H	6	W	94	95	124.02	124.03	7907.4	3.96E+07	1.30E+06	4.10E+05	2.39E+05	3.13E+07	2.68E+05	8.43E+04	7.11E+04	7.43E+04
318	U1357	B	15	H	4	W	12	14	126.12	126.14	8051.0	1.11E+07	3.21E+05	1.03E+05	6.55E+04	8.67E+06	5.93E+04	1.94E+04	1.96E+04	2.37E+04
318	U1357	B	15	H	4	W	42	43	132.15	132.16	8246.7	2.24E+07	7.29E+05	2.21E+05	1.17E+05	1.83E+07	1.42E+05	4.74E+04	3.62E+04	4.20E+04
318	U1357	B	15	H	5	W	43	44	132.15	132.16	8247.1	1.54E+07	4.58E+05	1.44E+05	8.36E+04	1.29E+07	9.00E+04	4.00E+04	3.33E+04	3.06E+04
318	U1357	B	15	H	6	W	85	86	134.08	134.09	8242.5	2.06E+07	5.96E+05	1.89E+05	1.12E+05	1.66E+07	1.12E+05	4.62E+04	3.93E+04	3.52E+04
318	U1357	B	15	H	6	W	86	88	134.09	134.11	8252.2	1.91E+07	5.56E+05	1.78E+05	1.08E+05	1.54E+07	1.13E+05	5.38E+04	4.13E+04	3.83E+04
318	U1357	B	16	H	1	W	63	65	136.13	136.14	8496.9	1.33E+07	3.84E+05	1.26E+05	6.43E+04	9.63E+06	1.12E+05	2.74E+04	1.77E+04	2.33E+04
318	U1357	B	16	H	1	W	65	67	136.15	136.17	8498.1	3.85E+07	1.04E+06	3.32E+05	1.92E+05	3.17E+07	1.53E+05	6.45E+04	6.34E+04	6.36E+04
318	U1357	B	16	H	3	W	9	11	138.26	138.28	8597.1	2.15E+07	6.50E+05	2.22E+05	1.11E+05	1.34E+07	1.13E+05	1.67E+04	1.67E+04	1.82E+04
318	U1357	B	16	H	3	W	11	13	138.28	138.29	8598.4	3.16E+07	9.18E+05	2.97E+05	1.65E+05	2.48E+07	1.88E+05	4.77E+04	5.00E+04	5.22E+04
318	U1357	B	16	H	4	W	63	64	140.17	140.18	8695.5	1.90E+07	5.28E+05	1.67E+05	9.68E+04	1.12E+07	9.17E+04	4.96E+04	4.02E+04	3.94E+04
318	U1357	B	16	H	4	W	64	65	140.18	140.19	8696.0	4.57E+07	1.17E+06	3.87E+05	2.39E+05	3.74E+07	3.21E+05	8.31E+04	8.88E+04	8.31E+04
318	U1357	B	16	H	5	W	124	126	142.28	142.3	8820.4	4.05E+07	1.04E+06	4.36E+05	2.69E+05	3.44E+07	2.83E+05	5.95E+04	4.84E+04	5.29E+04
318	U1357	B	16	H	5	W	126	128	142.32	142.34	8821.7	6.32E+07	1.68E+06	5.91E+05	3.60E+05	4.94E+07	2.24E+05	7.51E+04	6.67E+04	6.94E+04
318	U1357	B	16	H	7	W	5	7	144.09	144.11	8936.7	1.59E+07	1.51E+06	4.84E+05	2.94E+05	4.35E+07	2.43E+05	8.67E+04	8.13E+04	9.42E+04
318	U1357	B	16	H	7	W	7	9	144.11	144.13	8937.9	1.49E+07	4.69E+05	1.55E+05	8.69E+04	1.12E+07	7.90E+04	3.19E+04	2.40E+04	2.81E+04
318	U1357	B	17	H	1	W	117	119	146.17	146.19	9127.9	3.97E+07	1.13E+06	3.87E+05	2.18E+05	3.01E+07	1.93E+05	5.51E+04	4.69E+04	5.53E+04
318	U1357	B	17	H	1	W	119	120	146.19	146.2	9129.7	5.01E+07	1.23E+06	4.33E+05	2.89E+05	3.79E+07	1.85E+05	5.50E+04	4.21E+04	4.81E+04
318	U1357	B	17	H	3	W	13	15	148.13	148.15	9228.6	4.93E+07	1.22E+06	4.22E+05	2.84E+05	4.12E+07	2.32E+05	9.00E+04	7.99E+04	8.54E+04
318	U1357	B	17	H	4	W	61	62	150.11	150.12	9378.5	1.33E+07	3.97E+05	1.38E+05	7.70E+04	1.09E+07	7.56E+04	2.34E+04	2.00E+04	2.39E+04
318	U1357	B	17	H	4	W	99	99	151.99	151.99	9513.8	1.85E+07	4.93E+05	1.61E+05	1.10E+05	1.49E+07	6.53E+04	3.54E+04	3.01E+04	3.25E+04



EXP	SITE	HOLE	CORE	SECTION	upper interval	lower interval	upper depth (mbsf)	lower depth (mbsf)	average depth (mbsf)	Age (yr BP)	GDGT-0	GDGT-1	GDGT-2	GDGT-3	Crenarchaeol	Crenarchaeol regio-isomer	GDGT-I	GDGT-II	GDGT-III		
318	U1357	B	17	H	5	W	99	101	151.99	152.01	152	1.47E+07	4.13E+05	1.39E+05	8.39E+04	1.07E+07	7.43E+04	2.99E+04	2.16E+04	2.70E+04	
318	U1357	B	17	H	7	W	14	16	154.14	154.16	154.15	9696.4	4.33E+07	1.07E+06	3.76E+05	2.60E+05	3.52E+07	7.26E+04	7.11E+04	7.33E+04	
318	U1357	B	17	H	7	W	16	17	154.16	154.17	154.165	9697.8	2.11E+07	5.39E+05	1.85E+05	1.28E+05	1.70E+07	7.96E+04	4.35E+04	3.87E+04	4.27E+04
318	U1357	B	18	H	1	W	59	61	155.09	155.11	155.1	9897.2	3.42E+07	9.59E+05	3.11E+05	1.80E+05	2.74E+07	1.92E+04	4.91E+04	4.57E+04	5.88E+04
318	U1357	B	18	H	1	W	61	62	155.11	155.12	155.115	9898.6	4.51E+06	1.40E+05	4.60E+04	2.73E+04	3.35E+06	2.08E+04	7.56E+03	6.04E+03	7.86E+03
318	U1357	B	18	H	2	W	112	114	157.12	157.14	157.13	10088.2	4.10E+07	1.03E+06	3.46E+05	2.42E+05	3.15E+07	1.43E+05	7.30E+04	7.16E+04	7.04E+04
318	U1357	B	18	H	2	W	114	116	157.14	157.16	157.15	10090.6	2.28E+07	5.79E+05	2.02E+05	1.54E+05	1.70E+07	1.27E+05	4.01E+04	2.73E+04	3.70E+04
318	U1357	B	18	H	4	W	0	2	159	159.02	159.01	10291.6	6.30E+07	1.51E+06	5.06E+05	3.32E+05	5.01E+07	2.99E+05	1.06E+05	1.08E+05	1.21E+05
318	U1357	B	18	H	4	W	2	3	159.03	159.05	159.025	10293.5	1.32E+07	3.15E+05	1.15E+05	7.69E+04	9.96E+06	8.29E+04	1.96E+04	1.85E+04	2.53E+04
318	U1357	B	18	H	5	W	57	59	161.07	161.09	161.08	10518.3	9.11E+07	2.50E+06	9.54E+05	4.78E+05	7.49E+07	3.07E+05	1.32E+05	1.38E+05	1.72E+05
318	U1357	B	18	H	6	W	117	118	163.17	163.18	163.175	10740.7	2.10E+07	5.17E+05	1.62E+05	1.19E+05	1.55E+07	7.57E+04	2.84E+04	2.94E+04	4.46E+04
318	U1357	B	18	H	6	W	118	120	163.18	163.2	163.19	10742.0	2.14E+07	5.41E+05	1.81E+05	1.19E+05	1.45E+07	9.18E+04	3.43E+04	2.78E+04	4.92E+04
318	U1357	B	19	H	1	W	6	8	164.06	164.08	164.07	10879.3	7.09E+06	1.86E+05	6.22E+04	3.76E+04	5.58E+06	2.84E+04	1.49E+04	1.66E+04	2.18E+04
318	U1357	B	19	H	1	W	8	9	164.08	164.09	164.085	10880.6	6.23E+06	1.53E+05	5.54E+04	2.70E+04	4.02E+06	2.36E+04	1.14E+04	1.35E+04	1.66E+04
318	U1357	B	19	H	2	W	39	40	165.88	165.89	165.885	11031.1	3.28E+07	6.90E+05	2.58E+05	1.99E+05	2.31E+07	1.30E+05	3.50E+04	3.04E+04	3.90E+04
318	U1357	B	19	H	2	W	40	41	165.89	165.9	165.895	11032.0	1.29E+07	2.79E+05	1.04E+05	8.29E+04	8.80E+06	3.77E+04	1.35E+04	8.72E+03	1.77E+04
318	U1357	B	19	H	3	W	110	111	168.09	168.1	168.095	11202.2	6.62E+07	1.66E+06	6.03E+05	3.39E+05	6.35E+07	2.86E+05	1.28E+05	1.21E+05	1.46E+05
318	U1357	B	19	H	4	W	119	121	169.68	169.7	169.69	11344.4	8.65E+07	2.22E+06	6.86E+05	4.18E+05	6.83E+07	2.99E+05	1.33E+05	1.28E+05	1.42E+05
318	U1357	B	19	H	4	W	121	122	169.7	169.71	169.705	11345.7	1.93E+07	5.09E+05	1.57E+05	9.53E+04	1.42E+07	9.19E+04	3.26E+04	2.29E+04	3.01E+04

Holocene paleoenvironment and paleoclimate at the Adélie Basin

EXP SITE	HOLE CORE	SECTION	upper interval	lower interval	upper depth (mbsf)	lower depth (mbsf)	average depth (mbsf)	age (yr BP)	TEX86	GDGT-3 / GDGT-3	lower 90% conf. interv.	upper 90% conf. interv.	lower SE boundary	BAYSPAR subt	upper SE boundary	upper 90% conf. interv.
318 U1357 B	1 H	2 W	40	42	1.9	1.92	1.91	65.3	0.4172	1.641791	-4.32813439	-1.9273328	1.79484	5.2760534	7.521435842	
318 U1357 B	1 H	2 W	42	44	1.92	1.94	1.93	66.5	0.410247	1.5783133	-4.05628437	-2.095696	0.933774	4.2440311	6.379146632	
318 U1357 B	2 H	2 W	4	6	4.04	4.06	4.05	191.4	0.413448	1.6642755	-5.73045098	-3.0884305	1.007775	4.118036	6.124186435	
318 U1357 B	2 H	2 W	6	8	4.06	4.08	4.07	192.9	0.416667	1.5658915	-4.78339573	-2.5349684	0.949415	4.961485	7.54927002	
318 U1357 B	2 H	3 W	72	74	6.22	6.24	6.23	297.9	0.422558	1.6078431	-4.1841658	-2.0932729	1.314057	5.2121101	7.763654559	
318 U1357 B	2 H	3 W	74	76	6.24	6.26	6.25	298.9	0.404818	1.7358692	-5.0540735	-2.8390915	0.594989	4.083845	6.334156962	
318 U1357 B	2 H	4 W	111	113	8.11	8.13	8.12	391.1	0.424488	1.6520227	-3.49602597	-1.5319703	1.513077	5.1227475	7.450984838	
318 U1357 B	2 H	4 W	113	115	8.13	8.15	8.14	392.2	0.412495	1.6630824	-5.13432118	-2.8568657	0.674073	4.4339646	6.859049436	
318 U1357 B	2 H	6 W	6	8	10.06	10.08	10.07	491.6	0.394967	1.6987179	-5.35306428	-3.193829	0.153685	3.0946313	4.991541518	
318 U1357 B	2 H	6 W	8	10	10.08	10.1	10.09	492.6	0.417067	1.5959105	-4.476545	-2.0504835	1.715852	5.0012215	7.123509642	
318 U1357 B	2 H	CC	W	2	12.05	12.07	12.06	602.4	0.393869	1.6380952	-5.93580435	-3.5237355	0.215906	3.3644048	5.395186365	
318 U1357 B	2 H	CC	W	2	12.07	12.09	12.08	603.8	0.423259	1.5740741	-3.30991455	-1.2980372	1.821152	5.1967295	7.37976672	
318 U1357 B	3 H	1 W	97	99	12.97	12.99	12.98	679.6	0.418295	1.6268657	-3.9846629	-1.9670293	1.161085	4.3655098	6.432363872	
318 U1357 B	3 H	1 W	99	101	12.99	13.01	13	681.0	0.42002	1.677686	-2.89567651	-1.0966673	1.693379	5.1903675	7.445924726	
318 U1357 B	3 H	3 W	8	10	15.08	15.1	15.09	795.6	0.411123	1.7383333	-3.94544574	-1.9579256	1.123501	3.7367687	5.422326453	
318 U1357 B	3 H	4 W	70	72	17.2	17.22	17.21	893.3	0.424916	1.5079365	-4.04102108	-1.7893326	1.701657	4.8850116	6.938275187	
318 U1357 B	3 H	4 W	72	74	17.22	17.24	17.23	894.0	0.443701	1.5384619	-3.33003985	-0.9727772	2.681894	6.2482307	8.548518074	
318 U1357 B	3 H	5 W	97	99	18.97	18.98	18.98	968.4	0.422151	1.5098039	-3.71027013	-1.5527777	1.792172	5.201742	7.400914747	
318 U1357 B	3 H	5 W	99	101	18.99	19.01	19	969.4	0.424929	1.4952381	-2.6143446	-0.8340347	1.926136	5.1900695	7.295306932	
318 U1357 B	3 H	7 W	8	10	21.08	21.1	21.09	1055.2	0.426628	1.5311203	-3.84667187	-1.3934077	2.410103	5.6682393	7.769737384	
318 U1357 B	3 H	7 W	10	12	21.1	21.12	21.11	1056.0	0.419913	1.5675676	-3.77902367	-1.5400111	1.931326	5.0146134	7.003337394	
318 U1357 B	4 H	2 W	95	97	23.95	23.97	23.96	1194.1	0.415819	1.61	-4.96855688	-2.5092585	1.303607	4.3972438	6.392369326	
318 U1357 B	4 H	3 W	61	63	25.13	25.13	25.13	1245.3	0.408365	1.5266272	-4.85504766	-2.6705157	0.716356	4.5077544	6.953206676	
318 U1357 B	4 H	3 W	63	64	25.13	25.14	25.135	1246.1	0.409264	1.5195246	-3.97331719	-1.9801694	1.105982	4.1272377	6.073367507	
318 U1357 B	4 H	4 W	118	120	27.18	27.2	27.19	1358.2	0.425487	1.6408451	-3.08104213	-1.2115245	1.686953	4.9115358	6.991397043	
318 U1357 B	4 H	4 W	120	122	27.2	27.22	27.21	1359.1	0.423862	1.5646259	-4.33499128	-2.0365558	1.526961	5.0505504	7.323265531	
318 U1357 B	4 H	6 W	17	19	29.17	29.19	29.18	1456.6	0.377735	1.6315789	-7.87141177	-5.2414046	-1.163874	2.0820525	4.175675905	
318 U1357 B	4 H	6 W	19	21	29.19	29.21	29.2	1457.7	0.414384	1.5302594	-4.98990875	-2.7092435	0.826672	3.9189253	5.913428964	
318 U1357 B	4 H	7 W	37	39	30.87	30.89	30.88	1550.4	0.404122	1.6575875	-5.84378667	-3.2561452	0.755702	4.02214	6.128992446	
318 U1357 B	4 H	7 W	39	41	30.89	30.91	30.9	1551.6	0.430524	1.65	-3.5146661	-1.339816	2.032045	5.6649351	8.008149454	
318 U1357 B	5 H	1 W	122	124	32.22	32.24	32.23	1704.3	0.444444	1.3679654	-2.54328087	-0.3176729	3.32882	6.7942522	9.155835865	
318 U1357 B	5 H	1 W	124	126	32.24	32.26	32.25	1705.3	0.427567	1.546748	-4.5597077	-1.7764192	2.538757	6.2740213	8.683266873	
318 U1357 B	5 H	3 W	6	8	34.06	34.08	34.07	1804.9	0.409955	1.50192639	-2.6713916	0.739127	4.6456801	7.165406646		
318 U1357 B	5 H	3 W	8	10	34.08	34.1	34.09	1806.2	0.399779	1.5402844	-5.67137062	-3.234884	0.234884	3.3158136	5.303013438	
318 U1357 B	5 H	4 W	54	56	36.04	36.06	36.05	1922.1	0.428285	1.6382979	-4.92081459	-2.246281	1.900283	5.192538	7.316037668	
318 U1357 B	5 H	4 W	54	56	36.04	36.06	36.05	1923.4	0.426679	1.5396825	-3.15833688	-1.129507	2.015966	4.535557	6.160693493	
318 U1357 B	5 H	5 W	114	116	38.14	38.16	38.15	2060.3	0.460627	1.571929	-1.88647931	0.68107507	4.66178	8.0854408	10.29370236	
318 U1357 B	5 H	5 W	116	118	38.16	38.18	38.17	2062.0	0.399361	1.6347239	-2.8326913	0.429127	4.5829633	7.262187561		
318 U1357 B	5 H	7 W	5	7	40.05	40.07	40.06	2237.3	0.411318	1.65625	-4.48831788	-2.1336778	1.517702	4.6455331	6.602984154	
318 U1357 B	5 H	7 W	7	9	40.07	40.08	40.08	2239.1	0.417285	1.5947467	-4.83249582	-2.475473	1.17882	4.140555	6.050873993	
318 U1357 B	6 H	2 W	15	17	42.15	42.17	42.16	2527.7	0.410334	1.6476684	-5.03524443	-2.6780219	0.976587	3.9571477	5.879609473	
318 U1357 B	6 H	2 W	17	19	42.17	42.19	42.18	2529.9	0.376715	1.673595	-7.23232806	-4.7931915	-1.010174	2.7267216	5.137019001	
318 U1357 B	6 H	3 W	44	46	43.94	43.95	43.945	2674.9	0.439303	1.7258883	-2.4717339	-0.4207086	2.759176	6.2077154	8.433023698	
318 U1357 B	6 H	3 W	46	48	43.96	43.98	43.955	2675.8	0.392931	1.7649254	-5.64987928	-3.3845311	0.127637	3.4399664	5.576419142	
318 U1357 B	6 H	4 W	86	88	45.86	45.88	45.87	2871.8	0.412916	1.6480867	-4.48402651	-2.315519	1.046508	4.4481225	6.643808875	
318 U1357 B	6 H	4 W	88	89	45.88	45.89	45.885	2873.2	0.406755	1.7180157	-5.23340747	-0.061087	0.306852	3.8802091	6.185024604	
318 U1357 B	6 H	6 W	16	18	48.03	48.05	48.04	2995.0	0.405641	1.6618076	-5.18755858	-2.8036703	0.89228	3.7560968	5.603259401	
318 U1357 B	6 H	7 W	69	71	50.06	50.07	50.07	3205.0	0.415235	1.6477273	-3.21128699	-1.4612074	1.252094	4.9220955	7.289246178	

EXP SITE	HOLE CORE	SECTION	upper interval	lower interval	upper depth (mbsf)	lower depth (mbsf)	average depth (mbsf)	depth (yr BP)	TEX86 /GDGT-3	lower 90% conf. interv.	boundary	lower SE boundary	BAYSPAR subit	upper SE boundary	lower 90% conf. interv.	
318 U1357 B	6 H	7 W	71	73	50.8	50.1	50.9	3207.6	0.391088	1.748765	-6.45107794	-0.0035275	-0.208876	3.1198781	5.266924269	
318 U1357 B	7 H	1 W	107	109	51.07	51.09	51.08	3324.4	0.410488	1.559392	-4.36615139	-2.2654725	0.991394	3.936885	5.836725763	
318 U1357 B	7 H	1 W	109	110	51.09	51.1	51.095	3534.5	0.410423	1.6	-4.56609801	-2.4143389	0.9211671	4.0628414	6.08889657	
318 U1357 B	7 H	3 W	47	49	53.07	53.07	53.07	3728.1	0.406542	1.6	-5.30312799	-2.887372	0.857986	3.7647142	6.539535896	
318 U1357 B	7 H	3 W	49	50	53.07	53.08	53.075	3729.5	0.44159	1.66666667	-5.76078488	-0.7718955	2.320956	5.9815353	6.342608798	
318 U1357 B	7 H	5 W	2	4	55.04	55.06	55.05	3865.5	0.388163	1.7986111	-1.06704822	-4.3645262	-0.174567	2.5652828	4.332485919	
318 U1357 B	7 H	5 W	4	6	55.06	55.08	55.07	3867.3	0.401008	1.5802469	-4.70949111	-2.638871	0.571454	3.3826091	5.195804179	
318 U1357 B	7 H	6 W	43	44	56.95	56.96	56.955	4022.4	0.423868	1.5741445	-3.13623083	-1.2786636	1.601286	5.0352167	7.250102131	
318 U1357 B	7 H	6 W	44	46	56.96	56.98	56.97	4023.3	0.418255	1.5732087	-3.47437453	-1.4997152	1.561772	4.3853584	6.206571565	
318 U1357 B	8 H	1 W	66	68	60.16	60.18	60.17	4308.2	0.39852	1.5819666	-4.74640183	-2.8202648	0.165994	3.621322	5.857921155	
318 U1357 B	8 H	1 W	68	70	60.18	60.2	60.19	4309.4	0.40616	1.5802469	-5.29072997	-3.0638496	0.388678	3.4216999	5.377999092	
318 U1357 B	8 H	2 W	109	111	62.09	62.11	62.1	4416.9	0.423868	1.6091176	-3.34936908	-1.3093536	1.859907	5.0829589	7.161519754	
318 U1357 B	8 H	2 W	111	113	62.11	62.13	62.12	4418.1	0.425972	1.5269166	-3.6960967	-1.5578264	1.757322	5.2813689	7.554379447	
318 U1357 B	8 H	4 W	11	12	64.11	64.12	64.115	4520.3	0.439668	1.5176471	-2.30974911	-0.6065731	2.03401	5.634974	7.957595805	
318 U1357 B	8 H	4 W	12	14	64.12	64.14	64.13	4521.0	0.417445	1.401649	-4.82719283	-2.2579687	1.725324	5.0832308	7.249080469	
318 U1357 B	8 H	5 W	77	79	66.27	66.29	66.28	4613.0	0.402973	1.5123095	-4.82898952	-2.2830809	1.664064	4.498561	6.326811495	
318 U1357 B	8 H	5 W	79	81	66.29	66.31	66.3	4614.0	0.409578	1.4540541	-4.2305427	-2.143837	1.091366	4.6745728	6.968741467	
318 U1357 B	9 H	1 W	112	114	70.12	70.14	70.13	4827.7	0.444009	1.448938	-1.88268473	-0.0304099	2.841334	6.2592678	8.668835155	
318 U1357 B	9 H	1 W	114	116	70.14	70.16	70.15	4828.8	0.428408	1.4282574	-3.49501245	-1.2075957	2.245764	5.3963034	7.428401945	
318 U1357 B	9 H	3 W	13	15	71.92	71.94	71.93	4911.8	0.398817	1.6324324	-5.91176886	-3.5101829	0.213206	3.2896157	5.273899764	
318 U1357 B	9 H	4 W	79	81	74.08	74.1	74.09	5007.9	0.432277	1.4275362	-3.63165478	-1.3718193	2.131801	5.802115	8.169467226	
318 U1357 B	9 H	4 W	81	83	74.1	74.12	74.11	5009.1	0.418087	1.4265734	-4.98454615	-2.4274076	1.537148	5.0385861	7.297013518	
318 U1357 B	9 H	5 W	137	138	76.16	76.17	76.165	5116.2	0.403895	1.4176245	-6.50007239	-3.49308218	0.052512	3.7967841	6.211839331	
318 U1357 B	9 H	5 W	138	139	76.17	76.18	76.175	5118.8	0.39881	1.5980392	-4.21485512	-2.4778629	0.215148	3.4949358	5.610398787	
318 U1357 B	10 H	1 W	4	5	78.54	78.55	78.545	3317.8	0.449957	1.5192508	-2.89776667	-0.2959712	3.73782	7.0348199	9.161384736	
318 U1357 B	10 H	1 W	5	6	78.55	78.56	78.555	3318.5	0.424283	1.3708609	-2.55560523	-0.6188574	2.383852	5.467522	7.456488868	
318 U1357 B	10 H	2 W	28	30	80.28	80.3	80.29	5402.0	0.403948	1.5644172	-5.78545995	-3.3174368	5.508956	3.4337875	5.320304028	
318 U1357 B	10 H	2 W	30	32	80.3	80.32	80.31	5403.3	0.400638	1.5263158	-5.49869797	-3.0621012	0.715568	4.282118	5.582542569	
318 U1357 B	10 H	3 W	78	80	82.26	82.28	82.27	5484.3	0.399284	1.7355372	-5.89753328	-3.5849485	0.000454	3.1515746	5.18404725	
318 U1357 B	10 H	3 W	80	82	82.28	82.3	82.29	5485.4	0.406198	1.6917295	-4.90186222	-2.883675	0.365993	3.6569945	5.779631987	
318 U1357 B	10 H	4 W	97	98	83.9	83.9	83.905	5551.7	0.421137	1.6030534	-3.8787319	-1.6894846	1.563831	4.84131549	6.958318703	
318 U1357 B	10 H	4 W	98	99	83.91	83.92	83.915	5552.2	0.462075	1.7666667	-2.76942493	-0.144165	3.926005	7.8155468	10.324031004	
318 U1357 B	10 H	5 W	73	74	85.16	85.17	85.165	5611.5	0.495438	1.4316547	-1.26256122	3.34325612	6.569	10.15824	16.119152992	
318 U1357 B	10 H	5 W	74	76	85.17	85.19	85.18	5612.2	0.475945	1.5241379	-0.72154871	1.58079558	5.150322	8.7514247	11.07413624	
318 U1357 B	10 H	7 W	15	17	87.09	87.11	87.1	5712.0	0.43831	1.5780591	-2.60436945	-0.5125719	2.730325	6.3293299	8.650559123	
318 U1357 B	10 H	7 W	17	19	87.11	87.13	87.12	5713.1	0.409198	1.5077519	-4.01829322	-2.0974457	1.034317	4.8265578	7.272552992	
318 U1357 B	11 H	2 W	50	52	89.13	89.15	89.14	5910.1	0.430498	1.5169231	-3.0096742	-1.0195668	2.075053	5.6219105	9.709633856	
318 U1357 B	11 H	2 W	52	53	89.15	89.16	89.155	5911.0	0.408881	1.5628672	-4.38396711	-2.2131464	1.152467	4.1717291	6.119152992	
318 U1357 B	11 H	3 W	100	102	91.12	91.14	91.13	6000.5	0.428289	1.48	-3.3018319	-1.3723789	1.619021	4.8073718	6.863858103	
318 U1357 B	11 H	3 W	102	103	91.14	91.15	91.145	6001.6	0.417411	1.416235955	-4.10723457	-2.0447606	1.152873	4.6515005	9.908115046	
318 U1357 B	11 H	5 W	12	14	93.04	93.06	93.05	6097.7	0.424074	1.4411765	-4.11145683	-1.8803128	1.578825	5.0012353	7.208689791	
318 U1357 B	11 H	5 W	14	16	93.06	93.08	93.07	6099.0	0.425976	1.5649241	-3.59537884	-1.3780308	1.965999	5.284037	7.424717815	
318 U1357 B	11 H	6 W	72	74	95.14	95.16	95.15	6200.0	0.425094	1.4962406	-3.82644099	-3.3673755	1.757073	4.9581226	7.02279935	
318 U1357 B	11 H	6 W	74	76	95.16	95.18	95.17	6201.1	0.417642	1.5611511	-4.832688236	-2.5389766	1.008292	4.4590282	6.684753239	
318 U1357 B	11 H	CC	W	13	15	97.18	97.2	97.19	6289.2	0.428571	1.3826087	-3.47401162	-1.3369827	1.97624	5.631035	7.991780216
318 U1357 B	11 H	CC	W	15	16	97.2	97.21	97.205	6290.0	0.410589	1.4758065	-4.94914554	-2.4685261	1.377395	4.5769198	6.64061984
318 U1357 B	12 H	2 W	3	5	98.09	98.11	98.1	6410.5	0.409328	1.5242494	-4.57242016	-2.6120489	0.427287	4.4668884	7.072431688	
318 U1357 B	12 H	3 W	44	46	99.99	100.01	100	6488.1	0.444444	1.55349351	-2.47250539	-0.9990468	2.815618	6.3564511	8.6402889551	
318 U1357 B	12 H	3 W	46	48	100.01	100.03	100.02	6489.2	0.42963	1.5689655	-3.37864781	-1.4298702	1.59149	5.0045436	7.205962843	

Holocene paleoenvironment and paleoclimate at the Adélie Basin

EXP SITE	HOLE	CORE	SECTION	upper interval	lower interval	upper depth (mbsf)	lower depth (mbsf)	average depth (mbsf)	Age (yr BP)	TEX86	GDGT-2 /GDGT-3	lower 90% conf. interv.	lower SE boundary	BAYSPAR subt	upper SE boundary	upper 90% conf. interv.
318 U1357 B	12 H	4 W	116	118	102.03	102.05	102.04	102.04	6572.0	0.421512	1.6075949	-4.00779473	-1.810688	1.595679	4.7157169	6.728141348
318 U1357 B	12 H	4 W	118	120	102.05	102.07	102.06	102.06	6573.1	0.417399	1.5997101	-3.23578822	-1.5149967	1.514296	4.7223484	6.791541985
318 U1357 B	12 H	6 W	10	12	103.97	103.99	103.98	103.98	6649.0	0.442458	1.5006821	-1.5149967	0.13602807	1.695576	5.6620384	7.575290348
318 U1357 B	12 H	6 W	12	13	103.99	104.2	103.995	104.2	6649.7	0.426042	1.47107044	-4.8331286	-2.2034331	1.873089	4.7821186	6.658442786
318 U1357 B	12 H	7 W	81	83	106.18	106.2	106.19	106.19	6740.0	0.418326	1.5339060	-4.07582666	-1.8413438	1.622971	4.40347	6.196804485
318 U1357 B	12 H	7 W	83	84	106.2	106.21	106.205	106.205	6740.8	0.424409	1.5006002	-4.13539436	-1.9063809	1.549454	4.7123821	6.752470758
318 U1357 B	13 H	1 W	108	109	108.08	108.09	108.085	108.085	6941.5	0.421053	1.4505405	-4.17244825	-1.7638784	1.970338	5.1078835	7.131602028
318 U1357 B	13 H	1 W	109	110	108.09	108.09	108.095	108.095	6942.0	0.412538	1.4805654	-5.80893934	-3.0848511	1.138542	4.447729	6.582154944
318 U1357 B	13 H	3 W	29	31	110.02	110.04	110.03	110.03	7029.0	0.428212	1.5434873	-2.95885496	-1.1187134	1.734219	5.1922159	7.422623815
318 U1357 B	13 H	3 W	31	32	110.04	110.05	110.045	110.045	7030.0	0.447219	1.5188679	-2.33728945	0.0305891	3.701132	6.5308301	8.355985628
318 U1357 B	13 H	4 W	83	85	112.06	112.08	112.07	112.07	7140.0	0.429708	1.5323741	-3.38880519	-1.1891813	2.221088	5.0470317	6.869765335
318 U1357 B	13 H	4 W	85	86	112.08	112.09	112.085	112.085	7141.0	0.421087	1.6481994	-4.0931585	-1.6685988	2.088856	5.097171	7.037594365
318 U1357 B	13 H	6 W	12	14	114.12	114.14	114.13	114.13	7249.3	0.413862	1.6732283	-4.3702349	-2.1014932	2.416029	4.943442	6.231623637
318 U1357 B	13 H	6 W	14	16	114.14	114.16	114.15	114.15	7250.9	0.412538	1.6632940	-4.39838805	-2.1289822	1.387156	4.581203	5.945392379
318 U1357 B	13 H	7 W	46	47	115.96	115.97	115.965	115.965	7382.4	0.391616	1.4754508	-5.4715463	-3.351178	0.063785	2.8062594	4.657348292
318 U1357 B	13 H	7 W	49	49	115.97	115.99	115.98	115.98	7383.5	0.411508	1.5635714	-3.8265259	-1.9817085	0.878515	4.707659	5.167921938
318 U1357 B	14 H	2 W	98	98	118.09	118.1	118.095	118.095	7618.9	0.4383954	1.9597315	-6.95725136	-4.9333048	-0.418423	3.1673586	5.4801879
318 U1357 B	14 H	2 W	99	101	118.1	118.12	118.11	118.11	7620.2	0.408816	1.845414	-4.4830325	-2.3980897	0.8579	4.5671807	6.959666647
318 U1357 B	14 H	4 W	4	5	120.15	120.16	120.155	120.155	7737.8	0.426511	1.6823899	-3.79220652	-1.5810144	1.84719	4.9041846	6.875945819
318 U1357 B	14 H	5 W	48	49	122.09	122.1	122.095	122.1	7837.5	0.409463	1.7868852	-4.53930562	-2.3488925	1.04709	4.2350988	6.29135996
318 U1357 B	14 H	5 W	49	51	122.1	122.12	122.11	122.11	7838.2	0.422065	1.6629834	-4.65093523	-2.2877098	3.76206	4.807683	7.024416266
318 U1357 B	14 H	6 W	92	94	124	124.02	124.01	124.01	7906.6	0.424217	1.875	-3.73726808	-1.5659474	1.800441	4.7788047	6.699849069
318 U1357 B	14 H	6 W	94	95	124.02	124.03	124.025	124.025	7907.4	0.413622	1.7154812	-4.13704551	-2.0510472	1.260578	3.9707324	5.718781793
318 U1357 B	14 H	1 W	12	14	126.12	126.14	126.13	126.13	8051.0	0.415087	1.5725191	-3.95893944	-1.827647	1.476676	4.9647371	7.214536831
318 U1357 B	15 H	2 W	75	76	128.25	128.26	128.255	128.255	8117.0	0.416551	1.5371429	-4.40216014	-2.0391985	1.624308	4.9147602	7.037102033
318 U1357 B	15 H	2 W	78	79	128.28	128.29	128.285	128.285	8118.2	0.406332	1.6033058	-5.01837858	-2.8134865	0.604951	3.6790047	5.661769454
318 U1357 B	15 H	4 W	8	9	130.3	130.31	130.305	130.305	8184.4	0.432513	1.6284153	-3.37857722	-0.9574333	3.796278	6.0612675	8.167185535
318 U1357 B	15 H	4 W	9	11	130.31	130.33	130.32	130.32	8185.0	0.401261	1.6903073	-5.73953107	-3.3990766	0.229535	3.4316729	5.497051851
318 U1357 B	15 H	5 W	42	43	132.14	132.15	132.145	132.145	8246.7	0.397022	1.8888869	-6.0408941	-3.6865625	-0.03644	3.7107183	6.127635556
318 U1357 B	15 H	5 W	43	44	132.15	132.16	132.155	132.155	8247.1	0.409489	1.7724868	-3.92277439	-1.1994395	0.99483	4.4895645	6.743667924
318 U1357 B	15 H	6 W	85	86	134.08	134.09	134.085	134.085	8324.5	0.409316	1.6875	-4.1131211	-2.3190418	0.462476	3.8872919	6.096297841
318 U1357 B	15 H	6 W	88	88	134.09	134.11	134.1	134.1	8325.2	0.417801	1.6481481	-3.64001123	-1.7318374	1.226572	5.0635698	7.538433633
318 U1357 B	16 H	1 W	63	65	136.13	136.15	136.14	136.14	8496.9	0.439198	1.9595564	-5.9207986	-0.8925768	2.251953	5.6409916	7.826921361
318 U1357 B	16 H	1 W	65	67	136.15	136.17	136.16	136.16	8498.1	0.394292	1.7291667	-5.39894073	-3.4465904	-0.419691	2.6989103	4.710407932
318 U1357 B	16 H	3 W	9	11	138.26	138.28	138.27	138.27	8597.1	0.406934	2	-4.48604965	-2.4863608	0.613932	3.9763837	6.145165124
318 U1357 B	16 H	3 W	11	13	138.28	138.3	138.29	138.29	8598.4	0.412668	1.769697	-5.60929294	-2.7461887	1.072479	4.0084753	5.893968062
318 U1357 B	16 H	4 W	63	64	140.17	140.18	140.175	140.175	8695.4	0.403727	1.6902834	-4.25362079	-3.8876477	0.090605	3.2890328	5.352018745
318 U1357 B	16 H	4 W	64	65	140.18	140.19	140.185	140.185	8696.0	0.414121	1.5606695	-4.157196387	-2.3718305	1.039229	4.6024753	6.668804108
318 U1357 B	16 H	5 W	124	126	142.28	142.3	142.29	142.29	8820.4	0.433714	1.6208178	-2.78975624	-0.9269288	1.961176	4.9157509	6.82145192
318 U1357 B	16 H	5 W	126	128	142.3	142.32	142.31	142.31	8821.7	0.411559	1.6416667	-5.78141448	-3.1351857	0.967495	4.015541	5.981530492
318 U1357 B	16 H	7 W	5	7	144.09	144.11	144.1	144.1	8936.7	0.403398	1.6462585	-4.84215107	-2.7854706	0.603158	3.1647316	4.945946313
318 U1357 B	16 H	7 W	7	9	144.11	144.13	144.12	144.12	8937.9	0.407754	1.7433521	-4.66918796	-2.5966044	0.816704	3.7685783	5.801537464
318 U1357 B	17 H	1 W	117	119	146.17	146.19	146.18	146.18	9126.7	0.409651	1.7752294	-5.11683856	-2.5749788	1.365889	4.186544	6.005866492
318 U1357 B	17 H	1 W	120	120	146.19	146.2	146.195	146.195	9127.9	0.424427	1.4982699	-4.08559375	-1.7418089	1.891966	4.9208943	6.874552984
318 U1357 B	17 H	3 W	13	15	148.13	148.15	148.14	148.14	9228.6	0.434662	1.4859155	-3.23963092	-1.1657329	2.049613	5.7008098	8.055831675
318 U1357 B	17 H	4 W	61	62	150.11	150.12	150.115	150.115	9378.5	0.422629	1.9272078	-3.40266847	-1.3208598	0.906751	5.9714208	8.593133078
318 U1357 B	17 H	5 W	97	99	151.97	151.99	151.98	151.98	9513.8	0.405523	1.4636564	-4.18083872	-2.2643988	0.706826	3.8432059	5.866170953
318 U1357 B	17 H	5 W	99	101	151.99	152.01	152	152	9515.6	0.418474	1.6567942	-4.07191916	-1.8605992	1.567804	4.89393555	7.088336294
318 U1357 B	17 H	7 W	14	16	154.14	154.16	154.15	154.15	9696.4	0.434162	1.4461538	-3.06083957	-0.9484489	2.326575	5.7443153	7.948757605

EXP SITE	HOLE CORE	SECTION	upper interval	lower interval	upper depth (mbsf)	lower depth (mbsf)	average depth (mbsf)	Age (yr BP)	TEX86	GDGT-2 /GDGT-3	lower 90% conf. interv.	lower SE boundary	BAYSPAR subt	upper SE boundary	upper 90% conf. interv.
318 U1357 B	17 H	7 W	16	17	154.16	154.17	154.165	9697.8	0.421426	1.4453125	-5.47716364	-2.7544324	1.466856	4.4941527	6.4446758885
318 U1357 B	18 H	1 W	59	61	155.09	155.11	155.1	9897.2	0.415956	1.7277778	-4.17487863	-2.0726228	1.186688	4.6883207	6.946873455
318 U1357 B	18 H	1 W	61	62	155.11	155.12	155.115	9898.6	0.401965	1.6849817	-6.27120431	-3.6640014	0.378174	3.5700653	5.628835412
318 U1357 B	18 H	2 W	112	114	157.12	157.14	157.13	10088.2	0.415105	1.4297521	-5.27039252	-2.8151927	0.991319	4.0528734	6.027576152
318 U1357 B	18 H	2 W	114	116	157.14	157.16	157.15	10090.6	0.454802	1.3116883	-1.46427264	0.68455389	4.016068	7.0358792	8.983657574
318 U1357 B	18 H	4 W	0	2	159	159.02	159.01	10291.6	0.429543	1.5240964	-3.45535158	-1.2925096	2.060734	5.6143733	7.906470843
318 U1357 B	18 H	4 W	2	3	159.02	159.03	159.025	10293.5	0.465921	1.4954486	-1.33054223	0.86013347	4.25653	7.6392662	9.821131142
318 U1357 B	18 H	5 W	57	59	161.07	161.09	161.08	10518.3	0.410238	1.9958159	-4.28663387	-2.1987426	1.038298	4.4173345	6.59681301
318 U1357 B	18 H	6 W	117	118	163.17	163.18	163.175	10740.7	0.408264	1.3613445	-5.53985641	-3.2989671	0.17528	3.7012297	5.975467344
318 U1357 B	18 H	6 W	118	120	163.18	163.2	163.19	10742.0	0.420026	1.5210084	-4.52060943	-2.0095018	1.883688	5.2655208	7.446802675
318 U1357 B	19 H	1 W	6	8	164.06	164.08	164.07	10879.3	0.40802	1.6542553	-4.77068916	-2.5537342	0.883405	3.7565606	5.609745844
318 U1357 B	19 H	1 W	8	9	164.08	164.09	164.085	10880.6	0.409266	2.0518519	-4.94477687	-2.5623366	1.131369	4.1304323	6.064828099
318 U1357 B	19 H	2 W	39	40	165.88	165.89	165.885	11031.1	0.459671	1.2964824	-1.55939475	0.58410614	3.907363	7.6075451	9.994162311
318 U1357 B	19 H	2 W	40	41	165.89	165.9	165.895	11032.0	0.445989	1.2545235	-1.98681952	-0.0913757	2.847297	5.7728699	7.659866479
318 U1357 B	19 H	3 W	110	111	168.09	168.1	168.095	11202.2	0.425208	1.7787611	-4.82167513	-2.2137731	1.829486	5.5571738	7.961532601
318 U1357 B	19 H	4 W	119	121	169.68	169.7	169.69	11344.4	0.387248	1.6411483	-6.6735171	-4.455465	-1.016625	2.844943	5.335653985
318 U1357 B	19 H	4 W	121	122	169.7	169.71	169.705	11345.7	0.403422	1.6474292	-4.6021678	-2.6743243	0.31458	3.3866736	5.368173679

Chapter 5

Sea-ice, primary productivity and ocean temperatures at the Antarctic marginal zone during late Pleistocene

Abstract

While Pleistocene glacial-interglacial cycles are commonly associated with strong waxing and waning of Northern Hemisphere ice sheets, the response of the Antarctic ice sheet and regional changes in oceanographic and environmental conditions to Pleistocene climate dynamics remain poorly constrained. We present a reconstruction of sea-ice cover, sea surface temperature and primary productivity off the Ross Sea margin (Adare Basin at the slope of the Drygalski Basin) during the marine isotope stages (MIS) 9 to 5 (350-70 thousands years ago, encompassing Terminations IV to II). Our multiproxy study relies on micropaleontology (diatoms, dinoflagellate cysts, benthic foraminifers), organic and inorganic geochemistry proxies (carbon and nitrogen isotopes, lipid biomarkers, XRF-data), and sedimentology (IRD) obtained from deep-sea core AS05-10. For each glacial-interglacial transition a clear succession of events can be observed: (near-)permanent sea ice cover during glacial stages is followed by ice-shelf break-up with episodic ice-free areas and surface water stratification. Notably, ice-shelf break-up precedes the increase in air temperature as measured in the Vostok ice core for each glacial-interglacial transition. Generally, air temperature over Vostok starts rising once sea-ice cover at site AS05-10 has significantly decreased, becoming seasonal, as indicated by the diatom species composition. This is also reflected by the high diatom productivity and increased water mixing at site AS05-10, which is indicative of its proximity to the Marginal Ice Zone. At the onset of Termination II (MIS6 to 5), high export productivity and dysoxic bottom water conditions occurred, while water temperature increased about 5°C. During each interglacial spring/summer sea-ice cover is most reduced, and highest productivity occurs. Following each interglacial, the warm and cold fluctuations match the sawtooth character of the temperatures over Vostok. This record illustrates that at the Ross Sea margin, sea surface conditions and (export) productivity were strongly influenced by the natural climate variability of the Pleistocene. In light of this, current global warming may lead to increased ice-shelf break-up, water column stratification and shifts in the position/size of the Marginal Ice Zone with implications for algal species composition and diversity, and for primary productivity.

1 Introduction

Antarctic sea ice plays a key role in regional polar climate and biology, and global ocean circulation. It forms a regional physical barrier between the atmosphere and the ocean, limiting gas exchange (Stephens and Keeling, 2000), and between warm ocean waters and the ice sheet (Rintoul, 2018). Its reflective surface, which covers 18.2×10^6 km² at its maximum extent (1981-2010 monthly mean, National Snow and Ice Data Center), is fundamental for Earth's albedo. In addition, the seasonal melting of sea ice and release of nutrients is responsible for up to 35% of the total primary production (PP) in the Southern Ocean (Garrison and Close, 1993; Lizotte, 2001). The PP within the sea ice also 'seeds' surface waters upon melting and the entire polar ecosystem depends on the annual cycle of melting and formation of sea ice (Stoecker et al., 2000; Lizotte, 2001; Garrison et al., 2005; Murphy et al., 2017). While, over the last decades, global warming is clearly negatively affecting the sea-ice extent in the Arctic (Comiso and Nishio, 2008; Kay et al., 2011; Notz and Marotzke, 2012), sea-ice extent around Antarctica is more variable and shows strong local differences (Comiso and Nishio, 2008; Turner et al., 2009; Parkinson and Cavalieri, 2012; Parkinson, 2019). The lack of a clear trend in recent times makes future Antarctic sea-ice projections highly uncertain (Arzel et al., 2006; Bracegirdle et al., 2008; Bintanja et al., 2015). In recent years (2016-2017) sea ice has reached a springtime low (Turner et al., 2017), particularly in the Ross Sea sector, that includes the Adare Basin (Parkinson, 2019). Sea ice decline will likely act as a positive feedback to current global warming (e.g., Serreze & Barry 2011; Park et al. 2015; Abe et al. 2016; Haumann et al. 2016; Andry et al. 2017), which increases the relevance of understanding future sea ice conditions.

The biological response to sea ice decline is difficult to project (Sarmiento et al., 2004). Increased sea ice meltback will promote primary productivity (PP) by increasing available light and nutrient release, so that CO₂ uptake through photosynthesis acts as a negative feedback to global warming (Peck et al., 2010; Fernandez-Mendez et al., 2015). However, with a retreating sea-ice margin, global displacement of high-productivity areas to higher latitudes will reduce their size (Sarmiento et al., 2004). Furthermore, stratification (by melting) and reduced mixing could limit nutrient availability and promote ecosystem changes, which reduces CO₂ drawdown to the ocean floor (Arrigo et al., 1999; Steinacher et al., 2010; Vancoppenolle et al., 2013).

One way to understand the response of PP and sea-ice changes to different climate conditions is to reconstruct these parameters for past warmer than present periods, using sediment records. The Last Interglacial (LIG, 130-116 ka) or Marine Isotope Stage (MIS) 5e is the most recent of these periods. During the LIG, the ocean-area-weighted average sea surface temperature (SSTs) was about 0.7 ± 0.6 °C warmer than preindustrial temperatures

(McKay et al., 2011). The LIG may not be the perfect analogue for future climate, because global warmth was induced by Earth's orbital configuration rather than higher atmospheric CO₂ (Petit et al., 1999; Lüthi et al., 2008; Berg et al., 2011). Still, the response of sea-ice concentrations to warmer air and seawater temperatures during the LIG and in a future 2°C-warming scenario is likely very similar because of a (near) equal geographic setting, ice sheet configuration and oceanography. Tracking the summer sea-ice extension and the associated Marginal Ice Zone (MIZ), defined as the region experiencing most recent sea-ice melting/retreat, across MIS5e is particularly interesting because the MIZ is the region in the Southern Ocean with the highest summer PP (Fitch and Moore, 2007; Arrigo et al., 2008). The latitudinal position of the summer sea-ice edge is therefore important for the size of the high-productivity area associated with the MIZ. Changes in the position of the sea-ice edge in the late Pleistocene have affected the total Southern Ocean PP, as is clear from paleoproductivity reconstructions: PP was enhanced north of the Polar Front (PF) during glacial times, and south of the PF during interglacial times (Mortlock et al., 1991). A shift of the summer sea-ice edge (SSE) towards higher latitudes or changes in the size of the MIZ will also likely affect PP in the future (Sarmiento et al., 2004; Arrigo et al., 2008; Deppeler and Davidson, 2017). However, many Southern Ocean sea-ice reconstructions have focused on the winter sea ice edge (WSE) during glacial times instead (Gersonde and Zielinski, 2000; Bianchi and Gersonde, 2002; Howe et al., 2002; Crosta et al., 2004; Gersonde et al., 2005; Ferry et al., 2015), because sea ice expansion and related stratification have been proposed as a mechanism for glacial CO₂ reduction by prohibiting the air-sea CO₂ exchange during glacial periods (Stephens and Keeling, 2000; Sigman et al., 2004, 2010, 2021; Martínez-García et al., 2009; Ferrari et al., 2014).

In this paper we use sediment core AS05-10 collected off the Ross Sea continental slope (Fig. 1) to reconstruct the position of the SSE and the MIZ over the late Pleistocene glacial-interglacials and its influence on PP in the Adare Basin. The core is studied at high resolution (1-3 cm intervals) with paleobiological (diatoms, dinoflagellate cysts, benthic foraminifera), geochemical and sedimentological proxies. It straddles an interval between ~350 and 70 ka (see the age model below and Supplementary Information) and thus allows reconstructing the stepwise evolution of each glacial and interglacial stage.

High-resolution records close to the Antarctic margin, covering multiple glacial and interglacial stages have only become available over the last decade (Hillenbrand et al., 2009; Xiao et al., 2016b; Wilson et al., 2018), but none are from the Ross Sea area. With only one previously published low-resolution record from the Ross Sea (Ceccaroni et al., 1998), the record of AS05-10 thus substantially increases our knowledge on sea-ice variability and paleoproductivity for this area on glacial-interglacial timescales.

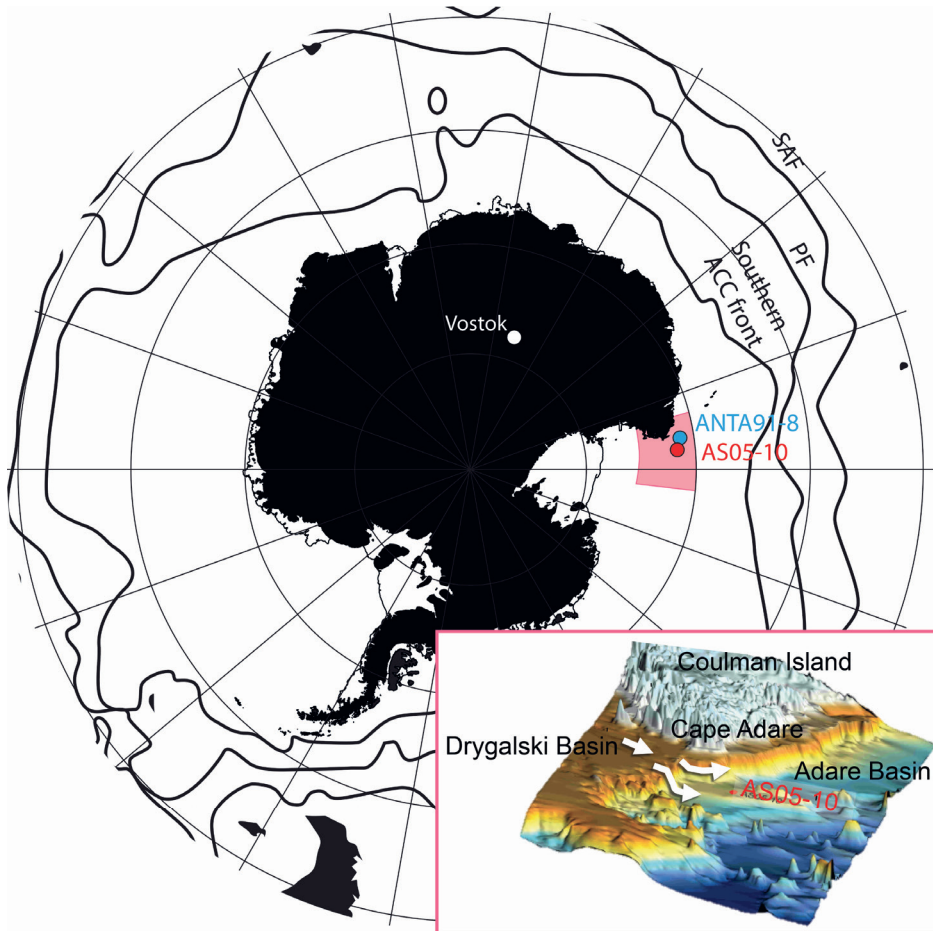


Figure 1: Map of the study site. Details of the bathymetry and topography of the pink area are shown. ACC front = Antarctic Circumpolar Current front; PF = Polar Front; SAF = Subantarctic Front (Orsi et al., 1995)

2 Oceanographic and geological setting

Core AS05-10 was drilled at the continental slope offshore the Drygalski Basin, which is called the Adare Basin, western Ross Sea (173.065°E, 70.835°S), at a water depth of 2377 m (Fig. 1) during the XX Antarctic Italian Cruise (01/15/2005-02/27/2005). Investigations are within the frame of the PNRA (Antarctic Italian National Research Program) projects 2004/4.08 “Bottom water production in the Ross Sea during the Late Quaternary: a geochemical and micropaleontological study” and 2009/A2.01 “Sub-milankovian paleoclimatic variations and deep circulation linkages during the Late Quaternary (MIS 5-7) in the Ross Sea slope (Antarctica)”.

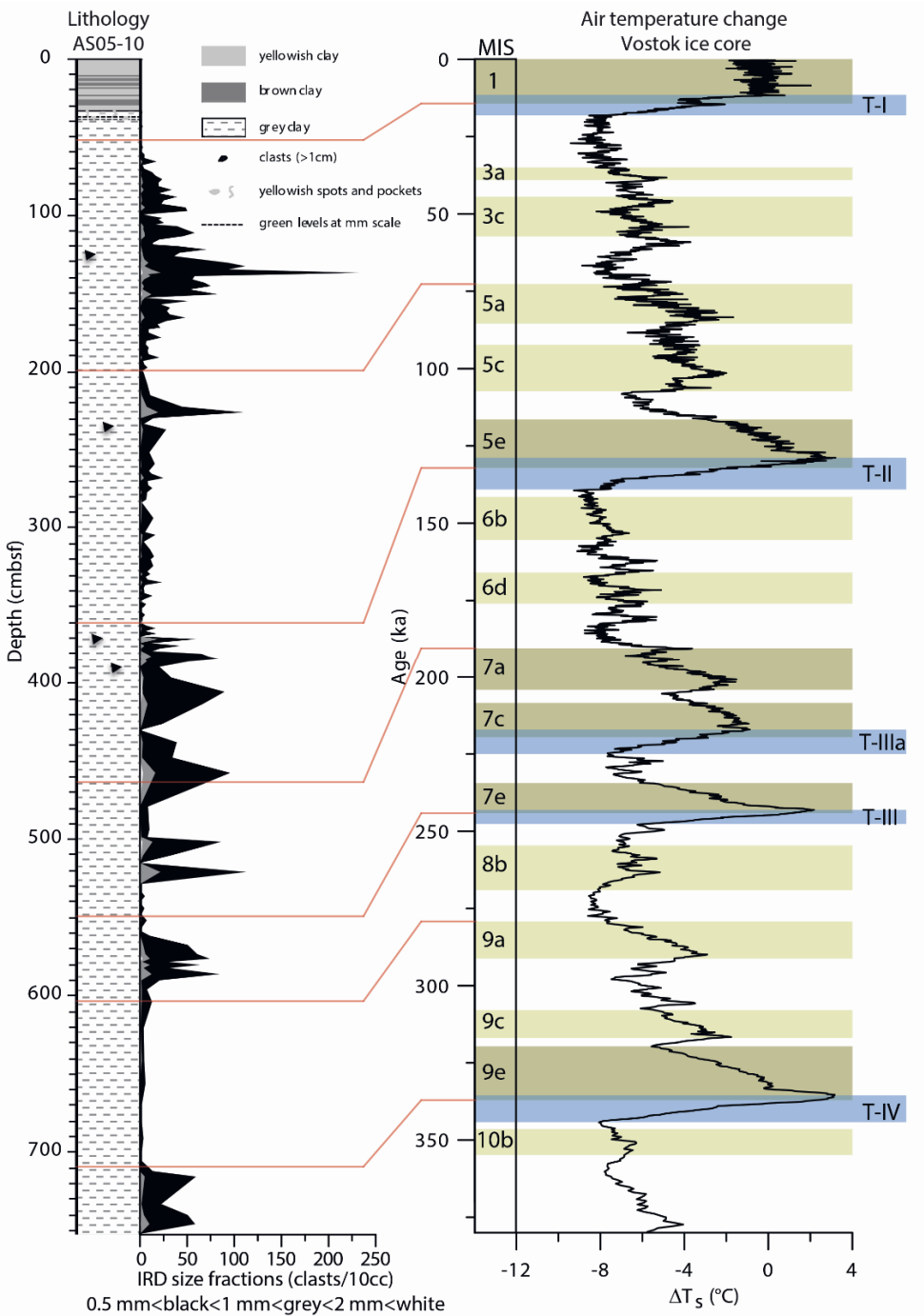


Figure 2 (previous page): Lithology of core AS05-10, including IRD (left). Relative air temperature change recorded in the Vostok ice core (Petit et al., 1999). The dark and light shaded areas mark the interglacials versus the interstadials, respectively, following Past Interglacial Working Group of PAGES (2016) with nomenclature following Railsback et al. (2015). Terminations (T) are marked in blue. Red lines mark the position of the onset of each Marine Isotope Stages (MIS) within the lithology based on the age model (Suppl. Inf.).

Today, the drill site of core AS05-10 is overlain by Circumpolar Deep Water (CDW) (Orsi and Wiederwohl, 2009), and influenced by occasional gravity currents that flow along the Drygalski Basin slope (Gordon et al., 2009). These gravity currents form through local mixing of relatively warm oceanic thermocline waters with relatively cold Modified CDW (MCDW; CDW that has been mixed with Ross Sea shelf waters) and High Salinity Shelf Water (HSSW) (Orsi and Wiederwohl, 2009). This very dense HSSW forms in the western sector of the Ross Sea as a result of the ongoing formation and removal of new sea ice in the Terra Nova Bay Polynya (Jacobs et al., 1985; Budillon et al., 1999), due to strong katabatic winter winds blowing over the Ross Ice Shelf (Bromwich and Kurtz, 1984). HSSW flows northward over the shelf and mixes with surface waters and MCDW at the shelf edge to form Antarctic Bottom Water (AABW) (Jacobs et al., 1970; Jacobs, 1991; Budillon et al., 2002, 2003; Bergamasco et al., 2004; Orsi and Wiederwohl, 2009). Surface and shelf waters in the Ross Sea are characterized by relatively high oxygen concentrations and low dissolved silica (DSi), and also determine the oxygen and DSi concentrations of the HSSW and AABW through bottom-water formation (Jacobs, 1989). Submarine canyons and basins, such as the Drygalski Basin, serve as conduits for bottom-water formation (Jacobs, 1989; Davey and Jacobs, 2007).

Spring warming and seaward winds cause northward sea ice retreat along the western Ross Sea coast (Spren et al., 2008; Smith et al., 2012), while the offshore sea-ice melt-back progresses southward. These two open water systems connect early January (Spren et al., 2008), so that, by definition, the Marginal Ice Zone (MIZ) is overlying AS05-10 in January (Fitch and Moore, 2007). Water column stratification, low wind speeds and nutrient release after sea-ice retreat trigger large phytoplankton blooms (Fitch and Moore, 2007; Arrigo et al., 2008; Smith et al., 2012). Together with the MIZ, the Ross Sea shelf surface waters are among the most productive areas of the Southern Ocean, with the shelf area alone contributing one third of the Southern Ocean total primary production (PP) (Arrigo et al., 2008; Smith et al., 2012). *Phaeocystis antarctica*, which is able to maintain high photosynthetic rates in the deeply-mixed Ross Sea polynya (Arrigo et al., 1999, 2003; Sedwick et al., 2000; Peloquin and Smith Jr., 2007), is responsible for the bulk of this high PP. However, when surface waters stratify due to the melting sea ice in summer, diatoms replace *P. antarctica* (Arrigo et al., 1999, 2003), taking advantage of the iron release from the melting sea ice (Arrigo et al., 2003; De Jong et al., 2013; McGillicuddy et al., 2015).

Similar to today, the surface waters of Site AS05-10 may have experienced shifts towards diatom-dominated PP during past interglacials.

About 90% of the total carbon and 30% of total biogenic silica production by *P. antarctica* and diatom blooms is seasonally recycled in the upper water column (Nelson et al., 1996). Still, organic carbon (OC) and biogenic silica (BSi) export to the seafloor is large in the Ross Sea, but varies strongly between years (Nelson et al., 1996; Smith Jr. et al., 2011) and regions (Nelson et al., 1996). OC export in the central Ross Sea occurs mainly through aggregate and fecal pellet formation (Asper and Smith, 1999; Smith Jr. et al., 2011). While high sinking rates of these fecal pellets imply that most sedimentary OC originated from the surface waters overlying Site AS05-10, part is shown to be derived from resuspended sediments from shallow banks (Nelson et al., 1996) through gravity flows (Gordon et al., 2009). Out of all the material that reaches the Ross Sea floor, another ~95% of OC and 80% of BSi gets remineralized (Nelson et al., 1996) under the influence of the high-oxygen low-DSi bottom waters (Jacobs, 1989).

3 Material

Core AS05-10 recovered 750 cm of fine-grained sediment. The top 40 cm is an alternation of brown and yellow clays; the rest of the core is homogeneous greyish clay with occasional clasts (>1 cm) (Fig. 2). The core has always been kept at -20°C. At ISMAR-CNR Bologna laboratory the sections of the core have been subsequently cut frozen in slices ca. 1 cm thick (Asioli and Langone, 2010).

4 Construction of the age model and terminology used

Comparison between the whole-core magnetic susceptibility (MS) in core AS05-10 and in the nearby core ANTA91-8 (Fig. 1 for its location) previously published at lower resolution (Ceccaroni et al., 1998) suggests our core contains at least MIS5 and MIS7.

We studied the section between 180 and 750 cm below sea floor (cmbsf) at high resolution and constructed an age model for this interval. The age model is based on two diatom datums: the last occurrence (LO) of *Rouxia leventerae* (0.138 Ma; the end of MIS6; Xiao et al., 2016b) at about 388±20 cmbsf; and the LO of *Rouxia constricta* (0.28 Ma; mid-MIS8; Zielinski and Gersonde, 2002) at about 594±19 cmbsf. The position of Termination I (18–11.5 ka) was estimated from a marked decrease in the %BSi and a sharp increase in the MS record between 115 and 147 cmbsf (see Supplementary Information).

The cyclic behavior of measured parameters in core AS05-10 has been used to improve dating by correlating these cycles to known orbital parameters and glacial-interglacial cyclicity. In the Southern Ocean records south of the Polar Front (PF), cycles of biogenic barium (Ba_{bio}) and %BSi are tightly linked, representing glacial-interglacial changes

in PP with higher values during the interglacials (Shimmield et al., 1994; Bonn et al., 1998; Pudsey and Howe, 1998; Hillenbrand and Fütterer, 2001; Hillenbrand et al., 2003, 2009; Wilson et al., 2018). Other geochemical elements have also shown a relation with glacial-interglacial variation related to provenance or terrigenous supply (Bertram et al., 2018; Jimenez-Espejo et al., 2020). In several other Southern Ocean records, glacial-interglacial cyclicity has been observed in MS: high BSi production dilutes lithogenic detritus input, which results in anti-correlation of MS with BSi (and Ba_{bio}) (Hillenbrand et al., 2009; Collins et al., 2012; Xiao et al., 2016b). In addition, some siliceous microfossils, such as the diatom *Eucampia antarctica*, show cyclic glacial-interglacial variation in relative abundance (Burckle and Cooke 1983; Burckle and Burak, 1988; Collins et al., 2012; Xiao et al., 2016b).

To build an age model for core AS05-10, we have tested several proxies for orbitally-driven cyclicity, using the diatom event datums and the position of Termination I for a first-order age model (see Suppl. Inf.). Successively, the Ti/Al record was used to tune core AS05-10 to the 19-kyr precession by using evolutive harmonic analysis (EHA) and evolutive spectral misfit analysis (e-ASM) of the Astrochron program in R (Meyers and Sageman, 2007; Meyers et al., 2012). The Ti/Al record was chosen as the cyclicities obtained from this record matched the expected astronomical cycle lengths based on the microfossil occurrence datums best. In addition, Al and Ti are found mainly in aluminosilicates and heavy minerals (Calvert and Pedersen, 2007), although both elements can be concentrated in diatom frustules, which means that at site AS05-10 the Ti/Al is likely influenced by the diatom export productivity in addition to a lithogenic signal. Nevertheless, Ti and Al are poorly mobilized during diagenesis, which means this proxy is least susceptible to changes in post-depositional remobilization and/or bottom-water oxygenation in comparison to for example Ba_{bio} and BSi. A final age model was obtained by tuning the obliquity pacing in the Ti/Al record to that within the deuterium-based air temperature reconstructions (ΔT_s) of the Vostok ice core (Petit et al., 1999). The Vostok ice core ΔT_s age model is based on the Antarctic Ice Core Chronology (AICC2012), which is based on a multi-proxy synchronization of multiple ice cores (Bazin et al., 2013; Veres et al., 2013). In our approach, we note that the 19-kyr precession signal within the Ti/Al record follows the precession signal of local (70.8°S) insolation (see Suppl. Inf.).

Names and ages for the individual marine isotope stages and glacial terminations were adopted from Railsback et al. (2015). Notably, this results in the designation of MIS9a to what is also known as MIS8.5. The relation between our stratigraphic record, the marine isotope stages according to Railsback et al. (2015), the ΔT_s record from the Vostok ice core, and the glacial Terminations in the ΔT_s record is shown in Figure 2.

Core AS05-10 continuously covers an interval between ~350 and 70 ka and thus allows reconstructing oceanographic conditions of each glacial and interglacial stage in

that interval and comparing the late Pleistocene interglacials. The definition of an interglacial is based on the comparative study of interglacials of the past 800 kyr by the Past Interglacials Working Group of PAGES (2016). Interglacials thus include MIS 9e, 7e, 7a-c and 5e. Following Cheng et al. (2009), the glacial Termination prior to MIS7a-c is termed Termination IIIa. We use the terms '(glacial) Termination' and '(onset of) Marine Isotope Stage, MIS' as the rapid shift from a glacial to an interglacial period marked by the steep temperature shift recorded in the Vostok ice core. The term 'glacial-interglacial transition' indicates the environmental changes related to the transition from a cold to a warm period, not necessarily synchronous to the Termination. We will describe several phases of each glacial-interglacial transition based on the proxy data.

5 Methods and proxy interpretations

5.1 Magnetic susceptibility

The gravity core AS05-10 was frozen at -20°C immediately after collection and scanned onboard for the magnetic susceptibility by means of a Bartington ring sensor for whole-core magnetic susceptibility with measurements at 2-cm steps.

Magnetic susceptibility is determined by the grain size and concentration of ferromagnetic minerals, which is determined by the source of the terrigenous material as well as the degree of dilution by biogenic input (Pudsey and Howe, 1998; Collins et al., 2012). Magnetic susceptibility has been used to correlate marine sediment cores as well as ice cores on glacial-interglacial timescales (Pudsey and Camerlenghi, 1998; Pudsey and Howe, 1998; Pugh et al., 2009; Xiao et al., 2016b).

5.2 X-ray fluorescence analyses

Geochemical analyses of 255 bulk sediment samples have been performed by X-ray fluorescence (XRF) located at the Department of Geosciences of Padova University (Italy). Dried sediment samples (1.5 g) were ground with an agate mortar and fused with lithium tetraborate (1:10; sample:lithium tetraborate). The obtained panes were analyzed with a Philips PW2400 spectrometer to measure the concentrations of the chemical elements by using several international geologic standards. Loss on ignition (LOI) was measured after heating samples to 980°C. The instrumental precision is within 0.6% for the major elements and within 3% for trace elements.

Subsequently, biogenic barium (Ba_{bio}) was calculated as the concentration of barium exceeding the detrital contribution observed in shales (Dymond et al., 1992). Barium is generally considered a proxy for paleoproductivity (Bonn et al., 1998; Ceccaroni et al., 1998; Pudsey and Howe, 1998; Hillenbrand et al., 2003, 2009; Xiao et al., 2016b). However, in some cases barium records are influenced by detrital input (Klump et al., 2000) and/or

changes in redox conditions (McManus et al., 1998). To account for this, elemental ratios considered in this paper are V/Cr, Ni/Co, and U/Th, which are indicative of bottom-water oxygenation (Jones and Manning, 1994), and Zr/Rb, which reflects the relative grain size (Dypvik and Harris, 2001) of the sediments and is indicative of increased detrital input at a lower shelf setting such as AS05-10. Because of low uranium concentrations a cut-off value of 2 ppm for was used for uranium to construct the U/Th record.

5.3 Biogenic silica

Biogenic silica was measured on 162 samples at ISMAR-CNR Bologna, following the dissolution method of DeMaster (1981) and the colorimetric analysis of Strickland and Parsons (1972) using a 0.5 M NaOH solution as extracting agent with an uncertainty of about 10%.

Changes in paleoproductivity in the Southern Ocean have been determined by measuring biogenic silica (BSi) (Shimmield et al., 1994; Bonn et al., 1998; Ceccaroni et al., 1998; Pudsey and Howe, 1998; Hillenbrand and Fütterer, 2001; Hillenbrand et al., 2003, 2009; Xiao et al., 2016b), often in combination with Ba_{bio} . Here, BSi is also considered a proxy for paleoproductivity.

5.4 Organic carbon, total nitrogen and $\delta^{15}N$

Total organic carbon (OC) and total nitrogen (TN) contents, and their stable isotope compositions were measured at ISMAR-CNR Bologna on 2 different aliquotes by a Finnigan DeltaPlus XP mass spectrometer directly coupled to a FISONs NA2000 Element Analyzer via a ConFlo III interface for continuous flow measurements (Tesi et al., 2007). Samples for OC analysis were first decarbonated in silver capsules after acid treatment (HCl 1.5 M). Samples for OC and TN contents and $\delta^{15}N$ were weighted in tin capsules and directly inserted in the EA autosampler. The average standard deviation of each measurement, determined by replicate analyses of the same sample, was $\pm 0.07\%$ for OC and $\pm 0.009\%$ for TN. The isotopic composition of nitrogen is presented in the conventional δ notation and reported as parts per thousand (‰). The internal standard for ^{15}N isotopic measurements was IAEA-N-1 (ammonium sulfate, $+0.4\%$ vs. air). Errors for replicate analyses of the standards were $\pm 0.2\%$.

The %OC and %TN in the sediments reflect the relative abundance in weight percentage of organic matter in the sediments. High %OC and %TN could either be the result of increased primary productivity or increased preservation.

Nitrogen fractionation by phytoplankton in the surface waters due to preferred uptake of ^{14}N over ^{15}N , makes $\delta^{15}N$ a proxy for surface water nutrient utilization; utilization being the ratio between phytoplankton uptake and nutrient supply (Altabet and Francois, 1994, 2001). The higher the $\delta^{15}N$ value, the higher the nutrient utilization is. Post-

depositional alteration of the $\delta^{15}\text{N}$ value due to early diagenesis at the sediment-water interface may, however, result in an increase of the bulk $\delta^{15}\text{N}$ value in the sediments, particularly at oxic pelagic sites with low accumulation rates (Robinson et al., 2012). However, empirical data across a range of sedimentation rates and sediment compositions at different water depths, suggest that even in slowly accumulating regions the study site bulk sedimentary $\delta^{15}\text{N}$ records will primarily reflect changes in the $\delta^{15}\text{N}$ of exported nitrogen in most cases. For example, in sediments with poor organic matter preservation, such as the Mediterranean marls (Higgins et al., 2010), or in millions-of-years-old sediments, such as the Cretaceous black shales (Higgins et al., 2012), the bulk $\delta^{15}\text{N}$ values are indicative of the biogeochemical cycling of nitrogen. Nevertheless, a bias due to the presence of inorganic nitrogen or input of terrestrial organics can be detected in a %OC-versus-%TN plot as a nonzero y-intercept of the linear regression line (Robinson et al., 2012).

5.5 Archaeal lipid (GDGT) processing and analyses

A total of 39 samples covering the period between 90 and 313 ka (243 – 665 cmbsf) were processed for analysis of glycerol dialkyl glycerol tetraethers (GDGTs) to derive TEX_{86} -based temperatures (Schouten et al., 2002). Sample processing involved extraction of freeze-dried and manual powdered sediments through accelerated solvent extraction (ASE; with dichloromethane (DCM)/methanol (MeOH) mixture, 9:1 v/v, at 100°C and 7.6×10^6 Pa). The polar GDGTs were separated from non-polar molecules through Al_2O_3 column chromatography using hexane/DCM (9:1, v/v), hexane/DCM (1:1, v/v) and DCM/MeOH (1:1, v/v) for separating apolar, ketone and polar fractions, respectively. The polar fractions were dried under N_2 , dissolved in hexane/isopropanol (99:1, v/v) and filtered through a $0.45 \mu\text{m}$ 4 mm diameter polytetrafluorethylene filter. After that, the dissolved polar fractions were injected and analyzed by ultra-high performance liquid chromatography/mass spectrometry (UHPLC/MS) at Utrecht University according to the method described by Hopmans et al. (2016). GDGT chromatogram peaks were integrated using Chemstation software. All samples containing low concentrations of GDGT-3 (below 3×10^3 mV) were not used for TEX_{86} -based temperature reconstructions and Branched and Isoprenoid Tetraether (BIT) index calculations (Hopmans et al., 2004).

For the TEX_{86} -based subsurface sea water temperature reconstruction we used the BAYSPAR calibration of Tierney and Tingley (2014), which gives a depth-integrated temperature estimate for the top 200 m of the surface water column based on surface sediment samples with a 90% confidence interval based on a linear regression with a slope and intercept specific for the region (a $20^\circ \times 20^\circ$ grid box) of our study. We have chosen this calibration as Thaumarchaeota are virtually absent in the upper 0-45 m (Kalanetra et al.,

2009), and reconstructed temperatures thus likely reflect a subsurface signal (Kim et al., 2012a). Based on Tierney & Tingley (2015), the expected slope and intercept of the TEX₈₆-subT calibration curve for our study area are 0.012 and 0.37 respectively, with a standard error (1σ) of 7.2°C. The standard error depends on the number of core tops used in the calibration. The number of available surface sediment samples used in the calibration at high southern latitude is low, which gives a high standard error. Despite this, reconstructed trends are reliable, as globally there is little variation in slope (values between 0.005 and 0.016) and intercept (values between 0.3 and 0.4) (Tierney and Tingley, 2015).

The (expected) normal pelagic marine distribution of isoprenoideal GDGTs (iGDGTs) in the sediments, and therefore TEX₈₆ values, can be affected by the iGDGT input of methanogenic or methanotrophic archaea (Koga et al., 1998), or other non-temperature related biases, such as archaeal growth phase (Elling et al., 2014), oxygen concentrations (Qin et al., 2015), and ammonia oxidation rates (Hurley et al., 2016). To search for possible biases, several indices have been developed, which we applied to our samples. These include the methane index (MI) (Zhang et al., 2011), the GDGT-0/crenarchaeol ratio (Blaga et al., 2009; Sinninghe Damsté et al., 2009), the GDGT-2/crenarchaeol ratio (Weijers et al., 2011) and the Ring Index ($|\Delta RI|$) (Zhang et al., 2016) (Suppl. Table S1).

In addition, we explore other proxies related to *in situ* production of branched GDGTs (brGDGTs). While initially considered purely soil-derived (Hopmans et al., 2004; Dearing Crampton-Flood et al., 2019), it was subsequently shown that brGDGTs are also produced within marine sediments (Peterse et al., 2009) and the water column (Zell et al., 2014). The relative abundance of brGDGTs versus iGDGTs is known as the BIT index, which is defined as (brGDGT-I + brGDGT-II + brGDGT-III) / (brGDGT-I + brGDGT-II + brGDGT-III + Crenarchaeol) (Hopmans et al., 2004). Other proxies based on brGDGTs, such as the degree of cyclization, have been suggested as indicators of *in-situ* sedimentary GDGT production versus soil-derived input of brGDGTs (Weijers et al., 2014; Sinninghe Damsté, 2016). The degree of cyclization within tetramethylated brGDGTs is called #ring_{Stetra}, is defined as ($[\text{brGDGT-Ib}] + 2 * [\text{brGDGT-Ic}]$) / ($[\text{brGDGT-Ia}] + [\text{brGDGT-Ib}] + [\text{brGDGT-Ic}]$) (Sinninghe Damsté, 2016) and is particularly varying as a function of *in situ* production.

5.6 Palynology

A total of 49 samples taken between 71 and 313 ka (195 and 665 cmsbf) were prepared for examination of palynomorphs by using established palynological processing methods. Samples were freeze-dried and a known amount of *Lycopodium clavatum* spores was added to c.a. 10 g of material. Samples were treated with 30% HCl to remove the carbonates and with 38% cold HF to remove silicates. After each acid treatment, samples were washed with water, left standing for 24 h to let the material settle, and subsequently

decanted. The HF treatment included 2 h of shaking at ~250 rpm and adding of 30% HCl to remove fluoride gels. The residue was then sieved through a 10- μ m mesh sieve and subsequently placed in an ultrasonic bath to break up clumps of organic matter and removal of heavy minerals. The remaining material was concentrated in ~1 ml of glycerin water used to make microscope slides. At least 200 dinoflagellate cysts were counted for each sample, if possible.

Dinoflagellate cysts can be used for reconstructing the presence of sea-ice (De Vernal and Hillaire-Marcel, 2000; Esper and Zonneveld, 2007; Bonnet et al., 2010; De Vernal et al., 2013) and primary productivity (Radi and De Vernal, 2008; Prebble et al., 2013). Moreover, based on the link between dinoflagellate cyst assemblages and the Antarctic and Polar Front Zones (Marret and De Vernal, 1997; Marret et al., 2001; Esper and Zonneveld, 2002; Prebble et al., 2013), dinoflagellate cysts have been used as an indicator of glacial-interglacial shifts of the Polar Front (Howe et al., 2002; Esper and Zonneveld, 2007). Dinoflagellate cysts are here grouped as being gonyaulacoid or protoperidinioid. It has been shown by infrared analysis that the cyst wall chemistry of phototrophic usually transparent gonyaulacoid dinoflagellates is distinctly different from that of the brown, heterotrophic protoperidinioids, and probably determined by the different feeding strategy of the dinoflagellates that produced the cyst (Ellegaard et al., 2013). Abundances of gonyaulacoid dinoflagellate cysts are typically less than 20% in surface sediments south of the PF and mostly represented by *Impagidinium pallidum* (Marret and De Vernal, 1997; Esper and Zonneveld, 2007; Prebble et al., 2013; Marret et al., 2020). High abundances of *I. pallidum* are associated with seasonal sea-ice in both the Arctic and Antarctic (Marret and De Vernal, 1997; De Vernal et al., 2001; Kunz-Pirrung et al., 2001; Esper and Zonneveld, 2007; Bonnet et al., 2010; Pieńkowski et al., 2013b; Zonneveld et al., 2013; Marret et al., 2020). Around Antarctica it is most dominant in nutrient-rich waters south of the PF and the seasonal sea-ice zone (SSIZ) upon seasonal melting of sea ice (Marret and De Vernal, 1997; Marret et al., 2001; Esper and Zonneveld, 2007).

Protoperidinioid cysts are dominant in present-day Subantarctic and Antarctic surface sediments where sea ice coverage and productivity are high (Marret and De Vernal, 1997; Esper and Zonneveld, 2002; Pieńkowski et al., 2013b; Prebble et al., 2013; Zonneveld et al., 2013). Protoperidinioid cysts are more sensitive than gonyaulacoid cysts to degradation in oxic environments (Versteegh and Zonneveld, 2002; Zonneveld et al., 2010). High abundances of protoperidinioid cysts in an assemblage could be representative of a high primary productivity environment as well as decreased bottom water oxygenation, which enhances their preservation. A way to at least partially circumvent this bias is the use of the concentration of protoperidinioid cysts (cysts/gram

sediment) and/or of total dinocysts as proxy for primary productivity (Reichart and Brinkhuis, 2003).

Other palynomorphs considered here include the gymnodinioid dinoflagellate cyst *Gymnodinium* spp., the prasinophycean alga *Cymatiosphaera* spp. and the acritarch *Leiosphaeridia* spp. *Cymatiosphaera* spp. is considered to be the phycoma of the chlorophyte *Pterosperma* (Mudie et al., 2010; **Chapter 2**). *Gymnodinium* spp., *Cymatiosphaera* spp., and *Leiosphaeridia* spp. have all been associated with surface water stratification due to fresh (melt)water (Mudie, 1992; Hannah, 2006; Warny et al., 2006, 2016; Ribeiro et al., 2016; **Chapter 2**).

5.7 Benthic foraminifers

The 103 samples between 180 and 578 cmbsf were treated in the laboratory for the analysis of foraminiferal assemblages and IRD. The samples were washed with a 0.063-mm mesh sieve, and thoroughly examined while they were wet with Leica M165C (11.7-192x) reflective optical stereomicroscope. The distribution of foraminifers is expressed in terms of absolute abundances (number of individuals/10 cc).

Benthic foraminifera are indicative of export productivity from the surface waters to the sea floor (Jorissen et al., 1995, 2007; Thomas and Gooday, 1996). Here, two species of benthic foraminifer are considered: *Martinottiella nodulosa* and *Eggerella bradyi*. These species have been reported at nearby surface sediment sample sites and core sites (Asioli, 1995; Barbieri et al., 1999). The occurrence of *M. nodulosa* seems to be linked to the availability of well-sorted quartz grains that it needs for constructing its test (Lindenberg and Auras, 1984). *M. nodulosa* is likely an infaunal species as its close relative, *Martinottiella communis*, has been shown to live at 1–3 cm sediment depth (Sabbatini et al., 2004). *E. bradyi* appears to be epifaunal with occurrences of living specimens in the 0–0.5 cm depth range (Asioli, 1995; Asioli and Langone, 2010).

5.8 Ice Rafted Debris (IRD)

The fraction larger than 0.500 mm in the 120 samples washed for foraminifera were dried and examined for IRD content with the same microscope used for the foraminifer study. Three fractions were chosen (>2 mm, 1-2 mm, and 0.5-1 mm), counting only the lithic clasts and excluding all remains of organisms. The content of the three fractions is expressed as a concentration (number of clasts/10 cc).

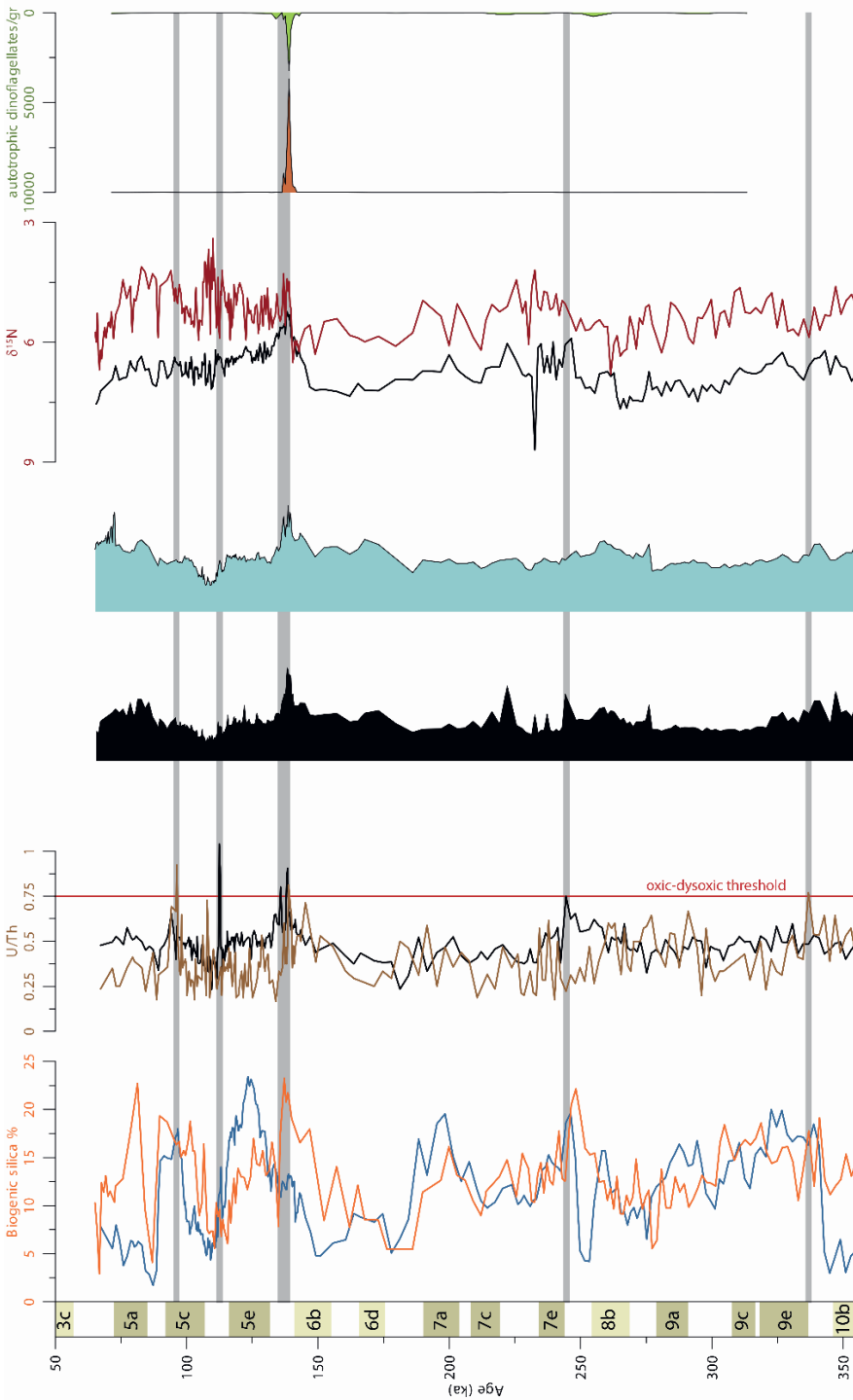


Figure 3: Geochemical elements, biogenic silica organic, carbon and nitrogen data obtained from core AS05-10. The grey shading marks periods of dysoxic bottom-water conditions.

IRD is indicative of icebergs reaching the depositional site and thus can be expected at ice-proximal sites. In the North Atlantic, high concentrations have been associated with glacial collapse as well as ice sheet growth (Heinrich, 1988; Cofaigh, 2012). Around Antarctica, however, a relation between glacial collapse and IRD is not as evident as in the northern hemisphere (Cofaigh, 2012) and in some records lags glacial Terminations (Grobe and Mackensen, 1992). Notably, increased IRD concentrations can simply be the result of decreased sedimentation rates and winnowing (Cofaigh et al., 2001). However, in the absence of high-energy bottom currents, increased IRD concentrations deposited in hemipelagic muds with biogenic material have been related to both periods of ice sheet advance and periods of intense calving and ice-shelf break-up around the Antarctic Peninsula (Pudsey and Camerlenghi, 1998; Lucchi et al., 2002; Minzoni et al., 2015). Furthermore, IRD layers have been associated with rapid ice-shelf break-up of the George VI ice shelf and associated iceberg release during the Holocene (Bentley et al., 2005).

5.9 Diatoms

Diatoms were processed according to the standard method, as described by Bernárdez et al. (2008) and Rigual-Hernández et al. (2017). A fixed amount of 0.5 g of sediment was placed in 600 ml beakers and treated with HCl and H₂O₂ in order to remove carbonate and organic matter. Bi-distilled water was added and left to settle over a night. The excess of liquid was removed with a vacuum pump. This process was repeated several times, until a neutral pH was achieved. For each sample, total volume and suspension volume used to mount the slides were known. For slide preparation, suspension was strewn evenly onto cleaned 18x18 mm cover slips placed in a Petri dish, after stirring the solution for homogenization. Slides were mounted with a toluene based synthetic resin mounting medium (Permout™, Fisher Scientific).

A total of 193 samples was analyzed at Salamanca University using a Leica DMLB microscope with phase contrast illumination at x1000 magnification for counting diatoms. Samples have been taken about every 5 cm, except for the interval between 428 and 472 cmbfs (168 – 197 ka), where sample spacing is about 10 cm, followed by a gap between 472 and 518 cmbfs (197 – 225 ka). The counts were performed following the method of Schrader and Gersonde (1978). A minimum of 400 valves was counted for each sample, where possible. For samples with a high amount of *Chaetoceros* resting spores (RS) at least 100 valves of non-dominant taxa were counted (Schrader and Gersonde 1978). The state of preservation of the fossil association was estimated by visual examination.

Diatom relative abundances are used to reconstruct sea-ice and temperatures in Southern Ocean sedimentary records (e.g., Bárcena et al., 1998, 2002; Crosta et al., 2008; Denis et al., 2010; Esper and Gersonde, 2014). To be able to reconstruct sea-ice dynamics

in this study, species with the same cryophylic and open-ocean ecological requirements were grouped: the seasonal sea-ice group and open-ocean group, respectively. Other species that are considered here are *Eucampia antarctica*, *Chaetoceros* resting spores (RS), *Fragilariopsis rhombica* and *Fragilariopsis kerguelensis*.

E. antarctica is a proxy for sea-ice cover, as it forms long chains of diatom valves during winter or in areas with extensive sea-ice cover (Kaczmarska et al., 1993). In the Atlantic sector of the Southern Ocean, percentages in surface sediment samples south of the SSE lie between 5 and 12.5% (Esper et al., 2010). Although increased abundances of *E. antarctica* have been associated with surface water temperatures up to 5.5°C within the Polar Frontal and Subantarctic Frontal Zones (Zielinski and Gersonde, 1997; Esper et al., 2010), this is likely because no distinction was made between *E. antarctica* var. *antarctica* and *E. antarctica* var. *recta*, the former being associated with the SSIZ (Fryxell and Prasad 1990; Esper et al. 2010). As of yet, a sediment distribution pattern for the two varieties for the Southern Ocean has to be documented (Armand et al., 2005, 2008). However, based on a study of the Amundsen and Weddell Seas the distribution of the two varieties offer a promising potential as quantitative proxy for austral summer SSTs (Allen, 2014). This study shows that core tops with high relative abundances of *E. antarctica*, as well as relatively high amounts of symmetrical and terminal valves, typical for the short colonies of *E. antarctica* var. *recta*, are associated with SSTs below 0.5°C and 10 to 12 months sea-ice cover (Allen, 2014).

In today's surface sediments *Chaetoceros* valves and RS show a bimodal distribution, because *Chaetoceros* species do not all have the same environmental preferences (Esper et al., 2010). Although certain species of *Chaetoceros* prefer near shore sea-ice environments (Garibotti et al., 2005), fossil Pleistocene *Chaetoceros* RS cannot easily be distinguished at species level (Gersonde and Zielinski, 2000; Esper et al., 2010), making them unsuitable as a proxy for sea ice. Generally, however, high percentages of *Chaetoceros* RS are associated with stratification of the surface waters, either through glacial runoff and sea-ice melting close to the Antarctic margin or through iceberg melting in the open ocean (Crosta et al., 1997). *Chaetoceros* subgenus *Hyalochaete* is known to overwinter in sea ice and may be able to seed the water column once the sea ice melts, leading to early-season blooms until nutrients are depleted (Alley et al., 2018). The formation of *Chaetoceros* RS is typically associated with nutrient depletion after phytoplankton blooms (Leventer et al., 1996). The highly silicified RS are highly resistant to water column and surface sediment dissolution (Crosta et al., 1997) and sink rapidly down the water column, thereby avoiding grazing (Rembauville et al., 2015). This makes them important contributors to carbon export to the ocean floor (Rembauville et al., 2016).

The seasonal sea-ice group is composed of *Fragilariopsis curta*, *F. cylindriciformis*, *F. cylindrus*, *F. obliquocostata*, *F. ritscheii*, *F. sublinearis*, and *F. vanheurkii*, which are all commonly found in the sea ice and highest in abundance (more than 20%) in surface sediments close to the summer sea-ice edge (SSE) with 9 – 11 months/yr sea-ice cover (e.g., Gersonde and Zielinski, 2000; Armand et al., 2005; Esper et al., 2010). The diatom species within the seasonal sea-ice group, such as *F. curta* and *F. cylindrus*, bloom during late summer and dominate the surface waters south of the PF and are particularly associated with the MIZ (Gersonde and Zielinski, 2000; Grigorov et al., 2014; Malinverno et al., 2016). It has been suggested that in an upper water column that is stabilized by the overlying meltwater lens from melting sea ice, *F. curta* and other seasonal sea-ice diatoms have an advantage over other diatoms due to a combination of their small size and low settling rates, while other species require mixing to stay in suspension (Leventer, 1998). However, because these seasonal sea-ice diatoms are very susceptible to dissolution (Grigorov et al., 2014), abundances are relatively low in the surface sediments underlying the high-productivity surface waters. Generally, their abundances increase towards Antarctica, which makes them good indicators of high annual sea-ice cover (Zielinski and Gersonde, 1997; Bárcena et al., 1998, 2002; Gersonde and Zielinski, 2000; Armand et al., 2005), also within fossil diatom records (Leventer et al., 1996; Leventer, 1998; Gersonde and Zielinski, 2000; Gersonde et al., 2003; Crosta et al., 2007, 2008; Riesselman and Dunbar, 2013). In particular, relative abundances of 3% *F. curta* and *F. cylindrus* have been used to trace the WSE in various Southern Ocean sediment cores (Gersonde and Zielinski, 2000; Bianchi and Gersonde, 2002).

F. rhombica is considered separately from the other seasonal sea-ice diatoms. Although generally very low in abundance in modern surface sediments, this species shows relatively highest abundances within the SSIZ, preferring slightly warmer summer SSTs in comparison to *F. curta* (Armand et al., 2005; Esper et al., 2010). An increased abundance of *F. rhombica* with respect to *F. curta* has been interpreted as a reduced competitiveness of *F. curta* due to slightly warmer temperatures and/or a reduction of sea ice during spring/summer (Denis et al., 2006; Crosta et al., 2007, 2008).

In Southern Ocean surface sediments, *F. kerguelensis* can be found in highest abundances north of the SSE (Crosta et al., 2005b). Surface-sediment abundances of *F. kerguelensis* increase sharply when summer SSTs reach values above 1°C (Crosta et al., 2005b, 2007). Instead, surface-sediment abundances of *F. curta* decrease sharply when summer SSTs reach values above 1°C (Armand et al., 2005), which is the reason that shifts between *F. curta* and *F. kerguelensis* have been interpreted as SST change (Crosta et al., 2007). Furthermore, high (>20%) surface-sediment abundances of *F. kerguelensis* are associated with <9 months of annual sea-ice cover, while highest abundances of *F. curta*

Figure 4 (next page): **(A)** Ternary diagram of the relative abundances of tetra-, penta-, and hexamethylated brGDGTs in samples obtained from core AS05-10 compared to global soils and peats, and sediments obtained from the Svalbard shelf. **(B)** iGDGT and brGDGT data and a TEX₈₆-based subsurface temperature reconstruction obtained from core AS05-10. Error bars of the subsurface temperature reconstruction show the width of the 10%-confidence interval according to the BAYSPAR calibration method. The blue shading marks the position of the Terminations (as in Fig. 2).

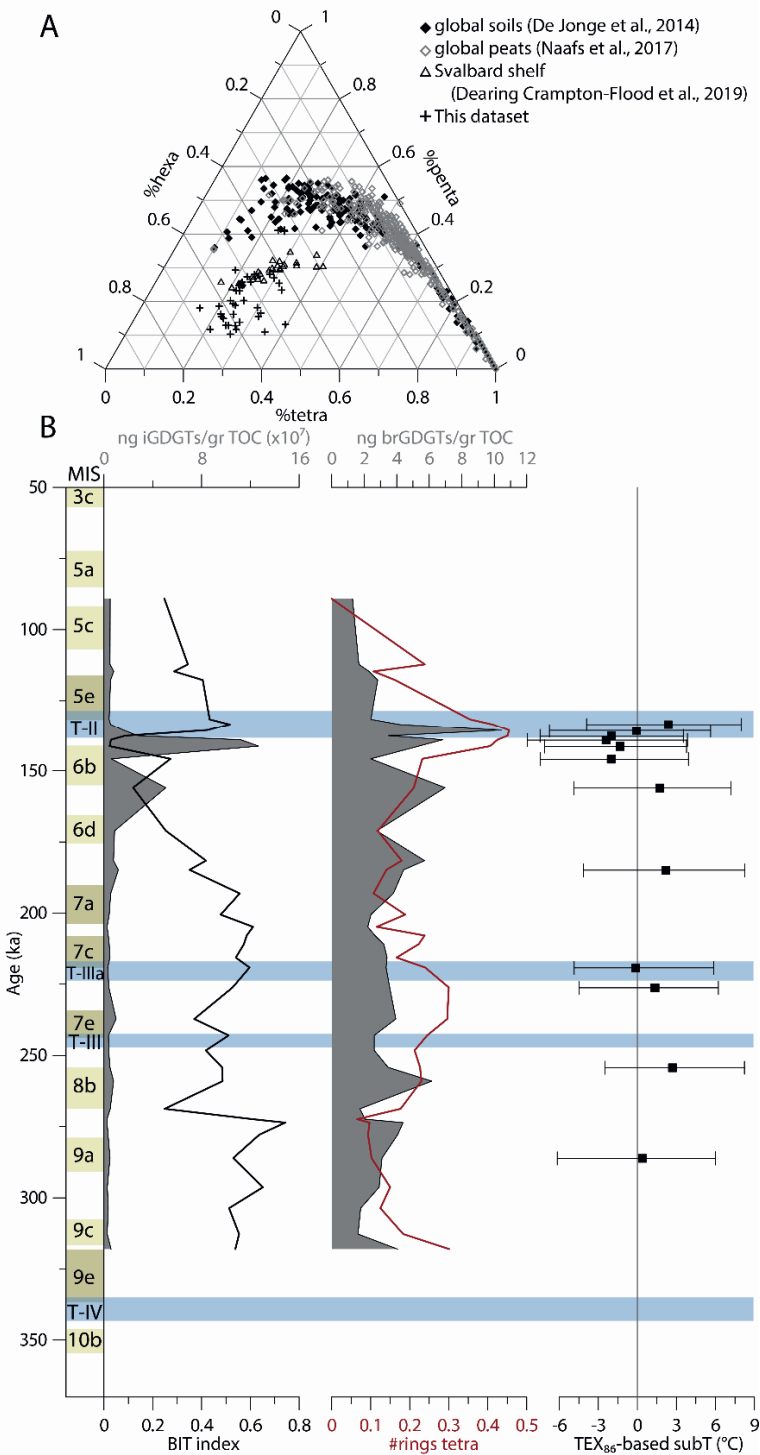
(20 – 30% in the Ross Sea sector of the Southern Ocean) are found between 9 and 11 months of sea ice (Armand et al., 2005; Crosta et al., 2005b). The shift in dominance between these two species therefore seems to mark the position of the SSE (Esper et al., 2010; Esper and Gersonde, 2014).

The open-ocean group is composed of *Thalassiosira eccentrica*, *Shionodiscus gracilis* (= *Thalassiosira gracilis*), *T. lentiginosa*, *Shionodiscus oestrupii*, *T. oliverana*, and *T. tumida*, as the genus *Thalassiosira* is typically associated with open water conditions (generally less than 4 months sea ice per year) during the growing season (Johansen and Fryxell, 1985; Crosta et al., 2005b; Campagne et al., 2016). However, differences between species within this group are important for our study. Highest relative abundances (>8%) of *S. gracilis* are particularly found in surface sediments underlying the SSIZ where it prefers much higher sea-ice conditions, while highest relative abundances (>12%) of *T. lentiginosa* (and highest relative abundances of other *Thalassiosira* species) are found north of the WSE (Esper et al., 2010). Notably, *Thalassiosira* species in general show increased relative abundances within the sediments when summer SSTs lie above ~1°C, with the exception of *S. gracilis* which is associated with summer SSTs lying between -1°C and 1°C (Crosta et al., 2005b; Esper et al., 2010).

6 Results

6.1 Magnetic susceptibility

Pronounced magnetic susceptibility (MS) minima correspond to pronounced biogenic silica (BSi) maxima, which precede each interglacial stage (Suppl. Fig. S1). This anti-correlation between MS and BSi records is in line with expectations, as increased biogenic input dilutes the terrigenous magnetic component of the sediment (Pudsey and Howe, 1998; Collins et al., 2012; Xiao et al., 2016b). High maximum values of MS are recorded at 722 cmbsf, 455 cmbsf and 291 cmbsf (Suppl. Fig. S1). The MS record is mainly used for age model reconstruction (see Suppl. Inf.) and will not be further discussed here.



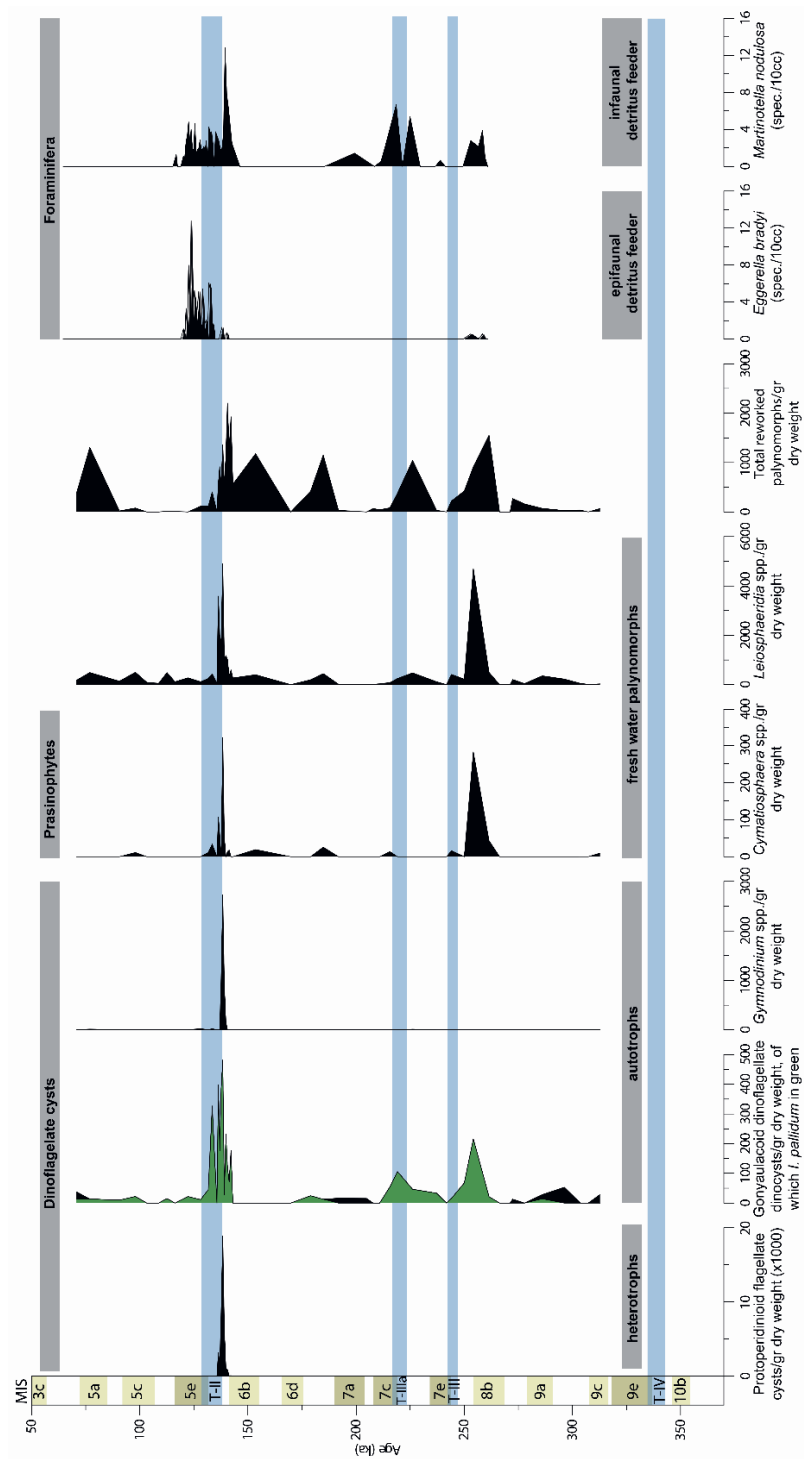


Figure 5: Palynological and foraminifer data obtained from core AS05-10. The blue shading marks the position of the Terminations (as in Fig. 2).

6.2 Ice-rafted debris

Ice-Rafted Debris (IRD) is present throughout the core (Fig. 2). High abundances of IRD (up to 135 clasts/10 cc) occur at 225, 383, 404, 499, 519, 584 and 743 cmbsf (~83, 140, 152, 213, 226, 265, and 360 ka, respectively). Peaks in the largest relative grain size (more than 5% of the IRD is larger than 2 mm) are located at 193, 233, 278, 395, 546 and 654 cmbsf (~70, 86, 103, 147, 242, and 307 ka, respectively). In general, the amount of IRD per 10 cc of sediment is higher during the glacial periods.

6.3 XRF: Biogenic barium (Ba_{bio}) and elemental ratios

Ba_{bio} concentrations were never below 230 ppm. Ba_{bio} shows no significant correlation with elemental ratios most sensitive to detrital input (Zr/Rb) or redox conditions (V/Cr, Ni/Co, U/Th) (Suppl. Fig. S13). Therefore, this proxy is a reliable indicator of biogenic production. The elemental ratios for bottom water oxygenation V/Cr, Ni/Co and U/Th are generally within the oxic field defined by Jones and Manning (1994) (respectively below 2.0, 5.0, and 0.75, Suppl. Fig S13)). However, the V/Cr and U/Th values occasionally cross the oxic-dysoxic threshold, suggesting dysoxic bottom-water conditions around 96, 112, 138, 244, and 337 ka (Fig. 3). Ni/Co never shows values above the oxic-dysoxic threshold as defined by Jones and Manning (1994) (Suppl. Fig. S13). Within these intervals where V/Cr and U/Th ratios suggest dysoxic bottom waters, Ba_{bio} might be reduced due to post-depositional remobilization (McManus et al., 1998).

The reliability of Ba_{bio} as a proxy for paleoproductivity is confirmed by the resemblance of the Ba_{bio} record to the BSi record, especially in the lower part of the core (Fig. 3). The tight link between Ba_{bio} and BSi has been used for reconstructing paleoproductivity at other Southern Ocean sites, with increased Ba_{bio} and BSi values during interglacials south of the PF (Bonn et al., 1998; Pudsey and Howe, 1998; Hillenbrand and Fütterer, 2001; Hillenbrand et al., 2003, 2009). Interestingly, our record shows that the timing of each Ba_{bio} peak lags that of the BSi around the onset of each interglacial (MIS 9e, 7e, 7a-c and 5e, Fig. 3). The largest lag can be observed around the onset of MIS5e.

6.4 Biogenic silica

Biogenic silica (BSi) weight percentages vary between 4% and 23%. Maxima are recorded during Terminations (Fig. 3). Highest values are recorded during T-III (~248 ka) and T-II (~137 ka), but also during MIS5c (~90-100 ka) and MIS5a (~81 ka).

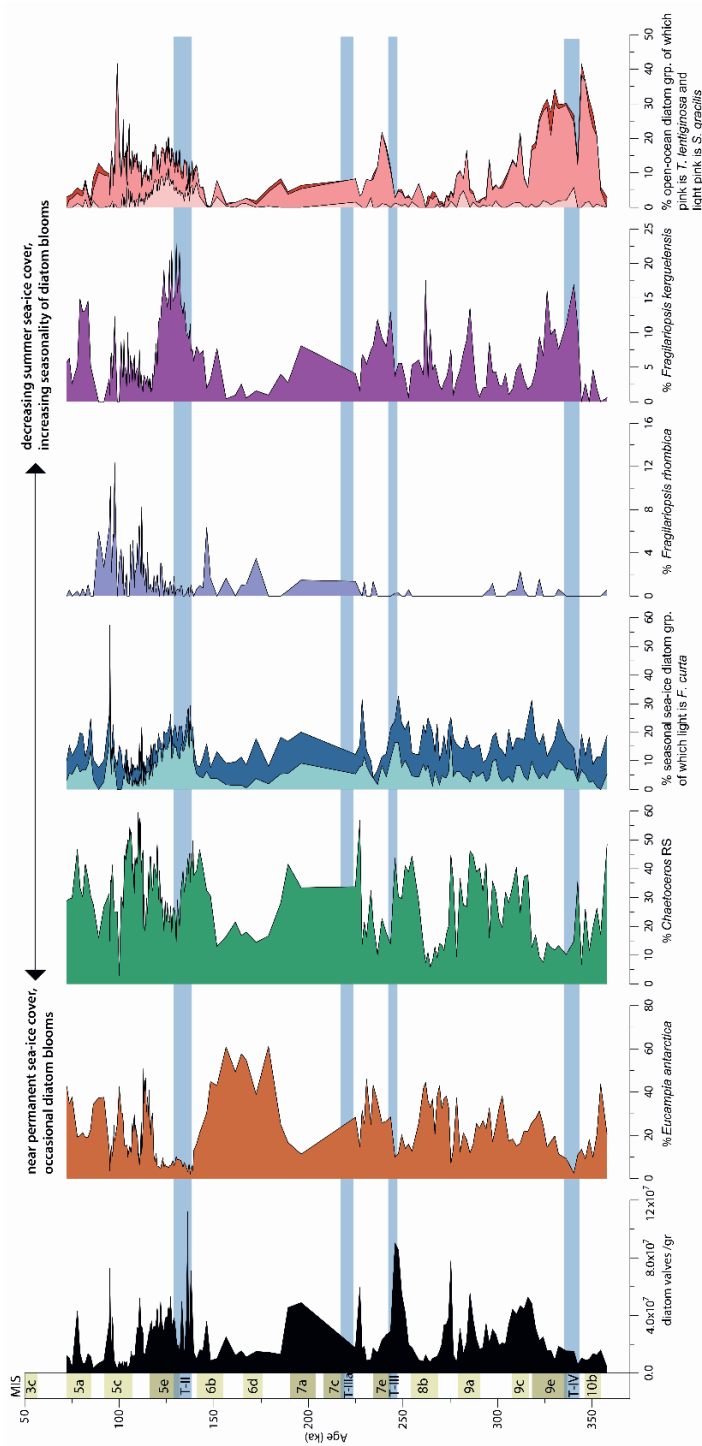


Figure 6: The relative abundances of diatoms obtained from core AS05-10. The blue shading marks the position of the Terminations (as in Fig. 2).

6.5 Organic carbon and nitrogen content and isotopes

Trends in weight percent organic carbon (%OC) and total nitrogen (%TN) are very comparable and show highest percentages at the onset of each interglacial stage. Peak values in both %OC and %TN coincide with maxima in BSi and/or Ba_{bio} (Fig. 3).

$\delta^{15}\text{N}$ values range between 3.4 and 6.8‰. Minima in $\delta^{15}\text{N}$ generally coincide with the onset of each major interglacial stage (MIS9e, MIS7e, MIS7a-c, MIS5e). Apart from those, three additional minima can be recognized at the onset of MIS9c (~310 ka), MIS5c (~110 ka), and MIS5a (~90 ka), respectively.

The intercept with the y-axis of the linear regression line of the %OC versus %TN plot lies at 0.013 %TN (Suppl. Fig. S14), indicating no significant influence on the $\delta^{15}\text{N}$ value due to the presence of inorganic nitrogen or due to terrestrial input.

6.6 Branched versus isoprenoid GDGTs and TEX₈₆-based subsurface temperatures

Maximum iGDGT concentrations around 140 ka (between 375 and 380 cmbsf) co-occur with maximum %OC values (Fig. 3; Fig. 4B). As abundances of branched GDGTs (brGDGTs) are relatively constant throughout the record, iGDGT concentrations determine the BIT index. The BIT shows a strong minimum of around 140 ka, otherwise being generally above 0.3 (Fig. 4B). The ternary diagram (Fig. 4A) shows that brGDGT compositions are very similar to those found on the Svalbard shelf (De Jonge et al., 2014; Sinninghe Damsté, 2016; Naafs et al., 2017; Dearing Crampton-Flood et al., 2019). In addition, the relative abundance of 6-methyl hexamethylated brGDGTs is high (between 56% and 94% of the total hexamethylated brGDGTs), which has been suggested to represent an adaptation to environments with a higher pH (i.e. sea water) (De Jonge et al., 2014), although such high relative abundances of 6-methyl brGDGTs are not commonly observed in a marine setting (values generally below 70%) (Sinninghe Damsté, 2016).

The composition of brGDGTs suggests that all brGDGTs are produced either *in situ* or have been transported from the Ross Sea shelf and are not derived from Antarctic soils. This was not unexpected, as soil production in glacial settings is low (Peterse et al., 2009). Nevertheless, our record shows #rings_{tetra} values increasing and decreasing during interglacial and glacial periods, respectively (Fig. 4).

Only 12 of 38 samples selected contained sufficient iGDGTs to calculate a reliable TEX₈₆ value. Most of these samples lie between 170 and 130 ka. The iGDGT data shows no indications of input from methanogenic or methanotrophic archaea (GDGT-0/Cren < 2 following Blaga et al. (2009), GDGT-2/Cren < 0.4 following Weijers et al. (2011), and MI < 0.5 following Zhang et al. (2011)) or other non-temperature related biases ($|\Delta\text{RI}| < 0.6$ following (Zhang et al., 2016)) (see Suppl. Table S1). Because all brGDGTs are produced *in*

situ, no samples have been discarded, because of high BIT values. TEX₈₆ values range between 0.34 and 0.44. When converted to subsurface temperatures using the BAYSPAR calibration, temperatures vary between -2.4°C and 2.7°C with a 90%-confidence interval of ±5.8°C (Fig. 4). Notably, our temperature reconstruction shows a minimum prior to Termination II and an increase towards the onset of MIS5e. Considering the much higher concentrations of iGDGTs in this interval compared to the rest of the record, these reconstructed temperatures are most reliable and most likely reflect subsurface warming at the onset of MIS5e.

6.7 Palynology

Only trace amounts of palynomorphs have been found: 34 out of 49 samples contain less than a 1000 palynomorphs per gram sediment. Four samples were completely barren. The *in situ* protoperidinioid dinoflagellate cysts in our samples include *Cryodinium meridianum*, *Nucicla umbiliphora* (**Chapter 3**), *Selenopemphix antarctica* and *Selenopemphix sp. 1* sensu Esper and Zonneveld (2007). *In situ* gonyaulacoids include *Impagidinium aculeatum*, *I. pallidum* and *I. variaseptum*. Generally, increased amounts of *in situ* palynomorphs co-occur with increased %OC (see Fig. 5). Notably, there is one prominent peak of dinoflagellate cyst (dinocyst) abundance between 143 and 134 ka (preceding the onset of MIS5e), coinciding with maximum %OC. Between 141 and 137 ka this peak is dominated by protoperidinioid (heterotrophic) dinocyst species: mainly *Selenopemphix antarctica* and *Cryodinium meridianum*. Apart from these protoperidinioids, also increased gonyaulacoid (mainly *Impagidinium pallidum*) and gymnodinioid (*Gymnodinium* spp.) dinoflagellate cysts are found in this interval, however in much lower absolute abundances (Figs. 5 and 7). Peak abundances of *I. pallidum* are also present downcore, in particular around 255 ka. Abundances of protoperidinioid dinocysts remain below 100 specimens/gram outside the 143–134 ka interval. Intervals with high abundances of the autotrophic species *I. pallidum* also show increased absolute abundances of *Leiosphaeridia* spp. and the prasinophyte *Cymatiosphaera* spp. (Fig. 5). Furthermore, several intervals with increased abundances of reworked Paleogene dinoflagellate cysts occur (*Vozzhenikova apertura* and *Spinidinium macmurdoense* (Bijl et al., 2013b)), as well as Paleogene pollen and spores. Generally, these high abundances of reworked material precede the peaks of *I. pallidum*, *Cymatiosphaera* spp. and *Leiosphaeridia* spp.

6.8 Benthic foraminifers

Low numbers of agglutinated foraminifer species have been found in parts of the record associated with interglacial deposition. Most dominant species are *E. bradyi* and *M. nodulosa*. *E. bradyi* shows highest values during MIS5e. *M. nodulosa* is most abundant in 198

the interval before MIS5e (Termination II). In comparison to *E. bradyi*, *M. nodulosa* is also more abundant during MIS7 (Fig. 5).

6.9 Diatoms

Absolute diatom valve counts show peak values at 137 and 245 ka, coeval with highest percentages of biogenic silica during Termination III and II (Fig. 6). Just prior to Termination IIIa diatom counts also peak, but there is no diatom data available for the period that encompasses Termination IIIa and interglacial 7a-c. Instead, diatom counts during Termination IV are relatively low, while BSi percentages are relatively high. Diatom valve counts only reach higher abundances during MIS9c and MIS9a. Diatom assemblages are dominated by alternating *Eucampia antarctica* and *Chaetoceros* resting spores (RS) (Fig. 6).

In core AS05-10 the highest abundances of *E. antarctica* are typically associated with the glacials, when also diatom abundance is low. Of the two varieties of *E. antarctica* only *E. antarctica* var. *recta* were found and no specimens of *E. antarctica* var. *antarctica*. *E. antarctica* in our paper thus refers to var. *recta*. %*E. antarctica* during MIS8 are lower than during MIS6, and the onset and termination of glacial MIS8 are also less pronounced in comparison to MIS6. Following the high %*E. antarctica* during the glacials, each glacial-interglacial transition is characterized by a clear sequence of increased relative abundances of individual diatom species (Fig. 6): reduction of %*E. antarctica*, an increase in %*Chaetoceros* RS, increase of %seasonal sea-ice diatom group, and finally increased %*Fragilariopsis kerguelensis* and %*Thalassiosira lentiginosa*. In general, this sequence of diatom species abundances is reversed when transitioning from an interglacial to a glacial state.

%*Chaetoceros* RS are always higher than 10%, but generally highest during and preceding maxima of diatom valve counts (Fig. 6). These peak values precede each glacial-interglacial transition, where declining %*E. antarctica* are replaced by a dominance of *Chaetoceros* RS, rising above 40%. After or coincident with the increase in %*Chaetoceros* RS preceding each interglacial, the seasonal sea-ice diatom group reaches values of 20% or higher (Fig. 6). Still *Chaetoceros* RS make up the largest part of the diatom assemblage. Notably, maxima in the seasonal sea-ice diatom group are coeval with maxima in the absolute diatom abundance and its overall trend is dominated by the changes in %*Fragilariopsis curta*, especially during T-II and T-III.

Following peak %*F. curta*, the %*Fragilariopsis kerguelensis* (>10%) rises to a maximum together with or followed by the open-ocean group (>15%) during each interglacial. Although the open-ocean diatom group follows the distribution pattern of *F. kerguelensis* during MIS5e, they peak after *F. kerguelensis* during MIS9e and MIS7e. This

group mainly consists of *Thalassiosira lentiginosa*. Notably, there are also increased % *Shionodiscus gracilis* during MIS5e, while it is generally very low in abundance in the rest of the record.

The glacial inception following each interglacial is characterized by increased % *Fragilariopsis rhombica*. Particularly high abundances occur during MIS5d and MIS5c. Minor peak abundances occur during the glacial stages.

7 Discussion

7.1 Glacial-interglacial sea-ice variability and primary productivity

7.1.1 Glacial phases

The low diatom valve abundances in combination with high relative abundance of *Eucampia antarctica* during glacial periods at site AS05-10 (Figs. 6 and 7), especially MIS6, is consistent with other Southern Ocean records (Kaczmarek et al., 1993; Xiao et al., 2016b). *E. antarctica* percentages in our record exceed those found in surface sediment samples south of the winter sea ice edge (WSE) within the seasonal sea-ice zone (SSIZ) (2%) (Zielinski and Gersonde, 1997; Esper et al., 2010), and even those found in surface sediment samples at or south of the summer sea-ice edge (SSE) (5%) (Esper et al., 2010). The high abundances of *E. antarctica* characterize what we define as the glacial phase in core AS05-10 (see Fig. 7) and suggest that the site was nearly permanently covered by sea ice during this phase. In support of this are the relatively high and/or increasing $\delta^{15}\text{N}$ values during the glacial phases of MIS6 and MIS8 (and the onset of MIS4) that coincide with relatively low Ba_{bio} values and BSi percentages (Fig. 7). This suggests high nutrient utilization during periods of low export productivity, indicating the $\delta^{15}\text{N}$ record reflects decreased nutrient supply, during glacial periods. A similar relation between $\delta^{15}\text{N}$ and glacial-interglacials was recorded in other locations south of the PF and is interpreted as reduced vertical deep-water nutrient supply resulting from (surface-water) stratification (François et al., 1997; Studer et al., 2015). A reduced nutrient availability is also supported by the low amounts of diatom valves/gr deposited during the glacial stages.

The presence of *Chaetoceros* RS during glacial phases (Fig. 7) suggests that despite the presence of sea ice, diatoms occasionally bloomed in – likely stratified – rare open-water conditions. Because *Chaetoceros* RS is characterized by high growth rates and high preservation potential (Crosta et al., 1997; Rembauville et al., 2015), occasional intense blooms would still allow the preservation of RS within the sediments resulting in *Chaetoceros* being the most abundant species after *E. antarctica* during the glacials. The relatively low Ba_{bio} values and BSi percentages are in accordance with rare open-water conditions that allow for primary productivity. Considering that Antarctic ice sheet

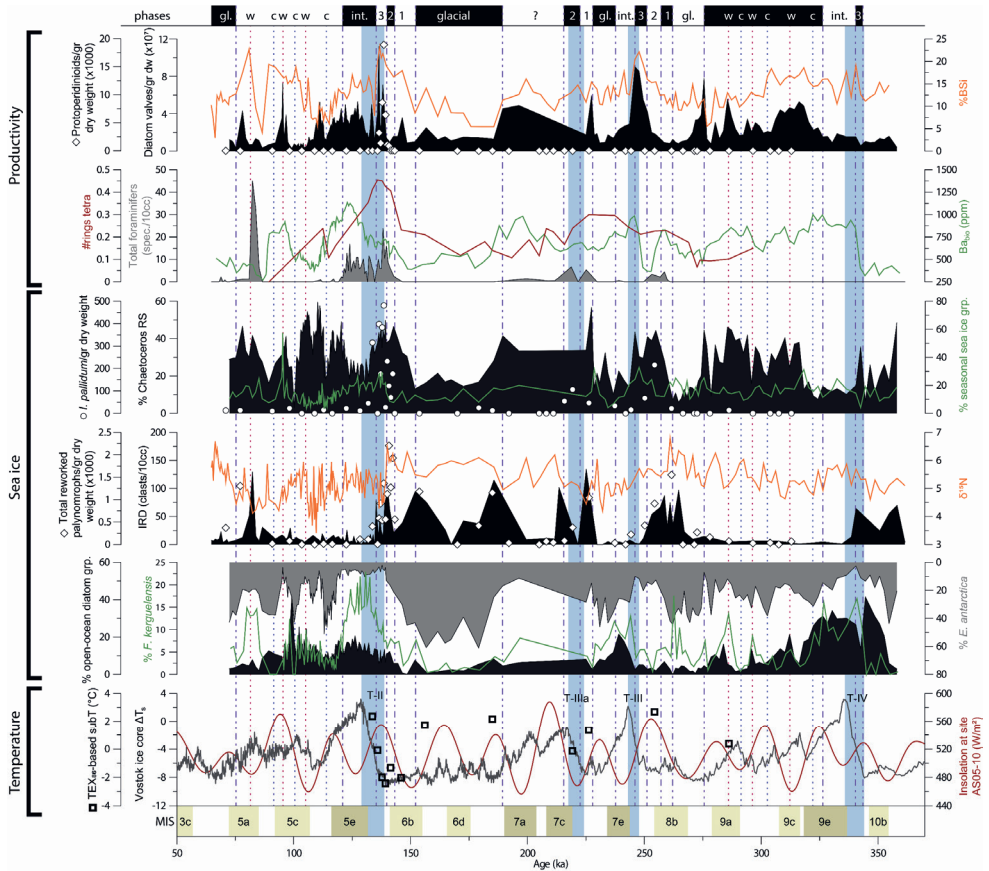


Figure 7: The proxies that are indicative of temperature, sea ice and productivity combined and related to the air temperature record of the Vostok ice core and local insolation. The blue shading marks the position of the Terminations (as in Fig. 2). The phases of each glacial (gl.) - interglacial (int.) transitions (see text) are indicated at the top of the figure. Dotted vertical lines correspond to warm (w) and cold (c) oscillations of the glacial inception following interglacial conditions.

reconstructions during the Last Glacial Maximum (LGM) suggest that the ice shelf edge was close to site AS05-10 (Denton and Hughes, 2002), such rare open-water conditions could be early-spring, ice-free areas that formed through spring warming and advection of sea ice from the ice shelf edge by katabatic winds or possibly polynya formation, which would allow for occasional diatom blooms of especially *E. antarctica* and *Chaetoceros*. Support for polynya formation near AS05-10 comes from a nearby sedimentary record of the LGM where the presence of the planktonic foraminifer *Neogloboquadrina pachyderma* has been interpreted as related to a polynya-driven environment (Bonaccorsi et al., 2007; Smith et al., 2010). Polynyas at the shelf edge may in general have been more frequent during glacial phases than today, due to the proximity of upwelling intermediate waters at

the Antarctic slope and strong katabatic winds that are funneled along depressions in the nearby paleo-ice sheet surface (Smith et al., 2010). However, the data do not indicate a permanent and/or efficient polynya present over AS05-10, because the relative abundance of *Chaetoceros* RS and high $\delta^{15}\text{N}$ values do not support upwelling of deeper waters at AS05-10 during the glacials (Denis et al., 2009b). Moreover, a diatom assemblage of an efficient latent-heat polynya would contain higher abundances of *F. curta* (Mezgec et al., 2017). We therefore interpret the *E. antarctica*/*Chaetoceros* RS dominated diatom assemblages as evidence for occasional wind-driven open-water conditions at the shelf edge in early spring (Fig. 8). The presence of generally high concentrations of IRD during the glacial phases (Fig. 7) supports a nearby ice shelf, although such high concentration could also be the result of the lower sediment accumulation rates during the glacials (Cofaigh et al., 2001).

The reconstructed low productivity during the glacial phases (MIS6 and MIS8 in Fig. 3) seems to disagree with the relatively high %OC and %TN found during the periods of glacial inception (MIS7a-b and MIS9a-d in Fig. 3). This could be the result of a closed sum effect resulting from the decreased influx of biogenic and terrigenous siliciclastics during glacials. Alternatively, the transport of OC and TN to the seafloor might be enhanced during the glacial phase with respect to the period of glacial inception due to the short intense blooms and the effective transport of the heavy silicified diatom species *E. antarctica* and *Chaetoceros* RS, that dominate the glacial assemblages. *Chaetoceros* and *E. antarctica* RS have been shown to contribute substantially to the organic matter flux to the sea floor at other Southern Ocean sites (Salter et al., 2012; Rembauville et al., 2015, 2016). The relatively high OC and TN could also be originating from an increase of organic matter derived from reworked (non-marine) sediments from times when Antarctica was vegetated. Indeed, part of the reworked palynomorph assemblage consists of reworked pollen and spores, which represent up to 40% of the total palynomorph assemblage during glacials. However, as the intercept with the y-axis in the %OC versus %TN plot equals nearly 0 (Suppl. Fig. S14), a substantial influence of (non-marine) reworked organic matter can be excluded.

During the glacial, quite surprisingly, sufficient iGDGTs were found in the samples, which allowed to reconstruct water temperature based on TEX_{86} (Fig. 4). It is possible that during the glacials at site AS05-10, some of the occasional diatom blooms allowed for sufficient transportation of iGDGTs and their preservation within the sediments. Diatom blooms in general have been shown to contribute to the transportation and preservation of iGDGTs within surface sediments (Yamamoto et al., 2012; Schouten et al., 2013; Mollenhauer et al., 2015). Subsurface temperatures between -2°C and 1°C (with a 90%-confidence interval of $\pm 5.8^{\circ}\text{C}$) have been reconstructed for the glacial periods (Figs. 4 and

7). However, the highest temperatures are derived from sediments with low iGDGTs concentrations and may therefore be less reliable. The *E. antarctica* assemblage only consists of the symmetrical valves of the variety *recta*. As high relative amounts of symmetrical and terminal valves of *E. antarctica* var. *recta* versus asymmetrical and intercalary valves have been associated with SST values below 0.5°C (Allen, 2014), diatom findings support the TEX₈₆-based temperature reconstructions.

A comparison between the glacial phases of MIS8 and MIS6 shows that MIS8 has higher Ba_{bio} and %BSi and is characterized by relatively lower abundances of *E. antarctica* and higher abundances of *F. kerguelensis*, in agreement with other Southern Ocean diatom records (Kaczmarek et al., 1993; Xiao et al., 2016b). This suggests that MIS8 may have been characterized by milder conditions in comparison to MIS6, allowing for more frequent open water, either through the retreat of the SSE to the glacial Ross Sea ice edge or through more efficient polynya activity (Mezgec et al., 2017). As a final remark, values for Ba_{bio}, %BSi and %*E. antarctica* during the glacial phase of MIS8 are very similar to those of MIS7d, also considered a glacial phase.

7.1.2 The glacial-interglacial transitions

We recognize three recurrent phases during each glacial-interglacial transition, representing a shift from dense sea-ice cover to seasonal sea ice: (1) ice-shelf break-up, (2) freshwater discharge and (3) the establishment of the MIZ over site AS05-10 (Figs. 7 and 8). The timing of these transitions coincides with air temperatures warming in the Vostok record of ~4°C warming (Fig. 7).

Phase 1: the diatoms show a shift from an *E. antarctica*-dominated assemblage to an assemblage dominated by *Chaetoceros* RS, indicative of nutrient depleted waters (Leventer et al., 1996). Peaks in ice-rafted debris (IRD) and in the concentration of reworked dinoflagellate cysts during (but also just prior and after) this phase (Fig. 7), suggest ice shelf break-up and transport of sediments from the Antarctic shelf towards the coring site, possibly aided by iceberg rafting. In support, the reworked palynomorphs recovered from AS05-10 are of Eocene-Oligocene age. Sediments of this age are known to be exposed at the seafloor in the Ross Sea (Wilson et al., 1998; Hannah and Fielding, 2001). Furthermore, high concentrations of IRD and low diatom concentrations have been associated with ice-shelf break-up and associated iceberg release (Bentley et al., 2005; Minzoni et al., 2015). Peak $\delta^{15}\text{N}$ values during phase 1 (and phase 2 prior to MIS5e) also suggest higher nutrient utilization. Icebergs can supply iron and are known to fertilize the Southern Ocean (Duprat et al., 2016). As the growth of *Chaetoceros* RS is iron limited (Salter et al., 2012; Rembauville et al., 2015, 2016), stratified waters and iron fertilization through the break-up of the Ross Sea ice shelf would provide an ideal environment for

Chaetoceros blooms, in line with our results (Fig. 8). Likely, increased stratification resulting from the increased input of freshwater due to the retreat of local glaciers and the associated break-off of large icebergs from ice shelves prohibits nutrient replenishment through vertical mixing. Enhanced nutrient utilization due to increased productivity is instead induced by a higher light penetration due to a decrease in sea ice cover. We interpret the combination of the proxy trends as an early warming signal. Although a direct relation with local insolation cannot be proven, phase 1 remarkably coincides with a period of increasing local insolation. Interestingly, this initial warming in our record precedes the atmospheric warming as recorded in the Vostok ice core, which could mean that ice shelf break-up was initiated by warming of the ocean waters. Although the Earth's climate is currently in a different state, the process of ice-shelf thinning and iceberg break-off due to basal warming occurs also today (Liu et al., 2015; Paolo et al., 2015) and results in an increased freshwater release, which seems to be promoting expansion of the sea-ice covered area around Antarctica (Bintanja et al., 2013).

Phase 2 is characterized by increasing fresh- and brackish water palynomorphs (*Cymatiosphaera* spp. and *Leiosphaeridia* spp.), while *Chaetoceros* RS reach peak abundances (Figs. 5 and 7). Although the taxonomic affinities of leiospheres are unknown, they have been associated with extensive presence of sea ice in paleoclimatic reconstructions (Wrenn et al., 1998; Troedson and Riding, 2002; **Chapter 2**). High abundances are associated with a freshwater surface layer: the summer sea-ice margin and disintegrating pack ice during spring (Mudie, 1992; Mudie and Harland 1996). Similarly, *Cymatiosphaera* spp. are typically associated with normal-to-low salinity and nutrient-rich surface waters and stratified waters (Mudie, 1992; Mudie et al., 2011) and have been interpreted as freshwater indicators in Antarctic paleo-reconstructions (Wrenn et al., 1998; Hannah, 2006). During this second phase, the gonyaulacoid autotrophic dinoflagellate cyst *Impagidinium pallidum* increased its abundances (Fig. 7). *I. pallidum* has been found in surface sediments underlying recently collapsed ice shelves (Pieńkowski et al., 2013b) and is known to withstand low-salinity waters (Zonneveld et al., 2013). This ecological niche may explain its absence during the interglacial phase, when longer open water conditions may favor other autotrophic dinoflagellates. Compared to phase 1, palynology and the relatively high amounts of *Chaetoceros* RS suggest the spring/summer melt and likely the retreat of the Ross Sea ice shelf results in a more frequent establishment of highly stratified fresh-brackish water lenses, promoting blooms of *Chaetoceros* and *I. pallidum* (Fig. 8). However, similar to phase 1, the relatively low abundance of seasonal sea-ice diatoms and the presence of IRD and reworked palynomorphs suggest that surface waters were still influenced by the presence of sea-ice and icebergs throughout most of the year. Such sea-ice coverage would have limited

productivity, which is confirmed by low total diatom abundances (valves/g, Fig. 7). Periodical freshening of the surface waters and stratification during phase 2 may have favored the formation of sea ice in the Ross Sea (Zhang, 2007). Notably, modern-day sea-ice concentrations in the Ross Sea show a non-linear, but on average increasing trend prior to 2014 (Comiso and Nishio, 2008; Parkinson, 2019), while the different water masses of the Ross Sea have also been freshening prior to 2014 (Castagno et al., 2019).

Phase 3: total diatom abundances (valves/g) and %BSi increase to a maximum during this phase (Fig. 7). *Chaetoceros* RS is still the dominant diatom species. *Chaetoceros* RS are heavily silicified and account for most of the high total diatoms in the sediment, being likely responsible for the peak in %BSi. During this phase, *Chaetoceros* RS is accompanied by peak abundances of the seasonal sea-ice diatom group, in particular *F. curta*. At present, this group appears during early spring when the sea ice is still present and dominates the surface waters during summer, particularly in the Marginal Ice Zone (MIZ) (Gersonde and Zielinski, 2000; Armand et al., 2005; Grigorov et al., 2014; Malinverno et al., 2016), the most productive ecological province of the Southern Ocean today (Fitch and Moore, 2007; Arrigo et al., 2008). *F. curta* and other seasonal sea-ice diatoms are small and they can easily float in stratified waters (Leventer, 1998). However, because of their small size, these seasonal sea-ice diatoms are very prone to dissolution (Grigorov et al., 2014), and only a high-productivity environment, like that of the MIZ, will favor their high occurrence in the sediment. The proximity of our site to the MIZ and therefore to the SSE during phase 3 is supported by the high total diatom abundance, %BSi and increasing $B_{a_{bio}}$. Today, the seasonal spring diatom blooms of the MIZ are suppressed by seasonal mixing of the surface waters during late summer due to increased winds (Arrigo et al., 1998a; Fitch and Moore, 2007). Disruption of the pycnocline allows for the settling and preservation of these dissolution-susceptible diatom species (Denis et al., 2006). Increased mixing of deeper waters with the surface waters during this phase is reflected in the decrease in $\delta^{15}N$ values, which is particularly clear during the MIS6/MIS5 glacial-interglacial transition. The drop in $\delta^{15}N$ values suggests decreased nutrient utilization during this phase, and probably an increased nitrogen supply from mixing with deeper waters. In contrast to phase 2, the relatively low amounts of IRD during phase 3, suggest surface water stratification during phase 3 are much less the result of the retreat of the Ross Sea ice shelf. Instead, the presence of *F. curta* in combination with high total diatom abundances and low $\delta^{15}N$ values suggests approximately three months of ice-free surface waters (Armand et al., 2005) and stratification due to the seasonal meltback of sea ice in spring/summer, then disrupted by (late) summer mixing (Fig. 8).

For the glacial-interglacial transition related to Termination IIIa (the onset of MIS7c), we lack the diatom data to fully recognize all three phases of the transition. Phase 1 and 2

Figure 8 (next page): An illustration the environmental conditions over site AS05-10 for the different phases of the glacial-interglacial transition described in the text based on the combined proxy records (see Fig. 7)

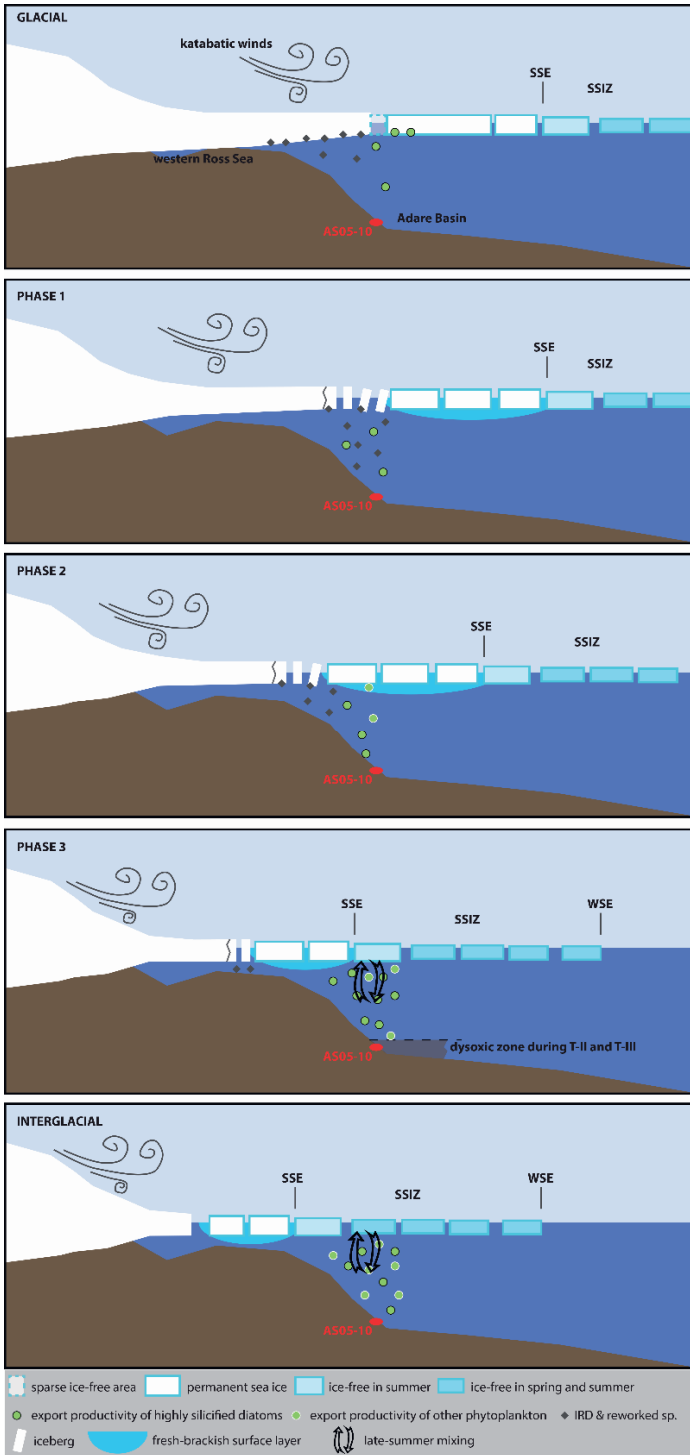
could be recognized based on high amounts of reworked palynomorphs together with IRD and high increased abundances of *I. pallidum*, respectively. Notably, Termination IIIa has been associated with ice-shelf break-up in the northern hemisphere as well, due to unusually high summer insolation following unusually low summer insolation at 65°N (Cheng et al., 2009).

Assuming we have recovered the full extent of the MIS10/MIS9 transition starting with the sharp drop in *E. antarctica* abundances around 355 ka, this glacial-interglacial transition differs in some respects from the MIS8/MIS7 and MIS6/MIS5 transitions. Surface water stratification appears to have been less intense/permanent prior to Termination IV (relatively low amounts of *Chaetoceros* RS and $\delta^{15}\text{N}$ values). Possibly, surface waters were already seasonally ice-free during MIS10 and/or meltwater release from the retreat of the ice shelf was less during this glacial-interglacial transition. Still increased IRD around 355 ka indicates ice-shelf break-up at that time, although the amounts are relatively low in comparison to the other glacial-interglacial transitions (Fig. 7).

During the MIS10/MIS9 transition, sea ice-free waters seem to have been reached very rapidly in spring, as *E. antarctica* is replaced by very high relative abundances of *T. lentiginosa*, which is a spring bloomer preferring low sea-ice concentrations (Crosta et al., 2005c; Esper et al., 2010). However, as *T. lentiginosa* produces large highly silicified valves (Shemesh et al., 1989), the record may be affected by preservation bias if silica dissolution or high bottom-water strength have removed the smaller (e.g., *Chaetoceros* RS, *E. antarctica*) and more dissolution-susceptible (e.g., *F. kerguelensis*, *F. curta*) diatom valves.

Both glacial-interglacial transitions related to Termination II (MIS6/MIS5) and III (MIS8/MIS7) show signs of oxygen-depleted bottom-water conditions (high V/Cr ratios, high %OC and high %TN; Fig. 3) in association with increased surface-water PP. But several differences between the MIS6/MIS5 and MIS8/MIS7 transitions suggest that bottom-water conditions at the onset of Termination II were more oxygen-depleted (Fig.7):

- 1) %BSi starts increasing during phase 1 comparably, reaching a maximum during phase 3, while Ba_{bio} shows a different trend, with a plateau during phase 3 of the MIS6/MIS5 transition, while rising sharply during phase 3 of the MIS8/MIS7 transition. Low oxygen conditions can result in post-depositional remobilization of barium (McManus et al., 1998).



- 2) Only phase 3 of the MIS6/MIS5 transition shows a peak in the concentration of heterotrophic protoperidinioid cysts. Protoperidinioid cysts are sensitive to oxic degradation (Versteegh and Zonneveld, 2002; Reichart and Brinkhuis, 2003), which also explains their absence in most of the record, while they typically dominate Southern Ocean surface sediments south of the PF (Esper and Zonneveld, 2002; Zonneveld et al., 2013).
- 3) BIT values show a decrease, reaching minimum values, during the transition phases preceding Termination II and not during the transition phases preceding Termination III. iGDGTs degrade more easily than brGDGTs (which, in our record, are exclusively marine-produced) in oxygen-rich environments (Huguet et al., 2008, 2009). Increasing iGDGT concentrations preceding Termination II, while concentrations of brGDGTs show little change (Fig. 4), therefore suggest increased organic matter preservation.

The abundant presence of iGDGTs during the second and third phase of the MIS6/MIS5 transition allows for the reconstruction of subsurface (0-200 m) temperatures (subT) based on TEX₈₆. Temperature increases from -2.4 to 2.3 (with a 90%-confidence interval of $\pm 5.8^\circ\text{C}$) (Fig. 4, 7). GDGTs are here interpreted to represent a spring/summer temperature signal, because archaeal communities bloom in spring after the sea-ice retreat (Murray et al., 1998; Church et al., 2003). Furthermore, GDGTs acquire pelleting to sink effectively to the sea floor (Schouten et al., 2013), and highest sedimentary GDGT fluxes are closely linked to highest organic matter, opal (diatom frustules) and lithogenic particle fluxes during the spring/summer season (Yamamoto et al., 2012; Mollenhauer et al., 2015). Today the difference between the summer SST and the 0-200 m depth-integrated temperature is 2°C . Assuming this difference has remained constant, reconstructed summer SSTs rose from -0.4 to 4.3°C during Termination II. The high abundances of *F. curta* and *Chaetoceros* RS in this interval would suggest sea surface temperatures between -1.5 and 1°C (Armand et al., 2005), in agreement with reconstructed TEX₈₆-based temperatures. The reconstructed (sub-)surface temperatures preceding peak warmth of MIS5e are 2.5°C warmer than (sub-)surface temperatures today (Locarnini et al., 2010). The few temperature estimates around the time of the MIS8/MIS7 transition show similar subsurface temperature estimates as those reconstructed for the MIS6/MIS5 transition (between 0 and 2°C with a 90%-confidence interval of $\pm 5.8^\circ\text{C}$), although these subTs are based on much lower iGDGT concentrations and could therefore be less reliable.

7.1.3 Interglacial phase

Maximum atmospheric temperatures over Vostok during peak interglacials coincide with decreasing seasonal sea-ice diatom abundances and a sharp rise in *F. kerguelensis* (although never > 25%), and subsequently an increase in open-ocean diatoms (mainly *T. lentiginosa*) (glacial phase in Fig. 7). The transition from relatively more *F. curta* to relatively more *F. kerguelensis* within the diatom assemblage marks the transition to a surface-water environment that more frequently experiences a longer sea ice-free season and summer SSTs above 1°C (Armand et al., 2005; Crosta et al., 2005b, 2007). Considering that *F. kerguelensis* and *T. lentiginosa* are early bloomers with respect to *F. curta* and other seasonal sea-ice diatoms (Grigorov et al., 2014), their increased abundances seem to reflect an advancement of the spring/summer melt and a prolongation of the blooming season. Increased annual PP is further supported by peak Ba_{bio} values, indicating increased export productivity. The longer blooming season and therefore increased export productivity of biogenic silica to the seafloor has attributed to the increased sedimentation rates during the interglacial phases with respect to the glacial phases, particularly for MIS5e (see Supplementary Information). For comparison, the depth interval containing 50 kyr of MIS6 is 60 cm, while the depth interval containing 10 kyr of MIS5e is 75 cm. However, this is not reflected in the height of %BSi or the diatom counts per gram, probably because of the simultaneous increase in detrital flux. Alternatively, other non-siliceous plankton species than diatoms have contributed to the maximum export productivity during the interglacial phase.

The high abundances of *F. kerguelensis*, which dominates the region north of the SSE today (Esper et al., 2010), reflect a more southward position of the SSE during MIS9e, MIS7e and MIS5e (no data for MIS7a-c available). The increase of *T. lentiginosa* during MIS9e, MIS7e and MIS5e (often coincident with a decrease in *F. kerguelensis*) could represent an even further reduction of annual sea-ice cover and proximity of the WSE (Crosta et al., 2005b; Esper et al., 2010). Still, *Chaetoceros* RS and the seasonal sea-ice diatoms account for at least 40% of the total diatom assemblage, suggesting that the surface waters overlying Site AS05-10 are still affected by the seasonal melt and lie within the SSIZ (Fig. 8).

Comparing the various interglacial phases, highest abundances of *F. kerguelensis* are found during MIS5e, suggesting this interglacial phase experienced furthest-reduced sea-ice cover, most-frequently reduced sea-ice cover, or both. However, a notable difference of MIS5e with the other interglacials is that a larger fraction of the open-ocean diatom group is composed of *S. gracilis* (Fig. 6). Although *S. gracilis* is an early bloomer like *F. kerguelensis* and *T. lentiginosa* (Grigorov et al., 2014), it is associated with cooler summer SSTs (Crosta et al., 2005b; Esper et al., 2010). This would suggest that SSTs during

MIS5e might have been cooler than during MIS9e and MIS7e, which is in contrast to deuterium-based air temperature reconstructions from the Vostok ice core (Petit et al., 1999). However, in contrast to *T. lentiginosa*, both *S. gracilis* and *F. kerguelensis* also bloom later during summer (Grigorov et al., 2014). Therefore, a more likely scenario would be that MIS5e experienced a longer blooming season due to more open waters in late summer, which allowed for the production and preservation of relatively more *S. gracilis* and *F. kerguelensis* versus *T. lentiginosa*.

Alternatively, shifts in relative abundances between the seasonal sea-ice diatoms, *F. kerguelensis* and the open-ocean diatoms *T. lentiginosa* and *S. gracilis* can be caused by differences in the susceptibility of these diatoms to dissolution. In general, however, the constant presence of dissolution-susceptible diatoms like *F. curta* and other seasonal sea-ice diatoms suggests that large changes in silica dissolution have not significantly influenced the record of site AS05-10.

The relatively high abundances of *F. kerguelensis*, *S. gracilis* and *T. lentiginosa* during MIS5e would suggest summer SSTs of at least 1°C (Crosta et al., 2005b; Esper et al., 2010). Although we have no TEX₈₆-based temperature reconstruction during the peak interglacial period, surface temperatures were possibly at or higher than the ~4°C reconstructed for Termination II. A recent compilation of several (summer) sea surface temperatures of the Southern Ocean for MIS5e, based on various proxies, shows estimates for the modern-day Antarctic Zone (50 - 60°S) between 3.1 and 6.1°C (Chadwick et al., 2020). One diatom-based temperature estimate from the SSIZ in the Weddell Sea (58.72°S) lies around 1.3°C (Bianchi and Gersonde, 2002; Chadwick et al., 2020). Considering the latitudinal position of site AS05-10 (70.835°S), our TEX₈₆-based temperature estimate for MIS5e appears therefore relatively high. However, our TEX₈₆-based temperature difference of 2.5°C warmer than today is supported by other polar estimates (McKay et al., 2011), which are higher than the 0.7°C global average difference (McKay et al., 2011), in part due to the effect of polar amplification. Together with other estimates, our results would contradict the conclusions by Serreze and Barry (2011) who suggested no Antarctic polar amplification in the near future, because surface waters around Antarctica probably remain cold enough to support sea ice, due to the presence of the Antarctic ice sheet and the cold katabatic outflow of surface winds over the coastal waters. In the Ross Sea, katabatic winds are particularly strong during winter (Nylen et al., 2004), where they control the ongoing formation of sea ice in Terra Nova Bay (Bromwich and Kurtz, 1984; Jacobs et al., 1985; Budillon et al., 1999). Although our diatom data also support sea ice during the winter, the summer temperatures are higher than at present. Seasonality seems to have increased during the last interglacial, and may therefore also increase due to future warming.

7.1.4 The glacial inception

In line with the study of the Past Interglacials Working Group of PAGES (2016), we have termed the period following an interglacial “the glacial inception”. Focusing on MIS5, the glacial inception following MIS5e is characterized by relatively lower PP and increased sea-ice concentrations, as indicated by the increased abundances of *Chaetoceros* RS, lower abundances of *F. kerguelensis*, and generally lower BSi and Ba_{bio} values (Figs. 6 and 7). During MIS5a-d, warm and cold periods can be inferred by the changes in abundance of the various diatom species, Ba_{bio} and %BSi. Peak Ba_{bio} and BSi values, high relative abundances of *F. kerguelensis* and open-ocean diatoms, and relative abundances of *E. antarctica* reaching a minimum, characterize the warmest phases, while the coldest phases are characterized by the opposite (red and blue dotted vertical lines in Fig. 7). The cold and warm phases correspond to stadials (MIS5b and d) and interstadials (MIS5a and c) in the Vostok ice core record. However, low relative abundances of *E. antarctica* and relatively high abundance of seasonal sea-ice diatoms suggest an additional warm/sea ice reduced phase during the late part of MIS5c, which coincides with peak solar insolation. Notably, peak local insolation at site AS05-10 during MIS5c also coincides with the highest abundances of *F. rhombica* (Figs. 6 and 7), a species that has been associated with relatively warm surface waters and/or low sea-ice concentrations compared to other sea-ice diatoms (Denis et al., 2006; Crosta et al., 2007, 2008). Although the data resolution is lower, a similar pattern of cold and warm oscillations can be observed for MIS9a-d.

7.2 Productivity at the sediment surface

Productivity at the sediment surface seems to be tightly linked to productivity in the surface waters. Increased abundances of the benthic foraminifer species *Martinottiella nodulosa* and *eggerella bradyi* occur during the period of highest PP, MIS5e (Figs. 5 and 7). Peak abundances of benthic foraminifers, particularly *M. nodulosa*, just prior to MIS5e show strong correlation with the IRD record and the abundance of reworked palynomorphs (prior to Termination III, IIIa and II), thus suggesting these peak abundances are caused by local reworking.

A dominant association of *eggerella* and *Martinottiella*, but in low amounts, is generally associated with a depositional environment below the calcite compensation depth (CCD) as they have high preservation potential (Mackensen et al., 1990; Harloff and Mackensen, 1997). Currently, a very diverse agglutinated benthic foraminifer assemblage dominates the calcareous benthic foraminifer assemblage in the western Ross Sea (Asioli, 1995). Furthermore, calcareous planktonic foraminifera are common in the western Ross Sea in the surface waters (Asioli and Langone, 1997; Bergami et al., 2009 and references therein). The absence in the AS05-10 record of both planktic and benthic calcareous

foraminifer species, as well as the lack of a diverse agglutinated benthic foraminifer assemblage, of which most use some form of calcite to glue their tests, seems to suggest carbonate dissolution by corrosive bottom waters.

In response to increased surface water productivity, sedimentary archaeal productivity was likely also promoted. Indeed, highest brGDGT concentrations are recorded during peak diatom export productivity during Termination II (Fig. 4). Increased archaeal productivity is, however, mostly reflected in the #rings_{tetra} (Figs. 4 and 7). Because input of soil-derived brGDGTs can be expected to be very low in glacial settings (Peterse et al., 2009) and dust-blown soil-derived brGDGTs have been shown to be of minor contribution to distal marine settings (Weijers et al., 2014), the input on acyclic brGDGTs must be very low. Therefore, the recorded trends of increased #rings_{tetra} during the interglacials and decreased #rings_{tetra} during the glacials must simply reflect increased input of marine brGDGTs at Site AS05-10. Alternatively, these marine brGDGTs were transported from the Ross Sea shelf to Site AS05-10.

8 Conclusions and implications for future warming

Core AS05-10 retrieved from the slope between the Drygalski basin and the Adare Basin records the response of the surface-water environment to glacial-interglacial variability in the late Pleistocene. Our multiproxy study identified three phases in each glacial-interglacial transition, which reflect the retreat of the seasonal sea-ice margin and warming of the surface waters.

Phase 1 is characterized by ice-shelf break-up and occasional ice-free areas. Phase 2 is characterized by meltwater runoff resulting in highly stratified waters. The progressive warming caused a retreat of the summer sea-ice edge, and brought the marginal sea-ice zone over site AS05-10 during Phase 3. During this phase the surface waters were seasonally stratified, instead of permanently stratified like during glacials, allowing for the replenishment of nutrients from the deep water through vertical mixing. Following the glacial-interglacial transition, an increased duration of ice-free conditions during the interglacials allowed open-water diatoms to proliferate. Increased (export) productivity during the interglacials is also reflected in the increased abundances of benthic agglutinated foraminifers and branched GDGTs. The highest productivity was reached during MIS5e due to an increased length of the blooming season and an increased supply of nutrients. TEX₈₆-based temperature values suggest summer temperatures of 2.5°C warmer than today during MIS5e.

Our record clearly reflects the migration of the highly productive marginal ice zone to higher latitudes during interglacials. It is therefore clear evidence that the position of the summer sea ice edge and therefore the size of the marginal ice zone (MIZ) are

influenced by past global warming phases. Future warming might shift the northern boundary of MIZ of the Ross Sea to even higher latitudes and could thereby reduce the size of this high-productivity zone (Sarmiento et al., 2004; Arrigo et al., 2008; Deppeler and Davidson, 2017).

Our record shows that warming is accompanied by an increased meltwater influx to the surface waters. Notably, the initial phases of ice-shelf break-up and surface water stratification precede the increase in air temperatures over Vostok and point to the fundamental role of the ocean on the cryosphere melting. It has been suggested that increased stratification could result in a shift from a *Phaeocystis*-dominated environment (like today) to a diatom-dominated environment, which could reduce the drawdown of CO₂ to the ocean floor (Arrigo et al., 1999; Steinacher et al., 2010; Vancoppenolle et al., 2013). We did reconstruct increased abundances of the fresh- and brackish water indicators *Leiosphaeridia* spp. and the prasinophyte *Cymatiosphaera* spp. in association with these highly stratified waters. Although initial conditions during current global warming are different from a glacial period, sea-ice cover in the Southern Ocean today is increasing due to increased meltwater runoff from the continent (Comiso and Nishio, 2008; Turner et al., 2009; Bintanja et al., 2013). If the melt phase at the onset of each glacial Termination in our record is equivalent to the increased freshwater release into the Southern Ocean today, we can expect sea-ice cover to decrease eventually in the Southern Ocean, like is happening in the Arctic already (Kay et al., 2011; Notz and Marotzke, 2012).

Supplementary information of chapter 5

Appendix A: Age model

This study focuses on the interval between 180 and 750 cm below sea floor (cmbsf) of core AS05-10. To construct an age model for this interval two tie points based on diatom event datums are available. However, a third tie point is obtained from the upper part of the core (<180 cmbsf) to get an estimate for the sedimentation rate above 388 cmbsf, which is the position of the upper diatom event. A final age model is established by subsequent tuning of the obliquity cycle captured within the Ti/Al record to the obliquity signal of the orbital signals captured in the deuterium isotope-based surface air temperature record (ΔT_s) of the Vostok ice core (Petit et al., 1999; Lüthi et al., 2008), with its age model based on the AICC2012 chronology (Bazin et al., 2013; Veres et al., 2013). We have chosen the Vostok ice core as a representation of regional surface air temperature, because it lies relatively close to our study site and is one of the few ice cores dating back to 400 kyr, thereby covering the age range captured within core AS05-10.

The diatom tie points

The diatom events present in core AS05-10 are the last occurrence (LO) of *Rouxia leventerae* and the LO of *Rouxia constricta*.

In the Atlantic sector of the Southern Ocean (Scotia Sea), the LO of *R. leventerae* (relative abundances below 1%) has been calibrated to 137.7 ± 4.1 ka based on a magnetic susceptibility chronology, which is correlated to dust Antarctic ice core dust concentrations (Xiao et al., 2016b). The LO of *R. leventerae* therefore marks the transition of glacial Marine Isotope Stage (MIS) 6 to interglacial MIS5.

In core AS05-10, *R. leventerae* shows a strong decline between 433 and 409 cmbsf (Fig. S1). Above 409 cmbsf there are some reoccurrences, which might be due to reworking. However, between 409 and 328 cmbsf relative abundances of *R. leventerae* still lie between 1% and 2% of the total diatom assemblage. We estimate the LO of *R. leventerae* between 409 and 368 cmbsf, at which point the presence of *R. leventerae* becomes more discontinuous and remains below 1% for a larger part of the record (Fig. S1). Its placement between 409 and 368 cmbsf is consistent with decreasing abundances of the diatom species *Eucampia antarctica*, associated with the MIS6-MIS5 transition (see also Xiao et al., 2016b). In agreement with Xiao et al. (2016b), the strongest decline of *R. leventerae* is recorded earlier, within MIS6.

Based on oxygen isotope-calibrated records (Ocean Drilling Program Sites 1093 and 1094) from within the Antarctic Zone of the Atlantic sector of the Southern Ocean, the LO of *R. constricta* was placed with high confidence at 0.28 Ma (Zielinski and Gersonde, 2002).

Notably, the LO of *R. constricta* is positioned earlier (0.44–0.64 Ma) in records from the Subantarctic and Polar Front Zone (Zielinski and Gersonde, 2002).

Within core AS05-10, influxes of between 1% and 3% of *R. constricta* are present between 603 cmbsf and 562 cmbsf, above which they disappear (Fig. S1). Reoccurrences of less than 1% of the total diatom assemblage occur above 409 cmbsf, which are likely caused by reworking. The youngest influxes of *R. constricta* above 1% lie between 603 cmbsf and 575 cmbsf. Considering the high concentrations of *E. antarctica* within this interval (Fig. S1), placement of the LO of *R. constricta* within this interval would be consistent with a LO datum for *R. constricta* during the middle of the glacial MIS8 (Zielinski and Gersonde, 2002).

The position of Termination I

A third tie point is obtained from the biogenic silica (BSi) and magnetic susceptibility (MS) records. Between the top of the core and 115 cmbsf, BSi percentages are plateauing at an average of 18%, after which there is a marked downcore decrease to 4% BSi at 147 cmbsf (Fig. S1). Similarly, MS values are relatively constant around 30 (10^{-5} SI) between the top of the core and 115 cmbsf, after which there is a sharp increase to peak values of around 64 (10^{-5} SI) at 132 cmbsf (Fig. S1). These BSi and MS shifts mark the establishment of the high-productivity conditions of the Holocene and therefore the position of Termination I (approx. 11.2–16.9 ka, Petit et al., 1999).

Orbital cyclicity

We have tested the records of biogenic silica percentages (BSi), biogenic barium (Ba_{bio}), titanium aluminum ratio (Ti/Al), magnetic susceptibility (MS), and the relative abundances of the diatom species *Eucampia antarctica* for orbital cyclicity. In many records these proxies show a marked difference between glacial and interglacial stages and have been used for age model reconstruction in previously published records (Burckle & Cooke, 1983; Burckle and Burak, 1988; Kaczmarek et al., 1993; Bertrand et al., 1996; Bonn et al., 1998; Pudsey and Howe, 1998; Brughmans, 2003; Hillenbrand et al., 2003, 2009; Collins et al., 2012; Xiao et al., 2016b). A different expression of glacial and interglacial stages can also be observed for each of these four proxies in core AS05-10. For example, the transition from MIS6 to MIS5e, marked by the position of *R. leventerae*, can be recognized in the four proxy records as an increase in the Ba_{bio} , Ti/Al and BSi records, and a decrease in both the MS and *E. antarctica* records. Notably, however, maximum/minimum values that mark peak productivity during MIS5e are not positioned at the same depth (Fig. S2). This suggests that orbital insolation affects the different proxies in different ways and/or each of the proxies is affected by different post-depositional processes.

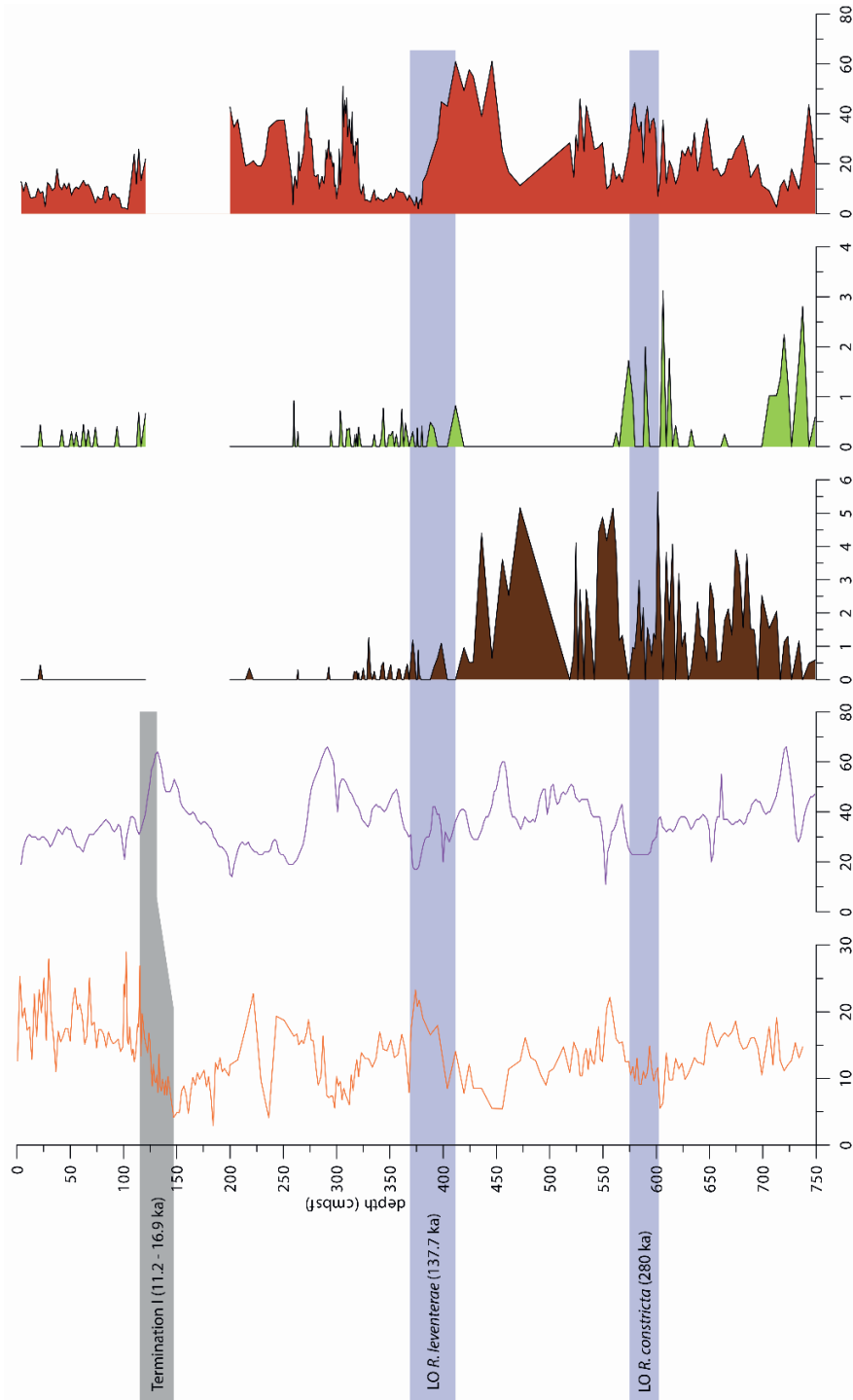


Figure S1: Diatom event tie points and the position of Termination I obtained from the biogenic silica, magnetic susceptibility, *Rouxia leventerae*, *Rouxia constricta*, and *Eucampia antarctica* records.

To see which of the proxy records best matches orbital insolation, the cycles filtered from the proxy records are compared to the cycles obtained from the orbital solution of Laskar et al., (2004) for the past 1 Ma: the 94-kyr eccentricity, 41-kyr obliquity, and the 23.7-, 22.3-, and 19.0-kyr precession cycles (Fig. S2). Based on the estimated positions of the diatom event datums, we expect that the length of one eccentricity cycle is 126 ± 26 cm, the length of one obliquity cycle is 55 ± 7 cm, and the length of a precession cycles range between 25 ± 3 and 32 ± 4 cm below 390 cmbsf (sedimentation rate is 1.34 ± 0.17 cm/kyr). Based on the estimated position of the LO of *R. leventerae* and the approximate position of Termination I, we expect that the length of one eccentricity cycle is between 202 ± 14 cm, one obliquity cycle is 88 ± 6 cm, and the length of precession cycles ranges between 41 ± 3 and 51 ± 3 above 390 cmbsf (sedimentation rate is 2.14 ± 0.15 cm/kyr).

Initial evaluation of cyclicity within the proxy records

Although it is apparent from the diatom datums and the position of Termination I that there are changes in sedimentation rate within this record, we test the full extent of each proxy record for significant cycles as a first approach. Using the Multi-Taper Method (MTM) of Meyers et al. (2012), cycle frequencies which are statistically significant (AR1 confidence levels $>90\%$ and MTM harmonic F-test confidence levels $>80\%$; Meyers, 2012) and lie within the estimated eccentricity, obliquity and precession frequencies have been plotted for each of the five proxy records (Fig. S2).

High AR1 confidence levels and harmonic F-test confidence levels above 95% within the eccentricity-cycle depth range (126 ± 26 – 202 ± 14 cm/cycle) can be observed for the Ba_{bio} , Ti/Al, BSi, and MS records. However, highest AR1 and harmonic F-test confidence levels within the obliquity-cycle depth range (55 ± 7 – 88 ± 6 cm/cycle) and within the shorter precession-cycle depth range (25 ± 3 – 41 ± 3 cm/cycle) are observed for the Ba_{bio} and Ti/Al records. Because of the presence of eccentricity, obliquity and precession cycles within the Ba_{bio} and Ti/Al records, we consider these records best suited for astronomical tuning. However, mismatches between the Ba_{bio} and BSi records as well as V/Cr ratios above 2 in parts of the record suggesting dysoxic conditions (Jones and Manning, 1994), particularly around 375 cmbsf, could indicate that Ba_{bio} may have been remobilized (McManus et al., 1998). Because, such post-depositional processes do not influence the Ti/Al record, which shows a strong correlation to the Ba_{bio} record, we have chosen to tune the AS05-10 core to the eccentricity, obliquity and precession cycles within the Ti/Al record. The cycles in depth domain that are observed within the Ti/Al records are 157 cm, 73 cm, and 30 cm in length. The 157-cm cycle lies half-way the expected eccentricity cycle range and similarly the 73-cm cycle lies half-way the expected obliquity cycle range. The 30-cm cycle lies within the expected precession cycle length for the core section below the LO of *R. leventerae*.

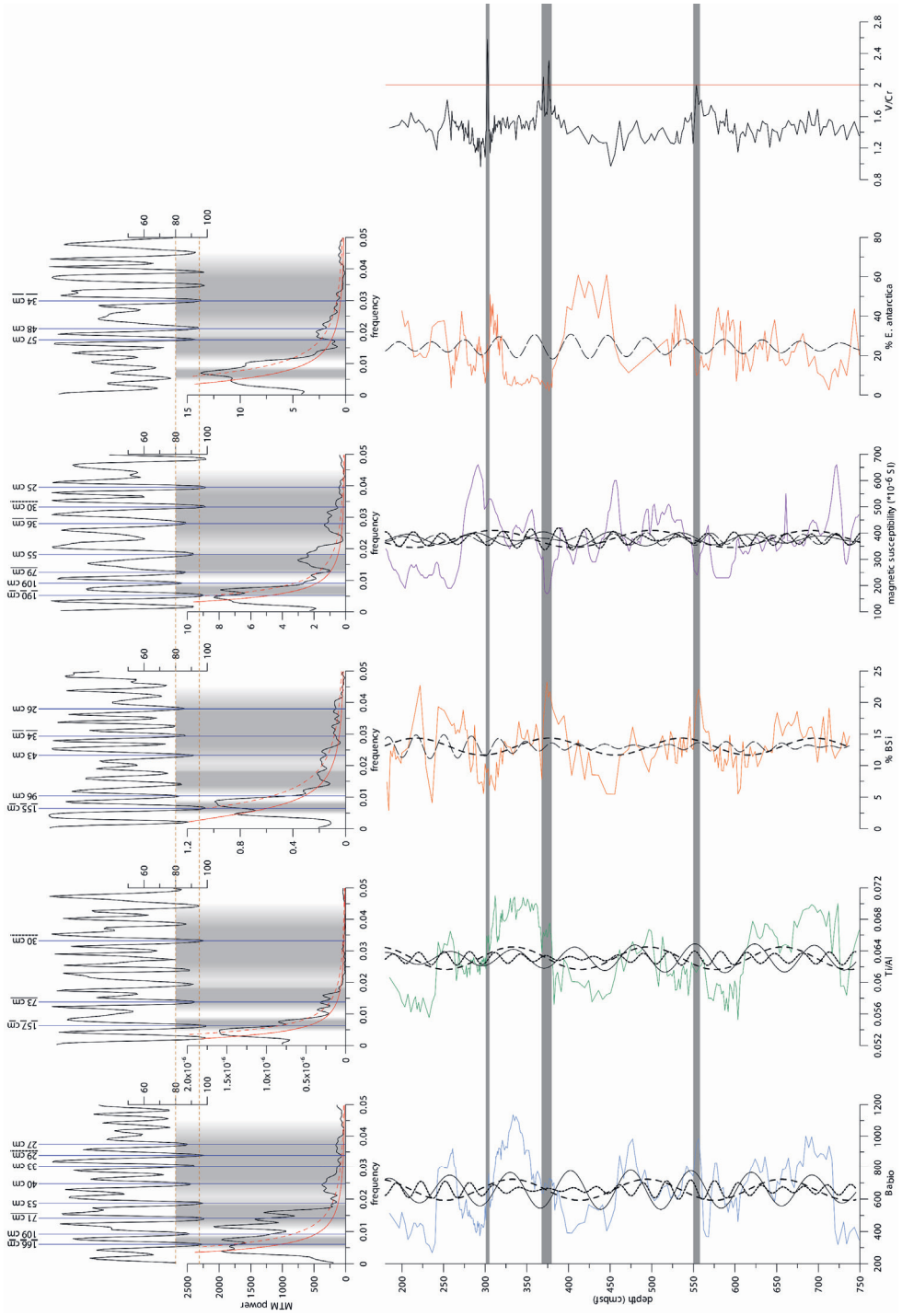


Figure S2 (previous page): Frequency spectra with AR1 confidence levels (90%, dotted red line in the MTM power spectrum) and Harmonic F-test confidence levels (dotted orange lines at 80% and 95% in the top figures) for the biogenic barium, Ti/Al, biogenic silica, magnetic susceptibility, and Eucampia antarctica records. V/Cr record on the far right shows intervals with possibly dysoxic conditions (values >2) (Dymond et al., 1992). Periods (in cm) are listed above the Harmonic F-test confidence levels. Those periods that are underlined (continuous and dotted black lines) are also plotted as a bandpass filter in the proxy record below it.

Evolutionary Harmonic Analysis and Evolutionary Average Spectral Misfit Analysis

As is evident from the diatom datums and the position of Termination I the sedimentation rate decreases downcore. However, considering that deposition at Site AS05-10 is partly controlled by biogenic sedimentation, it can be expected that sedimentation rates will change between glacial and interglacial stages. To account for these changes in sedimentation rate, we will further improve the age model by applying an evolutionary harmonic analysis (EHA) and an evolutionary average spectral misfit analysis (e-ASM) on the Ti/Al record using the Astrochron program in R (Meyers and Sageman, 2007; Meyers et al., 2012).

The EHA calculates a power spectrum for a set depth/time range (window) which moves along the entire record. In this way changes in the spectral features with depth/time can be evaluated and changes in sedimentation rate can be identified. Subsequently, the e-ASM tests a range of plausible sedimentation rates (i.e. time scales) given a set of target frequencies (i.e. orbital frequencies) for each of these depth/time slices and simultaneously evaluates the presence of these target frequencies statistically (Meyers and Sageman, 2007; Meyers et al., 2012). This method has been applied at deep-time records covering a few million years (Meyers et al., 2012; Fu et al., 2016; Salabarnada et al., 2018), but to our knowledge not yet at more recent shorter records in which orbital frequencies are expected to influence also the sedimentation rate.

Based on the initial tie points a moving-window size of 4 m was considered sufficient for the EHA to detect the short-term eccentricity signal and was shifted every 10 cm along the Ti/Al record, thereby producing a total of 26 frequency spectra (Fig. S3). The target frequencies for the e-ASM analysis were obtained from the orbital solution of Laskar et al. (2004) using the period between 0 and 1 Ma. By applying MTM analysis on the orbital solution the following five periods were obtained: 94.5, 41.0, 23.7, 22.3, and 19.0 kyr. A range of 50 sedimentation rates was tested between 1 cm/kyr and 3 cm/kyr, which covers the calculated sedimentation rates based on the initial tie points. All the spectral peaks with 80% F-test confidence level in each of the 26 frequency spectra of the EHA, are analyzed by the e-ASM analysis, and Monte-Carlo significance testing utilizing 10,000 simulations. Only those frequency spectra that have a Null Hypothesis Significance Level

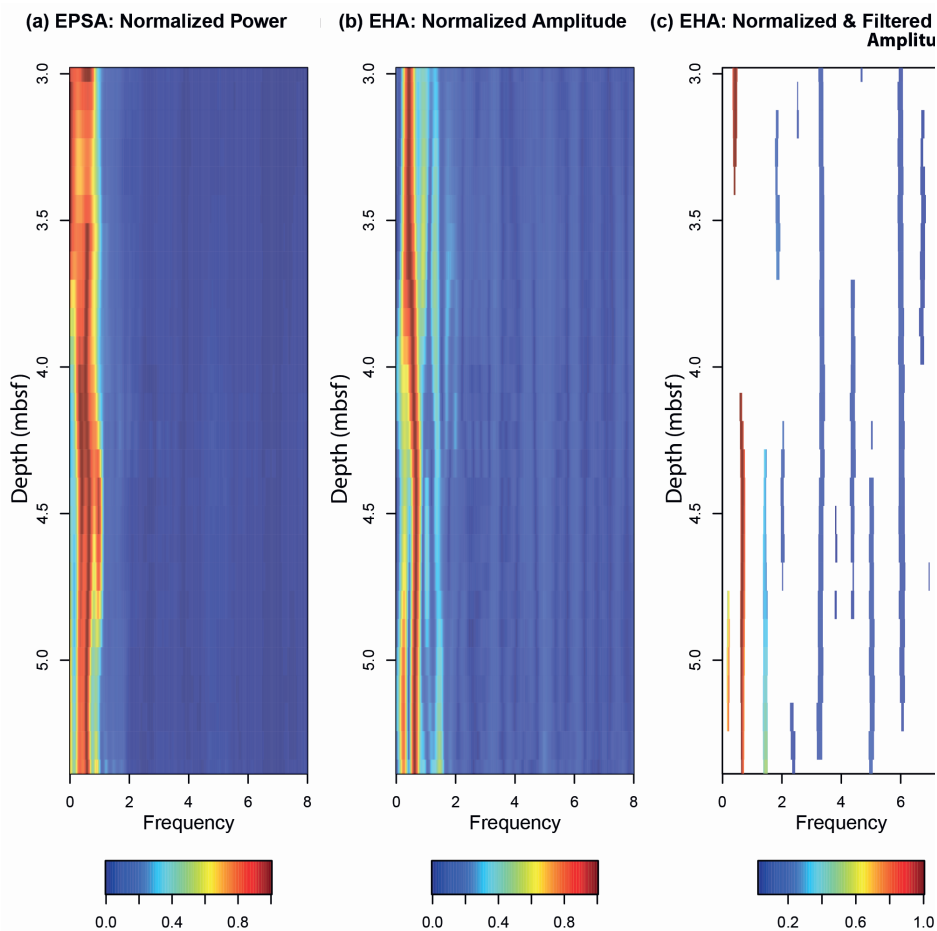


Figure S3: Evolutive Harmonic Analysis frequency spectrum of the original Ti/Al record in depth range.

(Ho-SL) below or equal to 0.1% are used for evaluation of the orbital target frequencies (Fig. S4, S5). To tune the Ti/Al record to time, the target period of 94.5 kyr was tracked in the EHA frequency spectrum using the e-ASM results for guidance (Fig. S6). The tracked eccentricity frequency in the EHA frequency spectrum is continuous and stable around ~ 0.75 cycle/m between 7.5 and 4.0 mbsf. Around 3.8 mbsf the tracked eccentricity frequency shifts to ~ 0.4 cycle/m, indicating an increase in sedimentation rate. This is consistent with the initial tie points, which indicate higher sedimentation rates above the LO of *R. leventerae*, which is also positioned around 3.8 mbsf. The tuning to the 94.5-kyr eccentricity cycle (Fig. S7) was further improved upon by repeating the EHA and e-ASM analyses on this eccentricity-tuned Ti/Al record to track also the 41.0-kyr obliquity

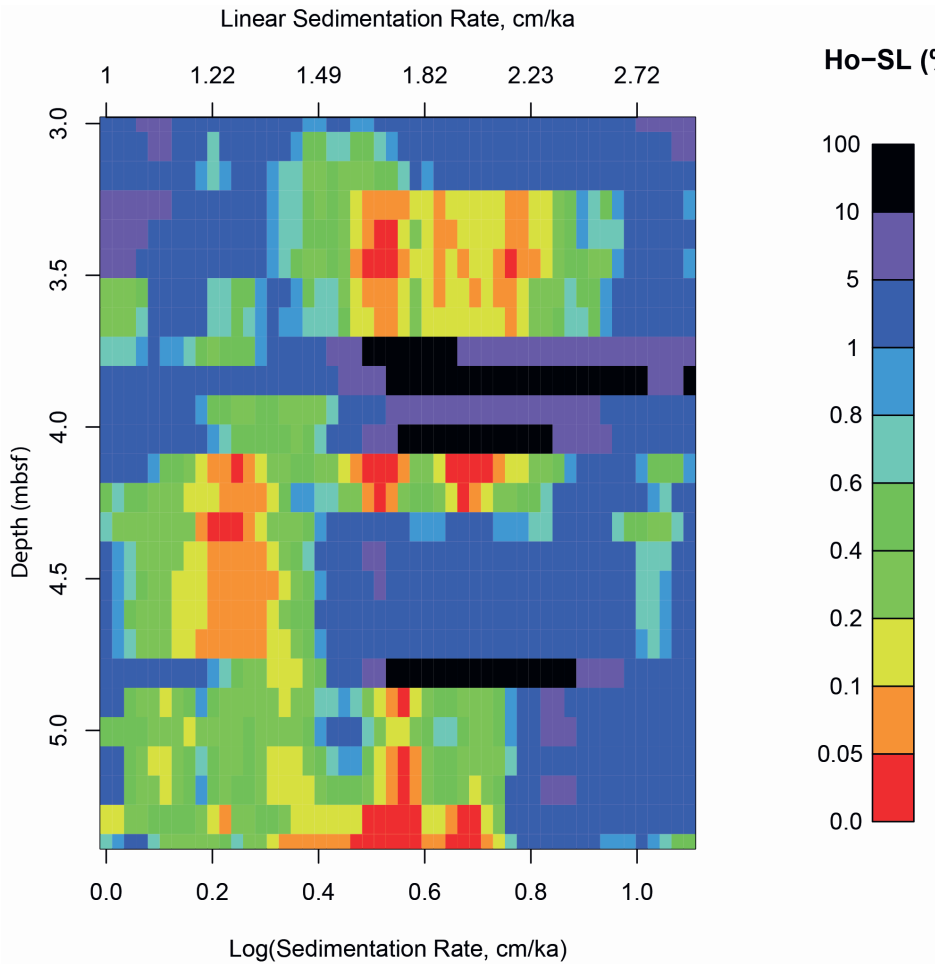


Figure S4: Probability of the linear sedimentation rates to be analyzed by the evolutive Average Spectral Misfit analysis of the original Ti/Al record in depth range.

frequency in the EHA frequency spectrum (Fig. S8), and subsequently to track the 19.0-kyr precession cycle in the obliquity-tuned Ti/Al record (Fig. S9).

The tracked obliquity frequency in the EHA frequency spectrum of the eccentricity-tuned Ti/Al record is discontinuous and increases between 200 and 150 kyrs (these kyrs are not the true age (ka) as this data series is not yet calibrated to any age model and therefore a floating tuned data series), indicating a decrease in sedimentation rate (Fig. S8). A decrease in sedimentation rate between 200 and 150 kyrs is consistent with the tuned position of MIS6 (Fig. S7) and with higher continuous frequency paths in the EHA frequency spectrum, which also show an upcore increasing trend (Fig. S8).

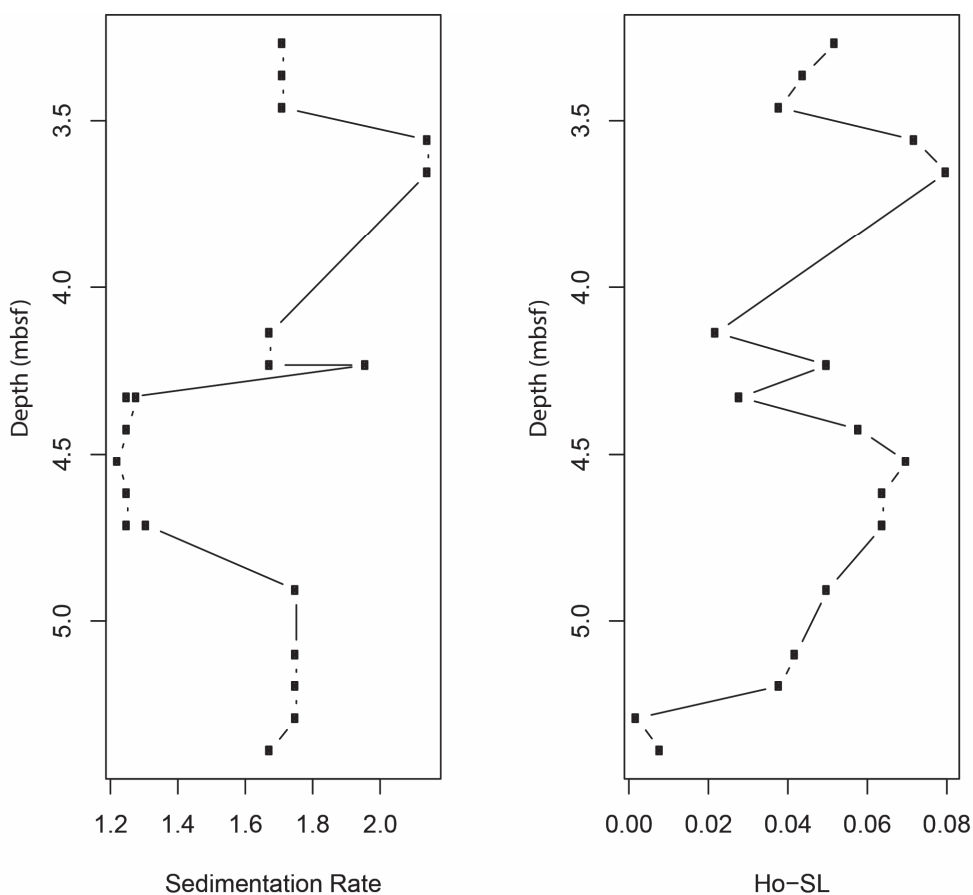


Figure S5: Estimated linear sedimentation rates based on the evolutive Average Spectral Misfit analysis of the original Ti/Al record in depth range.

Between 335 and 190 kyr, the tracked precession frequency in the EHA frequency spectrum of the obliquity-tuned Ti/Al record is relatively stable around 0.05 cycle/kyr (Fig. S9). At 190 kyr there is a sharp break, above which the EHA frequency spectrum shows two frequency pathways for tracking: around 0.04 cycle/kyr and around 0.055 cycle/kyr. The tracked frequency path below 190 kyr seems to be more continuous towards the lower frequency of 0.04 cycle/kyr, as are higher continuous frequency paths in the EHA frequency spectrum, indicating increased sedimentation rates. In addition, the break in the EHA frequency spectrum is located at the tuned position of the MIS6/MIS5 transition, so an increase in sedimentation rate can be expected. This all motivates our choice to track the lower frequency path around 0.04 cycle/kyr above 190 kyr. After tracking the precession frequency in the EHA frequency spectrum of the obliquity-tuned Ti/Al record a

final floating tuned data series was established. At this point, however, this tuned data series is still uncalibrated to an age model (Fig. S10, S11) (see also the R-code in Appendix B).

Evaluation of the tuned records

To evaluate the tuning of the AS05-10 core to the Ti/Al record, an MTM analysis has been performed on the tuned Ti/Al, Ba_{bio}, BSi, MS, and *E. antarctica* records to see if the orbital frequencies are expressed in these records now that changes in sedimentation rate are accounted for (Fig. S12). High AR1 confidence levels (>90%) and high Harmonic F-test confidence levels (>80%) can be observed for the eccentricity (91 kyr), obliquity (40 kyr) and the short precession (19 kyr) frequencies in the MTM frequency spectrum of the tuned Ti/Al record. Eccentricity and both short and long precession frequencies show high AR1 and Harmonic F-test confidence levels in the frequency spectra of the tuned Ba_{bio}, BSi, MS and *E. antarctica* records. Instead, the obliquity frequency is generally absent and only shows high powers in Ba_{bio} frequency spectrum, but with very low Harmonic F-test confidence levels. Notably, there are other frequencies that show high confidence levels for multiple of the studied proxy records: a 60±4-kyr period and a 32±3-kyr period.

As a representation of regional climate, we compare our tuned records to the reconstructed atmospheric temperature change (ΔT_s) recorded in the nearby Vostok ice core (Petit et al., 1999) with its age model based on the AICC chronology (Bazin et al., 2013). Regional air temperature is likely linked to surface water temperature, and therefore also sea-ice concentration and the related changes in primary productivity (PP). There is a remarkable similarity between the periodicities recorded in the five proxy records to the periodicities recorded within the Vostok ΔT_s record (with 106-kyr, 40-kyr, 30-kyr, 23-kyr and 19-kyr cycles). Because of this, we place high confidence in our reconstructed floating tuned record for core AS05-10. Notably, also a 30-kyr period is present in the Vostok ΔT_s record, which could be equivalent to the 32±3-kyr period recognized in the Ti/Al, Ba_{bio} and MS records of AS05-10.

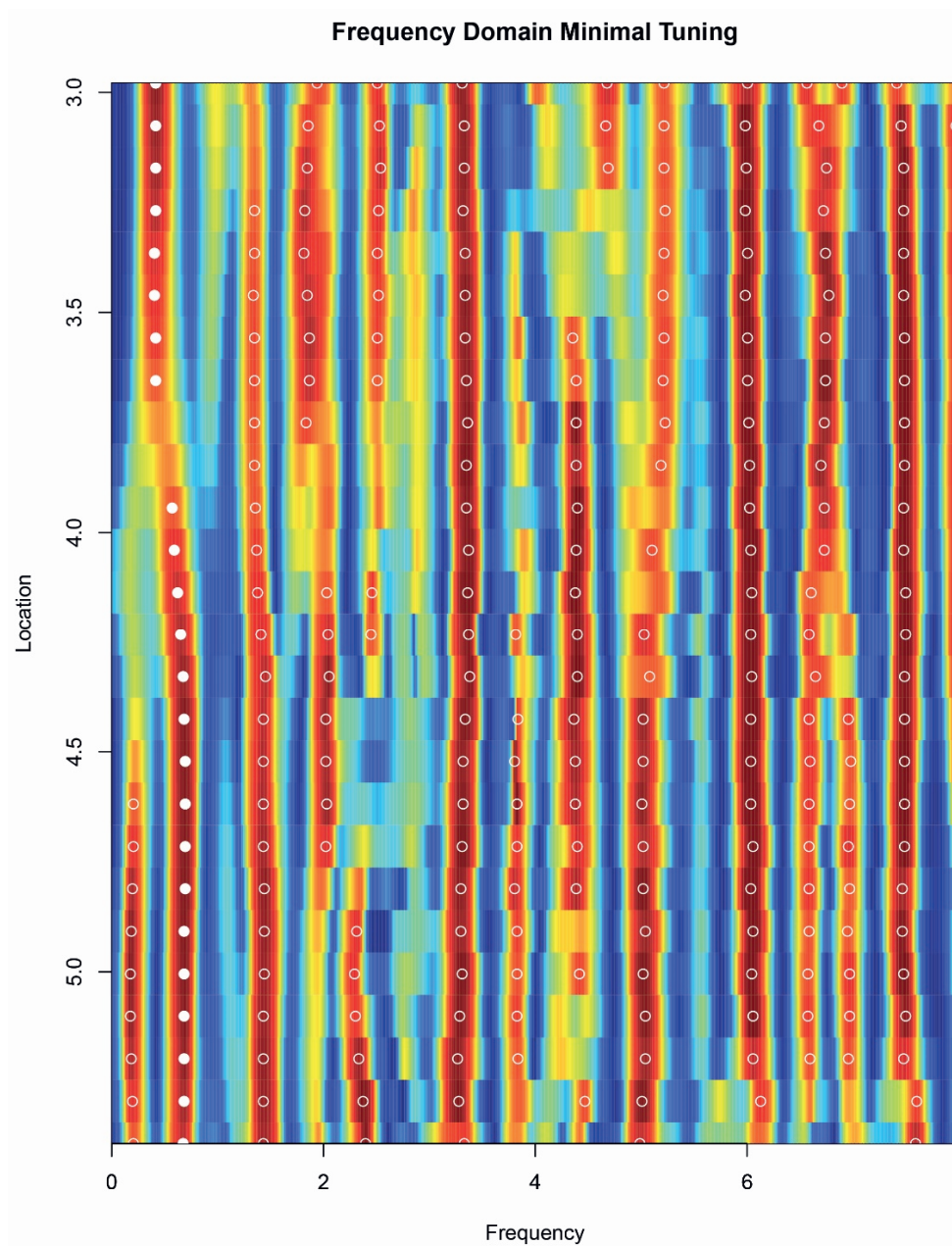


Figure S6: Tracking the eccentricity signal within the EHA of the original Ti/Al record in depth range.

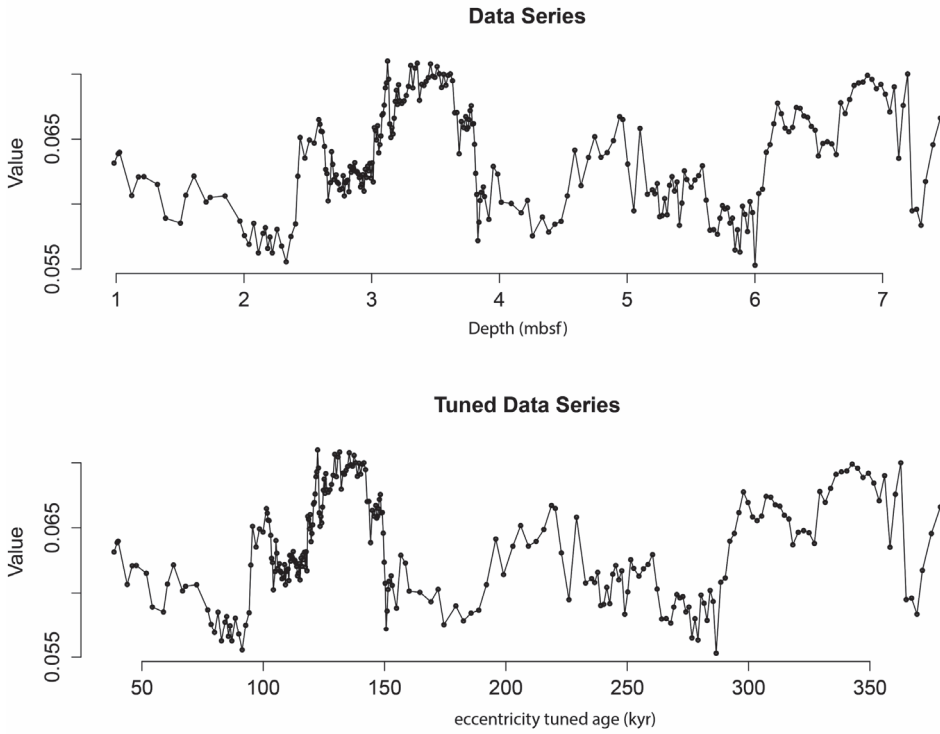


Figure S7: Comparison between the original Ti/Al record (in mbsf) and the eccentricity-tuned Ti/Al record (in kyr).

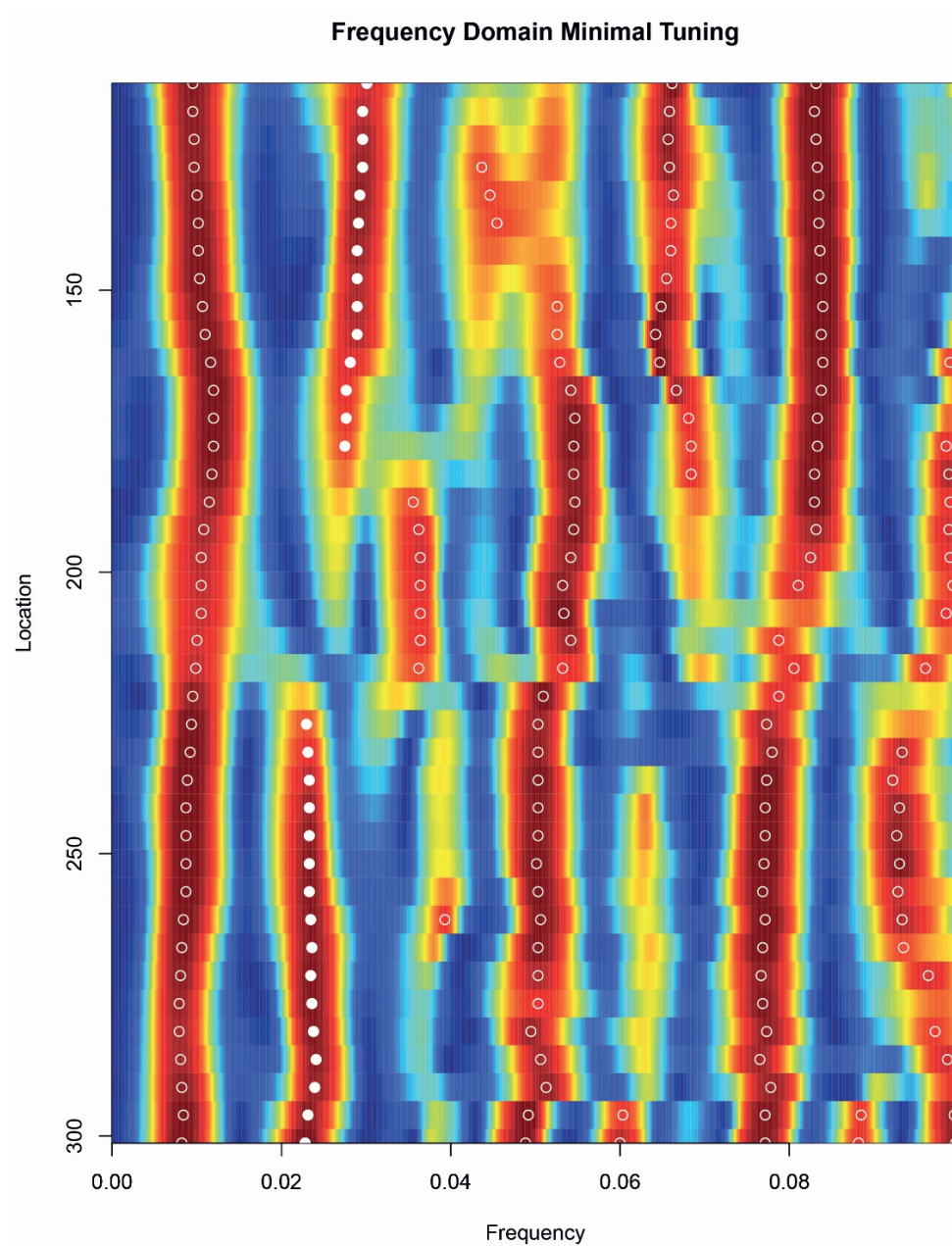


Figure S8: Tracking the obliquity signal within the EHA of the eccentricity-tuned Ti/Al record in depth time.

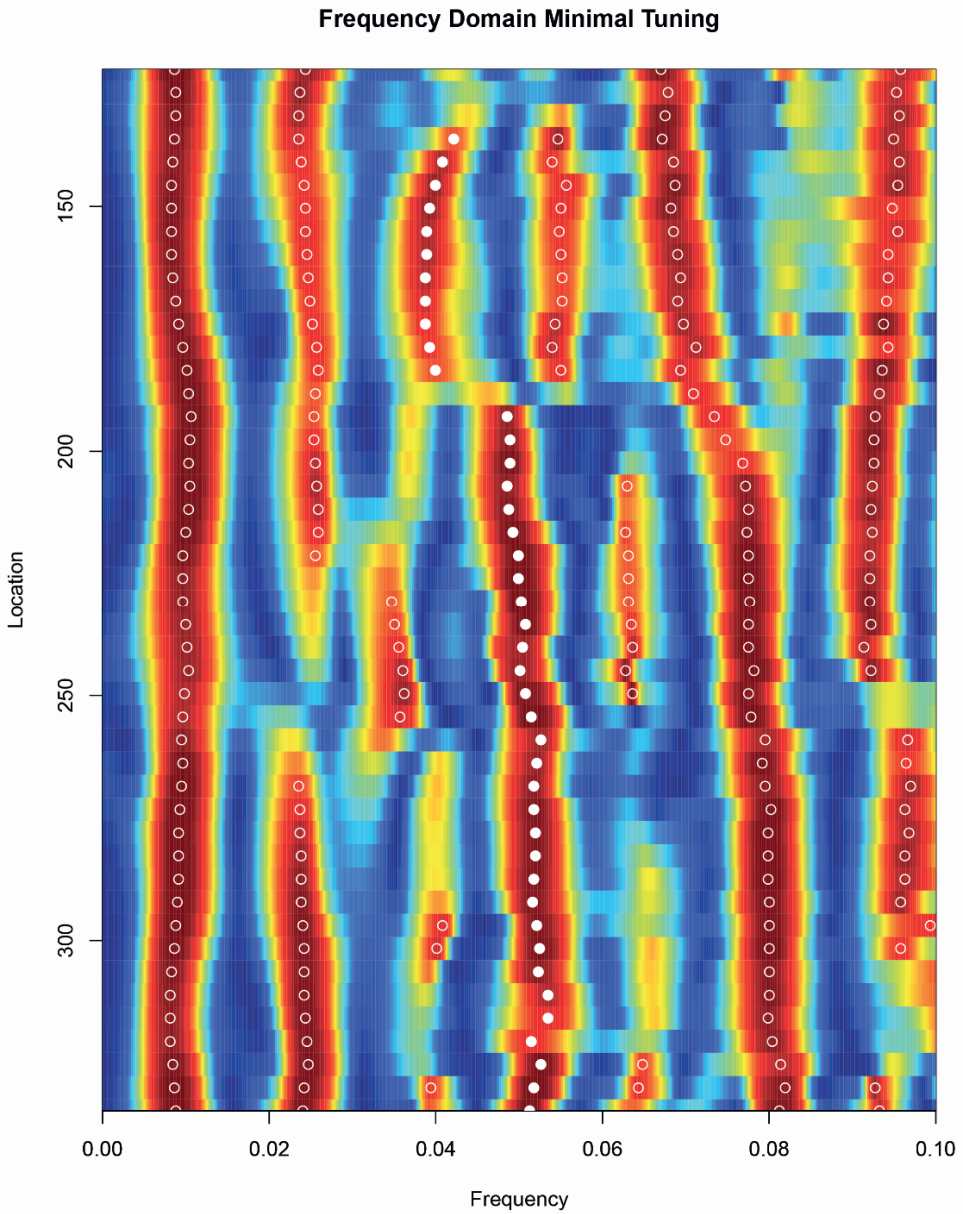


Figure S9: Tracking the 19-kyr precession signal within the EHA of the obliquity-tuned Ti/Al record in depth time.

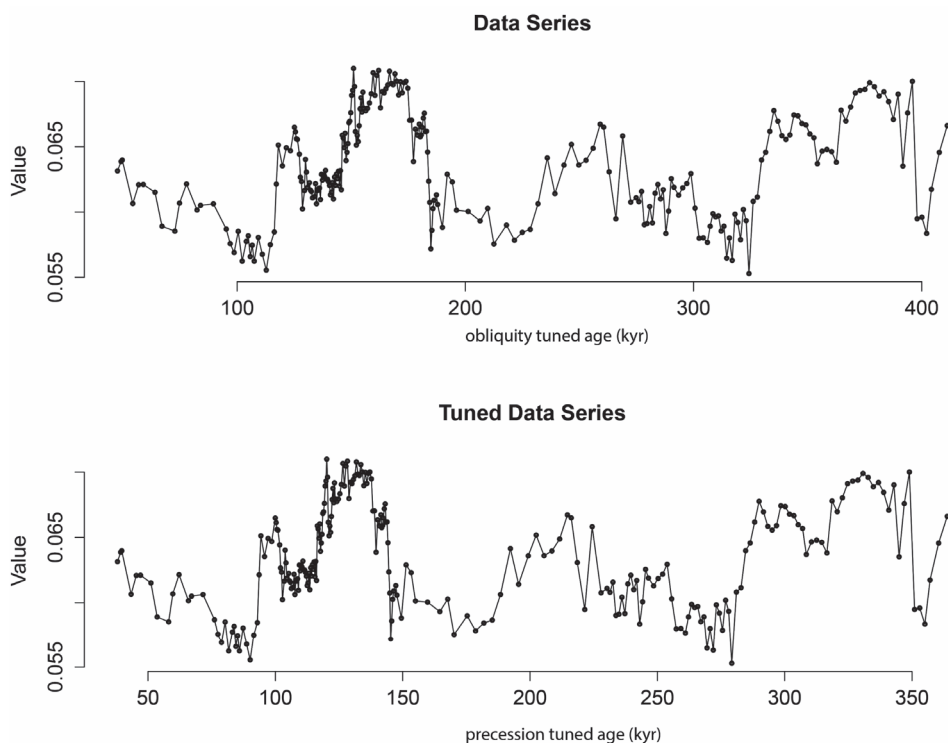


Figure S10: Comparison between the obliquity-tuned Ti/Al record (in kyr) and the precession-tuned Ti/Al record (in kyr)

Calibration of the tuned floating Ti/Al record to age

To establish a final age model for core AS05-10, the Ti/Al filtered obliquity was calibrated to the obliquity signal in the Vostok ΔT_s record. The obliquity signal in the Vostok ΔT_s record lags the obliquity signal present in the modeled local 70.8°S insolation (Fig. S12) by 3.4 kyr. We have chosen to calibrate the Ti/Al record to the AICC chronology of the Vostok ΔT_s record and not local insolation, because we expect that changes in the Ti/Al ratio are tied to the variations in regional climate reflected in the Vostok ΔT_s record. The exact mechanisms that determine the Ti/Al ratio at our study site are, however, not well known. Several mechanisms may play a role. For instance, the Ti/Al ratio could reflect changes in average grain size, which are driven by the strength of the bottom water currents. In turn, bottom-water current strength is likely tied to the formation of sea ice through bottom-water formation, which depends on the efficiency of coastal polynya formation in the Ross Sea and therefore wind strength and atmospheric conditions (Mezgec et al., 2017). Instead, changes in sediment provenance could have led to shifts in

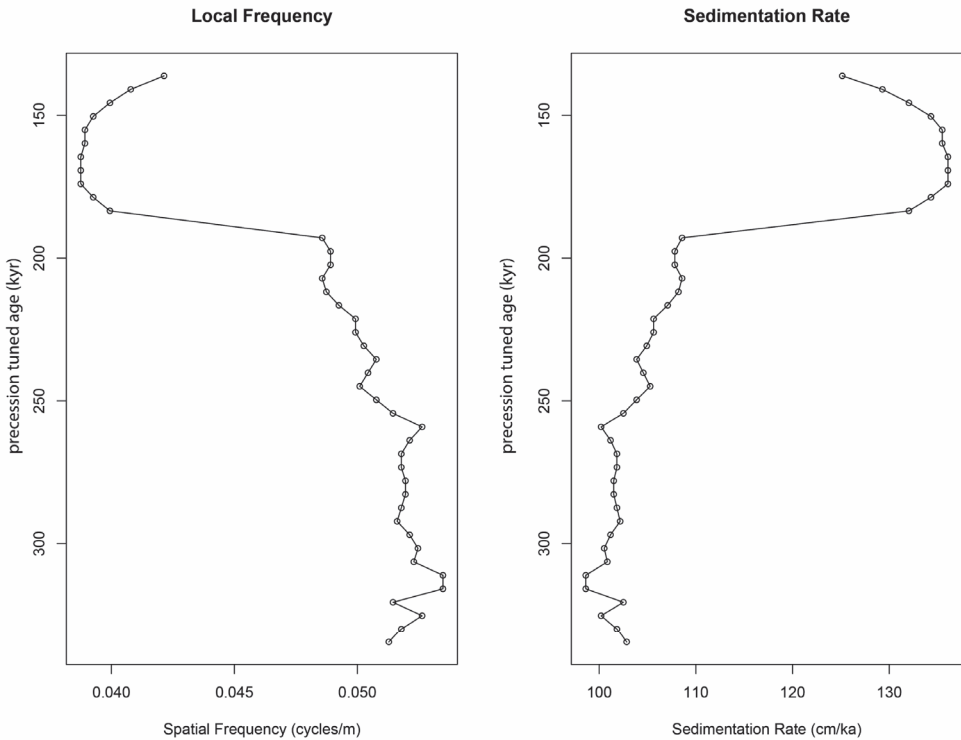


Figure S11: Calculated sedimentation rates based on the precession-tuned Ti/Al record.

the Ti/Al ratio at AS05-10, for instance through an increased input of dust (Calvert and Pedersen, 2007). The flux of dust towards Antarctica is known to increase during the glacial periods (Delmonte et al., 2020), which means that when ice shelves start retreating during the interglacials this dust is released into the water column, causing a shift in the Ti/Al ratio in the sediments. However, both Ti and Al can be incorporated in diatom frustules from the sea water, in which case changes in Ti/Al ratios can reflect changes in export productivity of opal to the sea floor (Dymond et al., 1997; Kryc et al., 2003). Because sedimentation at site AS05-10 is strongly influenced by diatom export productivity, this makes the Ti/Al ratio unreliable as a proxy for lithogenic input. The Ti/Al ratio thus likely reflects a combination of lithogenic input and export productivity. Nevertheless, considering that both Ti and Al are poorly mobilized during diagenesis, the Ti/Al ratio reflects the pristine sediment composition, meaning that also the filtered obliquity signal is not affected by post-depositional transformation.

Because the mechanism linking the Vostok atmospheric temperature to the Ti/Al record at site AS05-10 is not fully understood, we note that our tuning to the Vostok ΔT_s

record is a pragmatic choice, which means there is a certain degree of uncertainty about the exact tuning of the age model. If the obliquity signal within the Ti/Al record is a direct response to local insolation the onset of the glacial-interglacial transitional phases described in the main text would be 3.4 kyr earlier. Alternatively, it has been shown that the obliquity signal in the benthic $\delta^{18}\text{O}$ stack, reflecting northern hemisphere ice sheet waxing and waning, lags the Vostok ice core record by 3.5 kyr (Suwa and Bender, 2008). If the Ti/Al ratio at site AS05-10 is in any way determined by the strength of the thermohaline circulation, which is controlled by the extent of the northern hemisphere ice sheet, this would place the onset of the glacial-interglacial transitional phases described in the main text 3.5 kyr later. This ± 3.5 kyr uncertainty with respect to the chosen tuning to the Vostok ΔT_s record, does not affect the conclusions in the main text significantly, because the onset of phase 1 of the glacial-interglacial transition precedes the glacial Terminations by more than 3.5 kyr.

We place confidence in our age model, because this tuning independently places sharp increases in the Ba_{bio} record and the relative abundance of *F. kerguelensis* coeval with the sharp rise of the Vostok ΔT_s associated with the glacial Terminations. These proxies, reflecting primary productivity and sea ice-free surface waters in summer are expected to respond directly to increased atmospheric temperatures. By calibrating to the obliquity signal in the Vostok ΔT_s record, we find also that maxima in the 19-kyr precession cycle filtered from the Ti/Al record line up with the 19-kyr precession cycle within the modeled local 70.8°S insolation (Fig. S12). This strongly supports our age calibration and indicates that in addition to a response to obliquity, synchronous with atmospheric temperatures, the Ti/Al record is also influenced directly by local insolation. Notably, this means that precession filtered from the Ti/Al record does not follow the precession within the Vostok ΔT_s record, which behaves opposite to local 70.8°S insolation and tracks northern hemisphere insolation (Suwa and Bender, 2008).

In further support of this age calibration is the fact that the calibrated age for the LO of *R. leventerae* (at 137.7 ka) by Xiao et al., (2016) falls within the upper end of the estimated range for the position of the LO of *R. leventerae* (Fig. S12). Similar to the records from the Scotia Sea the largest decline of *R. leventerae*, marked by the lower boundary of the estimated range for the position of the LO of *R. leventerae* (at 409 cmbsf, Fig. S1), is positioned within MIS6 (Xiao et al., 2016b). According to our age model for AS05-10, the position of the LO of *R. constricta* is younger than 280 ka (Fig. S12), which is its position at ODP Site 1093 (Atlantic sector of the Southern Ocean), but falls within the range of 240–300 ka given for its position in ODP Site 1094 (Atlantic sector of the Southern Ocean) (Zielinski and Gersonde, 2002). Based on these records, it seems that in the Atlantic sector of the Southern Ocean *R. constricta* disappears earlier in the more northerly located

records. As AS05-10 is positioned about 20° further south than Site 1093, a younger LO of *R. constricta* at site AS05-10 would be consistent with the observations in the Atlantic sector of the Southern Ocean.

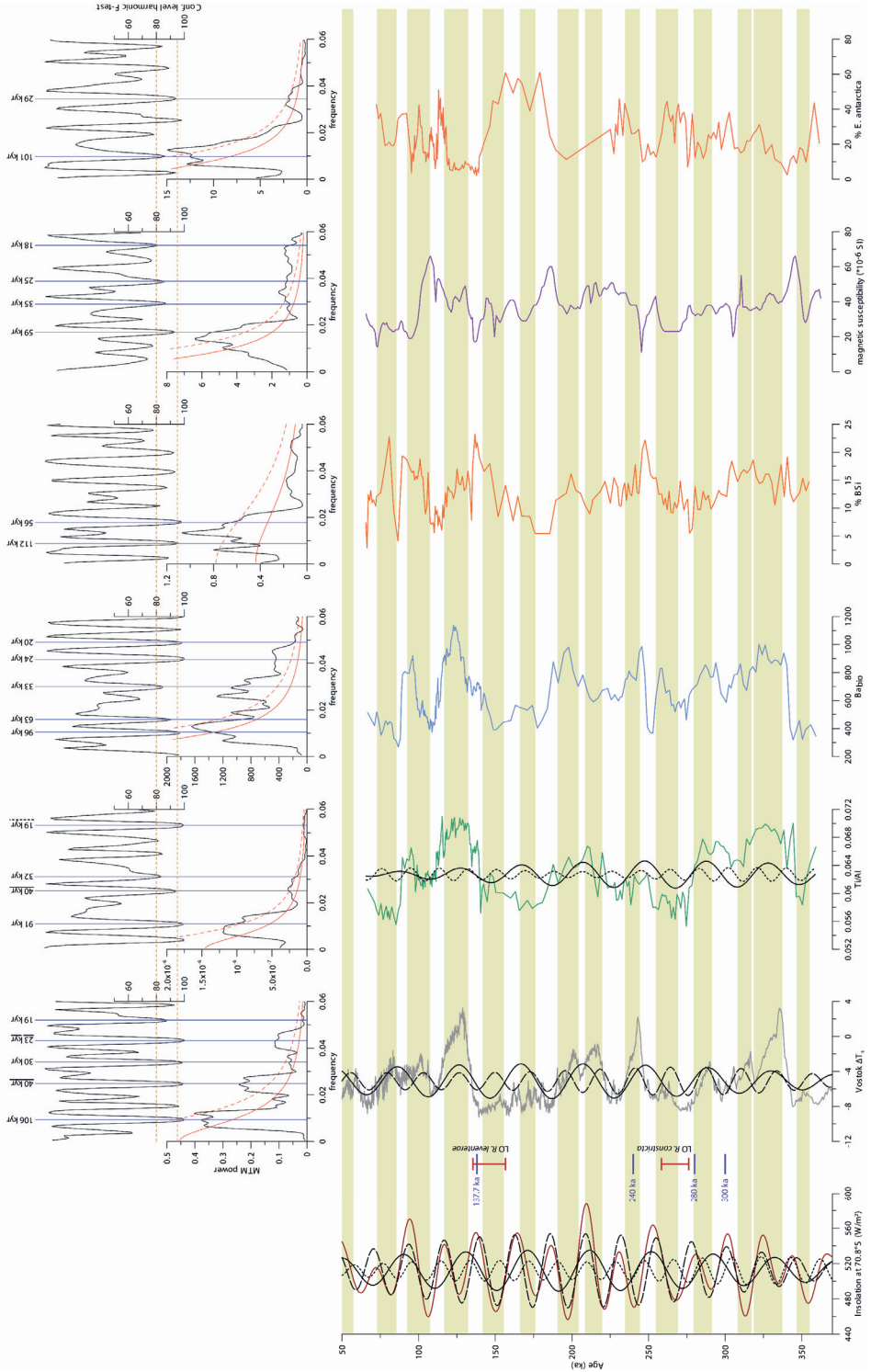


Figure S12 (previous page): Frequency spectra with AR1 confidence levels and Harmonic F-test confidence levels for the tuned and age calibrated Ti/Al record, biogenic barium, biogenic silica, magnetic susceptibility and Eucompia antarctica. Precession and obliquity periods are filtered from the Ti/Al record and compared to the modeled insolation at site AS05-10 (far left) and the reconstructed atmospheric temperatures from the Vostok ice core (in grey). Ranges of diatom event datums within core AS05-10 (in red) are plotted against the ages for these diatom events known from the Atlantic sector of the Southern Ocean (in blue).

Appendix B: R-script for the age model

```
#####  
### SET WORKING DIRECTORY AND LOAD ASTROCHRON PROGRAM  
#####  
setwd("C:/Users/...")  
library(astrochron)  
  
#####  
### READ THE Titanium/Aluminium DATA FILE  
#####  
  
TiAl<-read.csv("Ti_Al_csv.csv")  
summary(TiAl)  
  
#####  
### CALCULATE SEDIMENTATION RATE AND CONVERT DEPTH SCALE TO AGE BASED ON INITIAL TIE POINTS  
#####  
  
#####  
###PREPARE THE DATA-TO-AGE DATASET FOR ANALYSIS  
#####  
#LINEAR INTERPOLATION  
TiAl_res=linterp(TiAl)  
  
#THE DATASET IS RESAMPLED AT THE MEDIAN SAMPLING INTERVAL OF 0.0193 m  
  
#####  
###PERFORM EVOLUTIVE HARMONIC ANALYSIS  
#####  
#INITIAL TIE POINTS ARE:  
#TERMINATION I: 1.32 - 1.47 mbsf, 16.9 ka.  
#DIATOM EVENT DATUM: LO of Rouxia leventerae at 3.88 - 4.09 mbsf, 137.7 ka  
#DIATOM EVENT DATUM: LO of Rouxia constricta at 5.75 - 6.03 mbsf, 280 ka  
#BASED ON THESE DIATOM EVENTS 2 m SHOULD BE SUFFICIENT FOR A WINDOW WITH THREE 3pi DPSS TAPERS  
#FOR EHA ANALYSIS TO CAPTURE THE SMALLEST ORBITAL FREQUENCY OF INTEREST  
  
#THE FREQUENCIES OF INTEREST ARE THE ECCENTRICITY, OBLIQUITY AND PRECESSION TERMS BETWEEN 10 AND  
100 ka  
#BASED ON THE DIATOM EVENT DATUMS 10 ka WOULD CORRESPOND TO ~8 cycle/m,  
#WHICH IS THE MAXIMUM FREQUENCY THAT IS ANALYZED  
  
window=4  
  
eha_TiAl<-  
eha(TiAl_res,tbw=2,fmax=8,output=4,genplot=4,pl=2,detrend=T,pad=5000,win=window,step=0.1,ydir=-1)
```

#THE NYQUIST FREQUENCY AND RAYLEIGH FREQUENCY FOR THIS INTERPOLATED DATASET AND WINDOW SIZE ARE:

TiAl_ehanyquist=25.92593
TiAl_rayleigh=0.2492878

###EXTRACT TARGET PERIODS FOR THE EVOLUTIVE AVERAGE SPECTRAL MISFIT ANALYSIS

#ECCENTRICITY, OBLIQUITY AND PRECESSION TERMS ARE OBTAINED FROM Laskar et al. (2004) FOR THE PERIOD BETWEEN 0 AND 1 Ma

model=etp(tmin=0,tmax=1000)
mtm_La<-mtm(model,tbw=2,ar1=T,output=2,xmax=0.1,pl=2,sigID=T,siglevel=0.9)
target_La<-mtm_La[,1]

#THE FIVE TARGET PERIODS ARE 94.5, 41.0, 23.7, 22.3, 19.0 kyr

###PERFORM EVOLUTIVE AVERAGE SPECTRAL MISFIT ANALYSIS

#THE TARGET FREQUENCIES USED ARE DETERMINED FROM Laskar et al. (2004) WITH A 5% UNCERTAINTY RANGE

#BASED ON THE DIATOM EVENT DATUMS AND THE POSITION OF TERMINATION I, SEDIMENTATION RATES ARE CALCULATED
#BETWEEN 1.32 AND 4.09 m THE SEDIMENTATION RATE IS 2.29 cm/kyr
#BETWEEN 4.09 AND 5.75 m THE SEDIMENTATION RATE IS 1.17 cm/kyr
#MINIMUM AND MAXIMUM SEDIMENTATION RATE ARE THEREFORE SET TO 1 AND 3 cm/kyr, RESPECTIVELY

TiAl_easm<-eAsm(eha_TiAl,target_La,fper=c(rep(0.05,times=length(target_La))),rayleigh = TiAl_rayleigh,nyquist = TiAl_ehanyquist,siglevel=0.8,numsed=50,iter=50000,output=4,sedmin=1,sedmax=3,ydir=-1)

###EXAMINE EVOLUTIVE ASM SPECTRA WITH MINIMUM Ho-SL VALUES

#TRACK Ho-SL MINIMA FROM EVOLUTIVE ASM RESULTS
#AND IDENTIFY THOSE WITH Ho-SL LESS OR EQUAL TO 0.1%

pl(1); TiAl_easmtrack<-eAsmTrack(TiAl_easm[1],threshold=0.1,ydir=-1,genplot=T)

#LIST ALL PERIODS WITH 80% F-TEST CONFIDENCE LEVEL FOR EACH SPECTRUM WITH Ho-SL LESS OR EQUAL TO 0.1%

TiAl_easmperiods<-numeric(length(TiAl_easmtrack[,1]))
for(a in 1:length(TiAl_easmtrack[,1])){

```

TiAl_easmperiods[a]<-
(1/(peak(extract(eha_TiAl,get=TiAl_easmtrack[a,1]),level=0.8)[2]*(TiAl_easmtrack[a,2]*0.01)))
}
names(TiAl_easmperiods)<-TiAl_easmtrack[,1]
TiAl_easmperiods

#####
###TUNE THE Ti/Al RECORD USING FREQUENCY-DOMAIN MINIMAL TUNING (Meyers et al., 2001)
#####
#GIVEN THE ASM-CALIBRATED PERIODS, TRACK THE SHORT-TERM (94.5 kyr) ECCENTRICITY PERIOD IN ALL
SPECTRA

TiAl_freqs_ecc=trackFreq(eha_TiAl,threshold=0.8,ydir=-1)
write.csv(TiAl_freqs_ecc,file="TiAl_chosenfreqs-fortuning.csv")

#CALCULATE SEDIMENTATION RATES BASED ON THE TRACKED FREQUENCY

TiAl_sedrate_ecc=freq2sedrate(TiAl_freqs_ecc,period=(1/target_La[1]),ydir=-1)

#SEDIMENTATION RATES BASED ON THE POSITION OF TERMINATION I (C14 DATA),
#WHICH LIES OUTSIDE OF THE EXAMINED INTERVAL DUE TO THE WINDOW SIZE ARE NOT ADDED HERE,
#AND INTERPOLATE SEDIMENTATION RATES TO THE TOP AND BOTTOM OF THE RECORD

TiAl_sedrate_ecc_ext=data.frame(c(0,TiAl_sedrate_ecc[,1],max(TiAl[,1])+0.1),c(TiAl_sedrate_ecc[,2],TiAl_sedrat
e_ecc[,2],TiAl_sedrate_ecc[length(TiAl_sedrate_ecc[,1]),2]))
names(TiAl_sedrate_ecc_ext)<-c("Depth/Height","Sedrate")

#COVERT SEDIMENTATION RATES TO THE ECCENTRICITY-BASED AGE MODEL FOR THE Ti/Al RECORD

TiAl_time_ecc=sedrate2time(TiAl_sedrate_ecc_ext)
TiAl_tuned_ecc=tune(TiAl,TiAl_time_ecc)
idPts(TiAl_tuned_ecc)

#####
###REPEAT THESE TUNING STEPS FOR THE OBLIQUITY AND PRECESSION TERMS TO FURTHER IMPROVE THE AGE
MODEL
#####
#PREPARE THE ECCENTRICITY-TUNED DATASET AND PERFORM EHA AND E-ASM ANALYSIS
#THE WINDOW SIZE IS SET TO 150 kyr AND MAXIMUM FREQUENCY TO 0.1 cycle/kyr
#TO CAPTURE ALL PERIODS BETWEEN 10 AND 100 kyr
#SEDIMENTATION RATE IS ALLOWED TO VARY BETWEEN 80 AND 125% OF THE CURRENT SEDIMENTATION RATE
#THIS IS BASED ON THE UNCERTAINTY IN THE POSITION OF THE PEAK OF MISS.5 IN THE ECCENTRICITY-TUNED
Ti/Al RECORD,
#AND THEREFORE THE LENGTH OF MIS6, WHICH NOW RANGES BETWEEN 50 OR 70 kyr,
#WHILE IT IS 60 kyr LONG IN THE VOSTOK ICE CORE RECORD.
#50/60 = 0.833; 70/60 = 1.166

```

```
TiAlecc_res=linterp(TiAl_tuned_ecc)

windowecc=150
eha_TiAlecc<-
eha(TiAlecc_res,tbw=2,fmax=0.1,output=4,genplot=4,pl=2,detrend=T,pad=5000,win=windowecc,step=5,ydir=-1)
TiAlecc_ehanyquist=0.404422
TiAlecc_rayleigh=0.006629869
TiAlecc_easm<-eAsm(eha_TiAlecc,target_La,fper=c(rep(0.05,times=length(target_La))),rayleigh =
TiAlecc_rayleigh,nyquist =
TiAlecc_ehanyquist,siglevel=0.8,numsed=90,iter=50000,output=4,sedmin=80,sedmax=125,ydir=-1)

pl(1); TiAlecc_easmtrack<-eAsmTrack(TiAlecc_easm[1],threshold=0.1,ydir=-1,genplot=T)

TiAlecc_easmperiods<-numeric(length(TiAlecc_easmtrack[,1]))
for(a in 1:length(TiAlecc_easmtrack[,1])){
  TiAlecc_easmperiods[a]<-
  (1/(peak(extract(eha_TiAlecc,get=TiAlecc_easmtrack[a,1]),level=0.8)[2]*(TiAlecc_easmtrack[a,2]*0.01)))
}
names(TiAlecc_easmperiods)<-TiAlecc_easmtrack[,1]
TiAlecc_easmperiods

#TRACE OBLIQUITY 41 kyr CYCLE FOR TUNING
TiAl_freqs_obl=trackFreq(eha_TiAlecc,threshold=0.8,ydir=-1)

TiAl_sedrate_obl=freq2sedrate(TiAl_freqs_obl,period=(1/target_La[2]),ydir=-1)

#THE POSITION OF TERMINATION I AT 16.150 ka WAS NOT ADDED TO THE CALCULATED SEDIMENTATION RATES
#AND LIES OUTSIDED OF THE PART THAT COULD BE ANALYZED BY EHA DUE TO WINDOW SIZE

TiAl_sedrate_obl_ext=data.frame(c(0,TiAl_sedrate_obl[,1],max(TiAl_tuned_ecc[,1])+5),c(TiAl_sedrate_obl[,1,2],TiAl_sedrate_obl[,2],TiAl_sedrate_obl[length(TiAl_sedrate_obl[,1]),2]))
names(TiAl_sedrate_obl_ext)<-c("Depth/Height","Sedrate")
TiAl_time_obl=sedrate2time(TiAl_sedrate_obl_ext)
TiAl_tuned_obl=tune(TiAl_tuned_ecc,TiAl_time_obl)
idPts(TiAl_tuned_obl)
#write.csv(TiAl_tuned_obl,file="TiAl_tuned_obl.csv")

#PREPARE THE OBLIQUITY-TUNED DATASET FOR EHA AND E-ASM ANALYSIS

TiAlobl_res=linterp(TiAl_tuned_obl)

windowobl=150
eha_TiAlobl<-
eha(TiAlobl_res,tbw=2,fmax=0.1,output=4,genplot=4,pl=2,detrend=T,pad=5000,win=windowobl,step=5,ydir=-1)
TiAlobl_ehanyquist=0.4231034
TiAlobl_rayleigh=0.00663045
```

```

TiAlobl_easm<-eAsm(eha_TiAlobl,target_La,fper=c(rep(0.05,times=length(target_La))),rayleigh =
TiAlobl_rayleigh,nyquist =
TiAlobl_ehanyquist,siglevel=0.8,numsed=90,iter=50000,output=4,sedmin=80,sedmax=125,ydir=-1)

pl(1); TiAlobl_easmtrack<-eAsmTrack(TiAlobl_easm[1],threshold=0.1,ydir=-1,genplot=T)

TiAlobl_easmperiods<-numeric(length(TiAlobl_easmtrack[,1]))
for(a in 1:length(TiAlobl_easmtrack[,1])){
  TiAlobl_easmperiods[a]<-
(1/(peak(extract(eha_TiAlobl,get=TiAlobl_easmtrack[a,1],level=0.8)[2]*(TiAlobl_easmtrack[a,2]*0.01)))
}
names(TiAlobl_easmperiods)<-TiAlobl_easmtrack[,1]
TiAlobl_easmperiods

TiAl_freqs_prec=trackFreq(eha_TiAlobl,threshold=0.8,ydir=-1)

TiAl_sedrate_prec=freq2sedrate(TiAl_freqs_prec,period=1/target_La[5],ydir=-1)

TiAl_sedrate_prec_ext=data.frame(c(0,TiAl_sedrate_prec[1],max(TiAl_tuned_obl[,1])+5),c(TiAl_sedrate_prec[1,2
],TiAl_sedrate_prec[2],TiAl_sedrate_prec[length(TiAl_sedrate_prec[,1]),2]))
names(TiAl_sedrate_prec_ext)<-c("Depth/Height","Sedrate")
TiAl_time_prec=sedrate2time(TiAl_sedrate_prec_ext)
TiAl_tuned_prec=tune(TiAl_tuned_obl,TiAl_time_prec)
idPts(TiAl_tuned_prec)

#CALCULATE SEDIMENTATION RATE THROUGHOUT THE RECORD
#BASED ON FINAL TUNING TO PRECESSION AND THE ORIGINAL SAMPLE DEPTHS

TiAl_final_time<-data.frame(TiAl[,1],TiAl_tuned_prec[,1])
TiAl_final_sed<-data.frame(TiAl_final_time,c(rep(0,times=length(TiAl_final_time[,1])))

for(c in 1:length(TiAl_final_time[,1])){
  TiAl_final_sed[c,3]<-(TiAl_final_sed[c+1,1]-TiAl_final_sed[c,1])*100/(TiAl_final_sed[c+1,2]-TiAl_final_sed[c,2])
}
names(TiAl_final_sed)<-c("depth_m","TiAl","sedrate_m.kyr")
TiAl_final_sed[length(TiAl_final_sed[,1]),3]<-TiAl_final_sed[(length(TiAl_final_sed[,1])-1),3]
TiAl_final_sedrate<-
data.frame(c(0,TiAl_final_sed[,1],TiAl_final_sed[length(TiAl_final_sed[,1]),1]+0.2),c(TiAl_final_sed[1,3],TiAl_final_
sed[,3],TiAl_final_sed[length(TiAl_final_sed[,1]),3]))
names(TiAl_final_sedrate)<-c("meters","sedrate")

write.csv(TiAl_final_sedrate,file="TiAl_final_sedrate.csv")

#For applying the age model to other records extract sedimentation rates from data file
TiAl_final_sedrate<-read.csv(file="TiAl_final_sedrate.csv")[,2:3]
TiAl_sedrate_prec_ext<-TiAl_final_sedrate
TiAl_time_prec=sedrate2time(TiAl_sedrate_prec_ext)

```



```
TiAl_tuned_prec=tune(TiAl,TiAl_time_prec)
#write.csv(TiAl_tuned_prec,file="TiAl_tuned_afterTiAl.csv")

#####
###PREPARE AND EVALUATE THE FLOATING TI/AL RECORD BY MULTITAPER METHOD SPECTRAL ANALYSIS AND
BANDPASS FILTERING
#####

TiAl_tunedres<-linterp(TiAl_tuned_prec)
mtm_TiAlTuned<-mtm(TiAl_tunedres,tbw=2,ar1=T,pl=2,xmax=0.1,detrend=T,output=2,padfac=5,siglevel=0.8)
mtm_TiAlTunedall<-mtm(TiAl_tunedres,tbw=2,ar1=T,pl=2,xmax=0.1,detrend=T,output=1,padfac=5,siglevel=0.8)
freq_TiAlTuned<-mtm_TiAlTuned[,1]
bp1_TiAlTuned<-bandpass(TiAl_tunedres,flow=freq_TiAlTuned[1]-
0.1*freq_TiAlTuned[1],fhigh=freq_TiAlTuned[1]+0.1*freq_TiAlTuned[1],detrend=T)
bp2_TiAlTuned<-bandpass(TiAl_tunedres,flow=freq_TiAlTuned[2]-
0.1*freq_TiAlTuned[2],fhigh=freq_TiAlTuned[2]+0.1*freq_TiAlTuned[2],detrend=T)
bp3_TiAlTuned<-bandpass(TiAl_tunedres,flow=freq_TiAlTuned[3]-
0.1*freq_TiAlTuned[3],fhigh=freq_TiAlTuned[3]+0.1*freq_TiAlTuned[3],detrend=T)
bp4_TiAlTuned<-bandpass(TiAl_tunedres,flow=freq_TiAlTuned[4]-
0.1*freq_TiAlTuned[4],fhigh=freq_TiAlTuned[4]+0.1*freq_TiAlTuned[4],detrend=T)
bp5_TiAlTuned<-bandpass(TiAl_tunedres,flow=freq_TiAlTuned[5]-
0.1*freq_TiAlTuned[5],fhigh=freq_TiAlTuned[5]+0.1*freq_TiAlTuned[5],detrend=T)

write.csv(mtm_TiAlTunedall,file="powerspec_TiAl_tuned.csv")
write.csv(mtm_TiAlTuned,file="freqs_TiAl_tuned.csv")
write.csv(data.frame(bp1_TiAlTuned,bp2_TiAlTuned,bp3_TiAlTuned,bp4_TiAlTuned,bp5_TiAlTuned),file="bandpas
ses_TiAl-tuned.csv")

#THE FLOATING TI/AL RECORD CAN NOW BE TUNED EITHER TO LOCAL OBLIQUITY INSOLATION
#OR TO THE OBLIQUITY SIGNAL CAPTURED WITHIN THE VOSTOK AIR TEMPERATURE RECORD, WHICH SLIGHTLY
LAGS THE OBLIQUITY AND PRECESSION SIGNAL OF 65 DEGREES NORTHERN SUMMER INSOLATION
#AIR TEMPERATURES AT VOSTOK FOLLOW THE NORTHERN MID-LATITUDE OBLIQUITY AND PRECESSION SIGNAL
DUE TO ENERGY TRANSFER THROUGH OCEAN-ATMOSPHERE COUPLING
#WE INVESTIGATE BOTH OPTIONS AND COMPARE THE RESULTS TO THE DIATOM EVENT DATUMS

#####
#MODEL LOCAL SUMMER INSOLATION AT 70.8 DEGREES SOUTHERN LATITUDE
#####

library(palinsol)
insolation<-function(times, astrosol=la04)
  sapply(times,function(tt) Insol(orbit=astrosol(tt), long=3*pi/2, lat=-70.8*pi/180))

tts<-seq(from=-400e3, to=0, by=1e2)
isl<-insolation(tts,la04)
```

```
insolDec70.8<-data.frame(as.vector(rbind(-.001*tts[order(tts*-.001,isl)])),as.vector(rbind(isl[order(tts*-.001,isl)])))
names(insolDec70.8)<-c("age_kyr", "insolation")
```

```
mtm_insol<-mtm(insolDec70.8,tbw=2,ar1=T,pl=2,xmax=0.1,detrend=T,output=2,padfac=5,siglevel=0.8)
mtm_insolall<-mtm(insolDec70.8,tbw=2,ar1=T,pl=2,xmax=0.1,detrend=T,output=1,padfac=5,siglevel=0.8)
freq_insol<-mtm_insol[,1]
bp1_insol<-bandpass(insolDec70.8,flow=freq_insol[1]-
0.1*freq_insol[1],fhigh=freq_insol[1]+0.1*freq_insol[1],detrend=T)
bp2_insol<-bandpass(insolDec70.8,flow=freq_insol[2]-
0.1*freq_insol[2],fhigh=freq_insol[2]+0.1*freq_insol[2],detrend=T)
bp3_insol<-bandpass(insolDec70.8,flow=freq_insol[3]-
0.1*freq_insol[3],fhigh=freq_insol[3]+0.1*freq_insol[3],detrend=T)
bp4_insol<-bandpass(insolDec70.8,flow=freq_insol[4]-
0.1*freq_insol[4],fhigh=freq_insol[4]+0.1*freq_insol[4],detrend=T)
bp5_insol<-bandpass(insolDec70.8,flow=freq_insol[5]-
0.1*freq_insol[5],fhigh=freq_insol[5]+0.1*freq_insol[5],detrend=T)
```

```
write.csv(insolDec70.8,file="summer-insolation-at-AS05-10.csv")
write.csv(mtm_insolall,file="powerspec_insol.csv")
write.csv(mtm_insol,file="freqs_insol.csv")
write.csv(data.frame(bp1_insol,bp2_insol,bp3_insol,bp4_insol,bp5_insol),file="bandpasses_insol.csv")
```

#EXTRACT THE OBLIQUITY CYCLE IDENTIFIED IN THE INSOLATION RECORD FROM THE FLOATING TI/AL RECORD

```
bp2_insolTiAl<-bandpass(TiAl_tunedres,flow=freq_insol[2]-
0.1*freq_insol[2],fhigh=freq_insol[2]+0.1*freq_insol[2],detrend=T)
```

```
#####
#PERFORM MTM ANALYSIS ON VOSTOK ICE CORE DELTA-T RECORD
#####
```

```
Vostok<-read.csv(file="Vostok_T_csv.csv")
```

```
Vostokres<-linterp(Vostok,dt=0.1)
mtm_Vostok<-mtm(Vostokres,tbw=2,ar1=T,pl=2,xmax=0.1,detrend=T,output=2,padfac=5,siglevel=0.8)
mtm_Vostokall<-mtm(Vostokres,tbw=2,ar1=T,pl=2,xmax=0.1,detrend=T,output=1,padfac=5,siglevel=0.8)
freq_Vostok<-mtm_Vostok[,1]
bp1_Vostok<-bandpass(Vostokres,flow=freq_Vostok[1]-
0.1*freq_Vostok[1],fhigh=freq_Vostok[1]+0.1*freq_Vostok[1],detrend=T)
bp2_Vostok<-bandpass(Vostokres,flow=freq_Vostok[2]-
0.1*freq_Vostok[2],fhigh=freq_Vostok[2]+0.1*freq_Vostok[2],detrend=T)
bp3_Vostok<-bandpass(Vostokres,flow=freq_Vostok[3]-
0.1*freq_Vostok[3],fhigh=freq_Vostok[3]+0.1*freq_Vostok[3],detrend=T)
bp4_Vostok<-bandpass(Vostokres,flow=freq_Vostok[4]-
0.1*freq_Vostok[4],fhigh=freq_Vostok[4]+0.1*freq_Vostok[4],detrend=T)
```

```
bp5_Vostok<-bandpass(Vostokres,flow=freq_Vostok[5]-
0.1*freq_Vostok[5],fhigh=freq_Vostok[5]+0.1*freq_Vostok[5],detrend=T)

write.csv(mtm_Vostokall,file="powerspec_Vostok.csv")
write.csv(mtm_Vostok,file="freqs_Vostok.csv")
write.csv(data.frame(bp1_Vostok,bp2_Vostok,bp3_Vostok,bp4_Vostok,bp5_Vostok),file="bandpasses_Vostok.csv
")
```

```
#EXTRACT THE OBLIQUITY CYCLE IDENTIFIED IN THE VOSTOK DELTA-T RECORD FROM THE FLOATING TI/AL
RECORD
```

```
bp2_VostokTiAl<-bandpass(TiAl_tunedres,flow=freq_Vostok[2]-
0.1*freq_Vostok[2],fhigh=freq_Vostok[2]+0.1*freq_Vostok[2],detrend=T)
```

```
#####
#IDENTIFY 40-KYR INSOLATION MAXIMA AND 40-KYR MAXIMA IN TI/AL RECORD
#####
```

```
#OBTAIN OBLIQUITY PEAKS IN MODELED SUMMER INSOLATION AT 70.8 DEGREES SOUTHERN LATITUDE
```

```
start3<-
if(bp2_insol[1,2]<bp2_insol[2,2]){match(min(bp2_insol[1:(10*(1/freq_insol[2])),2)),bp2_insol[1:(10*(1/freq_insol
[2])),2])}else{match(min(bp2_insol[1:(5*(1/freq_insol[2])),2)),bp2_insol[1:(5*(1/freq_insol[2])),2])}

insol40kyrmax<-data.frame(numeric(400/(1/freq_insol[2])),numeric(400/(1/freq_insol[2])))
for(f in 1:(length(insol40kyrmax[,2]))){
  if(bp2_insol[1,2]<bp2_insol[2,2]){
    insol40kyrmax[1,2]<-max(bp2_insol[1:(5*(1/freq_insol[2])),2])
    insol40kyrmax[(f+1),2]<-max(bp2_insol[((f-1)*(1/freq_insol[2])*10+start3):(f*(1/freq_insol[2])*10+start3),2])
  }else{
    insol40kyrmax[f,2]<-max(bp2_insol[((f-1)*(1/freq_insol[2])*10+start3):(f*(1/freq_insol[2])*10+start3),2])
  }
}

for(g in 1:(length(insol40kyrmax[,1]))){
  if(bp2_insol[1,2]<bp2_insol[2,2]){
    insol40kyrmax[1,1]<-
bp2_insol[match(max(bp2_insol[1:(5*(1/freq_insol[2])),2)),bp2_insol[1:(5*(1/freq_insol[2])),2]),1]
    insol40kyrmax[(g+1),1]<-bp2_insol[match(insol40kyrmax[(g+1),2],(bp2_insol[((g-
1)*(1/freq_insol[2])*10+start3):(g*(1/freq_insol[2])*10+start3),2]))+as.integer(((g-
1)*(1/freq_insol[2])*10+start3))-1,1]
  }else{
    insol40kyrmax[g,1]<-bp2_insol[match(insol40kyrmax[g,2],(bp2_insol[((g-
1)*(1/freq_insol[2])*10+start3):(g*(1/freq_insol[2])*10+start3),2]))+as.integer(((g-
1)*(1/freq_insol[2])*10+start3))-1,1]
  }
}
```

```

insol40kyrmax<-na.omit(insol40kyrmax)

#OBTAIN POSITION OF OBLIQUITY PEAKS IN FLOATING TI/AL RECORD

start4<-
if(bp2_insolTiAl[1,2]<bp2_insolTiAl[2,2]){match(min(bp2_insolTiAl[1:(1/1.163226)*(1/freq_insol[2]),2]),bp2_insolTiAl[1:(1/1.163226)*(1/freq_insol[2]),2])}else{match(min(bp2_insolTiAl[1:(0.5*(1/1.163226)*(1/freq_insol[2]),2]),bp2_insolTiAl[1:(0.5*(1/1.163226)*(1/freq_insol[2]),2])}

TiAl40kyrmax<-
data.frame(numeric(max(bp2_insolTiAl[,1])/(1/freq_insol[2])),numeric(max(bp2_insolTiAl[,1])/(1/freq_insol[2])))
for(h in 1:(length(TiAl40kyrmax[,2]))){
  if(bp2_insolTiAl[1,2]<bp2_insolTiAl[2,2]){
    TiAl40kyrmax[1,2]<-max(bp2_insolTiAl[1:(0.5*(1/1.163226)*(1/freq_insol[2]),2])
    TiAl40kyrmax[(h+1),2]<-max(bp2_insolTiAl[((h-1)*(1/freq_insol[2])*(1/1.163226)+start4):(h*(1/freq_insol[2])*(1/1.163226)+start4),2])
  }else{
    TiAl40kyrmax[h,2]<-max(bp2_insolTiAl[((h-1)*(1/freq_insol[2])*(1/1.163226)+start4):(h*(1/freq_insol[2])*(1/1.163226)+start4),2])
  }
}

TiAl40kyrmax<-na.omit(TiAl40kyrmax)
for(i in 1:(length(TiAl40kyrmax[,1]))){
  if(bp2_insolTiAl[1,2]<bp2_insolTiAl[2,2]){
    TiAl40kyrmax[1,1]<-
bp2_insolTiAl[match(max(bp2_insolTiAl[1:(0.5*(1/1.163226)*(1/freq_insol[2]),2]),bp2_insolTiAl[1:(0.5*(1/1.163226)*(1/freq_insol[2]),2]),1]
    TiAl40kyrmax[(i+1),1]<-bp2_insolTiAl[match(TiAl40kyrmax[(i+1),2],(bp2_insolTiAl[((i-1)*(1/freq_insol[2])*(1/1.163226)+start4):(i*(1/freq_insol[2])*(1/1.163226)+start4),2]))+as.integer(((i-1)*(1/freq_insol[2])*(1/1.163226)+start4))-1,1]
  }else{
    TiAl40kyrmax[i,1]<-bp2_insolTiAl[match(TiAl40kyrmax[i,2],(bp2_insolTiAl[((i-1)*(1/freq_insol[2])*(1/1.163226)+start4):(i*(1/freq_insol[2])*(1/1.163226)+start4),2]))+as.integer(((i-1)*(1/freq_insol[2])*(1/1.163226)+start4))-1,1]
  }
}

TiAl40kyrmax<-na.omit(TiAl40kyrmax)

comparisonTiAlinsol<-numeric(length(TiAl40kyrmax[,1]))
for(j in 1:(length(comparisonTiAlinsol))){
  comparisonTiAlinsol[j]<-TiAl40kyrmax[j,1]-insol40kyrmax[(j+1),1]
}

mean_insol40kyr_diff<-mean(comparisonTiAlinsol)

```

```
write.csv(data.frame(c(0,TiAl40kyrmax[,1],0),insol40kyrmax[,1],c(0,comparisonTiAlinsol,0)),file="40kyr_insol-TiAl-difference.csv")
```

```
#####  
#IDENTIFY 40-KYR INSOLATION MAXIMA AND 40-KYR MAXIMA IN TI/AL RECORD  
#####
```

```
#OBTAIN OBLIQUITY PEAKS IN VOSTOK DELTA-T RECORD
```

```
start1<-  
if(bp2_Vostok[1,2]<bp2_Vostok[2,2]){match(min(bp2_Vostok[1:(10*(1/freq_Vostok[2])),2]),bp2_Vostok[1:(10*(1/freq_Vostok[2])),2])}else{match(min(bp2_Vostok[1:(5*(1/freq_Vostok[2])),2]),bp2_Vostok[1:(5*(1/freq_Vostok[2])),2])}
```

```
Vostok40kyrmax<-data.frame(numeric(400/(1/freq_Vostok[2])),numeric(400/(1/freq_Vostok[2])))  
for(a in 1:(length(Vostok40kyrmax[,2])))  
  if(bp2_Vostok[1,2]<bp2_Vostok[2,2]){  
    Vostok40kyrmax[1,2]<-max(bp2_Vostok[1:(5*(1/freq_Vostok[2])),2])  
    Vostok40kyrmax[(a+1),2]<-max(bp2_Vostok[1:(a-  
1)*(1/freq_Vostok[2])*10+start1):(a*(1/freq_Vostok[2])*10+start1),2])  
  }else{  
    Vostok40kyrmax[a,2]<-max(bp2_Vostok[1:(a-  
1)*(1/freq_Vostok[2])*10+start1):(a*(1/freq_Vostok[2])*10+start1),2])  
  }  
}
```

```
for(b in 1:(length(Vostok40kyrmax[,1])))  
  if(bp2_Vostok[1,2]<bp2_Vostok[2,2]){  
    Vostok40kyrmax[1,1]<-  
bp2_Vostok[match(max(bp2_Vostok[1:(5*(1/freq_Vostok[2])),2]),bp2_Vostok[1:(5*(1/freq_Vostok[2])),2]),1]  
    Vostok40kyrmax[(b+1),1]<-bp2_Vostok[match(Vostok40kyrmax[(b+1),2],(bp2_Vostok[1:(b-  
1)*(1/freq_Vostok[2])*10+start1):(b*(1/freq_Vostok[2])*10+start1),2]))+as.integer(((b-  
1)*(1/freq_Vostok[2])*10+start1))-1,1]  
  }else{  
    Vostok40kyrmax[b,1]<-bp2_Vostok[match(Vostok40kyrmax[b,2],(bp2_Vostok[1:(b-  
1)*(1/freq_Vostok[2])*10+start1):(g*(1/freq_Vostok[2])*10+start1),2]))+as.integer(((b-  
1)*(1/freq_Vostok[2])*10+start1))-1,1]  
  }  
}
```

```
#OBTAIN POSITION OF OBLIQUITY PEAKS IN FLOATING TI/AL RECORD
```

```
start2<-  
if(bp2_VostokTiAl[1,2]<bp2_VostokTiAl[2,2]){match(min(bp2_VostokTiAl[1:((1/1.163226)*(1/freq_Vostok[2])),2]),  
bp2_VostokTiAl[1:((1/1.163226)*(1/freq_Vostok[2])),2])}else{match(min(bp2_VostokTiAl[1:(0.5*(1/1.163226)*(1/  
/freq_Vostok[2])),2]),bp2_VostokTiAl[1:(0.5*(1/1.163226)*(1/freq_Vostok[2])),2])}
```

```

TiAlVostok40kyrmax<-
data.frame(numeric(max(bp2_VostokTiAl[,1])/(1/freq_Vostok[2])),numeric(max(bp2_VostokTiAl[,1])/(1/freq_Vostok[2])))
for(c in 1:(length(TiAlVostok40kyrmax[,2]))){
  if(bp2_VostokTiAl[1,2]<bp2_VostokTiAl[2,2]){
    TiAlVostok40kyrmax[1,2]<-max(bp2_VostokTiAl[1:(0.5*(1/1.163226)*(1/freq_Vostok[2])),2])
    TiAlVostok40kyrmax[(c+1),2]<-max(bp2_VostokTiAl[((c-1)*(1/freq_Vostok[2])*(1/1.163226)+start2):(c*(1/freq_Vostok[2])*(1/1.163226)+start2),2])
  }else{
    TiAlVostok40kyrmax[h,2]<-max(bp2_VostokTiAl[((c-1)*(1/freq_Vostok[2])*(1/1.163226)+start2):(c*(1/freq_Vostok[2])*(1/1.163226)+start2),2])
  }
}

TiAlVostok40kyrmax<-na.omit(TiAlVostok40kyrmax)
for(d in 1:(length(TiAlVostok40kyrmax[,1]))){
  if(bp2_VostokTiAl[1,2]<bp2_VostokTiAl[2,2]){
    TiAlVostok40kyrmax[1,1]<-
bp2_VostokTiAl[match(max(bp2_VostokTiAl[1:(0.5*(1/1.163226)*(1/freq_Vostok[2])),2]),bp2_VostokTiAl[1:(0.5*(1/1.163226)*(1/freq_Vostok[2])),2]),1]
    TiAlVostok40kyrmax[(d+1),1]<-bp2_VostokTiAl[match(TiAlVostok40kyrmax[(d+1),2],(bp2_VostokTiAl[((d-1)*(1/freq_Vostok[2])*(1/1.163226)+start2):(d*(1/freq_Vostok[2])*(1/1.163226)+start2),2]))+as.integer(((d-1)*(1/freq_Vostok[2])*(1/1.163226)+start2))-1,1]
  }else{
    TiAlVostok40kyrmax[d,1]<-bp2_VostokTiAl[match(TiAlVostok40kyrmax[d,2],(bp2_VostokTiAl[((d-1)*(1/freq_Vostok[2])*(1/1.163226)+start2):(d*(1/freq_Vostok[2])*(1/1.163226)+start2),2]))+as.integer(((d-1)*(1/freq_Vostok[2])*(1/1.163226)+start2))-1,1]
  }
}
TiAlVostok40kyrmax<-na.omit(TiAlVostok40kyrmax)

comparisonTiAlVostok<-numeric(length(TiAlVostok40kyrmax[,1]))
for(e in 1:(length(comparisonTiAlVostok))){
  comparisonTiAlVostok[e]<-TiAlVostok40kyrmax[e,1]-Vostok40kyrmax[(e+1),1]
}

mean_Vostok40kyr_diff<-mean(comparisonTiAlVostok)

write.csv(data.frame(c(0,TiAlVostok40kyrmax[,1],0),Vostok40kyrmax[,1],c(0,comparisonTiAlVostok,0)),file="40kyr_Vostok-TiAl-difference.csv")

#####
###TUNE THE FLOATING TI/AL RECORD TO INSOLATION BASED ON OBLIQUITY MAXIMA
#####

```

```
#THE MEAN DIFFERENCE BETWEEN THE OBLIQUITY PEAKS OF THE TI/AL RECORD AND 70.8 SOUTHERN LATITUDE  
SUMMER INSOLATION IS 1.0 KYR (+- ONE OBLIQUITY CYCLE)  
#THE MEAN DIFFERENCE BETWEEN THE OBLIQUITY PEAKS OF THE TI/AL RECORD AND THE VOSTOK DELTA-T  
RECORD IS 4.4 KYR (+- ONE OBLIQUITY CYCLE)
```

```
chosendiff=mean_Vostok40kyr_diff  
TiAl_trueages<-data.frame((TiAl_tuned_prec[,1]-chosendiff),TiAl_tuned_prec[,2])  
idPts(TiAl_trueages)  
write.csv(TiAl_trueages,file="TiAl_trueages.csv")
```

```
#TUNING TO THE 1.0-KYR DIFFERENCE RESULTS IN A TUNED AGE FOR THE DIATOM EVENT DATUMS OF 148±10  
AND 270±10 KA  
#TUNING TO THE 4.4-KYR DIFFERENCE RESULTS IN A TUNED AGE FOR THE DIATOM EVENT DATUMS OF 145±10  
AND 267±10 KA  
#VERSUS THE ORIGINAL AGES AT 138 AND 280 KA (OR 240-300 KA), RESPECTIVELY  
#WE CHOSE TO TUNE TO THE OBLIQUITY SIGNAL IN THE VOSTOK DELTA-T RECORD
```

```
TiAl_trueres<-linterp(TiAl_trueages)  
mtm_TiAltrueages<-mtm(TiAl_trueres,tbw=2,ar1=T,pl=2,xmax=0.1,detrend=T,output=2,padfac=5,siglevel=0.8)  
mtm_TiAltrueagesall<-mtm(TiAl_trueres,tbw=2,ar1=T,pl=2,xmax=0.1,detrend=T,output=1,padfac=5,siglevel=0.8)  
freq_TiAltrueages<-mtm_TiAltrueages[,1]  
bp1_TiAltrueages<-bandpass(TiAl_trueres,flow=freq_TiAltrueages[1]-  
0.1*freq_TiAltrueages[1],fhigh=freq_TiAltrueages[1]+0.1*freq_TiAltrueages[1],detrend=T)  
bp2_TiAltrueages<-bandpass(TiAl_trueres,flow=freq_TiAltrueages[2]-  
0.1*freq_TiAltrueages[2],fhigh=freq_TiAltrueages[2]+0.1*freq_TiAltrueages[2],detrend=T)  
bp3_TiAltrueages<-bandpass(TiAl_trueres,flow=freq_TiAltrueages[3]-  
0.1*freq_TiAltrueages[3],fhigh=freq_TiAltrueages[3]+0.1*freq_TiAltrueages[3],detrend=T)  
bp4_TiAltrueages<-bandpass(TiAl_trueres,flow=freq_TiAltrueages[4]-  
0.1*freq_TiAltrueages[4],fhigh=freq_TiAltrueages[4]+0.1*freq_TiAltrueages[4],detrend=T)  
bp5_TiAltrueages<-bandpass(TiAl_trueres,flow=freq_TiAltrueages[5]-  
0.1*freq_TiAltrueages[5],fhigh=freq_TiAltrueages[5]+0.1*freq_TiAltrueages[5],detrend=T)
```

Appendix C: additional data and figures

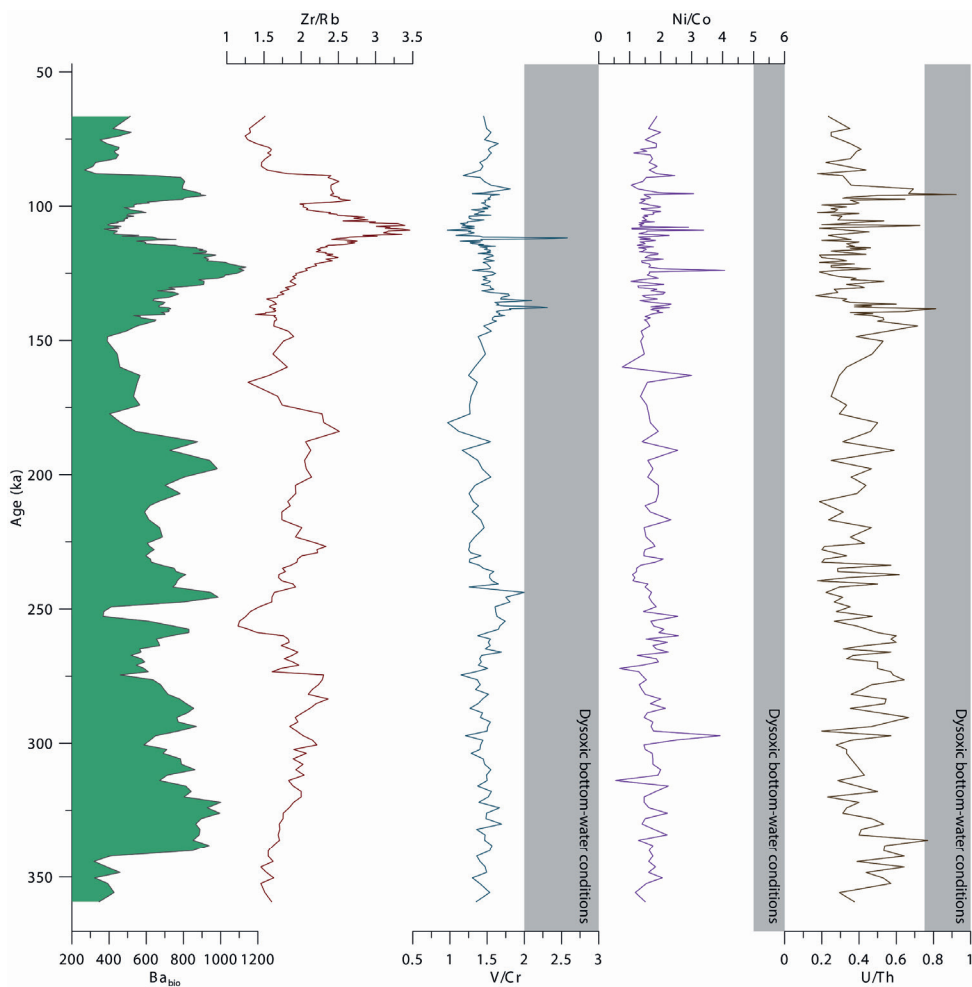


Figure S13: Record of the elemental ratios Zr/Rb, V/Cr, Ni/Co and U/Th compared to the biogenic barium record.

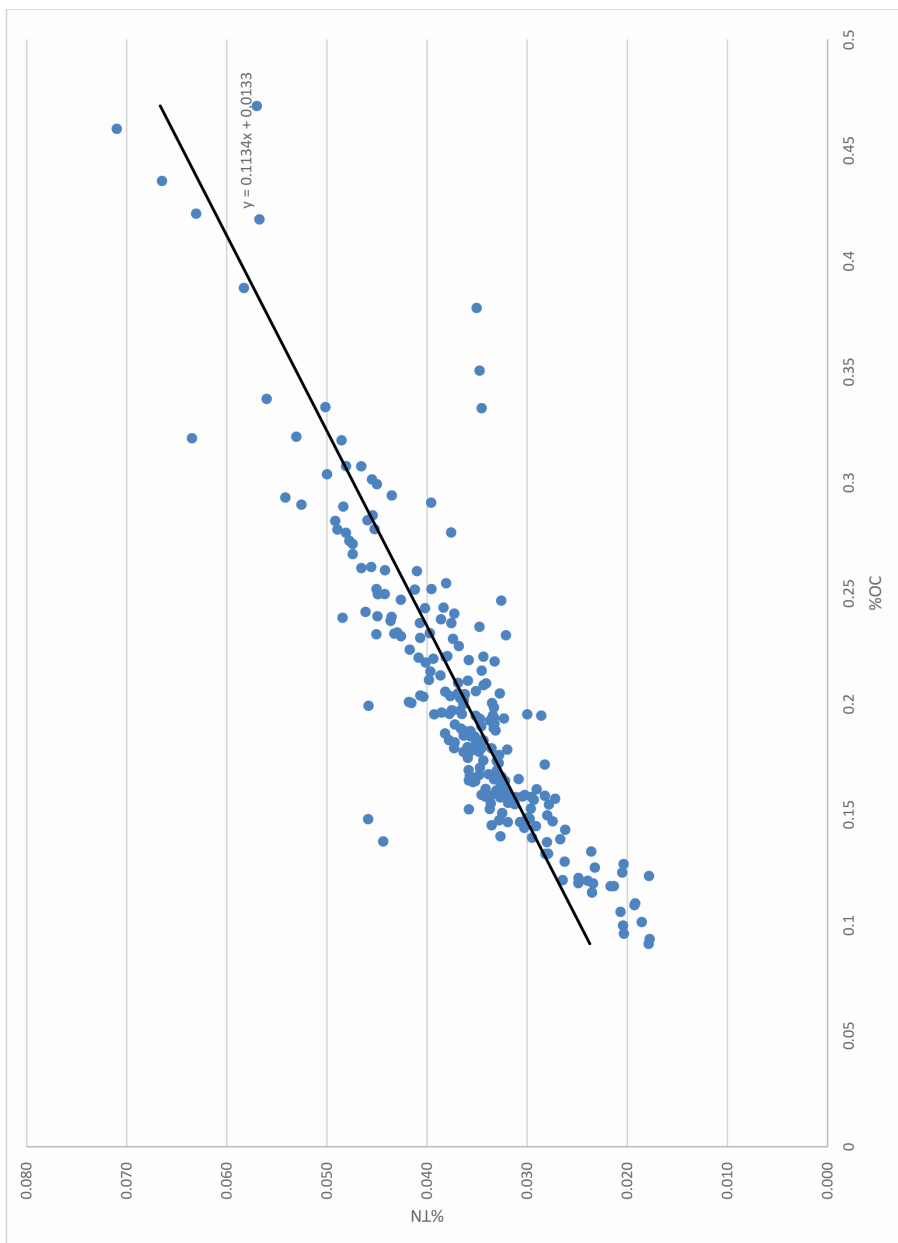


Figure S14. % total nitrogen plotted against total organic carbon with a linear regression line showing an intercept at 0.013 %TN

Chapter 6

Paleoceanography and ice sheet variability offshore Wilkes Land, Antarctica – Insights from Oligocene-Miocene TEX₈₆-based sea surface temperature reconstructions

Abstract

The volume of the Antarctic continental ice sheet(s) varied substantially during the Oligocene and Miocene (~34-5 Ma) from smaller to substantially larger than today, both on million-year and on orbital timescales. However, reproduction through physical modeling of a dynamic response of the ice sheets to climate forcing remains problematic, suggesting the existence of complex feedback mechanisms between the cryosphere, ocean, and atmosphere systems. There is therefore an urgent need to improve the models for better predictions of these systems, including resulting potential future sea level change. To assess the interactions between the cryosphere, ocean, and atmosphere, knowledge of ancient sea surface conditions close to the Antarctic margin is essential. Here, we present a new TEX_{86} -based sea surface water paleotemperature record measured on Oligocene sediments from Integrated Ocean Drilling Program (IODP) Site U1356, offshore Wilkes Land, East Antarctica. The new data are presented along with previously published Miocene temperatures from the same site. Together the data cover the interval between ~34 and ~11 Ma and encompasses two hiatuses. This record allows us to accurately reconstruct the magnitude of sea surface temperature (SST) variability and trends on both million-year and on glacial-interglacial timescales. On average, TEX_{86} values indicate SSTs ranging between 10 and 21°C during the Oligocene and Miocene, which is on the upper end of the few existing reconstructions from other high-latitude Southern Ocean sites. SST maxima occur around 30.5, 25 and 17 Ma. Our record suggests generally warm to temperate ocean offshore Wilkes Land. Based on lithological alternations detected in the sedimentary record, which are assigned to glacial-interglacial deposits, an SST variability of 1.5–3.1°C at glacial-interglacial timescales can be established. This variability is slightly larger than that of deep-sea temperatures recorded in Mg/Ca data. Our reconstructed Oligocene temperature variability has implications for Oligocene ice volume estimates based on benthic $\delta^{18}O$ records. If the long-term and orbital-scale SST variability at Site U1356 mirrors that of the nearby region of deep-water formation, we argue that a substantial portion of the variability and trends contained in long-term $\delta^{18}O$ records can be explained by variability in Southern high-latitude temperature and that the Antarctic ice volume may have been less dynamic than previously thought. Importantly, our temperature record suggests that Oligocene-Miocene Antarctic ice sheets were generally of smaller size compared to today.

1 Introduction

Numerical paleoclimate models predict that with the current rate of ice volume loss (up to 109 ± 56 Gt/yr, The IMBRIE team, 2018) several sectors of the West Antarctic marine-based ice sheet will disappear within the coming few centuries (e.g., Joughin et al., 2014; The IMBRIE team, 2018) favored by ocean warming-induced collapse. Observations show that glaciers on East Antarctica are also vulnerable to basal melt through warming of the ocean waters when they are grounded below sea level (Greenbaum et al., 2015; Miles et al., 2016; Shen et al., 2018; The IMBRIE team, 2018), making the East Antarctic Ice Sheet (EAIS) not as stable as previously thought (McMillan et al., 2014). Recent numerical modeling studies have improved on reproducing the observed ice sheet volume decrease, as they incorporate positive feedbacks (e.g., bedrock topography) to global warming and more complicated physics (e.g., hydrofracturing and ice-cliff failure) into these models (Fogwill et al., 2014; Austermann et al., 2015; Pollard et al., 2015; DeConto and Pollard, 2016; Golledge et al., 2017). These models indeed show that sensitivity to global warming is particularly high where the ice sheet is grounded below sea level (Fretwell et al., 2013), such as in the Wilkes Land Basin (Golledge et al., 2017; Shen et al., 2018).

On both glacial-interglacial (Parrenin et al., 2013) and longer-term Cenozoic timescales (Zachos et al., 2008; Pagani et al., 2011), Antarctic ice volume changes have been mostly linked to changes in atmospheric CO_2 concentrations ($p\text{CO}_2$; see e.g., Foster and Rohling, 2013; Crampton et al., 2016; Liebrand et al., 2017), modulated by astronomically forced changes in insolation (e.g., Westerhold et al., 2005; Pälike et al., 2006b; Holbourn et al., 2013; Liebrand et al., 2017; Miller et al., 2017). Foster and Rohling (2013) compiled $p\text{CO}_2$ proxy data and associated sea level reconstructions for the last 40 million years (Myr). These data suggest that if the past is projected to the future all ice on West Antarctica and Greenland may be lost under current and near-future atmospheric CO_2 conditions (400–450 ppmv) in equilibrium state. Projections of $p\text{CO}_2$ for future emission scenarios of the latest IPCC Report (2014) show a range from 500 to 1000 ppmv for the year 2100, which could lead to additional ice sheet volume loss from East Antarctica. This range in atmospheric $p\text{CO}_2$ is similar to that reconstructed for the warmest intervals of the Oligocene and Miocene epochs (full range: 200–1000 ppmv; e.g., Zhang et al., 2013; Super et al., 2018). Given that observations clearly link the recent instability of marine-based ice sheets to ocean warming, it becomes important to better constrain near-field sea surface temperatures (SSTs) from the Antarctic margin during the Oligocene and Miocene to improve our understanding of past ice sheet dynamics and the projections for the future.

EAIS volume changes have been suggested for the Oligocene and Miocene based on a number of deep-sea $\delta^{18}\text{O}$ records, which reflect a combination of bottom-water

temperature and ice volume (e.g., Shevenell et al., 2004; Westerhold et al., 2005; Pekar et al., 2006; Pekar and Christie-Blick, 2008; Liebrand et al., 2017; Miller et al., 2017), as well as sedimentary paleo-sea level reconstructions (John et al., 2011; Gallagher et al., 2013; Stap et al., 2017). These records show long-term (1-3 Myr) trends punctuated by strong but transient glaciation events (Oi and Mi events) (Westerhold et al., 2005; Pälike et al., 2006b; Liebrand et al., 2016; Hauptvogel et al., 2017; Liebrand et al., 2017; Miller et al., 2017). Following the onset of the Oligocene, marked by the Oi-1 glaciation event, the long-term trend shows a shift towards lighter $\delta^{18}\text{O}$ values and a steady increase towards 27 Ma, then a decrease to 24 Ma and a final increase leading into the Miocene, marked by the Mi-1 glaciation event (Zachos, 2001; Cramer et al., 2009; Beddow et al., 2016; Liebrand et al., 2016). Miocene benthic $\delta^{18}\text{O}$ long-term trends show a sudden increase at 16.9 Ma, which marks the onset of the mid-Miocene Climatic Optimum (MMCO), a plateau phase, and a subsequent stepwise decrease known as the mid-Miocene Climatic Transition (MCT) (Shevenell et al., 2004; Westerhold et al., 2005; Holbourn et al., 2007, 2013, 2015). The Oligocene and Miocene glaciations are paced by periods of strong 110-kyr eccentricity fluctuations of up to 1‰ (Liebrand et al., 2011, 2016, 2017). These $\delta^{18}\text{O}$ fluctuations may mostly result from the waxing and waning of the EAIS, in which case the ice sheet was highly dynamic, or they mostly reflect large changes in deep-sea temperature, in which case large SST fluctuations in the region of deep-water formation were to be expected. Considering the former, fluctuations between 50% and 125% of the present-day EAIS have been suggested for the Oligocene (Pekar et al., 2006; DeConto et al., 2008; Pekar and Christie-Blick, 2008), but this amount of variability has not yet been entirely reproduced by numerical modeling studies (DeConto et al., 2008; Pollard et al., 2015; Gasson et al., 2016). Considering the latter, several studies have suggested that during the Oligocene the southern high latitudes were the prevalent source for cold deep-water formation (Katz et al. 2011; Goldner et al. 2014; Borelli & Katz 2015). Hence, deep-water temperature records from the southern high latitudes, particularly those capturing temperature changes on million-year as well as orbital timescales, may provide information on the relative contribution of deep-sea temperature variability to the $\delta^{18}\text{O}$ records. However, reconstructions of deep-water temperature based on $\delta^{18}\text{O}$ and Mg/Ca ratios of benthic foraminifera are hampered by the poor preservation of carbonates on the high-latitude Southern Ocean floor and rely on critical assumptions about past composition of seawater chemistry. Therefore, one needs to assume that the deep-sea temperature trend captured in the Oligocene and Miocene $\delta^{18}\text{O}$ records is related to surface water temperature in the Southern Ocean similar to today (Jacobs, 1991; Baines, 2009) and in the Eocene (Bijl et al., 2009). Based on this assumption, Southern Ocean SSTs would potentially gauge deep-sea temperature variability. Only few Oligocene SST estimates are available for the Southern

Ocean and they relate to the early Oligocene (Plancq et al., 2014; Petersen and Schrag, 2015). Few Southern Ocean SST records are available for the early and mid-Miocene (14–17 Ma) (Shevenell et al., 2004; Kuhnert et al., 2009; Majewski and Bohaty, 2010) and only two (Levy et al., 2016; Sangiorgi et al., 2018) are derived from south of the Polar Front (PF). Obstacles for reconstructing Oligocene and Miocene SST in the Southern Ocean are the paucity of stratigraphically well-calibrated sedimentary archives, as well as suitable indicator fossils/compounds within these sediments that can be used to reconstruct SST.

In 2010, the Integrated Ocean Drilling Program (IODP) cored a sedimentary archive at the boundary of the continental rise and the abyssal plain offshore Wilkes Land with a well-dated Oligocene and Miocene sequence: IODP Site U1356 (Fig. 1), suitable for paleoclimatological analysis. In this study we use the now well-established ratio between several isoprenoid glycerol dialkyl glycerol tetraethers (GDGTs), the so-called TEX₈₆ proxy (Schouten et al., 2002, 2013), to reconstruct SSTs at this high-latitude Southern Ocean site. We present new SST data based on TEX₈₆, covering almost the entire Oligocene, along with published TEX₈₆ values for the mid-Miocene section (Sangiorgi et al., 2018). Detailed lithological logging of both the Oligocene and Miocene sections of Site U1356 allows for the distinction of glacial and interglacial deposits (Salabarnada et al., 2018). This enables us to assess long-term evolution of SSTs in proximity of the ice sheet as well as the temperature differences between glacials and interglacials on orbital timescales, which have implications on the dynamics of the Antarctic ice sheet and its sensitivity to climate change. We compare our record with the few existing early Oligocene and mid-Miocene SST data from other high-latitude Southern Ocean sites as well as with deep-water $\delta^{18}\text{O}$ and Mg/Ca-based bottom-water temperature (BWT) records from lower latitudes (Billups and Schrag, 2002; Lear et al., 2004; Shevenell et al., 2004), and we discuss the implications of our findings.

Together with the companion papers by Salabarnada et al. (2018) and Bijl et al. (2018b) on the lithology and dinocyst assemblages of Site U1356, we contribute significantly to the limited knowledge that exists on Oligocene-Miocene paleoceanographic conditions close to the Antarctic margin.

2 Materials & Methods

2.1 Site description

Integrated Ocean Drilling Program (IODP) Expedition 318 Site U1356 was cored about 300 kilometers off the Wilkes Land coast (63°54.61'S, 135°59.94'E) at the boundary between the continental rise and the abyssal plain at a water depth of 3992 m (Expedition 318 Scientists, 2011a, see Fig. 1). Today, this site is south of the Antarctic PF and is under the influence of by Antarctic Bottom Water (AABW), Lower Component Deep Water

(LCDW), Upper Component Deep Water (UCDW), and Antarctic Surface Water (AASW) (Orsi et al., 1995). Modern-day annual SST values lie around 0°C (summer SSTs are about 1–2°C) (Locarnini et al., 2010).

2.2 Sedimentology

At present, IODP Site U1356 receives sediments transported from the shelf and the slope as well as the in situ pelagic component. Although we have no quantitative constraints on the water depth during the Oligocene and Miocene, the sediments as well as the biota suggest a deep-water setting at Site U1356 during these times (Houben et al., 2013; Escutia et al., 2014). Sedimentary units of Hole U1356A have been defined in the shipboard report (Expedition 318 Scientists, 2011a). Detailed logging of the sediments recovered in Hole U1356A has revealed that the Oligocene and Miocene sedimentary record (between 95.40 and 894.80 meters below sea floor, mbsf) consists mostly of alternations of (diatomaceous) laminated and bioturbated sediments, gravity flow deposits, and carbonate beds (Salabarnada et al., 2018; Sangiorgi et al., 2018) (Fig. 2). Gravity flow deposits include mass-transport deposits (MTDs) formed by the slump and debris flow sediments of the Miocene, Oligocene and Eocene-Oligocene transition (EOT), and the late Oligocene-Miocene turbidite-type facies as defined by Salabarnada et al. (2018). Samples from the MTDs contain the largest contribution of reworked older material transported from the continental shelf (Bijl et al., 2018b), while in the other lithologies, this component is reduced or absent.

Between 593.4 and 795.1 mbsf, there are clear alternations between greenish carbonate-poor laminated and grey bioturbated deposits with some carbonate-rich bioturbated intervals. These deposits are interpreted as contourite deposits recording glacial-interglacial environmental variability (Salabarnada et al., 2018). Above 600 mbsf, sediments mostly consist of MTDs with low to abundant clasts (Fig. 2). However, between the MTDs greenish or grey laminated deposits and greenish or grey bioturbated deposits are preserved. Near the bottom of Unit III as defined in the shipboard report (around 433 mbsf and below), a different depositional setting is represented with alternations between pelagic clays and (ripple) cross-laminated sandstone beds (Expedition 318 Scientists, 2011a). These sandy (ripple) cross-laminated beds are interpreted as turbidite deposits (Salabarnada et al., 2018). Above these turbidite deposits, there are diatomaceous silty clays that are characterized by an alternation of green laminated and grey homogeneous (bioturbated) silty clays. Apart from their diatom content, these deposits are very similar to the Oligocene alternations between carbonate-poor laminated and carbonate-containing bioturbated deposits, and are therefore interpreted likewise (Salabarnada et al., 2018). Up-core within the Miocene section, the alternations between laminated and

homogeneous diatomaceous silty clays become more frequent. In the upper Miocene sections (95.4–110 mbsf) laminations become less clear as the sediments become less consolidated; however green and grey alternations can still be distinguished. The more diatomaceous green deposits are interpreted as interglacial stages. Samples analyzed for TEX₈₆ were chosen from all the different lithologies (Fig. 2). In particular the (diatomaceous) laminated and bioturbated deposits were sampled, so we can test whether the glacial-interglacial variability inferred from the lithology is reflected in our TEX₈₆ data.

2.3 Oligocene and Miocene paleoceanographic setting

The Oligocene and Miocene Southern Ocean paleoceanographic configuration is still obscure and controversial. Some studies suggest that most Southern Ocean surface and deep-water masses were already in place by Eocene-Oligocene boundary times (Katz et al., 2011). Neodymium isotopes on opposite sides of Tasmania suggest that an eastward-flowing deep-water current has been present since 30 Ma (Scher et al., 2015). A westward-flowing Antarctic Circumpolar Counter Current (ACCC) was already established during the middle Eocene (49 Ma; Bijl et al., 2013a) (Fig. 1). The Tasmanian Gateway opening also allowed the proto-Leeuwin current (PLC) flowing along southern Australia to continue eastward (Carter et al., 2004; Stickley et al., 2004) (Fig. 1). However, numerical modeling studies show that throughflow of the Antarctic Circumpolar Current (ACC) was still limited during the Oligocene (Hill et al., 2013) because Australia and South America were substantially closer to Antarctica (Fig. 1) than today (Markwick, 2007). Moreover, tectonic reconstructions and stratigraphy of formations on Tierra del Fuego suggest that following open conditions in the middle and late Eocene, the seaways at Drake Passage underwent uplift starting at 29 Ma and definitive closure around 22 Ma (Lagabrielle et al., 2009). Evidence for active spreading and transgressional deposits in the Tierra del Fuego area records the widening of Drake Passage from 15 Ma onwards. The timing of the Drake Passage opening, which allowed for significant ACC throughflow, is still heavily debated (Lawver and Gahagan, 2003; Livermore et al., 2004; Scher and Martin, 2006, 2008; Barker et al., 2007; Dalziel, 2014; Maldonado et al., 2014). Contourite deposits suggest that strong Antarctic bottom-water currents first appeared in the early Miocene (21.3 Ma) and that Weddell Sea Deep Water has been able to flow westwards into the Scotia Basin since the middle Miocene (~12.1 Ma) (Maldonado et al., 2003, 2005). It has been suggested that the closure and the reopening of Drake Passage are responsible for the warmer late Oligocene and the mid-Miocene Climatic Optimum (MMCO), and the subsequent cooling during the mid-Miocene Climate Transition (MMCT), respectively, as inferred from the benthic $\delta^{18}\text{O}$ records (Lagabrielle et al., 2009). If the throughflow at the Drake Passage was

limited in the late Oligocene and early Miocene, the ACCC was more dominant than the ACC during these times according to the model study of Hill et al. (2013).

Antarctica was positioned more eastward during the Oligocene and Miocene relative to today (due to true polar wander; van Hinsbergen et al. 2015), and Site U1356 was more to the north during the Oligocene and Miocene compared to today (approximately 59°S at 34 Ma to 61°S at 10 Ma). Reconstructions of the position of the PF based on the distribution of calcareous and siliceous microfossils, place the PF at 60°S during the early Oligocene (Scher et al., 2015), which means that Site U1356 may have crossed the PF between 34 and 10 Ma. The more northerly position of Site U1356 may have facilitated the influence of warmer waters during the mid-Miocene at Site U1356 (Sangiorgi et al., 2018), and therefore bottom-water formation may have been absent or limited at Site U1356. Bottom-water formation is expected in more southerly positioned shallow basins, such as the nearby Ross Sea, where glaciers extended onto the Antarctic shelf (Sorlien et al., 2007). However, neodymium isotopes obtained from Site U1356 suggest that bottom water formed offshore the Adélie and Wilkes Land coast during the early Eocene, which seems in contrast with the globally high temperature of that time (Huck et al., 2017). Modeling studies have, however, suggested that density contrasts created by seasonal changes in SST and salinity (with or without sea ice) may have induced deep-water formation and downwelling around Antarctica (Lunt et al., 2010; Goldner et al., 2014).

2.4 Age model U1356

Oligocene sediments were recovered in the section from 894.68 mbsf (first occurrence (FO) *Malvinia escutiana*) to 432.64 mbsf (base of subchron C6Cn.2n) at IODP Hole U1356A (Bijl et al., 2018a). The shipboard age model (Tauxe et al., 2012) was based on biostratigraphy with magnetostratigraphic tie points and chronostratigraphically calibrated to the Geologic Time Scale of 2004 (Gradstein et al., 2004). We follow Bijl et al. (2018a), who recalibrated the existing age tie points to the Geologic Timescale of 2012 (GTS2012, Gradstein et al., 2012). The FO of *Malvinia escutiana* (894.68 mbsf; 33.5 Ma; Houben et al., 2011) and the last occurrence (LO) of *Reticulofenestra bisecta* (431.99 mbsf; 22.97 Ma) and the paleomagnetic tie points were used to convert the data to the time domain (see Fig. 4). For the Oligocene-Miocene boundary, we also follow Bijl et al. (2018a) who infer a hiatus spanning from ~22.5 to 17.0 Ma between Cores 44R and 45R (~421 mbsf). It is unknown whether additional short hiatuses exist within the Oligocene record, but this is likely considering the presence of MTDs (Salabarnada et al., 2018; Fig. S1). In addition, the poor core recovery in some intervals dictates caution in making detailed stratigraphic comparisons with other records.

For the Miocene section of Hole U1356A we follow Sangiorgi et al. (2018), who applied the constrained optimization methodology (CONOP) of Crampton et al. (2016) to diatom and radiolarian biostratigraphic events to construct an age model. Based on the application of CONOP to the diatom and radiolarian biostratigraphic events a second hiatus was identified spanning approximately the interval between 13.4 and 11 Ma.

2.5 Glycerol dialkyl glycerol tetraether extraction and analysis

In addition to the 29 samples from the Miocene section presented in Sangiorgi et al. (2018), a total of 132 samples from the Oligocene and early Miocene part of the sedimentary record (Table S1) were processed for the analysis of GDGTs used for TEX₈₆. Spacing varies due to variability in core recovery and GDGT preservation. Furthermore, sampling of disturbed strata was avoided. Sample processing involved manual powdering of freeze-dried sediments after which lipids were extracted through accelerated solvent extraction (ASE; with a dichloromethane (DCM)/methanol (MeOH) mixture, 9:1 v/v, at 100°C and 7.6 x 10⁶ Pa). The lipid extract was separated using Al₂O₃ column chromatography and hexane/DCM (9:1, v/v), hexane/DCM (1:1, v/v) and DCM/MeOH (1:1, v/v) for separating apolar, ketone, and polar fractions, respectively. Then, 99 ng of C₄₆ internal standard was added to the polar fraction, containing the GDGTs, for quantification purposes (see Huguet et al., 2006). The polar fraction of each sample was dried under N₂, dissolved in hexane/isopropanol (99:1, v/v) and filtered through a 0.45 µm 4 mm diameter polytetrafluorethylene filter. After that the dissolved polar fractions were injected and analyzed by high-performance liquid chromatography–mass spectrometry (HPLC–MS) at Utrecht University. Most samples were analyzed following HPLC–MS settings in Schouten et al. (2007), while some samples (see Table S1) were analyzed by ultra-high-performance liquid chromatography–mass spectrometry (UHPLC–MS) according to the method described by Hopmans et al. (2016). Only a minor difference between TEX₈₆ index values generated by the different methods was recorded by Hopmans et al. (2016) (on average 0.005 TEX₈₆ units). Reruns of five samples with the new method show an average difference between the two methods of 0.011 TEX₈₆ units (see Table S2), which translates to a 0.6°C temperature difference based on TEX₈₆^H of Kim et al. (2010) and lies well within the calibration error of 2.5°C. GDGT peaks in the (U)HPLC chromatograms were integrated using ChemStation software. A total of 16 of the 132 samples had too low concentrations of GDGTs to obtain a reliable TEX₈₆ value and have been discarded (i.e., with a peak height less than 3x background, as well as peak areas below 5*10³ mV and 3*10³ mV for HPLC-MS and UHPLC–MS, respectively).

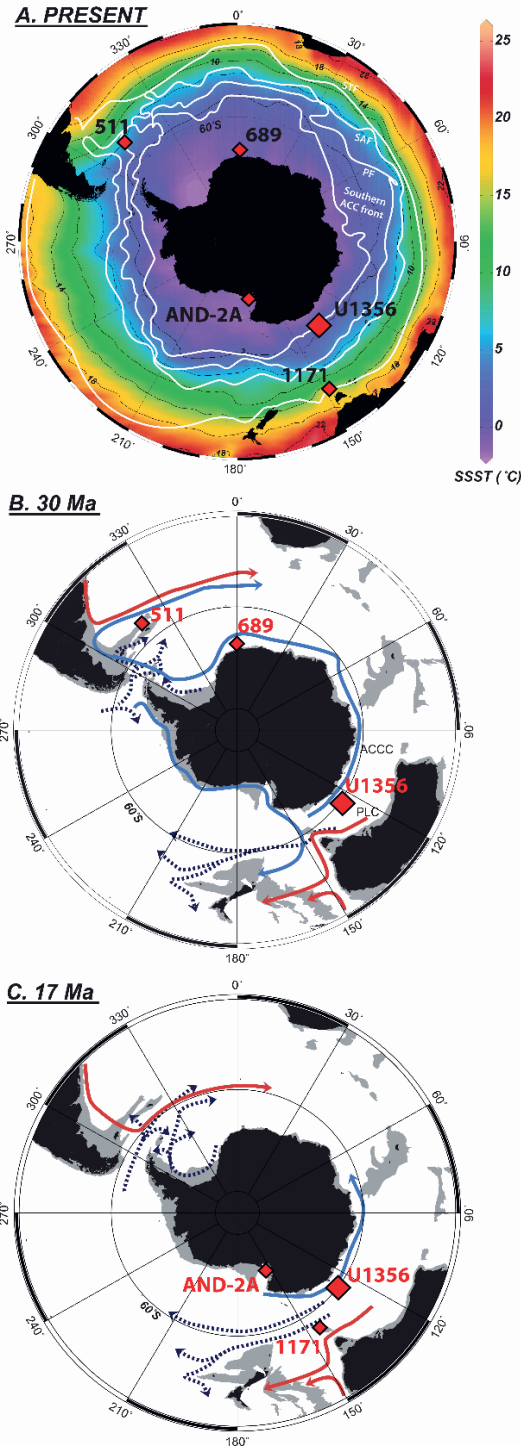


Figure 1: (A) Present-day Southern Ocean summer temperatures and geography obtained from the World Ocean Atlas (Locarnini et al., 2010) using Ocean Data View and Southern Ocean fronts obtained from Orsi et al. (1995). PF: Polar Front, SAF: Sub-Antarctic Front, STF: Sub-Tropical Front. Red diamonds indicate DSDP/ODP/IODP site locations.

(B) Map of Antarctica around 30 Ma, a modified reconstruction by the Ocean Drilling Stratigraphic Network Plate Tectonic Reconstruction Service (continents in black, shelf areas in grey). Paleolatitudes calculated with paleolatititude.org (van Hinsbergen et al., 2015). Reconstructed cold (light blue) and warm (red) surface currents are based on publications by Stickley et al. (2004), Warnaar (2006), Bijl et al. (2011), Bijl et al., (2013), and Douglas et al. (2014). Reconstructed bottom-water currents (dotted dark blue) are based on publications by Carter et al. (2004), Livermore et al. (2007), Maldonado et al. (2014) and Scher et al. (2015). ACCC: Antarctic Circumpolar Current, PLC: proto-Leeuwin Current.

(C) The same as the middle figure, but then for the period around 17 Ma.

We have used the branched and isoprenoid tetraether (BIT) index (Hopmans et al., 2004) to verify the relative contribution of terrestrial GDGTs in our samples, compared to marine GDGTs. As isoprenoid GDGTs (isoGDGTs), used for the TEX_{86} proxy, are also produced in terrestrial soils, albeit in minor amounts, they can alter the marine signal when there is a large contribution of soil organic matter to marine sediments. This contribution can be identified by determining the relative amount of branched GDGTs (brGDGTs), which are primarily derived from soil (Weijers et al., 2006), to that of the isoGDGT crenarchaeol (Hopmans et al., 2004). Samples with BIT index values above 0.3 indicate that the TEX_{86} -based temperature may be affected by a contribution of soil-derived isoGDGTs and thus should be discarded (see Weijers et al. 2006), although, a high BIT value can sometimes also result from production of brGDGTs in marine sediments and the water column (Peterse et al., 2009; Sinninghe Damsté, 2016). The composition of the brGDGTs can be used to distinguish between marine and soil-derived GDGT input, in particular by using the $\#ring_{\text{tetra}}$ index (Sinninghe Damsté, 2016). The $\#rings_{\text{tetra}}$ index can discriminate between marine and soil-derived brGDGTs as the composition of soil-derived GDGTs typically shows high amounts of the acyclic tetramethylated GDGT-Ia, while a dominance of cyclic tetramethylated (Ib and Ic) brGDGTs has been attributed to *in situ* production within the sediments (Sinninghe Damsté, 2016).

Oxic degradation of GDGTs does not affect the relative amounts of individual isoGDGTs (Huguet et al., 2009; Kim et al., 2009). However, oxic degradation may lead to an increased relative influence of soil-derived isoGDGTs, which could bias the TEX_{86} in different ways depending on the composition of the soil-derived isoGDGTs (Huguet et al., 2009). Higher BIT index values are expected in samples with enhanced amounts of soil-derived isoGDGTs due to oxic degradation and will be discarded. In addition, we calculated the methane index (MI) (Zhang et al., 2011), GDGT-0 / crenarchaeol (Blaga et al., 2009; Sinninghe Damsté et al., 2009), GDGT-2 / crenarchaeol ratios (Weijers et al., 2011), and ring index (Zhang et al., 2016) to check for input of methanogenic or methanotrophic archaea, or any other non-temperature-related biases to TEX_{86} .

2.6 TEX_{86} calibrations

The TEX_{86} proxy is based on the distribution of isoGDGTs preserved in sediments (Schouten et al., 2002, 2013). In marine sediments these lipids are assumed to originate from cell membranes of marine Thaumarchaeota, which are one of the dominant prokaryotes in today's ocean and occur throughout the entire water column (e.g., Karner et al., 2001; Church et al., 2003, 2010). Applying TEX_{86} in polar oceans has been challenged by the observation that high scatter in the cold end of the core-top dataset for TEX_{86} is present (Kim et al., 2010; Ho et al., 2014). To overcome some of the scatter as well as the

nonlinearity of the TEX_{86} -SST relationship, Kim et al. (2010) proposed two isoGDGT-based proxies and calibrations: $\text{TEX}_{86}^{\text{L}}$ and $\text{TEX}_{86}^{\text{H}}$. The latter is not considered here as it was particularly developed for low-latitude high-temperature surface waters, and high-latitude core-top values were left out of the calibration (Kim et al., 2010). The former was particularly developed for high-latitude low-temperature surface waters. However, it has been shown that $\text{TEX}_{86}^{\text{L}}$ is sensitive to changes in the GDGT-2/GDGT-3 ratio ($[2]/[3]$), which are unrelated to SST (Taylor et al., 2013; Hernández-Sánchez et al., 2014). Instead these $[2]/[3]$ changes result from changes in the Thaumarchaeota community structure in the water column because the community that thrives in deeper (>1000 mbsl) nutrient and ammonia-rich waters produces significantly more GDGT-2 and thereby introduces a water-depth dependency into the calibration (Taylor et al., 2013; Hernández-Sánchez et al., 2014; Villanueva et al., 2015). Close to the Antarctic margin, the abundance of shallow versus deep-water Thaumarchaeota communities at deep-water sites, like Site U1356 during the Oligocene-Miocene, could be affected by the presence of sea ice and the relative influence of (proto-)UCDW and (proto-)LCDW upwelling. For this reason, $\text{TEX}_{86}^{\text{L}}$ -based calibrations are also not the focus of our study. Instead, we focus on TEX_{86} -based calibrations only. All existing $\text{TEX}_{86}^{\text{(H)}}$ and $\text{TEX}_{86}^{\text{L}}$ calibrations have, however, been applied to our data and are presented as a figure in the Supplement (Figure S1).

In addition to the $\text{TEX}_{86}^{\text{L}}$ and $\text{TEX}_{86}^{\text{H}}$ calibrations, Kim et al. (2010) also constructed a linear SST calibration based on TEX_{86} that does include the high-latitude core-top values. Despite the scatter at the cold end of the calibration that results from the inclusion of Arctic surface sediment samples with deviating TEX_{86} -SST relations, this calibration ($\text{SST} = 81.5 \cdot \text{TEX}_{86} - 26.6$ with a calibration error of $\pm 5.2^\circ\text{C}$) has been shown to plot onto the annual mean sea surface temperatures of the World Ocean Atlas 2009 (WOA2009; Locarnini et al., 2010) for the surface sample TEX_{86} values obtained in the Pacific sector of the Southern Ocean (Ho et al., 2014). However, this calibration is likely to be influenced by regional differences in water depth, oceanographic setting and archaeal communities (Trommer et al., 2009; Tierney and Tingley, 2014; Kim et al., 2015; Villanueva et al., 2015; Kim et al., 2016). In addition, this calibration suffers from regression dilution bias caused by the uncertainty in the measured TEX_{86} values plotted on the x axis (Tierney and Tingley, 2014). Regression dilution bias causes flattening of the slope (Hutcheon et al., 2010) and therefore affects reconstructed TEX_{86} -based temperatures at the lower and upper end of the calibration range. Modern-analogue calibration methods exist today to overcome this regression dilution bias as well as some of the regional variability in TEX_{86} -SST relationships (Tierney and Tingley, 2014, 2015). These calibrations are based on a Bayesian spatially varying regression model (BAYSPAR), which infers a best estimate for intersection and slope of the calibration based on an assembly of 20° by 20° spatial grid boxes that

statistically fit best with an estimate of the prior distribution of temperature (i.e. the prior) (Tierney and Tingley, 2014). As for deep-time temperature reconstructions this prior cannot be based on modern-day annual mean SSTs, the BAYSPAR method requires a user-specified mean and variance for this prior (Tierney and Tingley, 2014). The prior for Site U1356 is obtained from recent clumped isotope measurements (Δ_{47}) on planktonic foraminifers from Maud Rise (ODP Site 689) (Petersen and Schrag, 2015), which show early Oligocene temperatures of 12°C. The BAYSPAR approach (Tierney and Tingley, 2014, 2015) selects only those TEX_{86} values from the calibration set of Kim et al. (2010) and an additional 155 core tops from regional core-top TEX_{86} studies that are relevant for the study site, thereby generating a more regional calibration. Application of BAYSPAR on Site U1356 using a prior mean of 12°C does, however, result in the exclusion of the high-latitude core-top values. For this reason we find it useful to compare the BAYSPAR results to the results obtained by using the linear calibration of Kim et al. (2010). The BAYSPAR calibration method provides an estimate for SST and an upper and lower 90% confidence interval. For comparison to the linear calibration of Kim et al. (2010) a standard error (SE) has been calculated from these confidence intervals by assuming a normal distribution around the mean, in which case the 90% confidence interval boundaries can be calculated as the mean plus or minus 1.645 times the SE.

Despite these recent efforts in improving the TEX_{86} -SST relationship, TEX_{86} is known to overestimate temperatures at high latitudes due to multiple possible biases, such as seasonality (Schouten et al., 2013; Ho et al., 2014) and the incorporation of a subsurface signal (0-200 mbsl) at deep-ocean sites (>1000 mbsl) (Huguet et al., 2007; Yamamoto et al., 2012; Hernández-Sánchez et al., 2014; Rodrigo-Gámiz et al., 2015). There is, however, general consensus that TEX_{86} is able to capture decadal and longer-term temperature trends (Richey and Tierney, 2016), which is why the main focus of this work is on relative SST changes. Indeed, subsurface export of GDGTs is implicitly incorporated into the global TEX_{86} -SST calibration and has therefore no implications for reconstructing SST (Hernández-Sánchez et al., 2014). The highest GDGT fluxes are closely linked to the highest organic matter, opal (diatom frustules) and lithogenic particle fluxes (Yamamoto et al., 2012; Mollenhauer et al., 2015) and the lack of production of sinking particles that can incorporate GDGTs formed in deeper waters prevents biasing of surface-sediment TEX_{86} values towards deep-water temperatures (Yamamoto et al., 2012; Basse et al., 2014; Mollenhauer et al., 2015). Still, particular environmental settings (e.g., upwelling regions, regions with oxygen-depleted deep waters, freshwater surface waters) might favor the transport of a subsurface temperature (T_{sub}) signal to the sediments (Lopes dos Santos et al., 2010; Kim et al., 2012a, 2012b; Mollenhauer et al., 2015). Also for polar oceans it has been suggested that reconstructed temperatures reflect T_{sub} since today Thaumarchaeota

are virtually absent in the upper 0-45 m of Antarctic low-salinity surface waters formed by seasonal retreat of sea ice (Kalanetra et al., 2009). Surface water conditions over Site U1356 during the Oligocene and the MMCO were much like present-day regions south of the STF and likely not under the influence of a seasonal sea ice system (see Fig. 1) (Bijl et al., 2018b; Sangiorgi et al., 2018). For these time intervals, there is no reason to believe that surface waters were devoid of Thaumarchaeota due to the presence of sea ice and that TEX_{86} values are influenced by an increased subsurface signal. For the earliest Oligocene and the MMCT, the presence of *Selenopemphix antarctica* suggests that Site U1356 was under the influence of a seasonal sea ice system (Bijl et al., 2018b). For these periods, a reconstruction of T_{sub} values may be more appropriate, but this would still imply that SSTs are warmer. We limit our discussion to the TEX_{86} -based reconstructions of SST, notably, because it has been shown that TEX_{86} -based SST estimates based on the linear calibration of Kim et al. (2010) obtained from core-top samples from today's sea-ice-influenced Southern Ocean, are in accordance with WOA2009 mean annual SST (Ho et al., 2014). This suggests that the effect of sea ice on surface and subsurface isoGDGT production is incorporated into the linear calibration of Kim et al. (2010). We therefore consider that despite the potential absence of Thaumarchaeota in the surface waters during the early Oligocene and the MMCT, the calibration of Kim et al. (2010) does provide a reliable estimate of SST for these time intervals. Moreover, [2]/[3] ratios for the earliest Oligocene and the MMCT are relatively low and show much less variability compared to the rest of the record (Fig. 2), which is opposite of what is expected when the relative influence of deep-water Thaumarchaeota increases (Hernández-Sánchez et al., 2014; Villanueva et al., 2015). Calibrations to T_{sub} (Kim et al., 2012a, 2012b; Tierney and Tingley, 2015) are therefore not considered here, but are included in Figure S1 in the Supplement.

To obtain an estimate for the long-term average SST trends and confidence levels, a local polynomial regression model (LOESS) has been applied using R, which is based on the local regression model “cloess” of Cleveland et al. (1992). This method of estimating the long-term average trend is preferred over a running average, because it accounts for the variable sample resolution. For the parameter “span”, which controls the degree of smoothing a value was automatically selected through generalized cross-validation (R-package fANCOVA; Wang 2010).

3 Results

3.1 Discarding potentially biased TEX_{86} values

A total of 116 samples spanning the Oligocene and earliest Miocene were analyzed for TEX_{86} in this study. When the Miocene samples of Sangiorgi et al. (2018) are included, the total number of samples with sufficiently high GDGT concentrations is 145. However,

only 77 of these 145 TEX₈₆ values could be used for SST reconstruction for reasons discussed below.

Although sampling of disturbed strata was avoided, a total of 46 Oligocene and Miocene samples proved to be obtained from MTDs after detailed logging by Salabarnada et al. (2018). Hence, samples from these beds may not reflect *in situ* material exclusively. For the EOT slumps, this is supported by a high degree of reworked Eocene specimens within the dinoflagellate cyst assemblage below 880.08 mbsf (Houben et al., 2013). In addition, the clast-bearing deposits of Units II and IV and decimeter-thick granule-rich interbeds of Unit VIII (Fig. 2) are interpreted as ice-rafted debris (IRD) deposits (Expedition 318 Scientists, 2011a; Sangiorgi et al., 2018) and thus indicate the presence of icebergs above the site during deposition of these intervals. To avoid potential bias due to allochthonous input and reworking of older sediments, all samples from MTDs are excluded from the SST reconstructions.

A contribution of terrestrial isoGDGTs can also bias the marine pelagic TEX₈₆ signal and can be verified by the BIT index (Weijers et al., 2006; Hopmans et al. 2004). In 17 samples – none of which were derived from MTDs – the BIT index value was >0.3, which indicates that the reconstructed TEX₈₆ temperatures are likely affected by a contribution of soil-derived isoGDGTs (Weijers et al., 2006; Hopmans et al. 2004). For selected samples, the composition of brGDGTs was analyzed by UHPLC–MS (Hopmans et al., 2016), which showed that #rings_{tetra} values were below 0.7 (Sinninghe Damsté, 2016) meaning that a significant portion of the brGDGTs was likely derived from soil. Furthermore, the TEX₈₆ signal may be influenced by a potential input of isoGDGTs from methanogenic archaea. Since methanogenic Euryarchaeota are known to produce GDGT-0 and small amounts of GDGT-1, GDGT-2, and GDGT-3 (Koga et al., 1998), but not crenarchaeol, such a contribution may be recognized by GDGT-0/crenarchaeol values >2 (Blaga et al., 2009; Sinninghe Damsté et al., 2009). Similarly, methanotrophic Euryarchaeota may contribute significant amounts of GDGT-1, GDGT-2 and GDGT-3 that can be identified by values >0.3 for the MI (Zhang et al., 2011) and/or GDGT-2 / crenarchaeol values >0.4 (Weijers et al., 2011). In total 19 non-MTD-derived samples have too high GDGT-0 / crenarchaeol ratios, too high MI values, or too high GDGT-2 / crenarchaeol values. Of these 19 samples, 14 also have too high BIT values, meaning that in total 22 samples are discarded because of a potential contribution of soil-derived and methanogenic or methanotrophic archaeal isoGDGT input. As a final exercise, the ring index ($|\Delta RI|$) was calculated for our dataset to identify all other non-temperature-related influences on the distribution of isoGDGTs in the samples (Zhang et al., 2016). In addition to the non-temperature-related influences discussed above, these could include oxygen concentrations (Qin et al., 2015), archaeal growth phase (Elling et al.,

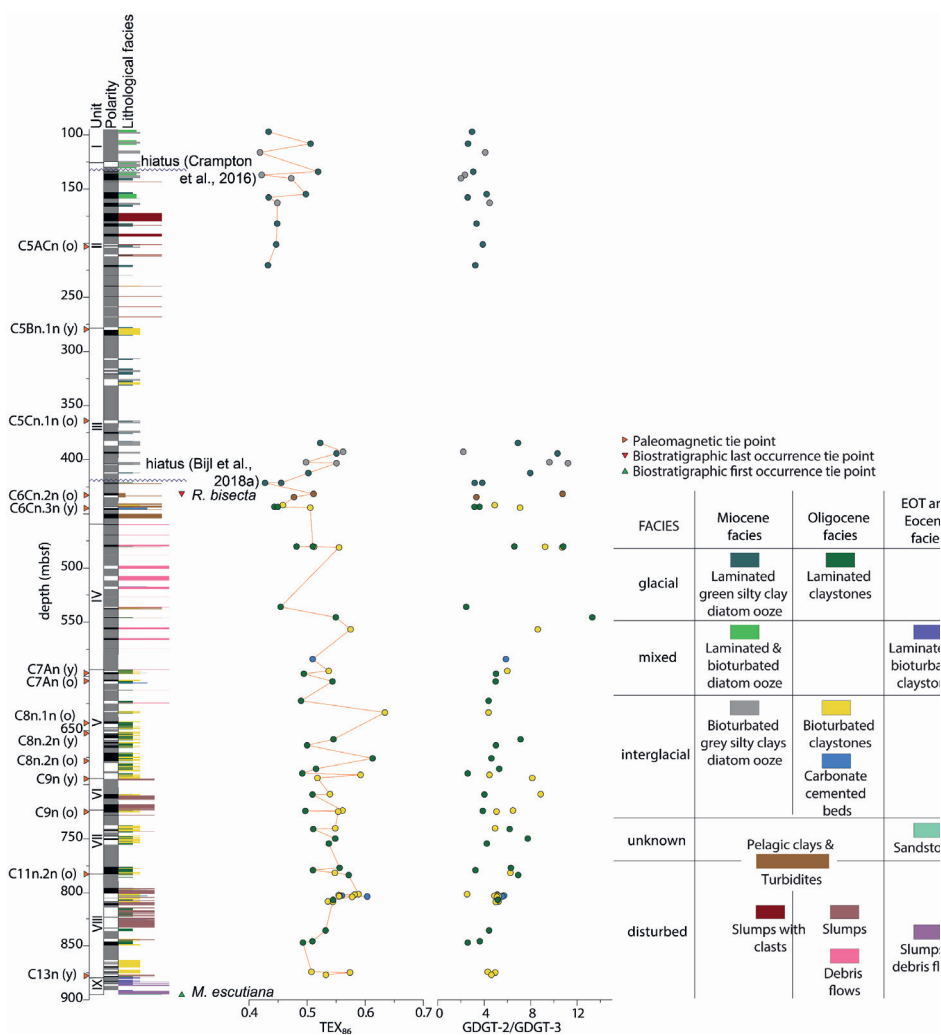


Figure 2: Lithology, TEX₈₆ values and GDGT-2 / GDGT-3 ratios of Hole U1356A plotted against depth (mbsf) with units according to Expedition 318 Scientists (2011a) and chronostratigraphic tie points and paleomagnetic polarities obtained from Tauxe et al. (2012), adjusted by Crampton et al. (2016) and Bijl et al. (2018a). Depositional facies and interpretation are indicated with colors following Salabarnada et al. (2018), see legend to the right. Colors of the TEX₈₆ and GDGT-2 / GDGT-3 values reflect the lithology they have been sampled from.

2014), ammonia oxidation rates (Hurley et al., 2016) and ecological factors (Elling et al., 2015). Using $|\Delta RI| > 0.6$ as a cutoff, no additional samples were discarded. All GDGT data and TEX₈₆ values, including those of the discarded samples, are presented in the Supplement (Fig. S2, Table S1).

3.2 Relation between TEX₈₆ values and lithology

After excluding samples with potentially biased TEX₈₆ values, the remaining record shows short-term variability that is strongly linked to the lithology (see Fig. 2). Sediments from the greenish laminated, carbonate-poor (glacial) facies produce statistically significant (t test p value < 0.005) lower TEX₈₆ values than values obtained from the grey carbonate-rich bioturbated (interglacial) facies. For the entire record, TEX₈₆ values are on average 0.50 and 0.53 for the glacial (laminated) and interglacial (bioturbated) lithologies, respectively. Paleoceanographic changes between glacial and interglacial periods may have affected the community structure of the Thaumarchaeota living over Site U1356, which may have introduced a nonthermal component to the TEX₈₆ record that could contribute to the observed difference between TEX₈₆ values from laminated and bioturbated facies. To test if changes in the composition of the Thaumarchaeota community have contributed significantly to the observed difference between TEX₈₆ values from laminated facies and bioturbated facies, a t test was also performed on the [2]/[3] ratios of laminated and bioturbated lithologies for the entire record (Fig. 2). No significant difference was observed between the laminated and bioturbated facies (t test p value > 0.2).

3.3 Oligocene and Miocene long-term sea surface temperature trend

Based on the linear temperature calibration of Kim et al. (2010) (black curve in Fig. 3A), our TEX₈₆ values yield the highest temperatures around 30.5 Ma (up to $22.6 \pm 5.2^\circ\text{C}$), 25.5 Ma (up to $25.1 \pm 5.2^\circ\text{C}$) and around 17 Ma (up to $19.2 \pm 5.2^\circ\text{C}$), whereas the lowest temperatures are recorded between 22 and 23.5 Ma (minimum temperatures are $8.3 \pm 5.2^\circ\text{C}$) and around 13 and 10.5 Ma (minima around $7.6 \pm 5.2^\circ\text{C}$). On average SSTs based on the linear calibration of Kim et al. (2010) are 16.6°C , 16.7°C and 10.6°C for the Oligocene, MMCO and MMCT, respectively. Oligocene SST variability increases significantly (p value < 0.001 in F test) after 26.5 Ma (see Fig. 3B). Before 26.5 Ma, the variation in the record (2σ) is about 3.6°C , while the 2σ is 6.8°C after 26.5 Ma. We note a strong (9.5°C) SST drop at the lower boundary of what is interpreted to represent subchron C6Cn.2n (23.03 Ma) (see Fig. 2 and 4), at the stratigraphic position of maximum $\delta^{18}\text{O}$ values related to Mi-1 in the deep-sea records (Pälike et al., 2006b; Liebrand et al., 2011; Beddow et al., 2016). Unfortunately, due to core recovery issues and limited high-resolution chronobiostatigraphic control in this interval, the age model generally lacks the resolution to identify some of the other known transient temperature drops in our record (~ 30 Ma, ~ 24 Ma) to Oligocene glaciation-related Oi events (Fig. 4).

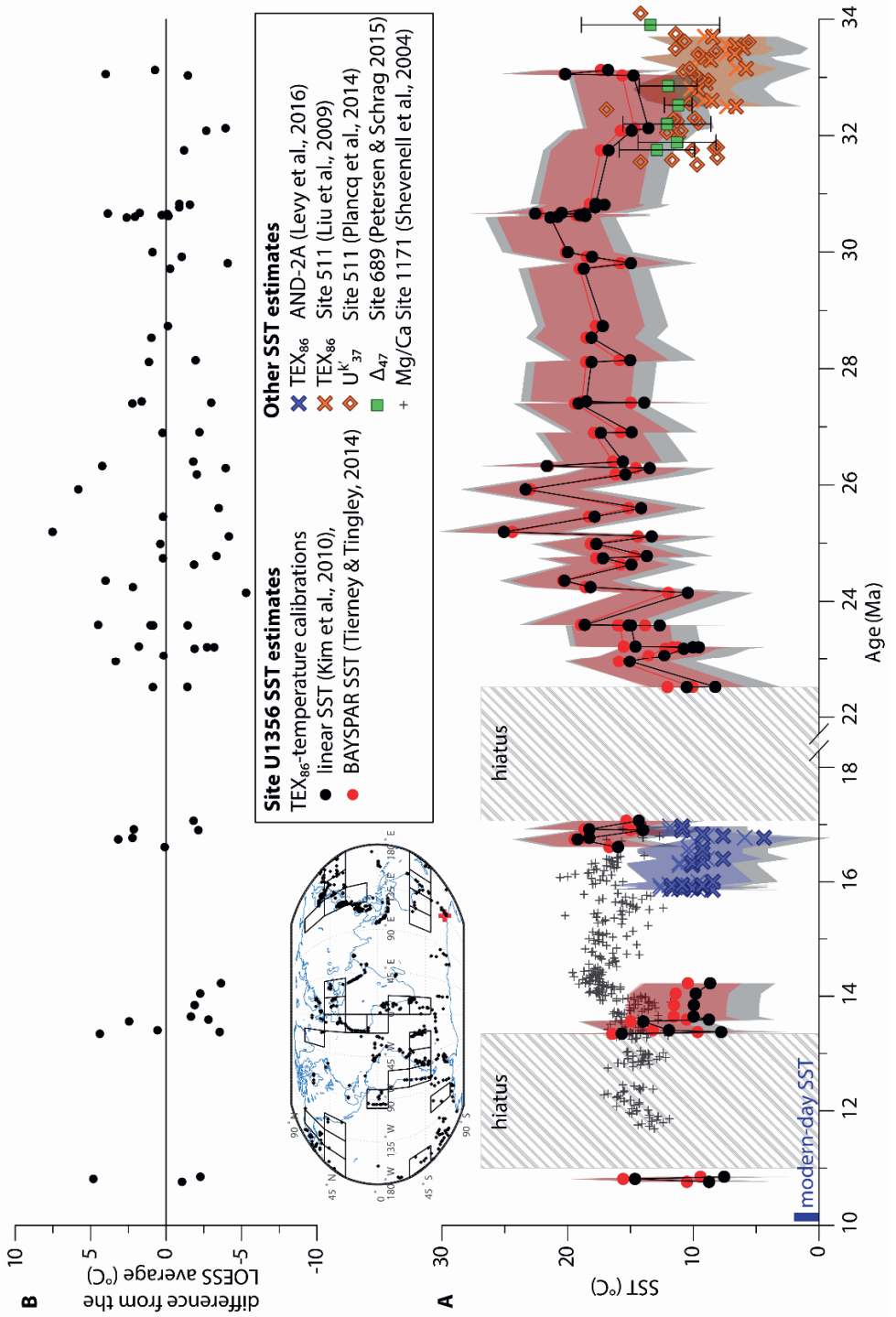


Figure 3 (previous page): **(A)** TEX_{86} -based SSTs plotted against age (Ma), using the linear calibration of Kim et al. (2010) and the BAYSPAR method (see text). The map (center left) indicates the $20^\circ \times 20^\circ$ grid cells from which core-top values (black dots) were obtained for the BAYSPAR calibration. The red + in the map indicates the location of Site U1356. Other SST estimates are plotted for comparison. For the TEX_{86} -based temperature estimates (blue and orange crosses), the symbols with both fill and outline are based on the linear calibration of Kim et al. (2010), those with the fill color only are based on the BAYSPAR SST calibration (Tierney & Tingley, 2014). The standard error of the Kim et al. (2010) calibration is indicated by grey shading and the standard error of the BAYSPAR calibration is indicated by colored shading. **(B)** The SST difference from the LOESS average based on the linear calibration of Kim et al. (2010) plotted against age. Modern-day temperature range indicated along the y axis.

The SST record for Site U1356 based on the BAYSPAR model shows the same trend as the SST record generated with the linear calibration, but for SST values below 20.5°C it is offset towards slightly warmer values for SSTs based on the linear calibration. Above 20.5°C , BAYSPAR-based SSTs are slightly offset towards cooler values. On average, BAYSPAR-based SSTs are 0.8°C warmer than the SSTs based on the linear calibration of Kim et al. (2010), and they have a smaller calibration SE ($\pm 4.0^\circ\text{C}$) (red curve in Fig. 3A). This offset and the smaller calibration error result primarily from the fact that the BAYSPAR calibration does not take the TEX_{86} values for polar core tops into account. Instead, it bases its calibration mostly on the modern $30\text{--}50^\circ$ northern and southern latitudinal bands (see map in Fig. 3). Nevertheless, the BAYSPAR-based SSTs lie well within the $\pm 5.2^\circ\text{C}$ SE of the transfer function from Kim et al. (2010), as well as within the SE of about $\pm 4.0^\circ\text{C}$ for the BAYSPAR SST calibration. Average SSTs for the Oligocene, MMCO and MMCT based on the BAYSPAR SST calibration are 17.2°C , 17.3°C and 12°C , respectively.

4 Discussion

4.1 Oligocene and Miocene Southern Ocean sea surface temperatures

Our TEX_{86} -derived SST record is the first for the Southern Ocean that covers almost the entire Oligocene. Absolute temperature values are relatively high considering the high-latitude position of Site U1356 ($\sim 59^\circ\text{S}$, van Hinsbergen et al., 2015), but confidence can be obtained from the observation that TEX_{86} -based reconstructed SSTs from glacial lithologies are generally lower than those from interglacial lithologies (Fig. 4). Several lines of evidence support the relatively high Oligocene and mid-Miocene temperatures reconstructed for Site U1356. Dinoflagellate cyst assemblages from the same site (Bijl et al., 2018b; Sangiorgi et al., 2018) mostly contain taxa related to those found between the PF and the STF today, where mean annual SST is between 8 and 16°C (Prebble et al. 2013). This is on the low end of our reconstructed SSTs for the Oligocene and the MMCO but very comparable to SSTs for the MMCT. Furthermore, the abundance of *in situ* pollen of temperate vegetation in these sediments (Strother et al., 2017; Sangiorgi et al., 2018),

which are most likely derived from the Antarctic shores, also suggests a relatively mild climate. Finally, the abundance of pelagic carbonaceous facies in some of the Oligocene interglacial intervals of these high-latitude strata is interpreted to occur under the influence of warmer northern-sourced surface waters at Site U1356 (Salabarnada et al., 2018). Our reconstructed SST values for U1356 add to a picture of globally very warm SSTs during the Oligocene and MMCO, as was also reconstructed for the North Atlantic based on TEX₈₆ with SST values ranging between 24 and 35°C (Super et al., 2018).

In general, Oligocene SST estimates are higher than the SST estimates reconstructed with other proxies at other high-latitude Southern Ocean Sites 511 and 689 (Fig. 3A). However, the reconstructed ~12°C (standard error: ±1.1-3.5°C) based on clumped isotopes from Site 689 is derived from thermocline-dwelling foraminifera, whereas the temperature of the surface waters was likely higher than that at the thermocline (Petersen and Schrag, 2015). In addition, when the newest calibration for clumped isotope data is applied (Kelson et al., 2017), higher temperature estimates, 12.8-14.5°C, are also obtained. Temperature estimates between 6 and 10°C have been obtained from ODP Site 511 (see Fig. 1) based on U^K₃₇ (Plancq et al., 2014) and TEX₈₆ values (Liu et al., 2009), the latter recalculated with the linear calibration of Kim et al. (2010) and the BAYSPAR calibration used here (Fig. 3A). The influence of the cold Antarctic-derived surface current at Site 511 (Bijl et al., 2011; Douglas et al., 2014) (Fig. 1) might be the reason for these colder estimates. Similar to the Eocene, Site U1356 was probably one of the warmest regions around Antarctica during the early Oligocene (Pross et al., 2012), situated at a relatively northerly latitude (van Hinsbergen et al., 2015) and still under the influence of the relatively warm PLC (Fig. 1) (Bijl et al., 2011, 2018b).

Sangiorgi et al. (2018) compared TEX₈₆^L-based reconstructed temperatures (based on the 0-200 depth-integrated calibration of Kim et al., 2012a) from the Miocene section of Site U1356 with Mg/Ca-based SST values from planktic foraminifera from ODP Site 1171, South Tasman Rise (Shevenell et al., 2004), and TEX₈₆^L-based seawater temperatures from the ANDRILL AND-2A core, Ross Sea (Levy et al., 2016). Based on these temperature reconstructions it was established that temperatures at Site U1356 during the MMCO are very comparable to the Mg/Ca-based SSTs from the South Tasman Rise and are a few degrees cooler during the MMCT, which was further supported by pollen and dinocyst assemblages (Sangiorgi et al., 2018). We reach the same conclusion based on the reconstructed SSTs using the linear calibration of Kim et al. (2010) and the BAYSPAR calibration for the Miocene TEX₈₆ values from Site U1356 as well as site AND-2A (Fig. 3). Based on these recalibrated SST values, we conclude, like Sangiorgi et al. (2018), that during the MMCO there was a much reduced SST gradient between Site U1356 and Site 1171, which were at that time positioned at approximately 60°S and 54°S, respectively

(van Hinsbergen et al., 2015). Notably, however, the latitudinal difference between Site U1356 and Site 1171 after the MMCO increased and may be partly responsible for the increased temperature gradient between the two sites at 14 Ma.

Biota-based temperature reconstructions at such high latitudes are likely skewed towards summer conditions, as has also been suggested for Site 689 and Site 511 (Plancq et al., 2014; Petersen and Schrag, 2015). An important reason for this could be the light limitation at high latitudes during winter (e.g., Spilling et al. 2015), which is unfavorable for the growth and bloom of phytoplankton and organisms feeding on phytoplankton. The potential summer bias in high-latitude TEX_{86} -based SST reconstructions has been discussed extensively for other past warm periods (e.g., Sluijs et al., 2008; Bijl et al., 2009, 2010, 2013a). Like in these past warm climates, we expect that primary productivity in the Oligocene Southern Ocean was in sync with seasonal availability of light, irrespective of the presence of sea ice or overall climate conditions. Indeed, isoGDGTs likely require pelleting to sink effectively through the water column to the ocean floor (e.g., Schouten et al. 2013) and therefore depend on the presence of larger zooplankton that feed on the phytoplankton. As phytoplankton blooms mostly occur during Antarctic summer-autumn, when their predators also thrive (Schnack-Schiel, 2001), we expect the highest isoGDGT fluxes to the sediment during the summer in the Southern Ocean, despite their highest production during a different season (Murray et al., 1998; Church et al., 2003; Rodrigo-Gámiz et al., 2015; Richey and Tierney, 2016). A bias towards summer temperatures is confirmed by the presence of sea ice dinoflagellate cysts in some parts of the record, which would suggest SSTs near freezing point during winter.

4.2 Long-term Oligocene and Miocene sea surface temperature trends

We aim to explore the implications of the long-term trends in our TEX_{86} -based SST record by placing it in the context of the global benthic $\delta^{18}\text{O}$ and benthic foraminiferal Mg/Ca-based BWT records, in order to infer oceanographic changes or changes in ice volume. Due to the relatively low sample resolution, and discontinuous sampling due to core gaps, in comparison to the complete and quasi-continuous $\delta^{18}\text{O}$ records (Billups et al., 2004; Pälike et al., 2006a, 2006b; Holbourn et al., 2015; Beddow et al., 2016; Liebrand et al., 2016; Hauptvogel et al., 2017; Liebrand et al., 2017), we will here focus on the long-term temperature trends. However, we can use the glacial-interglacial alternations in the lithology, which cover the period between 32 and 10 Ma, to differentiate between glacial and interglacial SST and assess amplitudes (see Fig. 2). As was mentioned, SSTs derived from the glacial facies show a significantly lower mean than SSTs derived from interglacial facies. Separating glacial and interglacial signals allows us to interpret the long-term SST

trend, as this removes a potential sampling bias caused by irregularly spaced glacial or more interglacial samples. To obtain both long-term glacial and interglacial SST trends, LOESS curves are plotted through SST estimates from the glacial and interglacial subsets of the Oligocene (Fig. 4). For the Miocene we averaged SSTs from glacial and interglacial samples for the three sample clusters (at ~17, ~13.5 and ~10.5 Ma). For both the SST estimates based on the linear calibration of Kim et al. (2010) and those based on the BAYSPAR calibration, the glacial and interglacial LOESS curves plotted through these SST estimates show the same trend. Therefore, we have chosen to show only the BAYSPAR-based SST data and LOESS curves in Figure 4. The SST LOESS curves based on the linear calibration of Kim et al. (2010) lie slightly below the BAYSPAR SST LOESS curves (i.e. a 0.9°C offset for the glacial LOESS curve and a 0.4°C offset for the interglacial LOESS curve).

A global benthic foraminiferal stacked $\delta^{18}\text{O}$ curve has been constructed by combining the benthic $\delta^{18}\text{O}$ records of the far-field Site 1218, eastern equatorial Pacific (Pälike et al., 2006b); Sites 1264 and 1265, Walvis Ridge, southeast Atlantic (Liebrand et al., 2016, 2017); Sites 926 and 929, Ceara Rise, equatorial Atlantic (Zachos et al., 2001; Pälike et al., 2006a); Site U1334, eastern equatorial Pacific (Beddow et al., 2016); Site 1090, Agulhas Ridge, Atlantic sector of the Southern Ocean (Billups et al., 2004); Site U1337, eastern equatorial Pacific (Holbourn et al., 2015); and Site 588, southwest Pacific (Flower and Kennett, 1993). To obtain a global benthic $\delta^{18}\text{O}$ stack in which the global long-term trends are best represented, we have normalized the data to the Site 1264 and 1265 record of Liebrand et al. (2016, 2017), on which all records now overlap (Fig.4). Mg/Ca-based BWT records are obtained from Site 1218, eastern equatorial Pacific (Lear et al., 2004); Site 747, Kerguelen Plateau, Southern Ocean (Billups and Schrag, 2002); and Site 1171, Tasman Rise, Southern Ocean (Shevenell et al., 2004). LOESS curves have been plotted through the benthic $\delta^{18}\text{O}$ stack as well as the individual Mg/Ca-based BWT records (Fig. 4).

The LOESS curves through the glacial and interglacial data show similar trends and show a good resemblance to the global benthic $\delta^{18}\text{O}$ stack (Fig. 4), particularly when considering the compromised sample resolution of our record. The temperature optima and minima in the LOESS curves can be directly linked to periods of relatively low and high benthic $\delta^{18}\text{O}$ values (maximum and minimum ice volume and BWT), respectively. Temperatures increase from the earliest Oligocene towards 30.5 Ma, while benthic $\delta^{18}\text{O}$ values show a decrease in the same interval, but reach a minimum earlier, around 32 Ma. It is difficult to determine whether SSTs are truly lagging the benthic $\delta^{18}\text{O}$ values in this interval or whether this is an artifact caused by the age model in this part of the record. The recorded post-Oi-1 SST warming coincides with the disappearance of IRD (Expedition 318 Scientists, 2011a) and sea-ice-related dinoflagellate cysts (Houben et al., 2013) in the

same record (Fig. 4). Following this temperature optimum, there is a cooling trend until a minimum is reached around 28–27 Ma, which coincides with relatively high benthic $\delta^{18}\text{O}$ values and the Oi-2a and Oi-2b glacials. Subsequently, there is a warming towards a long-term temperature optimum around 25 Ma, which coincides with a minimum in the benthic $\delta^{18}\text{O}$ record known as the late Oligocene warming. This temperature optimum around 25 Ma is characterized by the influx of the temperate dinocyst species *Nematosphaeropsis labyrinthus* (Bijl et al., 2018b). This seems to indicate a strong influence of northern-sourced surface waters at Site U1356, as this species is currently associated with the SF and winter and summer temperatures of 6–13°C and 8–17°C, respectively (Marret and De Vernal, 1997; Esper and Zonneveld, 2007; Prebble et al., 2013). Finally, the Oligocene LOESS temperature curves show a cooling towards the Oligocene-Miocene transition at 23 Ma. In comparison to the benthic $\delta^{18}\text{O}$ record this cooling trend is rather gradual and starts 1 Myr earlier than the steeper benthic $\delta^{18}\text{O}$ record increase that starts at 24 Ma and continues towards the Mi-1 glaciation. We consider this to represent a realistic climate signal, notably so since the age model is sufficiently well constrained in this part of the record. Glacial and interglacial averages for the Miocene data clustered around 17, 13.5, and 10.5 Ma show a declining trend and follow the increasing benthic $\delta^{18}\text{O}$ trend that characterizes the MMCT. High amounts of *N. labyrinthus* within the MMCO interval support warm surface water conditions (Sangiorgi et al., 2018). After the MMCO, increased amounts of sea ice dinoflagellates and IRD indicate that Site U1356 came under the influence of seasonal sea ice, and therefore cooler conditions. However, increases in *N. labyrinthus* after the MMCT indicate that warmer northern-sourced waters still periodically influenced Site U1356 (Sangiorgi et al., 2018).

The fact that the LOESS temperature trends mirror the benthic $\delta^{18}\text{O}$ record may suggest that (1) changes in the Wilkes Land SST correspond to SST changes in the region of deep-water formation, which is reflected in the benthic $\delta^{18}\text{O}$ records, and (2) changes in the Wilkes Land SST reflect long-term changes in paleoceanography that simultaneously affect or are related to the size of the Antarctic Ice Sheet (AIS) and therefore the deep-sea $\delta^{18}\text{O}$ of the sea water, or a combination of both.

Considering (1), in the modern-day Southern Ocean, bottom water forms through mixing along the Antarctic Slope Front (ASF) of Circumpolar Deep Water (CDW) and High-Salinity Shelf Water (HSSW), which forms as a consequence of sea ice formation (Gill, 1973; Jacobs, 1991). Associated with the ASF is the westward-flowing Antarctic Slope Current (ASC), which contributes to the bottom-water formation and results from the geostrophic adjustment of Ekman transport to the south, which is driven by the predominantly easterly winds around Antarctica (Gill, 1973). It has been suggested that, after the establishment of its shallower westward-flowing counterpart, the ACCC, around

49 Ma (Bijl et al., 2013a), an ASC was established near Site U1356 in the early Oligocene (Scher et al., 2015). In areas where sea ice was formed during the Oligocene and Miocene the ASC could have enhanced mixing between HSSW and CDW similar to today. For the Wilkes Land margin this might have been the case for the earliest Oligocene and MMCT for which we find sea ice indicators in the dinoflagellate cyst assemblages (Houben et al., 2013; Bijl et al., 2018a). These sea ice dinoflagellate cysts seem to indicate that winter temperatures at the Wilkes Land margin were cold enough to allow sea ice formation and therefore maybe formation of deep waters along the Wilkes Land coast during the earliest Oligocene and MMCT. However, most of the record is devoid of sea ice indicators, suggesting that modern-day processing of deep-water formation is unlikely to have occurred at the Wilkes Land margin. Still, neodymium isotopes of fossil fish teeth from Site U1356 have suggested that deep-water formation took place at the Adélie and Wilkes Land margin during the Eocene (Huck et al., 2017), when pollen indicates near-tropical warmth (Pross et al., 2012). Model studies have suggested that during such warm periods seasonal density differences may still induce deep-water formation or downwelling of waters around Antarctica (Lunt et al., 2010; Goldner et al., 2014). Alternatively and more likely, sea ice may have formed in the cooler Ross Sea and been transported along the Wilkes Land coast similar to today during the Oligocene and Miocene, meaning that deep water formed in the Ross Sea where glaciers extended onto the Antarctic shelf (see Sorlien et al., 2007). In that case, the absence of sea ice dinoflagellate cysts during most of the Oligocene and the MMCO at Site U1356 would mean that, in contrast to the earliest Oligocene and MMCT, sea ice coming from the Ross Sea was prevented from reaching Site U1356 by too warm winter SSTs. This is in accordance with the relatively warmer (summer) SST values for Site U1356 during most of the Oligocene and the MMCO. If the reconstructed SST trends of Site U1356 are representative for the climatic trends of a larger region (i.e., including the Ross Sea as a potential region for deep-water formation), this climatic signal may have been relayed to the deep ocean and recorded in the stable oxygen isotope composition of benthic foraminifera at far-field sites. In fact, Southern Ocean-sourced deep waters may have reached as far as the north Pacific during the Oligocene (Borrelli and Katz, 2015). If this is the case, the consistent long-term trends between the SST of Site U1356 and the benthic $\delta^{18}\text{O}$ record would imply that the size of the AIS is less variable on these long-term timescales than the benthic $\delta^{18}\text{O}$ record would suggest under the assumption of constant BWT (e.g., Liebrand et al., 2017; see Figure 4): much of the variation will be due to deep-sea temperature variation. The small AIS may have been relatively stable during the Oligocene and Miocene, most likely because there was less marine-based ice in comparison to land-based ice as topographic reconstructions of Antarctica would suggest (Wilson et al., 2012; Gasson et al., 2016).

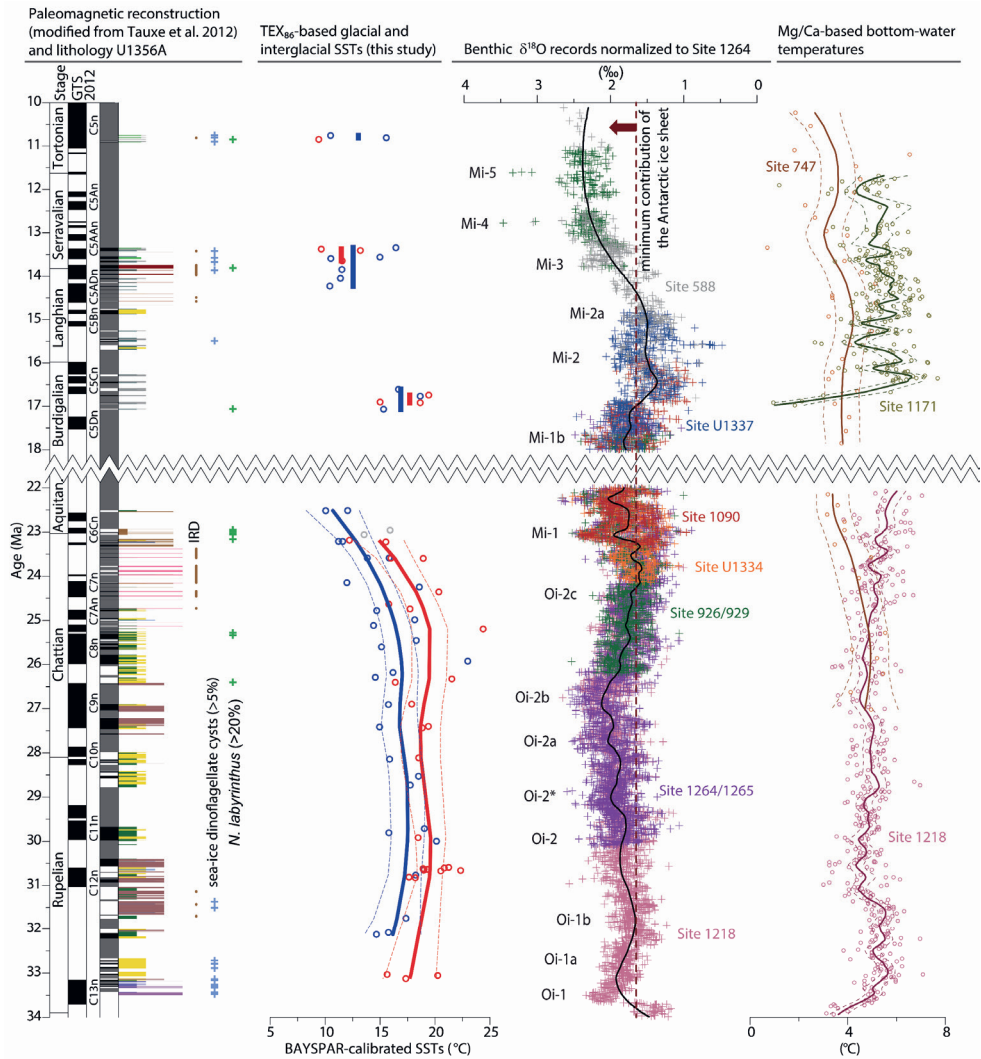


Figure 4: Lithology and paleomagnetic polarities as in Fig. 2, but plotted against age (Ma), updated to the GTS2012 timescale (Gradstein et al., 2012). Sections with IRD and samples with sea ice and *Nematosphaeropsis labyrinthus* dinoflagellate cysts are indicated. SST values are based on the BAYSPAR calibration with blue and red open circles indicating glacial and interglacial temperature estimates, respectively, based on the lithology (see text). For the Oligocene, thick blue and red lines are the LOESS average glacial and interglacial trends with their 95% confidence interval (dotted lines). For the Miocene, thick blue and red straight lines indicate glacial and interglacial means for the corresponding data clusters. Benthic $\delta^{18}\text{O}$ records are normalized to the $\delta^{18}\text{O}$ record of Site 1264 (in purple). Colored + signs indicate the different DSDP/ODP/IODP sites (refs. in text) and the black line is the LOESS average. Oi and Mi glaciation events are indicated. The area below the benthic $\delta^{18}\text{O}$ record on the left side of the dark red dotted line (1.65‰) indicates the minimum contribution (‰) of the Antarctic Ice Sheet to the benthic $\delta^{18}\text{O}$ record, assuming BWT at Site 1264 did not drop below its modern-day value (see Liebrand et al. (2017)). Mg/Ca-based BWT records of three ODP/IODP sites with LOESS averages (solid lines) and 95% confidence intervals (dotted lines) on the far right (refs. in text).

Only one BWT record is available for the Oligocene, which is based on Mg/Ca ratios from Site 1218 (equatorial Pacific). Mg/Ca was obtained from the benthic foraminifer *Oridorsalis umbonatus* (Lear et al., 2004; Fig. 4), an infaunal species that is to some extent insulated from long-term changes in carbonate ion concentrations (Lear et al., 2015; Ford et al., 2016). Although absolute temperatures may depend on local factors, such as pore water chemistry, the long-term trends should reflect the trends in BWT (Lear et al., 2015). The BWT record of Site 1218 shows a long-term deep-sea warming between 27 and 25 Ma, similar to our SST record. The temperature optimum at 30.5 Ma in our TEX₈₆-based SST record cannot be recognized in the BWT record of Site 1218. Similar to the benthic $\delta^{18}\text{O}$ record, an optimum is reached earlier (~32 Ma) and this mismatch could be due to uncertainties in the age model of the lower part of the Oligocene section of Hole U1356A. The continued temperature rise after 25 Ma in the BWT record of Site 1218 is also not observed in our TEX₈₆-based temperature trend. This could be because the equatorial Pacific mainly receives bottom water from a warmer Pacific sector of the Southern Ocean, east of the Tasmanian Gateway, and not from the Wilkes Land margin, and the Pacific sector is influenced by warming. Alternatively, there is an increasing influence of a warmer deep-water mass from elsewhere. Notably, Mg/Ca-based BWTs from the Kerguelen Plateau (Site 747) show a temperature optimum around 25 Ma preceding the $\delta^{18}\text{O}$ minimum at 24 Ma, similar to the SST trend at Site U1356. For the mid-Miocene, BWT records of both Site 747 (Kerguelen Plateau) and Site 1171 (South Tasman Rise) show slowly decreasing trends consistent with decreasing TEX₈₆-based SSTs of Site U1356. The similarities of the three Mg/Ca records to our TEX₈₆-based SST record support the transfer of a regional SST signal towards the deep ocean through deep-water formation. However, the temperature differences between temperature optima (e.g., the late Oligocene and MMCO) and minima (e.g., the mid-Oligocene and MMCT) are much larger for the TEX₈₆-based SSTs than for the Mg/Ca-based BWTs. This difference in the degree of change could be explained by the fact that the formation of deep waters during winter is constrained at the lower end by the freezing point of water, which would limit the degree of change during relatively cold intervals. The degree of change could also be reduced by a shift in the location of deep-water formation to higher latitudes during warmer intervals.

Alternatively, long-term SST trends as well as Southern Ocean BWT trends (Sites 747 and 1171) are governed by large-scale tectonic processes, such as the opening and closure of the Drake Passage, as was suggested by Lagabrielle et al. (2009). Opening of the Drake Passage could result in increased isolation of the Antarctic continent through the establishment of a (proto-)ACC. In turn, this would result in effective blocking of northerly sourced warmer waters as well as ice sheet expansion, thereby resulting in a simultaneous benthic $\delta^{18}\text{O}$ increase and SST decrease.

As an alternative hypothesis, reconstructed SSTs at Wilkes Land may depend on the volume of the ice sheet in the hinterland. In that scenario most of the long-term trends in the $\delta^{18}\text{O}$ record are due to ice volume growth and decline. A more expanded ice sheet will lower SSTs and enhance the formation of sea ice around Antarctica (Goldner et al., 2014). Expansion of this cool (proto-)AASW and the ocean frontal systems to lower latitudes during glacials may have cooled SSTs at Site U1356, while ice volume decrease and the retreat of the ocean frontal systems during interglacials may have resulted in warmer SSTs at Site U1356. However, the warmth of even the glacial SSTs in our SST record, as well as the overall absence of sea ice indicators during most of the Oligocene in these glacial intervals, strongly argues against this alternative. Only during the MMCT, when dinoflagellate cysts and IRD suggest an increased influence of icebergs or sea ice (Sangiorgi et al., 2018), might the ice sheet have been large enough during the glacial periods to allow the influence of a cool (proto-)AASW at Site U1356.

4.3 Sea surface temperature variability at glacial–interglacial time scales

For the Oligocene, the offset between the glacial and interglacial LOESS curves is constant over time (Fig. 4). Irrespective of the chosen calibration (i.e., TEX₈₆ or BAYSPAR), SSTs are on average 1.5–3.1°C higher during interglacial intervals than during adjacent glacial times. Notably, this glacial–interglacial SST difference is smaller than the variability that can be observed in samples from within one sedimentary facies. Particularly around 31 Ma, when we have a higher sampling resolution within a short interval, temperature variability shows a 5°C range and is therefore larger than the glacial–interglacial temperature difference. We emphasize that the glacial–interglacial facies changes reflect obliquity-paced shifts in the position of bottom-water currents (Salabarnada et al., 2018).

This glacial–interglacial SST difference is also smaller than the observed amplitude of the variability in our temperature record ($2\sigma = 3.6^\circ\text{C}$ before 27 Ma), because it takes relatively warm glacials and cool interglacial SST values into account. Also considering that part of the 2σ variability is due to the relatively large calibration error of the BAYSPAR calibration ($\pm 4.0^\circ\text{C}$), the difference of 1.5–3.1°C may be a better representation of average glacial–interglacial SST variation than the 2σ . It has been shown that glacial–interglacial variability could be overestimated due to increased GDGT export from deeper waters during Pleistocene glacial periods (Hertzberg et al., 2016). These authors showed that during the Last Glacial Maximum in the equatorial Pacific a reduced nutrient availability and primary productivity lowered the nitrite maximum in the water column and consequently the position of the highest Thaumarchaeota export production. If export of GDGTs consistently took place in deeper waters during the glacial periods in our record, we

would expect that [2]/[3] ratios were higher during the glacials. We show (Fig. 2) that this is not the case. In addition, dinoflagellate cysts suggest that the surface waters overlying Site U1356 become more oligotrophic during the interglacial periods, meaning that the nitrite maximum in the water column and therefore GDGT export production would be deeper during the interglacials. Interglacial TEX₈₆-derived temperatures would hence underestimate true SST values.

The average consistent offset between glacial and interglacial values seems to disappear for each of the Miocene data clusters at ~17, ~13.5, and ~10.5 Ma. Several causes could explain this. It could be the result of a less variable climate during the Miocene, which causes both subsets to overlap more. Indeed, for the MMCO this may be the case, because the MMCO is a time interval of exceptional warmth, with retreated ice sheets and vegetated coastlines of Wilkes Land (Sangiorgi et al., 2018). In such a climate, the glacial intervals may not have been fundamentally colder than the interglacials. We cannot, however, explain the apparent absence of glacial-interglacial temperature variability around 14 and 10.5 Ma, when dinoflagellate cysts suggest profound variability in sea ice extent, upwelling and temperature (Sangiorgi et al., 2018). It could be that the samples taken by Sangiorgi et al. (2018) do not capture the true glacial and interglacial extremes, but this cannot be verified at this stage. Because a detailed lithological log was not available to Sangiorgi et al. (2018), there is also an uneven distribution between glacial and interglacial samples.

If the recorded glacial-interglacial SST variability in the Oligocene is representative for the SST variability at the region of deep-water formation, it should be considered when interpreting benthic foraminiferal $\delta^{18}\text{O}$ records in terms of ice volume variability. As such, a larger part of the variability in $\delta^{18}\text{O}$ than so far assumed (Hauptvogel et al., 2017; Liebrand et al., 2017) should be ascribed to deep-sea temperature rather than ice volume changes. If the region of deep-water formation experienced the same SST variability, 40-70% of the 1‰ deep-sea $\delta^{18}\text{O}$ variability over Oligocene glacial-interglacial cycles can be related to deep-sea temperature. However, it is plausible that not the entire range of SST variability is relayed to the deep sea and that in the more southerly positioned Ross Sea, the most likely region of Oligocene deep-water formation, temperatures were not as variable as in the Wilkes Land sector. Indeed, Mg/Ca-based reconstructed bottom-water temperatures from Site 1218 show much less glacial-interglacial variation (1.1°C, Fig. 5) (Lear et al., 2004) than our record. Still, our record provides evidence that polar SST experienced considerable variability, both on the short-term glacial-interglacial cycles as well as in the long-term.

A considerable influence of deep-sea temperature on benthic $\delta^{18}\text{O}$ could explain the level of symmetry in glacial-interglacial cycles in the Oligocene (Liebrand et al., 2017), as the temperature would vary in a sinusoidal fashion, whereas ice sheets would respond

nonlinearly to climate forcing. The sedimentary record of Site U1356 lacks the potential of obtaining a resolution comparable to that of deep-sea $\delta^{18}\text{O}$ records in order to verify these claims. However, ice volume reconstructions from $\delta^{18}\text{O}$ records on both long-term and short-term timescales should consider that an important component of the signal could potentially be ascribed to temperature variability.

5 Conclusions

We reconstruct (summer-biased) SSTs of around 17°C on average for the Wilkes Land margin during the Oligocene, albeit with a high degree of variability (up to a 6.8°C double standard deviation during the late Oligocene). The reconstructed temperatures are a few degrees higher than previously published high-latitude early Oligocene Southern Ocean estimates. Because alternations in the lithology reflect glacial-interglacial cycles, an estimated temperature difference of 1.5 to 3.1°C between glacials and interglacials could be interpreted for the Oligocene. The long-term trends in both glacial and interglacial records show a temperature increase towards 30.5 Ma, followed by a minimum around 27 Ma, an optimum around 25 Ma and finally a decrease towards the end of the Oligocene, generally following the long-term trends in the global benthic $\delta^{18}\text{O}$ record as well as parts of the available Mg/Ca-based BWT records for the Oligocene. Recalibrated SSTs based on previously published TEX_{86} data for the mid-Miocene decrease from around 17°C to 11°C between ~ 17 and ~ 10.5 Ma. A distinct glacial-interglacial SST difference was not observed for the mid-Miocene. Nevertheless, the recorded temperature decline also follows the trend observed in benthic $\delta^{18}\text{O}$ and Mg/Ca-based BWT records. Our results suggest that considerable SST variability prevailed during the Oligocene and Miocene. This may have implications for the dynamics of marine-based ice sheets, if present, and the extent of the Antarctic ice sheet in general. Assuming that the reconstructed SST trends and glacial-interglacial variability have been relayed to the deep water at nearby bottom-water formation sites, our results indicate that the long-term $\delta^{18}\text{O}$ trend may be controlled for a considerable part by bottom-water temperature. This implies that the Antarctic Ice Sheet was less dynamic during the Oligocene and Miocene, which could be due to the presence of relatively more land-based versus marine-based ice.

Supplementary information of chapter 6

Appendix A: Supplementary figures

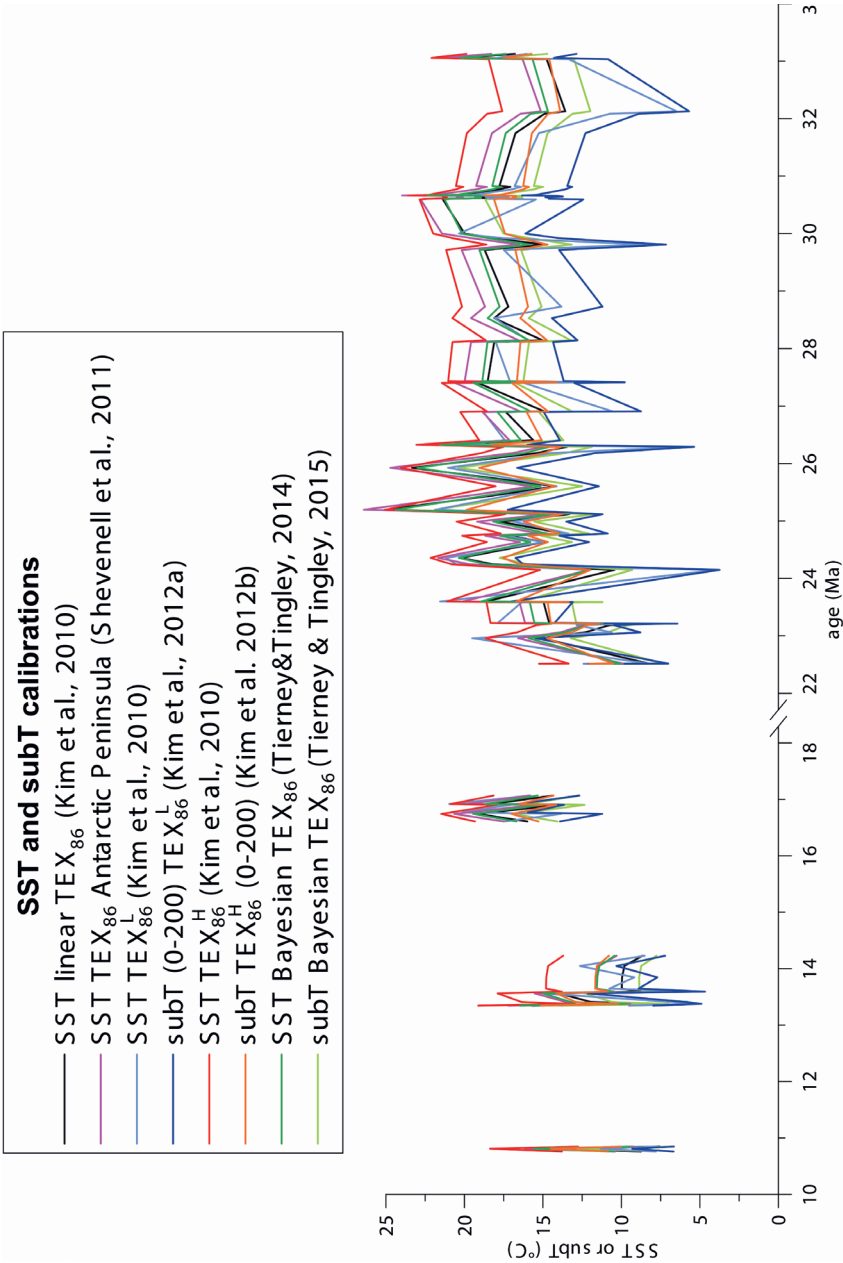


Figure S1: Sea surface temperature and subsurface temperature reconstructions using all existing calibrations for the TEX_{86} , TEX_{86}^L , and TEX_{86}^H proxies, plotted against age.

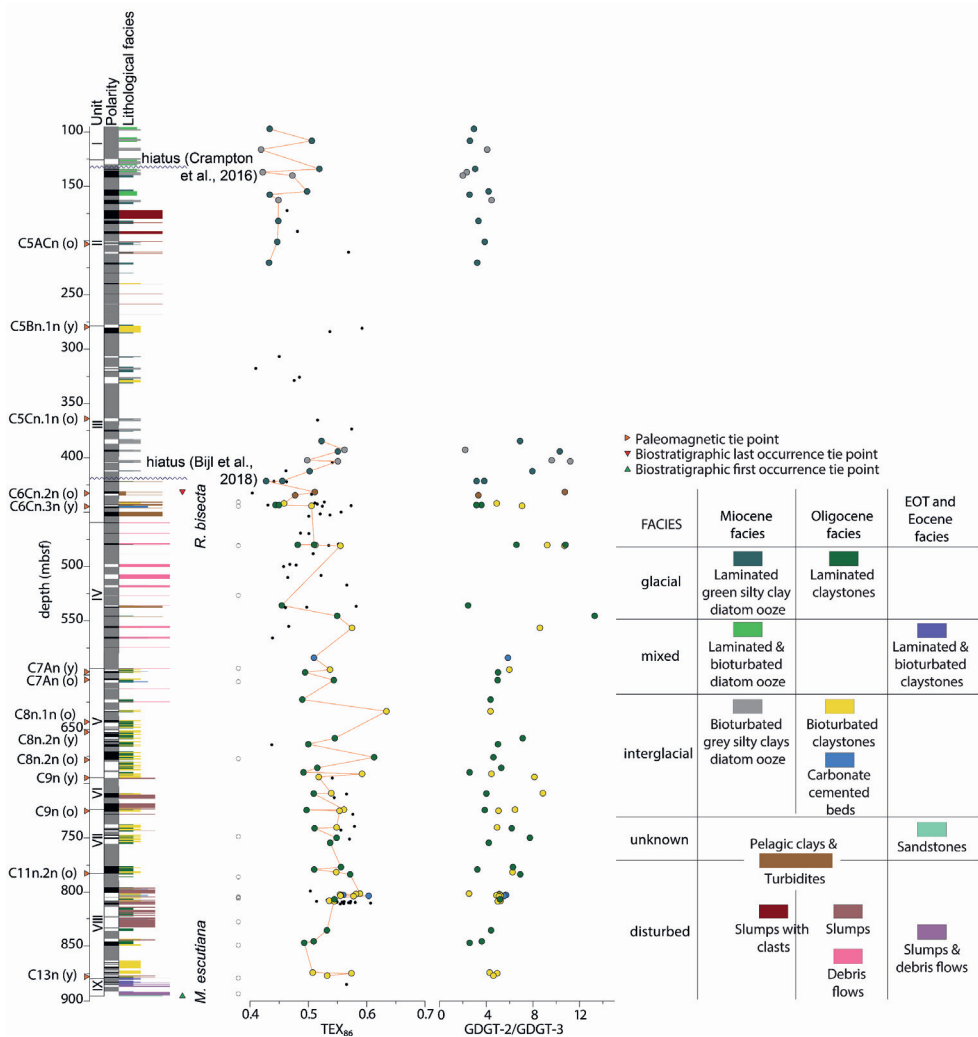


Figure S2: As Figure 2, but with black dots indicating TEX_{86} values from samples that have been discarded for the SST reconstruction. Furthermore, open circles indicate the position of samples taken from Hole U1356A that did not provide sufficient amounts of isoGDGTs for a reliable TEX_{86} value.

Core	Section	Coring Interval	Gm. top depth (m)	Gm. bottom depth (m)	Age (Ma)	Method	GGT0	GGT-1	GGT-2	GGT-3	Cen	Cen*	GGT-III	GGT-IV	GGT-5	GGT-6	BIT	Mertens Index (M)	GGT-2 /Cen	GGT-0 /Cen	JARI	GGT-2 /GGT-3	Hf/Al ³⁺ /Al ³⁺	
54R	1W	185-89			498.65	23.27 (HPLC/MS)	1.0504E+07	5.0839E+05	2.3759E+05	6.7557E+04	1.0146E+07	1.4217E+06	5.7513E+05	1.2711E+05	8.2788E+04	9.7200E+05	0.13	0.07	0.02	1.04	1.00	1.02	1.46	
54R	1W	185-89			498.93	23.27 (HPLC/MS)	1.0504E+07	5.0839E+05	2.3759E+05	6.7557E+04	1.0146E+07	1.4217E+06	5.7513E+05	1.2711E+05	8.2788E+04	9.7200E+05	0.13	0.07	0.02	1.04	1.00	1.02	1.46	
54R	1W	185-89			500.27	23.27 (HPLC/MS)	1.2819E+06	1.5553E+06	1.0397E+06	1.6727E+04	2.1430E+06	3.6761E+04	1.5413E+04	1.8221E+05	1.8933E+05	6.5218E+05	0.15	0.10	0.01	0.97	0.95	0.97	5.16	
54R	3W	0-4			510.13	23.96 (HPLC/MS)	4.4174E+06	3.6973E+05	1.4757E+05	1.0591E+04	6.42E+05	4.81E+04	1.29E+05	1.13E+05	1.45E+05	1.6560E+05	0.4477E+06	0.38	0.22	0.12	1.95	1.04	0.004	4.81
54R	1W	15-12	0		517.19	23.96 (HPLC/MS)	1.25E+06	1.02E+05	7.9E+04	7.24E+03	2.08E+07	3.9E+05	8.24E+04	1.13E+05	1.45E+05	1.6560E+05	0.4477E+06	0.38	0.22	0.12	1.95	1.04	0.004	4.81
57R	1W	4-8			535.84	24.15 (HPLC/MS)	2.90E+07	1.13E+06	3.89E+05	1.57E+05	2.88E+04	2.8E+04	2.8E+04	1.4E+04	9.58E+05	5.4447E+05	0.09	0.20	0.11	1.69	0.72	0.07	2.45	
57R	1W	8-8.4	0		536.6	24.15 (HPLC/MS)	2.90E+07	1.13E+06	3.89E+05	1.57E+05	2.88E+04	2.8E+04	2.8E+04	1.4E+04	9.58E+05	5.4447E+05	0.09	0.20	0.11	1.69	0.72	0.07	2.45	
57R	1W	8-8.4	0		537.86	24.15 (HPLC/MS)	7.16E+06	5.09E+05	2.64E+05	3.97E+04	5.62E+06	1.21E+05	2.85E+05	1.94E+05	1.58E+05	0.4669E+06	0.10	0.12	0.02	1.27	0.89	0.27	6.70	
57R	1W	25-29			537.86	24.15 (HPLC/MS)	7.16E+06	5.09E+05	2.64E+05	3.97E+04	5.62E+06	1.21E+05	2.85E+05	1.94E+05	1.58E+05	0.4669E+06	0.10	0.12	0.02	1.27	0.89	0.27	6.70	
58R	1W	14-18			545.54	24.25 (HPLC/MS)	3.01E+06	3.59E+05	2.45E+05	1.91E+04	2.7E+06	1.55E+05	4.03E+05	6.1E+04	3.8E+04	0.5494E+06	0.07	0.18	0.09	1.11	0.26	0.38	13.29	
58R	1W	17-12			545.54	24.25 (HPLC/MS)	6.8772E+05	3.2933E+04	1.5749E+04	4.310E+03	7.4530E+05	7.5942E+05	2.0167E+04	1.8252E+04	6.172E+04	0.4663E+06	0.08	0.07	0.02	0.92	1.21	0.14	45.55	
58R	1W	17-12			555.16	24.36 (HPLC/MS)	1.02E+06	1.02E+05	7.9E+04	9.24E+03	4.97E+04	9.8E+04	6.02E+04	6.02E+04	6.02E+04	6.02E+04	0.7481E+06	0.24	0.20	0.11	1.44	0.58	0.77	8.60
65R	2W	19-21			563.3	24.65 (HPLC/MS)	3.7788E+05	1.6489E+05	6.5039E+04	2.4619E+04	4.0398E+04	1.6293E+04	1.0424E+05	1.5033E+05	0.4385E+06	0.09	0.06	0.02	0.94	0.36	0.14	0.93	2.68	
65R	2W	19-21			563.3	24.65 (HPLC/MS)	3.7788E+05	1.6489E+05	6.5039E+04	2.4619E+04	4.0398E+04	1.6293E+04	1.0424E+05	1.5033E+05	0.4385E+06	0.09	0.06	0.02	0.94	0.36	0.14	0.93	2.68	
65R	2W	19-21			594.95	24.74 (HPLC/MS)	1.3774E+06	1.0973E+06	6.9851E+05	1.1650E+04	1.1650E+04	1.8094E+06	4.6977E+04	8.3282E+04	4.6941E+04	5.1727E+04	0.11	0.10	0.04	0.83	0.03	0.03	5.98	
64R	2W	19-21			597.54	24.79 (HPLC/MS)	6.3354E+06	4.5174E+05	2.3817E+05	6.7455E+04	1.6358E+06	1.6589E+06	1.1503E+05	1.1503E+05	1.6589E+06	0.4442E+07	0.06	0.10	0.03	0.92	0.04	0.38	5.01	
64R	2W	18-21			604.72	24.79 (HPLC/MS)	1.1593E+06	4.3112E+05	2.2837E+05	1.6644E+04	1.6509E+06	1.5059E+06	1.1509E+05	1.1509E+05	1.6509E+06	0.4442E+07	0.06	0.10	0.03	0.92	0.04	0.38	5.01	
66R	1W	26-28			627.58	25.19 (HPLC/MS)	4.72E+05	8.15E+05	7.29E+05	1.68E+05	6.8E+05	1.58E+05	2.3E+05	2.3E+05	1.03E+05	0.6359E+06	0.72	0.10	0.04	1.07	0.09	0.07	4.37	
66R	1W	26-28			633.38	25.19 (HPLC/MS)	4.72E+05	8.15E+05	7.29E+05	1.68E+05	6.8E+05	1.58E+05	2.3E+05	2.3E+05	1.03E+05	0.6359E+06	0.72	0.10	0.04	1.07	0.09	0.07	4.37	
66R	1W	26-28			633.38	25.19 (HPLC/MS)	4.72E+05	8.15E+05	7.29E+05	1.68E+05	6.8E+05	1.58E+05	2.3E+05	2.3E+05	1.03E+05	0.6359E+06	0.72	0.10	0.04	1.07	0.09	0.07	4.37	
66R	1W	26-28			633.38	25.19 (HPLC/MS)	4.72E+05	8.15E+05	7.29E+05	1.68E+05	6.8E+05	1.58E+05	2.3E+05	2.3E+05	1.03E+05	0.6359E+06	0.72	0.10	0.04	1.07	0.09	0.07	4.37	
66R	1W	26-28			633.38	25.19 (HPLC/MS)	4.72E+05	8.15E+05	7.29E+05	1.68E+05	6.8E+05	1.58E+05	2.3E+05	2.3E+05	1.03E+05	0.6359E+06	0.72	0.10	0.04	1.07	0.09	0.07	4.37	
66R	1W	26-28			633.38	25.19 (HPLC/MS)	4.72E+05	8.15E+05	7.29E+05	1.68E+05	6.8E+05	1.58E+05	2.3E+05	2.3E+05	1.03E+05	0.6359E+06	0.72	0.10	0.04	1.07	0.09	0.07	4.37	
66R	1W	26-28			633.38	25.19 (HPLC/MS)	4.72E+05	8.15E+05	7.29E+05	1.68E+05	6.8E+05	1.58E+05	2.3E+05	2.3E+05	1.03E+05	0.6359E+06	0.72	0.10	0.04	1.07	0.09	0.07	4.37	
66R	1W	26-28			633.38	25.19 (HPLC/MS)	4.72E+05	8.15E+05	7.29E+05	1.68E+05	6.8E+05	1.58E+05	2.3E+05	2.3E+05	1.03E+05	0.6359E+06	0.72	0.10	0.04	1.07	0.09	0.07	4.37	
66R	1W	26-28			633.38	25.19 (HPLC/MS)	4.72E+05	8.15E+05	7.29E+05	1.68E+05	6.8E+05	1.58E+05	2.3E+05	2.3E+05	1.03E+05	0.6359E+06	0.72	0.10	0.04	1.07	0.09	0.07	4.37	
66R	1W	26-28			633.38	25.19 (HPLC/MS)	4.72E+05	8.15E+05	7.29E+05	1.68E+05	6.8E+05	1.58E+05	2.3E+05	2.3E+05	1.03E+05	0.6359E+06	0.72	0.10	0.04	1.07	0.09	0.07	4.37	
66R	1W	26-28			633.38	25.19 (HPLC/MS)	4.72E+05	8.15E+05	7.29E+05	1.68E+05	6.8E+05	1.58E+05	2.3E+05	2.3E+05	1.03E+05	0.6359E+06	0.72	0.10	0.04	1.07	0.09	0.07	4.37	
66R	1W	26-28			633.38	25.19 (HPLC/MS)	4.72E+05	8.15E+05	7.29E+05	1.68E+05	6.8E+05	1.58E+05	2.3E+05	2.3E+05	1.03E+05	0.6359E+06	0.72	0.10	0.04	1.07	0.09	0.07	4.37	
66R	1W	26-28			633.38	25.19 (HPLC/MS)	4.72E+05	8.15E+05	7.29E+05	1.68E+05	6.8E+05	1.58E+05	2.3E+05	2.3E+05	1.03E+05	0.6359E+06	0.72	0.10	0.04	1.07	0.09	0.07	4.37	
66R	1W	26-28			633.38	25.19 (HPLC/MS)	4.72E+05	8.15E+05	7.29E+05	1.68E+05	6.8E+05	1.58E+05	2.3E+05	2.3E+05	1.03E+05	0.6359E+06	0.72	0.10	0.04	1.07	0.09	0.07	4.37	
66R	1W	26-28			633.38	25.19 (HPLC/MS)	4.72E+05	8.15E+05	7.29E+05	1.68E+05	6.8E+05	1.58E+05	2.3E+05	2.3E+05	1.03E+05	0.6359E+06	0.72	0.10	0.04	1.07	0.09	0.07	4.37	
66R	1W	26-28			633.38	25.19 (HPLC/MS)	4.72E+05	8.15E+05	7.29E+05	1.68E+05	6.8E+05	1.58E+05	2.3E+05	2.3E+05	1.03E+05	0.6359E+06	0.72	0.10	0.04	1.07	0.09	0.07	4.37	
66R	1W	26-28			633.38	25.19 (HPLC/MS)	4.72E+05	8.15E+05	7.29E+05	1.68E+05	6.8E+05	1.58E+05	2.3E+05	2.3E+05	1.03E+05	0.6359E+06	0.72	0.10	0.04	1.07	0.09	0.07	4.37	
66R	1W	26-28			633.38	25.19 (HPLC/MS)	4.72E+05	8.15E+05	7.29E+05	1.68E+05	6.8E+05	1.58E+05	2.3E+05	2.3E+05	1.03E+05	0.6359E+06	0.72	0.10	0.04	1.07	0.09	0.07	4.37	
66R	1W	26-28			633.38	25.19 (HPLC/MS)	4.72E+05	8.15E+05	7.29E+05	1.68E+05	6.8E+05	1.58E+05	2.3E+05	2.3E+05	1.03E+05	0.6359E+06	0.72	0.10	0.04	1.07	0.09	0.07	4.37	
66R	1W	26-28			633.38	25.19 (HPLC/MS)	4.72E+05	8.15E+05	7.29E+05	1.68E+05	6.8E+05	1.58E+05	2.3E+05	2.3E+05	1.03E+05	0.6359E+06	0.72	0.10	0.04	1.07	0.09	0.07	4.37	
66R	1W	26-28			633.38	25.19 (HPLC/MS)	4.72E+05	8.15E+05	7.29E+05	1.68E+05	6.8E+05	1.58E+05	2.3E+05	2.3E+05	1.03E+05	0.6359E+06	0.72	0.10	0.04	1.07	0.09	0.07	4.37	
66R	1W	26-28			633.38	25.19 (HPLC/MS)	4.72E+05	8.15E+05	7.29E+05	1.68E+05	6.8E+05	1.58E+05	2.3E+05	2.3E+05	1.03E+05	0.6359E+06	0.72	0.10	0.04	1.07	0.09	0.07	4.37	
66R	1W	26-28			633.38	25.19 (HPLC/MS)	4.72E+05	8.15E+05	7.29E+05	1.68E+05	6.8E+05	1.58E+05	2.3E+05	2.3E+05	1.03E+05	0.6359E+06	0.72	0.10	0.04	1.07	0.09	0.07	4.37	
66R	1W	26-28			633.38	25.19 (HPLC/MS)	4.72E+05	8.15E+05	7.29E+05	1.68E+05	6.8E+05	1.58E+05	2.3E+05	2.3E+05	1.03E+05	0.6359E+06	0.72	0.10	0.04	1.07	0.09	0.07	4.37	
66R	1W	26-28			633.38	25.19 (HPLC/MS)	4.72E+05	8.15E+05	7.29E+05	1.68E+05	6.8E+05	1.58E+05	2.3E+05	2.3E+05	1.03E+05	0.6359E+06	0.72	0.10	0.04	1.07	0.09	0.07	4.37	
66R	1W	26-28			633.38	25.19 (HPLC/MS)	4.72E+05	8.15E+05	7.29E+05	1.68E+05	6.8E+05	1.58E+05	2.3E+05	2.3E+05	1.03E+05	0.6359E+06	0.72	0.10	0.04	1.07	0.09	0.07	4.37	
66R	1W	26-28			633.38	25.19 (HPLC/MS)	4.72E+05	8.15E+05	7.29E+05	1.68E+05	6.8E+05	1.58E+05	2.3E+05	2.3E+05	1.03E+05	0.6359E+06	0.72	0.10	0.04	1.07	0.09	0.07	4.37	
66R	1W	26-28			633.38	25.19 (HPLC/MS)	4.72E+05	8.15E+05	7.29E+05	1.68E+05	6.8E+05	1.58E+05	2.3E+05	2.3E+05	1.03E+05	0.6359E+06	0.72	0.10	0.04	1.07	0.09	0.07	4.37	
66R	1W	26-28			633.38	25.19 (HPLC/MS)	4.72E+05	8.15E+05	7.29E+05	1.68E+05	6.8E+05	1.58E+05	2.3E+05	2.3E+05	1.03E+05	0.6359E+06	0.72	0.10	0.0					

Core Section	Core interval	Core depth (mbsf)	Core top	Core bottom	Age (Ma)	Used method	GDGT-0	GDGT-1	GDGT-2	GDGT-3	Cren	Cren*	GDGT-III	GDGT-II	GDGT-I	TEX86	BIT	Methane Index (MI) /Cren	GDGT-2 /Cren	GDGT-0 /Cren	IAH	GDGT-2 /GDGT-3	ifringe-3 beta
B5R	5W	59-66	810.38	810.45	30.50	HPLC/MS	1.56655E+05	1.53478E+05	1.28848E+05	2.72077E+04	2.05111E+06	8.75478E+04	2.67762E+04	3.78674E+04	3.18862E+04	0.550654	0.05	0.14	0.06	0.81	0.019406	5.67	0.81
B5R	3W	80-84	835.66	835.7	31.75	HPLC/MS	1.69339E+05	1.64494E+05	1.02774E+05	3.26654E+04	2.66544E+06	7.44434E+04	2.49092E+04	4.96265E+04	4.58454E+04	0.518185	0.06	0.13	0.06	0.79	0.020492	4.41	0.79
B5R	3W	84-87	845.71	845.75	32.08	HPLC/MS	3.97955E+05	4.09168E+05	1.89315E+05	5.24693E+04	5.03454E+06	1.82231E+05	1.36529E+05	1.17033E+05	1.68454E+04	0.509221	0.06	0.11	0.04	0.79	0.156168	3.62	0.79
B5R	4W	847.01	847.05	847.05	32.13	HPLC/MS	1.17E+05	5.59E+04	2.17E+04	8.41E+03	1.18E+06	2.43E+04	5.13E+04	5.09E+04	7.00E+04	0.492921	0.13	0.07	0.02	0.99	0.003988	2.58	0.99
B5R	3W	874.04	874.08	874.08	33.03	HPLC/MS	4.17962E+05	2.76287E+05	1.44751E+05	3.37198E+04	4.18849E+06	1.06268E+05	1.31564E+05	1.48132E+05	2.04077E+05	0.507478	0.10	0.10	0.03	1.00	0.055645	4.29	1.00
B5R	3W	874.74	874.77	874.77	33.06	HPLC/MS	7.27973E+05	8.80532E+04	5.93566E+04	1.20147E+04	1.08277E+06	4.72115E+04	4.99433E+04	5.19098E+04	3.81779E+04	0.573873	0.11	0.12	0.05	0.74	0.040389	4.94	0.74
B5R	3W	878.84	878.88	878.88	33.12	HPLC/MS	1.80534E+05	1.80534E+05	1.80534E+05	1.80534E+05	1.80534E+06	1.80534E+06	1.80534E+06	1.80534E+06	1.80534E+06	0.5259	0.14	0.11	0.04	0.78	0.035451	4.81	0.78
B5R	3W	884.95	884.95	884.95	33.20	HPLC/MS	5.26055E+05	7.10739E+04	4.89331E+04	9.21084E+03	8.8825E+05	3.23285E+04	1.60717E+04	1.89227E+04	2.38114E+04	0.38554	0.07	0.12	0.02	0.62	0.152452	4.88	0.62

Table S2: Comparison between TEX86 and temperature values derived from samples analyzed with both HPLC/MS and UHPLC/MS.

Core	Section	Core interval (cm)	average cum. depth (mbsf)	TEX86 on			Δ SST (lin. cal. Kim et al., 2010)	Δ SST (TEX86H cal. Kim et al., 2010)
				HPLC/MS	UHPLC/MS	Δ TEX86		
48R	2W	19-21	451.6	0.520	0.504	0.016	0.998	0.930
63R	4W	19-21	597.55	0.494	0.506	0.011	0.744	0.677
70R	3W	21-23	663.67	0.500	0.510	0.010	0.625	0.574
84R	6W	40-44	802.79	0.556	0.547	0.008	0.449	0.450
92R	3W	2-6	874.06	0.507	0.499	0.009	0.568	0.520
Average						0.011	0.677	0.630

References

- Abe, M., Nozawa, T., Ogura, T., Takata, K., 2016. Effect of retreating sea ice on Arctic cloud cover in simulated recent global warming. *Atmos. Chem. Phys.* 16, 14343–14356. <https://doi.org/10.5194/acp-16-14343-2016>
- Agatha, S., 2010. A Light and Scanning Electron Microscopic Study of the Closing Apparatus in Tintinnid Ciliates (Ciliophora, Spirotricha, Tintinnida): A Forgotten Synapomorphy. *J. Eukaryot. Microbiol.* 57, 297–307. <https://doi.org/10.1111/j.1550-7408.2010.00490.x>
- Agatha, S., Laval-Peuto, M., Simon, P., 2013. The Tintinnid Lorica, in: Dolan, J.R., Montagnes, D.J.S., Agatha, S., Coats, D.W., Stoecker, D.K. (Eds.), *The Biology and Ecology of Tintinnid Ciliates: Models for Marine Plankton*. Wiley-Blackwell, Hoboken, New Jersey, USA, pp. 17–41.
- Agatha, S., Simon, P., 2012. On the Nature of Tintinnid Loricae (Ciliophora: Spirotricha: Tintinnina): a Histochemical, Enzymatic, EDX, and High-resolution TEM Study. *Acta Protozool.* 51, 1–19. <https://doi.org/10.4467/16890027AP.12.001.0384>
- Agatha, S., Strüder-Kypke, M.C., 2013. Systematics and Evolution of Tintinnid Ciliates, in: Dolan, J.R., Montagnes, D.J.S., Agatha, S., Coats, D.W., Stoecker, D.K. (Eds.), *The Biology and Ecology of Tintinnid Ciliates: Models for Marine Plankton*. Wiley-Blackwell, Hoboken, New Jersey, USA, pp. 42–84.
- Agatha, S., Strüder-Kypke, M.C., 2012. Reconciling Cladistic and Genetic Analyses in Choreotrichid Ciliates (Ciliophora, Spirotricha, Oligotrichea). *J. Eukaryot. Microbiol.* 59, 325–350. <https://doi.org/10.1111/j.1550-7408.2012.00623.x>
- Alder, V.A., 1999. Tintinninea, in: Boltovskoy, D. (Ed.), *South Atlantic zooplankton*. Vol. 1. Backhuys Publishers, Leiden, pp. 321–384.
- Alder, V.A., Boltovskoy, D., 1991. Microplanktonic distributional patterns west of the Antarctic Peninsula, with special emphasis on the Tintinnids. *Polar Biol.* 11, 103–112.
- Allen, C.S., 2014. Proxy development: A new facet of morphological diversity in the marine diatom *Eucampia antarctica* (Castracane) Mangin. *J. Micropalaeontol.* 33, 131–142.
- Alley, K., Patacca, K., Pike, J., Dunbar, R., Leventer, A., 2018. Iceberg Alley, East Antarctic Margin: Continuously laminated diatomaceous sediments from the late Holocene. *Mar. Micropaleontol.* 140, 56–68. <https://doi.org/10.1016/j.marmicro.2017.12.002>
- Alley, R.B., Ágústssdóttir, A.M., 2005. The 8k event: cause and consequences of a major Holocene abrupt climate change. *Quaternary Sci. Rev.* 24, 1123–1149. <https://doi.org/10.1016/j.quascirev.2004.12.004>
- Altabet, M.A., Francois, R., 2001. Nitrogen isotope biogeochemistry of the Antarctic Polar Frontal Zone at 170°W. *Deep-Sea Res. Pt II* 48, 4247–4273.
- Altabet, M.A., Francois, R., 1994. Sedimentary nitrogen isotopic ratio as a recorder for surface ocean nitrate utilization. *Global Biogeochem. Cy.* 8, 103–116.
- Altiero, T., Bertolani, R., Rebecchi, L., 2010. Hatching phenology and resting eggs in tardigrades. *J. Zool.* 280, 290–296. <https://doi.org/10.1111/j.1469-7998.2009.00664.x>
- Amenábar, C.R., Candel, M.S., Guerstein, G.R., 2014. Small Antarctic Late Cretaceous Chorate Dinoflagellate Cysts: Biological and Palaeoenvironmental Affinities. *Palynology* 38, 303–323.
- Amorim, A., Dale, B., Godinho, R., Brotas, V., 2001. *Gymnodinium catenatum*-like cysts (Dinophyceae) in recent sediments from the coast of Portugal. *Phycologia* 40, 572–582. <https://doi.org/10.2216/i0031-8884-40-6-572.1>
- Anderson, D.M., Fukuyo, Y., Matsuoka, K., 2003. Cyst methodologies, in: Hallegraeff, G.M., Anderson, D.M., Cembella, A.D. (Eds.), *Manual of Harmful Marine Microalgae*. UNESCO Monographs on oceanographic methodology 11, Paris, France, pp. 165–189.

- Anderson, D.M., Jacobson, D.M., Bravo, I., Wrenn, J.H., 1988. The unique, microreticulate cyst of the naked dinoflagellate *Gymnodinium catenatum*, J. Phycol. 24, 255–262.
- Andreoli, C., Moro, I., La Rocca, N., Valle, L.D., Masiero, L., Rascio, N., Vecchia, F.D., 2000. Ecological, physiological, and biomolecular surveys on microalgae from Ross Sea (Antarctica). Ital. J. Zool. 67, 147–156. <https://doi.org/10.1080/11250000009356370>
- Andreoli, C., Tolomio, C., Moro, I., Radice, M., Moschin, E., Bellato, S., 1995. Diatoms and dinoflagellates in Terra Nova Bay (Ross Sea-Antarctica) during austral summer 1990. Polar Biol. 15, 465–475. <https://doi.org/10.1007/BF00237460>
- Andry, O., Bintanja, R., Hazeleger, W., 2017. Time-Dependent Variations in the Arctic's Surface Albedo Feedback and the Link to Seasonality in Sea Ice. J. Climate 30, 393–410. <https://doi.org/10.1175/JCLI-D-15-0849.1>
- Apstein, C., 1909. Die Pyrocysteen der Plankton-Expedition, in: Ergebnisse der Plankton-Expedition der Humboldt-Stiftung, Bd. IV M.c., Lipsius and Tischer, Kiel and Leipzig, 1–27.
- Arai, M., Koutsoukos, E.A.M., 1998. Palynoforaminifera (Foraminiferal Organic Linings and Allied Material): a New Tool for Petroleum Exploration. Am. Assoc. Petr. Geol. AAPG Int. Conf. Exhib. Ext. Abstr. Vol. 82, 584–585.
- Armand, L.K., Crosta, X., Quéguiner, B., Mosseri, J., Garcia, N., 2008. Diatoms preserved in surface sediments of the northeastern Kerguelen Plateau. Deep-Sea Res. Pt II 55, 677–692. <https://doi.org/10.1016/j.dsr2.2007.12.032>
- Armand, L.K., Crosta, X., Romero, O., Pichon, J.J., 2005. The biogeography of major diatom taxa in Southern Ocean sediments: 1. Sea ice related species. Palaeogeogr. Palaeoclimatol. 223, 93–126. <https://doi.org/10.1016/j.palaeo.2005.02.015>
- Armbrrecht, L.H., Eriksen, R., Leventer, A., Armand, L.K., 2017. First observations of living sea-ice diatom agglomeration to tintinnid loricae in East Antarctica. J. Plankton Res. 39, 795–802. <https://doi.org/10.1093/plankt/fbx036>
- Arrigo, K.R., Robinson, D.H., Worthen, D.L., Dunbar, R.B., DiTullio, G.R., VanWoert, M., Lizotte, M.P., 1999. Phytoplankton Community Structure and the Drawdown of Nutrients and CO₂ in the Southern Ocean. Science 283, 365–367. <https://doi.org/10.1126/science.283.5400.365>
- Arrigo, K.R., van Dijken, G.L., 2003. Phytoplankton dynamics within 37 Antarctic coastal polynya systems. J. Geophys. Res. 108, 3271. <https://doi.org/10.1029/2002JC001739>
- Arrigo, K.R., van Dijken, G.L., Bushinsky, S., 2008. Primary production in the Southern Ocean, 1997 – 2006. J. Geophys. Res. 113, C08004. <https://doi.org/10.1029/2007JC004551>
- Arrigo, K.R., Weiss, A.M., Smith, W.O.J., 1998a. Physical forcing of phytoplankton dynamics in the southwestern Ross Sea. J. Geophys. Res. 103, 1007–1021.
- Arrigo, K.R., Worthen, D., Schnell, A., Lizotte, M.P., 1998b. Primary production in Southern Ocean waters. J. Geophys. Res. 103, 15587–15600. <https://doi.org/10.1029/98JC00930>
- Arrigo, K.R., Worthen, D.L., Robinson, D.H., 2003. A coupled ocean-ecosystem model of the Ross Sea: 2. Iron regulation of phytoplankton taxonomic variability and primary production. J. Geophys. Res.-Oceans 108, 3231. <https://doi.org/10.1029/2001JC000856>
- Arzel, O., Fichet, T., Goosse, H., 2006. Sea ice evolution over the 20th and 21st centuries as simulated by current AOGCMs. Ocean Model. 12, 401–415. <https://doi.org/10.1016/j.ocemod.2005.08.002>
- Ashley, K.E., McKay, R., Eturneau, J., Jimenez-espejo, F.J., Condrón, A., Albot, A., Crosta, X., Riesselman, C., Seki, O., Massé, G., Golléde, N.R., Gasson, E., Lowry, D.P., Barrand, N.E.,

- Johnson, K., Bertler, N., Escutia, C., Dunbar, R., Bendle, J.A., 2021. Mid-Holocene Antarctic sea-ice increase driven by marine ice sheet retreat. *Clim. Past* 17, 1–19.
- Asioli, A., 1995. Living (stained) benthic Foraminifera distribution in the Western Ross Sea (Antarctica). *Palaeopelagos* 5, 201–214.
- Asioli, A., Langone, L., 2010. “Living” (CTG vs Rose Bengal) benthic foraminifera distribution in Western Ross Sea (Antarctica). *International Symposium on Foraminifera, FORAMS 2010 Abstracts*, 51.
- Asioli, A., Langone, L., 1997. Relationship between recent planktic foraminifera and water mass properties in the Western Ross Sea (Antarctica). *Geogr. Fis. Din. Quat.* 20, 193–198.
- Askin, R.A., Raine, J.I., 2000. Oligocene and Early Miocene Terrestrial Palynology of the Cape Roberts Drillhole CRP-2/2a, Victoria Land Basin, Antarctica. *Terra Ant.* 7, 493–501.
- Asper, V.L., Smith, W.O., 1999. Particle fluxes during austral spring and summer in the southern Ross Sea, Antarctica. *J. Geophys. Res.* 104, 5345–5359.
- Assmy, P., Cisewski, B., Henjes, J., Klaas, C., Montresor, M., Smetacek, V., 2014. Response of the protozooplankton assemblage during the European Iron Fertilization Experiment (EIFEX) in the Antarctic circumpolar current. *J. Plankton Res.* 36, 1175–1189. <https://doi.org/10.1093/plankt/fbu068>
- Atanassova, J., 2005. Palaeoecological setting of the western Black Sea area during the last 15000 years. *Holocene* 15, 576–584.
- Atkinson, A., 1998. Life cycle strategies of epipelagic copepods in the Southern Ocean. *J. Marine Syst.* 15, 289–311.
- Atkinson, A., Hunt, B.P.V., Pakhomov, E.A., Hosie, G.W., 2012. Overview of Southern Ocean Zooplankton data: Abundance, Biomass, Feeding and Functional Relationships. *CCAMLR Sci.* 19, 171–218.
- Attaran-Fariman, G., de Salas, M.F., Negri, A.P., Bolch, C.J.S., 2007. Morphology and phylogeny of *Gymnodinium trapeziforme* sp. nov. (Dinophyceae): a new dinoflagellate from the southeast coast of Iran that forms microreticulate resting cysts. *Phycologia* 46, 644–656. <https://doi.org/10.2216/07-05.1>
- Austermann, J., Pollard, D., Mitrovica, J.X., Moucha, R., Forte, A.M., DeConto, R.M., Rowley, D.B., Raymo, M.E., 2015. The impact of dynamic topography change on Antarctic ice sheet stability during the mid-Pliocene warm period. *Geology* 43, 927–930. <https://doi.org/10.1130/G36988.1>
- Australian Antarctic Data Centre, 2017. Electron Micrograph Database - Marine Specimens. Occurrence Dataset <https://doi.org/10.15468/Subdem> accessed via GBIF.org on 2018-02-08.
- Baines, P.G., 2009. A model for the structure of the Antarctic Slope Front. *Deep-Sea Res. Pt II* 56, 859–873. <https://doi.org/10.1016/j.dsr2.2008.10.030>
- Balech, E., 1973. Segunda contribucion al conocimiento del microplancton del mar de Bellingshausen. *Contrib. del Inst. Antart. Argentino* 107, 1–63.
- Balech, E., 1958a. Plancton de la Campaña Antártica Argentina. *Physis* 21, 75–108.
- Balech, E., 1958b. Dinoflagellés et Tintinnides de la Terre Adélie (Secteur Français Antarctique). *Vie Milieu* 8, 382–408.
- Ball, E.E., Miller, D.J., 2006. Phylogeny: The Continuing Classificatory Conundrum of Chaetognaths. *Curr. Biol.* 16, R593–R596. <https://doi.org/10.1016/j.cub.2006.07.005>
- Barber, D.C., Dyke, A., Hillaire-Marcel, C., Jennings, A.E., Andrews, J.T., Kerwin, M.W., Bilodeau, G., McNeely, R., Southon, J., Morehead, M.D., Gagnon, J.-M., 1999. Forcing of the cold

- event of 8,200 years ago by catastrophic drainage of Laurentide lakes. *Nature* 400, 344–348. <https://doi.org/10.1038/22504>
- Barbieri, R., D'Onofrio, S., Melis, R., Westall, F., 1999. r-Selected benthic foraminifera with associated bacterial colonies in Upper Pleistocene sediments of the Ross Sea (Antarctica): implications for calcium carbonate preservation. *Palaeogeogr. Palaeoclimatol.* 149, 41–57. [https://doi.org/10.1016/S0031-0182\(98\)00191-6](https://doi.org/10.1016/S0031-0182(98)00191-6)
- Bárcena, M.Á., Gersonde, R., Ledesma, S., Fabrés, J., Calafat, A.M., Canals, M., Sierro, F.J., Flores, J.A., 1998. Record of Holocene glacial oscillations in Bransfield Basin as revealed by siliceous microfossil assemblages. *Antarct. Sci.* 10, 269–285.
- Bárcena, M.Á., Isla, E., Plaza, A., Flores, J.A., Sierro, F.J., Masqué, P., Sanchez-Cabeza, J.A., Palanques, A., 2002. Bioaccumulation record and paleoclimatic significance in the Western Bransfield Strait. The last 2000 years. *Deep-Sea Res. Pt II* 49, 935–950.
- Barker, P.F., Filippelli, G.M., Florindo, F., Martin, E.E., Scher, H.D., 2007. Onset and role of the Antarctic Circumpolar Current. *Deep-Sea Res. Pt II* 54, 2388–2398. <https://doi.org/10.1016/j.dsr2.2007.07.028>
- Bartels, P.J., Pilato, G., Lisi, O., Nelson, D.R., 2009. *Macrobiotus* (Eutardigrada, Macrobiotidae) from the Great Smoky Mountains National Park, Tennessee/North Carolina, USA (North America): two new species and six new records. *Zootaxa* 2022, 45–57. <https://doi.org/10.5281/zenodo.186100>
- Barwell, L.J., Isaac, N.J.B., Kunin, W.E., 2015. Measuring β -diversity with species abundance data. *J. Anim. Ecol.* 84, 1112–1122. <https://doi.org/10.1111/1365-2656.12362>
- Basse, A., Zhu, C., Versteegh, G.J.M., Fischer, G., Hinrichs, K.-U., 2014. Distribution of intact and core tetraether lipids in water column profiles of suspended particulate matter off Cape Blanc, NW Africa. *Org. Geochem.* 72, 1–13. <https://doi.org/10.1016/j.orggeochem.2014.04.007>
- Bauer, E., Ganopolski, A., Montoya, M., 2004. Simulation of the cold climate event 8200 years ago by meltwater outburst from Lake Agassiz. *Paleoceanography* 19, PA3014. <https://doi.org/10.1029/2004PA001030>
- Bazin, L., Landais, A., Lemieux-Dudon, B., Toyé Mahamadou Kele, H., Veres, D., Parrenin, F., Martinerie, P., Ritz, C., Capron, E., Lipenkov, V., Loutre, M.-F., Raynaud, D., Vinther, B., Svensson, A., Rasmussen, S.O., Severi, M., Blunier, T., Leuenberger, M., Fischer, H., Masson-Delmotte, V., Chappellaz, J., Wolff, E., 2013. An optimized multi-proxy, multi-site Antarctic ice and gas orbital chronology (AICC2012): 120–800 ka. *Clim. Past* 9, 1715–1731. <https://doi.org/10.5194/cp-9-1715-2013>
- Beddow, H.M., Liebrand, D., Sluijs, A., Wade, B.S., Lourens, L.J., 2016. Global change across the Oligocene-Miocene transition: High-resolution stable isotope records from IODP Site U1334 (equatorial Pacific Ocean). *Paleoceanography* 31, 81–97. <https://doi.org/10.1002/2015PA002820>. Received
- Beijerinck, M.W., 1890. Culturversuche mit Zoochlorellen, Lichenengonidien und anderen niederen Algen, *Botanische Zeitung* 48, 725–739, 741–754, 757–768, 781–785.
- Bell, E.M., Laybourn-Parry, J., 2003. Mixotrophy in the Antarctic phytoflagellate, *Pyramimonas gelidicola* (Chlorophyta: Prasinophyceae). *J. Phycol.* 39, 644–649.
- Belmonte, G., 1998. The egg morphology of 7 Acartiidae species: a preliminary survey of the ootaxonomy of calanoids. *J. Marine Syst.* 15, 35–39.
- Belmonte, G., 1992. Diapause egg production in *Acartia* (*Paracartia*) *latisetosa* (Crustacea, Copepoda, Calanoida). *B. Zool.* 59, 363–366. <https://doi.org/10.1080/11250009209386694>

- Belt, S.T., Massé, G., Rowland, S.J., Poulin, M., Michel, C., LeBlanc, B., 2007. A novel chemical fossil of palaeo sea ice: IP₂₅. *Org. Geochem.* 38, 16–27.
<https://doi.org/10.1016/j.orggeochem.2006.09.013>
- Benedek, P.N., 1972. Phytoplanktonen aus dem Mittel- und Oberoligozän von Tönisberg (Niederrheingebiet), *Palaeontographica*, Abt. B 137, 1–71.
- Bentley, M., Hodgson, D.A., Sugden, D., Roberts, S.J., Smith, J.A., Leng, M.J., Bryant, C., 2005. Early Holocene retreat of the George VI Ice Shelf, Antarctic Peninsula. *Geology* 33, 173–176. <https://doi.org/10.1130/G21203.1>
- Bentley, M.J., Hodgson, D.A., Smith, J.A., Cofaigh, C.Ó., Domack, E.W., Larter, R.D., Roberts, S.J., Brachfeld, S., Leventer, A., Hjort, C., Hillenbrand, C.-D., Evans, J., 2009. Mechanisms of Holocene palaeoenvironmental change in the Antarctic Peninsula region. *Holocene* 19, 51–69.
- Bérard-Therriault, L., Poulin, M., Bossé, L., 1999. Guide d'identification du phytoplancton marin de l'estuaire et du golfe du Saint-Laurent incluant également certains protozoaires. Publication spéciale canadienne des sciences halieutiques et aquatiques 128, NRC Research Press, p. 387.
- Berasategui, A.A., Hoffmeyer, M.S., Dutto, M.S., Biancalana, F., 2012. Seasonal variation in the egg morphology of the copepod *Eurytemora americana* and its relationship with reproductive strategy in a temperature estuary in Argentina. *ICES J. Mar. Sci.* 69, 380–388.
- Berg, W.J. Van De, Broeke, M. Van Den, Ettema, J., Meijgaard, E. Van, 2011. Significant contribution of insolation to Eemian melting of the Greenland ice sheet. *Nat. Geosci.* 4, 679–683. <https://doi.org/10.1038/ngeo1245>
- Bergamasco, A., Defendi, V., Budillon, G., Spezie, G., 2004. Downslope flow observations near Cape Adare shelf-break. *Antarct. Sci.* 16, 199–204.
<https://doi.org/10.1017/S0954102004001981>
- Bergami, C., Capotondi, L., Langone, L., Giglio, F., Ravaioli, M., 2009. Distribution of living planktonic foraminifera in the Ross Sea and the Pacific sector of the Southern Ocean (Antarctica). *Mar. Micropaleontol.* 73, 37–48.
<https://doi.org/10.1016/j.marmicro.2009.06.007>
- Bernárdez, P., González-Álvarez, R., Francés, G., Prego, R., Bárcena, M.A., Romero, O.E., 2008. Late Holocene history of the rainfall in the NW Iberian peninsula — Evidence from a marine record. *J. Marine Syst.* 72, 366–382.
<https://doi.org/10.1016/j.jmarsys.2007.03.009>
- Bertolani, R., Rebecchi, L., 1993. A revision of the *Macrobotus hufelandi* group (Tardigrada, Macrobiotidae), with some observations on the taxonomic characters of eutardigrades. *Zool. Scr.* 22, 127–152. <https://doi.org/10.1111/j.1463-6409.1993.tb00347.x>
- Bertolani, R., Rebecchi, L., Claxton, S.K., 1996. Phylogenetic significance of egg shell variation in tardigrades. *Zool. J. Linn. Soc.-Lond.* 116, 139–148.
- Bertram, R.A., Wilson, D.J., Fliedert, T. van de, McKay, R.M., Patterson, M.O., Jimenez-Espejo, F.J., Escutia, C., Duke, G.C., Taylor-Silva, B.I., Riesselman, C.R., 2018. Pliocene deglacial event timelines and the biogeochemical response offshore Wilkes Subglacial Basin, East Antarctica. *Earth Planet. Sc. Lett.* 494, 109–116.
<https://doi.org/10.1016/j.epsl.2018.04.054>
- Bertrand, P., Shimmield, G., Martinez, P., Grousset, F., Jorissen, F., Paterne, M., Pujol, C., Bouloubassi, I., Buat Menard, P., Peypouquet, J.-P., Beaufort, L., Sicre, M.-A., Lallier-Verges, E., Foster, J.M., Ternois, Y., Other Participants of the Sedorqua Program, 1996.

- The glacial ocean productivity hypothesis: the importance of regional temporal and spatial studies. *Mar. Geol.* 130, 1–9. [https://doi.org/10.1016/0025-3227\(95\)00166-2](https://doi.org/10.1016/0025-3227(95)00166-2)
- Bianchi, C., Gersonde, R., 2002. The Southern Ocean surface between Marine Isotope Stages 6 and 5d: Shape and timing of climate changes. *Palaeogeogr. Palaeoclimatol.* 187, 151–177. [https://doi.org/10.1016/S0031-0182\(02\)00516-3](https://doi.org/10.1016/S0031-0182(02)00516-3)
- Bijl, P.K., Bendle, J.A.P., Bohaty, S.M., Pross, J., Schouten, S., Tauxe, L., Stickley, C.E., McKay, R.M., Röhl, U., Olney, M., Sluijs, A., Escutia, C., Brinkhuis, H., 2013a. Eocene cooling linked to early flow across the Tasmanian Gateway. *P. Natl. Acad. Sci. USA* 110, 9645–9650. <https://doi.org/10.1073/pnas.1220872110>
- Bijl, P.K., Houben, A.J.P., Bruls, A., Pross, J., Sangiorgi, F., 2018a. Stratigraphic calibration of Oligocene – Miocene organic-walled dinoflagellate cysts from offshore Wilkes Land, East Antarctica, and a zonation proposal. *J. Micropalaeontol.* 37, 105–138.
- Bijl, P.K., Houben, A.J.P., Hartman, J.D., Pross, J., Salabarnada, A., Escutia, C., Sangiorgi, F., 2018b. Paleooceanography and ice sheet variability offshore Wilkes Land, Antarctica – Part 2: Insights from Oligocene–Miocene dinoflagellate cyst assemblages. *Clim. Past* 14, 1015–1033. <https://doi.org/10.5194/cp-14-1015-2018>
- Bijl, P.K., Houben, A.J.P., Schouten, S., Bohaty, S.M., Sluijs, A., Reichert, G.-J., Sinninghe Damsté, J.S., Brinkhuis, H., 2010. Transient Middle Eocene Atmospheric CO₂ and Temperature Variations. *Science* 330, 819–821. <https://doi.org/10.1126/science.1193654>
- Bijl, P.K., Pross, J., Warnaar, J., Stickley, C.E., Huber, M., Guerin, R., Houben, A.J.P., Sluijs, A., Visscher, H., Brinkhuis, H., 2011. Environmental forcings of Paleogene Southern Ocean dinoflagellate biogeography. *Paleoceanography* 26, PA1202. <https://doi.org/10.1029/2009PA001905>
- Bijl, P.K., Schouten, S., Sluijs, A., Reichert, G.-J., Zachos, J.C., Brinkhuis, H., 2009. Early Palaeogene temperature evolution of the southwest Pacific Ocean. *Nature* 461, 776–779. <https://doi.org/10.1038/nature08399>
- Bijl, P.K., Sluijs, A., Brinkhuis, H., 2013b. A magneto- and chemostratigraphically calibrated dinoflagellate cyst zonation of the early Palaeogene South Pacific Ocean. *Earth-Sci. Rev.* 124, 1–31. <https://doi.org/10.1016/j.earscirev.2013.04.010>
- Billups, K., Pälike, H., Channell, J.E.T., Zachos, J.C., Shackleton, N.J., 2004. Astronomic calibration of the late Oligocene through early Miocene geomagnetic polarity time scale. *Earth Planet. Sc. Lett.* 224, 33–44. <https://doi.org/10.1016/j.epsl.2004.05.004>
- Billups, K., Schrag, D.P., 2002. Paleotemperatures and ice volume of the past 27 Myr revisited with paired Mg/Ca and ¹⁸O/¹⁶O measurements on benthic foraminifera. *Paleoceanography* 17, 1003. <https://doi.org/10.1029/2000PA000567>
- Bintanja, R., Oldenborgh, G.J.V.A.N., Katsman, C.A., 2015. The effect of increased fresh water from Antarctic ice shelves on future trends in Antarctic sea ice. *Ann. Glaciol.* 56, 120–126. <https://doi.org/10.3189/2015AoG69A001>
- Bintanja, R., Oldenborgh, G.J. Van, Drijfhout, S.S., Wouters, B., Katsman, C.A., 2013. Important role for ocean warming and increased ice-shelf melt in Antarctic sea-ice expansion. *Nat. Geosci.* 6, 376–379. <https://doi.org/10.1038/ngeo1767>
- Bjørnsen, P.K., Kuparinen, J., 1991. Growth and herbivory by heterotrophic dinoflagellates in the Southern Ocean, studied by microcosm experiments. *Mar. Biol.* 109, 397–405. <https://doi.org/10.1007/BF01313505>
- Blaga, C.I., Reichert, G.-J., Heiri, O., Sinninghe Damsté, J.S., 2009. Tetraether membrane lipid distributions in water-column particulate matter and sediments: a study of 47 European

- lakes along a north–south transect. *J. Paleolimnol.* 41, 523–540.
<https://doi.org/10.1007/s10933-008-9242-2>
- Boere, A.C., Abbas, B., Rijpstra, W.I.C., Versteegh, G.J.M., Volkman, J.K., Sinninghe Damsté, J.S., Coolen, M.J.L., 2009. Late-Holocene succession of dinoflagellates in an Antarctic fjord using a multi-proxy approach: Paleoenvironmental genomics, lipid biomarkers and palynomorphs. *Geobiology* 7, 265–281. <https://doi.org/10.1111/j.1472-4669.2009.00202.x>
- Bogus, K., Harding, I.C., King, A., Charles, A.J., Zonneveld, K.A.F., Versteegh, G.J.M., 2012. The composition and diversity of dinosporin in species of the *Apectodinium* complex (Dinoflagellata). *Rev. Palaeobot. Palyno.* 183, 21–31.
<https://doi.org/10.1016/j.revpalbo.2012.07.001>
- Bogus, K., Mertens, K.N., Lauwaert, J., Harding, I.C., Vrieliinck, H., Zonneveld, K.A.F., Versteegh, G.J.M., 2014. Differences in the chemical composition of organic-walled dinoflagellate resting cysts from phototrophic and heterotrophic dinoflagellates. *J. Phycol.* 50, 254–266. <https://doi.org/10.1111/jpy.12170>
- Bohaty, S.M., Zachos, J.C., Delaney, M.L., 2012. Foraminiferal Mg/Ca evidence for Southern Ocean cooling across the Eocene–Oligocene transition. *Earth Planet. Sc. Lett.* 317–318, 251–261. <https://doi.org/10.1016/j.epsl.2011.11.037>
- Bolch, C., Negri, A.P., Hallegraeff, G.M., 1999. *Gymnodinium microreticulatum* sp. nov. (Dinophyceae): a naked, microreticulate cyst-producing dinoflagellate, distinct from *Gymnodinium catenatum* and *Gymnodinium nolleri*. *Phycologia* 38, 301–313.
<https://doi.org/10.2216/i0031-8884-38-4-301.1>
- Bolch, C.J.S., Reynolds, M.J., 2002. Species resolution and global distribution of microreticulate dinoflagellate cysts. *J. Plankton Res.* 24, 565–578.
- Boltovskoy, D., Dinofrio, E.O., Alder, V.A., 1990. Intraspecific variability in Antarctic tintinnids: the *Cymatocylis affinis/convallaria* species group. *J. Plankton Res.* 12, 403–413.
- Bonaccorsi, R., Quaiá, T., Burckle, L.H., Anderson, R.F., Melis, R., Brambati, A., 2007. C-14 age control of pre- and post-LGM events using *N. pachyderma* preserved in deep-sea sediments (Ross Sea, Antarctica), in: Cooper, A.K., Raymond, C.R., the 10th ISAES Editorial Team (Eds.), *Antarctica: A Keystone in a Changing World - Online Proceedings for the 10th International Symposium on Antarctic Earth Sciences*. USGS Open-File Report 2007-1047, pp. 4, Extended Abstract 098.
- Bonn, W.J., Gingele, F.X., Grobe, H., Mackensen, A., Ffitterer, D.K., 1998. Paleoproductivity at the Antarctic continental margin: opal and barium records for the last 400 ka. *Palaeogeogr. Palaeoclimatol.* 139, 195–211.
- Bonnet, S., De Vernal, A., Hillaire-Marcel, C., Radi, T., Husum, K., 2010. Variability of sea-surface temperature and sea-ice cover in the Fram Strait over the last two millennia. *Mar. Micropaleontol.* 74, 59–74. <https://doi.org/10.1016/j.marmicro.2009.12.001>
- Booth, R.K., Jackson, S.T., Forman, S.L., Kutzbach, J.E., Bettis, E.A., Kreig, J., Wright, D.K., 2005. A severe centennial-scale drought in mid- continental North America 4200 years ago and apparent global linkages. *Holocene* 15, 321–328.
- Borrelli, C., Katz, M.E., 2015. Dynamic deep-water circulation in the northwestern Pacific during the Eocene: Evidence from Ocean Drilling Program Site 884 benthic foraminiferal stable isotopes ($\delta^{18}\text{O}$ and $\delta^{13}\text{C}$). *Geosphere* 11, 1204–1225.
<https://doi.org/10.1130/GES01152.1>
- Borromei, A.M., Coronato, A., Franzén, L.G., Ponce, J.F., Sáez, J.A.L., Maidana, N., Rabassa, J., Candel, M.S., 2010. Multiproxy record of Holocene paleoenvironmental change, Tierra

- del Fuego, Argentina. *Palaeogeogr. Palaeocl.* 286, 1–16.
<https://doi.org/10.1016/j.palaeo.2009.11.033>
- Bova, S., Rosenthal, Y., Liu, Z., Godad, S.P., Yan, M., 2021. Seasonal origin of the thermal maxima at the Holocene and the last interglacial. *Nature* 589, 548–553.
<https://doi.org/10.1038/s41586-020-03155-x>
- Bracegirdle, T.J., Connolley, W.M., Turner, J., 2008. Antarctic climate change over the twenty first century. *J. Geophys. Res.* 113, 1–13. <https://doi.org/10.1029/2007JD008933>
- Brassell, S.C., Eglinton, G., Marlowe, I.T., Pflaumann, U., Sarntheim, M., 1986. Molecular stratigraphy: a new tool for climatic assessment. *Nature* 320, 129–133.
- Brenner, W.W., Biebow, N., 2001. Missing autofluorescence of recent and fossil dinoflagellate cysts—an indicator of heterotrophy? *Neues Jahrbuch für Geologie und Paläontologie Abhandlungen*, 219, pp. 229–240.
- Brinkhuis, H., Munsterman, D.K., Sengers, S., Sluijs, A., Warnaar, J., Williams, G.L., 2003. Late Eocene-Quaternary dinoflagellate cysts from ODP Site 1168, off Western Tasmania. *Proc. ODP, Sci. Results* 189, 1–36.
- Bromwich, D.H., Kurtz, D., 1984. Katabatic wind forcing of the Terra Nova Bay Polynya. *J. Geophys. Res.* 89, 3561–3572.
- Brugmans, N., 2003. Marine productivity and terrigenous matter supply: The variability of the Subtropical Convergence around Tasmania during the last 500 ka. Christian-Albrechts University, Kiel, Germany.
- Brünnich, M. T., 1772: *Zoologiae fundamenta praelectionibus academicis accomodata*. Grunde i dyrelaeren, Friderik Christian Pelt, Hafnia et Lipsia, p. 253.
- Buck, K.R., Bolt, P.A., Bentham, W.N., Garrison, D.L., 1992. A dinoflagellate cyst from Antarctic sea ice. *J. Phycol.* 28, 15–18.
- Budillon, G., Gremes Cordero, S., Salusti, E., 2002. On the dense water spreading off the Ross Sea shelf (Southern Ocean). *J. Marine Syst.* 35, 207–227.
[https://doi.org/10.1016/S0924-7963\(02\)00082-9](https://doi.org/10.1016/S0924-7963(02)00082-9)
- Budillon, G., Pacciaroni, M., Cozzi, S., Rivaro, P., Catalano, G., Ianni, C., Cantoni, C., 2003. An optimum multiparameter mixing analysis of the shelf waters in the Ross Sea. *Antarct. Sci.* 15, 105–118. <https://doi.org/10.1017/S095410200300110X>
- Budillon, G., Tucci, S., Artegiani, A., Spezie, G., 1999. Water masses and suspended matter characteristics of the western Ross Sea, in: Faranda, F.M., Guglielmo, L., Ianora, A. (Eds.), *Ross Sea Ecology*. Springer-Verlag, Milan, pp. 63–93.
- Bujak, J.P., 1984. Cenozoic Dinoflagellate Cysts and Acritarchs from the Bering Sea and Northern North Pacific, DSDP Leg 19. *Micropaleontology* 30, 180–212.
<https://doi.org/10.2307/1485717>
- Bujak, J. P., Davies, E. H., 1998. *Protoperidiniaceae* fam. nov. – Type: *Protoperidinium* Bergh, *Taxon* 47, 729.
- Bujak, J. P., Davies, E. H., 1983. Modern and fossil Peridiniineae, American Association of Stratigraphic Palynologists, Contribution Series, no. 13, p. 202.
- Burckle, L.H., Burak, R.W., 1988. Fluctuations in Late Quaternary Diatom abundances: Stratigraphy and Paleoclimatic implications from Subantarctic Deep Sea Cores. *Palaeogeogr. Palaeocl.* 67, 147–156.
- Burckle, L.H., Cooke, D.W., 1983. Late Pleistocene *Eucampia antarctica* abundance stratigraphy in the Atlantic sector of the Southern Ocean. *Micropaleontology* 29, 6–10.

- Burke, K.D., Williams, J.W., Chandler, M.A., Haywood, A.M., Lunt, D.J., Otto-Bliesner, B.L., 2018. Pliocene and Eocene provide best analogues for near-future climates. *PNAS* 115(52), 13288-13293. DOI: 10.1073/pnas.1809600115.
- Bütschli, O., 1885. Dr. H. G. Bronn's Klassen und Ordnungen Thier-Reichs, wissenschaftlich dargestellt in Wort und Bild, C. F. Winter'sche Verlagshandlung, Leipzig and Heidelberg, p. 1096.
- Calvert, S.E., Pedersen, T.F., 2007. Elemental Proxies for Palaeoclimatic and Palaeoceanographic Variability in Marine Sediments: Interpretation and Application, in: *Developments in Marine Geology*. Elsevier B.V., pp. 567–644. [https://doi.org/10.1016/S1572-5480\(07\)01019-6](https://doi.org/10.1016/S1572-5480(07)01019-6)
- Campagne, P., Crosta, X., Houssais, M.N., Swingedouw, D., Schmidt, S., Martin, A., Devred, E., Capo, S., Marieu, V., Closset, I., Masse, G., 2015. Glacial ice and atmospheric forcing on the Mertz Glacier Polynya over the past 250 years. *Nat. Commun.* 6, 6642. <https://doi.org/10.1038/ncomms7642>
- Campagne, P., Crosta, X., Schmidt, S., Houssais, M.N., Ther, O., Massé, G., 2016. Sedimentary response to sea ice and atmospheric variability over the instrumental period off Adélie Land, East Antarctica. *Biogeosciences* 13, 4205–4218. <https://doi.org/10.5194/bg-2015-610>
- Candel, M.S., Borromei, A.M., Martínez, M.A., Bujalesky, G., 2013. Palynofacies analysis of surface sediments from the Beagle Channel and its application as modern analogues for Holocene records of Tierra del Fuego, Argentina. *Palynology* 37, 62–76. <https://doi.org/10.1080/01916122.2012.718994>
- Cărăuș, I., 2017. Algae of Romania. A distributional checklist of actual algae. *Stud. Cercet.-Biologie* 7, 1–1002.
- Carter, L., Carter, R.M., McCave, I.N., 2004. Evolution of the sedimentary system beneath the deep Pacific inflow off eastern New Zealand. *Mar. Geol.* 205, 9–27. [https://doi.org/10.1016/S0025-3227\(04\)00016-7](https://doi.org/10.1016/S0025-3227(04)00016-7)
- Castagno, P., Capozzi, V., DiTullio, G.R., Falco, P., Fusco, G., Rintoul, S.R., Spezie, G., Budillon, G., 2019. Rebound of shelf water salinity in the Ross Sea. *Nat. Commun.* 5441. <https://doi.org/10.1038/s41467-019-13083-8>
- Castellani, C., Lucas, I.A.N., 2003. Seasonal variation in egg morphology and hatching success in the calanoid copepods *Temora longicornis*, *Acartia clausi* and *Centropages hamatus*. *J. Plankton Res.* 25, 527–537.
- Cavalier-Smith, T., 2010. Kingdoms Protozoa and Chromista and the eozoan root of the eukaryotic tree, *Biol. Letters* 6, 342–345.
- Cavalier-Smith, T., 2002. The phagotrophic origin of eukaryotes and phylogenetic classification of Protozoa, *Int. J. Syst. Evol. Micr.* 52, 297–354.
- Cavalier-Smith, T., 1998. A revised six-kingdom system of life, *Biol. Rev.* 73, 203–266.
- Cavalier-Smith, T., 1991. Cell diversification in heterotrophic flagellates, in: Patterson, D.J., Larsen, J. (Eds.), *The Biology of Free-Living Heterotrophic Flagellates*, Oxford University Press, Oxford, UK, pp. 113–131.
- Cavalier-Smith, T., 1987. The origin of eukaryotic and archaeobacterial cells, *Ann. N.Y. Acad. Sci.* 503, 17–54.
- Cavalier-Smith, T., 1981. Eukaryote kingdoms: Seven or nine?, *BioSystems* 14, 461–481.
- Ceccaroni, L., Frank, M., Frignani, M., Langone, L., Ravaoli, M., Mangini, A., 1998. Late Quaternary fluctuations of biogenic component fluxes on the continental slope of the

- Ross Sea, Antarctica. *J. Marine Syst.* 17, 515–525. [https://doi.org/10.1016/S0924-7963\(98\)00061-X](https://doi.org/10.1016/S0924-7963(98)00061-X)
- Chadefaud, M., 1950. Les cellules nageuses de algues dans l'embranchement de Chromophycées, *C. R. Acad. Sci. Paris* 231, 788–790.
- Chadwick, M., Allen, C.S., Sime, L.C., Hillenbrand, C.-D., 2020. Analysing the timing of peak warming and minimum winter sea-ice extent in the Southern Ocean during MIS 5e. *Quaternary Sci. Rev.* 229, 106134.
- Chamberlin, R.V., 1919. The Annelida Polychaeta, *Memoirs of the Museum of Comparative Zoölogy at Harvard Collage* 48, 1–514.
- Cheng, H., Edwards, R.L., Broecker, W.S., Denton, G.H., Kong, X., Wang, Y., Zhang, R., Wang, X., 2009. Ice Age Terminations. *Science* 326, 248–252. <https://doi.org/10.1126/science.1177840>
- Choi, K.-S., Park, K.-I., 2010. Review on the Protozoan Parasite *Perkinsus olseni* (Lester and Davis 1981) Infection in Asian Waters, in: Ishimatsu, A., Lie, H.-J. (Eds.), *Coastal Environmental and Ecosystem Issues of the East China Sea*. TERRAPUB and Nagasaki University, Nagasaki, Japan, pp. 269–281.
- Church, M.J., DeLong, E.F., Ducklow, H.W., Karner, M.B., Preston, C.M., Karl, D.M., 2003. Abundance and distribution of planktonic Archaea and Bacteria in the waters west of the Antarctic Peninsula. *Limnol. Oceanogr.* 48, 1893–1902. <https://doi.org/10.4319/lo.2003.48.5.1893>
- Church, M.J., Wai, B., Karl, D.M., DeLong, E.F., 2010. Abundances of crenarchaeal amoA genes and transcripts in the Pacific Ocean. *Environ. Microbiol.* 12, 679–688. <https://doi.org/10.1111/j.1462-2920.2009.02108.x>
- Claparède, E., Mecznikow, E., 1869. Beitrage zur Kenntniss der Entwicklungsgeschichte der Chaetopoden, *Zeitschrift für Wissenschaftliche Zoologie* 19, 163–205.
- Clarke, A., Leakey, R.J.G., 1996. The seasonal cycle of phytoplankton, macronutrients, and the microbial community in a nearshore Antarctic marine ecosystem. *Limnol. Oceanogr.* 41, 1281–1294.
- Cleve, P.T., 1899. Some Atlantic Tintinnodea. *Öfversigt af Konglig Vetenskaps-Akademiens Förhandlingar* 10, 969–975.
- Cleveland, W.S., Grosse, E., Shyu, W.M., 1992. Local regression models, in: Chambers, J.M., Hastie, T.J. (Eds.), *Statistical Models in S*, chapter 8, 309–376.
- Clowes, C.D., Hannah, M.J., Wilson, G.J., Wrenn, J.H., 2016. Marine palynostratigraphy and new species from the Cape Roberts drill-holes, Victoria land basin, Antarctica. *Mar. Micropaleontol.* 126, 65–84. <https://doi.org/10.1016/j.marmicro.2016.06.003>
- Cofaigh, C.Ó., 2012. Ice sheets viewed from the ocean: the contribution of marine science to understanding modern and past ice sheets. *Phil. Trans. R. Soc. A* 370, 5512–5539. <https://doi.org/10.1098/rsta.2012.0398>
- Cofaigh, C.Ó., Dowdeswell, J.A., Pudsey, C.J., 2001. Late Quaternary Iceberg Rafting along the Antarctic Peninsula Continental Rise and in the Weddell and Scotia Seas. *Quaternary Res.* 56, 308–321. <https://doi.org/10.1006/qres.2001.2267>
- Colbath, G.K., Grenfell, H.R., 1995. Review of biological affinities of Paleozoic acid-resistant, organic-walled eukaryotic algal microfossils (including “acritarchs”). *Rev. Palaeobot. Palyno.* 86, 287–314.
- Colleoni, F., Santis, L. De, Naish, T.R., DeConto, R.M., Escutia, C., Stocchi, P., Uenzelmann-neben, G., Hochmuth, K., Hillenbrand, C.-D., Flierdt, T. van de, Pérez, L.F., Leitchenkov, G., Sangiorgi, F., Jamieson, S., Bentley, M.J., Wilson, D.J., the PAIS Community, 2022. Past

- Antarctic ice sheet dynamics (PAIS) and implications for future sea-level change, in: Antarctic Climate Evolution. Elsevier B.V., pp. 689–768. <https://doi.org/10.1016/B978-0-12-819109-5.00010-4>
- Collins, L.G., Hounslow, M.W., Allen, C.S., Hodgson, D.A., Pike, J., Karloukovski, V.V., 2012. Quaternary Geochronology Palaeomagnetic and biostratigraphic dating of marine sediments from the Scotia Sea, Antarctica: First identification of the Laschamp excursion in the Southern Ocean. *Quat. Geochronol.* 7, 67–75. <https://doi.org/10.1016/j.quageo.2011.10.002>
- Comiso, J.C., Nishio, F., 2008. Trends in the sea ice cover using enhanced and compatible AMSR-E, SSM/I, and SMMR data. *J. Geophys. Res.* 113, C02S07. <https://doi.org/10.1029/2007JC004257>
- Concheyro, A., Caramés, A., Amenábar, C.R., Lescano, M., 2014. Nannofossils, foraminifera and microforaminiferal linings in the Cenozoic diamicrites of Cape Lamb, Vega Island, Antarctica. *Pol. Polar Res.* 35, 1–26. <https://doi.org/10.2478/popore-2014-0-003>
- Convey, P., Gibson, J.A.E., Hillenbrand, C.-D., Hodgson, D.A., Pugh, P.J.A., Smellie, J.L., Stevens, M.I., 2008. Antarctic terrestrial life – challenging the history of the frozen continent? *Biol. Rev.* 83, 103–117. <https://doi.org/10.1111/j.1469-185X.2008.00034.x>
- Convey, P., McInnes, S.J., 2005. Exceptional tardigrade-dominated ecosystems in Ellsworth Land, Antarctica. *Ecology* 86, 519–527.
- Cookson, I.C., Eisenack, A., 1962. Additional microplankton from the Australian Cretaceous sediments, *Micropaleontology* 8, 485–507.
- Corliss, B.H., 1991. Morphology and microhabitat preferences of benthic foraminifera from the northwest Atlantic Ocean. *Mar. Micropaleontol.* 17, 195–236. [https://doi.org/10.1016/0377-8398\(91\)90014-W](https://doi.org/10.1016/0377-8398(91)90014-W)
- Costello, O.P., Bauch, H.A., 1997. Late Pleistocene-Holocene productivity record of benthic foraminifera from the Iceland Plateau (Core PS 1246-2), in: Hass, H.C., Kaminski, M.A. (Eds.), *Contributions of the Micropaleontology and Paleoceanography of the Northern North Atlantic*. Grzybowski Foundation Special Publication, Krakow, pp. 141–148.
- Coxall, H.K., Wilson, P.A., Pälike, H., Lear, C.H., Backman, J., 2005. Rapid stepwise onset of Antarctic glaciation and deeper calcite compensation in the Pacific Ocean. *Nature* 433, 53–57. <https://doi.org/10.1038/nature03186.1>
- Cramer, B.S., Toggweiler, J.R., Wright, J.D., Katz, M.E., Miller, K.G., 2009. Ocean overturning since the late Cretaceous: Inferences from a new benthic foraminiferal isotope compilation. *Paleoceanography* 24, 1–14. <https://doi.org/10.1029/2008PA001683>
- Crampton, J.S., Cody, R.D., Levy, R., Harwood, D., Mckay, R., Naish, T.R., 2016. Southern Ocean phytoplankton turnover in response to stepwise Antarctic cooling over the past 15 million years. *P. Natl. Acad. Sci. USA* 113, 6868–6873. <https://doi.org/10.1073/pnas.1600318113>
- Cremer, H., Heiri, O., Wagner, B., Wagner-Cremer, F., 2007. Abrupt climate warming in East Antarctica during the early Holocene. *Quaternary Sci. Rev.* 26, 2012–2018. <https://doi.org/10.1016/j.quascirev.2006.09.011>
- Cromer, L., Gibson, J.A.E., McInnes, S.J., Agius, J.T., 2008. Tardigrade remains from lake sediments. *J. Paleolimnol.* 39, 143–150. <https://doi.org/10.1007/s10933-007-9102-5>
- Cromer, L., Gibson, J.A.E., Swadling, K.M., Ritz, D.A., 2005. Faunal microfossils: Indicators of Holocene ecological change in a saline Antarctic lake. *Palaeogeogr. Palaeocl.* 221, 83–97. <https://doi.org/10.1016/j.palaeo.2005.02.005>

- Crosta, X., Crespin, J., Billy, I., Ther, O., 2005a. Major factors controlling Holocene $\delta^{13}\text{C}_{\text{org}}$ changes in a seasonal sea-ice environment, Adélie Land, East Antarctica. *Global Biogeochem. Cy.* 19, GB4029. <https://doi.org/10.1029/2004GB002426>
- Crosta, X., Debret, M., Denis, D., Courty, M.A., Ther, O., 2007. Holocene long- and short-term climate changes off Adélie Land, East Antarctica. *Geochem. Geophys. Geosy.* 8, Q11009. <https://doi.org/10.1029/2007GC001718>
- Crosta, X., Denis, D., Ther, O., 2008. Sea ice seasonality during the Holocene, Adélie Land, East Antarctica. *Mar. Micropaleontol.* 66, 222–232. <https://doi.org/10.1016/j.marmicro.2007.10.001>
- Crosta, X., Pichon, J.J., Labracherie, M., 1997. Distribution of *Chaetoceros* resting spores in modern peri-Antarctic sediments. *Mar. Micropaleontol.* 29, 283–299. [https://doi.org/10.1016/S0377-8398\(96\)00033-3](https://doi.org/10.1016/S0377-8398(96)00033-3)
- Crosta, X., Romero, O., Armand, L.K., Pichon, J., 2005b. The biogeography of major diatom taxa in Southern Ocean sediments: 2 . Open ocean related species 223, 66–92. <https://doi.org/10.1016/j.palaeo.2005.03.028>
- Crosta, X., Shemesh, A., Etourneau, J., Yam, R., Billy, I., Pichon, J.J., 2005c. Nutrient cycling in the Indian sector of the Southern Ocean over the last 50,000 years. *Global Biogeochem. Cy.* 19, 1–10. <https://doi.org/10.1029/2004GB002344>
- Crosta, X., Sturm, A., Armand, L., Pichon, J., 2004. Late Quaternary sea ice history in the Indian sector of the Southern Ocean as recorded by diatom assemblages. *Mar. Micropaleontol.* 50, 209–223. [https://doi.org/10.1016/S0377-8398\(03\)00072-0](https://doi.org/10.1016/S0377-8398(03)00072-0)
- Crouch, E.M., Mildenhall, D.C., Neil, H.L., 2010. Distribution of organic-walled marine and terrestrial palynomorphs in surface sediments, offshore eastern New Zealand. *Mar. Geol.* 270, 235–256. <https://doi.org/10.1016/j.margeo.2009.11.004>
- Dahl, E., 1956. Some crustacean relationships, in: Wingstrand, K.G. (Ed.), *Festschrift für Bertil Hanström: Zoological Papers in Honour of his Sixty-Fifth Birthday*, Zoological Institute, Lund, pp. 138–147.
- Dalziel, I.W.D., 2014. Drake Passage and the Scotia arc: A tortuous space-time gateway for the Antarctic Circumpolar Current. *Geology* 42, 367–368. <https://doi.org/10.1130/focus042014.1>
- Dastych, H., Harris, J.M., 1995. A new species of the genus *Macrobiotus* from inland nunataks in western Dronning Maud Land, continental Antarctica (Tardigrada). *Entomol. Mitt. zool. Mus. Hamburg* 11, 175–182.
- Daugbjerg, N., 2000. *Pyramimonas tychoireta*, sp. nov. (Prasinophyceae), a new marine species from Antarctica: light and electron microscopy of the motile stage and notes on growth rates. *J. Phycol.* 36, 160–171.
- Davey, F.J., Jacobs, S.S., 2007. Influence of submarine morphology on bottom water flow across the western Ross Sea continental margin, in: Cooper, A.K., Raymond, C.R., the 10th ISAES Editorial Team (Eds.), *Antarctica: A Keystone in a Changing World - Online Proceedings for the 10th International Symposium on Antarctic Earth Sciences*. USGS Open-File Report 2007-1047, pp. 5, Short Research Paper 067.
- Davies C., Watts D., 2017. The Australian Phytoplankton Database (1844 onwards). CSIRO Oceans and Atmosphere. Occurrence Dataset <https://doi.org/10.15468/my3fxc> accessed via GBIF.org on 2018-02-08.
- Davis, B.A.S., Brewer, S., 2009. Orbital forcing and role of the latitudinal insolation/temperature gradient. *Clim. Dynam.* 32, 143–165. <https://doi.org/10.1007/s00382-008-0480-9>

- De Jong, J., Schoemann, V., Maricq, N., Mattielli, N., Langhorne, P., Haskell, T., Tison, J.L., 2013. Iron in land-fast sea ice of McMurdo Sound derived from sediment resuspension and wind-blown dust attributes to primary productivity in the Ross Sea, Antarctica. *Mar. Chem.* 157, 24–40. <https://doi.org/10.1016/j.marchem.2013.07.001>
- De Jonge, C., Hopmans, E.C., Zell, C.I., Kim, J., Schouten, S., Sinninghe Damsté, J.S., 2014. Occurrence and abundance of 6-methyl branched glycerol dialkyl glycerol tetraethers in soils: Implications for palaeoclimate reconstruction. *Geochim. Cosmochim. Ac.* 141, 97–112. <https://doi.org/10.1016/j.gca.2014.06.013>
- De Schepper, S., Fischer, E.I., Groeneveld, J., Head, M.J., Matthiessen, J., 2011. Deciphering the palaeoecology of Late Pliocene and Early Pleistocene dinoflagellate cysts. *Palaeogeogr. Palaeocl.* 309, 17–32. <https://doi.org/10.1016/j.palaeo.2011.04.020>
- De Vernal, A., 2009. Marine palynology and its use for studying nearshore environments. *IOP C. Ser. Earth Env.* 5, 1–13. <https://doi.org/10.1088/1755-1307/5/1/012002>
- De Vernal, A., Goyette, C., Rodrigues, C.G., 1989. Contribution palynostratigraphique (dinokystes, pollen et spores) à la connaissance de la mer de Champlain: coupe de Saint-Césaire, Québec. *Can. J. Earth Sci.* 26, 2450–2464.
- De Vernal, A., Henry, M., Matthiessen, J., Mudie, P.J., Rochon, A., Boessenkool, K.P., Eynaud, F., Grøsfjeld, K., Joel, G., Hamel, D., Harland, R., Head, M.J., Kunz-Pirrung, M., Levac, E., Loucheur, V., Peyron, O., Pospelova, V., Radi, T., Turon, J., Voronina, E., 2001. Dinoflagellate cyst assemblages as tracers of sea-surface conditions in the northern North Atlantic, Arctic and sub-Arctic seas: the new “n = 677” data base and its application for quantitative palaeoceanographic reconstruction. *J. Quaternary Sci.* 16, 681–698. <https://doi.org/10.1002/jqs.659>
- De Vernal, A., Hillaire-Marcel, C., 2000. Sea-ice cover, sea-surface salinity and halo-/thermocline structure of the northwest North Atlantic: Modern versus full glacial conditions. *Quaternary Sci. Rev.* 19, 65–85. [https://doi.org/10.1016/S0277-3791\(99\)00055-4](https://doi.org/10.1016/S0277-3791(99)00055-4)
- De Vernal, A., Marret, F., 2007. Organic-Walled Dinoflagellate Cysts: Tracers of Sea-Surface Conditions, in: *Developments in Marine Geology*. Elsevier B.V., Amsterdam and London, pp. 371–408. [https://doi.org/10.1016/S1572-5480\(07\)01014-7](https://doi.org/10.1016/S1572-5480(07)01014-7)
- De Vernal, A., Rochon, A., Fréchette, B., Henry, M., Radi, T., Solignac, S., 2013. Reconstructing past sea ice cover of the Northern Hemisphere from dinocyst assemblages: Status of the approach. *Quaternary Sci. Rev.* 79, 122–134. <https://doi.org/10.1016/j.quascirev.2013.06.022>
- De Vernal, A., Rochon, A., Turon, J.-L., Matthiessen, J., 1997. Organic-walled Dinoflagellate Cysts: Palynological Tracers of Sea-surface Conditions in Middle to High Latitude Marine Environments. *Geobios* 30, 905–920.
- Dearing Crampton-Flood, E., Peterse, F., Sinninghe Damsté, J.S., 2019. Production of branched tetraethers in the marine realm: Svalbard fjord sediments revisited. *Org. Geochem.* 138, 103907.
- D’Orbigny, M.D., 1826. Tableau méthodique de la classe des Céphalopodes, *Ann. Sci. Nat.* 7, 245–314.
- DeConto, R.M., Pollard, D., 2016. Contribution of Antarctica to past and future sea-level rise. *Nature* 531, 591–597. <https://doi.org/10.1038/nature17145>
- DeConto, R.M., Pollard, D., Wilson, P.A., Pälike, H., Lear, C.H., Pagani, M., 2008. Thresholds for Cenozoic bipolar glaciation. *Nature* 455, 652–656. <https://doi.org/10.1038/nature07337>

- Defaye, D., Cuoc, C., Brunet, M., 2000. Genital structures and spermatophore placement in female Paradiaptominae (Copepoda, Calanoida, Diaptomidae). *J. Crustacean Biol.* 20, 245–261. [https://doi.org/10.1651/0278-0372\(2000\)020\[0245:GSASPI\]2.0.CO;2](https://doi.org/10.1651/0278-0372(2000)020[0245:GSASPI]2.0.CO;2)
- Deflandre, G., 1937. Microfossiles des Silex Crétacés. Deuxième partie: Flagellés incertae sedis, Hystrichosphaeridés, Sarconidés, Organismes divers. *Ann. Paléontologie* 26, 51–103.
- Del Carlo, P., Di Roberto, A., Di Vincenzo, G., Bertagnini, A., Landi, P., Pompilio, M., Colizza, E., Giordano, G., 2015. Late Pleistocene-Holocene volcanic activity in northern Victoria Land recorded in Ross Sea (Antarctica) marine sediments. *Bull. Volcanol.* 77, 36.
- Delmonte, B., Winton, H., Baroni, M., Baccolo, G., Hansson, M., Andersson, P., Baroni, C., Salvatore, M.C., Lanci, L., Maggi, V., 2020. Holocene dust in East Antarctica: Provenance and variability in time and space. *Holocene* 30, 546–558. <https://doi.org/10.1177/0959683619875188>
- DeMaster, D.J., 1981. The supply and accumulation of silica in the marine environment. *Geochim. Cosmochim. Ac.* 45, 1715–1732.
- Denis, D., Crosta, X., Barbara, L., Massé, G., Renssen, H., Ther, O., Giraudeau, J., 2010. Sea ice and wind variability during the Holocene in East Antarctica: insight on middle-high latitude coupling. *Quaternary Sci. Rev.* 29, 3709–3719. <https://doi.org/10.1016/j.quascirev.2010.08.007>
- Denis, D., Crosta, X., Schmidt, S., Carson, D.S., Ganeshram, R.S., Renssen, H., Bout-Roumazeilles, V., Zaragosi, S., Martin, B., Cremer, M., Giraudeau, J., 2009a. Holocene glacier and deep water dynamics, Adélie Land region, East Antarctica. *Quaternary Sci. Rev.* 28, 1291–1303. <https://doi.org/10.1016/j.quascirev.2008.12.024>
- Denis, D., Crosta, X., Schmidt, S., Carson, D.S., Ganeshram, R.S., Renssen, H., Crespin, J., Ther, O., Billy, I., Giraudeau, J., 2009b. Holocene productivity changes off Adélie Land (East Antarctica). *Paleoceanography* 24, PA3207. <https://doi.org/10.1029/2008PA001689>
- Denis, D., Crosta, X., Zaragosi, S., Romero, O., Martin, B., Mas, V., 2006. Seasonal and subseasonal climate changes recorded in laminated diatom ooze sediments, Adélie Land, East Antarctica. *Holocene* 16, 1137–1147.
- Denton, G.H., Hughes, T.J., 2002. Reconstructing the Antarctic Ice Sheet at the Last Glacial Maximum. *Quaternary Sci. Rev.* 21, 193–202. [https://doi.org/10.1016/S0277-3791\(01\)00090-7](https://doi.org/10.1016/S0277-3791(01)00090-7)
- Deppeler, S.L., Davidson, A.T., 2017. Southern Ocean Phytoplankton in a Changing Climate. *Front. Mar. Sci.* 4, 40. <https://doi.org/10.3389/fmars.2017.00040>
- Divine, D. V, Koç, N., Isaksson, E., Nielsen, S., Crosta, X., Godtliebsen, F., 2010. Holocene Antarctic climate variability from ice and marine sediment cores: Insights on ocean – atmosphere interaction. *Quaternary Sci. Rev.* 29, 303–312. <https://doi.org/10.1016/j.quascirev.2009.11.012>
- Doflein, F., 1901. Die Protozoen als Parasiten und Krankheitserreger nach biologischen Gesichtspunkten dargestellt, Jena, Gustav Fischer, p. 274.
- Dolan, J.R., Montagnes, D.J.S., Agatha, S., Coats, D.W., Stoecker, D.K., 2013a. The Biology and Ecology of Tintinnid Ciliates: Models for Marine Plankton, 1st ed. Wiley-Blackwell, Hoboken, New Jersey, USA.
- Dolan, J.R., Pierce, R.W., 2013. Diversity and Distributions of Tintinnids, in: Dolan, J.R., Montagnes, D.J.S., Agatha, S., Coats, D.W., Stoecker, D.K. (Eds.), The Biology and Ecology of Tintinnid Ciliates: Models for Marine Plankton. Wiley-Blackwell, Hoboken, New Jersey, USA, pp. 214–243.

- Dolan, J.R., Pierce, R.W., Yang, E.J., Kim, S.Y., 2012. Southern ocean biogeography of tintinnid ciliates of the marine plankton. *J. Eukaryot. Microbiol.* 59, 511–519. <https://doi.org/10.1111/j.1550-7408.2012.00646.x>
- Dolan, J.R., Yang, E.J., Lee, S.H., Kim, S.Y., 2013b. Tintinnid ciliates of Amundsen Sea (Antarctica) plankton communities. *Polar Res.* 32, 19784. <https://doi.org/10.3402/polar.v32i0.19784>
- Domack, E., Leventer, A., Dunbar, R., Taylor, F., Brachfeld, S., Sjunneskogs, C., ODP Leg 178 Scientific Party, 2001. Chronology of the Palmer Deep site, Antarctic Peninsula: a Holocene palaeoenvironmental reference for the circum-Antarctic. *Holocene* 11, 1–9.
- Douglas, P.M.J., Affek, H.P., Ivany, L.C., Houben, A.J.P., Sijp, W.P., Sluijs, A., Schouten, S., Pagani, M., 2014. Pronounced zonal heterogeneity in Eocene southern high-latitude sea surface temperatures. *P. Natl. Acad. Sci. USA* 111, 1–6. <https://doi.org/10.1073/pnas.1321441111>
- Downie, C. Evitt, W.R., Sarjeant, W.A.S., 1963. Dinoflagellates, hystrichospheres, and the classification of the acritarchs: *Stanford Univ. Pubs. Geol. Sci.*, Vol. 7, part 3, p. 16.
- Dumont, H.J., Nandini, S., Sarma, S.S.S., 2002. Cyst ornamentation in aquatic invertebrates: a defence against egg-predation. *Hydrobiologia* 486, 161–167.
- Duncan, B., McKay, R., Levy, R., Naish, T., Prebble, J.G., Sangiorgi, F., Krishnan, S., Hoem, F., Clowes, C., Dunkley Jones, T., Gasson, E., Kraus, C., Kulhanek, D.K., Meyers, S.R., Moossen, H., Warren, C., Willmott, V., Ventura, G.T., Bendle, J., 2022. Climatic and tectonic drivers of late Oligocene Antarctic ice volume. *Nat. Geosci.* 15, 819–825. <https://doi.org/10.1038/s41561-022-01025-x>
- Dunkley Jones, T., Eley, Y.L., Thomson, W., Greene, S.E., Mandel, I., Edgar, K., Bendle, J.A., 2020. OPTiMAL: a new machine learning approach for GDGT-based palaeothermometry. *Clim. Past* 16, 2599–2617.
- Duprat, L.P.A.M., Bigg, G.R., Wilton, D.J., 2016. Enhanced Southern Ocean marine productivity due to fertilization by giant icebergs. *Nat. Geosci.* 9, 219–221. <https://doi.org/10.1038/ngeo2633>
- Dymond, J., Collier, R., McManus, J., Honjo, S., Manganini, S., 1997. Can the aluminum and titanium contents of ocean sediments be used to determine the paleoproductivity of the oceans? *Paleoceanography* 12, 586–593. <https://doi.org/10.1029/97PA01135>
- Dymond, J., Suess, E., Lyle, M., 1992. Barium in Deep-Sea Sediment: a Geochemical proxy for Paleoproductivity. *Paleoceanography* 7, 163–181.
- Dypvik, H., Harris, N.B., 2001. Geochemical facies analysis of fine-grained siliciclastics using Th/U, Zr/Rb and (Zr+Rb)/Sr ratios. *Chem. Geol.* 181, 131–146.
- Eaton, G.L., 1971. A morphogenetic series of dinoflagellate cysts from the Bracklesham Beds of the Isle of Wight, Hampshire, England, in: Farinacci, A. (Ed.), *Proceedings of the Second Planktonic Conference, Rome, 1970*, Edizioni Tecnoscienza, Rome, pp. 355–379.
- Ehrenberg, C.G., 1831. *Animalia evertebrata*, in: Hemprich, P. C., Ehrenberg, C. G. (Eds.), *Symbolae physicae seu icones et descriptiones naturalium novorum aut minus cognitorum quae ex itineribus Lybiam Aegyptum Nubiam Dongalam Syriam Arabiam et Habessiniam. Pars Zoologica*, *Abhandlungen der deutschen Akademie der Wissenschaften*.
- Eisenack, A., 1958. Mikroplankton aus dem norddeutsche Apt nebst einigen Bemerkungen über fossile Dinoflagellaten, *Neues Jahrbuch für Geologie und Paläontologie, Abhandlungen* 106, 383–422.

- Ellegaard, M., Moestrup, Ø., 1999. Fine structure of the flagellar apparatus and morphological details of *Gymnodinium nolleri* sp. nov. (Dinophyceae), an unarmored dinoflagellate producing a microreticulate cyst, *Phycologia* 38, 289–300.
- Ellegaard, M., Figueroa, R.L., Versteegh, G.J.M., 2013. Dinoflagellate life cycles, strategy and diversity: key foci for future research, in: Lewis, J.M., Marret, F., Bradley, L.R. (Eds.), *Biological and Geological Perspectives of Dinoflagellates*, London, The Micropalaeontological Society, Special Publications, pp. 249–261.
- Elling, F.J., Könneke, M., Lipp, J.S., Becker, K.W., Gagen, E.J., Hinrichs, K.-U., 2014. Effects of growth phase on the membrane lipid composition of the thaumarchaeon *Nitrosopumilus maritimus* and their implications for archaeal lipid distributions in the marine environment. *Geochim. Cosmochim. Ac.* 141, 579–597.
<https://doi.org/10.1016/j.gca.2014.07.005>
- Elling, F.J., Könneke, M., Mußmann, M., Greve, A., Hinrichs, K.-U., 2015. Influence of temperature, pH, and salinity on membrane lipid composition and TEX₈₆ of marine planktonic thaumarchaeal isolates. *Geochim. Cosmochim. Ac.* 171, 238–255.
<https://doi.org/10.1016/j.gca.2015.09.004>
- Escutia, C., Brinkhuis, H., Expedition 318 Scientists, 2014. From Greenhouse to Icehouse at the Wilkes Land Antarctic Margin: IODP Expedition 318 Synthesis of Results, in: Stein, R., Blackman, D., Inagaki, F., Larsen, H.-C. (Eds.), *Developments in Marine Geology: Earth and Life Processes Discovered from Subseafloor Environments*. Elsevier B.V., pp. 295–328. <https://doi.org/10.1017/CBO9781107415324.004>
- Esper, O., Gersonde, R., 2014. New tools for the reconstruction of Pleistocene Antarctic sea ice. *Palaeogeogr. Palaeoclimatol.* 399, 260–283. <https://doi.org/10.1016/j.palaeo.2014.01.019>
- Esper, O., Gersonde, R., Kadagies, N., 2010. Diatom distribution in southeastern Pacific surface sediments and their relationship to modern environmental variables. *Palaeogeogr. Palaeoclimatol.* 287, 1–27. <https://doi.org/10.1016/j.palaeo.2009.12.006>
- Esper, O., Zonneveld, K.A.F., 2007. The potential of organic-walled dinoflagellate cysts for the reconstruction of past sea-surface conditions in the Southern Ocean. *Mar. Micropaleontol.* 65, 185–212. <https://doi.org/10.1016/j.marmicro.2007.07.002>
- Esper, O., Zonneveld, K.A.F., 2002. Distribution of organic-walled dinoflagellate cysts in surface sediments of the Southern Ocean (eastern Atlantic sector) between the Subtropical Front and the Weddell Gyre. *Mar. Micropaleontol.* 46, 177–208.
[https://doi.org/http://dx.doi.org/10.1016/S0377-8398\(02\)00041-5](https://doi.org/http://dx.doi.org/10.1016/S0377-8398(02)00041-5)
- Evitt, W.R., 1985. Sporopollenin dinoflagellate cysts. Their morphology and interpretation, American Association of Stratigraphic Palynology Foundation, Austin, Texas, 333.
- Evitt, W.R., 1963. A discussion and proposals concerning fossil dinoflagellates, hystrichospheres and acritarchs, II, *P. Natl. Acad. Sci. USA*, 49, 298–302.
- Expedition 318 Scientists, 2011a. Expedition 318 summary, in: Escutia, C., Brinkhuis, H., Klaus, A., Expedition 318 Scientists (Eds.), *Proceedings of the Integrated Ocean Drilling Program*. Integrated Ocean Drilling Program Management International, Inc., Tokyo, pp. 1–59. <https://doi.org/10.2204/iodp.proc.318.101.2011>
- Expedition 318 Scientists, 2011b. Site U1357, in: Escutia, C., Brinkhuis, H., Klaus, A., the Expeditions 318 Scientists (Eds.), *Proceedings of the Integrated Ocean Drilling Program*. Integrated Ocean Drilling Program Management International, Inc., Tokyo, pp. 1–74. <https://doi.org/10.2204/iodp.proc.318.105.2011>

- Fabiano, M., Chiantore, M., Povero, P., Cattaneo-Vietti, R., Pusceddu, A., Misic, C., Albertelli, G., 1997. Short-term variations in particulate matter flux in Terra Nova Bay, Ross Sea. *Antarct. Sci.* 9, 143–149. <https://doi.org/10.1017/S0954102097000187>
- Fan, G., Han, Z., Ma, W., Chen, S., Chai, F., Mazloff, M.R., Pan, J., Zhang, H., 2020. Southern Ocean carbon export efficiency in relation to temperature and primary productivity. *Sci. Rep.* 10:13494. <https://doi.org/10.1038/s41598-020-70417-z>
- Fauchald, K., 1977. The Polychaete Worms. Definitions and Keys to the Orders, Families and Genera. *Nat. Hist. Museum Los Angeles Cty. Sci. Ser.* 28, 1–188.
- Fensome, R.A., Bujak, J., Dale, B., Davies, E.H., Dodge, J.D., Edwards, L.E., Harland, R., Head, M.J., Lentin, J.K., Lewis, J., Matsuoka, K., Norris, G., Sarjeant, W.A.S., Taylor, F.J.R., Williams, G.L., 1998. Proposal to conserve the name Protoperidiniaceae against Congruentidiaceae, Diplopsalaceae, and Kolkwitzellaceae (Dinophyceae), *Taxon* 47, 727–730.
- Fensome, R.A., Guerin, G.R., Williams, G.L., 2006. New insights on the Paleogene dinoflagellate cyst genera *Enneadocysta* and *Licracysta* gen. nov. based on material from offshore eastern Canada and southern Argentina. *Micropaleontology* 52, 385–410.
- Fensome, R.A., Taylor, F.J.R., Norris, G., Sarjeant, W.A.S., Wharton, D.I., Williams, G.L., 1993. A classification of fossil and living dinoflagellates. *Micropaleontology Press Special Paper*, no.7, 351 p.
- Fernandez-Mendez, M., Katlein, C., Rabe, B., Nicolaus, M., Peeken, I., Bakker, K., Flores, H., Boetius, A., 2015. Photosynthetic production in the central Arctic Ocean during the record sea-ice minimum in 2012. *Biogeosciences* 12, 3525–3549. <https://doi.org/10.5194/bg-12-3525-2015>
- Ferrari, R., Jansen, M.F., Adkins, J.F., Burke, A., Stewart, A.L., Thompson, A.F., 2014. Antarctic sea ice control on ocean circulation in present and glacial climates. *P. Natl. Acad. Sci. USA* 111, 8753–8758. <https://doi.org/10.1073/pnas.1323922111>
- Ferry, A.J., Crosta, X., Quilty, P.G., Fink, D., Howard, W., Armand, L.K., 2015. First record of winter sea ice concentration in the southwest Pacific sector of the Southern Ocean. *Paleoceanography* 30, 1525–1539. <https://doi.org/10.1002/2014PA002764>. Received
- Fertouna-Bellakhal, M., Dhib, A., Béjaoui, B., Turki, S., Aleya, L., 2014. Driving factors behind the distribution of dinocyst composition and abundance in surface sediments in a western Mediterranean coastal lagoon: Report from a high resolution mapping study. *Mar. Pollut. Bull.* 84, 347–362. <https://doi.org/10.1016/j.marpolbul.2014.04.041>
- Filipova-Marinova, M., 2007. Archaeological and paleontological evidence of climate Dynamics, sea level change, and coastline migration in the Bulgarian sector of the Circum-Pontic Region, in: Yanko-Hombach, V., Gilbert, A.S., Panin, N., Dolukhanov, P.M. (Eds.), *The Black Sea Flood Question: Changes in Coastline, Climate and Human Settlement*. Springer, New York, pp. 453–481.
- Filipova-Marinova, M., Pavlov, D., Vergiev, S., Slavchev, V., Giosan, L., 2013. Palaeoecology and Geoarchaeology of Varna Lake, Northeastern Bulgaria. *Comptes rendus l'Académie Bulg. des Sci.* 66, 377–392.
- Fitch, D.T., Moore, J.K., 2007. Wind speed influence on phytoplankton bloom dynamics in the Southern Ocean Marginal Ice Zone. *J. Geophys. Res.* 112, C08006. <https://doi.org/10.1029/2006JC004061>
- Fjellså, A., Nordberg, K., 1996. Toxic dinoflagellate “blooms” in the Kattegat, North Sea, during the Holocene. *Palaeogeogr. Palaeoclimatol.* 124, 87–105. [https://doi.org/10.1016/0031-0182\(96\)00009-0](https://doi.org/10.1016/0031-0182(96)00009-0)

- Flower, B.P., Kennett, J.P., 1993. Middle Miocene Ocean-Climate Transition: High-resolution oxygen and carbon isotopic records from Deep Sea Drilling Project Site 588A, Southwest Pacific. *Paleoceanography* 8, 811–843.
- Fogwill, C.J., Turney, C.S.M., Meissner, K.J., Golledge, N.R., Spence, P., Roberts, J.L., England, M.H., Jones, R.T., Carter, L., 2014. Testing the sensitivity of the East Antarctic Ice Sheet to Southern Ocean dynamics: past changes and future implications. *J. Quaternary Sci.* 29, 91–98. <https://doi.org/10.1002/jqs.2683>
- Foissner, W., Müller, H., Agatha, S., 2007. A comparative fine structural and phylogenetic analysis of resting cysts in oligotrich and hypotrich Spirotrichea (Ciliophora). *Eur. J. Protistol.* 43, 295–314. <https://doi.org/10.1016/j.ejop.2007.06.001>
- Fonda Umani, S., Monti, M., Bergamasco, A., Cabrini, M., De Vittor, C., Burba, N., Del Negro, P., 2005. Plankton community structure and dynamics versus physical structure from Terra Nova Bay to Ross Ice Shelf (Antarctica). *J. Marine Syst.* 55, 31–46. <https://doi.org/10.1016/j.jmarsys.2004.05.030>
- Ford, H.L., Sosdian, S.M., Rosenthal, Y., Raymo, M.E., 2016. Gradual and abrupt changes during the Mid-Pleistocene Transition. *Quaternary Sci. Rev.* 148, 222–233. <https://doi.org/10.1016/j.quascirev.2016.07.005>
- Foster, G.L., Rohling, E.J., 2013. Relationship between sea level and climate forcing by CO₂ on geological timescales. *P. Natl. Acad. Sci. USA* 110, 1209–1214. <https://doi.org/10.1073/pnas.1216073110>
- François, R., Altabet, M.A., Yu, E.-F., Sigman, D.M., Bacon, M.P., Frank, M., Bohrmann, G., Bareille, G., Labeyrie, L.D., 1997. Contribution of Southern Ocean surface-water stratification to low atmospheric CO₂ concentrations during the last glacial period. *Nature* 389, 929–935. <https://doi.org/10.1038/40073>
- Fretwell, P., Pritchard, H.D., Vaughan, D.G., Bamber, J.L., Barrand, N.E., Bell, R., Bianchi, C., Bingham, R.G., Blankenship, D.D., Casassa, G., Catania, G., Callens, D., Conway, H., Cook, A.J., Corr, H.F.J., Damaske, D., Damm, V., Ferraccioli, F., Forsberg, R., Fujita, S., Gim, Y., Gogineni, P., Griggs, J.A., Hindmarsh, R.C.A., Holmlund, P., Holt, J.W., Jacobel, R.W., Jenkins, A., Jokat, W., Jordan, T., King, E.C., Kohler, J., Krabill, W., Riger-Kusk, M., Langley, K.A., Leitchenkov, G., Leuschen, C., Luyendyk, B.P., Matsuoka, K., Mouginot, J., Nitsche, F.O., Nogi, Y., Nost, O.A., Popov, S. V., Rignot, E., Rippin, D.M., Rivera, A., Roberts, J., Ross, N., Siegert, M.J., Smith, A.M., Steinhage, D., Studinger, M., Sun, B., Tinto, B.K., Welch, B.C., Wilson, D., Young, D.A., Xiangbin, C., Zirizzotti, A., 2013. Bedmap2: Improved ice bed, surface and thickness datasets for Antarctica. *Cryosphere* 7, 375–393. <https://doi.org/10.5194/tc-7-375-2013>
- Frieling, J., Reichert, G.-J., Middelburg, J.J., Röhl, U., Westerhold, T., Bohaty, S.M., Slujs, A., 2018. Tropical Atlantic climate and ecosystem regime shifts during the Paleocene–Eocene Thermal Maximum. *Clim. Past* 14, 39–55. <https://doi.org/10.5194/cp-14-39-2018>
- Froneman, P.W., Pakhomov, E.A., 1998. Trophic importance of the chaetognaths *Eukrohnia hamata* and *Sagitta gazellae* in the pelagic system of the Prince Edward Islands (Southern Ocean). *Polar Biol.* 19, 242–249.
- Fryxell, G.A., Prasad, A.K.S.K., 1990. *Eucampia antarctica* var. *recta* (Mangin) stat. nov. (Biddulphiaceae, Bacillariopyceae): life stages at the Weddel Sea ice edge. *Phycologia* 29 (1): 27–38.

- Fu, W., Jiang, D.Y., Montañez, I.P., Meyers, S.R., Motani, R., Tintori, A., 2016. Eccentricity and obliquity paced carbon cycling in the Early Triassic and implications for post-extinction ecosystem recovery. *Sci. Rep.* 6, 27793. <https://doi.org/10.1038/srep27793>
- Fujiwara, A., Hirawake, T., Suzuki, K., Imai, I., Saitoh, S.-I., 2014. Timing of sea ice retreat can alter phytoplankton community structure in the western Arctic Ocean. *Biogeosciences* 11, 1705–1716. <https://doi.org/10.5194/bg-11-1705-2014>
- Gaarder, K.R., 1954. Coccolithineae, Silicoflagellatae, Pterospermataceae and other forms from the 'Michael Sars' North Atlantic Deep-Sea Expedition 1910, Report on the Scientific Results of the 'Michael Sars' North Atlantic Deep-Sea Expedition 1910 2(4), 1–20.
- Gaarder, K.R., 1938. Phytoplankton Studies from the Trømso District 1930-31. Trømso Museums Arshefter Naturh. Avd. Nr. 11, 55(1), 1–159.
- Galeotti, S., DeConto, R., Naish, T., Stocchi, P., Florindo, F., Pagani, M., Barrett, P., Bohaty, S.M., Lanci, L., Pollard, D., Sandroni, S., Talarico, F.M., Zachos, J.C., 2016. Antarctic Ice Sheet variability across the Eocene-Oligocene boundary climate transition. *Science* 352, 76–80. <https://doi.org/10.1126/science.aab0669>
- Gallagher, S.J., Villa, G., Drysdale, R.N., Wade, B.S., Scher, H., Li, Q., Wallace, M.W., Holdgate, G.R., 2013. A near-field sea level record of East Antarctic Ice Sheet instability from 32 to 27 Myr. *Paleoceanography* 28, 1–13. <https://doi.org/10.1029/2012PA002326>
- Gambi, M.C., Lorenti, M., Russo, G.F., Scipione, M.B., 1994. Benthic associations of the shallow hard bottoms off Terra Nova Bay, Ross Sea: zonation, biomass and population structure. *Antarct. Sci.* 6, 449–462.
- Garibotti, I.A., Vernet, M., Smith, R.C., Ferrario, M.E., 2005. Interannual variability in the distribution of the phytoplankton standing stock across the seasonal sea-ice zone west of the Antarctic Peninsula. *J. Plankton Res.* 27, 825–843. <https://doi.org/10.1093/plankt/fbi056>
- Garrison, D.L., Buck, K.R., 1989. Protozooplankton in the Weddell Sea, Antarctica: Abundance and Distribution in the Ice-Edge Zone. *Polar Biol.* 9, 341–351.
- Garrison, D.L., Close, A.R., 1993. Winter ecology of the sea ice biota in Weddell Sea pack ice. *Mar. Ecol. Prog. Ser.* 96, 17–31.
- Garrison, D.L., Gibson, A., Coale, S.L., Gowing, M.M., Okolodkov, Y.B., Fritsen, C.H., Jeffries, M.O., 2005. Sea-ice microbial communities in the Ross Sea: autumn and summer biota. *Mar. Ecol. Prog. Ser.* 300, 39–52. <https://doi.org/10.3354/meps300039>
- Garzio, L.M., Steinberg, D.K., 2013. Microzooplankton community composition along the Western Antarctic Peninsula. *Deep-Sea Res. Pt I* 77, 36–49. <https://doi.org/10.1016/j.dsr.2013.03.001>
- Gasson, E., DeConto, R.M., Pollard, D., Levy, R.H., 2016. Dynamic Antarctic ice sheet during the early to mid-Miocene. *P. Natl. Acad. Sci. USA* 113, 3459–3464. <https://doi.org/10.1073/pnas.1516130113>
- Gautier, A., 2023. Antarctic sea ice settles on record low extent, again. National Snow and Ice Data Center, (see <https://nsidc.org/arcticseaicenews/2023/02/antarctic-sea-ice-minimum-settles-on-record-low-extent-again/>)
- Gersonde, R., Abelman, A., Brathauer, U., Becquey, S., Bianchi, C., Cortese, G., Grobe, H., Kuhn, G., Niebler, H.-S., Segl, M., Sieger, R., Zielinski, U., Fütterer, D.K., 2003. Last glacial sea surface temperatures and sea-ice extent in the Southern Ocean (Atlantic-Indian sector): A multiproxy approach. *Paleoceanography* 18, 1–18. <https://doi.org/10.1029/2002PA000809>

- Gersonde, R., Crosta, X., Abelmann, A., Armand, L., 2005. Sea-surface temperature and sea ice distribution of the Southern Ocean at the EPILOG Last Glacial Maximum—a circum-Antarctic view based on siliceous microfossil records. *Quaternary Sci. Rev.* 24, 869–896. <https://doi.org/10.1016/j.quascirev.2004.07.015>
- Gersonde, R., Zielinski, U., 2000. The reconstruction of late Quaternary Antarctic sea-ice distribution — the use of diatoms as a proxy for sea-ice. *Palaeogeogr. Palaeoclimatol.* 162, 263–286.
- Gibson, J.A.E., Cromer, L., Agius, J.T., McInnes, S.J., Marley, N.J., 2007. Tardigrade eggs and exuviae in Antarctic lake sediments: Insights into Holocene dynamics and origins of the fauna. *J. Limnol.* 66, 65–71. <https://doi.org/10.4081/jlimnol.2007.s1.65>
- Gibson, J.A.E., Zale, R., 2006. Holocene development of the fauna of Lake Boeckella, northern Antarctic Peninsula. *Holocene* 16, 625–634. <https://doi.org/10.1191/0959683606h1959rp>
- Gill, A.E., 1973. Circulation and bottom water production in the Weddell Sea. *Deep-Sea Res.* 20, 111–140. [https://doi.org/10.1016/0011-7471\(73\)90048-X](https://doi.org/10.1016/0011-7471(73)90048-X)
- Goldner, A., Herold, N., Huber, M., 2014. Antarctic glaciation caused ocean circulation changes at the Eocene–Oligocene transition. *Nature* 511, 574–577. <https://doi.org/10.1038/nature13597>
- Golledge, N.R., Levy, R.H., McKay, R.M., Naish, T.R., 2017. East Antarctic ice sheet most vulnerable to Weddell Sea warming. *Geophys. Res. Lett.* 44, 2343–2351. <https://doi.org/10.1002/2016GL072422>
- Gordon, A.L., Orsi, A.H., Muench, R., Huber, B.A., Zambianchi, E., Visbeck, M., 2009. Western Ross Sea continental slope gravity currents. *Deep-Sea Res. Pt II* 56, 796–817. <https://doi.org/10.1016/j.dsr2.2008.10.037>
- Gowing, M.M., Garrison, D.L., 1992. Abundance and feeding ecology of larger protozooplankton in the ice edge zone of the Weddell and Scotia Seas during the austral winter. *Deep-Sea Res.* 39, 893–919.
- Gradstein, F.M., Ogg, J.G., Smith, A.G. (Eds.), 2004. *A Geologic Time Scale 2004*. Cambridge University Press, Cambridge, p. 589.
- Gradstein, F.M., Ogg, J.G., Schmitz, M.D., Ogg, G. (Eds.), 2012. *The Geologic Time Scale 2012*. Elsevier, Boston, USA, p. 1127, DOI: 10.1016/B978-0-444-59425-9.00004-4.
- Greenbaum, J.S., Blankenship, D.D., Young, D.A., Richter, T.G., Roberts, J.L., Aitken, A.R.A., Legresy, B., Schroeder, D.M., Warner, R.C., van Ommen, T.D., Siegert, M.J., 2015. Ocean access to a cavity beneath Totten Glacier in East Antarctica. *Nat. Geosci.* 8, 294–298. <https://doi.org/10.1038/NGEO2388>
- Grigorov, I., Rigual-Hernandez, A.S., Honjo, S., Kemp, A.E.S., Armand, L.K., 2014. Settling fluxes of diatoms to the interior of the Antarctic circumpolar current along 170 °W. *Deep-Sea Res. Pt I* 93, 1–13. <https://doi.org/10.1016/j.dsr.2014.07.008>
- Grobe, H., Mackensen, A., 1992. Late Quaternary Climatic Cycles as recorded in sediments from the Antarctic Continental Margin, in: Kennett, J.P., Warkne, D.A. (Eds.), *The Antarctic Paleoenvironment: A Perspective on Global Change - Part One*. American Geophysical Union, Antarctic Research Series, Washington, D.C., pp. 349–376.
- Grube, A. E., 1850. *Die Familien der Anneliden*, Archiv für Naturgeschichte 16, Bd. 1, 249–364.
- Gudmundsson, G.H., Paolo, F.S., Adusumilli, S., Fricker, H.A., 2019. Instantaneous Antarctic ice sheet loss driven by thinning ice shelves. *Geophysical Research Letters*. *Geophys. Res. Lett.* 46, 13903–13909. <https://doi.org/10.1029/2019GL085027>

- Guillou, L., Eikrem, W., Chrétiennot-Dinet, M.-J., Le Gall, F., Massana, R., Romari, K., Pedrós-Alió, C., Vaulot, D., 2004. Diversity of Picoplanktonic Prasinophytes Assessed by Direct Nuclear SSU rDNA Sequencing of Environmental Samples and Novel Isolates Retrieved from Oceanic and Coastal Marine Ecosystems. *Protist* 155, 193–214.
- Guilloux, L., Rigaut-Jalabert, F., Jouenne, F., Ristori, S., Viprey, M., Not, F., Vaulot, D., Simon, N., 2013. An annotated checklist of Marine Phytoplankton taxa at the SOMLIT-Astan time series off Roscoff (Western English Channel, France): data collected from 2000 to 2010. *Cah. Biol. Mar.* 54, 247–256.
- Haeckel, E., 1894. Systematische Phylogenie. Entwurf eines natürlichen Systems der Organismen auf Grund ihrer Stammesgeschichte, Erster Theil: Systematische Phylogenie der Protisten und Pflanzen, Georg Reimer, Berlin, p. 400.
- Haeckel, E., 1873. Ueber einige neue pelagische Infusorien, *Jenaische Zeitschrift für Naturwissenschaft* 7 (year 1871), 561–568.
- Haeckel, E., 1866. Generelle Morphologie der Organismen. Allgemeine Grundzüge der organischen Formenwissenschaft, mechanisch begründet durch die von Charles Darwin reformirte Descendenz-Theorie, Bd. 2: Allgemeine Entwicklungsgeschichte der Organismen, Georg Reimer, Berlin, p. 462.
- Hajós, M., 1966. A mecseki miocén diatomaföld rétegek mikroplanktonja. (Das Mikroplankton der Kieselgurschichten im Miozän des Mecsekgebirges), *Magyar Állami Földtani Intézet jelentése az 1964. évről.*, 139–171.
- Hallegraeff, G.M., 1998. Transport of toxic dinoflagellates via ships' ballast water: bioeconomic risk assessment and efficacy of possible ballast water management strategies. *Mar. Ecol. Prog. Ser.* 168, 297–309.
- Hällfors, G., 2004. Checklist of Baltic Sea phytoplankton species (including some heterotrophic protistan groups). *Baltic Sea Environment Proceedings* 95, 1–208.
- Hammer, Ø., Harper, D.A.T., Ryan, P.D., 2001. PAST: Paleontological Statistics software package for education and data analysis. *Palaeontologia Electronica* 4(1), pp. 9.
- Hannah, M.J., 2006. The palynology of ODP site 1165, Prydz Bay, East Antarctica: A record of Miocene glacial advance and retreat. *Palaeogeogr. Palaeoclimatol.* 231, 120–133. <https://doi.org/10.1016/j.palaeo.2005.07.029>
- Hannah, M.J., Fielding, C.R., 2001. Chronostratigraphy of the CRP-3 Drillhole, Victoria Land Basin, Antarctica. *Terra Ant.* 8, 615–620.
- Hannah, M.J., Wilson, G.J., Wrenn, J.H., 2000. Oligocene and Miocene Marine Palynomorphs from CRP-2/2A, Victoria Land Basin, Antarctica. *Terra Ant.* 7, 503–511.
- Hannah, M.J., Wrenn, J.H., Wilson, G.J., 2001. Preliminary Report on Early Oligocene and ?Latest Eocene Marine Palynomorphs from CRP-3 Drillhole, Victoria Land Basin, Antarctica. *Terra Ant.* 8, 383–388.
- Hannah, M.J., Wrenn, J.H., Wilson, G.J., 1998. Early Miocene and Quaternary Marine Palynomorphs from Cape Roberts Project CRP-1, McMurdo Sound, Antarctica. *Terra Ant.* 5, 527–538.
- Hansen, B.W., Drillet, G., Kristensen, R.M., Sørensen, T.F., Tøttrup, M.T., 2010. Production, hatching success and surface ornamentation of eggs of calanoid copepods during a winter at 57°N. *Mar. Biol.* 157, 59–68. <https://doi.org/10.1007/s00227-009-1295-x>
- Harðardóttir, S., Lundholm, N., Moestrup, Ø., Nielsen, T.G., 2014. Description of *Pyramimonas diskoicola* sp. nov. and the importance of the flagellate *Pyramimonas* (Prasinophyceae) in Greenland sea ice during the winter-spring transition. *Polar Biol.* 37, 1479–1494. <https://doi.org/10.1007/s00300-014-1538-2>

- Harland, R., FitzPatrick, M.E.J., Pudsey, C.J., 1999. Latest Quaternary dinoflagellate cyst climatostratigraphy for three cores from the Falkland Trough, Scotia and Weddell Seas, Southern Ocean. *Rev. Palaeobot. Palyno.* 107, 265–281. [https://doi.org/10.1016/S0034-6667\(99\)00023-8](https://doi.org/10.1016/S0034-6667(99)00023-8)
- Harland, R., Pudsey, C.J., 1999. Dinoflagellate cysts from sediment traps deployed in the Bellingshausen, Weddell and Scotia seas, Antarctica. *Mar. Micropaleontol.* 37, 77–99. [https://doi.org/10.1016/S0377-8398\(99\)00016-X](https://doi.org/10.1016/S0377-8398(99)00016-X)
- Harland, R., Pudsey, C.J., Howe, J.A., Fitzpatrick, M.E.J., 1998. Recent dinoflagellate cysts in a transect from the Falkland Trough to the Weddell Sea, Antarctica. *Palaeontology* 41, 1093–1131.
- Harloff, J., Mackensen, A., 1997. Recent benthic foraminiferal associations and ecology of the Scotia Sea and Argentine Basin. *Mar. Micropaleontol.* 31, 1–29.
- Harmsworth, R. V., 1968. The Developmental History of Blelham Tarn (England) as Shown by Animal Microfossils, with Special Reference to the Cladocera. *Ecol. Monogr.* 38, 223–241.
- Harris, R., 2001. Copepods, in: Steele, J.H., Thorpe, S.A., Turekian, K.K. (Eds.), *Encyclopedia of Ocean Sciences*. Academic Press, San Diego, pp. 640–650.
- Hartman, J.D., Bijl, P.K., Sangiorgi, F., 2018a. A review of the ecological affinities of marine organic microfossils from a Holocene record offshore of Adélie Land (East Antarctica). *J. Micropalaeontol.* 37, 445–497.
- Hartman, J.D., Sangiorgi, F., Bijl, P.K., Versteegh, G.J.M., 2018b. *Nucicla umbiliphora* gen. et sp. nov.: a Quaternary peridinioid dinoflagellate cyst from the Antarctic margin. *Palynology* 43, 94–103. <https://doi.org/10.1080/01916122.2018.1430070>
- Hartman, J.D., Sangiorgi, F., Salabarnada, A., Peterse, F., Houben, A.J.P., Schouten, S., Brinkhuis, H., Escutia, C., Bijl, P.K., 2018c. Paleooceanography and ice sheet variability offshore Wilkes Land, Antarctica-Part 3: Insights from Oligocene-Miocene TEX₈₆-based sea surface temperature reconstructions. *Clim. Past* 14, 1275–1297. <https://doi.org/10.5194/cp-14-1275-2018>
- Hashihama, F., Hirawake, T., Kudoh, S., Kanda, J., Furuya, K., Yamaguchi, Y., Ishimaru, T., 2008. Size fraction and class composition of phytoplankton in the Antarctic marginal ice zone along the 140°E meridian during February-March 2003. *Polar Sci.* 2, 109–120. <https://doi.org/10.1016/j.polar.2008.05.001>
- Haumann, F.A., Gruber, N., Münnich, M., Frenger, I., Kern, S., 2016. Sea-ice transport driving Southern Ocean salinity and its recent trends. *Nature* 537, 89–92. <https://doi.org/10.1038/nature19101>
- Hauptvogel, D.W., Pekar, S.F., Pincay, V., 2017. Evidence for a heavily glaciated Antarctica during the late Oligocene “warming” (27.8–24.5 Ma): Stable isotope records from ODP Site 690. *Paleoceanography* 32, 384–396. <https://doi.org/10.1002/2016PA002972>
- Hazel, J.E., Stewart, A.L., 2019. Are the Near-Antarctic Easterly Winds Weakening in Response to Enhancement of the Southern Annular Mode? *J. Climate* 32, 1895–1918. <https://doi.org/10.1175/JCLI-D-18-0402.1>
- Head, M., 1996. Modern dinoflagellate cysts and their biological affinities, in: Jansonius, J., McGregor, D.C. (Eds.), *Palynology: Principles and Applications*. American Association of Stratigraphic Palynologists Foundation, Salt Lake City, Utah, pp. 1197–1248.
- Head, M.J., 1993. Dinoflagellate cysts, sporomorphs, and other palynomorphs from the marine uppermost Pliocene St. Erth Beds, Cornwall, southwestern England. *The Paleontological Society, Memoir* 31 (Suppl. to *J. Paleontol.* 67, 3), 1–62.

- Head, M.J., Harland, R., Matthiessen, J., 2001. Cold marine indicators of the late Quaternary: The new dinoflagellate cyst genus *Islandinium* and related morphotypes. *J. Quaternary Sci.* 16, 621–636. <https://doi.org/10.1002/jqs.657>
- Head, M.J., Riding, J.B., Eidvin, T., Chadwick, R.A., 2004. Palynological and foraminiferal biostratigraphy of (Upper Pliocene) Nordland Group mudstones at Sleipner, northern North Sea. *Mar. Petrol. Geol.* 21, 277–297. <https://doi.org/10.1016/j.marpetgeo.2003.12.002>
- Heikkilä, M., Pospelova, V., Hochheim, K.P., Kuzyk, Z.Z.A., Stern, G.A., Barber, D.G., Macdonald, R.W., 2014. Surface sediment dinoflagellate cysts from the Hudson Bay system and their relation to freshwater and nutrient cycling. *Mar. Micropaleontol.* 106, 79–109. <https://doi.org/http://dx.doi.org/10.1016/j.marmicro.2013.12.002>
- Heinrich, H., 1988. Origin and Consequences of Cyclic Ice Rafting in the Northeast Atlantic Ocean during the Past 130,000 Years. *Quaternary Res.* 29, 142–152.
- Hemleben, C., Bé, A.W.H., Anderson, O.R., Tuntivate, S., 1977. The morphology, organic layers and chamber formation of the planktonic foraminifer *Globorotalia menardii* (d'Orbigny). *J. Foramin. Res.* 7, 1–25.
- Hernández-Sánchez, M.T., Woodward, E.M.S., Taylor, K.W.R., Henderson, G.M., Pancost, R.D., 2014. Variations in GDGT distributions through the water column in the South East Atlantic Ocean. *Geochim. Cosmochim. Ac.* 132, 337–348. <https://doi.org/10.1016/j.gca.2014.02.009>
- Hertzberg, J.E., Schmidt, M.W., Bianchi, T.S., Smith, R.W., Shields, M.R., Marcantonio, F., 2016. Comparison of eastern tropical Pacific TEX₈₆ and *Globigerinoides ruber* Mg/Ca derived sea surface temperatures: Insights from the Holocene and Last Glacial Maximum. *Earth Planet. Sc. Lett.* 434, 320–332. <https://doi.org/10.1016/j.epsl.2015.11.050>
- Higgins, M.B., Robinson, R.S., Carter, S.J., Pearson, A., 2010. Evidence from chlorin nitrogen isotopes for alternating nutrient regimes in the Eastern Mediterranean Sea. *Earth Planet. Sc. Lett.* 290, 102–107. <https://doi.org/10.1016/j.epsl.2009.12.009>
- Higgins, M.B., Robinson, R.S., Husson, J.M., Carter, S.J., Pearson, A., 2012. Dominant eukaryotic export production during ocean anoxic events reflects the importance of recycled NH₄⁺. *P. Natl. Acad. Sci. USA* 109, 2269–2274. <https://doi.org/10.1073/pnas.1104313109>
- Hill, D.J., Haywood, A.M., Valdes, P.J., Francis, J.E., Lunt, D.J., Wade, B.S., Bowman, V.C., 2013. Paleogeographic controls on the onset of the Antarctic circumpolar current. *Geophys. Res. Lett.* 40, 5199–5204. <https://doi.org/10.1002/grl.50941>
- Hill, R.S., Scriven, L.J., 1995. The angiosperm-dominated woody vegetation of Antarctica: A review. *Rev. Palaeobot. Palyno.* 86, 175–198. [https://doi.org/10.1016/0034-6667\(94\)00149-E](https://doi.org/10.1016/0034-6667(94)00149-E)
- Hillenbrand, C.-D., Fütterer, D.K., 2001. Neogene to Quaternary deposition of opal on the continental rise west of the Antarctic Peninsula, ODP Leg 178, Sites 1095, 1096, and 1101, in: Barker, P.F., Camerlenghi, A., Acton, G.D., Ramsay, A.T.S. (Eds.), *Proceedings of the Ocean Drilling Program, Scientific Results*. pp. 1–33.
- Hillenbrand, C.-D., Grobe, H., Diekmann, B., Kuhn, G., Fütterer, D.K., 2003. Distribution of clay minerals and proxies for productivity in surface sediments of the Bellingshausen and Amundsen seas (West Antarctica) - Relation to modern environmental conditions. *Mar. Geol.* 193, 253–271.
- Hillenbrand, C.-D., Kuhn, G., Frederichs, T., 2009. Record of a Mid-Pleistocene depositional anomaly in West Antarctic continental margin sediments: an indicator for ice-sheet

- collapse? *Quaternary Sci. Rev.* 28, 1147–1159.
<https://doi.org/10.1016/j.quascirev.2008.12.010>
- Hiscock, M.R., Marra, J., Smith Jr., W.O., Goericke, R., Measures, C., Vink, S., Olson, R.J., Sosik, H.M., Barber, R.T., 2003. Primary productivity and its regulation in the Pacific Sector of the Southern Ocean. *Deep-Sea Res. Pt II* 50, 533–558. [https://doi.org/10.1016/S0967-0645\(02\)00583-0](https://doi.org/10.1016/S0967-0645(02)00583-0)
- Ho, S.L., Mollenhauer, G., Fietz, S., Martínez-García, A., Lamy, F., Rueda, G., Schipper, K., Méheust, M., Rosell-Melé, A., Stein, R., Tiedemann, R., 2014. Appraisal of TEX₈₆ and TEX₈₆⁺ thermometries in subpolar and polar regions. *Geochim. Cosmochim. Ac.* 131, 213–226. <https://doi.org/10.1016/j.gca.2014.01.001>
- Hodell, D.A., Kanfoush, S.L., Shemesh, A., Crosta, X., Charles, C.D., Guilderson, T.P., 2001. Abrupt Cooling of Antarctic Surface Waters and Sea Ice Expansion in the South Atlantic Sector of the Southern Ocean at 5000 cal yr B.P. *Quaternary Res.* 56, 191–198.
<https://doi.org/10.1006/qres.2001.2252>
- Hoem S.A., 2018. Norwegian Biodiversity Information Centre - Other datasets. Version 31.127. Natural History Museum, University of Oslo. Occurrence Dataset
<https://doi.org/10.15468/tm56sc> accessed via GBIF.org on 2018-02-08.
- Hoem, F.S., Sauermilch, I., Hou, S., Brinkhuis, H., Sangiorgi, F., Bijl, P.K., 2021a. Late Eocene – early Miocene evolution of the southern Australian subtropical front: a marine palynological approach. *J. Micropalaeontol.* 40, 175–193.
- Hoem, F.S., Valero, L., Evangelinos, D., Escutia, C., Duncan, B., McKay, R.M., Brinkhuis, H., Sangiorgi, F., Bijl, P.K., 2021b. Temperate Oligocene surface ocean conditions offshore of Cape Adare, Ross Sea, Antarctica. *Clim. Past* 17, 1423–1442.
- Holbourn, A., Kuhnt, W., Clemens, S., Prell, W., Andersen, N., 2013. Middle to late Miocene stepwise climate cooling: Evidence from a high-resolution deep water isotope curve spanning 8 million years. *Paleoceanography* 28, 688–699.
<https://doi.org/10.1002/2013PA002538>
- Holbourn, A., Kuhnt, W., Kochhann, K.G.D., Andersen, N., Meier, K.J.S., 2015. Global perturbation of the carbon cycle at the onset of the Miocene Climatic Optimum. *Geology* 43, 123–126. <https://doi.org/10.1130/G36317.1>
- Holbourn, A., Kuhnt, W., Schulz, M., Flores, J.-A., Andersen, N., 2007. Orbitally-paced climate evolution during the middle Miocene “Monterey” carbon-isotope excursion. *Earth Planet. Sc. Lett.* 261, Supplementary Material.
- Hopcroft, R., 2016. Phytoplankton from the White Sea, Barents Sea, Norwegian Sea and Arctic Basin 1993-2003. Conservation of Arctic Flora and Fauna. Occurrence Dataset
<https://doi.org/10.15468/tvpmov> accessed via GBIF.org on 2018-02-08.
- Hopkins, C.C.E., 1978. The male genital system, and spermatophore production and function in *Euchaeta norvegica* Boeck (Copepoda: Calanoida). *J. Exp. Mar. Biol. Ecol.* 35, 197–231.
[https://doi.org/10.1016/0022-0981\(78\)90076-X](https://doi.org/10.1016/0022-0981(78)90076-X)
- Hopmans, E.C., Schouten, S., Sinninghe Damsté, J.S., 2016. The effect of improved chromatography on GDGT-based palaeoproxies. *Org. Geochem.* 93, 1–6.
<https://doi.org/10.1016/j.orggeochem.2015.12.006>
- Hopmans, E.C., Weijers, J.W.H., Schefuß, E., Herfort, L., Sinninghe Damsté, J.S., Schouten, S., 2004. A novel proxy for terrestrial organic matter in sediments based on branched and isoprenoid tetraether lipids. *Earth Planet. Sc. Lett.* 224, 107–116.
<https://doi.org/10.1016/j.epsl.2004.05.012>

- Houben, A.J.P., Bijl, P.K., Guerin, G.R., Sluijs, A., Brinkhuis, H., 2011. *Malvinia escutiana*, a new biostratigraphically important Oligocene dinoflagellate cyst from the Southern Ocean. *Rev. Palaeobot. Palyno.* 165, 175–182.
<https://doi.org/10.1016/j.revpalbo.2011.03.002>
- Houben, A.J.P., Bijl, P.K., Pross, J., Bohaty, S.M., Passchier, S., Stickley, C.E., Röhl, U., Sugisaki, S., Tauxe, L., van de Flierdt, T., Olney, M., Sangiorgi, F., Sluijs, A., Escutia, C., Brinkhuis, H., Dotti, C.E., Klaus, A., Fehr, A., Williams, T., Bendle, J.A.P., Carr, S.A., Dunbar, R.B., Flores, J.-A., González, J.J., Hayden, T.G., Iwai, M., Jimenez-Espejo, F.J., Katsuki, K., Kong, G.S., McKay, R.M., Nakai, M., Pekar, S.F., Riesselman, C., Sakai, T., Salzmann, U., Shrivastava, P.K., Tuo, S., Welsh, K., Yamane, M., 2013. Reorganization of Southern Ocean plankton ecosystem at the onset of Antarctic glaciation. *Science* 340, 341–344.
<https://doi.org/10.1126/science.1223646>
- Howe, J.A., Harland, R., Pudsey, C.J., 2002. Dinoflagellate cyst evidence for Quaternary palaeoceanographic change in the northern Scotia Sea, South Atlantic Ocean. *Mar. Geol.* 191, 55–69. [https://doi.org/10.1016/S0025-3227\(02\)00498-X](https://doi.org/10.1016/S0025-3227(02)00498-X)
- Huck, C.E., van de Flierdt, T., Bohaty, S.M., Hammond, S.J., 2017. Antarctic climate, Southern Ocean circulation patterns, and deep water formation during the Eocene. *Paleoceanography* 32, 674–691. <https://doi.org/10.1002/2017PA003135>
- Huguet, C., de Lange, G.J., Gustafsson, Ö., Middelburg, J.J., Sinninghe Damsté, J.S., Schouten, S., 2008. Selective preservation of soil organic matter in oxidized marine sediments (Madeira Abyssal Plain). *Geochim. Cosmochim. Ac.* 72, 6061–6068.
<https://doi.org/10.1016/j.gca.2008.09.021>
- Huguet, C., Hopmans, E.C., Febo-Ayala, W., Thompson, D.H., Sinninghe Damsté, J.S., Schouten, S., 2006. An improved method to determine the absolute abundance of glycerol dibiphytanyl glycerol tetraether lipids. *Org. Geochem.* 37, 1036–1041.
<https://doi.org/10.1016/j.orggeochem.2006.05.008>
- Huguet, C., Kim, J., Lange, G.J. De, Sinninghe, J.S., Schouten, S., 2009. Effects of long term oxic degradation on the U^K₃₇, TEX₈₆ and BIT organic proxies. *Org. Geochem.* 40, 1188–1194.
<https://doi.org/10.1016/j.orggeochem.2009.09.003>
- Huguet, C., Schimmelmann, A., Thunell, R., Lourens, L.J., Sinninghe Damsté, J.S., Schouten, S., 2007. A study of the TEX₈₆ paleothermometer in the water column and sediments of the Santa Barbara Basin, California. *Paleoceanography* 22, PA3203.
<https://doi.org/10.1029/2006PA001310>
- Hurley, S.J., Elling, F.J., Könnike, M., Buchwald, C., Wankel, S.D., Santoro, A.E., Lipp, J.S., Hinrichs, K.-U., Pearson, A., 2016. Influence of ammonia oxidation rate on thaumarchaeal lipid composition and the TEX₈₆ proxy. *P. Natl. Acad. Sci. USA* 113, 7762–7767. <https://doi.org/10.1073/pnas.1518534113>
- Hutcheon, J.A., Chioloro, A., Hanley, J.A., 2010. Random measurements error and regression dilution bias. *Brit. Med. J.* 340, c2289.
- Ichinomiya, M., Nakamachi, M., Fukuchi, M., Taniguchi, A., 2008. Resting cells of microorganisms in the 20–100µm fraction of marine sediments in an Antarctic coastal area. *Polar Sci.* 2, 27–32. <https://doi.org/10.1016/j.polar.2007.12.001>
- Inouye, I., Hori, T., Chihara, M., 1990. Absolute configuration analysis of the flagellar apparatus of *Pterosperma cristatum* (Prasinophyceae) and consideration of its phylogenetic position. *J. Phycol.* 26, 329–344.
- IPCC, 2023. Climate Change 2023: Synthesis Report. A Report of the Intergovernmental Panel on Climate Change. Contribution of Working Groups I, II and III to the Sixth Assessment

- Report of the Intergovernmental Panel on Climate Change, Core Writing Team, Lee, H., Romero, J. (Eds.), IPCC, Geneva, Switzerland, (in press).
- IPCC, 2014. AR5 Climate Change 2014: Synthesis Report. Contribution of Working Groups I, II and III to the Fifth Assessment Report of the Intergovernmental Panel on Climate Change, IPCC, Geneva, Switzerland.
- IPCC, 2013. AR5 Climate Change 2013: The Physical Science Basis. Contribution of Working Group I to the Fifth Assessment Report of the Intergovernmental Panel on Climate Change, Stocker, T.F., Qin, D., Plattner, G.-K., Tignor, M., Allen, S.K., Boschung, J., Nauels, A., Xia, Y., Bex, V., Midgley, P.M. (Eds.), Cambridge University Press, Cambridge, United Kingdom and New York, NY, USA, p. 1535.
- Ivany, L.C., Van Simaeys, S., Domack, E.W., Samson, S.D., 2006. Evidence for an earliest Oligocene ice sheet on the Antarctic Peninsula. *Geology* 34, 377–380. <https://doi.org/10.1130/G22383.1>
- Jacobs, S.S., 1991. On the nature and significance of the Antarctic Slope Front. *Mar. Chem.* 35, 9–24. [https://doi.org/10.1016/S0304-4203\(09\)90005-6](https://doi.org/10.1016/S0304-4203(09)90005-6)
- Jacobs, S.S., 1989. Marine controls on modern sedimentation on the Antarctic continental shelf. *Mar. Geol.* 85, 121–153.
- Jacobs, S.S., Amos, A.F., Bruchhausen, P.M., 1970. Ross sea oceanography and antarctic bottom water formation. *Deep-Sea Res.* 17, 935–962. [https://doi.org/10.1016/0011-7471\(70\)90046-X](https://doi.org/10.1016/0011-7471(70)90046-X)
- Jacobs, S.S., Fairbanks, R.C., Horibe, Y., 1985. Origin and evolution of water masses near the Antarctic continental margin: evidence from $H_2^{18}O / H_2^{16}O$ ratios in seawater, in: Jacobs, S.S. (Ed.), *Oceanology of the Antarctic Continental Shelf*, vol. 3, pp. 59–85.
- Jacobs, S.S., Giulivi, C.F., Mele, P.A., 2002. Freshening of the Ross Sea During the Late 20th Century. *Science* 297, 386–389.
- Jacobson, D.M., 1999. A brief history of dinoflagellate feeding research. *J. Eukaryot. Microbiol.* 46, 376–381.
- Janssen, H.H., Gradinger, R., 1999. Turbellaria (Archoophora: Acoela) from Antarctic sea ice endofauna - examination of their micromorphology. *Polar Biol.* 21, 410–416.
- Jimenez-Espejo, F.J., Presti, M., Kuhn, G., McKay, R., Crosta, X., Escutia, C., Lucchi, R.G., Yoshimura, T., Ortega, M., Macrì, P., Caburlotto, A., Santis, L. De, 2020. Late Pleistocene oceanographic and depositional variations along the Wilkes Land margin (East Antarctica) reconstructed with geochemical proxies in deep-sea sediments. *Global Planet. Change* 184, 103045. <https://doi.org/10.1016/j.gloplacha.2019.103045>
- Johansen, J.R., Fryxell, G.A., 1985. The genus *Thalassiosira* (Bacillariophyceae): studies on species occurring south of the Antarctic Convergence Zone. *Phycologia* 24(2), 155–179.
- John, C.M., Karner, G.D., Browning, E., Leckie, R.M., Mateo, Z., Carson, B., Lowery, C., 2011. Timing and magnitude of Miocene eustasy derived from the mixed siliciclastic-carbonate stratigraphic record of the northeastern Australian margin. *Earth Planet. Sc. Lett.* 304, 455–467. <https://doi.org/10.1016/j.epsl.2011.02.013>
- Jones, B., Manning, D.A.C., 1994. Comparison of geochemical indices used for the interpretation of palaeoredox conditions in ancient mudstones. *Chem. Geol.* 111, 111–129. [https://doi.org/10.1016/0009-2541\(94\)90085-X](https://doi.org/10.1016/0009-2541(94)90085-X)
- Jones, T.R., Cuffey, K.M., Roberts, W.H.G., Markle, B.R., Steig, E.J., Stevens, C.M., Valdes, P.J., Fudge, T.J., Sigl, M., Hughes, A.G., Morris, V., Vaughn, B.H., Garland, J., Vinther, B.M., Rozmiarek, K.S., Brashear, C.A., White, J.W.C., 2023. Seasonal temperatures in West

- Antarctica during the Holocene. *Nature* 613, 292–297. <https://doi.org/10.1038/s41586-022-05411-8>
- Jørgensen, E., 1924. Mediterranean Tintinnidae. Report of the Danish Oceanographical Expeditions 1908-1910 to the Mediterranean and adjacent seas, Vol. 2, Biology, No. 8, J.3 (Thor Expedition), Copenhagen, p. 109.
- Jorissen, F.J., de Stigter, H.C., Widmark, J.G. V, 1995. A conceptual model explaining benthic foraminiferal microhabitats. *Mar. Micropaleontol.* 26, 3–15. [https://doi.org/10.1016/0377-8398\(95\)00047-X](https://doi.org/10.1016/0377-8398(95)00047-X)
- Jorissen, F.J., Fontanier, C., Thomas, E., 2007. Paleoceanographical Proxies Based on Deep-Sea Benthic Foraminiferal Assemblage Characteristics, in: *Developments in Marine Geology*. Elsevier B.V., pp. 263–325. [https://doi.org/10.1016/S1572-5480\(07\)01012-3](https://doi.org/10.1016/S1572-5480(07)01012-3)
- Joughin, I., Smith, B.E., Medley, B., 2014. Marine Ice Sheet Collapse Potentially Under Way for the Thwaites Glacier Basin, West Antarctica. *Science* 344, 735–738. <https://doi.org/10.1126/science.1249055>
- Kaczmarek, I., Barbrick, N.E., Ehrman, J.M., Cant, G.P., 1993. *Eucampia* Index as an indicator of the Late Pleistocene oscillations of the winter sea-ice extent at the ODP Leg 119 Site 745B at the Kerguelen Plateau. *Hydrobiologia* 269/270, 103–112.
- Kalanetra, K.M., Bano, N., Hollibaugh, J.T., 2009. Ammonia-oxidizing Archaea in the Arctic Ocean and Antarctic coastal waters. *Environ. Microbiol.* 11, 2434–2445. <https://doi.org/10.1111/j.1462-2920.2009.01974.x>
- Kamiyama, T., 2013. Comparative Biology of Tintinnid Cysts, in: Dolan, J.R., Montagnes, D.J.S., Agatha, S., Coats, D.W., Stoecker, D.K. (Eds.), *The Biology and Ecology of Tintinnid Ciliates: Models for Marine Plankton*. Wiley-Blackwell, Hoboken, New Jersey, USA, pp. 171–185.
- Kamykowski, D., Reed, R.E., Kirkpatrick, G.J., 1992. Comparison of sinking velocity, swimming velocity, rotation and path characteristics among six marine dinoflagellate species. *Mar. Biol.* 113, 319–328. <https://doi.org/10.1007/BF00347287>
- Kang, S.-H., Fryxell, G.A., 1993. Phytoplankton in the Weddell Sea, Antarctica: composition, abundance and distribution in water-column assemblages of the marginal ice-edge zone during austral autumn. *Mar. Biol.* 116, 335–348.
- Karner, M.B., DeLong, E.F., Karl, D.M., 2001. Archaeal dominance in the mesopelagic zone of the Pacific Ocean. *Nature* 409, 507–510. <https://doi.org/10.1038/35054051>
- Katajisto, T., 2003. Development of *Acartia bifilosa* (Copepoda: Calanoida) eggs in the northern Baltic Sea with special reference to dormancy. *J. Plankton Res.* 25, 357–364.
- Katz, M.E., Cramer, B.S., Toggweiler, J.R., Esmay, G., Liu, C., Miller, K.G., Rosenthal, Y., Wade, B.S., Wright, J.D., 2011. Impact of Antarctic Circumpolar Current development on late Paleogene ocean structure. *Science* 332, 1076–1079. <https://doi.org/10.1126/science.1202122>
- Kawachi, M., 2017. Microbial Culture Collection, National Institute for Environmental Studies. Version 5.5. National Institute of Genetics, ROIS. Occurrence Dataset <https://doi.org/10.15468/8rml10> accessed via GBIF.org on 2018-02-08.
- Kay, J.E., Holland, M.M., Jahn, A., 2011. Inter-annual to multi-decadal Arctic sea ice extent trends in a warming world. *Geophys. Res. Lett.* 38, L15708. <https://doi.org/10.1029/2011GL048008>
- Kelson, J.R., Huntington, K.W., Schauer, A.J., Saenger, C., Lechler, A.R., 2017. Toward a universal carbonate clumped isotope calibration: Diverse synthesis and preparatory methods

- suggest a single temperature relationship. *Geochim. Cosmochim. Ac.* 197, 104–131.
<https://doi.org/10.1016/j.gca.2016.10.010>
- Kemp, E.M., 1975. Palynology of Leg 28 drill sites, Deep Sea Drilling Project. Initial Rep. DSDP 28, 699–623.
- Kennett, J.P., Barker, Peter F, 1990. Latest Cretaceous to Cenozoic Climate and Oceanographic Developments in the Weddell Sea, Antarctica: an Ocean-Drilling Perspective, in: Barker, P.F., Kennett, J.P., O’Connell, S., Pisias, N.G. (Eds.), *Proceedings of the Ocean Drilling Program, Scientific Results*. pp. 937–960.
- Kim, J.-H., Crosta, X., Willmott, V., Renssen, H., Bonnin, J., Helmke, P., Schouten, S., Sinninghe Damsté, J.S., 2012a. Holocene subsurface temperature variability in the eastern Antarctic continental margin. *Geophys. Res. Lett.* 39, L06705.
<https://doi.org/10.1029/2012GL051157>
- Kim, J.-H., Huguet, C., Zonneveld, K.A.F., Versteegh, G.J.M., Roeder, W., Sinninghe Damsté, J.S., Schouten, S., 2009. An experimental field study to test the stability of lipids used for the TEX₈₆ and U^K₃₇ palaeothermometers. *Geochim. Cosmochim. Ac.* 73, 2888–2898.
<https://doi.org/10.1016/j.gca.2009.02.030>
- Kim, J.-H., Romero, O.E., Lohmann, G., Donner, B., Laepple, T., Haam, E., Sinninghe Damsté, J.S., 2012b. Pronounced subsurface cooling of North Atlantic waters off Northwest Africa during Dansgaard – Oeschger interstadials. *Earth Planet. Sc. Lett.* 339–340, 95–102.
<https://doi.org/10.1016/j.epsl.2012.05.018>
- Kim, J.-H., Schouten, S., Hopmans, E.C., Donner, B., Sinninghe Damsté, J.S., 2008. Global sediment core-top calibration of the TEX₈₆ paleothermometer in the ocean. *Geochim. Cosmochim. Ac.* 72, 1154–1173. <https://doi.org/10.1016/j.gca.2007.12.010>
- Kim, J.-H., Schouten, S., Rodrigo-Gámiz, M., Rampen, S., Marino, G., Huguet, C., Helmke, P., Buscail, R., Hopmans, E.C., Pross, J., Sangiorgi, F., Middelburg, J.B.M., Sinninghe Damsté, J.S., 2015. Influence of deep-water derived isoprenoid tetraether lipids on the TEX₈₆^H paleothermometer in the Mediterranean Sea. *Geochim. Cosmochim. Ac.* 150, 125–141.
<https://doi.org/10.1016/j.gca.2014.11.017>
- Kim, J.-H., van der Meer, J., Schouten, S., Helmke, P., Willmott, V., Sangiorgi, F., Koç, N., Hopmans, E.C., Sinninghe Damsté, J.S., 2010. New indices and calibrations derived from the distribution of crenarchaeal isoprenoid tetraether lipids: Implications for past sea surface temperature reconstructions. *Geochim. Cosmochim. Ac.* 74, 4639–4654.
<https://doi.org/10.1016/j.gca.2010.05.027>
- Kim, J.-H., Villanueva, L., Zell, C., Sinninghe Damsté, J.S., 2016. Biological source and provenance of deep-water derived isoprenoid tetraether lipids along the Portuguese continental margin. *Geochim. Cosmochim. Ac.* 172, 177–204.
<https://doi.org/10.1016/j.gca.2015.09.010>
- Kim, S.Y., Choi, J.K., Dolan, J.R., Shin, H.C., Lee, S., Yang, E.J., 2013. Morphological and Ribosomal DNA-based Characterization of Six Antarctic Ciliate Morphospecies from the Amundsen Sea with Phylogenetic Analyses. *J. Eukaryot. Microbiol.* 60, 497–513.
<https://doi.org/10.1111/jeu.12057>
- Klump, J., Hebbeln, D., Wefer, G., 2000. The impact of sediment provenance on barium-based productivity estimates. *Mar. Geol.* 169, 259–271.
- Klumpp, B., 1953. Beitrag zur Kenntnis der Mikrofossilien des mittleren und oberen Eozän, *Palaeontographica, Abteilung A* 103, 377–406.

- Kofoid, C.A., 1911. Dinoflagellata of the San Diego region, IV. The Genus *Gonyaulax*, with notes on its skeletal morphology and a discussion of its generic and specific characters, University of California Publications in Zoology., 8(4), 187-286 + plates 9-17.
- Kofoid, C.A., Campbell, A.S., 1929. A conspectus of the marine and freshwater ciliata belonging to the suborder Tintinnoinea, with descriptions of new species principally from the Agassiz expedition to the Eastern Tropical Pacific 1904–1905, Univ. Calif. Publ. Zool. 34, 1–403.
- Koga, F., 1968. On the Pelagic Eggs of Copepoda. J. Oceanogr. Soc. Japan 24, 16–20.
- Koga, Y., Morii, H., Akagawa-Matsushita, M., Ohga, M., 1998. Correlation of Polar Lipid Composition with 16S rRNA Phylogeny in Methanogens. Further Analysis of Lipid Component Parts. Biosci. Biotechnol. Biochem. 62, 230–236.
<https://doi.org/10.1271/bbb.62.230>
- Kozłowski, W.A., Deutschman, D., Garibotti, I., Trees, C., Vernet, M., 2011. An evaluation of the application of CHEMTAX to Antarctic coastal pigment data. Deep-Sea Res. Pt I 58, 350–364. <https://doi.org/10.1016/j.dsr.2011.01.008>
- Kramer, M., Swadling, K.M., Meiners, K.M., Kiko, R., Scheltz, A., Nicolaus, M., Werner, I., 2011. Antarctic sympagic meiofauna in winter: Comparing diversity, abundance and biomass between perennially and seasonally ice-covered regions. Deep-Sea Res. Pt II 58, 1062–1074. <https://doi.org/10.1016/j.dsr2.2010.10.029>
- Kryc, K.A., Murray, R.W., Murray, D.W., 2003. Al-to-oxide and Ti-to-organic linkages in biogenic sediment: Relationships to paleo-export production and bulk Al/Ti. Earth Planet. Sc. Lett. 211, 125–141. [https://doi.org/10.1016/S0012-821X\(03\)00136-5](https://doi.org/10.1016/S0012-821X(03)00136-5)
- Kuhnert, H., Bickert, T., Paulsen, H., 2009. Southern Ocean frontal system changes precede Antarctic ice sheet growth during the middle Miocene. Earth Planet. Sc. Lett. 284, 630–638. <https://doi.org/10.1016/j.epsl.2009.05.030>
- Kunz-Pirung, M., Matthiessen, J., De Vernal, A., 2001. Relationships between dinoflagellate cyst assemblages in surface sediment and hydrographic conditions in the Bering and Chukchi seas. J. Quaternary Sci. 16, 667–680. <https://doi.org/10.1002/jqs.652>
- Kvenvolden, K.A., Rapp, J.B., Golan-Bac, M., Hostettler, F.D., 1987. Multiple sources of alkanes in Quaternary oceanic sediment of Antarctica. Org. Geochem. 11, 291–302.
[https://doi.org/10.1016/0146-6380\(87\)90040-4](https://doi.org/10.1016/0146-6380(87)90040-4)
- La, H.S., Park, K., Wåhlin, A., Arrigo, K.R., Kim, D.S., Yang, E.J., Atkinson, A., Fielding, S., Im, J., Kim, T.-W., Shin, H.C., Lee, S., Ha, H.K., 2019. Zooplankton and micronekton respond to climate fluctuations in the Amundsen Sea polynya, Antarctica. Sci. Rep. 9, 10087.
<https://doi.org/10.1038/s41598-019-46423-1>
- Laackmann, H., 1910. Die Tintinnodeen der Deutschen Südpolar-Expedition 1901-1903, in: Von Drygalski, E. (Ed.), Deutschen Südpolar-Expedition, Im Auftrage Des Reichsamtes Des Innern, Bd. 11. Georg Reimer, Berlin, pp. 341–496.
- Laackmann, H., 1907. Antarktische Tintinnen. Zool. Anz. 31, 235–239.
- Lagabriele, Y., Malavieille, J., Suárez, M., 2009. The tectonic history of Drake Passage and its possible impacts on global climate. Earth Planet. Sc. Lett. 279, 197–211.
<https://doi.org/10.1016/j.epsl.2008.12.037>
- Lamarck, J.B.P.A., 1809. Philosophie Zoologique ou Exposition des Considérations relatives à l'histoire naturelle des Animaux, Tome Premier, Paris, p. 428.
- Lankester, E.R., 1885. Protozoa, in: The Encyclopedia Britannica, 9th ed., Vol. 19, pp. 830–866.

- Laskar, J., Robutel, P., Joutel, F., Gastineau, M., Correia, A.C.M., Levrard, B., 2004. A long term numerical solution for the insolation quantities of the Earth. *Astron. Astrophys.* 428, 261–285.
- Lawler, K.-A., Cortese, G., Civel-Mazens, M., Bostock, H., Crosta, X., Leventer, A., Lowe, V., Rogers, J., Armand, L.K., 2021. The Southern Ocean Radiolarian (SO-RAD) dataset: a new compilation of modern radiolarian census data. *Earth Syst. Sci. Data* 13, 5441–5453.
- Lawver, L.A., Gahagan, L.M., 2003. Evolution of cenozoic seaways in the circum-antarctic region. *Palaeogeogr. Palaeoclimatol.* 198, 11–37. [https://doi.org/10.1016/S0031-0182\(03\)00392-4](https://doi.org/10.1016/S0031-0182(03)00392-4)
- Leander, B.S., Hoppenrath, M., 2008. Ultrastructure of a novel tube-forming, intracellular parasite of dinoflagellates: *Parvilucifera prorocentri* sp. nov. (Alveolata, Myzozoa). *Eur. J. Protistol.* 44, 55–70. <https://doi.org/10.1016/j.ejop.2007.08.004>
- Lear, C.H., Coxall, H.K., Foster, G.L., Lunt, D.J., Mawbey, E.M., Rosenthal, Y., Sosdian, S.M., Thomas, E., Wilson, P.A., 2015. Neogene ice volume and ocean temperatures: Insights from infaunal foraminiferal Mg/Ca paleothermometry. *Paleoceanography* 30, 1437–1454. <https://doi.org/10.1002/2015PA002833>. Received
- Lear, C.H., Elderfield, H., Wilson, P.A., 2000. Cenozoic Deep-Sea Temperatures and Global Ice Volumes from Mg/Ca in Benthic Foraminiferal Calcite. *Science* 287, 269–272. <https://doi.org/10.1126/science.287.5451.269>
- Lear, C.H., Rosenthal, Y., Coxall, H.K., Wilson, P.A., 2004. Late Eocene to early Miocene ice sheet dynamics and the global carbon cycle. *Paleoceanography* 19, PA4015. <https://doi.org/10.1029/2004PA001039>
- Lee, S., Hwang, J., Ducklow, H.W., Hahn, D., Lee, S.H., Kim, D., Hyun, J.-H., Park, J., Ha, H.K., Kim, T.-W., Yang, E.J., Shin, H.C., 2017. Evidence of minimal carbon sequestration in the productive Amundse Sea polynya. *Geophys. Res. Lett.* 44, 7892–7899. <https://doi.org/10.1002/2017GL074646>
- Lentin, J.K., Williams, G.L., 1976. A monograph of fossil peridinioid dinoflagellate cysts, Bedford Institute of Oceanography, Report Series BI-R-75-16, 1–237.
- Leventer, A., 1998. The fate of Antarctic “sea ice diatoms” and their use as paleoenvironmental indicators. *Antarct. Res. Ser.* 73, 121–137.
- Leventer, A., Brachfeld, S., Domack, E., Dunbar, R., Manley, P., McClennen, C., 2001. Coring Holocene Antarctic Ocean Sediments – NBP0101 Cruise Report, p. 190.
- Leventer, A., Domack, E., Barkoukis, A., McAndrews, B., Murray, J., 2002. Laminations from the Palmer Deep: A diatom-based interpretation. *Paleoceanography* 17, PAL 3-1-PAL 3-15.
- Leventer, A., Domack, E.W., Ishman, S.E., Brachfeld, S., McClennen, C.E., Manley, P., 1996. Productivity cycles of 200-300 years in the Antarctic Peninsula region: Understanding linkages among the sun, atmosphere, oceans, sea-ice and biota. *Geol. Soc. Am. Bull.* 108, 1626–1644. [https://doi.org/10.1130/0016-7606\(1996\)108<1626](https://doi.org/10.1130/0016-7606(1996)108<1626)
- Levy, R.H., Harwood, D.M., 2000. Tertiary marine palynomorphs from McMurdo Sound erratics, Antarctica, in: Stilwell, J.D., Feldman, R.M. (Eds.), *Paleobiology and Paleoenvironments of Eocene Rocks, McMurdo Sound, East Antarctica*, Antarctic Research Series 76, American Geophysical Union, Washington D.C., pp. 183–242.
- Levy, R., Harwood, D., Florindo, F., Sangiorgi, F., Tripathi, R., von Eynatten, H., Gasson, E., Kuhn, G., Tripathi, A., DeConto, R., Fielding, C., Field, B., Golledge, N., McKay, R., Naish, T., Olney, M., Pollard, D., Schouten, S., Talarico, F., Warny, S., Willmott, V., Acton, G., Panter, K., Paulsen, T., Taviani, M., the SMS Science Team, 2016. Antarctic ice sheet sensitivity to atmospheric CO₂ variations in the early to mid-Miocene. *P. Natl. Acad. Sci. USA* 113, 3453–3458. <https://doi.org/10.1073/pnas.1516030113>

- Li, Z., Pospelova, V., Liu, L., Zhou, R., Song, B., 2017. High-resolution palynological record of Holocene climatic and oceanographic changes in the northern South China Sea. *Palaeogeogr. Palaeoclimatol. 483*, 94–124. <https://doi.org/10.1016/j.palaeo.2017.03.009>
- Liebrand, D., Bakker, A.T.M. De, Beddow, H.M., Wilson, P.A., Bohaty, S.M., 2017. Evolution of the early Antarctic ice ages. *P. Natl. Acad. Sci. USA* 114, 3867–3872. <https://doi.org/10.1073/pnas.1615440114>
- Liebrand, D., Beddow, H.M., Lourens, L.J., Pälike, H., Raffi, I., Bohaty, S.M., Hilgen, F.J., Saes, M.J.M., Wilson, P.A., Dijk, A.E. Van, Hodell, D.A., Kroon, D., Huck, C.E., Batenburg, S.J., 2016. Cyclostratigraphy and eccentricity tuning of the early Oligocene oxygen and carbon isotope records from Walvis Ridge Site 1264. *Earth Planet. Sc. Lett.* 450, 392–405. <https://doi.org/10.1016/j.epsl.2016.06.007>
- Liebrand, D., Lourens, L.J., Hodell, D.A., De Boer, B., Van De Wal, R.S.W., Pälike, H., 2011. Antarctic ice sheet and oceanographic response to eccentricity forcing during the early Miocene. *Clim. Past* 7, 869–880. <https://doi.org/10.5194/cp-7-869-2011>
- Lindemann, E., 1928. Abteilung Peridineae (Dinoflagellatae), in: Engler, A., Prantl, K. (Eds.), *Die Natürlichen Pflanzenfamilien nebst ihren Gattungen und wichtigeren Arten insbesondere den Nutzpflanzen. Zweite stark vermehrte und verbesserte Auflage herausgegeben von A. Engler. Bd. 2, Wilhelm Engelmann, Leipzig*, pp. 3–104.
- Lindenberg, H.G., Auras, A., 1984. Distribution of arenaceous foraminifera in depth profiles of the Southern Ocean (Kerguelen Plateau area). *Palaeogeogr. Palaeoclimatol.* 48, 61–106.
- Linnaeus, C., 1758: *Systema Naturae per Regna Tria Naturae, secundum Classes, Ordines, Genera, Species cum characteribus, differentiis, synonymis, locis*, Tomus I, 10th edition, Laurentius Salvius, Holmiae, p. 824.
- Lipps, J.H., Stoeck, T., Dunthorn, M., 2013. Fossil Tintinnids, in: Dolan, J.R., Montagnes, D.J.S., Agatha, S., Coats, D.W., Stoecker, D.K. (Eds.), *The Biology and Ecology of Tintinnid Ciliates: Models for Marine Plankton*. Wiley-Blackwell, Hoboken, New Jersey, USA, pp. 186–197.
- Lisiecki, L.E., Raymo, M.E., 2005. A Pliocene-Pleistocene stack of 57 globally distributed benthic $\delta^{18}\text{O}$ records. *Paleoceanography* 20, PA1003. <https://doi.org/10.1029/2004PA001071>
- Liu, Y., Moore, J.C., Cheng, X., Gladstone, R.M., Bassis, J.N., Liu, H., Wen, J., Hui, F., 2015. Ocean-driven thinning enhances iceberg calving and retreat of Antarctic ice shelves. *P. Natl. Acad. Sci. USA* 112, 3263–3268. <https://doi.org/10.1073/pnas.1415137112>
- Liu, Z., Pagani, M., Zinniker, D., DeConto, R., Huber, M., Brinkhuis, H., Shah, S.R., Leckie, R.M., Pearson, A., 2009. Global Cooling During the Eocene-Oligocene Climate Transition. *Science* 323, 1187–1190. <https://doi.org/10.1126/science.1166368>
- Livermore, R., Eagles, G., Morris, P., Maldonado, A., 2004. Shackleton Fracture Zone: No barrier to early circumpolar ocean circulation. *Geology* 32, 797–800. <https://doi.org/10.1130/G20537.1>
- Livermore, R., Hillenbrand, C.D., Meredith, M., Eagles, G., 2007. Drake Passage and Cenozoic climate: An open and shut case? *Geochem. Geophys. Geosy.* 8, Q01005. <https://doi.org/10.1029/2005GC001224>
- Lizotte, M.P., 2001. The Contributions of Sea Ice Algae to Antarctic Marine Primary Production. *Am. Zool.* 41, 57–73. [https://doi.org/10.1668/0003-1569\(2001\)041\[0057:TCOSIA\]2.0.CO;2](https://doi.org/10.1668/0003-1569(2001)041[0057:TCOSIA]2.0.CO;2)
- Ljung, K., Björk, S., Renssen, H., Hammarlund, D., 2008. South Atlantic island record reveals a South Atlantic response to the 8.2 kyr event. *Clim. Past* 4, 35–45.

- Locarnini, R.A., Mishonov, A.V., Antonov, J.I., Boyer, T.P., Garcia, H.E., Baranova, O.K., Zweng, M.M., Johnson, D.R., 2010. World Ocean Atlas 2009, Volume 1 : Temperature. NOAA Atlas NESDIS 68, U.S. Government Printing Office, Washington, D.C.
- Long, M.C., Stephens, B.B., Mckain, K., Sweeney, C., Keeling, R.F., Kort, E.A., Morgan, E.J., Bent, J.D., Chandra, N., Chevallier, F., Commane, R., Daube, B.C., Krummel, P.B., Loh, Z., Luijkx, I.T., Munro, D., Patra, P., Peters, W., Ramonet, M., Rödenbeck, C., Stavert, A., Tans, P., Wofsy, S.C., 2021. Strong Southern Ocean carbon uptake evident in airborne observations. *Science* 374, 1275–1280.
- Loots, C., Swadling, K.M., Koubbi, P., 2009. Annual cycle of distribution of three ice-associated copepods along the coast near Dumont d’Urville, Terre Adélie (Antarctica). *J. Marine Syst.* 78, 599–605. <https://doi.org/10.1016/j.jmarsys.2009.01.003>
- Lopes dos Santos, R.A., Prange, M., Castañeda, I.S., Schefuß, E., Mulitza, S., Schulz, M., Niedermeyer, E.M., Sinninghe Damsté, J.S., Schouten, S., 2010. Glacial – interglacial variability in Atlantic meridional overturning circulation and thermocline adjustments in the tropical North Atlantic. *Earth Planet. Sc. Lett.* 300, 407–414. <https://doi.org/10.1016/j.epsl.2010.10.030>
- Lucchi, R.G., Rebesco, M., Camerlenghi, A., Busetti, M., Tomadin, L., Villa, G., Persico, D., Morigi, C., Bonci, M.C., Giorgetti, G., 2002. Mid-late Pleistocene glacial marine sedimentary processes of a high-latitude, deep-sea sediment drift (Antarctic Peninsula Pacific margin). *Mar. Geol.* 189, 343–370.
- Lunt, D.J., Valdes, P.J., Jones, T.D., Ridgwell, A., Haywood, A.M., Schmidt, D.N., Marsh, R., Maslin, M., 2010. CO₂-driven ocean circulation changes as an amplifier of Paleocene-Eocene thermal maximum hydrate destabilization. *Geology* 38, 875–878. <https://doi.org/10.1130/G31184.1>
- Lüthi, D., Le Floch, M., Bereiter, B., Blunier, T., Barnola, J.-M., Siegenthaler, U., Raynaud, D., Jouzel, J., Fischer, H., Kawamura, K., Stocker, T.F., 2008. High-resolution carbon dioxide concentration record 650,000–800,000 years before present. *Nature* 453, 379–382. <https://doi.org/10.1038/nature06949>
- Mackensen, A., Grobe, H., Kuhn, G., Fittlerer, D.K., 1990. Benthic foraminiferal assemblages from the eastern Weddell Sea between 68 and 73°S : Distribution, ecology and fossilization potential. *Mar. Micropaleontol.* 16, 241–283.
- Mackintosh, A., Golledge, N., Domack, E., Dunbar, R., Leventer, A., White, D., Pollard, D., Deconto, R., Fink, D., Zwart, D., Gore, D., Lavoie, C., 2011. Retreat of the East Antarctic ice sheet during the last glacial termination. *Nat. Geosci.* 4, 195–202. <https://doi.org/10.1038/ngeo1061>
- Maddison, E.J., Pike, J., Dunbar, R., 2012. Seasonally laminated diatom-rich sediments from Dumont d’Urville Trough, East Antarctic Margin: Late-Holocene Neoglacial sea-ice conditions. *Holocene* 22, 857–875. <https://doi.org/10.1177/0959683611434223>
- Magyar, I., Geary, D.H., Müller, P., 1999. Paleogeographic evolution of the Late Miocene Lake Pannon in Central Europe. *Palaeogeogr. Palaeoclimatol.* 147, 151–167. [https://doi.org/10.1016/S0031-0182\(98\)00155-2](https://doi.org/10.1016/S0031-0182(98)00155-2)
- Majewski, W., Bohaty, S.M., 2010. Surface-water cooling and salinity decrease during the Middle Miocene climate transition at Southern Ocean ODP Site 747 (Kerguelen Plateau). *Mar. Micropaleontol.* 74, 1–14. <https://doi.org/10.1016/J.Marmicro.2009.10.002>
- Maldonado, A., Barnolas, A., Bohoyo, F., Escutia, C., Galindo-Zaldívar, J., Hernández-Molina, J., Jabaloy, A., Lobo, F.J., Nelson, C.H., Rodríguez-Fernández, J., Somoza, L., Vázquez, J.-T., 2005. Miocene to Recent contourite drifts development in the northern Weddell Sea

- (Antarctica). *Global Planet. Change* 45, 99–129.
<https://doi.org/10.1016/j.gloplacha.2004.09.013>
- Maldonado, A., Barnolas, A., Bohoyo, F., Galindo-Zaldívar, J., Hernández-Molina, J., Lobo, F., Rodríguez-Fernández, J., Somoza, L., Vázquez, J.T., 2003. Contourite deposits in the central Scotia Sea: The importance of the Antarctic Circumpolar Current and the Weddell Gyre flows. *Palaeogeogr. Palaeoclimatol.* 198, 187–221.
[https://doi.org/10.1016/S0031-0182\(03\)00401-2](https://doi.org/10.1016/S0031-0182(03)00401-2)
- Maldonado, A., Bohoyo, F., Galindo-Zaldívar, J., Hernández-Molina, F.J., Lobo, F.J., Lodolo, E., Martos, Y.M., Pérez, L.F., Schreider, A. a., Somoza, L., 2014. A model of oceanic development by ridge jumping: Opening of the Scotia Sea. *Global Planet. Change* 123, 152–173. <https://doi.org/10.1016/j.gloplacha.2014.06.010>
- Malinverno, E., Maffioli, P., Gariboldi, K., 2016. Latitudinal distribution of extant fossilizable phytoplankton in the Southern Ocean: Planktonic provinces, hydrographic fronts and palaeoecological perspectives. *Mar. Micropaleontol.* 123, 41–58.
<https://doi.org/10.1016/j.marmicro.2016.01.001>
- Mangot, J.F., Debroas, D., Domaizon, I., 2011. Perkinsozoa, a well-known marine protozoan flagellate parasite group, newly identified in lacustrine systems: A review. *Hydrobiologia* 659, 37–48. <https://doi.org/10.1007/s10750-010-0268-x>
- Marchant, H.J., 2005. Prasinophytes, in: Scott, F., Marchant, H.J. (Eds.), *Antarctic Marine Protists*, Australian Biological Resources Study, Canberra and Australian Antarctic Division, Hobart, pp. 308–315.
- Marcus, E., 1927. Zur Anatomie und Ökologie mariner Tardigraden, *Zoologische Jahrbücher, Abteilung für Systematik* 53, 487–558.
- Marcus, N.H., 1996. Ecological and evolutionary significance of resting eggs in marine copepods: past, present, and future studies. *Hydrobiologia* 320, 141–152.
- Marin, B., Melkonian, M., 2010. Molecular Phylogeny and Classification of the Mamiellophyceae class. nov. (Chlorophyta) based on Sequence Comparisons of the Nuclear- and Plastid-encoded rRNA Operons. *Protist* 161, 304–336.
<https://doi.org/10.1016/j.protis.2009.10.002>
- Markwick, P.J., 2007. The palaeogeographic and palaeoclimatic significance of climate proxies for data-model comparisons, in: Williams, M., Haywood, A.M., Gregory, F.J., Schmidt, D.N. (Eds.), *Deep-Time Perspectives on Climate Change: Marrying the Signal from Computer Models and Biological Proxies*. The Micropalaeontological Society, Special Publications. The Geological Society, London, pp. 251–312.
- Marley, N.J., McInnes, S.J., Sands, C.J., 2011. Phylum Tardigrada: A re-evaluation of the Parachela. *Zootaxa* 2819, 51–64.
- Marret, F., Bradley, L., De Vernal, A., Hardy, W., Kim, S., Mudie, P., Penaud, A., Pospelova, V., Price, A.M., Radi, T., Rochon, A., 2020. From bi-polar to regional distribution of modern dinoflagellate cysts, an overview of their biogeography. *Mar. Micropaleontol.* 159, 101753. <https://doi.org/10.1016/j.marmicro.2019.101753>
- Marret, F., De Vernal, A., 1997. Dinoflagellate cyst distribution in surface sediments of the southern Indian Ocean. *Mar. Micropaleontol.* 29, 367–392.
[https://doi.org/10.1016/S0377-8398\(96\)00049-7](https://doi.org/10.1016/S0377-8398(96)00049-7)
- Marret, F., De Vernal, A., Benderra, F., Harland, R., 2001. Late Quaternary sea-surface conditions at DSDP Hole 594 in the Southwest Pacific Ocean based on dinoflagellate cyst assemblages. *J. Quaternary Sci.* 16, 739–751. <https://doi.org/10.1002/jqs.648>

- Marret, F., Zonneveld, K.A.F., 2003. Atlas of modern organic-walled dinoflagellate cyst distribution. *Rev. Palaeobot. Palyno.* 125, 1–200. [https://doi.org/10.1016/S0034-6667\(02\)00229-4](https://doi.org/10.1016/S0034-6667(02)00229-4)
- Marschalek, J.W., Zurli, L., Talarico, F., van de Flierdt, T., Vermeesch, P., Carter, A., Beny, F., Bout-Roumazeilles, V., Sangiorgi, F., Hemming, S.R., Pérez, L.F., Colleoni, F., Prebble, J.G., van Peer, T.E., Perotti, M., Shevenell, A.E., Browne, I., Kulhanek, D.K., Levy, R., Harwood, D., Sullivan, N.B., Meyers, S.R., Griffith, E.M., Hillenbrand, C.-D., Gasson, E., Siegert, M.J., Keisling, B., Licht, K.J., Kuhn, G., Dodd, J.P., Boshuis, C., De Santis, L., McKay, R.M., IODP Expedition 374 Scientists, 2021. A large West Antarctic Ice Sheet explains early Neogene sea-level amplitude. *Nature* 600, 450–455. <https://doi.org/10.1038/s41586-021-04148-0>
- Marsland, S.J., Church, J.A., Bindoff, N.L., Williams, G.D., 2007. Antarctic coastal polynya response to climate change. *J. Geophys. Res.* 112, C07009. <https://doi.org/10.1029/2005JC003291>
- Martin, F., 1993. Acritarchs: a review. *Biol. Rev. Camb. Philos.* 68, 475–538.
- Martínez-García, A., Rosell-Melé, A., Geibert, W., Gersonde, R., Masqué, P., Gaspari, V., Barbante, C., 2009. Links between iron supply, marine productivity, sea surface temperature, and CO₂ over the last 1.1 Ma. *Paleoceanography* 24, 1–14. <https://doi.org/10.1029/2008PA001657>
- Masson-Delmotte, V., Stenni, B., Jouzel, J., 2004. Common millennial-scale variability of Antarctic and Southern Ocean temperatures during the past 5000 years reconstructed from the EPICA Dome C ice core. *Holocene* 14, 145–151.
- Masson, V., Vimeux, F., Jouzel, J., Morgan, V., Delmotte, M., Ciais, P., Hammer, C., Johnsen, S., Lipenkov, V.Y., Mosley-Thompson, E., Petit, J.-R., Steig, E.J., Stievenard, M., Vaikmae, R., 2000. Holocene Climate Variability in Antarctica Based on 11 Ice-Core Isotopic Records. *Quaternary Res.* 54, 348–358. <https://doi.org/10.1006/qres.2000.2172>
- Matsuoka, K., Head, M., 2013. Clarifying cyst – motile stage relationships in dinoflagellates, in: Lewis, J.M., Marret, F., Bradley, L. (Eds.), *Biological and Geological Perspectives of Dinoflagellates*. The Micropalaeontological Society, Special Publications, London, pp. 325–350.
- McGillicuddy, D.J., Sedwick, P.N., Dinniman, M.S., Arrigo, K.R., Bibby, T.S., Greenan, B.J.W., Hofmann, E.E., Klinck, J.M., Smith, W.O., Mack, S.L., Marsay, C.M., Sohst, B.M., Van Dijken, G.L., 2015. Iron supply and demand in an Antarctic shelf ecosystem. *Geophys. Res. Lett.* 42, 8088–8097. <https://doi.org/10.1002/2015GL065727>
- McKay, N.P., Overpeck, J.T., Otto-Bliesner, B.L., 2011. The role of ocean thermal expansion in Last Interglacial sea level rise. *Geophys. Res. Lett.* 38, 4–9. <https://doi.org/10.1029/2011GL048280>
- McManus, J., Berelson, W.M., Klinkhammer, G.P., Johnson, K.S., Coale, K.H., Anderson, R.F., Kumar, N., Burdige, D.J., Hammond, D.E., Brumsack, H.J., McCorkle, D.C., Rushdi, A., 1998. Geochemistry of barium in marine sediments: Implications for its use as a paleoproxy. *Geochim. Cosmochim. Ac.* 62, 3453–3473. [https://doi.org/10.1016/S0016-7037\(98\)00248-8](https://doi.org/10.1016/S0016-7037(98)00248-8)
- McMillan, M., Shepherd, A., Sundal, A., Briggs, K., Muir, A., Ridout, A., Hogg, A., Wingham, D., 2014. Increased ice losses from Antarctica detected by CryoSat-2. *Geophys. Res. Lett.* 41, 3899–3906. <https://doi.org/10.1002/2014GL060111>. Received

- McMinn, A., 2002. Marine Quaternary dinoflagellate cysts of Australia, Papua-New Guinea, New Zealand and the Southern Ocean: a review. *Alcheringa* 26, 519–530. <https://doi.org/10.1080/03115510208619541>
- McMinn, A., 1995. Why are there no post-Paleogene dinoflagellate cysts in the Southern Ocean. *Micropaleontology* 41, 383–386.
- Medvedeva, L.A., Nikulina, T. V., 2014. Catalogue of freshwater algae of the southern part of the Russian Far East. *Dal'nauka*, Vladivostok.
- Melis, R., Capotondi, L., Torricella, F., Ferretti, P., Geniram, A., Trieste, U., Weiss, V.E., Gobetti, V., Ambientali, S., Statistica, I., Scienza, P., 2021. Last Glacial Maximum to Holocene paleoceanography of the northwestern Ross Sea inferred from sediment core geochemistry and micropaleontology at Hallett Ridge. *J. Micropalaeontol.* 40, 15–35.
- Menéndez, C.A., 1965. Microplancton fósil de sedimentos Terciarios y Cretácicos del norte de Tierra del Fuego (Argentina), *Ameghiniana* 4, 1, 7–18.
- Meredith, M.P., King, J.C., 2005. Rapid climate change in the ocean west of the Antarctic Peninsula during the second half of the 20th century. *Geophys. Res. Lett.* 32, L19604. <https://doi.org/10.1029/2005GL024042>
- Mertens, K.N., Gu, H., Takano, Y., Price, A.M., Pospelova, V., Bogus, K., Versteegh, G.J.M., Marret, F., Eugene, R., Rabalais, N.N., Matsuoka, K., Neil, K., Gu, H., Takano, Y., Price, A.M., Pospelova, V., Bogus, K., Versteegh, G.J.M., Marret, F., Turner, R.E., Rabalais, N.N., Matsuoka, K., 2017. The cyst-theca relationship of the dinoflagellate cyst *Trinovantedinium pallidifulum*, with erection of *Protoperidinium lousianensis* sp. nov. and their phylogenetic position within the *Conica* group. *Palynology* 41, 183–202. <https://doi.org/10.1080/01916122.2016.1147219>
- Mertens, K.N., Ribeiro, S., Bouimetarhan, I., Caner, H., Combourieu Nebout, N., Dale, B., De Vernal, A., Ellegaard, M., Filipova, M., Godhe, A., Goubert, E., Grøsfjeld, K., Holzwarth, U., Kotthoff, U., Leroy, S.A.G., Londeix, L., Marret, F., Matsuoka, K., Mudie, P.J., Naudts, L., Peña-Manjarrez, J.L., Persson, A., Popescu, S.-M., Pospelova, V., Sangiorgi, F., van der Meer, M.T.J., Vink, A., Zonneveld, K.A.F., Vercauteren, D., Vlassenbroeck, J., Louwye, S., 2009. Process length variation in cysts of a dinoflagellate, *Lingulodinium machaerophorum*, in surface sediments: Investigating its potential as salinity proxy. *Mar. Micropaleontol.* 70, 54–69. <https://doi.org/10.1016/j.marmicro.2008.10.004>
- Meyers, S.R., 2014. Astrochron: An R Package for Astrochronology. <http://cran.r-project.org/package=astrochron>.
- Meyers, S.R., 2012. Seeing red in cyclic stratigraphy: Spectral noise estimation for astrochronology. *Paleoceanography* 27, PA3228. <https://doi.org/10.1029/2012PA002307>
- Meyers, S.R., Sageman, B.B., 2007. Quantification of deep-time orbital forcing by average spectral misfit. *Am. J. Sci.* 307, 773–792. <https://doi.org/10.2475/05.2007.01>
- Meyers, S.R., Sageman, B.B., Arthur, M.A., 2012. Obliquity forcing of organic matter accumulation during Oceanic Anoxic Event 2. *Paleoceanography* 27, PA3212. <https://doi.org/10.1029/2012PA002286>
- Mezgec, K., Stenni, B., Crosta, X., Masson-Delmotte, V., Baroni, C., Braida, M., Ciardini, V., Colizza, E., Melis, R., Salvatore, M.C., Severi, M., Scarchilli, C., Traversi, R., Udisti, R., Frezzotti, M., 2017. Holocene sea ice variability driven by wind and polynya efficiency in the Ross Sea. *Nat. Commun.* 8, 1334. <https://doi.org/10.1038/s41467-017-01455-x>

- Michels, J., Gorb, S.N., 2015. Mandibular gnathobases of marine planktonic copepods – feeding tools with complex micro- and nanoscale composite architectures. *Beilstein J. Nanotech.* 6, 674–685. <https://doi.org/10.3762/bjnano.6.68>
- MICROBIS database. Occurrence Dataset <https://doi.org/10.15468/wi6v9k> accessed via GBIF.org on 2018-02-08.
- Mikhalevich, V.I., 2004. Major features of the distribution of Antarctic foraminifera. *Micropaleontology* 50, 179–194.
- Miles, B.W.J., Stokes, C.R., Jamieson, S.S.R., 2016. Pan – ice-sheet glacier terminus change in East Antarctica reveals sensitivity of Wilkes Land to sea-ice changes. *Sci. Adv.* 2, e1501350. <https://doi.org/10.1126/sciadv.1501350>
- Miller, K.G., Baluyot, R., Wright, J.D., Kopp, R.E., Browning, J. V., 2017. Closing an early Miocene astronomical gap with Southern Ocean $\delta^{18}\text{O}$ and $\delta^{13}\text{C}$ records: Implications for sea level change. *Paleoceanography* 32, 600–621. <https://doi.org/10.1002/2016PA003074>
- Miller, K.G., Browning, J. V., Schmelz, W.J., Kopp, R.E., Mountain, G.S., Wright, J.D., 2020. Cenozoic sea-level and cryospheric evolution from deep-sea geochemical and continental margin records. *Sci. Adv.* 6, eaaz1346.
- Milne-Edwards, M., 1840. Histoire naturelle des crustacés, comprenant l'anatomie, la physiologie et la classification de ces animaux, Tome Troisième, Librairie Encyclopedique de Roret, Paris, p. 638.
- Minzoni, R.T., Anderson, J.B., Fernandez, R., Wellner, J.S., 2015. Marine record of Holocene climate, ocean, and cryosphere interactions: Herbert Sound, James Ross Island, Antarctica. *Quaternary Sci. Rev.* 129, 239–259. <https://doi.org/10.1016/j.quascirev.2015.09.009>
- Moestrup, Ø., Inouye, I., Hori, T., 2003. Ultrastructural studies on *Cymbomonas tetramitiformis* (Prasinophyceae). I. General structure, scale microstructure, and ontogeny. *Can. J. Botany* 81, 657–671. <https://doi.org/10.1139/B03-055>
- Moita, M.T., Vilarinho, M.G., 1999. Checklist of phytoplankton species off Portugal: 70 years (1929-1998) of studies. *Portugaliae Acta Biol. Ser. B. Sist.* 18, 5–50.
- Mollenhauer, G., Basse, A., Kim, J.H., Sinninghe Damsté, J.S., Fischer, G., 2015. A four-year record of U^{K}_{37} - and TEX_{86} -derived sea surface temperature estimates from sinking particles in the filamentous upwelling region off Cape Blanc, Mauritania. *Deep-Sea Res. Pt I* 97, 67–79. <https://doi.org/10.1016/j.dsr.2014.11.015>
- Montagnes, D.J.S., 2013. Ecophysiology and Behaviour of Tintinnids, in: Dolan, J.R., Montagnes, D.J.S., Agatha, S., Coats, D.W., Stoecker, D.K. (Eds.), *The Biology and Ecology of Tintinnid Ciliates: Models for Marine Plankton*. Wiley-Blackwell, Hoboken, New Jersey, USA, pp. 85–121.
- Montesor, M., Lovejoy, C., Orsini, L., Procaccini, G., Roy, S., 2003. Bipolar distribution of the cyst-forming dinoflagellate *Polarella glacialis*. *Polar Biol.* 26, 186–194. <https://doi.org/10.1007/s00300-002-0473-9>
- Montesor, M., Procaccini, G., Stoecker, D.K., 1999. *Polarella glacialis*, Gen. Nov., Sp. Nov. (Dinophyceae): Suessiaceae are still alive. *J. Phycol.* 35, 186–197.
- Morales Maqueda, M.A., Willmott, A.J., Biggs, N.R.T., 2004. Polynya Dynamics: A review of observations and modeling. *Rev. Geophys.* 42, RG1004. <https://doi.org/10.1029/2002RG000116>
- Morehead, S., Montagna, P., Kennicutt II, M.C., 2008. Comparing fixed-point and probabilistic sampling designs for monitoring the marine ecosystem near McMurdo Station, Ross Sea, Antarctica. *Antarct. Sci.* 20, 471–484. <https://doi.org/10.1017/S0954102008001326>

- Moro, I., La Rocca, N., Valle, L.D., Moschin, E., Negrisolo, E., Andreoli, C., 2002. *Pyramonas australis* sp. nov. (Prasinophyceae, Chlorophyta) from Antarctica: fine structure and molecular phylogeny. *Eur. J. Phycol.* 37, 103–114.
- Moros, M., De Deckker, P., Jansen, E., Perner, K., Telford, R.J., 2009. Holocene climate variability in the Southern Ocean recorded in a deep-sea sediment core off South Australia. *Quaternary Sci. Rev.* 28, 1932–1940. <https://doi.org/10.1016/j.quascirev.2009.04.007>
- Mortlock, R.A., Charles, C.D., Froelich, P.N., Zibello, M.A., Saltzman, J., Hays, J.D., Burckle, L.H., 1991. Evidence for lower productivity in the Antarctic Ocean during the last glaciation. *Nature* 351, 220–223.
- Mousing, E.A., Ribeiro, S., Chisholm, C., Kuijpers, A., Moros, M., Ellegaard, M., 2017. Size differences of Arctic marine protists between two climate periods—using the paleoecological record to assess the importance of within-species trait variation. *Ecol. Evol.* 7, 3–13. <https://doi.org/10.1002/ece3.2592>
- Mudie, P.J., 1992. Circum-arctic Quaternary and Neogene marine palynofloras: paleoecology and statistical analysis, in: Head, M.X., Wrenn, J.H. (Eds.), *Neogene and Quaternary dinoflagellate cysts and acritarchs*. American Association of Stratigraphic Palynologists Foundation, Dallas, Texas, pp. 347–390.
- Mudie, P.J., Harland, R., 1996. Chapter 21. Aquatic Quaternary, in: Jansonius, J., McGregor, D.C. (Eds.), *Palynology: Principles and Applications*: American Association of Stratigraphic Palynologists Foundation, Dallas, Texas, v. 2, pp. 843–877.
- Mudie, P.J., Leroy, S.A.G., Marret, F., Gerasimenko, N.P., Kholeif, S.E.A., Sapelko, T., Filipova-Marinova, M., 2011. Nonpollen palynomorphs: indicators of salinity and environmental change in the Caspian – Black Sea – Mediterranean corridor, in: Buynovich, I.V., Yanko-Hombach, V., Gilbert, A.S., Martin, R.E. (Eds.), *Geology and Geoarchaeology of the Black Sea Region: Beyond the Flood Hypothesis*. The Geological Society of America Special Paper, Boulder, Colorado, pp. 89–115. [https://doi.org/10.1130/2011.2473\(07\)](https://doi.org/10.1130/2011.2473(07)).
- Mudie, P.J., Marret, F., Gurdebeke, P.R., Hartman, J.D., Reid, P.C., 2021. Marine dinocysts, acritarchs and less well-known NPP: tintinnids, ostracod and foraminiferal linings, copepod and worm remains, in: Marret, F., O’Keefe, J., Osterloff, P., Pound, M., Shumilovskikh, L. (Eds.), *Applications of Non-Pollen Palynomorphs: From Palaeoenvironmental Reconstructions to Biostratigraphy*. Geological Society, London, pp. 159–232.
- Mudie, P.J., Marret, F., Rochon, A., Aksu, A.E., 2010. Non-pollen palynomorphs in the Black Sea corridor. *Veg. Hist. Archaeobot.* 19, 531–544. <https://doi.org/10.1007/s00334-010-0268-9>
- Mudie, P.J., Rochon, A., Aksu, A.E., Gillespie, H., 2002. Dinoflagellate cysts, freshwater algae and fungal spores as salinity indicators in Late Quaternary cores from Marmara and Black seas. *Mar. Geol.* 190, 209–231.
- Müller, H., Wünsch, C., 1999. Seasonal dynamics of cyst formation of pelagic strombidiid ciliates in a deep prealpine lake. *Aquat. Microb. Ecol.* 17, 37–47.
- Murphy, E.J., Thorpe, S.E., Tarling, G.A., Watkins, J.L., Fielding, S., Underwood, P., 2017. Restricted regions of enhanced growth of Antarctic krill in the circumpolar Southern Ocean. *Sci. Rep.* 7, 6963. <https://doi.org/10.1038/s41598-017-07205-9>
- Murray, A.E., Preston, C.M., Massana, R., Taylor, T.L., Blakis, A., Wu, K., Delong, E.F., 1998. Seasonal and spatial variability of bacterial and archaeal assemblages in the coastal waters near Anvers Island, Antarctica. *Appl. Environ. Microb.* 64, 2585–2595.

- Naafs, B.D.A., Inglis, G.N., Zheng, Y., Amesbury, M.J., Biester, H., Bindler, R., Blewett, J., Burrows, M.A., del Castillo Torres, D., Chambers, F.M., Cohen, A.D., Evershed, R.P., Feakins, S.J., Gafka, M., Gallego-Sala, A., Gandois, L., Gray, D.M., Hatcher, P.G., Honorio Coronado, E.N., Hughes, P.D.M., Huguet, M., Könönen, M., Laggoun-Défarge, F., Lähteenoja, O., Lamentowitz, M., Marchant, R., McClymont, E., Pontevedra-Pombal, X., Ponton, C., Pourmand, A., Rizzuti, A.M., Rochefort, L., Schellekens, J., De Vleeschouwer, F., Pancost, R.D., 2017. Introducing global peat-specific temperature and pH calibrations based on brGDGT bacterial lipids. *Geochim. Cosmochim. Ac.* 208, 285–301.
- Nakayama, T., Marin, B., Kranz, H.D., Surek, B., Huss, V.A.R., Inouye, I., Melkonian, M., 1998. The Basal Position of Scaly Green Flagellates among the Green Algae (Chlorophyta) is Revealed by Analyses of Nuclear-Encoded SSU rRNA Sequences. *Protist* 149, 367–380. [https://doi.org/10.1016/S1434-4610\(98\)70043-4](https://doi.org/10.1016/S1434-4610(98)70043-4)
- National Oceanic and Atmospheric Administration, Global Monitoring Laboratory (<https://gml.noaa.gov/ccgg/trends/>)
- Nelson, D.M., DeMaster, D.J., Dunbar, B., Smith Jr, W.O., 1996. Cycling of organic carbon and biogenic silica in the Southern Ocean: Estimates of water-column and sedimentary fluxes on the Ross Sea continental shelf. *J. Geophys. Res.* 101, 18519–18532.
- Ní Fhlaithearta, S., Ernst, S.R., Nierop, K.G.J., de Lange, G.J., Reichart, G.-J., 2013. Molecular and isotopic composition of foraminiferal organic linings. *Mar. Micropaleontol.* 102, 69–78. <https://doi.org/10.1016/j.marmicro.2013.06.004>
- Nielsen, S.H.H., Koç, N., Crosta, X., 2004. Holocene climate in the Atlantic sector of the Southern Ocean: Controlled by insolation or oceanic circulation? *Geology* 32, 317–320. <https://doi.org/10.1130/G20334.1>
- Notz, D., Marotzke, J., 2012. Observations reveal external driver for Arctic sea-ice retreat. *Geophys. Res. Lett.* 39, L08502. <https://doi.org/10.1029/2012GL051094>
- Nylen, T.H., Fountain, A.G., Doran, P.T., 2004. Climatology of katabatic winds in the McMurdo dry valleys, southern Victoria Land, Antarctica. *J. Geophys. Res.* 109, D03114. <https://doi.org/10.1029/2003JD003937>
- O’Kelly, C.J., 2007. Origin and Early Evolution of Green Plants, in: Falkowski, P.G., Knoll, A.H. (Eds.), *Evolution of Primary Producers in the Sea*, Academic Press, Burlington, pp. 287–309.
- Ocean Biogeographic Information System. NODC WOD01 Plankton Database. Occurrence Dataset <https://doi.org/10.15468/ahpulo> accessed via GBIF.org on 2018-02-08.
- Orlova, T.Y., Morozova, T. V., Gribble, K.E., Kulis, D.M., Anderson, D.M., 2004. Dinoflagellate cysts in recent marine sediments from the east coast of Russia. *Bot. Mar.* 47, 184–201. <https://doi.org/10.1515/BOT.2004.019>
- Orsi, A.H., Whitworth, T., Nowlin, W.D., 1995. On the meridional extent and fronts of the Antarctic Circumpolar Current. *Deep-Sea Res. Pt I* 42, 641–673. [https://doi.org/10.1016/0967-0637\(95\)00021-W](https://doi.org/10.1016/0967-0637(95)00021-W)
- Orsi, A.H., Wiederwohl, C.L., 2009. A recount of Ross Sea waters. *Deep-Sea Res. Pt II* 56, 778–795. <https://doi.org/10.1016/j.dsr2.2008.10.033>
- Ostenfeld, C.H., Schmidt, J., 1902. Plankton fra det Røde Hav og Adenbugten (Plankton from the Red Sea and Gulf of Aden), in: *Videnskabilige Meddelelser Fra Dansk Naturhistorisk Forening, for Aaret 1901*. Bianco Lunos, Kjøbenhavn, pp. 141–182.
- Pagani, M., Huber, M., Liu, Z., Bohaty, S.M., Henderiks, J., Sijp, W., Krishnan, S., DeConto, R.M., 2011. The Role of Carbon Dioxide During the Onset of Antarctic Glaciation. *Science* 334, 1261–1265. <https://doi.org/10.1126/science.1203909>

- Pälike, H., Frazier, J., Zachos, J.C., 2006a. Extended orbitally forced palaeoclimatic records from the equatorial Atlantic Ceara Rise. *Quaternary Sci. Rev.* 25, 3138–3149.
<https://doi.org/10.1016/j.quascirev.2006.02.011>
- Pälike, H., Norris, R.D., Herrle, J.O., Wilson, P.A., Coxall, H.K., Lear, C.H., Shackleton, N.J., Tripathi, A.K., Wade, B.S., 2006b. The heartbeat of the Oligocene climate system. *Science* 314, 1894–8. <https://doi.org/10.1126/science.1133822>
- Pals, J.P., van Geel, B., Delfos, A., 1980. Paleoeoological studies in the Klokkeweel Bog near Hoogkarspel (Prov. of Noord-Holland). *Rev. Palaeobot. Palyno.* 30, 371–418.
- Pancost, R.D., Hopmans, E.C., Sinninghe Damsté, J.S., The MEDINAUT Shipboard Scientific Party, 2001. Archaeal lipids in mediterranean cold seeps: Molecular proxies for anaerobic methane oxidation. *Geochim. Cosmochim. Ac.* 65, 1611–1627.
[https://doi.org/10.1016/S0016-7037\(00\)00562-7](https://doi.org/10.1016/S0016-7037(00)00562-7)
- Panizzo, V., Crespin, J., Crosta, X., Shemesh, A., Massé, G., Yam, R., Mattioli, N., Cardinal, D., 2014. Sea ice diatom contributions to Holocene nutrient utilization in East Antarctica. *Paleoceanography* 29, 328–342. <https://doi.org/10.1002/2014PA002609>. Received
- Paolo, F.S., Fricker, H.A., Padman, L., 2015. Volume loss from Antarctic ice shelves is accelerating. *Science* 348, 327–332. <https://doi.org/10.1126/science.aaa0940>
- Park, J.-Y., Kug, J.-S., Bader, J., Rolph, R., Kwon, M., 2015. Amplified Arctic warming by phytoplankton under greenhouse warming. *P. Natl. Acad. Sci. USA* 112, 5921–5926.
<https://doi.org/10.1073/pnas.1416884112>
- Parke, M., Boalch, G.T., Jowett, R., Harbour, D.S., 1978. The genus *Pterosperma* (Prasinophyceae): species with a single equatorial ala. *J. Mar. Biol. Assoc. UK* 58, 239–276.
- Parkinson, C.L., 2019. A 40-y record reveals gradual Antarctic sea ice increases followed by decreases at rates far exceeding the rates seen in the Arctic. *P. Natl. Acad. Sci. USA* 116, 14414–14423. <https://doi.org/10.1073/pnas.1906556116>
- Parkinson, C.L., Cavalieri, D.J., 2012. The Cryosphere Antarctic sea ice variability and trends, 1979–2010. *Cryosphere* 6, 871–880. <https://doi.org/10.5194/tc-6-871-2012>
- Parrenin, F., Masson-Delmotte, V., Köhler, P., Raynaud, D., Paillard, D., Schwander, J., Barbante, C., Landais, A., Wegner, A., Jouzel, J., 2013. Synchronous Change of Atmospheric CO₂ and Antarctic Temperature During the Last Deglacial Warming. *Science* 339, 1060–1063.
- Pascher, A., 1914. Über Flagellaten und Algen, *Ber. Deut. Bot. Ges.* 32, 136–160.
- Past Interglacials Working Group of PAGES, 2016. Interglacials of the last 800,000 years. *Rev. Geophys.* 54, 162–219. <https://doi.org/10.1002/2015RG000482>
- Pasternak, A.F., Schnack-Schiel, S.B., 2001. Seasonal feeding patterns of the dominant Antarctic copepods *Calanus propinquus* and *Calanoides acutus* in the Weddell Sea. *Polar Biol.* 24, 771–784. <https://doi.org/10.1007/s003000100283>
- Paxton, H., Åkesson, B., 2007. Redescription of *Ophryotrocha puerilis* and *O. labronica* (Annelida, Dorvilleidae). *Mar. Biol. Res.* 3, 3–19.
<https://doi.org/10.1080/17451000601024373>
- Paxton, H., Davey, A., 2010. A new species of *Ophryotrocha* (Annelida : Dorvilleidae) associated with fish farming at Macquarie Harbour, Tasmania, Australia. *Zootaxa* 2509, 53–61.
<https://doi.org/10.5281/zenodo.196027>
- Paxton, H., Wiklund, H., Alexander, F., Taboada, S., 2017. Is the Antarctic *Ophryotrocha orensanzi* (Annelida: Dorvilleidae) a circumpolar non-specialized opportunist? *Syst. Biodivers.* 15, 105–114. <https://doi.org/10.1080/14772000.2016.1218371>

- Peck, L.S., Barnes, D.K.A., Cook, A.J., Fleming, A.H., Clarke, A., 2010. Negative feedback in the cold: ice retreat produces new carbon sinks in Antarctica. *Glob. Change Biol.* 16, 2614–2623. <https://doi.org/10.1111/j.1365-2486.2009.02071.x>
- Pekar, S.F., Christie-Blick, N., 2008. Resolving apparent conflicts between oceanographic and Antarctic climate records and evidence for a decrease in pCO₂ during the Oligocene through early Miocene (34–16 Ma). *Palaeogeogr. Palaeoclimatol.* 260, 41–49. <https://doi.org/10.1016/j.palaeo.2007.08.019>
- Pekar, S.F., DeConto, R.M., Harwood, D.M., 2006. Resolving a late Oligocene conundrum: Deep-sea warming and Antarctic glaciation. *Palaeogeogr. Palaeoclimatol.* 231, 29–40. <https://doi.org/10.1016/j.palaeo.2005.07.024>
- Peloquin, J.A., Smith Jr., W.O., 2007. Phytoplankton blooms in the Ross Sea, Antarctica: Interannual variability in magnitude, temporal patterns, and composition. *J. Geophys. Res.* 112, C08013. <https://doi.org/10.1029/2006JC003816>
- Percival, D.B., Walden, A.T., 1993. *Spectral Analysis for Physical Applications: Multitaper and Conventional Univariate Techniques*, Cambridge Univ. Press, Cambridge, U.K., p. 583. doi:10.1017/CBO9780511622762.
- Peterse, F., Kim, J., Schouten, S., Klitgaard, D., Koç, N., Sinninghe, J.S., 2009. Constraints on the application of the MBT/CBT palaeothermometer at high latitude environments (Svalbard, Norway). *Org. Geochem.* 40, 692–699. <https://doi.org/10.1016/j.orggeochem.2009.03.004>
- Petersen, S. V., Schrag, D.P., 2015. Antarctic ice growth before and after the Eocene-Oligocene Transition: New estimates from clumped isotope paleothermometry. *Paleoceanography* 30, 1–13. <https://doi.org/10.1002/2014PA002769>
- Petit, R.J., Raynaud, D., Basile, I., Chappellaz, J., Ritz, C., Delmotte, M., Legrand, M., Lorius, C., Pe, L., 1999. Climate and atmospheric history of the past 420,000 years from the Vostok ice core, Antarctica. *Nature* 399, 429–413. <https://doi.org/10.1038/20859>
- Petz, W., 2005. Ciliates, in: Scott, F., Marchant, H.J (Eds.), *Antarctic Marine Protists*. Australian Biological Resources Study, Canberra & Australian Antarctic Division, Hobart, pp. 347–448.
- Petz, W., Song, W., Wilbert, N., 1995. Taxonomy and ecology of the ciliate fauna (Protozoa, Ciliophora) in the endopagial and pelagial of the Weddell Sea, Antarctica. *Stapfia* 40, 1–223.
- Piasecki, S., Gregersen, U., Johannessen, P.N., 2002. Lower Pliocene dinoflagellate cysts from cored Utsira Formation in the Viking Graben, northern North Sea. *Mar. Petrol. Geol.* 19, 55–67. [https://doi.org/10.1016/S0264-8172\(01\)00053-8](https://doi.org/10.1016/S0264-8172(01)00053-8)
- Pieńkowski, A.J., England, J.H., Furze, M.F.A., Blasco, S., Mudie, P.J., MacLean, B., 2013a. 11,000 yrs of environmental change in the Northwest Passage: A multiproxy core record from central Parry Channel, Canadian High Arctic. *Mar. Geol.* 341, 68–85. <https://doi.org/10.1016/j.margeo.2013.04.008>
- Pieńkowski, A.J., England, J.H., Furze, M.F.A., MacLean, B., Blasco, S., 2014. The late Quaternary environmental evolution of marine Arctic Canada: Barrow Strait to Lancaster Sound. *Quaternary Sci. Rev.* 91, 184–203. <https://doi.org/10.1016/j.quascirev.2013.09.025>
- Pieńkowski, A.J., Marret, F., Scourse, J.D., Thomas, D.N., 2013b. Organic-walled microfossils from the north-west Weddell Sea, Antarctica: records from surface sediments after the collapse of the Larsen-A and Prince Gustav Channel ice shelves. *Antarct. Sci.* 25, 565–574. <https://doi.org/10.1017/S0954102012001186>

- Pieńkowski, A.J., Mudie, P.J., England, J.H., Smith, J.N., Furze, M.F.A., 2011. Late Holocene environmental conditions in Coronation Gulf, southwestern Canadian Arctic Archipelago: Evidence from dinoflagellate cysts, other non-pollen palynomorphs, and pollen. *J. Quaternary Sci.* 26, 839–853. <https://doi.org/10.1002/jqs.1503>
- Pilato, G., Binda, M.G., Lisi, O., 2004. Tardigrades of the Seychelles Islands, with the description of three new species. *Ital. J. Zool.* 71, 171–178. <https://doi.org/10.1080/11250000409356569>
- Plancq, J., Mattioli, E., Pittet, B., Simon, L., Grossi, V., 2014. Productivity and sea-surface temperature changes recorded during the late Eocene-early Oligocene at DSDP Site 511 (South Atlantic). *Palaeogeogr. Palaeoclimatol.* 407, 34–44. <https://doi.org/10.1016/j.palaeo.2014.04.016>
- Pollard, D., DeConto, R.M., Alley, R.B., 2015. Potential Antarctic Ice Sheet retreat driven by hydrofracturing and ice cliff failure. *Earth Planet. Sc. Lett.* 412, 112–121. <https://doi.org/10.1016/j.epsl.2014.12.035>
- Post, E., Bhatt, U.S., Bitz, C.M., Brodie, J.F., Fulton, T.L., Hebblewhite, M., Kerby, J., Kutz, S.J., Stirling, I., Walker, D.A., 2013. Ecological Consequences of Sea-Ice Decline. *Science* 341, 519–524.
- Pouchet, M., 1894. Chapter X. Histoire naturelle, in: Leroux, E. (Eds.), *Voyage de "La Manche" à l'île Jan-Mayen et au Spitzberg*, Paris, pp. 155–217.
- Prebble, J.G., Bostock, H.C., Cortese, G., Lorrey, A.M., Hayward, B.W., Calvo, E., Northcote, L.C., Scott, G.H., Neil, H.L., 2017. Evidence for a Holocene Climatic Optimum in the southwest Pacific: A multiproxy study. *Paleoceanography* 32, 763–779. <https://doi.org/10.1002/2016PA003065>
- Prebble, J.G., Crouch, E.M., Carter, L., Cortese, G., Bostock, H., Neil, H., 2013. An expanded modern dinoflagellate cyst dataset for the Southwest Pacific and Southern Hemisphere with environmental associations. *Mar. Micropaleontol.* 101, 33–48. <https://doi.org/10.1016/j.marmicro.2013.04.004>
- Prebble, J.G., Raine, J.I., Barrett, P.J., Hannah, M.J., 2006. Vegetation and climate from two Oligocene glacioeustatic sedimentary cycles (31 and 24 Ma) cored by the Cape Roberts Project, Victoria Land Basin, Antarctica. *Palaeogeogr. Palaeoclimatol.* 231, 41–57. <https://doi.org/10.1016/j.palaeo.2005.07.025>
- Pross, J., Brinkhuis, H., 2005. Organic-walled dinoflagellate cysts as paleoenvironmental indicators in the Paleogene; a synopsis of concepts. *Paläontologische Zeitschrift* 79, 53–59.
- Pross, J., Contreras, L., Bijl, P.K., Greenwood, D.R., Bohaty, S.M., Schouten, S., Bendle, J. a, Röhl, U., Tauxe, L., Raine, J.I., Huck, C.E., van de Flierdt, T., Jamieson, S.S.R., Stickle, C.E., van de Schootbrugge, B., Escutia, C., Brinkhuis, H., 2012. Persistent near-tropical warmth on the Antarctic continent during the early Eocene epoch. *Nature* 488, 73–77. <https://doi.org/10.1038/nature11300>
- Pudsey, C.J., Camerlenghi, A., 1998. Glacial-interglacial deposition on a sediment drift on the Pacific margin of the Antarctic Peninsula. *Antarct. Sci.* 10, 286–308.
- Pudsey, C.J., Howe, J.A., 1998. Quaternary history of the Antarctic Circumpolar Current: evidence from the Scotia Sea. *Mar. Geol.* 148, 83–112.
- Pugh, R.S., Mccave, I.N., Hillenbrand, C.D., Kuhn, G., 2009. Circum-Antarctic age modelling of Quaternary marine cores under the Antarctic Circumpolar Current: Ice-core dust – magnetic correlation. *Earth Planet. Sc. Lett.* 284, 113–123. <https://doi.org/10.1016/j.epsl.2009.04.016>

- Qin, W., Carlson, L.T., Armbrust, E.V., Devol, A.H., Moffett, J.W., Stahl, D.A., Ingalls, A.E., 2015. Confounding effects of oxygen and temperature on the TEX₈₆ signature of marine Thaumarchaeota. *P. Natl. Acad. Sci. USA* 112, 10979–10984. <https://doi.org/10.1073/pnas.1501568112>
- Radi, T., Bonnet, S., Cormier, M.-A., de Vernal, A., Durantou, L., Faubert, É., Head, M.J., Henry, M., Pospelova, V., Rochon, A., Van Nieuwenhove, N., 2013. Operational taxonomy and (paleo-)autecology of round, brown, spiny dinoflagellate cysts from the Quaternary of high northern latitudes. *Mar. Micropaleontol.* 98, 41–57. <https://doi.org/10.1016/j.marmicro.2012.11.001>
- Radi, T., De Vernal, A., 2008. Dinocysts as proxy of primary productivity in mid-high latitudes of the Northern Hemisphere. *Mar. Micropaleontol.* 68, 84–114. <https://doi.org/10.1016/j.marmicro.2008.01.012>
- Railsback, L.B., Gibbard, P.L., Head, M.J., Voarintsoa, N.R.G., Toucanne, S., 2015. An optimized scheme of lettered marine isotope substages for the last 1.0 million years, and the climatostratigraphic nature of isotope stages and substages. *Quaternary Sci. Rev.* 111, 94–106. <https://doi.org/10.1016/j.quascirev.2015.01.012>
- Ravara, A., Marçal, A.R., Wiklund, H., Hilário, A., 2015. First account on the diversity of *Ophryotrocha* (Annelida, Dorvilleidae) from a mammal-fall in the deep-Atlantic Ocean with the description of three new species. *Syst. Biodivers.* 13, 555–570. <https://doi.org/10.1080/14772000.2015.1047428>
- Razouls, C., de Boyée, F., Kouwenberg, J., Desreumaux, N., 2005-2017. Diversity and Geographic Distribution of Marine Planktonic Copepods. Available at <http://copepodes.obs-bayuls.fr/en> [Accessed 25-12-2017].
- Reichart, G., Brinkhuis, H., 2003. Late Quaternary *Protoperidinium* cysts as indicators of paleoproductivity in the northern Arabian Sea. *Mar. Micropaleontol.* 49, 303–315. [https://doi.org/10.1016/S0377-8398\(03\)00050-1](https://doi.org/10.1016/S0377-8398(03)00050-1)
- Reid, P.C., 1987. Mass encystment of a planktonic oligotrich ciliate. *Mar. Biol.* 95, 221–230.
- Reid, P.C., John, A.W.G., 1983. Resting Cysts in the Ciliate Class Polyhymenophorea: Phylogenetic Implications. *J. Protozool.* 30, 710–713.
- Rembauville, M., Blain, S., Armand, L., Quéguiner, B., Salter, I., 2015. Export fluxes in a naturally iron-fertilized area of the Southern Ocean – Part 2: Importance of diatom resting spores and faecal pellets for export. *Biogeosciences* 12, 3171–3195. <https://doi.org/10.5194/bg-12-3171-2015>
- Rembauville, M., Manno, C., Tarling, G.A., Blain, S., Salter, I., 2016. Strong contribution of diatom resting spores to deep-sea carbon transfer in naturally iron-fertilized waters downstream of South Georgia. *Deep-Sea Res. Pt I* 115, 22–35. <https://doi.org/10.1016/j.dsr.2016.05.002>
- Rengfors, K., Laybourn-Parry, J., Logares, R., Marshall, W.A., Hansen, G., 2008. Marine-Derived Dinoflagellates in Antarctic Saline Lakes: Community Composition and Annual Dynamics. *J. Phycol.* 44, 592–604. <https://doi.org/10.1111/j.1529-8817.2008.00517.x>
- Renssen, H., Goosse, H., Fichetef, T., Masson-Delmotte, V., Koç, N., 2005. Holocene climate evolution in the high-latitude Southern Hemisphere simulated by a coupled atmosphere-sea ice-ocean-vegetation model. *Holocene* 15, 951–964.
- Ribeiro, S., Amorim, A., Abrantes, F., Ellegaard, M., 2016. Environmental change in the Western Iberia Upwelling Ecosystem since the preindustrial period revealed by dinoflagellate cyst records. *Holocene* 26, 874–889. <https://doi.org/10.1177/0959683615622548>

- Ribeiro, S., Amorim, A., Andersen, T.J., Abrantes, F., Ellegaard, M., 2012a. Reconstructing the history of an invasion: the toxic phytoplankton species *Gymnodinium catenatum* in the Northeast Atlantic. *Biol. Invasions* 14, 969–985. <https://doi.org/10.1007/s10530-011-0132-6>
- Ribeiro, S., Moros, M., Ellegaard, M., Kuijpers, A., 2012b. Climate variability in West Greenland during the past 1500 years: evidence from a high-resolution marine palynological record from Disko Bay. *Boreas* 41, 68–83. <https://doi.org/10.1111/j.1502-3885.2011.00216.x>
- Richey, J.N., Tierney, J.E., 2016. GDGT and alkenone flux in the northern Gulf of Mexico: Implications for the TEX₈₆ and U^K₃₇ paleothermometers. *Paleoceanography* 31, 1547–1561. <https://doi.org/10.1002/2016PA003032>
- Riding, J.B., Hubbard, R.N.L.B., 1999. Jurassic (Toarcian to Kimmeridgian) dinoflagellate cysts and paleoclimates. *Palynology* 23, 15–30. <https://doi.org/10.1080/01916122.1999.9989516>
- Riesselman, C.R., Dunbar, R.B., 2013. Diatom evidence for the onset of Pliocene cooling from AND-1B, McMurdo Sound, Antarctica. *Palaeogeogr. Palaeoclimatol.* 369, 136–153. <https://doi.org/10.1016/j.palaeo.2012.10.014>
- Rigual-Hernández, A.S., Colmenero-Hidalgo, E., Martrat, B., Bárcena, M.A., Vernal, A. de Sierro, F.J., Flores, J.A., Grimalt, J.O., Henry, M., Lucchi, R.G., 2017. Svalbard ice-sheet decay after the Last Glacial Maximum: New insights from micropalaeontological and organic biomarker paleoceanographical reconstructions. *Palaeogeogr. Palaeoclimatol.* 465, 225–236. <https://doi.org/10.1016/j.palaeo.2016.10.034>
- Rintoul, S.R., 2018. The global influence of localized dynamics in the Southern Ocean. *Nature* 558, 209–218.
- Rintoul, S.R., Chown, S.L., DeConto, R.M., England, M.H., Fricker, H.A., 2018. Choosing the future of Antarctica. *Nature* 558, 233–241. <https://doi.org/10.1038/s41586-018-0173-4>
- Roberts, A.P., Wilson, G.S., Harwood, D.M., Verosub, K.L., 2003. Glaciation across the Oligocene-Miocene boundary in southern McMurdo Sound, Antarctica: New chronology from the CIROS-1 drill hole. *Palaeogeogr. Palaeoclimatol.* 198, 113–130. [https://doi.org/10.1016/S0031-0182\(03\)00399-7](https://doi.org/10.1016/S0031-0182(03)00399-7)
- Robinson, R.S., Kienast, M., Albuquerque, A.L., Altabet, M., Contreras, S., Holz, R.D.P., Dubois, N., Francois, R., Galbraith, E., Hsu, T., Ivanochko, T., Jaccard, S., Kao, S., Kiefer, T., Kienast, S., Lehmann, M., Martinez, P., Mccarthy, M., Möbius, J., Pedersen, T., Quan, T.M., Ryabenko, E., Schmittner, A., Schneider, R., Schneider-Mor, A., Shigemitsu, M., Sinclair, D., Somes, C., Studer, A., Thunell, R., Yang, J.-Y., 2012. A review of nitrogen isotopic alteration in marine sediments. *Paleoceanography* 27, PA4203. <https://doi.org/10.1029/2012PA002321>
- Rodrigo-Gámiz, M., Rampen, S.W., de Haas, H., Baas, M., Schouten, S., Sinninghe Damsté, J.S., 2015. Constraints on the applicability of the organic temperature proxies U^K₃₇, TEX₈₆ and LDI in the subpolar region around Iceland. *Biogeosciences* 12, 6573–6590. <https://doi.org/10.5194/bgd-12-1113-2015>
- Roncaglia, L., 2004a. Palynofacies analysis and organic-walled dinoflagellate cysts as indicators of palaeo-hydrographic changes: an example from Holocene sediments in Skálafjörður, Faroe Islands. *Mar. Micropaleontol.* 50, 21–42. [https://doi.org/10.1016/S0377-8398\(03\)00065-3](https://doi.org/10.1016/S0377-8398(03)00065-3)
- Roncaglia, L., 2004b. New acritarch species from Holocene sediments in central West Greenland. *Grana* 43, 81–88. <https://doi.org/10.1080/00173130410018966>

- Rozema, P.D., Venables, H.J., Poll, W.H. Van De, Clarke, A., Meredith, M.P., Buma, A.G.J., 2017. Interannual variability in phytoplankton biomass and species composition in northern Marguerite Bay (West Antarctic Peninsula) is governed by both winter sea ice cover and summer stratification. *Limnol. Oceanogr.* 62, 235–252. <https://doi.org/10.1002/lno.10391>
- Ruddiman, W.F., 2003. Orbital insolation, ice volume, and greenhouse gases. *Quaternary Sci. Rev.* 22, 1597–1629. [https://doi.org/10.1016/S0277-3791\(03\)00087-8](https://doi.org/10.1016/S0277-3791(03)00087-8)
- Ruggiero, M.A., Gordon, D.P., Orrell, T.M., Bailly, N., Bourgoin, T., Brusca, R.C., Cavalier-Smith, T., Guiry, M.D., Kirk, P.M., 2015. A higher level classification of all living organisms. *PLoS One* 10, 1–60. <https://doi.org/10.1371/journal.pone.0119248>
- Saba, G.K., Fraser, W.R., Saba, V.S., Iannuzzi, R.A., Coleman, K.E., Doney, S.C., Ducklow, H.W., Martinson, D.G., Miles, T.N., Patterson-Fraser, D.L., Stammerjohn, S.E., Steinberg, D.K., Schofield, O.M., 2014. Winter and spring controls on the summer food web of the coastal West Antarctic Peninsula. *Nat. Commun.* 5, 4318. <https://doi.org/10.1038/ncomms5318>
- Sabbatini, A., Morigi, C., Ravaioli, M., Negri, A., 2004. Abyssal benthic foraminifera in the Polar Front region (Pacific sector): Faunal composition, standing stock and size structure. *Chem. Ecol.* 20 (Supple, S117–S129).
- Sackett, W.M., 1986. Organic carbon in sediments underlying the Ross Ice Shelf. *Org. Geochem.* 9, 135–137. [https://doi.org/10.1016/0146-6380\(86\)90103-8](https://doi.org/10.1016/0146-6380(86)90103-8)
- Salabarnada, A., Escutia, C., Röhl, U., Nelson, C.H., McKay, R., Jiménez-Espejo, F., Bijl, P.K., Hartman, J.D., Strother, S.L., Salzmann, U., Evangelinos, D., López-Quirós, A., Flores, J.A., Sangiorgi, F., Ikehara, M., Brinkhuis, H., 2018. Paleocyanography and ice sheet variability offshore Wilkes Land, Antarctica – Part 1: Insights from late Oligocene astronomically paced contourite sedimentation. *Clim. Past* 14, 991–1014. <https://doi.org/10.5194/cp-14-1015-2018>
- Salter, I., Kemp, A.E.S., Moore, C.M., Lampitt, R.S., Wolff, G.A., Holtvoeth, J., 2012. Diatom resting spore ecology drives enhanced carbon export from a naturally iron-fertilized bloom in the Southern Ocean 26, 1–17. <https://doi.org/10.1029/2010GB003977>
- Sangiorgi, F., Bijl, P.K., Passchier, S., Salzmann, U., Schouten, S., McKay, R., Cody, R.D., Pross, J., Van De Flierdt, T., Bohaty, S.M., Levy, R., Williams, T., Escutia, C., Brinkhuis, H., 2018. Southern Ocean warming and Wilkes Land ice sheet retreat during the mid-Miocene. *Nat. Commun.* 9, 317. <https://doi.org/10.1038/s41467-017-02609-7>
- Sangiorgi, F., Donders, T.H., 2004. Reconstructing 150 years of eutrophication in the north-western Adriatic Sea (Italy) using dinoflagellate cysts, pollen and spores. *Estuar. Coast. Shelf S.* 60, 69–79. <https://doi.org/10.1016/j.ecss.2003.12.001>
- Santella, L., Ianora, A., 1990. Subitaneous and diapause eggs in Mediterranean populations of *Pontella mediterranea* (Copepoda: Calanoida): a morphological study. *Mar. Biol.* 105, 83–90.
- Sarjeant, W.A.S., 1981. A Restudy of some Dinoflagellate Cyst Holotypes in the University of Kiel Collections. II. The Eocene Holotypes of Barbara Klumpp (1953); with a Revision of the Genus *Cordosphaeridium* Eisenack, 1963. *Meyniana* 33, 97–132.
- Sarmiento, J.L., Slater, R., Barber, R., Bopp, L., Doney, S.C., Hirst, A.C., Kleypas, J., Matear, R., Mikolajewicz, U., Monfray, P., Soldatov, V., Spall, S.A., Stouffer, R., 2004. Response of ocean ecosystems to climate warming. *Global Biogeochem. Cy.* 18, 1–23. <https://doi.org/10.1029/2003GB002134>

- Scher, H.D., Martin, E.E., 2008. Oligocene deep water export from the North Atlantic and the development of the Antarctic Circumpolar Current examined with neodymium isotopes. *Paleoceanography* 23, 1–12. <https://doi.org/10.1029/2006PA001400>
- Scher, H.D., Martin, E.E., 2006. Timing and climatic consequences of the opening of Drake Passage. *Science* 312, 428–430. <https://doi.org/10.1126/science.1120044>
- Scher, H.D., Whittaker, J.M., Williams, S.E., Latimer, J.C., Kordesch, W.E.C., Delaney, M.L., 2015. Onset of Antarctic Circumpolar Current 30 million years ago as Tasmanian Gateway aligned with westerlies. *Nature* 523, 580–583. <https://doi.org/10.1038/nature14598>
- Schiller, J., 1925. Die planktonischen Vegetationen des adriatischen Meeres. B. Chryomonadina, Heterokontae, Cryptomonadina, Eugleninae, Volvocales. 1. Systematischer Teil, *Arch. Protistenkd.* 53, 59–123.
- Schmitz, F., 1879. Halosphaera, eine neue Gattung grüner Algen aus dem Mittelmeer, in: *Mitteilungen aus der zoologischen Station zu Neapel*, Bd. 1, Wilhelm Engelmann, Leipzig.
- Schnack-Schiel, S.B., 2001. Aspects of the study of the life cycles of Antarctic copepods. *Hydrobiologia* 453–454, 9–24. <https://doi.org/10.1023/A:1013195329066>
- Scholz, B., Liebezeit, G., 2012. Microphytobenthic dynamics in a Wadden Sea intertidal flat - Part II: Seasonal and spatial variability of non-diatom community components in relation to abiotic parameters. *Eur. J. Phycol.* 47, 120–137. <https://doi.org/10.1080/09670262.2012.665251>
- Schouten, S., Hopmans, E.C., M, E.S., 2002. Distributional variations in marine crenarchaeotal membrane lipids: a new tool for reconstructing ancient sea water temperatures? *Earth Planet. Sc. Lett.* 204, 265–274. [https://doi.org/10.1016/S0012-821X\(02\)00979-2](https://doi.org/10.1016/S0012-821X(02)00979-2)
- Schouten, S., Hopmans, E.C., Sinninghe Damsté, J.S., 2013. The organic geochemistry of glycerol dialkyl glycerol tetraether lipids: A review. *Org. Geochem.* 54, 19–61. <https://doi.org/10.1016/j.orggeochem.2012.09.006>
- Schouten, S., Hugué, C., Hopmans, E.C., Kienhuis, M.V.M., Sinninghe Damsté, J.S., 2007. Analytical Methodology for TEX₈₆ Paleothermometry by High-Performance Liquid Chromatography / Atmospheric Pressure Chemical Ionization-Mass Spectrometry. *Anal. Chem.* 79, 2940–2944. <https://doi.org/10.1029/2004PA001110>
- Schrader, H.J., Gersonde, R., 1978. Diatoms and silicoflagellates. Micropaleontological counting methods and techniques: an exercise on an eight metres section of the Lower Pliocene of Capo Rosello, Sicily. *Utrecht Bull. Micropaleontol.* 17, 129–176.
- Schrank, E., 2003. Small acritarchs from the Upper Cretaceous: taxonomy, biological affinities and palaeoecology. *Rev. Palaeobot. Palyno.* 123, 199–235.
- Schuster, R.O., Nelson, D.R., Grigarić, A.A., Christenberry, D., 1980. Systematic criteria of the Eutardigrada. *T. Am. Microsc. Soc.* 99, 3, 284–303.
- Sedwick, P.N., DiTullio, G.R., Mackey, D.J., 2000. Iron and manganese in the Ross Sea, Antarctica: Seasonal iron limitation in Antarctic shelf waters. *J. Geophys. Res.* 105, 11321. <https://doi.org/10.1029/2000JC000256>
- Seidenkrantz, M.-S., Roncaglia, L., Fischel, A., Heilmann-Clausen, C., Kuijpers, A., Moros, M., 2008. Variable North Atlantic climate seesaw patterns documented by a late Holocene marine record from Disko Bugt, West Greenland. *Mar. Micropaleontol.* 68, 66–83. <https://doi.org/10.1016/j.marmicro.2008.01.006>
- Serreze, M.C., Barry, R.G., 2011. Processes and impacts of Arctic amplification: A research synthesis. *Global Planet. Change* 77, 85–96. <https://doi.org/10.1016/j.gloplacha.2011.03.004>

- Shemesh, A., Burckle, L.H., Froelich, P.N., 1989. Dissolution and Preservation of Antarctic Diatoms and the Effect on Sediment Thanatocoenoses. *Quaternary Res.* 31, 288–308.
- Shen, Q., Wang, H., Shum, C.K., Jiang, L., Hsu, H.T., Dong, J., 2018. Recent high-resolution Antarctic ice velocity maps reveal increased mass loss in Wilkes Land, East Antarctica. *Sci. Rep.* 8, 4477. <https://doi.org/10.1038/s41598-018-22765-0>
- Shevenell, A.E., Ingalls, A.E., Domack, E.W., Kelly, C., 2011. Holocene Southern Ocean surface temperature variability west of the Antarctic Peninsula. *Nature* 470, 250–254. <https://doi.org/10.1038/nature09751>
- Shevenell, A.E., Kennett, J.P., Lea, D.W., 2004. Middle Miocene Southern Ocean cooling and Antarctic cryosphere expansion. *Science* 305, 1766–1770. <https://doi.org/10.1126/science.1100061>
- Shimmield, G., Derrick, S., Mackensen, A., Grobe, H., Pudsey, C., 1994. The history of barium, biogenic silica and organic carbon accumulation in the Weddell Sea and Antarctic Ocean over the last 150,000 years, in: Zahn, R., Kaminski, M.A., Labeyrie, L., Pedersen, T.F. (Eds.), *Carbon Cycling in the Glacial Ocean: Constraints on the Ocean's Role in Global Change*, NATO ASI Series, Springer, Berlin, Heidelberg, New York, 117, pp. 555–574.
- Sigman, D.M., Fripiat, F., Studer, A.S., Kerneny, P.C., Martínez-García, A., Hain, M.P., Ai, X., Wang, X., Ren, H., Haug, G.H., 2021. The Southern Ocean during the ice ages: A review of the Antarctic surface isolation hypothesis, with comparison to the North Pacific. *Quaternary Sci. Rev.* 254, 106732. <https://doi.org/10.1016/j.quascirev.2020.106732>
- Sigman, D.M., Hain, M.P., Haug, G.H., 2010. The polar ocean and glacial cycles in atmospheric CO₂ concentration. *Nature* 466, 47–55. <https://doi.org/10.1038/nature09149>
- Sigman, D.M., Jaccard, S.L., Haug, G.H., 2004. Polar ocean stratification in a cold climate. *Nature* 428, 59–63. <https://doi.org/10.1038/nature02378.1>
- Sinninghe Damsté, J.S., 2016. Spatial heterogeneity of sources of branched tetraethers in shelf systems: The geochemistry of tetraethers in the Berau River delta (Kalimantan, Indonesia). *Geochim. Cosmochim. Ac.* 186, 13–31. <https://doi.org/10.1016/j.gca.2016.04.033>
- Sinninghe Damsté, J.S., Ossebaar, J., Abbas, B., Schouten, S., Verschuren, D., 2009. Fluxes and distribution of tetraether lipids in an equatorial African lake: Constraints on the application of the TEX₈₆ palaeothermometer and BIT index in lacustrine settings. *Geochim. Cosmochim. Ac.* 73, 4232–4249. <https://doi.org/10.1016/j.gca.2009.04.022>
- Sluijs, A., Bijl, P.K., Schouten, S., Röhl, U., Reichert, G.-J., Brinkhuis, H., 2011. Southern ocean warming, sea level and hydrological change during the Paleocene-Eocene thermal maximum. *Clim. Past* 7, 47–61. <https://doi.org/10.5194/cp-7-47-2011>
- Sluijs, A., Brinkhuis, H., Stickley, C.E., Warnaar, J., Williams, G.L., Fuller, M., 2003. Dinoflagellate Cysts From the Eocene–Oligocene Transition in the Southern Ocean: Results From ODP Leg 189, in: Exon, N.F., Kennett, J.P., Malone, M.J. (Eds.), *Proceedings of the Ocean Drilling Program, Scientific Results*. pp. 1–42.
- Sluijs, A., Brinkhuis, H., Williams, G.L., Fensome, R.A., 2009. Taxonomic revision of some Cretaceous–Cenozoic spiny organic-walled peridiniacean dinoflagellate cysts. *Rev. Palaeobot. Palyno.* 154, 34–53. <https://doi.org/10.1016/j.revpalbo.2008.11.006>
- Sluijs, A., Röhl, U., Schouten, S., Brumsack, H.-J., Sangiorgi, F., Sinninghe Damsté, J.S., Brinkhuis, H., 2008. Arctic late Paleocene–Early Eocene paleoenvironments with special emphasis on the Paleocene-Eocene thermal maximum (Lomonosov Ridge, Integrated Ocean Drilling Program Expedition 302). *Paleoceanography* 23, PA1S11. <https://doi.org/10.1029/2007PA001495>

- Sluijs, A., Schouten, S., Pagani, M., Woltering, M., Brinkhuis, H., Sinninghe Damsté, J.S., Dickens, G.R., Huber, M., Reichart, G.-J., Stein, R., Matthiessen, J., Lourens, L.J., Pedentchouk, N., Backman, J., Moran, K., Clemens, S., Cronin, T., Eynaud, F., Gattacceca, J., Jakobsson, M., Jordan, R., Kaminski, M., King, J., Koc, N., Martinez, N.C., McInroy, D., Moore Jr., T.C., O'Regan, M., Onodera, J., Pälike, H., Rea, B., Rio, D., Sakamoto, T., Smith, D.C., St John, K.E.K., Suto, I., Suzuki, N., Takahashi, K., Watanabe, M., Yamamoto, M., 2006. Subtropical Arctic Ocean temperatures during the Palaeocene/Eocene thermal maximum. *Nature* 441, 610–613. <https://doi.org/10.1038/nature04668>
- Small, E.B., Lynn, D.H., 1985. Phylum Ciliophora, in: Lee, J.J., Hunter, S.H., Bovee, E.C. (Eds.), *An Illustrated Guide to the Protozoa*, Society of Protozoool. Spec. Publ., Lawrence, Kansas, pp. 393–575.
- Smith, J.A., Graham, A.G.C., Post, A.L., Hillenbrand, C., Bart, P.J., Powell, R.D., 2019. The marine geological imprint of Antarctic ice shelves. *Nat. Commun.* 10:5635. <https://doi.org/10.1038/s41467-019-13496-5>
- Smith, J.A., Hillenbrand, C., Pudsey, C.J., Allen, C.S., Graham, A.G.C., 2010. The presence of polynyas in the Weddell Sea during the Last Glacial Period with implications for the reconstruction of sea-ice limits and ice sheet history. *Earth Planet. Sc. Lett.* 296, 287–298. <https://doi.org/10.1016/j.epsl.2010.05.008>
- Smith Jr., W.O., Marra, J., Hiscock, M.R., Barber, R.T., 2000. The seasonal cycle of phytoplankton biomass and primary productivity in the Ross Sea, Antarctica. *Deep-Sea Res. Pt II* 47, 3119–3140. [https://doi.org/10.1016/S0967-0645\(00\)00061-8](https://doi.org/10.1016/S0967-0645(00)00061-8)
- Smith Jr., W.O., Shields, A.R., Dreyer, J.C., Peloquin, J.A., Asper, V., 2011. Interannual variability in vertical export in the Ross Sea: Magnitude, composition, and environmental correlates. *Deep-Sea Res. Pt I* 58, 147–159. <https://doi.org/10.1016/j.dsr.2010.11.007>
- Smith Jr., W.O., Shields, A.R., Peloquin, J.A., Catalano, G., Tozzi, S., Dinniman, M.S., Asper, V.A., 2006. Interannual variations in nutrients, net community production, and biogeochemical cycles in the Ross Sea. *Deep-Sea Res. Pt II* 53, 815–833. <https://doi.org/10.1016/j.dsr2.2006.02.014>
- Smith, W.O.J., Sedwick, P.N., Arrigo, K.R., Ainley, D.G., Orsi, A.H., 2012. The Ross Sea in a sea of change. *Oceanography* 25, 90–103.
- Sorlien, C.C., Luyendyk, B.P., Wilson, D.S., Decesari, R.C., Bartek, L.R., Diebold, J.B., 2007. Oligocene development of the West Antarctic Ice Sheet recorded in eastern Ross Sea strata. *Geology* 35, 467–470. <https://doi.org/10.1130/G23387A.1>
- Spallanzani, L., 1776. *Opuscoli di fisica animale, e vegetabile*, Volume Secondo, Presso la Societa Tipografica, p. 277.
- Spilling, K., Ylöstalo, P., Simis, S., Seppälä, J., 2015. Interaction Effects of Light, Temperature and Nutrient Limitations (N, P and Si) on Growth, Stoichiometry and Photosynthetic Parameters of the Cold-Water Diatom *Chaetoceros wighamii*. *PLoS One* 10, e0126308. <https://doi.org/10.1371/journal.pone.0126308>
- Spreen, G., Kaleschke, L., Heygster, G., 2008. Sea ice remote sensing using AMSR-E 89-GHz channels. *J. Geophys. Res.* 113, C02S03. <https://doi.org/10.1029/2005JC003384>
- Stammerjohn, S.E., Martinson, D.G., Smith, R.C., Yuan, X., Rind, D., 2008. Trends in Antarctic annual sea ice retreat and advance and their relation to El Niño – Southern Oscillation and Southern Annular Mode variability. *J. Geophys. Res.* 113, C03S90. <https://doi.org/10.1029/2007JC004269>

- Stap, L.B., van de Wal, R.S.W., de Boer, B., Bintanja, R., Lourens, L.J., 2017. The influence of ice sheets on temperature during the past 38 million years inferred from a one-dimensional ice sheet – climate model. *Clim. Past* 13, 1243–1257.
- Steinacher, M., Joos, F., Frölicher, T.L., Bopp, L., Cadule, P., Cocco, V., Doney, S.C., Gehlen, M., Lindsay, K., Moore, J.K., Schneider, B., Segschneider, J., 2010. Projected 21st century decrease in marine productivity: a multi-model analysis. *Biogeosciences* 7, 979–1005.
- Stephens, B.B., Keeling, R.F., 2000. The influence of Antarctic sea ice on glacial-interglacial CO₂ variations. *Nature* 404, 171–174.
- Stickley, C.E., Brinkhuis, H., Schellenberg, S.A., Sluijs, A., Röhl, U., Fuller, M., Grauert, M., Huber, M., Warnaar, J., Williams, G.L., 2004. Timing and nature of the deepening of the Tasmanian Gateway. *Paleoceanography* 19, 1–18.
<https://doi.org/10.1029/2004PA001022>
- Stickley, C.E., Pike, J., Leventer, A., Dunbar, R., Domack, E.W., Brachfeld, S., Manley, P., McClennan, C., 2005. Deglacial ocean and climate seasonality in laminated diatom sediments, Mac.Robertson Shelf, Antarctica. *Palaeogeogr. Palaeoclimatol.* 227, 290–310.
<https://doi.org/10.1016/j.palaeo.2005.05.021>
- Stirling, I., 1997. The importance of polynas, ice edges, and leads to marine mammals and birds. *J. Marine Syst.* 10, 9–21. [https://doi.org/10.1016/S0924-7963\(96\)00054-1](https://doi.org/10.1016/S0924-7963(96)00054-1)
- Stocchi, P., Escutia, C., Houben, A.J.P., Vermeersen, B.L.A., Bijl, P.K., Brinkhuis, H., DeConto, R.M., Galeotti, S., Passchier, S., Pollard, D., Brinkhuis, H., Escutia, C., Klaus, A., Fehr, A., Williams, T., Bendle, J.A.P., Bijl, P.K., Bohaty, S.M., Carr, S.A., Dunbar, R.B., Flores, J.A., González, J.J., Hayden, T.G., Iwai, M., Jimenez-Espejo, F.J., Katsuki, K., Kong, G.S., McKay, R.M., Nakai, M., Olney, M.P., Passchier, S., Pekar, S.F., Pross, J., Riesselman, C., Röhl, U., Sakai, T., Shrivastava, P.K., Stickley, C.E., Sugisaki, S., Tauxe, L., Tuo, S., van de Flierdt, T., Welsh, K., Yamane, M., 2013. Relative sea-level rise around East Antarctica during Oligocene glaciation. *Nat. Geosci.* 6, 380–384. <https://doi.org/10.1038/ngeo1783>
- Stoecker, D.K., 2013. Predators of Tintinnids, in: Dolan, J.R., Montagnes, D.J.S., Agatha, S., Coats, D.W., Stoecker, D.K. (Eds.), *The Biology and Ecology of Tintinnid Ciliates: Models for Marine Plankton*. Wiley-Blackwell, Hoboken, New Jersey, USA, pp. 122–144.
- Stoecker, D.K., Gustafson, D.E., Baier, C.T., Black, M.M.D., 2000. Primary production in the upper sea ice. *Aquat. Microb. Ecol.* 21, 275–287. <https://doi.org/10.3354/ame021275>
- Stoecker, D.K., Gustafson, D.E., Merrell, J.R., Black, M.M.D., Baier, C.T., 1997. Excystment and growth of chrysophytes and dinoflagellates at low temperatures and high salinities in Antarctic sea-ice. *J. Phycol.* 33, 585–595. <https://doi.org/10.1111/j.0022-3646.1997.00585.x>
- Storkey, C.A., 2006. *Distribution of Marine Palynomorphs in Surface Sediments, Prydz Bay, Antarctica*. Victoria University of Wellington.
- Stover, L.E., Evitt, W.R., 1978. Analyses of pre-Pleistocene organic-walled dinoflagellates, *Stanford Univ. Publ. Geol. Sci.* 15, 1–300.
- Stover, L.E., Williams, G.L., 1995. A revision of the Paleogene dinoflagellate genera *Areosphaeridium* Eaton 1971 and *Eatonicysta* Stover and Evitt 1978, *Micropaleontology* 41, 97–141.
- Strickland, J.D.H., Parsons, T.R., 1972. *A practical handbook of seawater analysis*, 2nd ed. Fisheries Research Board of Canada, Ottawa.
- Strother, S.L., Salzmann, U., Sangiorgi, F., Bijl, P.K., Pross, J., Escutia, C., 2017. A new quantitative approach to identify reworking in Eocene to Miocene pollen records from offshore

- Antarctica using red fluorescence and digital imaging. *Biogeosciences* 14, 2089–2100. <https://doi.org/10.5194/bg-14-2089-2017>
- Struck, T.H., Purschke, G., Halanych, K.M., 2006. Phylogeny of Eunicida (Annelida) and Exploring Data Congruence Using a Partition Addition Bootstrap Alteration (PABA) Approach. *Syst. Biol.* 55, 1–20.
- Strüder-Kypke, M.C., Lynn, D.H., 2008. Morphological versus molecular data – Phylogeny of tintinnid ciliates (Ciliophora, Choreotrichia) inferred from small subunit rRNA gene sequences. *Denisia* 23, 417–424.
- Studer, A.S., Sigman, D.M., Martínez-garcía, A., Benz, V., Winckler, G., Kuhn, G., Esper, O., Lamy, F., Jaccard, S.L., Wacker, L., Oleynik, S., Gersonde, R., Haug, G.H., 2015. Antarctic Zone nutrient conditions during the last two glacial cycles. *Paleoceanography* 30, 845–862. <https://doi.org/10.1002/2014PA002745>. Received
- Subramoniam, T., 2017. Spermatophore and Sperm Transfer Mechanisms, in: Subramoniam, T. (Ed.), *Sexual Biology and Reproduction in Crustaceans*. Academic Press, Amsterdam, pp. 325–367. <https://doi.org/10.1016/B978-0-12-809337-5.00012-5>
- Suda, S., Bhuiyan, M.A.H., Faria, D.G., 2013. Genetic diversity of *Pyramimonas* from Ryukyu Archipelago, Japan (Chlorophyceae, Pyramimonadales). *J. Mar. Sci. Technol.* 21, 285–296. <https://doi.org/10.6119/JMST-013-1220-16>
- Super, J.R., Thomas, E., Pagani, M., Huber, M., Brien, C.O., Hull, P.M., 2018. North Atlantic temperature and pCO₂ coupling in the early-middle Miocene. *Geology* 46, 519–522. <https://doi.org/https://doi.org/10.1130/G40228.1>
- Sütő, Z., Szegő, É., 2008. Szervesvázú mikroplankton-vizsgálatok az erdélyi-medencei marosorbói (Orba de Mures) szarmata és pannóniai emelet határsztratotípus rétegeiből. *Földtani Közlöny* 138, 279–296.
- Sütőné Szentai, M., 2012. Szervesvázú mikroplankton zónák a szarmata és a pannóniai emeletek határan Magyarországról. *Acta Nat. Pannonica* 4, 5–34.
- Suwa, M., Bender, M.L., 2008. Chronology of the Vostok ice core constrained by O₂/N₂ ratios of occluded air, and its implication for the Vostok climate records 27, 1093–1106. <https://doi.org/10.1016/j.quascirev.2008.02.017>
- Swadling, M.K., 1998. Influence of Seasonal Ice Formation on Life Cycle Strategies of Antarctic Copepods. University of Tasmania, Hobart.
- Szaniawski, H., 2002. New evidence for the protoconodont origin of chaetognaths. *Acta Palaeontol. Pol.* 47, 405–419.
- Szaniawski, H., Wrona, R., 1987. Polychaete jaws from the Cape Melville Formation (Lower Miocene) of King George Island, West Antarctica. *Palaeontologia Polonica* 49, 105–125.
- Taboada, S., Bas, M., Avila, C., 2015. A new *Parougia* species (Annelida, Dorvilleidae) associated with eutrophic marine habitats in Antarctica. *Polar Biol.* 38, 517–527. <https://doi.org/10.1007/s00300-014-1614-7>
- Taboada, S., Wiklund, H., Glover, A.G., Dahlgren, T.G., Cristobo, J., 2013. Two new Antarctic *Ophryotrocha* (Annelida: Dorvilleidae) described from shallow-water whale bones. *Polar Biol.* 36, 1031–1045. <https://doi.org/10.1007/s00300-013-1326-4>
- Takahashi, K., 1967. Upper Cretaceous and Lower Paleogene microfloras of Japan. *Rev. Palaeobot. Palyno.* 5, 227–234.
- Takahashi, K., 1964. Microplankton from the Asagai Formation in the Joban Coal-Field. *Trans. Proc. Paleontol. Soc. Japan N.S.* 54, 201–214.
- Takahashi, T., Sutherland, S.C., Sweeney, C., Poisson, A., MetzI, N., Tilbrook, B., Bates, N., Wanninkhof, R., Feely, R.A., Sabine, C., Olafsson, J., Nojiri, Y., 2002. Global sea-air CO₂

- flux based on climatological surface ocean pCO₂, and seasonal biological and temperature effects. *Deep-Sea Res. Pt II* 49, 1601–1622. [https://doi.org/10.1016/S0967-0645\(02\)00003-6](https://doi.org/10.1016/S0967-0645(02)00003-6)
- Takahashi, T., Sutherland, S.C., Wanninkhof, R., Sweeney, C., Feely, R.A., Chipman, D.W., Hales, B., Friederich, G., Chavez, F., Sabine, C., Watson, A., Bakker, D.C.E., Schuster, U., Metzl, N., Yoshikawa-Inoue, H., Ishii, M., Midorikawa, T., Nojiri, Y., Körtzinger, A., Steinhoff, T., Hoppema, M., Olafsson, J., Arnarson, T.S., Tilbrook, B., Johannessen, T., Olsen, A., Bellerby, R., Wong, C.S., Delille, B., Bates, N.R., de Baar, H.J.W., 2009. Climatological mean and decadal change in surface ocean pCO₂, and net sea-air CO₂ flux over the global oceans. *Deep-Sea Res. Pt II* 56, 554–577. <https://doi.org/10.1016/j.dsr2.2008.12.009>
- Tauxe, L., Stickley, C.E., Sugisaki, S., Bijl, P.K., Bohaty, S.M., Brinkhuis, H., Escutia, C., Flores, J.A., Houben, A.J.P., Iwai, M., Jiménez-Espejo, F., McKay, R., Passchier, S., Pross, J., Riesselman, C.R., Röhl, U., Sangiorgi, F., Welsh, K., Klaus, A., Fehr, A., Bendle, J.A.P., Dunbar, R., González, J., Hayden, T., Katsuki, K., Olney, M.P., Pekar, S.F., Shrivastava, P.K., van de Flierdt, T., Williams, T., Yamane, M., 2012. Chronostratigraphic framework for the IODP Expedition 318 cores from the Wilkes Land Margin: Constraints for paleoceanographic reconstruction. *Paleoceanography* 27, PA2214. <https://doi.org/10.1029/2012PA002308>
- Taylor, F.J.R., 1980. On dinoflagellate evolution, *BioSystems* 13, 65–108.
- Taylor, K.W.R., Huber, M., Hollis, C.J., Hernandez-Sanchez, M.T., Pancost, R.D., 2013. Re-evaluating modern and Palaeogene GDGT distributions: Implications for SST reconstructions. *Global Planet. Change* 108, 158–174. <https://doi.org/10.1016/j.gloplacha.2013.06.011>
- Teller, J.T., Leverington, D.W., Mann, J.D., 2002. Freshwater outburst to the oceans from glacial Lake Agassiz and their role in climate change during the last glaciation. *Quaternary Sci. Rev.* 21, 879–887.
- Terazaki, M., Takahashi, K.T., Odate, T., 2013. Zonal variations in abundance and body length of chaetognaths in the 140°E seasonal ice zone during the austral summer of 2001 / 02. *Polar Sci.* 7, 39–47. <https://doi.org/10.1016/j.polar.2013.02.002>
- Tesi, T., Miserocchi, S., Goñi, M.A., Langone, L., 2007. Source, transport and fate of terrestrial organic carbon on the western Mediterranean Sea, Gulf of Lions, France. *Mar. Chem.* 105, 101–117. <https://doi.org/10.1016/j.marchem.2007.01.005>
- The IMBRIE team, 2018. Mass balance of the Antarctic Ice Sheet from 1992 to 2017. *Nature* 558, 219–222.
- Thöle, L.M., Nootboom, P.D., Hou, S., Wang, R., Nie, S., Michel, E., Sauermilch, I., Marret, F., Sangiorgi, F., Bijl, P.K., 2023. An expanded database of Southern Hemisphere surface sediment dinoflagellate cyst assemblages and their oceanographic affinities. *J. Micropalaeontol.* 42, 35–56.
- Thomas, E., Booth, L., Maslin, M., Shackleton, N.J., 1995. Northeastern Atlantic benthic foraminifera during the last 45,000 years: Changes in productivity seen from the bottom up. *Paleoceanography*. <https://doi.org/10.1029/94PA03056>
- Thomas, E., Gooday, A.J., 1996. Cenozoic deep-sea benthic foraminifers: Tracers for changes in oceanic productivity? *Geology* 24, 355–358.
- Thompson, D.W.J., Wallace, J.M., 2000. Annular Modes in the Extratropical Circulation. Part I: Month-to-Month Variability. *J. Climate* 13, 1000–1016.

- Thompson, D.W.J., Wallace, J.M., Hegerl, G.C., 2000. Annular Modes in the Extratropical Circulation. Part II: Trends. *J. Climate* 13, 1018–1036.
- Thomson, P.G., McMinn, A., Kiessling, I., Watson, M., Goldsworthy, P.M., 2006. Composition and succession of dinoflagellates and chrysophytes in the upper fast ice of Davis Station, East Antarctica. *Polar Biol.* 29, 337–345. <https://doi.org/10.1007/s00300-005-0060-y>
- Thomson, P.G., Wright, S.W., Bolch, C.J.S., Nichols, P.D., Skerratt, J.H., McMinn, A., 2004. Antarctic distribution, pigment and lipid composition, and molecular identification of the brine dinoflagellate *Polarella glacialis* (Dinophyceae). *J. Phycol.* 40, 867–873. <https://doi.org/10.1111/j.1529-8817.2004.03169.x>
- Thorrington-Smith, M., 1970. Some new and little known phytoplankton forms from the West Indian Ocean. *Brit. Phycol. J.* 5, 51–56. <https://doi.org/10.1080/00071617000650071>
- Thorsen, T.A., Dale, B., Nordberg, K., 1995. 'Blooms' of the toxic dinoflagellate *Gymnodinium catenatum* as evidence of climatic fluctuations in the late Holocene of southwestern Scandinavia. *The Holocene* 5, 435–446.
- Thronsdon, J., 1997. The planktonic marine flagellates, in: Tomas, C.R. (Ed.), *Identifying marine phytoplankton*. Academic Press, San Diego, pp. 591–730.
- Thulin, G., 1928. Über die Phylogenie und das System der Tardigraden, *Hereditas*, 11, 207–266.
- Tierney, J.E., Tingley, M.P., 2015. A TEX₈₆ surface sediment database and extended Bayesian calibration. *Sci. Data* 2, 150029. <https://doi.org/10.1038/sdata.2015.29>
- Tierney, J.E., Tingley, M.P., 2014. A Bayesian, spatially-varying calibration model for the TEX₈₆ proxy. *Geochim. Cosmochim. Ac.* 127, 83–106. <https://doi.org/10.1016/j.gca.2013.11.026>
- Tragin, M., Lopes dos Santos, A., Christen, R., Vaulot, D., 2016. Diversity and ecology of green microalgae in marine systems: an overview based on 18S rRNA gene sequences. *Perspect. Phycol.* 3, 141–154. <https://doi.org/10.1127/pip/2016/0059>
- Traverse, A., Ginsburg, R.N., 1966. Palynology of the surface sediments of Great Bahama Bank, as related to water movement and sedimentation. *Mar. Geol.* 4, 417–459. [https://doi.org/10.1016/0025-3227\(66\)90010-7](https://doi.org/10.1016/0025-3227(66)90010-7)
- Troedson, A.L., Riding, J.B., 2002. Upper Oligocene to Lowermost Miocene Strata of King George Island, South Shetland Islands, Antarctica: Stratigraphy, Facies Analysis, and Implications for the Glacial History of the Antarctic Peninsula. *J. Sediment. Res.* 72, 510–523. <https://doi.org/10.1306/110601720510>
- Trommer, G., Siccha, M., van der Meer, M.T.J., Schouten, S., Sinninghe Damsté, J.S., Schulz, H., Hemleben, C., Kucera, M., 2009. Distribution of Crenarchaeota tetraether membrane lipids in surface sediments from the Red Sea. *Org. Geochem.* 40, 724–731. <https://doi.org/10.1016/j.orggeochem.2009.03.001>
- Truswell, E.M., 1982. Palynology of seafloor samples collected by the 1911–14 Australasian Antarctic Expedition: Implications for the geology of coastal East Antarctica. *J. Geol. Soc. Aust.* 29, 343–356. <https://doi.org/10.1080/00167618208729218>
- Turner, J., Bracegirdle, T.J., Phillips, T., Marshall, G.J., Scott Hosking, J., 2013. An initial assessment of antarctic sea ice extent in the CMIP5 models. *J. Climate* 26, 1473–1484. <https://doi.org/10.1175/JCLI-D-12-00068.1>
- Turner, J., Comiso, J., 2017. Solve Antarctica's sea-ice puzzle. *Nature* 547, 275–277.
- Turner, J., Comiso, J.C., Marshall, G.J., Lachlan-Cope, T.A., Bracegirdle, T., Maksym, T., Meredith, M.P., Wang, Z., Orr, A., 2009. Non-annular atmospheric circulation change induced by stratospheric ozone depletion and its role in the recent increase of Antarctic sea ice

- extent. *Geophysical Research Letters* 36, L08502.
<https://doi.org/10.1029/2009GL037524>
- Ulrich, E.O., Bassler, R.S., 1926. A Classification of the toothlike fossils, Conodonts, with descriptions of American Devonian and Mississippian species. *Proc. U.S. Natl. Museum* 68, 1–63.
- Van Hinsbergen, D.J.J., Groot, L.V. De, van Schaik, S.J., Spakman, W., Bijl, P.K., Sluijs, A., Langereis, C.G., Brinkhuis, H., 2015. A Paleolatitude Calculator for Paleoclimate Studies. *PLoS One* 10, 1–21. <https://doi.org/10.5281/zenodo.16166>.
- Van Waveren, I.M., 1992. Morphology of probable planktonic crustacean eggs from the Holocene of the Banda Sea (Indonesia), in: Head, M.J., Wrenn, J.H. (Eds.). *Neogene and Quaternary dinoflagellate cysts and acritarchs*. American Association of Stratigraphic Palynologists Foundation, Dallas, pp. 89–120.
- Vancoppenolle, M., Bopp, L., Madec, G., Dunne, J., Ilyina, T., Halloran, P.R., Steiner, N., 2013. Future Arctic Ocean primary productivity from CMIP5 simulations: Uncertain outcome, but consistent mechanisms. *Global Biogeochem. Cy.* 27, 605–619.
<https://doi.org/10.1002/gbc.20055>
- Varela, M., Fernandez, E., Serret, P., 2002. Size-fractionated phytoplankton biomass and primary production in the Gerlache and south Bransfield Straits (Antarctic Peninsula) in Austral summer 1995–1996. *Deep-Sea Res. Pt II* 49, 749–768.
- Veen, A., Hof, C.H.J., Kouwets, F.A.C., Berkhout, T., 2015. Rijkswaterstaat Waterdienst, Informatiehuis Water, <http://ipt.nlbif.nl/ipt/resource?r=checklist-twn>, consulted 08-02-2018 via GBIF.org
- Venkatesan, M.I., Kaplan, I.R., 1987. The lipid geochemistry of Antarctic marine sediments: Bransfield Strait. *Mar. Chem.* 21, 347–375.
- Veres, D., Bazin, L., Landais, A., Toyé Mahamadou Kele, H., Lemieux-Dudon, B., Parrenin, F., Martinerie, P., Blayo, E., Blunier, T., Capron, E., Chappellaz, J., Rasmussen, S.O., Severi, M., Svensson, A., Vinther, B., Wolff, E.W., 2013. The Antarctic ice core chronology (AICC2012): an optimized multi-parameter and multi-site dating approach for the last 120 thousand years. *Clim. Past* 9, 1733–1748. <https://doi.org/10.5194/cp-9-1733-2013>
- Verleye, T.J., Louwye, S., 2010. Recent geographical distribution of organic-walled dinoflagellate cysts in the southeast Pacific (25–53°S) and their relation to the prevailing hydrographical conditions. *Palaeogeogr. Palaeocl.* 298, 319–340.
<https://doi.org/10.1016/j.palaeo.2010.10.006>
- Versteegh, G.J.M., Zonneveld, K.A.F., 2002. Use of selective degradation to separate preservation from productivity. *Geology* 30, 615–618.
- Versteegh, G.J.M., Zonneveld, K.A.F., 1994. Determination of (palaeo-)ecological preferences of dinoflagellates by applying Detrended and Canonical Correspondence analysis to Late Pliocene dinoflagellate cyst assemblages of the south Italian Singa section. *Rev. Palaeobot. Palyno.* 84, 181–199. [https://doi.org/10.1016/0034-6667\(94\)90050-7](https://doi.org/10.1016/0034-6667(94)90050-7)
- Villanueva, L., Schouten, S., Sinninghe Damsté, J.S., 2015. Depth-related distribution of a key gene of the tetraether lipid biosynthetic pathway in marine Thaumarchaeota. *Environ. Microbiol.* 17, 3527–3539. <https://doi.org/10.1111/1462-2920.12508>
- Von Siebold, C.T., 1848. *Lehrbuch der vergleichenden Anatomie der wirbellosen Thiere*, in: Von Siebold, C.T., Stannius, H. (Eds.), *Lehrbuch der vergleichenden Anatomie, Erster Theil, Veit and Comp., Berlin*, pp. 1–679.
- Walker, M.J.C., Berkelhammer, M., Björck, S., Cwynar, L.C., Fisher, D.A., Long, A.J., Lowe, J.J., Newnham, R.M., Rasmussen, S.O., Weiss, H., 2012. Formal subdivision of the Holocene

- Series/Epoch: A Discussion Paper by a Working Group of INTIMATE (Integration of ice-core, marine and terrestrial records) and the Subcommission on Quaternary Stratigraphy (International Commission on Stratigraphy). *J. Quaternary Sci.* 27, 649–659. <https://doi.org/10.1002/jqs.2565>
- Wall, D., Dale, B., Harada, K., 1973. Description of new fossil dinoflagellates from the Late Quaternary of the Black Sea. *Micropaleontology* 19, pp. 18–31.
- Wang, X.-F., 2010. fANCOVA: Non-parametric analysis of covariance. <https://CRAN.R-project.org/package=fANCOVA>, accessed 27-08-2018
- Warnaar, J., 2006. Climatological implications of Australian-Antarctic separation, Utrecht University, Utrecht, The Netherlands.
- Warny, S., 2009. Species of the acritarch genus *Palaeostomocystis* Deflandre 1937: Potential indicators of neritic subpolar to polar environments in Antarctica during the Cenozoic. *Palynology* 33, 43–54. <https://doi.org/10.1080/01916122.2009.9989682>
- Warny, S., Askin, R.A., Hannah, M.J., Mohr, B.A.R., Raine, J.I., Harwood, D.M., Florindo, F., Team, the S.S., 2009. Palynomorphs from a sediment core reveal a sudden remarkably warm Antarctica during the middle Miocene. *Geology* 37, 955–958. <https://doi.org/10.1130/G30139A.1>
- Warny, S., Kymes, C.M., Askin, R.A., Krajewski, K.P., Bart, P.J., 2016. Remnants of Antarctic vegetation on King George Island during the early Miocene Melville Glaciation. *Palynology* 40, 66–82. <https://doi.org/10.1080/01916122.2014.999954>
- Warny, S., Wrenn, J.H., Bart, P.J., Askin, R., 2006. Palynology of the NBP03-01 A Transect in the Northern Basin, Western Ross Sea, Antarctica: a Late Pliocene Record. *Palynology* 30, 151–182.
- Wasik, A., 1998. Antarctic Tintinnids: Their Ecology, Morphology, Ultrastructure and Polymorphism. *Acta Protozool.* 37, 5–15.
- Wasik, A., Mikolajczyk, E., Ligowski, R., 1996. Agglutinated loricae of some Baltic and Antarctic Tintinnina species (Ciliophora). *J. Plankton Res.* 18, 1931–1940.
- Weijers, J.W.H., Lim, K.L.H., Aquilina, A., Sinninghe Damsté, J.S., Pancost, R.D., 2011. Biogeochemical controls on glycerol dialkyl glycerol tetraether lipid distributions in sediments characterized by diffusive methane flux. *Geochem. Geophys. Geosy.* 12, Q10010. <https://doi.org/10.1029/2011GC003724>
- Weijers, J.W.H., Schefuß, E., Kim, J., Sinninghe, J.S., Schouten, S., 2014. Constraints on the sources of branched tetraether membrane lipids in distal marine sediments. *Org. Geochem.* 72, 14–22. <https://doi.org/10.1016/j.orggeochem.2014.04.011>
- Weijers, J.W.H., Schouten, S., Hopmans, E.C., Geenevasen, J.A.J., David, O.R.P., Coleman, J.M., Pancost, R.D., Sinninghe Damsté, J.S., 2006. Membrane lipids of mesophilic anaerobic bacteria thriving in peats have typical archaeal traits. *Environ. Microbiol.* 8, 648–657. <https://doi.org/10.1111/j.1462-2920.2005.00941.x>
- Westerhold, T., Bickert, T., Röhl, U., 2005. Middle to late Miocene oxygen isotope stratigraphy of ODP site 1085 (SE Atlantic): New constrains on Miocene climate variability and sea-level fluctuations. *Palaeogeogr. Palaeoclimatol.* 217, 205–222. <https://doi.org/10.1016/j.palaeo.2004.12.001>
- Westerhold, T., Marwan, N., Drury, A.J., Liebrand, D., Agnini, C., Anagnostou, E., Barnet, J.S.K., Bohaty, S.M., Vleeschouwer, D. De, Florindo, F., Frederichs, T., Hodell, D.A., Holbourn, A.E., Kroon, D., Lauretano, V., Littler, K., Lourens, L.J., Lyle, M., Pälike, H., Röhl, U., Tian, J., Wilkens, R.H., Wilson, P.A., Zachos, J.C., 2020. An astronomically dated record of

- Earth's climate and its predictability over the last 66 million years. *Science* 369, 1383–1387.
- Wiersma, A.P., Renssen, H., 2006. Model – data comparison for the 8.2 ka BP event: confirmation of a forcing mechanism by catastrophic drainage of Laurentide Lakes. *Quaternary Sci. Rev.* 25, 63–88. <https://doi.org/10.1016/j.quascirev.2005.07.009>
- Wiersma, A.P., Roche, D.M., Renssen, H., 2011. Fingerprinting the 8.2 ka event climate response in a coupled climate model. *J. Quaternary Sci.* 26, 118–127. <https://doi.org/10.1002/jqs.1439>
- Williams, G.L., Fensome, R.A., MacRae, R.A., 2017. The Lentins and Williams Index of Fossil Dinoflagellates 2017 Edition. *Am. Assoc. Stratigr. Palynol. Contrib. Ser.* 48, 1–1097.
- Wilson, D.J., Bertram, R.A., Needham, E.F., Flierdt, T. Van De, Welsh, K.J., McKay, R.M., Mazumder, A., Riesselman, C.R., Jimenez-espejo, F.J., Escutia, C., 2018. Ice loss from the East Antarctic Ice Sheet during late Pleistocene interglacials. *Nature*. <https://doi.org/10.1038/s41586-018-0501-8>
- Wilson, D.S., Jamieson, S.S.R., Barrett, P.J., Leitchenkov, G., Gohl, K., Larter, R.D., 2012. Antarctic topography at the Eocene–Oligocene boundary. *Palaeogeogr. Palaeoclimatol.* 335–336, 24–34. <https://doi.org/10.1016/j.palaeo.2011.05.028>
- Wilson, G.J., 1967. Some new species of lower Tertiary Dinoflagellates from McMurdo sound, Antarctica. *New Zeal. J. Bot.* 5, 57–83. <https://doi.org/10.1080/0028825X.1967.10428735>
- Wilson, G.S., Roberts, A.P., Verosub, K.L., Florindo, F., Sagnotti, L., 1998. Magnetobiostratigraphic chronology of the Eocene-Oligocene transition in the CIROS-1 core, Victoria Land margin, Antarctica: Implications for Antarctic glacial history. *Bull. Geol. Soc. Am.* 110, 35–47. [https://doi.org/10.1130/0016-7606\(1998\)110<0035:MCOTEO>2.3.CO;2](https://doi.org/10.1130/0016-7606(1998)110<0035:MCOTEO>2.3.CO;2)
- Winski, D.A., Osterberg, E.C., Kreutz, K.J., Ferris, D.G., 2021. Seasonally Resolved Holocene Sea Ice Variability Inferred From South Pole Ice Core Chemistry. *Geophysical Research Letters*. *Geophys. Res. Lett.* 48, e2020GL091602. <https://doi.org/10.1029/2020GL091602>
- Wrenn, J.H., Hannah, M.J., Raine, J.I., 1998. Diversity and Palaeoenvironmental Significance of Late Cainozoic Marine Palynomorphs from the CRP-1 Core, Ross Sea, Antarctica. *Terra Ant.* 5, 553–570.
- Wrenn, J.H., Hart, G.F., 1988. Paleogene dinoflagellate cyst biostratigraphy of Seymour Island, Antarctica. *Geological Society of America, Memoir* 169, 321–447.
- Xiao, W., Esper, O., Gersonde, R., 2016a. Last Glacial - Holocene climate variability in the Atlantic sector of the Southern Ocean. *Quaternary Sci. Rev.* 135, 115–137. <https://doi.org/10.1016/j.quascirev.2016.01.023>
- Xiao, W., Frederichs, T., Gersonde, R., Kuhn, G., Esper, O., Zhang, X., 2016b. Quaternary Geochronology Constraining the dating of late Quaternary marine sediment records from the Scotia Sea (Southern Ocean). *Quat. Geochronol.* 31, 97–118. <https://doi.org/10.1016/j.quageo.2015.11.003>
- Yamamoto, M., Shimamoto, A., Fukuhara, T., Tanaka, Y., Ishizaka, J., 2012. Glycerol dialkyl glycerol tetraethers and TEX₈₆ index in sinking particles in the western North Pacific. *Org. Geochem.* 53, 52–62. <https://doi.org/10.1016/j.orggeochem.2012.04.010>
- Yamane, M., Yokoyama, Y., Miyairi, Y., Suga, H., Matsuzaki, H., Dunbar, R.B., Ohkouchi, N., 2014. Compound-specific ¹⁴C dating of IODP Expedition 318 Core U1357A obtained off the Wilkes Land Coast, Antarctica. *Radiocarbon* 56, 1000–1017.

- Yi, S., Batten, D.J., Joo, S., 2005. Provenance of recycled palynomorph assemblages recovered from surficial glaciomarine sediments in Bransfield Strait, offshore Antarctic Peninsula. *Cretaceous Res.* 26, 906–919. <https://doi.org/10.1016/j.cretres.2005.06.004>
- Yuan, N., Ding, M., Ludescher, J., Bunde, A., 2017. Increase of the Antarctic Sea Ice Extent is highly significant only in the Ross Sea. *Sci. Rep.* 7, 41096. <https://doi.org/10.1038/srep41096>
- Zachos, J., 2001. Trends, Rhythms, and Aberrations in Global Climate 65 Ma to Present. *Science* 292, 686–693. <https://doi.org/10.1126/science.1059412>
- Zachos, J.C., Breza, J.R., Wise, S.W., 1992. Early Oligocene ice-sheet expansion on Antarctica: stable isotope and sedimentological evidence from Kerguelen Plateau, southern Indian Ocean. *Geology* 20, 569–573. [https://doi.org/10.1130/0091-7613\(1992\)020<0569:EOISEO>2.3.CO;2](https://doi.org/10.1130/0091-7613(1992)020<0569:EOISEO>2.3.CO;2)
- Zachos, J.C., Dickens, G.R., Zeebe, R.E., 2008. An early Cenozoic perspective on greenhouse warming and carbon-cycle dynamics. *Nature* 451, 279–283. <https://doi.org/10.1038/nature06588>
- Zachos, J.C., Shackleton, N.J., Revenaugh, J.S., Pälike, H., Flower, B.P., 2001. Climate Response to Orbital Forcing Across the Oligocene-Miocene Boundary. *Science* 292, 274–278. <https://doi.org/10.1126/science.1058288>
- Zawierucha, K., Kolicka, M., Kaczmarek, Ł., 2016. Re-description of the Arctic tardigrade *Tenuibiotus voronkovi* (Tumanov, 2007) (Eutardigrada; Macrobiotidea), with the first molecular data for the genus. *Zootaxa* 4196, 498–510. <https://doi.org/10.11646/zootaxa.4196.4.2>
- Zell, C., Kim, J., Hollander, D., Lorenzoni, L., Baker, P., Guizan, C., Nittroer, C., 2014. Sources and distributions of branched and isoprenoid tetraether lipids on the Amazon shelf and fan: Implications for the use of GDGT-based proxies in marine sediments. *Geochim. Cosmochim. Ac.* 139, 293–312. <https://doi.org/10.1016/j.gca.2014.04.038>
- Zevenboom, D., Brinkhuis, H., Visscher, H., 1994. Dinoflagellate cysts palaeoenvironmental analysis of the Oligocene/Miocene transition in northwest and central Italy. *Giorn. di Geol.* 56(1), 3a, 155–169.
- Zhang, J., 2007. Increasing antarctic sea ice under warming atmospheric and oceanic conditions. *J. Climate* 20, 2515–2529. <https://doi.org/10.1175/JCLI4136.1>
- Zhang, Y.G., Pagani, M., Liu, Z., Bohaty, S.M., DeConto, R., 2013. A 40-million-year history of atmospheric CO₂. *Phil. Trans. R. Soc. A* 371, 20130096. <https://doi.org/10.1098/rsta.2013.0096>
- Zhang, Y.G., Pagani, M., Wang, Z., 2016. Ring Index: A new strategy to evaluate the integrity of TEX₈₆ paleothermometry. *Paleoceanography* 31, 220–232. <https://doi.org/10.1002/2015PA002848>. Received
- Zhang, Y.G., Zhang, C.L., Liu, X., Li, L., Hinrichs, K., Noakes, J.E., 2011. Methane Index: A tetraether archaeal lipid biomarker indicator for detecting the instability of marine gas hydrates. *Earth Planet. Sc. Lett.* 307, 525–534. <https://doi.org/10.1016/j.epsl.2011.05.031>
- Zielinski, U., Gersonde, R., 2002. Plio-Pleistocene diatom biostratigraphy from ODP Leg 177, Atlantic sector of the Southern Ocean. *Mar. Micropaleontol.* 45, 225–268. [https://doi.org/10.1016/S0377-8398\(02\)00031-2](https://doi.org/10.1016/S0377-8398(02)00031-2)
- Zielinski, U., Gersonde, R., 1997. Diatom distribution in Southern Ocean surface sediments (Atlantic sector): Implications for paleoenvironmental reconstructions. *Palaeogeogr. Palaeoclimatol.* 129, 213–250. [https://doi.org/10.1016/S0031-0182\(96\)00130-7](https://doi.org/10.1016/S0031-0182(96)00130-7)

- Zonneveld, K.A.F., 1997. New species of organic walled dinoflagellate cysts from modern sediments of the Arabian Sea (Indian Ocean), *Rev. Palaeobot. Palyno.* 97, 317–337.
- Zonneveld, K.A.F., Marret, F., Versteegh, G.J.M., Bogus, K., Bonnet, S., Bouimetarhan, I., Crouch, E., De Vernal, A., Elshanawany, R., Edwards, L., Esper, O., Forke, S., Grøsfjeld, K., Henry, M., Holzwarth, U., Kieft, J., Kim, S., Ladouceur, S., Ledu, D., Chen, L., Limoges, A., Londeix, L., Lu, S.-H., Mahmoud, M.S., Marino, G., Matsouka, K., Matthiessen, J., Mildenthal, D.C., Mudie, P., Neil, H.L., Pospelova, V., Qi, Y., Richerol, T., Rochon, A., Sangiorgi, F., Solignac, S., Turon, J., Verleye, T., Wang, Y., Wang, Z., Young, M., 2013. Atlas of modern dinoflagellate cyst distribution based on 2405 data points. *Rev. Palaeobot. Palyno.* 191, 1–197. <https://doi.org/10.1016/j.revpalbo.2012.08.003>
- Zonneveld, K.A.F., Versteegh, G.J.M., Kasten, S., Eglinton, T.I., Emeis, K.-C., Huguët, C., Koch, B.P., de Lange, G.J., de Leeuw, J.W., Middelburg, J.J., Mollenhauer, G., Prah, F.G., Rethemeyer, J., Wakeham, S.G., 2010. Selective preservation of organic matter in marine environments; processes and impact on the fossil record. *Biogeosciences* 7, 483–511. <https://doi.org/10.5194/bgd-6-6371-2009>

Nederlandse samenvatting

Het leven op Aarde zal meer en meer de effecten gaan ondervinden van de huidige klimaatverandering als gevolg van de uitstoot van broeikasgassen. Ten opzichte van de periode 1850-1900 is de temperatuur globaal met 1,1°C gestegen. De opwarming van de Aarde heeft ook gevolgen voor het ijs op de polen. Dit is nu al merkbaar door de reductie van zeeijs in het Arctisch gebied. Wat de gevolgen zijn voor het Antarctisch gebied, zowel het zeeijs als het landijs, is echter onzeker. De concentratie zeeijs rondom Antarctica laat geen duidelijke trend zien, alhoewel de concentratie zeeijs in februari 2023 een laagterecord heeft bereikt. Tevens is de gevoeligheid van het landijs voor opwarming niet goed bekend en zijn modellen niet goed in staat om de zeespiegel fluctuaties die over de afgelopen 25 miljoen jaar hebben plaatsgevonden te reconstrueren. Een belangrijk gegeven is dat veel van de Antarctische ijskap een basis heeft die onder zeeniveau ligt en dus gevoelig is voor relatief warmer water dat de ijskap van onderaf kan doen smelten, waardoor deze onstabiel kan worden en opbreken. Om de gevoeligheid van het Antarctisch gebied voor opwarming nader te onderzoeken kunnen we ons wenden tot periodes van opwarming in het geologisch verleden van de Aarde. Om dat verleden te onderzoeken wordt gebruik gemaakt van zogenaamde proxies: indirecte bepalingen op basis van chemische samenstelling of biologische resten, die over periodes van miljoenen jaren bewaard zijn gebleven op de oceanbodem.

Veel van de verschillende soorten plankton die rondom Antarctica leven produceren een 'huisje' van carbonaat, silica of een resistent organisch materiaal, waarvan een fractie uiteindelijk als sediment op de oceanbodem belandt en fossiliseert. Deze microfossielen kunnen gebruikt worden om de condities in het oppervlaktewater van de ocean te reconstrueren. Veel van deze reconstructies zijn gebaseerd op microfossielen van carbonaat of silica, maar in veel mindere mate zijn deze gebaseerd op organische microfossielen. Het is van belang om ook organische microfossielen te bestuderen, omdat rondom Antarctica microfossielen van carbonaat niet goed conserveren en ook microfossielen van silica beneden een bepaalde diepte onder de zeebodem, het zogenaamde diagenetisch front, rekristalliseren. Organische microfossielen kunnen daarom een waardevol alternatief, danwel een waardevolle toevoeging zijn aan de beschikbare proxies die ons in staat stellen het klimaat uit het verleden te reconstrueren. Het eerste deel van dit proefschrift is derhalve een uiteenzetting van alle verschillende soorten organische microfossielen (ookwel palynomorfen) die zijn gevonden in boorkern U1357, die is opgeboord vanaf de oceanbodem in het Adélie Bekken en die zo'n 170 meter aan Holoceen (de afgelopen 11.000 jaar) sediment bevat. In deze palynologische atlas worden 74 verschillende mariene microfossiele soorten beschreven tezamen met hun biologische oorsprong en ecologische affiniteiten voor zover bekend.

Naast organische microfossielen wordt gebruik gemaakt van moleculaire resten van Archaeobacteriën voor het reconstrueren van het klimaat in het verleden. Deze Archaeobacteriën, specifiek Thaumarchaeota, synthetiseren meer of minder cyclopentaaanringen in hun membraanlipiden afhankelijk van de temperatuur van het zeewater. Op basis van de verhouding tussen de overblijfselen van deze verschillende membraanlipiden (met de chemische afkorting GDGTs) met meer of minder cyclopentaaanringen is een proxy ontwikkeld, die bekend staat als TEX₈₆. Voor deze proxy zijn meerdere calibratiemethoden ontwikkeld om de absolute temperatuur van het zeewater te reconstrueren. Dit is met name uitdagend in de polaire gebieden, omdat de relatie tussen de temperatuur van het oppervlaktewater van de oceaan en de TEX₈₆ van de oppervlakte monsters afkomstig van de oceaانبodem beneden 5°C niet eenduidig is. Tevens blijkt in algemene zin sprake te zijn van regionale verschillen, die gedeeltelijk samenhangen met de aanwezigheid van zogenaamde 'diep water' Thaumarchaeota in de waterkolom. Om daarvoor te compenseren is in 2014 een calibratiemethode ontwikkeld op basis van een Bayesiaans ruimtelijk variërend regressiemodel (BAYSPAR). Dit calibratiemodel is toegepast op de TEX₈₆ van het monstermateriaal dat in dit proefschrift is onderzocht om de oppervlaktetemperatuur van het zeewater in het verleden te kunnen reconstrueren.

Op basis van de ratio tussen de lichtere en zwaardere zuurstofisotopen in benthische foraminiferen (microfossielen van carbonaat) is bekend dat een grote Antarctische ijsskap pas bestaat sinds 34 miljoen jaar geleden (Ma). In ijs bevinden zich namelijk met name lichtere zuurstofisotopen en hoe groter de ijsskap hoe lager het relatieve gehalte aan lichtere zuurstofisotopen in de oceaan, en daarmee ook het relatieve gehalte in de carbonaathuisjes van benthische foraminiferen. Belangrijke periodes sinds het bestaan van een grote Antarctische ijsskap, die inzicht kunnen bieden in wat het effect van de opwarming van de Aarde in de toekomst zal hebben op het Antarctisch zee- en landijs, zijn onder andere het Oligoceen (34 tot 23 Ma), de Laatste Interglaciaal (LIG; ca. 125 duizend jaar geleden (ka)) en de mid-Holocene warme periode (ca. 8 ka). Deze periodes worden in de verschillende hoofdstukken van dit proefschrift behandeld. Het Oligoceen wordt gekenmerkt door koolstofdioxideconcentraties (CO₂) in de atmosfeer die overeenkomen met vandaag de dag en wat in de rapporten van het IPCC voorspeld is voor de komende eeuw (400 tot 650 ppmv). CO₂ is het belangrijkste broeikasgas op Aarde als het gaat om het versterken van de warmtestraling van de zon. Het onderzoeken van periodes met vergelijkbare CO₂ concentraties als nu of de toekomst kan belangrijke inzichten geven in de stabiliteit van de Antarctische ijsskap bij dergelijke CO₂ concentraties. Uit de resultaten in dit proefschrift blijkt dat de temperatuur van het oppervlaktewater nabij Wilkesland tijdens het Oligoceen gemiddeld genomen 17°C was en gedurende het midden-Mioceen afnam naar zo'n 11°C, waarbij uit de resten van dinoflagellatencysten

(organische microfossielen) blijkt dat er over het algemeen geen zeeijs aanwezig was. De configuratie van de continenten op Aarde was in het Oligoceen echter anders dan tegenwoordig, wat van invloed kan zijn geweest op het warmtetransport via het oceaanwater naar Antarctica. Australië en Zuid-Amerika bevonden zich dicht bij Antarctica, waardoor de Antarctische Circumpolaire Strooming nog niet zo sterk was als nu. Het is belangrijk om daarom ook naar warmere periodes uit het recentere verleden te kijken, zoals de LIG en het mid-Holoceen, die qua continentale configuratie beter overeenkomen met de huidige configuratie.

Het verschuiven van continenten is een langetermijnproces, maar bij klimaatreconstructies is het tevens van belang om rekening te houden met de variatie op kortere termijn. Afhankelijk van de stand van de Aarde en de vorm haar baan rondom de Zon ontvangt de Aarde meer of minder zonnestraling en derhalve ook meer of minder warmte. Deze veranderingen zijn cyclisch en herhalen zich elke 19 tot 100 duizend jaar, die ook terug te zien is in de verhouding tussen lichte en zware zuurstofisotopen ($\delta^{18}\text{O}$ -ratio) van benthische foraminiferen, en zijn de reden voor het ontstaan en gaan van ijstijden. Deze glaciale-interglaciale variabiliteit is kenmerkend voor het Pleistoceen (2,5 Ma tot 11 ka) waar elk van de glaciale en interglaciale genummerd zijn als *Marine Isotope Stages* (MIS) en speelt even goed een rol tijdens het Oligoceen en Mioceen. Op basis van de variabiliteit in de $\delta^{18}\text{O}$ -ratio gedurende deze periodes zou de omvang van de Antarctische ijskap moeten fluctueren tussen de 50 en de 125% van zijn huidige omvang. Bij de bemonstering voor de reconstructie van de temperatuur tijdens het Oligoceen is daarom expliciet onderscheid aangebracht tussen monsters afkomstig uit glaciale afzettingen en monsters afkomstig uit interglaciale afzettingen. Uit de resultaten blijkt dat de temperatuur van het oceaanwater 1,5 tot 3,0°C warmer was tijdens interglaciale ten opzichte van glaciale periodes.

Voor het reconstrueren van de oppervlaktewatercondities gedurende MIS9 tot MIS5 is monstermateriaal afkomstig uit boorkern AS05-10 uit het Adara Bekken nabij de Ross Zee gebruikt. Naast organische microfossielen en TEX_{86} zijn ook diatomeeën (microfossielen van silica), benthische foraminiferen en andere geochemische proxies gebruikt. Daaruit blijkt dat elke glaciale-interglaciale transitie wordt gekenmerkt door het opbreken van het ijsplateau dat vanaf de gletsjer in zee uitkomt, vrijkomend smeltwater en een steeds verder zuidelijke terugtrekking van de zomerzeeijsgrens. De gereconstrueerde (zomer)temperatuur van het oceaanwater tijdens de LIG was 2,5°C warmer dan nu. Deze veranderingen zijn vergelijkbaar met de effecten van klimaatverandering vandaag de dag, gezien het feit dat de temperatuur van het oceaanwater ten westen van het Antarctisch Peninsula reeds met 1°C zijn gestegen sinds 1955 en sprake is van een toename van smeltwater van het Antarctisch continent dat uitstroomt in de Ross Zee.

Dankwoord (Acknowledgements)

Het lijkt inmiddels een eeuw geleden dat ik net een paar maanden afgestudeerd, zoekend naar een baan, ineens bericht kreeg van Francesca Sangiorgi of ik interesse had in een PhD-positie. Het onderzoek was gefinancierd door NWO op basis van een voorstel van Henk Brinkhuis en Francesca en daarna aan Peter Bijl aangeboden. Doordat Peter moest stoppen met dit onderzoek, omdat hij een Veni-beurs had gekregen, was deze Postdoc-positie nu vrijgekomen en omgezet naar een PhD-positie. Ik was blij verrast, want het was tot dan toe nog niet gelukt om ergens een baan te vinden en had stiekem de hoop dat ik nog een promotietraject zou kunnen starten. Met dinoflagellaten had ik dankzij Henk, Peter en Sander Houben al kennis gemaakt tijdens mijn bachelorscriptie en ik was erg enthousiast dat ik me verder in deze materie mocht verdiepen ten aanzien van een maatschappelijk zeer relevant onderwerp, klimaatverandering rondom Antarctica. Ik ben daarom Francesca, Peter en Henk en ook Appy Sluijs als hoofd van de afdeling Marine Palynology and Palaeoceanography zeer dankbaar dat zij mij na de sollicitatieprocedure de kans hebben gegeven om dit promotietraject te doen.

Ik ben geneigd om in mijn eentje heel erg diep in de materie te duiken en schema's te maken van alle informatie die voorhanden is. Ik heb tijdens mijn promotietraject ook echt moeten leren om vragen stellen, om hulp te vragen en knopen door te hakken. Op een gegeven moment moet je stoppen met uitpluizen en gewoon opschrijven wat je tot nu toe weet. Ik heb in de loop van de tijd veel geleerd over het verzamelen van informatie en hoe je dat gestructureerd kunt opschrijven, waar ik nu nog veel aan heb. Daarin ben ik voortdurend gecoached door Peter en Francesca. Ook nadat mijn contractperiode voorbij was, waren zij altijd blij om iets van mij te horen ook als het daarvoor door ziekte of thuissituatie een lange tijd stil was geweest of ik weinig voortgang had geboekt. Dank voor al jullie begrip, motivatie en steun. En ook al zagen we elkaar niet vaak, dankjewel ook Henk dat je ondanks je drukke baan als directeur van het NIOZ nog tijd kon vrij maken voor inhoudelijke discussies, voor je nuchtere kijk op zaken en het helpen zoeken naar de rode draad in de verschillende onderzoeksprojecten die ik heb mogen doen.

Ik wil daarnaast ook Stefan Schouten bedanken voor het ter beschikking stellen van monsters vanuit het NIOZ, voor het wekken van mijn interesse in de organische geochemie (al tijdens mijn studie), voor de kans om pilot-studies te doen met hydroxy-GDGT's hoewel daar helaas uiteindelijk niets van in het proefschrift terecht is gekomen.

Alhoewel ik zelf monsters heb opgewerkt voor GDGT-analyse en palynologische slides, kon ik dat niet zonder de hulp en ervaring van Natasja Welters, Dominica Kasjaniuk, Anita van Leeuwen, Michiel Kienhuis en Linda van Roij. Daarnaast heb tijdens mijn onderzoek gebruik mogen maken van materiaal dat al geprepareerd was en/of data was verzameld. Daarom dank ook aan Niels Schoffelen en Veronica Willmott.

Als je zo nu en dan eens vastloopt in je denkwerk ben je blij dat er ook afleiding om je heen is in de vorm van collega's. Ik was af en toe ook blij dat ik me met andermans problemen kon bezighouden of met tafelvoetbalpotjes, WK-poules of het PPGU-penningmeesterschap. Dank daarom ook aan mijn PhD-collega's en tevens leden van de PPGU, Tjerk Veenstra, Mariska Datema, Carolien van der Weijst, Margot Cramwinckel, Johann Vellekoop, Joost Frieling, Robin van der Ploeg, Loes van Bree, Fabian Ercan, Arjen Grothe, Ilja Kocken, Kim Hagemans en Niels van Helmond. Dankzij de bijdrage van alle PPGU-leden konden we regelmatig uitjes organiseren waar we veel lol hebben beleefd.

Voor hun betrokkenheid bij mijn wetenschappelijke ontwikkeling en hun interesse in hoe het met mij persoonlijk gaat in al die jaren dat ik hiermee bezig geweest, gaan dank uit naar Appy, Bas van de Schootbrugge, Timme Donders, Gerard Versteegh, Francien Peterse, Han Konijnenburg-van Cittert, Marjolein Mullen en in het bijzonder Wilma Wessels, die mij na mijn MSc-scriptie bij haar heeft voorgedragen voor deze promotieplek.

Niet alle monsters die je opwerkt leiden tot resultaten. Zeker niet als je met materiaal werkt van nabij de Antarctische kust. Het is daarom heel fijn als je de kans krijgt om de beperkte data die je zelf hebt vergaard te mogen combineren met andere gegevens van dezelfde kern. Daarom ook: thanks to my Italian colleagues that allowed me to use all of their collected data to add to my own to write down a truly multi-proxy study on core AS05-10. Alessandra Asioli and I had multiple discussions on whether we should divide the data over multiple articles, but I'm happy we eventually incorporated all into one. Thanks to Lines Barcena for everything that I've learned about diatoms and the useful papers that you could provide me with. Thanks to Leonardo Langone and Fabio Tateo for their insights into organic and trace metal chemistry.

Thanks also to all the international friends I have made during conferences and especially during the Urbino Summer School. It is nice to follow your careers and chat on Facebook every once in a while. I would like to mention in particular Carlota Escutia, Ari Salabarnada, Rob McKay, Martin Head, Amy Leventer and Kate Ashley for their contribution to this research.

Zo'n promotietraject gaat met ups en downs en dan is het fijn om daarop met studievrienden op te kunnen reflecteren. Dank daarom aan Anouk Klootwijk, Sjors van Broekhuizen en in het bijzonder ook Niels de Winter en Jesse Hennekam voor het delen van jullie ervaringen als PhD en omdat jullie mijn paranimfen willen zijn.

Het is nu negen jaar nadat ik aan dit promotietraject ben begonnen en in die tijd ben ik vader geworden van twee kinderen, ben ik verhuisd, heb ik een baan gevonden bij Arcadis en een pandemie meegemaakt. Ik heb na mijn contractperiode uiteindelijk nog 5 jaar hieraan gewerkt. Dat is toch nog vrij lang voor iets wat voor je gevoel bijna klaar is. Om de moed niet te verliezen wil ik daarom tenslotte mijn familie bedanken en in het

Acknowledgements

bijzonder natuurlijk mijn vriendin Froukje Henstra. Dankjewel lieverd voor alle steun en motiverende gesprekken, dat je me af en toe een spiegel voor hebt gehouden en dat ik kon putten uit jouw ervaring om in je eigen tijd nog een proefschrift af te schrijven.

Short Curriculum Vitae

Work experience

2023	Project Leader Soil and Subsurface, Arcadis Nederland B.V.
2018 – 2023	Specialist Soil and Subsurface, Arcadis Nederland B.V.
2014 – 2018	PhD researcher Marine Sciences, Utrecht University
2011 – 2012	KNAW Lab assistant, Utrecht University

Education

2011 – 2013	Master Earth, Life and Climate, Utrecht University
2008 – 2011	Bachelor Earth Sciences, Utrecht University
2006 – 2008	Bachelor Architecture, Delft University

Other completed courses

2018 – 2023	Various safety and gas trainings
2018	VCA VOL certificate
2016	Maintaining Scientific Integrity in Present-day Academic Reality
2016	Statistics in R
2015	Advanced Course in Organic-walled Dinoflagellate Cysts
2014	Presenting in English

Boards

2014 – 2017	Paleobotanisch en Palynologisch Genootschap Utrecht
2014 – 2016	Geograduates Utrecht, PhD council faculty of Geosciences
2009 – 2010	Nederlands Studenten Kamerkoor

Publications

- Hartman, J.D., Sangiorgi, F., Barcena, M.A., Tateo, F., Giglio, F., Albertazzi, S., Trincardi, F., Bijl, P.K., Langone, L., Asioli, A. (2021). "Sea-ice, primary productivity and ocean temperatures at the Antarctic marginal zone during late Pleistocene." *Quaternary Science Reviews* 266, 107069. <https://doi.org/10.1016/j.quascirev.2021.107069>
- Mudie, P.J., Marret, F., Gurdebeke, P.R., Hartman, J.D., Reid, P.C. (2021). "Marine dinocysts, acritarchs and less well-known NPP: tintinnid, ostracod and foraminiferal linings, copepod and worm remains." From: Marret, F., O'Keefe, J., Osterloff, P., Pound M., Shumilovskikh, L. (eds). "Applications of Non-Pollen Palynomorphs: from Palaeoenvironmental reconstructions to Biostratigraphy." Geological Society, London, Special Publications 511, 159-232. <https://doi.org/10.1144/SP511-2020-55>
- Hartman, J.D., Sangiorgi, F., Bijl, P.K., Versteegh, J.M. (2019). "*Nucicla umbiliphora* gen. et sp. nov.: a Quaternary peridinioid dinoflagellate cyst from the Antarctic margin". *Palynology* 43(1), 94-103. <https://doi.org/10.1080/01916122.2018.1430070>
- Hartman J.D., Van de Weerd, A.A., De Bruijn, H., Wessels, W. (2019) "An exceptionally large sample of the Early Miocene ctenodactyline rodent *Sayimys giganteus*, specific variation and taxonomic implications." *Fossil Imprint* 75 (3-4), 359-382. <https://doi.org/10.2478/if-2019-0023>
- Salabarnada, A., Escutia, C., Röhl, U., Nelson, C.H., McKay, R., Jiménez-Espejo, F.J., Bijl, P.K., Hartman, J.D., Strother, S.L., Salzmann, U., Evangelinos, D., López-Quirós, A., Flores, J.A., Sangiorgi, F., Ikehara, M., Brinkhuis, H. (2018). "Paleoceanography and ice sheet variability offshore Wilkes Land, Antarctica – Part 1: Insight from late Oligocene astronomically paced contourite sedimentation." *Climate of the Past* 14, 991-1014. <https://doi.org/10.5194/cp-14-991-2018>
- Bijl, P.K., Houben, A.J.P., Hartman, J.D., Pross, J., Salabarnada, A., Escutia, C., Sangiorgi, F. (2018). "Paleoceanography and ice sheet variability offshore Wilkes Land, Antarctica – Part 2: Insights from Oligocene-Miocene dinoflagellate cyst assemblages." *Climate of the Past* 14, 1015-1033. <https://doi.org/10.5194/cp-14-1015-2018>
- Hartman, J.D., Sangiorgi, F., Salabarnada, A., Peterse, F., Houben, A.J.P., Schouten, S., Escutia, C., Bijl, P.K. (2018). "Paleoceanography and ice sheet variability offshore Wilkes Land, Antarctica – Part 3: Insights from Oligocene-Miocene TEX86-based sea water temperature reconstructions". *Climate of the Past* 14, 1275-1297. <https://doi.org/10.5194/cp-14-1275-2018>
- Hartman, J.D., Bijl, P.K., Sangiorgi, F. (2018). "A review of the ecological affinities of marine organic microfossils from a Holocene record offshore of Adélie Land (East Antarctica)." *Journal of Micropalaeontology* 37, 445-497. <https://doi.org/10.5194/jm-37-445-2018>

Utrecht University
Faculty of Geosciences
Department of Earth Sciences